Structural and chemical characterisation of $LiCoO_2$ and $Li_7La_3Zr_2O_{12}$ from the micron to the atomic scales for solid-state Li-ion energy storage materials

Connor Thomas Murrill

Doctor of Philosophy

University of York

Chemistry

September 2023

Abstract

Solid-state devices, as the next generation of lithium-ion batteries, have the potential to improve performance characteristics, meeting growing demands for energy storage infrastructure. Electrode materials of importance focus on layered lithium metal oxides, while many candidates for solid-state electrolytes have emerged. Lithium lanthanum zirconium oxide ($Li_7La_3Zr_2O_{12}$) is an electrolyte of significant interest, based on a competitive lithium conductivity. Electron microscopy and associated spectroscopic techniques, from micron to atomic scales, can develop understanding of bulk and interfacial characteristics regarding features fundamental to battery performance, such as lithium intercalation routes and structural failure mechanisms. Atomic resolution microscopy has the potential to develop upon current imaging and spectroscopic studies of solid-state materials. In his project, GB spanning particle cross-sections and complex defect structures were revealed within both $LiCoO_2$ and $Li_7La_3Zr_2O_{12}$. Grain boundaries and defects exhibited variable potential impacts on Li mobility both beneficial and detrimental to performance. Significant interfacial decomposition occurs between $LiCoO_2$ and $Li_7La_3Zr_2O_{12}$ particles during annealing, forming Li_2CO_3 or $LaCoO_3$ depending on temperature. Pulsed laser deposition of $LiCoO_2$ onto Al_2O_3, $SrTiO_3$ and $Gd_5Ga_3O_{12}$ substrates, at low temperature formed multi-phase systems, with nanograins of rhombohedral $LiCoO_2$, rock salt CoO and spinel Co_3O_4. $Li_7La_3Zr_2O_{12}$ grown on $SrTiO_3$ and $Gd_5Ga_3O_{12}$ crystallised at 600 °C, either during deposition or through annealing of amorphous films. Lithium loss during deposition and annealing temperatures above 600 °C was a limitation for the studies conducted, forming large grains of $La_2Zr_2O_7$. Deposition of $LiCoO_2/Li_7La_3Zr_2O_{12}$ heterostructures provide samples where growth of crystalline interfaces and the influence of annealing are assessed down to atomic resolutions. Annealing improved the quantity and orientation consistency of rhombohedral $LiCoO_2$ within the electrode, although detrimental intermixing and crystallite formation occurred at the $LiCoO_2/Li_7La_3Zr_2O_{12}$ interface. $LiCoO_2$ crystallites growing into the $Li_7La_3Zr_2O_{12}$ layer may have a significant role to play in Li mobility through annealed solid electrode-electrolyte interfaces.

Contents

List of Tables

List of Figures

Acknowledgements

Formal acknowledgements

I would like to thank my supervisors, Dr Richard Douthwaite, Professor Vlado Lazarov and Dr Demie Kepaptsoglou for their support and guidance throughout the duration of this project. The insight and information you have both offered has been invaluable. I would also like to thank Dr Stuart Cavill for deposition of my thin film samples. Concerning training, both Dr Jonathan Barnard and Adam Kerrigan have provided extensive support on the operation of SEM, TEM and FIB instruments. I would also like to thank the members of both research groups that have been a help during my time at York.

Declaration

I declare that the work presented in this thesis is based on research carried out by myself in the Department of Chemistry and Physics, University of York, England. The results acquired within this thesis have not been presented elsewhere for any other degree or qualification. The work presented is all my personal undertaking; excluding pulsed laser deposition of $LiCoO_2$ and $Li_7La_3Zr_2O_{12}$ thin films, and supporting data referred to by in-text citations where comparisons are made to important work within the field of research.

Chapter 1

Introduction

Understanding the lithium (Li) intercalation processes within electrode and electrolyte materials with respect to their crystal structure and chemistry requires a range of approaches. These include bulk studies with X-ray diffraction (XRD), and scanning electron microscopy (SEM), through to high-resolution (HR) analysis using transmission electron microscopy (TEM). The latter can observe materials down to atomic resolution (AR), providing valuable insight into slight variations in structure, lattice orientation and grain boundaries (GB) throughout solid-state battery (SSB) electrodes and electrolytes.

The following chapter covers the two materials focused upon within the project, $LiCoO_2$ (LCO) and $Li_7La_3Zr_2O_{12}$ (LLZO), the latter doped with niobium to promote conductivity and stabilise the desired phase at lower temperatures. In addition to bulk studies, the chemistry of interfaces between these electrode and electrolyte materials is discussed with reference to literature-based theory and previous research into degradations resulting from redox reactions during charge cycling of devices. The specific applications and wider role of electron microscopy within the SSB field of research are presented, alongside potential applications at the forefront of microscopy. Questions aimed at advancing upon current state-of-the-art literature are introduced based on the observations and data presented in this chapter.

1.1 Motivation for High-Resolution Analysis SSB Materials

As reliance on Li-ion energy storage devices increases to ensure the supply demands of electric devices, such as phones and motor vehicles are met, there is a need to create battery compositions that are longer lasting, with higher capacities, as well as safer. With a wealth of different materials being discovered and refined, offering widely varying Li conductivities, research into understanding the materials from the macro to atomic scales is fundamental to optimisation and potential implementation on a commercial-scale[1, 2]. Important factors governing device performance are the degradation mechanisms within the electrodes and electrolyte, as well as the redox reactions raising impedance to ion transfer across the electrode-electrolyte interfaces (EEI)[3-6]. The current generation of commercial batteries is reliant on solvent-based electrolytes where lithium phosphate salts provide conductivities of approximately 1×10^{-2} S cm^{-1} (Siemens per centimetre)[4, 7]. These are prone to significant electrochemical decay at the EEI and well as flammability upon failure where air exposure of the Li ion devices has occurred. Solid-state alternatives are of significant interest as a replacement for liquid electrolytes (LEs). These include materials such as lithium phosphates (Li_3PO_4), sulphates (Li_3PS_4) and garnets or ceramics ($Li_7La_3Zr_2O_{12}$, $Li_{1+x}Al_xGe_{2-x}(PO_4)_3$, $Li_{0.34}La_{0.5}TiO_{2.94}$ etc.) proposed and under active research with respect to computational and experimental approaches[8-11].

$Li_7La_3Zr_2O_{12}$ is one such solid-sate electrolyte with optimised conductivities reaching $\times 10^{-3}$ S cm^{-1} for the cubic crystal phase, supported by the incorporation of transitional metal dopants.[12-14] The particle morphologies on the micron scale have the potential to form a high conductivity electrolyte with wider applications through the incorporation of binders and polymers, creating durable and flexible systems[15]. Studying the nanoscale structure of a fully solid-state device with respect to the bulk and interfacial characteristics of each layer has the potential to inform more accurate computational analysis of ion conduction routes and understand the deterioration mechanisms that occur[16]. Structural variations have the potential to arise through changes in Li content between a charged and discharged states of the electrode, as well as chemical reactivates based on windows of thermodynamic stability at the interface[10, 17]. Using HR electron microscopy and spectroscopic techniques available in the York JEOL Nanocentre, alongside time on instruments at SuperSTEM and ePSIC, it was possible in this project to pursue the objectives of understanding the crystallinity and grain structures of LCO and LLZO based on various deposition, substrate orientation and annealing conditions.

The understanding of phase dynamics in LCO provides potential insights into structural characteristics of other more complex Li metal oxide (LMO) electrodes (e.g. $LiMnO_2$ and $Li_{1.2}Ni_{0.4}Ru_{0.4}O_2$)[3, 18, 19]. Work on the HR imaging of LLZO aims to progress the understanding of structures and interface chemistry previously investigated at low resolutions on the micron-to-nanoscales[15, 20, 21]. The insights into atomic structures, that electron microscopy provides, has the potential to allow visualisation of specific characteristics adopted by crystalline solid-state Li-ion materials in relation to performance. There is significant scope to develop the understanding of grain boundary (GB) and interface structures, alongside techniques to optimised particle and controlled growth of thin films to model solid-state devices. Such data is fundamental for the refinement of solid-state electrolytes (SSEs), such that compatibility in a functional device can be achieved which improves upon the current generation of Li-ion batteries.

1.1.2 Overview of Chapter Contents and Aims

This thesis contains six chapters, where Chapter 1 provides an insight into the motivations and insights into the important areas covered within each chapter of the thesis, alongside the important theory and literature relating to LCO and LLZO studies. The introduction covers details relating to the chemistry and structural attributes of both the electrode ($LiCoO_2$) and electrolyte ($Li_7La_3Zr_2O_{12}$). This includes the attempts to achieve specific growth directions on single crystal substrates, alongside the stabilisation of the cubic electrolyte phase with transitional metal doping, to improve Li-ion conductivity. The potential of layered LMOs as electrodes is well documented, with multi-metal systems including compounds of Co, Ni and Mn, cited to reduce reliance on Co (environmental considerations) amidst other performance benefits[22, 23]. Similarly, for LLZO the optimisation of conductivity through preparation conditions and metal ion dopants enables this to be a SSE of significant interest. Interfacial chemical decomposition between electrodes and electrolytes are fundamental to retaining performance across multiple battery cycles, with the important changes to chemistry and crystallinity later lower Li mobility between the two materials[4, 5]. Finally, an overview of the roles electron microscopy can play with respect to structural and chemical analysis of battery materials are introduced.

Chapter 2 focuses on the experimental methods employed and theory behind them to collect the data that comprises the results sections of Chapters 3 to 5. The experimental techniques cover specific methods I have used to investigate SSB materials from micron to atomic scale analysis of samples, alongside the spectroscopy required to investigate interfaces of LCO and LLZO. Sample preparation methods (e.g. annealing, lamellae extraction and thinning) are also covered, as these comprised a considerable amount of project time and are important with respect to achieving electron microscope compatible samples.

Chapter 3 presents the work focusing on sintering particle-based samples, with features resolved on the micro and nanoscales in SEM and TEM where interfaces between particles of LCO and LLZO are investigated. Interfacial decomposition between electrode and electrolyte were detectable via energy dispersive spectroscopy (EDS), with GBs visible in electron backscatter diffraction (EBSD) maps. Bright and dark field (BF and DF) images in TEM provide insight into complex defect systems in both materials.

Chapter 4 covers work conducted on nanometre thick single layers of LCO and LLZO deposited on Al_2O_3 (ALO), $SrTiO_3$ (STO) and $Gd_3Gd_5O_{12}$ (GGG). HRTEM and scanning transmission electron microscopy (STEM) allow identification of multiple phases and respective orientations of crystal growth within LCO onto ALO(0001), STO(111) and (100), as well as GGG(111), achieved by pulsed laser deposition (PLD) at low temperature (LT). Thin films of LLZO on STO(111) and (100), alongside GGG(111) are similarly imaged to assess amorphous depositions at LT, as well as crystalline films relating to development of suitable ex-situ annealing or substrate temperatures during PLD. A significant focus is applied to the alignments between GB and the effects these may have on Li mobility within the electrode and electrolyte.

Chapter 5 focuses on the HR (S)TEM analysis of heterostructures deposited using conditions developed in Chapter 4. For STO/LCO/LLZO heterostructures subjected to annealing at 600 °C, the bulk of the LCO thin films is investigated to assess any change to the electrode's orientation and crystallographic characteristics of the three phases detected in single layers. Alongside the changes to the bulk of the electrode, the importance of intermixing and resultant changes along the EEI are analysed by STEM, EDS and electron energy loss spectroscopy (EELS). This provides insights into the presence of LCO crystallites at the interface, their phase, and orientations. Various annealing and deposition conditions allow the observation of crystalline-to-amorphous (STO substrates) and crystalline-to-crystalline (GGG substrate) interfaces between LCO and LLZO.

Chapter 6 concludes the project with a summary of how the important observations within each results chapter contribute to the areas of LCO, LLZO and interfacial research introduced in Chapter 1. In addition, potential alterations and future avenues of exploration are discussed with regarding adjustments to PLD and annealing such that Li retention is improved, alongside complications of ion milling and beam sensitivity of Li-ion battery electrolytes. Potential application of current samples to in-situ heating and biasing experiments are also considered as opportunities for future work.

Appendices include additional data and information, to support the results relating to phase assignments and ex-situ biasing described in respective results chapters.

1.1.3 What are Batteries and Their Important Features

Batteries are electrochemical devices functioning through the transfer of ions within the crystallographic structure of electrodes and electrolytes. Li is the most used ion within current commercial devices relying on the intercalation between an anode and cathode when subjected to a potential difference [24, 25]. The application of a bias in the range of 4 V between a graphitic anode and LMO cathode drives the Li-ions into the metal oxide (e.g. $LiCoO_2$), subsequently occupying sites within the respective crystallographic phases suitable for lithium intercalation[26]. The delivery of power drives the current through a device at a rate defined by the requirements of the system drawing current. Li is deintercalated from the cathode, through the EEI, electrolyte and into the graphitic anode. Li permeable separators between electrode and electrolyte are used to protect against dendrite formation and shorting of the device[27]. During this process, the device is susceptible to physical and chemical changes that influence the capacity and efficiency of the device over multiple charge cycles.

The industrial fabrication of Li-ion devices currently utilises a multistep process, whereby a suspension of electrode particles are supported in a polycarbonate binder, that acts as both a medium to allow processing of the devices layers but also as a matrix to bind the powder/particles together [28, 29]. Depending on the cells construction the electrode is pasted as a thin layer, rolled (calendering) to compact the particles prior to layering with the electrolyte and anode to increase the density of active material within the device. Heating the system during calendering aims to improve the grain size and remove defects resulting from the strain effects as particles compact [29-31]. Regarding the atomic ordering of electrode and electrolyte, crystallographic structures defining conductivity throughout the bulk are important influencers of Li mobility, alongside interfacial reactivity between electrode and electrolyte. EEI are most susceptible to decomposition during charge cycles, through electrochemical redox reactions. The rate of structural and chemical degradation within the device is also dependant on the rate of charge cycles. Rapid rates of charge and discharge result in faster decay in capacity and efficiency of the device [32, 33]. Similarly, if a device is over-charged or excessively depleted by application of voltages above the limits of specific cathode-anode combination (e.g. 4.2 V for a LCO-graphite battery), phase transitions and lithium plating can reduce capacity and induce structural fractures [33]. The overarching aim of literature is to develop electrodes and electrolytes that are compatible in electrochemically active systems, maximising the Li capacity per unit volume, alongside retaining of performance over numerous charge cycles. This is analysed through a range of techniques covering electrochemical measurements, x-ray spectroscopy and electron microscopy, each providing their own insight into characteristics that define the suitability of new materials of interest for the next generation of LIBs.

1.2 Structure, Phase and Lithium intercalation into Layered Cobalt Oxide Electrodes

The standard description of a battery details three defining parts; the cathode, anode and electrolyte. These determine the capacity and operating voltage of the battery, as well as mediate the movement of active ions (e.g. Li). Significant research has gone into optimising the capacity and lifespan of electrodes through structural and composition refinement [17, 22, 32, 34-37]. Similarly, electrolyte composition has been refined to maximise conductivity, thus facilitating efficient Li-ion transfer. Current commercial Li-ion batteries (LIB) utilise $LiMO_2$ (M = Co, Mn, Ni) cathodes and graphite anodes [38]. While electrolytes consist of $LiPF_6$ salt in dimethyl carbonate (DMC) and ethylene carbonate (EC) solvent mixtures [36]. These batteries can deliver power up to around 4 V, with lifespans suitable for small-scale, portable devices operating over 1 to 4 years. Improvements in electron microscope resolution and electrochemical impedance measurements across electrode-electrolyte boundaries have revealed thin (< 10 nm) solid electrode-electrolyte interface (SEI) layers. These SEIs grow through redox reactions at the respective anode and cathode. Importantly they play significant roles regarding electron and ion mobility across the EEI[4, 5, 39].

The process of producing high quality electrodes requires optimised synthesis conditions. By optimising structural characteristics, this can improve charge storage capacity and ion/charge transfer dynamics. LCO and graphite are two main choices for cathodes and anodes in industrial LIBs.[38] The rhombohedral structure (r-LCO, space group: $R\bar{3}m$), allows intercalation of Li ions between the CoO_6 layers. The occupancy between these layers increases during discharge cycles, with an applied potential moving Li-ion back into the anode to charge the device[19, 40]. Both Co and oxygen play a role in the changes in bonding environments during cathode cycling (Figure 1.1). Use of XPS to track shifts in bonding environments as the lithium content in LCO varies. While exact lithium contents are a challenge to accurately quantify, a reducing Li content (Li_xCoO_2, $x \leq 1$) can be seen within the changing shoulder to the Co 3s orbital XPS spectrum. In Figure 1.1, a) Co shifts between the low-spin Co^{3+} (t_2g^6) and high-spin Co^{4+} ($t_{2g}^3\ e_g^2$) states during the deintercalation of Li. Electron delocalisation between Co^{3+} and Co^{4+} at lower Li contents leads to Li_xCoO_2 ($x < 0.6$) showing traits of metallic conduction [35, 41]. With reducing Li content, the O 1s signal at 529.3 eV in $LiCoO_2$ shifts to a slightly lower binding energy, while intensity of the shoulder peak at 532 eV increases as Li content decreases. This sensitivity to changes in the binding energies of Co and O, allows deintercalation or deficiencies in Li content to be tracked within an electrode. The extent of Co and oxygen's role is thought to differ, with the oxygen interacting directly with the Li ion as an anion as well as being closer to the Li layers in the r-LCO phase [18, 35].

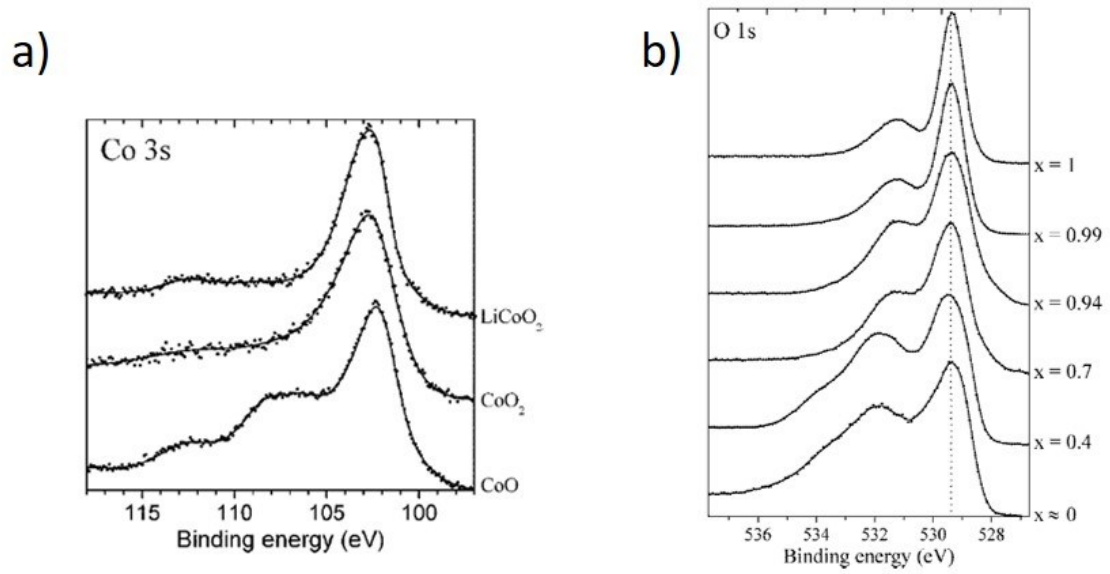

Figure 1.1: XPS of a) Co 3s for LCO, CoO_2 and CoO, showing decrease in the binding energy of the LCO signal at 103 eV, to 102 eV. b) O 1s orbitals during Li deintercalation, where intensity of to shoulder peak at 532 eV increases with reducing Li content (Li_xCoO_2, x=1 to x=0). This illustrates changes in bonding character of Co and O orbitals during deintercalation. Figure acquired from reference [18].

The ideal structure of $LiCoO_2$ allows lithium insertion between the CoO_6 layers, as detailed in (Figure 1.2). Altering specific structural characteristics through heat treatment/annealing is fundamental to maximising performance (capacity and conductivity). Using $LiCoO_2$ as an example, there is a clear difference between the structure obtained at temperatures below and above 550°C. The r-LCO (Figure 1.2, b) that forms above 550°C (Figure 1.2, a), is preferential for Li-ion intercalation dynamics, providing intercalation channels for the Li-ions to migrate along. The cubic structure (c-LCO, space group: $Fd\bar{3}m$) (Figure 1.2, c) has fewer channels of Li-ions and restricts mobility trough intermixing of half the Li and Co sites [19]. The structures have been viewed using high resolution (S)TEM, with phases varying in the bulk and Li deficiencies observed close to the surface of thinned LCO samples [22, 42, 43].

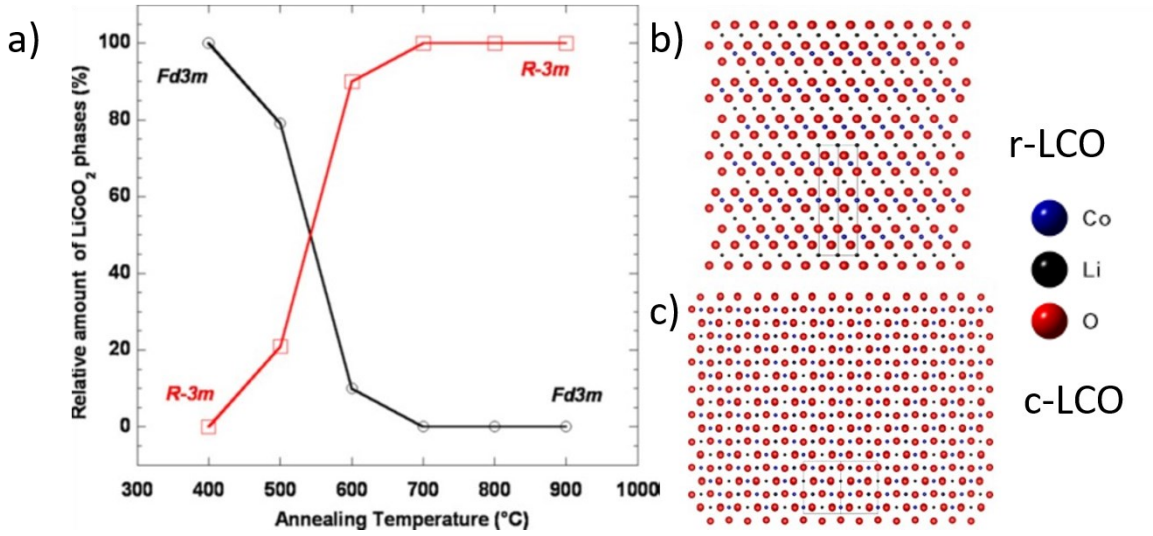

Figure 1.2: Plot of LCO phase transition between cubic and rhombohedral as a function of annealing temperature. Plot acquired from reference [19], atomic models derived from .cif files from literature and materials project databases[26, 44].

Layer spacing increases during intercalation, causing a volume change for the electrode. Conversely, these layers contract during deintercalation when charging the battery. The applied potential to reach lithium values below x ≈ 0.4 for Li_xCoO_2 becomes much higher, due to the decreased spacing [41]. Therefore, during charging, $LiCoO_2$ electrodes are not completely lithium depleted into CoO_2. Analysis shown in Figure 1.3 show the fracturing of a $LiNi_{0.6}Co_{0.2}Mn_{0.2}O_2$ cathode during cycling, especially during the first few cycles. In addition to several electrochemical (Li plating and SEI formation) degradation pathways, the change in lattice structure can also be cited as another reason for performance loss in LIBs [17, 22].

Performance of LIBs has been extensively modelled and evaluated, using electrochemical techniques. Voltage-capacity curves have investigated the retention of active Li content and achievable voltage delivery over numerous cycles, as well as the effect of charge/discharge rates on the rate of cell decay. Studies have progressed the understanding of where performance is lost, such as electrochemical electrode and electrolyte decay, as well as structural degradation [17, 45-47]. The use of low-resolution electron microscopy studies has enabled observation of increasing structural disorder and general deterioration of the electrodes bulk structure (Figure 1.3) [17, 22]. Combining information from both electrochemical and structural observations helps provide a clearer picture of the system.

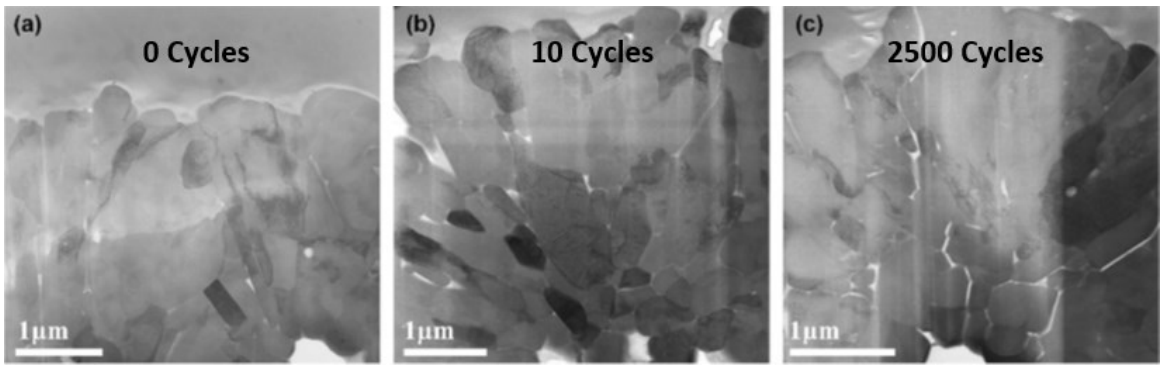

Figure 1.3: Progress in structure of $LiNi_{0.6}Co_{0.2}Mn_{0.2}O_2$ on the micron and nanoscales over multiple charge cycles, showing change in grain contrast after 10 cycles (b) and significant cracking after 2500 cycles (c), relative to the pristine electrode (a). Figure from reference [22].

During Li intercalation, the charges in stoichiometry within LCO can lead to the presence of four distinct phases (Figure 1.4). This can be distinguished using XRD, SAD or HR (S)TEM, with distinctive symmetries of atoms and lattice spacings (Table 4.1), allowing r-LCO, c-LCO and Li-deficient rock salt CoO (rs-CO) to be distinguished by their BF, HAADF and diffraction information. Some zone axis (ZA) have similar lattice spacings, within expected calibration errors (1% to 15%) of (S)TEM microscopes, leading to potential misidentification of r-LCO, rs-CO and s-CO along symmetrically equivalent ZA. Appendix I uses the known lattice parameters of substrates in PLD samples, where diffractograms from HR images are used as a reference/calibration for accurate assignment of diffraction patterns (DP) or diffractograms relating to the LCO and LLZO (Figure 1.10, a and b) phases in individual nanograins. A substrate image was taken as a calibration during each microscope session for each sample, allowing ALO, STO and GGG substrates to be effectively used as calibrations that are independent of Li or dopant content. Intensity differences within DP can also differentiate between the rs-CO and s-CO, as well as LLZO and LZO to determine the phase and extent of Li deficiency within electrode and electrolyte grains. However, double diffraction provides additional complexity to using intensities and absences of specific spots for effective assignment of these phases, so is mostly avoided [48-50].

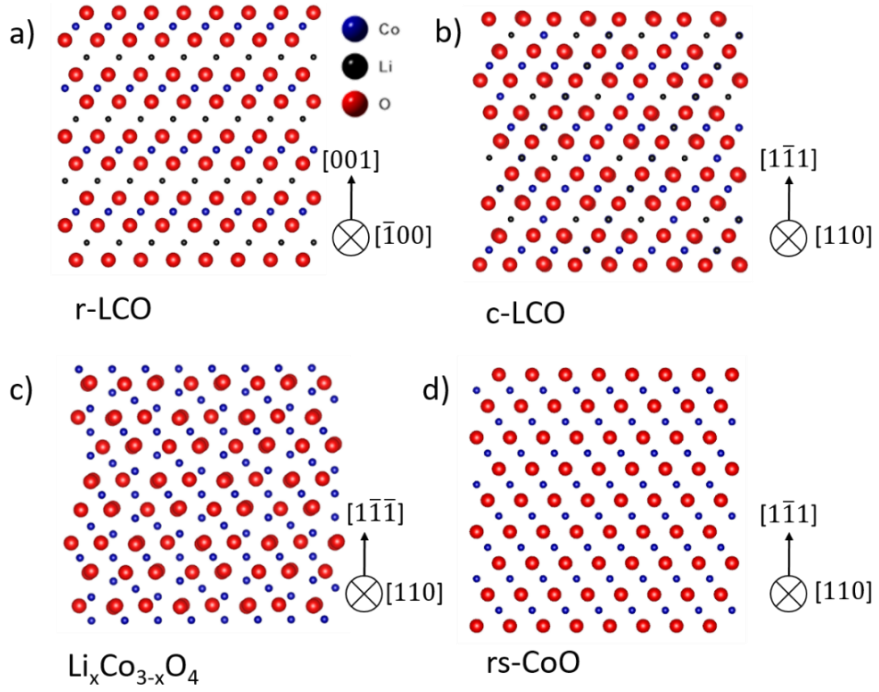

Figure 1.4: Atomic models of a) r-$LiCoO_2$, b) c-$LiCoO_2$, c) s-Co_3O_4 d) rs-CoO phases along a ZA commonly observed in sintered particles and PLD films on ALO, STO and GGG substrates in Chapters 3 to 5. Models formed using .cif files from literature databases and the Materials Project [51, 52].

Replacements for Co predominantly include Ni and Mn. These are more abundant and considered to be less environmentally invasive alternatives[53, 54]. Regarding their respective performance, research has determined good stability and improved capacity compared to $LiCoO_2$ (capacity: 140 mA h g^{-1}). Examples include $LiNi_{0.6}Co_{0.2}Mn_{0.2}O_2$, with an initial capacity of 170 mA h g^{-1} and capacity retention of 85% over 50 cycles, however only 40% over 2500 cycles [22]. Capacities up to 250 mA h g^{-1} were also achieved by Thackeray et al. for $LiMn_{0.65}Ni_{0.35}O_2$, illustrating better short term performance than $LiCoO_2$ [55].

The chemical reactions within a cell comprised of an LCO cathode and graphite anode require a route through which the electrons can flow, to facilitate the redox reactions as Li intercalates into and out of each material during charge cycles. The half reactions for the redox couple and associated standard potential ($E^{\ominus}$) for LCO and graphite are shown in Table 1.1. These combine to provide a standard potential of 3.6 V for the LCO-graphite redox couple. Equation 1 describes the method for calculating the standard potential ($E^{\ominus}_{overall}$) from the oxidation ($E^{\ominus}_{ox}$) and reduction ($E^{\ominus}_{red}$) potentials of the cathode and anode.

Table 1.1: Standard potentials and half reactions relating to a LCO – graphite cell

Cell state	Positive	Negative electrode
Charging (galvanic)	$Li^+ + CoO_2 + e^- \leftrightharpoons Li^+ + [CoO_2]^-$	$Li \leftrightharpoons Li^+ + e^-$
	(Cathode)	(Anode)
Discharge (electrolytic)	$Li^+ + [CoO_2]^- \leftrightharpoons Li^+ + CoO_2 + e^-$	$Li^+ + e^- \leftrightharpoons Li$
	(Anode)	(Cathode)
E^{Θ}	-3.04 V	0.56 V

Equation for $E^{\Theta}_{overall} = E^{\Theta}_{red} - E^{\Theta}_{ox}$ (Equation 1)

1.2.1 Alternatives to Lithium as the Active Ion

Alternative battery materials of interest included Na, Zn and other replacements for cobalt in LIBs. These have varying capacities compared to practical capacity of 140 mA h g^{-1} for $LiCoO_2$ [22, 47, 56, 57]. These may also help resolve issues around lifespan of the battery as well as abundance and toxicity of the exploited materials. With respect to cobalt alternatives, nickel and manganese are identified as more abundant, cheaper replacements. Cathodes incorporating these metals have recorded capacities up to 226 mA h g^{-1} and promising stability over 100 cycles [34, 58].

For example, sodium (Na) has been cited as a promising replacement to Li given its high abundance, supply security and low cost [56, 57, 59]. A few key Na cathodes have included titanates, layered metal oxides, and sulphides [56, 59]. Similarly to $LiCoO_2$, the structure of titanates allows intercalation and storage of ions between Ti_xO_y layers (Figure 1.5) [57]. These provide structures with sites of suitable size to intercalate Na ions (radius (r) = 0.99 Å), while achieving reasonable capacities (90 - 100 mA h g^{-1}) and reasonable stability (approx. 100 cycles) [57, 60]. Dependence of capacity and Na insertion appears to rely on specific stoichiometry, with improved performance for $Na_2Ti_3O_7$ compared to $Na_2Ti_6O_{13}$ [57]. Capacities up to 200 mA h g^{-1} were achieved for $Na_2Ti_3O_7$, however, these rapidly decrease to a more stable 100 mA h g^{-1} after a few charge cycles. This is thought to be a result of structural distortion upon insertion and removal of ions [60].

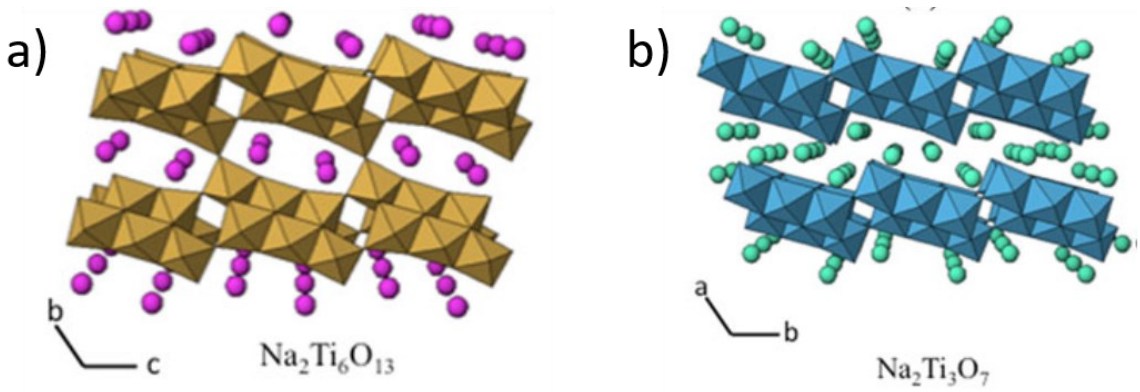

Figure 1.5: Structure of Na titanates, a) $NaTi_6O_{13}$ and b) $NaTi_3O_7$, displaying the Na ions (pink and light blue) positioned between the titanium oxide layers. Reprinted from reference [57].

The goal is to find systems like LIBs, which provide adequate performance compared to the current generation of batteries, but with improved resource security and device safety. As LIBs still dominate the global battery market, it is clear Na-ion batteries and other alternatives (e.g. zinc) are still not suitably advanced with capacity and long-term stability commonly cited as reasons [59, 60]. However, continuing research into these alternative cathodes means they remain potential replacements for LMOs in the future.

1.2.2 Battery Capacity

The capacity of a battery can be defined by the energy per unit volume (Watt-hours per litre, Wh l^{-1}) or per unit mass (Watt-hours per kilogram, Wh kg^{-1}). These two definitions describe the volume and weight of the battery required to deliver the required performance. The specific energy (Wh kg^{-1}) and energy density (Wh l^{-1}) are consequently related to the duration for which the battery can supply a given power output (Watts, W) in relation to its mass or volume when subject to a load during supplying power to a device. The electrode material, electrolyte volume and packing density all impact the capacity of the battery. Compressing the same mass of material with a specific capacity into a smaller volume will improve the energy density (Wh l^{-1}) of the battery [61].

In terms of application, the greater the capacity per unit volume and mass are the smaller the device can be, while still maintaining the capacity suitable for supply of a required load over a specific timespan. Solid-state devices have the potential to improve the energy density of a device, by excluding the substantial volume of electrolyte. The gravimetric capacity of the electrodes can then be maintained within a smaller, lighter device or used to enhance a cell's capacity by utilising the same battery volume, occupied by a greater capacity of active material (e.g. LCO and LLZO) incorporated within the cell [62, 63].

1.3 Structure, Doping and Conductivity of Electrolytes and Electrochemical Changes at EEIs

The main role of the electrolyte in a LIB is to mediate transfer of lithium ions between the cathode and anode, alongside limiting the potential for the device to short. The most common electrolyte in modern commercial devices is lithium phosphate hexafluoride ($LiPF_6$) salt, within ethylene carbonate (EC) and dimethyl carbonate (DMC) solvents. This therefore exists in liquid form, added after assembly of the battery electrodes [36]. A separator, with appropriate pore size, acts to allow both efficient charge transfer, protect against shorting and stop battery function upon overheating. Separators are commonly a thin, porous membrane of ceramic or polymer construction [64]. $LiPF_6$ in DMC:EC electrolytes are convenient as they exhibit conductivities up to 1×10^{-2} S cm^{-1} [36]. Ion mobility and conductivities can be calculated using Equations 2 to 4.

$$\mu = \frac{D}{k_B T} \qquad \text{(Equation 2)}$$

$$D = D_0 e^{-\frac{Ea}{k_B T}} \qquad \text{(Equation 3)}$$

μ being the mobility, relating to the ion diffusion coefficient D (Equation 2 and 3), where k_B and T are the Boltzmann constant and temperature (Kelvin).

Equation 4 relates conductivity σ, with E_A the activation energy of diffusion [65]. With respect to atomic structure analysis of batteries, some techniques require the use of high-vacuum conditions (e.g. (S)TEM and XPS). The volatility of LEs (LEs), including $LiPF_6$, makes them relatively incompatible to equipment such as electron microscopes [35, 41, 66, 67]. Alternatively, SSE can be used that avoid the use of volatile and flammable solvents and could in principle have other advantages with respect to stability and applications in extreme environments. Fully solid-sate devices are also more amenable to study using vacuum methods of analysis such as electron microscopies [10, 68].

$$\sigma = \frac{\sigma_0}{T} e^{-\frac{E_A}{k_B T}} \qquad \text{(Equation 4)}$$

Limitations of SSE arise from their lower conductivity and complexity of synthesis.[8, 69] These attributes still make LEs like $LiPF_6$ in EC:DMC solvents mixtures more attractive on an industrial scale for most applications. However, the selling point for SSEs is their improved safety. Dendrite growth through the liquid medium, gasification and combustion upon overheating are all safety implications with LEs. In addition, the lower volatility, slower rates of deterioration and resistance to shorting between electrodes would be significant benefits for the lifetime of SSEs [10, 68].

The direct contact between electrolyte and electrodes causes redox reactions at these interfaces and formation of an SEI. Numerous chemical and thermodynamic factors influence the formation rate and attributes of the decomposition layer [10, 17]. Figure 1.6 illustrates the respective charge transfer and energy profiles for reduction and oxidation in relation to theoretical redox potentials of the electrode. The electrodes operate at the standard potentials, defined by each specific material, during the charge/discharge cycles. The cathode-anode energy gap determines the voltage at which the battery can deliver power [5, 39]. Specific electrode and electrolyte combinations are fundamental to the efficient power delivery, practically and stability of a battery.

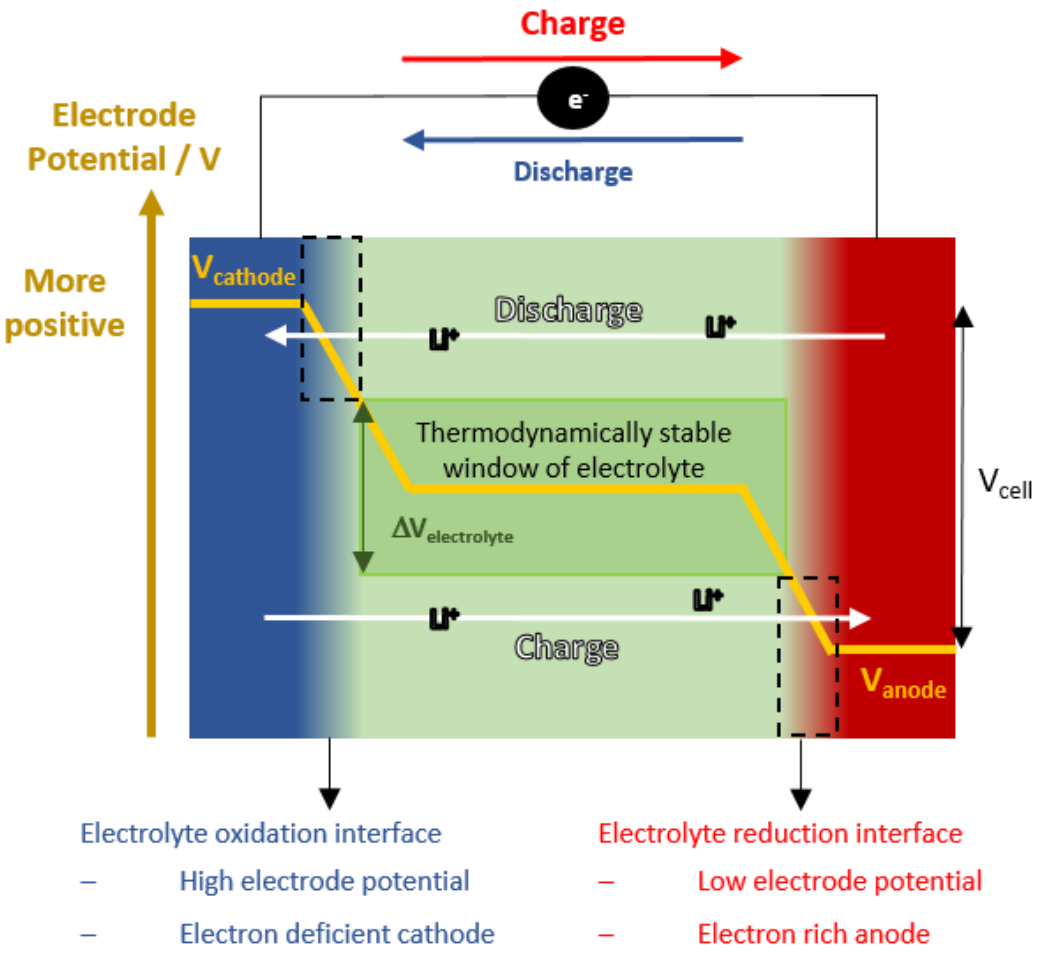

Figure 1.6: Model of electrode and electrolyte layout, displaying theoretical chemical potentials of the electrodes and direction of both electron and ion flow during charging and discharging. Dashed regions highlight energies outside the thermodynamically stable window (WOS) where redox reactions can occur to form SEIs [70].

The voltages at LIB interfaces are extreme with respect to the LE during the charging and discharging of a battery. Therefore, these interface sites become particularly reactive environments, with most initially conductive to both electrons and lithium ions [4, 71]. Feasibility of interfacial redox decomposition reactions depends on the chemical potential of the electrodes. The key parameters being their relation to the electrolyte's highest occupied molecular orbital (HOMO) and lowest unoccupied molecular orbital (LUMO) energies. The energy gaps of commonly researched electrolytes are known and the thermodynamic 'window of stability' (WOS), in relation to the chemical potential energies of the cathode and anode can be determined (Figure 1.7) for a given electrode-electrolyte combination [72-76]. A high potential anode in relation to the LUMO

band results in reduction of the electrolyte at this interface. Alternatively, if the chemical potential of the cathode is low enough to lie close to the HOMO energy levels, the electrolyte is susceptible to oxidation [5, 39]. The rate and extent to which these redox reactions occur during EEI formation, plays a role in overall battery performance.

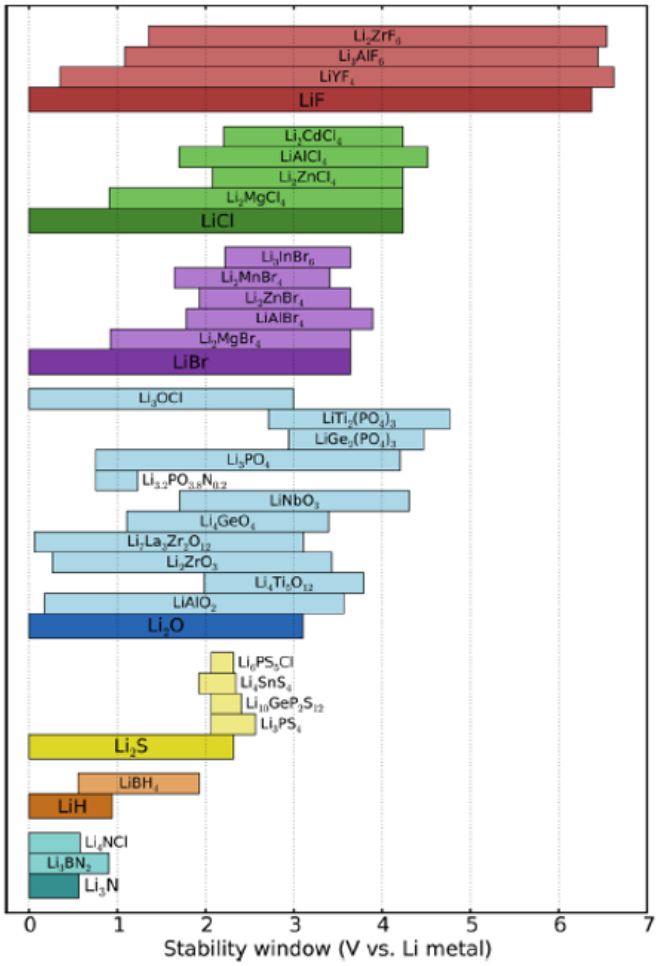

Figure 1.7: Electrolytes and their thermodynamic window of stability (WOS). A graphite anode's reduction potential lies close to 0 V vs Li/Li$^+$, reducing the interface with SSE with WOS above this value. LCO cathodes operate up to potentials of 4 V vs a Li/Li$^+$ electrode, resulting in oxidation at the boundary with SSE with WOS below this value. Figure acquired from reference [5].

Multiple reduction or oxidation products can be formed, depending on the constituent elements of the electrode and electrolyte. This can lead to the complex mixtures of solid compounds across the EEI [77, 78]. Experimental observations have seen increased impedance to electron flow, as well as ion mobility across the boundary. Despite being only a few nanometres thick, interface layers can be detrimental to the performance of the battery. This occurs once impedance to lithium transfer becomes the dominant factor compared to the bulk electrolyte [5,

78]. The formation of this layer can however provide the benefit of protecting the electrolyte from further decomposition. This occurs when the EEI supports ion transfer but becomes sufficiently insulating to the electrons required for continuation of redox-related decomposition. Structural characteristics and thickness of the stabilised EEI are important factors, in terms of overall resistance to ion transfer [16, 20, 39].

1.3.1 Interfacial Decomposition and LE Interfaces with Solid-State Electrodes

LEs are comprised of salts (e.g. $LiPF_6$) dissolved into appropriate solvent systems that can undergo oxidation and reduction reactions at the electrodes, giving a variety of solid decomposition products at the interfaces. For lithium-ion batteries with $LiPF_6$ in ethylene carbonate, some decomposition products include dilithium ethylene dicabonate, lithium carbonate and lithium oxide. Formation occurs through reduction reactions at a graphite or lithium metal oxide electrode. Combinations of these decomposition products produce complex SEI structures [20]. A reduction or oxidation peak on cyclic voltammograms, that disappears after a number of cycles, can be attributed to EEI formation [79]. Voltammetry techniques can therefore help identify the stability window of electrolyte through peaks in voltage values.

EEI and SEI can exhibit a complex mix of characteristics, across structural transitions, regional chemical composition, and local disorder. The point at which they become resistant to electron transfer, and hence stable, is also determined by the interface layer thickness. Equally important is the retention of ion conductivity upon formation of the stable, electronically insulating layer. The final thickness and composition help define the impedance to ion (e.g. Li^+, Na^+) transfer from the electrode to the electrolyte. Experimental observations have seen EEI layers from at least 3 nm (30 Å) thick on $LiMO_2$ (M = Co, Mn, Ni) and graphite electrodes [3, 80]. Figure 1.8 shows the formation of an SEI layer between $LiPF_6$-based LE and Li-Au alloy electrode. Thicker EEIs increase the distance required for ions to flow between the electrode and electrolyte. Consequently, they provide greater impedance across the boundary to Li^+ ions, reducing the transfer efficiency [6, 81]. Local structure also has a fundamental role to play in impedance of the SEI. Incompatible GB or high-energy barriers for ion migration between lattice sites will raise the interface's resistance.

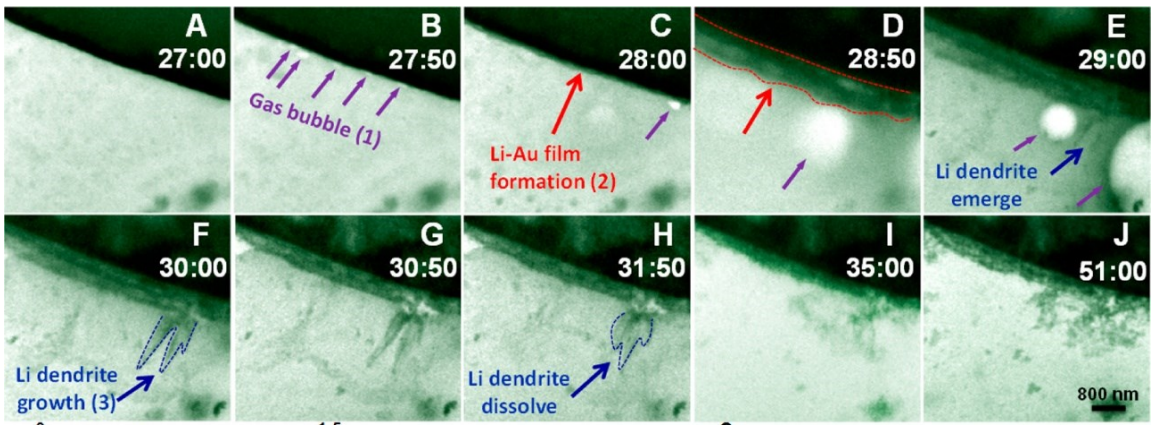

Figure 1.8: In-situ development of a SEI between Li-gold alloy electrode and commercial $LiPF_6$ salt-based LE. Degradation occurs on the timescale of seconds when cycling the device between 0 V and -3 V. Figure sourced from reference [82].

1.3.2 Formation and Properties of SSE EEIs

SSE that have seen interest in literature include glassy solids (e.g. Li_3PS_4) and lithium phosphorous oxynitride (LiPON). More recently, structures of greater complexity with garnet structure of $Li_7La_3Zr_2O_{12}$ and lithium lanthanum titanium oxides have seen development and application within novel electrolyte designs, as well as electron microscopy related research into their structure and chemistry [65]. A list of solid electrolytes and respective conductivities are found in Table 1.2. Solid electrolytes such as LiPON and NaPON are recorded to have significantly lower conductivities, compared to $LiPF_6$, of around 1 $\times 10^{-6}$ S cm^{-1} [83, 84]. Zhao et al. showed this conductivity is dependent on nitrogen pressure during deposition, hence content in the LiPON electrolyte. A nitrogen pressure of 200 mTorr during PLD, promoted the greatest conductivity of 1.6 $\times 10^{-6}$ S cm^{-1} for their electrolyte [85]. Another prominent glassy solid electrolyte is lithium thiophosphate (Li_3PS_4). With a conductivity up to 1 $\times 10^{-4}$ S cm^{-1}, Li_3PS_4 is significantly more conductive than LiPON electrolytes [8]. In addition, the doping of Li_3PS_4 and lithium titanate ($LiTi_2(PO_4)_3$) electrolytes can cause significant improvements in conductivity [8, 9].

Table 1.2: Optimised conductivities in Siemens per centimetre (S cm^{-1}) for several SSEs of interest, relevant to both Li- and Na-ion batteries.

Electrolyte	Conductivity / S cm^{-1}	Reference
$LiPF_6$ (liquid)	1×10^{-2}	[36]
$NaPF_6$ (liquid)	6.8×10^{-3}	[86]
LiPON / NaPON	$\leq 2 \times 10^{-6}$	[83, 84]
Li_3PS_4	1×10^{-4}	[8]
Li_4GeS_4 and Li_3PS_4	1.8×10^{-3}	[8]
$LiTi_2(PO_4)_3$	1×10^{-4}	[9]
$Li_{1.3}Al_{0.3}Ti_{1.7}(PO_4)_3$	3.8×10^{-3}	[9]
Na_3PS_4	2×10^{-4}	[10]
$Li_7La_3Zr_2O_{12}$	1×10^{-3}	[65]
$Li_{10}GeP_2S_{12}$	1×10^{-2}	[87]

While conductively is important, the transfer of ions at the electrode, electrolyte boundary is fundamental to the function of the battery. Incompatible interfaces, whether that be due to structure or morphology, will limit ion transfer efficiency through increased resistance. Therefore, studies into the charge dynamics between Li electrodes and the respective electrolyte have been carried out. These help to understand the effect of the interface at the point of charge intercalation into the electrodes. The charge transfer resistance from the electrolyte and electrode, such as $LiCoO_2$, reduces efficiency and restricts the charge or discharge rate of the battery [88]. Similarly, to LEs, the degradation of solid electrolytes at electrode interfaces is important in determining performance and capacity retention [5, 39, 77]. LEs can interface well with the electrode surface, given their fluid nature. SSE require either a complimentary structure or strong interfacial mechanics by design. This can be achieved through heat treatment or structurally compatible EEI formation. If the electrode and electrolyte are incompatible, then this will severally restrict the rate and efficiency of ion transfer [39, 71]. Therefore, for both liquid and solid electrolytes, research has gone into understanding and refining the compatibility with the electrode. Electrochemical, X-ray and nanoscale imaging techniques have been exploited to further understand the interfacial layers.

Like LEs, SSE are also susceptible to reduction and oxidation at the interface with a given anode or cathode. Again, the type of decomposition products, thickness, structural arrangement and conductivity are fundamental to determining battery performance and stability [21, 78]. Formation of only a thin electronically insulating but ionic conducting layer is ideal, to limit electrolyte decomposition and minimise ion impedance. However, with SSE it is important to ensure suitable structural integrity of the electrode-electrolyte boundary. A poor contact or structural mismatch will increase defect site density, as well as allowing gaps to exist between the electrode and electrolyte. Such a system would significantly increase impedance to ion mobility across the boundary, hindering efficiency [5, 39].

Many SSE have gained interest, with a range of elemental compositions, conductivities, structures, and thermodynamic stability windows. Electrolytes based on phosphates and thiophosphates are popular, with lithium phosphorus oxynitride (LiPON) and lithium thiophosphate (Li_3PS_4) laying foundations in SSE research [5, 65, 74, 89]. Recent refinement of electrolytes, doped with germanium or aluminium have achieved Li^+ conductivities close to industrial $LiPF_6$ – EC:DMC LEs. For example, Aono et al. achieved 1 $\times 10^{-3}$ S cm^{-1} for $Li_{1.3}Al_{0.3}Ti_{1.7}(PO_4)_3$, while 1.2 $\times 10^{-2}$ S cm^{-1} was measured for $Li_{10}GeP_2S_{12}$ by Kamaya et al [65, 90]. This compares to 1 $\times 10^{-2}$ S cm^{-1} of $LiPF_6$ – EC:DMC electrolyte [65]. If SSE bulk and interfacial properties enable performance and lifespans to equal that of current industry leading batteries, they offer safer alternatives to liquids.

Reasons why specific solid electrolytes show such high conductivity are explainable through concerted ion migration mechanisms. Classical ion transfer observes the movement of a single ion between different lattice sites, experiencing each energy transition barrier in sequence. However, this predicts much higher transition energies and lower conductivity than measured experimentally for SSE with high conductivities. In contrast, concerted migration illustrates a system where the movement of one ion between lattice sites triggers simultaneous transitions of adjacent ions. Electrolytes with high lithium density and ions in unstable lattice sites are most likely to facilitate concerted migration events. The energy profile for concerted systems does not view each ion individually. Instead the combination of ion transitions from high to low energy sites and vice versa, combine to reduce the net energy barrier [91, 92]. The concerted process therefore lowers the overall energy profile for lithium transfer, commonly between tetrahedral and octahedral sites. The result is significantly easier ion movement, hence higher conductivities observed for SSE like $Li_{1.3}Al_{0.3}Ti_{1.7}(PO_4)_3$ and $Li_{10}GeP_2S_{12}$.

Intercalation of lithium causes expansion and contraction of lithium metal oxide electrodes and therefore leads to mechanical strain at the EEI. Consequently, an initially well-bonded EEI may not retain its structural integrity over time. A SSE should be able to withstand these stresses and strains of electrode volume changes, while maintaining a good interface.[93] Interface fracturing will lead to greater defect site and grain boundary densities, plus vacant regions too large for ion transfer. Wu et al. highlight that such interface fracturing, from volume cycling in silicon electrodes, opens up fresh regions of unreacted electrolyte. This consequent continued decomposition will thicken a given EEI, further raising impedance to ion transfer [81].

Current exploration of solid electrolyte EEI formation in the literature, has uncovered a few key aspects. For Li_3PS_4 a dependence was found across aspects such as, degradation rate, temperature of preparation and use of protective oxide layers.[21] The interface between Li_xPS_y electrolytes and $LiCoO_2$ electrodes has a higher impedance to Li^+ flow than the bulk electrolyte. As mentioned, volume shifts during charge intercalation can put significant stress on the EEI, leading to decay in structural integrity and interfacial contact [71]. Kitaura et al. used the glass transition temperature of Li_3PS_4 (≈ 200^oC), to improve contact with the electrode through electrolyte softening. This technique also enhanced the capacity of the cell by 70 mA h g^{-1} [21]. Protective oxide layers, an example being $LiNbO_3$, have been used to improve the interface between electrodes and electrolytes [21]. In addition, to interface improvements, these must facilitate efficient Li-ion transfer.

The ability for modern electron microscopes to reach Angstrom resolutions has opened the window to exploring EEI in substantial detail. Solid-state structures provide the added benefit of enabling high-resolution imaging, without beam distortions or radiolysis associated with environmental liquid systems [94]. EEI are commonly around 3 to 10 nm thick, hence only a small number of unit cells across [4]. Therefore, understanding structure and ion diffusion mechanisms, on atomic scales, becomes an exciting prospect with the capabilities of modern electron microscopes [95]. Important aspects that can be resolved include; interface layer formation, regional structures and GB, plus how these develop over charge cycles [96]. One important area of research would be into routes ions travel between the electrode and electrolyte. Bulk structure / composition, defect density and grain boundary effects could provide insights into how EEI can be refined to maximise battery efficiency.

Focusing on the structural aspects of the EEI, if a mismatch or inhibiting grain boundary is present, impedance to Li^+ movement across the EEI increases [16, 21]. Therefore, a good match or efficient structural transition between the electrode and electrolyte is important. Tuning the lattice orientation may promote more efficient ion flow through the region by lowering energy barriers. Ion transitions can either occur through sequential movement between adjacent lattice sites, as well as through unoccupied sites or vacancies. Ideally, the exploitation of structures exhibiting concerted migration will help achieve high ion conductivities [91, 92]. A concerted system integrated into the EEI would minimise energy barriers for Li transition between EEI lattice sites, maximising efficiency [16, 39].

1.2.3 Use of Passivation Layers to Improve EEI

Electronically insulating and ionic conducting layers can form naturally or be pre-deposited between the electrode and electrolyte. Controlling the extent of electrolyte decomposition and subsequent impedance to ion flow across the EEI is appealing. This has led to research around methods to limit electrolyte decomposition and refine characteristics of the interface layer. As previously covered, the addition of fluoroethylene carbonate to a standard LE forms a separate protective EEI. This limited the extent of bulk electrolyte decomposition and helps increase battery lifetime [21, 79]. A few solid-state materials show promise, with windows of stability in the region of graphite and $LiMO_2$ (M = Co, Mn, Ni) electrode potentials (0 V and 4 V vs Li/Li^+). Figure 1.7 shows compounds including Li_3PO_4, $LiNbO_3$, $Li_4Ti_5O_{12}$ and Li metal halides (e.g. $LiAlCl_4$ and Li_3AlF_6) have thermodynamic WOS in the 4 V vs Li/Li^+ region [5]. Pre-depositing a thin (< 5 nm] layer of material, known to have low impedance to ion transfer but be electronically insulting (Figure 1.9), can reduce overall EEI thickness. This is achieved by limiting the extent the electrolyte decomposes, before reaching a stable electronically insulating state [5]. Reducing EEI thickness and ideally improving structural contact, ion transfer efficiency and stability over numerous cycles should improve. Kitaura et al. mention the effectiveness of $LiNbO_3$ in their Li_3PS_4 electrolyte / $LiCoO_2$ cathode / $Li_4Ti_5O_{12}$ anode arrangement. Here $LiNbO_3$ supressed resistive interfacial layers between electrode and electrolyte during cell preparation and hot pressing into a pellet [21].

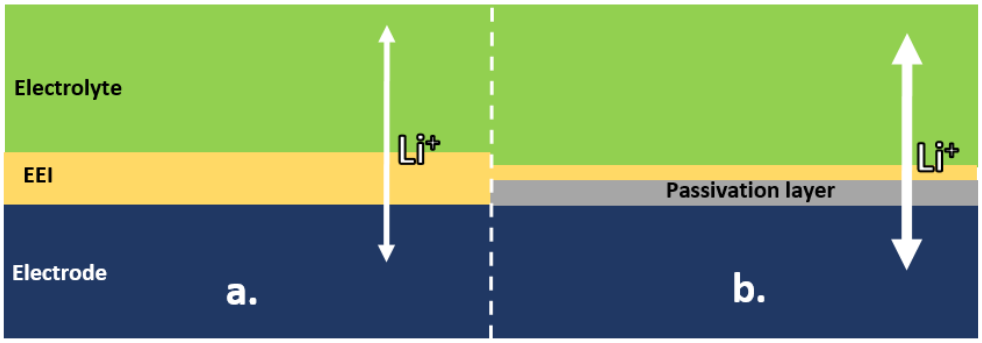

Figure 1.9: Diagram representing the effect of passivation layers on Li conductivity across an interface where an SEI forms. a) EEI without pre-deposited passivation layer, leading to formation of a thicker SEI. b) Use of passivation layer is likely to reduce electrolyte decomposition creating a thinner SEI and therefore improve Li mobility across the EEI.

Therefore, the following key points need consideration when selecting an effective passivation layer compound. It needs to be stable in relation to the oxidation or reduction potential of the respective electrode. Secondly, the layer should limit the extent to which the bulk electrolyte decomposes. Finally, the passivation layer or additive must not excessively hinder the efficiency of battery charging and discharging. If EEI formation from the bulk electrolyte cannot be easily controlled, passivation layers provide a feasible alternative to reduce bulk electrolyte decomposition and improve ion transfer.

1.3.1 Lithium Lanthanum Zirconium Oxide

The work in this thesis focuses on Lithium lanthanum zirconium oxide (LLZO) SSEs. LLZO is a garnet-type SSE with a formula unit of $Li_7La_3Zr_2O_{12}$. and either a cubic (space group) or tetragonal (space group), providing lithium conductivity of around 1×10^{-4} S cm^{-1} for the cubic phase. The cubic unit cell is built of eight formula units ($Li_{56}La_{24}Zr_{16}O_{96}$), totalling 192 atoms per unit cell, where the La and Zr atoms occupy LaO_8 and ZrO_6 dodecahedral and octahedral coordinated sites respectively. Synthesis is achieved through mixing suitable ratios of, La_2O_3, ZrO_2 and Li_2CO_3, prior to thermally decomposing the mixed powder at 750 °C to form tetragonal LLZO (Equation 5) [97]. Subsequent sintering above 700 °C should induce a phase change to a bulk cubic structure [98]. In addition, sintering at such elevated temperatures leads to lithium evaporation, thus causing regions of $La_2Zr_2O_7$ to form. However, an excess of approximately 10 wt% of lithium should be enough to compensate for any major lithium loss during the sintering process [97].

$$7Li_2CO_3+3La_2O_3+4ZrO_2 \rightarrow 2Li_7La_3Zr_2O_{12}+7CO_2 \qquad \text{Equation 5}$$

LLZO has a large complex unit cell (Table 4.1), although smaller regions of repeating symmetry occur within the backbone of La and Zr ions when viewed along the low-order ZA. These heavy atoms will dominate the image intensity within BF and HAADF images, of the tetragonal and cubic phases (Figure 1.10) [99, 100].

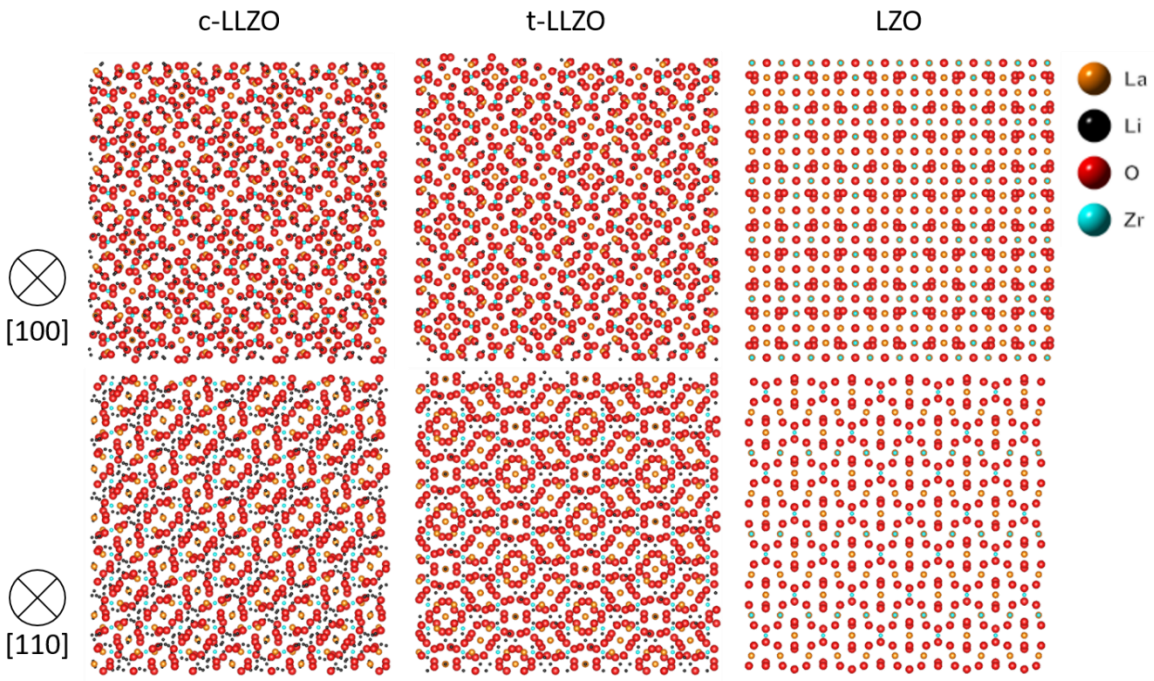

Figure 1.10: Models of cubic and tetragonal LLZO (c- and t-LLZO) and cubic LZO (c-LZO) phases along the [100] and [110] ZA. Structures from .cif files in computational and literature databases [44, 51].

The conductivity of the two phases is governed by a complex mechanism for lithium transfer between sites in the lattice's lithium network. In the low conductivity (1×10^{-6} S cm^{-1}) tetragonal phase, where all three distinct crystallographic sites are occupied by lithium [101]. This resulting lower energy states of lithium ions hinders the tetragonal structure from achieving the same conductivities as its cubic counterpart. In contrast, the potential sites which lithium can occupy in the cubic phase are not all filled, leading to an energy profile for site-to-site transitions that supports ion conductivity. Additional instability of lithium ions in specific sites lowers the energy required to promote the motion of lithium ions within the structure. Initial motion of the highest energy lithium ions can trigger a concerted process of local Li^+ rearrangement within the cubic phase. The experimentally measured energy barriers for lithium diffusion in c-LLZO (0.32 eV) match closely with the values relating to the concerted motion of lithium ions [92, 102, 103].

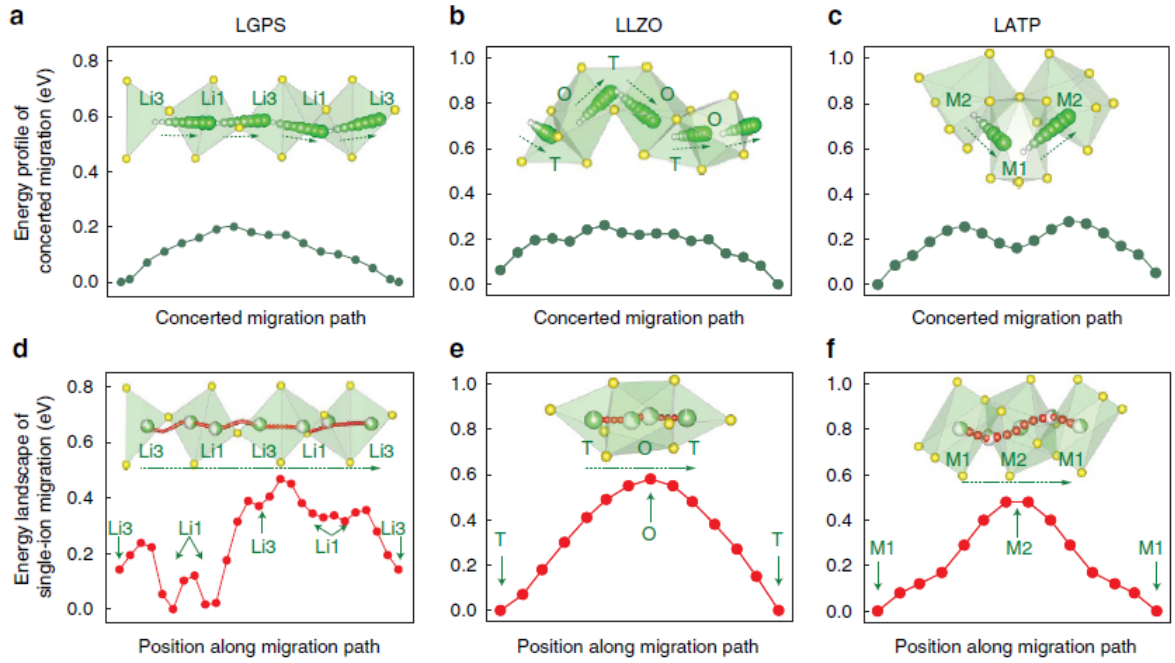

Figure 1.11: Theoretical pathways for Li conduction through ceramic electrolyte, including LLZO. Computational energy profiles show the differences between concerted (multi-ion) motion a-c) and conduction with each Li ion overcoming an individual energy barrier e to f). Energy profiles for concerted migration are shown to be lower than single ion migration mechanisms. Figure acquired from reference [104].

Given the cubic phase of LLZO does not form at standard temperature and pressure, either requiring temperatures above 700 °C or additionally doping with low weight percentages of metal ions. The latter option has the additional benefit of potentially improving the conductivity of the cubic phase if a suitable metal is chosen (e.g. Al, Bi, Ge, Ga, Nb, Nd, Ta, Ti, Y) [12, 13, 105-108]. Aluminium doping has achieved conductivity in excess of 1 $\times 10^{-3}$ S cm^{-1} and widely used in studies for maximising conductivity [11]. The dopant commonly occupies the La or Zr sites within the structure, depending on the oxidation state stability and size of the dopant ion. The substitution of raises the energy of the adjacent Li site, promoting a lower activation energy pathway for ion migration via this instability [92]. However, the purchase options for PLD targets meant the dopant in this project is niobium. doping can improve conductivities of the electrolyte but also stability of lithiated cathode materials [23]. Conductivities for Nb and Nd-doped LLZO have been measured up to 1 $\times 10^{-5}$ S cm^{-1} for Nb or Nd as the only dopant. This increases to over 1 $\times 10^{-4}$ S cm^{-1}, when combined with a secondary dopant (e.g. Al or Bi). Nd^{3+} occupies the La^{3+} site ($Li_7Nd_xLa_{3-x}Zr_2O_{12}$), while Nb occupies the Zr sites ($Li_7Nb_xLa_3Zr_{2-x}O_{12}$), with the effect of reducing the lattice constant when used as a sole dopant.

Phase stabilisation and lattice dimensions are important the size of the substituent ion needs avoid detrimental effects to the energetics of Li migration through raising the activation energy of concerted ion migration mechanisms [13, 105, 108]. Conductivities for Nb-doped LLZO have been measured at $\times 10^{-4}$ S cm^{-1}, promoted by destabilisation of Li sites by the large ionic radius of Nb^{3+} ions (0.72 Å) occupying Zr sites ($Li_7Nb_xLa_3Zr_{2-x}O_{12}$) [12]. Counteracting the stabilisation of the cubic phase and promotion of lower energy Li transitions, the smaller lattice constant after Nb doping limits the improvement in LLZO conductivity [108-110]. A co-dopant that occupies the La or Zr site but increases lattice parameter would be a method of offsetting the effect of compressed lattice parameters in Nb-doped LLZO. Purchase options for PLD targets meant the dopant in this project was niobium. Nb doping can improve conductivities of the electrolyte but also stability of lithiated cathode materials [23]. This may help acquire a cubic LLZO (c-LLZO) phase, stabilised at LT and with suitable conductivity for electrochemical in-situ experiments.

1.4 Anodes Materials and Ion Intercalation Characteristics

As with cathodes, it is important to have an anode for Li storage and delivery that allows for high capacity and longevity of performance during intercalation cycles. For Li batteries graphite functions effectively as an anode with capacities of 372mA h g^{-1}. Li inserts efficiently within the graphite layers, with an interlayer spacing of 0.34 nm (pure graphite) to 0.37 nm (LiC_6)), providing a measured conductivity at a magnitude of $\times 10^{-4}$ S cm^{-1} [26, 111]. The anode material is also fundamental to battery lifespan and performance. The bulk of research has been around understanding and modifying graphite for LIBs. However, given graphite has a limited capacity (372 mA h g^{-1}) and incompatibility with Na ions, silicones and hard carbons have also gained interest [112]. Graphite's layered structure, with a spacing of 0.34 nm, works well for incorporating Li ions of 0.76 Å in diameter [113]. Along with carbon's abundance and simple industrial deposition techniques, it is therefore the most common anode material in the LIB industry.

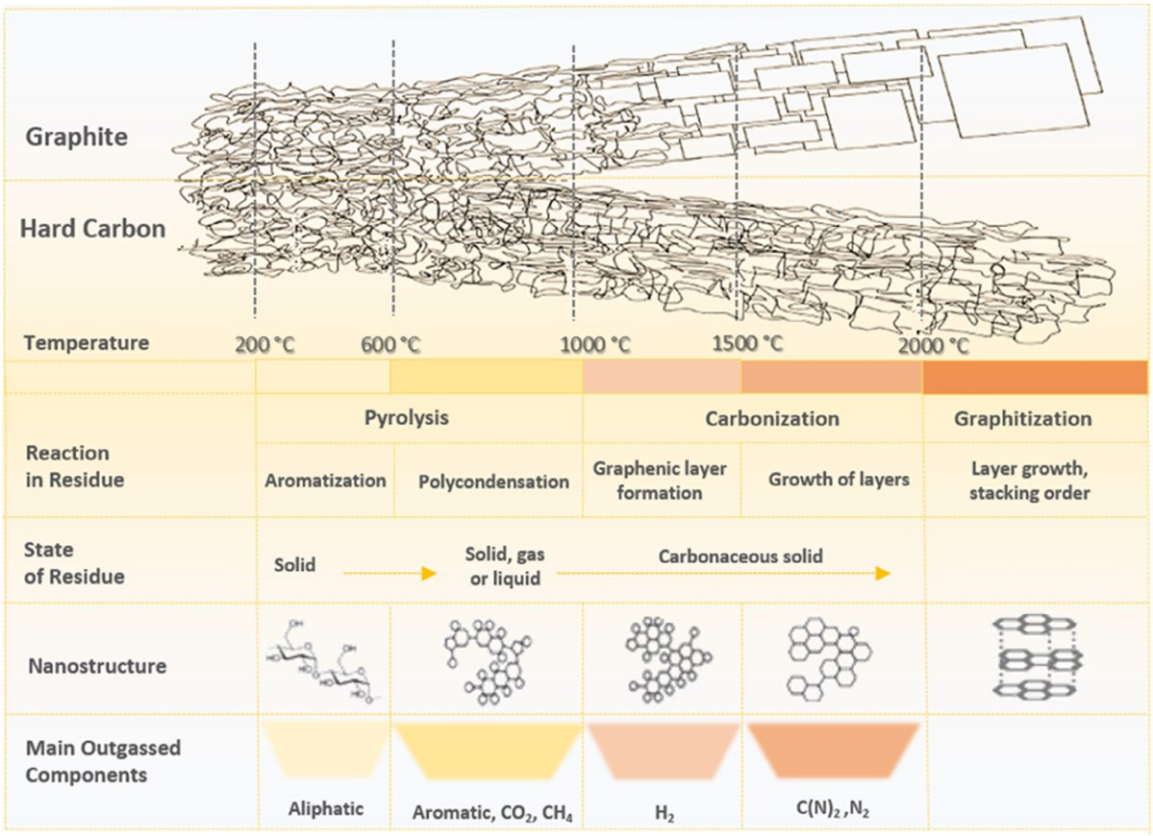

Figure 1.12: Temperature profile of graphitic and non-graphitic hard carbon structure, showing difference in the ordered layered and disordered structure of graphite and hard carbon respectively. Acquired from references [114, 115].

With respect to alternative active ions in energy storage devices, larger metal ions (e.g. potassium, calcium), will intercalate to some extent between graphite layers. However, the energetic potential of Na ions within graphite is unfavourable, compared to metal formation on the surface [115]. Hard carbons (Figure 1.12) have quoted capacities up to approximately 438 mA h g^{-1} for intercalation of lithium where optimally prepared. This higher capacity and ability to intercalate Na, has driven research into this class of anodes [115, 116]. The structure of hard carbons is still debated, with the precise formation seemingly dependent on the precursor. Consequently, there is no agreed intercalation mechanism for respective ions. It is thought the storage for ions occurs predominantly in defect sites, which depend on the internal porosity of the electrode [115]. Coating or doping of hard carbon anodes, has achieved improvements in their stability and capacity [116].

Research into silicon anodes has yielded some interesting findings and progress. A high theoretical capacity (approx. 4200 mA h g^{-1}), makes it an anode material of significant interest.[112] However, the underlying issue of large volume changes upon intercalation, leads to rapid structural deterioration. Consequently, the initial advantageous capacity of silicon anodes quickly decreases. Work on silicon anodes appears limited, despite the length of time since research in the field commenced. This is likely due to the significant challenges posed by structural deterioration. Methods including mixing silicon with graphite, as well as applying oxide coatings, have achieved improved stability over a greater number of charge cycles [117].

With respect to the research into solid-state devices, the implementation of graphite or other anodes is of less interest than the deposition and structural studies into the cathode and electrolyte materials. The formation of SEI between graphite and SSE are also important to the battery performance, and lattice orientations in relation to graphite planes [4, 118]. Analysis focuses on cathodes and electrolyte in this project, where similar studies into the solid-state interfaces with anode material would constitute a project focused on their specific interaction with an SSE.

1.5 Role of GB in Conduction and Trapping of Lithium within Solid-State Batteries

The role of GB within energy storage devices have the potential to provide significant advantages and disadvantages for the mobility of ions during charge cycles [119, 120]. The ability to acquire HR STEM images of crystal structures along regions were two different orientations of the same phase meet or where two different phases converge can provide insight into systems of Li transfer pathways. GBs can facilitate Li transfer within the space between two grains at a boundary where lattice misalignment is significant, facilitating ion motion around adjacent grains [120]. In contrast, the role of low-misorientation GB, good lattice match and therefore no unoccupied space between grains, will be more dependent on the mobility across the two ZA in contact. Where a highly conductive lattice directions align the Li flow through the GB will be more preferable (e.g. LCO(100)) than a lattice axis with higher impedance to Li intercalation (e.g. LCO[001]) [42, 121]. Three-dimensional contributions to the performance of electrodes and electrolytes can be measured and modelled using slice-by-slice imaging, EDS and EBSD, to build a picture of GB networks and potential features contributing to lithium migration or device failure hotspots [122, 123].

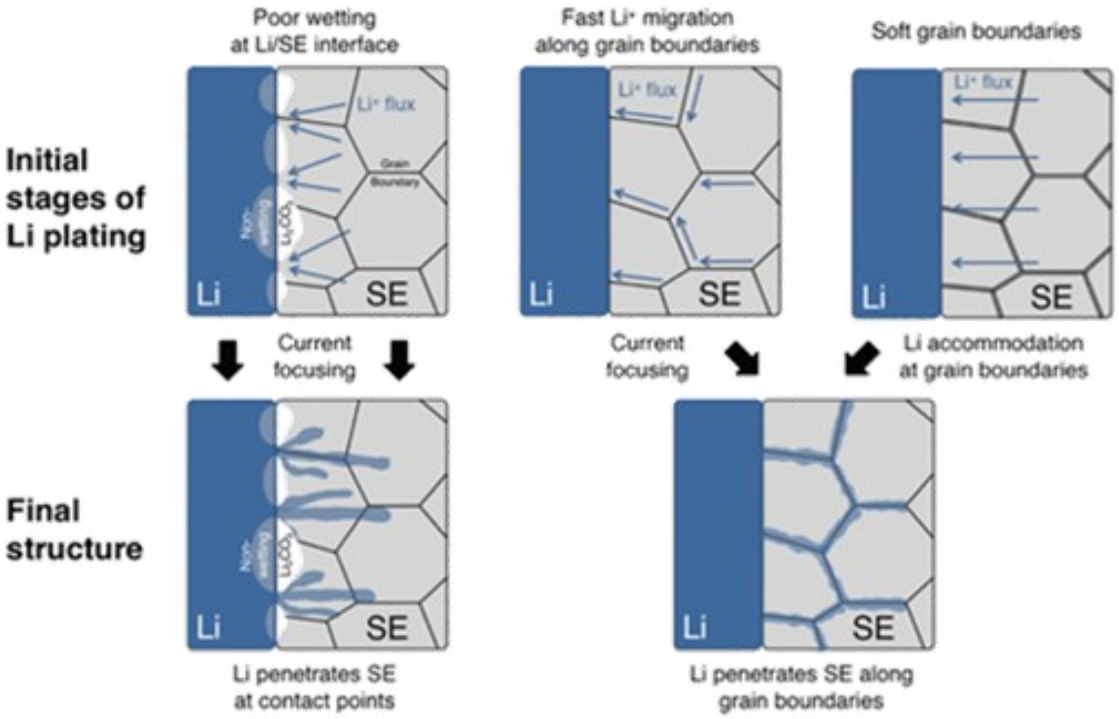

Figure 1.13: Degradations at GB and SSE resulting from routes of Li intercalation through a granular SSE. These include Li flux through grains and along GB, with degradation mechanisms show to be Li dendrite formation at the EEI or accumulation in the GB. Figure from reference [121].

Modelling of lithium movement through the grains and boundaries within lattices has been achieved, for example $LiOCl_3$. This study illustrated the greater probability of lithium ions occupying the GB due to spatial effects and lower local coordination. The ions in the GB are theoretically retained until they can pass into the bulk grain, limiting the rate to which they flow through the lattice [16]. This high resistance to ion transfer means Li ions experience delays in GB regions, before moving into the bulk material grain. Finding ways to control the density of GB in the EEI, may be important towards improving battery performance for specific materials.

Examples of such boundaries within Li materials have been approached with theory and modelling of the r-LCO phase boundaries observed in Li rich materials. Imaging allows aspects such as the angle at which twins of the same phase align and mixing of cobalt present between the offset layers of anti-phase twin (APT) boundaries [42, 48, 124]. Twin boundaries share points of symmetry between two adjacent planes of the same phase, in contact along a symmetrically equivalent plane/surface. A twin can include contact between equivalent crystallographic planes, misorientation between the two grains that creates a coherent fit between the atomic structure and a symmetry operation, commonly a mirror plane. The lithium diffusion across these boundaries is aided by the alignment of lithium channels in the misorientated twinned boundary; however, the

APT boundaries lithium is more susceptible to being blocked. The transition between cubic and rhombohedral phases occurs for predominantly rhombohedral $Li_{1.2}Ni_{0.4}Ru_{0.4}O_2$, creating a GB between the high-conductivity (rhombohedral)- and low-conductivity (cubic) grains, creating as a bottle neck to lithium mobility [42]. A phase change from rhombohedral to cubic is unlikely to be thermally induced at room temperature, rather it is a consequence of the charge transfer process where lithium content decreases and increases during charge cycles [22, 48]. Charge cycling of batteries results in the constant variation of lithium content in LMO's like Li_xCoO_2, where x=1 in the charged state and x<0.4 in a safe discharged state [125]. Reducing lithium content below x≤0.4 can result in locking lithium capacity into the c-LCO phase, with reduced reversibility between c-LCO and r-LCO. Such phase charges during discharge of a device are disadvantageous, with resultant greater contribution of the c-LCO as a volume percentage. Phase shifts not only result in the changing of conductivity and capacity of the electrode but also the strain within the electrode. The slight differences in lattice parameters and therefore strain of various GBs between r-LCO, rs-CO and s-CO have the potential to create sites more prone to structural failure [126]. Stain maybe eased through defect formation on the nanoscale, however across many microns of a device the combined strain has potential to contribute to fracturing. This may occur during synthesis, but is observed to be more detrimental to creating multiple failure sites within electrode materials after charge cycles [22].

Dynamical studies of the influence of GBs on micron scale devices have been performed. Diffusion along nanoscale GBs is observed using STEM-EELS, as a route through micron-scale regions of electrode material, with significant impact on net Li conductivity [127]. Fracturing of the materials over multiple charging cycles, and dendrite formation is observed (Figure 1.14), on the micron scale for LLZO when under electron beam irradiation [128]. This also highlights the susceptibility of SSEs to damage mechanisms relating to charging under the electron beam as well as illustration potential for Li accumulation along these GB during device operation. This potential of Li plating leading to failure mechanisms in SSEs could be important, although specific studies into Li dendrite formation at GB during charge cycles in a necessary dynamic experiment to carry out. Such experiments would need to be ex-situ or in-situ under beam sensitive conditions to avoid electron beam effects causing the Li accumulation [129].

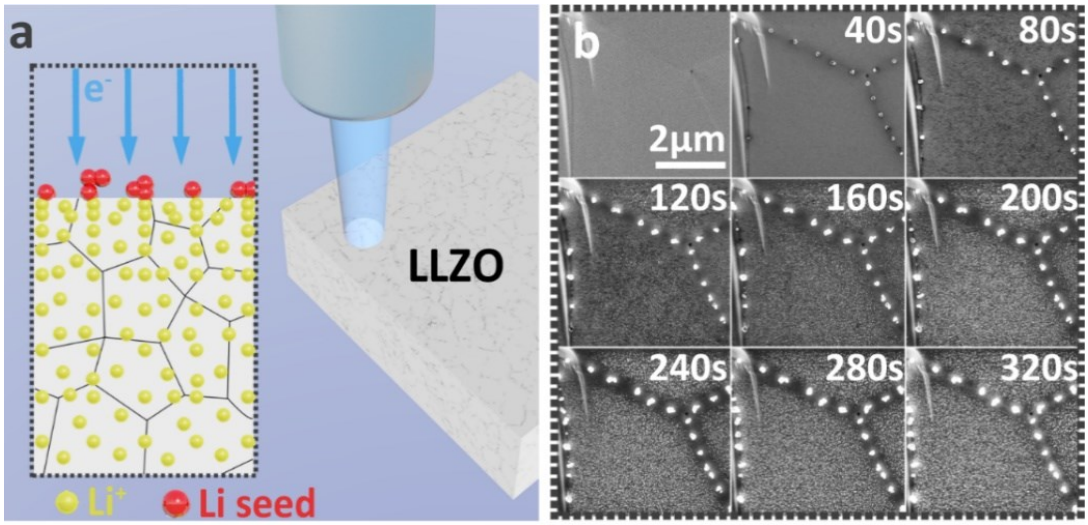

Figure 1.14: Li dendrite formation at GB within LLZO during electron beam irradiation. Appearance of bright spots along GB are indicative of Li accumulation resulting from LLZO charging under the electron beam/probe. Sourced from reference [128].

Control of GB within the project may be achieved in different ways, depending on whether the material is generally susceptible to GB growth via annealing or exhibits orientation dependant GB growth during thin film formation [130, 131]. In principle, film growth can lead to a single, optimised grain orientation between electrode and electrolyte with a defined interface. Of course, in practical devices many interfaces are present. In this thesis orientated films of LCO and LLZO resulted in polycrystalline films with dominant orientations containing several interfaces. Developing synthetic routes to analyse single and polycrystallinity within thin LCO and LLZO films is explored in results chapters 4 and 5.

1.6 Conditions and Crystallographic Considerations of Substrates during Pulsed Laser Deposition of Thin Films

Achieving consistent samples with fine control over their characteristics is desirable for the analysis of materials with important characteristics on atomic scales. Techniques including PLD, sputtering and atomic layer deposition (ALD), provide conditions such that thin crystalline films can be deposited, with control over stoichiometry, thickness, and crystallinity. These attributes are dependent on the chamber conditions, the substrate being deposited upon and the composition of the source/target [132, 133]. The PLD process is divisible into several key steps:

- Absorption of irradiation energy into the solid target material.
- Formation of a plume of material ejected from the target's surface.
- Three-dimensional expansion into vacuum chamber between target and substrate.
- Reduction in plume velocity and dispersion within residual air molecules or selected background gas (e.g. nitrogen, argon) pressure.
- Deposition of atoms and particles onto substrate, thus contributing to film growth.

As depicted in Figure 1.15 the setup for PLD consists of a laser incident on the target material within the vacuum chamber. The target rotates while under irradiation from the laser (wavelength) to ensure even ablation of material from the surface. The intensity of light incident on the target's surface defines the energy quota collected across a given area and time, the units, therefore, being J m^{-2} s^{-1}. Alternatively, the laser energy can be referred to as laser fluency in J m^{-2}, defining the energy per unit area incident on the target per laser pulse. Absorption of the energy from the laser beam requires the material to have a suitable band gap; otherwise, the material is transparent to the beam. Upon absorption of the beam's energy, a pocket of heat leads to explosive dispersion of material toward the substrate. The substrate is mounted around centimetres from the target, with background pressure and laser fluency moderating the flow and deposition rate, as well as the spread of the plume [134].

The choice of laser wavelength, as well as the materials compatible with a given PLD system, depends on the ability for the target to absorb the wavelength of the installed laser. For example, at York this is a Nd:YAG, laser, operating at 248 nm, 5 eV. Compatible materials are therefore required to be able to absorb the deep UV light of the Nd:YAG (248 nm) laser implemented in this project. The band gaps of LLZO can vary between 3.96 eV and 6 eV depending on preparation conditions and doping, with doping lowering the band gap [135, 136]. The band gap

of LCO can also vary but is much smaller, being measured between 1.7 to 2.7 eV [137]. The effective absorption of the excess energy within the 5 eV of incident Nd:YAG laser makes LCO and doped LLZO suitable for applications in PLD, where the excess energy is dissipated as heat in the target ablation process.

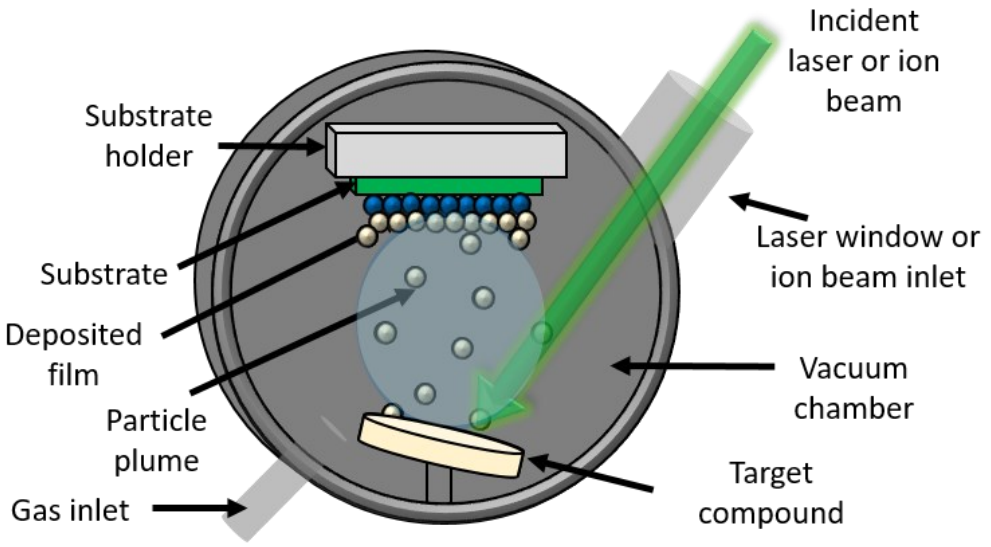

Figure 1.15: Diagram of PLD system with ablation of target by laser in order to deposit material on substrate located at a distance across the vacuum chamber. The type of laser, substrate temperature, repetition rate, background pressure and target-substrate distance are important parameters for each unique PLD design/setup.

During the ablation of the target material, the presence of a gaseous background element can introduce a concentration of dopant into the composition of the deposited form. This aims to acquire certain desirable characteristics, including stabilising a conductive phase and introducing defects (e.g. dopants) that can alter the energetics of ion migration, alter band gap profiles or facilitate surface reactions [133, 138-140]. Examples of this include the introduction of nitrogen into the structure of Li phosphate SSE, to improve the conductivity of Li through the Li_3PO_4 (P_{nm21}), through distortion of the structure [141, 142]. The LLZO target used in this project was niobium doped, as purchased from MSE Supplies, therefore no additional dopant gas was introduced during deposition of the electrolyte. Deficiency of lighter elements (e.g. Li and O) can occur within the deposited film, due to their susceptibility to lose their momentum in collisions with background molecules. For Li-based battery materials, this is a significant challenge to acquire stoichiometric films without the consequent Li deficiency seen in literature [140, 143]. This would be significantly detrimental to LCO and LLZO and therefore depositions are attempted at LT in this project, to limit Li evaporation. This also allows the effect of low substrate temperature on crystal structure to be

analysed at ARs in HRSTEM. Growth characteristics result from varying match between the atom spacings within the substrate's lattice and spacing of the atom arrangements along the growth direction of the thin film can be investigated, without the influence of elevated substrate temperature during PLD. While the match between lattice spacings is important to consider, the minimum displacement distances between repeating symmetry along the planes at which substrate and deposited material meet will drive epitaxial growth and determine strain. Ensuring ultra-high vacuum or using targets with 10% or even 20% weight excesses of Li could have also offset any significant Li deficiencies in deposited films. Excess sacrificial element mass in the target is not always desirable in terms of a waste or cost effectiveness viewpoint, hence alternative methods are preferable, including; shorter target-to-substrate distances, lower substrate temperatures, or increasing laser repetition rate [134, 140].

1.6.1 The strain of substrate

While substrate orientation is related to the epitaxial growth of thin films, the match between lattice constants for the deposited material and substrate can also have a significant effect on crystallinity and strain effects near the interface (Figure 1.16). A perfect match between the atom symmetries and their spacing, along preferentially aligned axis, is rare but small differences in atomic displacement conditions (<0.5 Å) between the substrate and the thin film will lead to minimal strain between the two materials across the interface region (roughly 10 nm into each film). Were the substrate or material symmetry and lattice dimensions are sufficiently mismatched, the film may be compressed or stretched close to the interface. This will lead to mechanisms whereby the strain energy is released in the form of defects. For example, this creates edge, screw or induced misorientations of the deposited material near the interface of the sample [134, 144]. Another consequence of strain at the substrate-film interface will be the overall crystallinity of the film's bulk structure. If multiple defect sites exist before the next layer of material deposition, there is a high likelihood for distinct grains to form, leading to a polycrystalline film .[145]. Depending on the material and scope for alignment of lattice rotations within the bulk of the film, the number of defects may increase of decrease with greater film thicknesses [144, 145]. Minimising the displacement between the periodic structure of substrate and lattice is important to ensure the electrode and electrolyte films have well oriented growth for optimising the plane along which Li diffuses, in addition to lower interfacial strain-induced defect or misorientation densities.

Bulk properties of the film often differ from the substrate-film interface, as initial defects within the first few layers of growth transition into a more stable growth [145]. However, if sufficient disorder occurs at the interface this will continue to influence disorder within the bulk of the film. In extreme cases, the extent of disorder at the film-substrate interface cannot be compensated and polycrystallinity dominates with minimal dependence on substrate orientation.

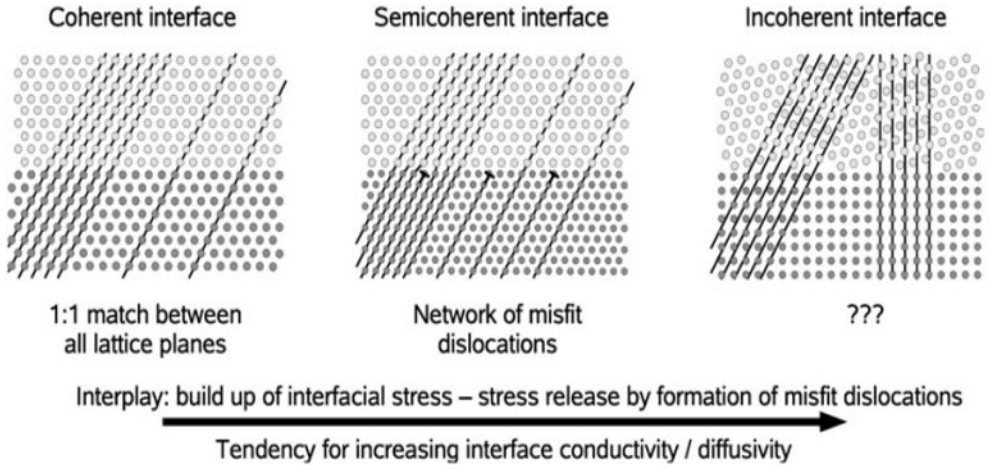

Figure 1.16: Diagrams of coherent, semi-coherent and incoherent interfaces, illustrating the effects of increasing lattice mismatch between the two distinct layers in a specimen, for example a substrate and deposited electrode or electrolyte. Reproduced from reference [146].

PLD of LCO can be carried out in such a way that epitaxial growth can be achieved on specific substrates. Al_2O_3(0001) and STO(111) can induce growth in the [001] direction parallel to the substrate surface (r-LCO(001)||ALO(0001) and STO(111)), while STO(100) can induce growth along the (014) plane (r-LCO(014)||STO(100)) [147, 148]. Films with the [001] ZA of growth have the CoO_2 layers perpendicular to the film's surface, although the faceted crystallite structure on the surface lends itself to exposure of the Li layers. The uncovered edges of r-LCO[001] films are then exposed to the electrolyte layer deposited on top of them. In contrast, LLZO has only shown epitaxial growth on a GGG substrate and is therefore expected to be fairly polycrystalline with either the cubic or the tetragonal phase present within the thin film [11, 149].

1.6.2 Growth of $LiCoO_2$ and $Li_7La_3Zr_2O_{12}$ on Substrates to Induce Desirable Crystallographic Orientations

LCO can be deposited in a controlled manner onto specific compositions and orientations of substrates. This includes STO and ALO, where [001] and [014] growth directions of LCO are obtainable, respectively [124, 150]. The ability to acquire such control over the crystalline growth of LCO is both interesting but also important in the formation of consistent interfaces within heterostructure devices in TEM, where electrode and electrolyte planes can be formed in contact with at least one layer being a fairly constant variable. Growth along the [001] plane of LCO is achievable on both ALO(0001) and STO(111) substrate orientations, with reasonable match between the lattice parameters, most apparent when looking at the periodic Co spacing relative to ALO and STO (Figure 1.17) [130, 151]. Similarly on STO(100) the more advantageous [014] plane of LCO is achievable, allowing easier Li intercalation to an electrolyte boundary at the surface along the exposed Li layers.[124] The high-temperature (HT) (> 400 °C) associated with such depositions promotes the formation of r-LCO dominated films. While higher temperatures help acquire the r-LCO phase, a 10 to 20% weight excess is beneficial for offsetting Li evaporation [152]. However, acquiring orientated film growth at LTs without sacrificial lithium content is also of interest. Assessing the atomic structure of LT LCO film deposition would give insight into the relative contribution of r-LCO before heating. This is where the project aims to build upon previous investigations.

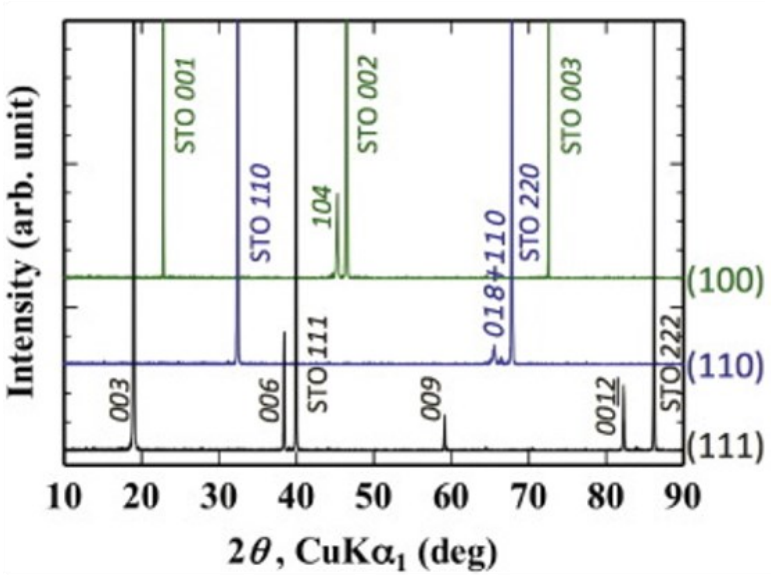

Figure 1.17: a) XRD of LCO films grown on STO substrates with (111), (110) and (100) surface orientations, showing dominant LCO growth planes relating to the (001), (110) and (104) r-LCO lattice vectors respectively. Acquired from reference [124].

In addition to the optimal r-LCO phase, there is potential contribution from lithium deficient or LT rock-salt phases [151]. With a LT (below 200 °C) pulsed laser deposition of LCO onto substrates a significant contribution from the c-LCO phase may be anticipated.[19] If regions of excessive lithium deficiency form within the electrode, a combination of cubic CoO and spinel Co_3O_4 grains also have the potential to appear. The intensities of every second site in HAADF images are indicative of lithium content in the cubic phase. Respective diffraction patterns also differentiate the lithium rich LCO phase from a structure closer to CoO [48, 153].

It has been shown to be possible to grow LLZO with a dominant orientation on GGG(111) and (001), with an electrolyte orientation matching that of the substrate (Figure 1.18) [131]. The importance of controlling the orientation of electrolyte growth, facilitates analysis of GB and Li diffusion characteristics between a specific plane of LLZO and grains of LCO. From a functionality perspective, the conductivity of the SSE may benefit from a dominant growth direction, more so than an epitaxial LCO electrode. Depositing electrode-electrolyte systems with PLD of LCO or LLZO onto suitable substrate can therefore provide different characteristics and perspectives for atomic-resolution TEM analysis within this project.

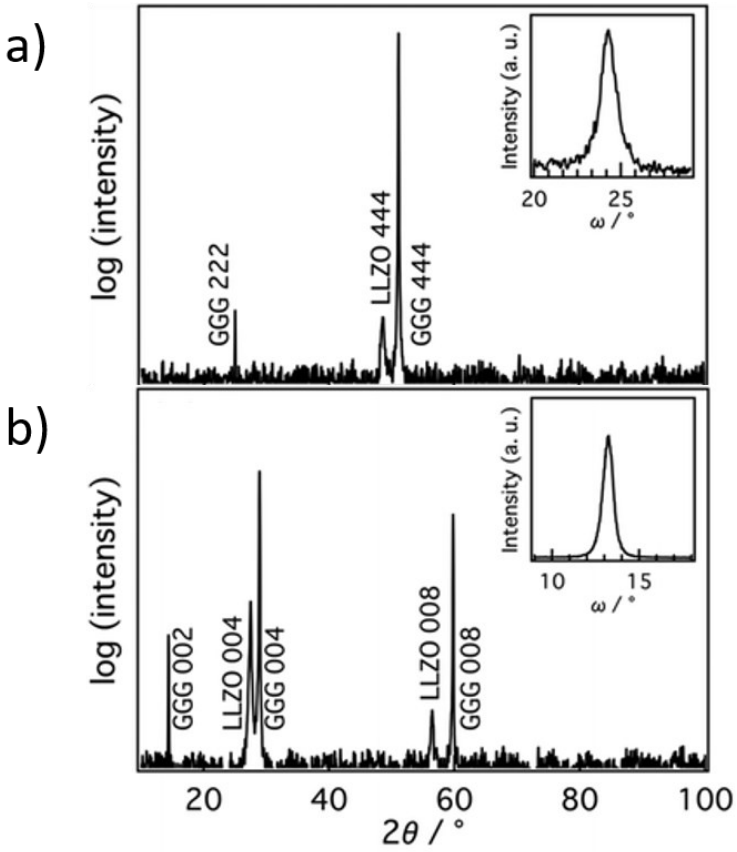

Figure 1.18: XRD spectra of LLZO grown on GGG substrates, showing a) LLZO growth achieved along the (111) plane on GGG(111), and b) Growth of LLZO along the (001) plane on GGG(001). Figures acquired from reference [131].

While contribution of Li-rich and deficient phases are easily tracked by XRD, in tandem with lower magnification TEM imaging the Li deficiency after annealing thin films is a clear limitation [154]. This provides the incentive to find deposition and annealing conditions were crystallinity and Li retention are sufficient to develop LCO/LLZO heterostructures where a crystalline-to-crystalline interface can be analysed.

1.6.3 Potential Alternative Methods to PLD

The process through which electrode and electrolyte films are deposited can involve methods including; vapour deposition, atomic layer deposition, sputtering, molecular beam epitaxy and evaporation. Each method has advantages as well as limitations, with respect to compatibility with materials, rate of deposition, uniformity of deposition, in-situ annealing effects and retention of stoichiometry [155]. The following briefly summaries the advantages and limitations of the above methods.

Sputtering uses either plasma (magnetron) or an ion beam to ablate material from the target. As with PLD sputtering can be achieved in chemically inert atmospheres, with a high degree of control over thickness and uniformity of the thin film. The method is compatible with a wide range of materials and can incorporate substrate temperature variation for in-situ annealing, alongside creating high-density films with good adhesion to substrates. Sputtering limitations include low deposition rates for creating thicker films, expensive and precise equipment setups, requiring high vacuum and alignment of material targets with the plasma/ion-beam and substrate. The incident plasma or ion-beam can also degrade heat sensitive target materials, potentially changing phase or, similarly to PLD, potentially inducing undesirable Li evaporation [156, 157]. Use of electron beams for dispersing material from the target may also induce charging effects and dendrite formation within Li-rich materials.

Evaporation can be induced thermally as well as through interaction with electron or ion beams. Particles within the vapour travel within the chamber towards the substrate. The thermal sensitivity of LCO and LLZO towards the high temperatures required for thermal evaporation make the method incompatible.

Vapour deposition techniques uses the volatility of a precursor within the target material, allowing the materials to be moved into the gaseous phase via heating the target, applying a plasma, laser or photochemical methods. Materials where the is a presence of Li makes continuous heating of the Li-rich target potentially detrimental to retention of stoichiometry, as Li evaporation rate will be in significant excess to heavier elements. Heating of the target may also induce undesired phases change relating to excessive Li evaporation. The requirement for precursors that may alter the electrode or electrolyte chemistry and Li retention within LCO and LLZO make vapour deposition less applicable despite a suitable growth rate (10 to 20 nm min^{-1}) [158].

1.7 Development and Compositional Analysis of Electrode-Electrolyte Heterostructures Using Electrochemical and Spectroscopic Studies

The ability to create systems that replicate the electrode/electrolyte/electrode layering of real-word devices, under carefully controlled conditions is fundamental for understanding the specific dynamics and decomposition mechanisms of these materials in a device. Attempts using numerous techniques including; PLD, hydrothermal, thermal evaporation, deposition and pressing powders, have created heterostructures to investigate interactions between a pair of electrode and electrolyte [151, 159, 160]. Sample preparation aimed at electrochemistry, spectroscopy and electron microscopy has developed insight into the performance degradation through multiple charge cycles. Electron microscopy has so far been able to monitor the chemical decompositions by spectroscopy (EDS and EELS), supporting studies using XRD and XPS [18, 161, 162]

The variety of electrodes and electrolytes combined into heterostructures in literature have differing chemistries and physical properties, which introduces complexity when comparing results. Nevertheless, valuable knowledge can be gained in studying model systems although any limitations must be acknowledged when drawing conclusions with systems including different transitional metals (e.g. Ti, Ni and Mn) [80, 161, 163]. The focus of such studies includes the measurement of increasing impedance over multiple charge cycles, and correlating this to the changes within electrodes and interface compositions with spectroscopy after ex-situ electrochemistry [88, 120]. This enables the understanding of chemical intermixing between lithium metal oxide and LiPON, LLZO or lithium sulphate electrolytes, although limits the understanding of any crystallinity within the variable chemistry along the interfaces [88, 164, 165]. It is clear that the intermixing of elements creates metal oxide layers with restricted Li mobility. For example, the mixing of Co and La into a lanthanum-cobalt-oxide phase will raise the interfacial impedance of an LCO/LLZO heterostructure. The low-conductivity of the most stable stoichiometry ($LaCoO_3$) is likely to define the interfacial mobility of Li in this system [51].

This project investigates the SEI region with HR (S)TEM, aiming to determine specific compositions and crystal orientations within the decomposition region. Charging or cycling LCO/LLZO heterostructures can be conducted ex-situ prior to extraction of cross-sectional lamella or in-situ within the microscope using MEMS chips. Advantages apply to both methods, when ex-situ work can collect data across hundreds of charge cycle measurements on a bulk sample. In-situ experiments on lamella suffer from fragility of the sample as well as changes induced by electron beam dose and current, although do allow insight into intermediate states of a solid-state heterostructure at ARs, while under the influence of biasing or heat.

It is important to consider that within this project and literature, the preparation method has the potential to induce changes to the structure and chemistry of materials prior to in-situ analysis. Mechanically polished samples may oxidise or be exposed to stresses that induce deformation during preparation. The use of FIB-SEM is likely to induce some charging, heating, and implantation related changes during lamella preparation and therefore it is reasonable to assume structural and chemical changes relating to these mechanisms may have altered to pristine sample. Changes may be inferred by XRD, XPS and other methods analysing the pristine sample, compared to observations in the lamella and FIB-SEM preparation. However, it is difficult to precisely determine the changes caused by the FIB on the nano and atomic scales, prior to an in-situ experiment [166, 167].

Studies on LCO/LiPON heterostructure highlight the potential for in-situ tracking of decomposition and lithium mobility through an interface using the O K-edges of Li (55 eV) and Co (60eV) in pristine, ex-situ biased and in situ experiments (Figure 1.19) [168]. Separating out the Co $M_{2,3}$-edge signal intensity from that of the Li core-loss signal can create challenges with respect to accurately mapping lithium within a metal oxide electrode. Work into single layers of LLZO and heterostructures where EELS data was collected as part of this project (Chapters 4 and 5) aimed to try and extract the Li K-edge from the background signal. The weak lithium signal strength and sample damage through radiolysis and noise in EELS data sets makes reliable detection of lithium a challenge. Accurate quantification of lithium content from low-loss EELS is unreliable given the contribution of Zr, La, Co and plasmons [169].

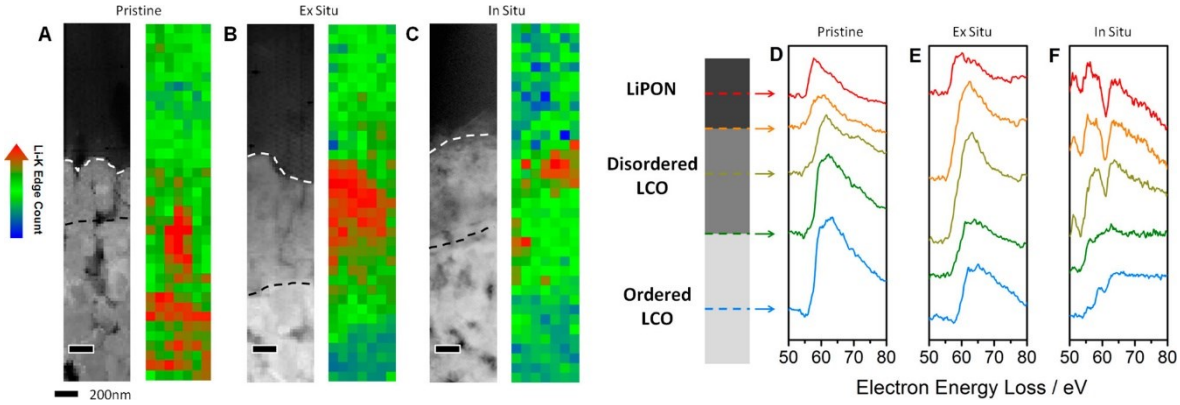

Figure 1.19: a, b, c) Li K-edge maps across the LCO/LiPON interface for pristine (a), ex-situ (b) and in-situ (c) biased heterostructures. d, e, f) respective Co $M_{2,3}$-edge low-loss EELS spectra with respect to their position across the interface for pristine (d), ex-situ biased (e) and in-situ biased (f) samples. Figure acquired from reference [168].

With respect to heterostructure studies of LMO in combination with LLZO, these have focused on the impact of sintering, by monitoring micron scale diffusions in a particle-based stack or thin film layering of LCO and LLZO using XRD and XPS. In some instances, a $LiNbO_3$ passivation layer is included to study the suppression of interface degradation with respect to retaining capacity and reduced interfacial impedance over multiple charge cycles [162, 163, 165, 170]. Sintering under dry oxygen, nitrogen, and CO_2 conditions, versus humid (2 wt% H_2O in O_2) the interfacial decomposition of a $LiNi_{0.6}Mn_{0.2}Co_{0.2}O_2$/LLZO interface showed dependence on the presence of CO_2 or humidity in the sintering environment. The XRD spectra (Figure 1.20) suggested Li_2CO_3 dominated the interfacial composition, up to 500 °C, while at 700 °C $La_2Zr_2O_7$ and lanthanum metal oxides developed between the electrode and electrolyte.

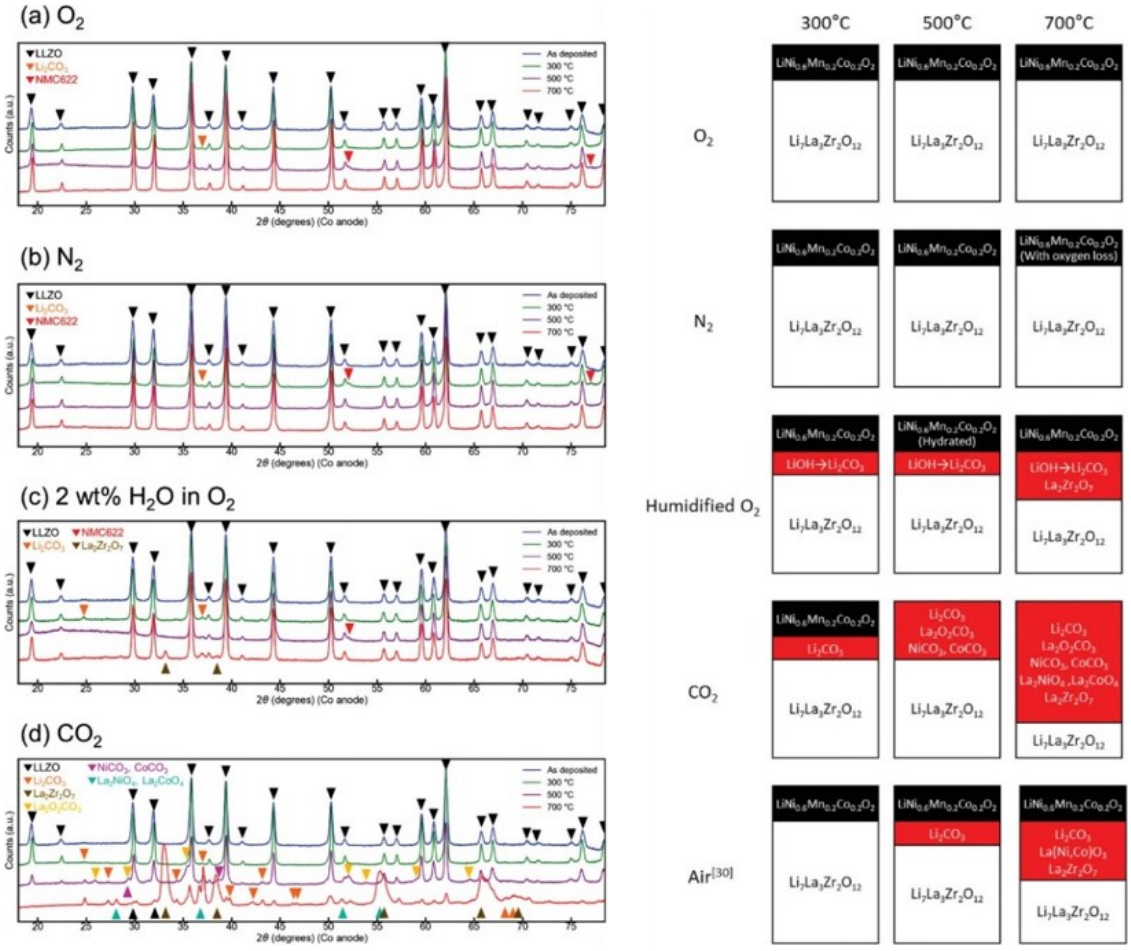

Figure 1.20: XRD and simplified schematic of interfacial products resulting from various annealing environments. Use of pure O_2 (a), N_2 (b), CO_2 (d), alongside humid O_2 (c), and air atmospheres within the furnace show H_2O and CO_2 were fundamental for interfacial decomposition into LiOH, Li_2CO_3, LZO and $LaCoO_3$. Reprinted from reference [170].

The application of passivation layers and analysis on resultant changes during annealing and cycling via a combination of STEM-EELS and electrochemistry has been studied for LCO/LLZO heterostructures relevant to this thesis and gives insights into the chemical changes along the interface influencing structure and charge transfer efficiency. Annealing at 500 ^{o}C shows a damaged interface and mixing of La, Zr and Co over 25nm, creating an inconsistent, fractured interface between LCO and LLZO [162]. A larger-scale system with $LiNbO_3$ layer between electrode and electrolyte, highlights similar extents of La and Co mixing through analysis of a FIB-SEM cross-section using EDS. With XPS measurements detecting Li_2CO_3 forming at the interface during the annealing (500 ^{o}C) process. The extent of interfacial intermixing was suppressible via the introduction of the $LiNbO_3$ interlayer.

The presence of $La_2Zr_2O_7$ (LZO) and lanthanum cobalt oxide is also anticipated, especially at greater sintering temperatures. With XRD the presence of the LZO phase may indicate lithium deficiency within the LLZO layer after annealing or be part of the interface layer. This is where AR analysis of the interfacial region is required to observe whether $LaCoO_3$ and LZO are present within the SEI. A $LaCoO_3$ stoichiometry is expected to dominate as the most stable form, although depending on the elemental rations in the SEI La_2CoO_4 may also be present [126]. The benefits of the interlayer were also reflected in the reduced impedance measurements of devices containing either LiNbO, LiAlO and LiTiO at the LCO/LLZO interface. Figure 1.21 also shows the enhanced retention of capacity with the presence of a passivation layer [163, 165].

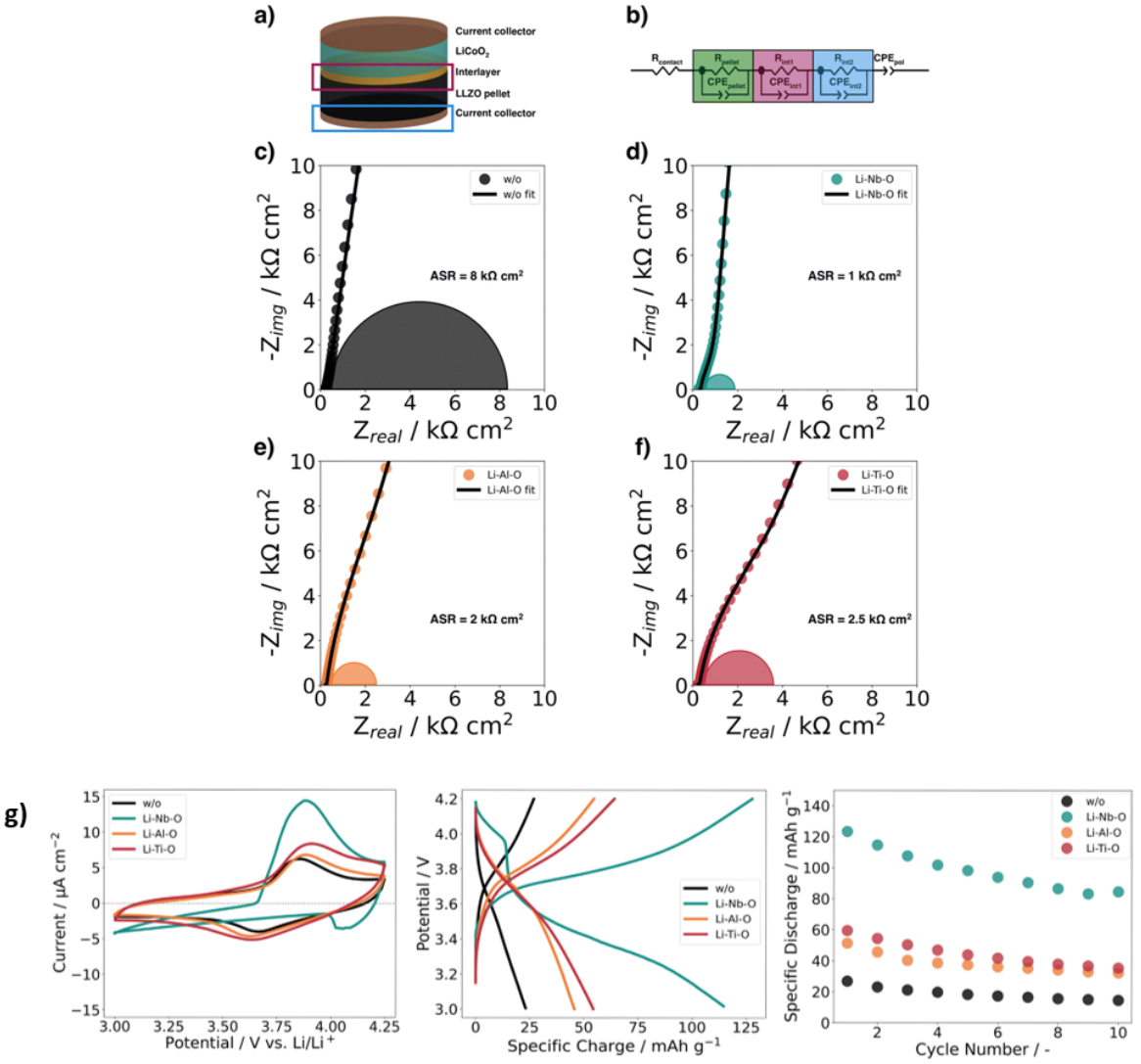

Figure 1.21: Influence of passivation layers between LCO/LLZO in a stacked device. a to f) Impedance measurements show significantly decreased interfacial resistance to Li transfer. g) Cyclic voltammograms and specific discharge capacity, versus cycle number indicate the retention of performance using different interfacial passivation layers. Figure acquired from references [163, 165].

1.8 Application of Electron Microscopy to Studying Battery Materials from the Micron to Atomic Scale

The applications of microscopy to battery research are extensive with the ability to conduct surface imaging, analysis of particle morphology and spectroscopic chemical mapping of samples from the micron the nanoscale. This provides the basis for understanding the size and shape of particles after different annealing processes and for varying composition [171, 172]. This includes focusing on cross-sections of pristine and used commercial cells as well as sample acquired from customised cell or thin film depositions [124, 131]. The former enables electron microscopy to observe the limitations of current Li-ion energy storage devices, while thin films can achieve controlled crystalline growth with characteristics compatible with effective preparation of samples for AR or in-situ microscope experiments. Figure 1.22 provides some example of microscopy applications for device cross-sections, with micron devices easily being scaled down to nanometre thick thin film devices [2].

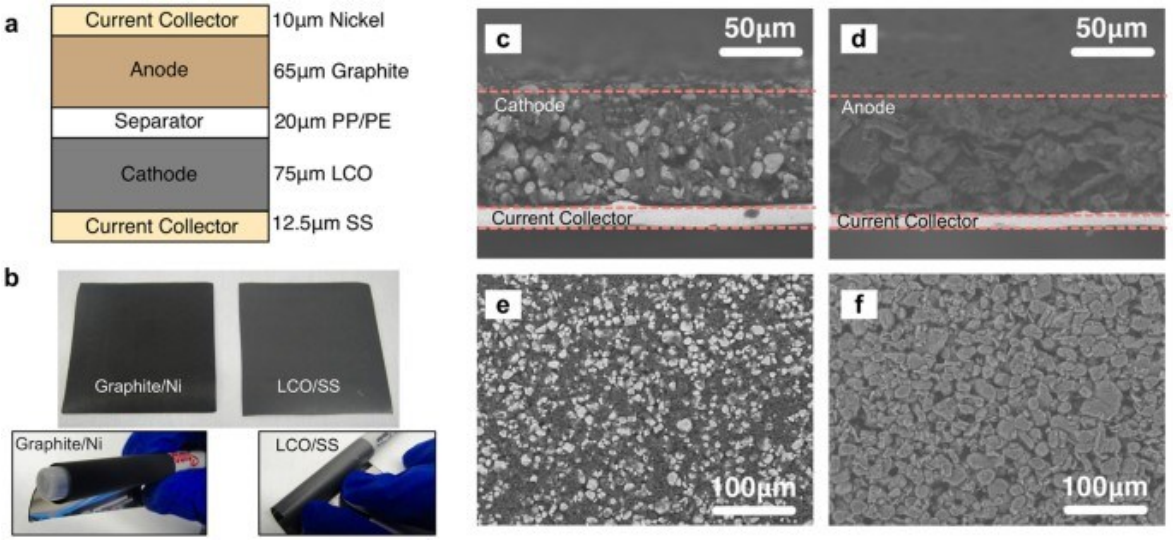

Figure 1.22: a, b) Battery cross-section with LCO electrolyte. SEM images of a device's cross-section where c) and e) relate to the particle structure of LCO, while d) and f) correspond to the graphite anode. Figure acquired from reference [2].

With SEM it is possible to analyse the cross-sections of samples on a larger scale with lower beam energies than materials may be subjected to for transmission microscopy. Although the resolutions of secondary electron (SE) and backscattered electron (BSE) signal does not allow for the visualisation of atom structures, insight into the topography of samples alongside supporting diffraction and spectroscopy methods provide a wealth of information. Examples of such imaging and spectroscopy are performed on LCO and graphite electrodes, alongside LiPON and LLZO SSEs. These contain information on particle size and morphology, with higher resolution imaging allowing for the analysis of film roughness, including crystallite shapes or porosity [2, 84, 172]. This data enables to understanding of the distribution and porosity on the micron scale relating to a variety of annealing conditions, alongside effective surface areas from which Li transfer can occur through between particles. Comparisons of preparation conditions between SEM and TEM allow for features comparisons between ideal morphology on the micron scale in relation to optimising crystal and grain structures on the nanoscale [100, 124]. Low magnification imaging and chemical mapping of battery materials can observe the grain structures and chemical changes occurring across the bulk and surface regions of particles and films [165].

The scope of experiments conducted in a TEM covers multiple avenues of structural imaging and spectroscopy of steady state and dynamic sample conditions. The applications of TEM to SSB materials are wide reaching, allowing comprehensive analysis of phases, grains and boundaries within electrode and electrolyte materials. The ability to conduct HR imaging, with the capabilities of resolving atomic structures provides insight into the structural dynamics influences intercalation of the active ion (Li) during charge cycling. In order to observe Li, soft-beam ptychography has the potential to observe Li ions through 4DSTEM phase reconstruction in appropriate situations [173]. Combined with EELS and EDS a highly detailed map of systems can be produced to investigate the different chemistries of grains and interfaces within a multi-compositional system [162, 168].

1.8.1 High-resolution Electron Microscopy of Well-Oriented LCO Growth

When studying the characteristics of crystalline materials, it is highly desirable to have control over the crystal phase and orientation of the sample. In an idealistic case this control extends to acquiring specific single crystal growth directions of a material. Atomic arrangements and dynamic characteristics including, but not limited to; conductivity, magnetism and charge transfer can be assessed in a controlled manner along specific axis of a material of interest. Choice of fluency, temperature and substrate material can strongly influence the phase and direction of growth (epitaxy). The single crystal substrate's influence on epitaxial growth is the most important as it has a defined orientation a lattice parameter at the surface. The match in lattice dimensions

and symmetry between the substrate and deposited material determines the subsequent crystallinity and orientation of the thin film. A good match will result in the target material adopting a preferential growth along a lattice vector. Figure 1.23 shows a project relevant growth of an epitaxial LCO layer at 600 °C. HTs favour the formation of epitaxial r-LCO layer but are dependent on excess Li to offset potential device limiting deficiencies [174]. Conditions for LCO and LLZO depositions covered in the results chapters focused on crystallinity and grain characteristics resulting from LT depositions to represent and analyse polycrystallinity, replicating aged devices. For LLZO, higher substrate temperatures were required for crystallisation but enabled other avenues of analysis aimed at progressing literature around growth and HR TEM of the electrolyte.

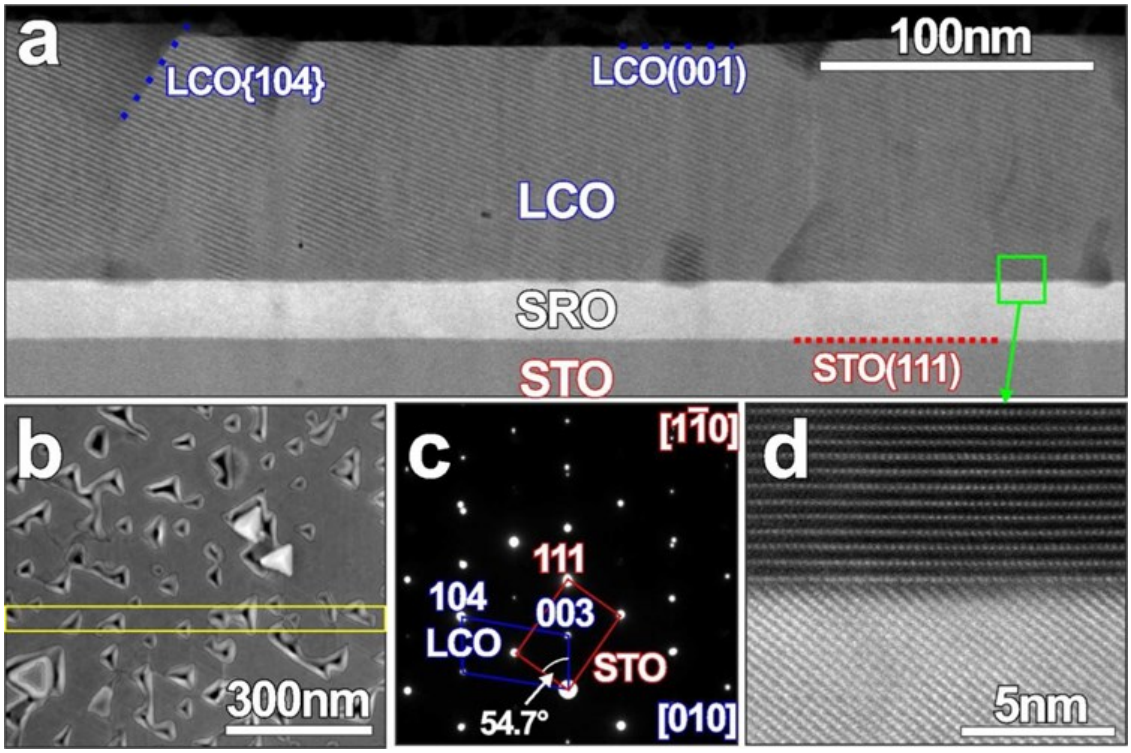

Figure 1.23: Epitaxial LCO layer grown onto a surface at 600 °C using PLD, showing orientation along the [001] plane when grown on an epitaxial $SrRuO_3$ (SRO) [111] buffer layer. a) HAADF image showing layering of STO, SRO and LCO. b) SEM image of the sample's surface, c) SAD DP from the cross-section containing LCO and STO with ZA and orientations labelled, d)HAADF image of interface between SRO and LCO. Reproduced from reference [174].

At micrometre scales, contrast based on the position of GB and orientation shifts provides visual reference to granular disorder from the nano to micron scale. It is also possible to detect the presence and analyse defects at low magnifications. These are important for understanding potential alternative mechanisms or traps within the crystalline structure effecting ion mobility [120]. While features on the micron scale are important for long-range conductivity and impedance to ion transfer through bulk and interfacial environments, investigation of the nano and atomic scale is fundamental to moving forward understanding of features influencing capacity, conductivity and overall performance of SSB materials [78, 120]. Investigation of atomic features relating to battery materials focuses on the observing the precise misorientations and alignment of atoms along GB of equivalent or differing phases. These attributes help understand the mechanisms through which lattice structures of existing materials align and can help predict the alignment of grains in similar ion intercalation materials. The alignment of grains is important within both the bulk of the structure as well as interfaces between two materials. Applying HR TEM and STEM imaging to controlled growth has provides the ability to assess the Li content and orientations of phases specific to electrode materials inclusive of LMOs where the metal is a combination of Co, Mn or Ni. The stability and resolutions of aberration corrected STEM provide the basis for imaging Co and O sites in LCO and columns containing La and Zr in LLZO. Figure 1.24 shows the potential of achieving atomistic images of phases within LMOs, showing suitable beam stability to achieve analysis of phases and GB within the bulk and electrode side of a solid-state electrode/electrolyte interface [42, 43].

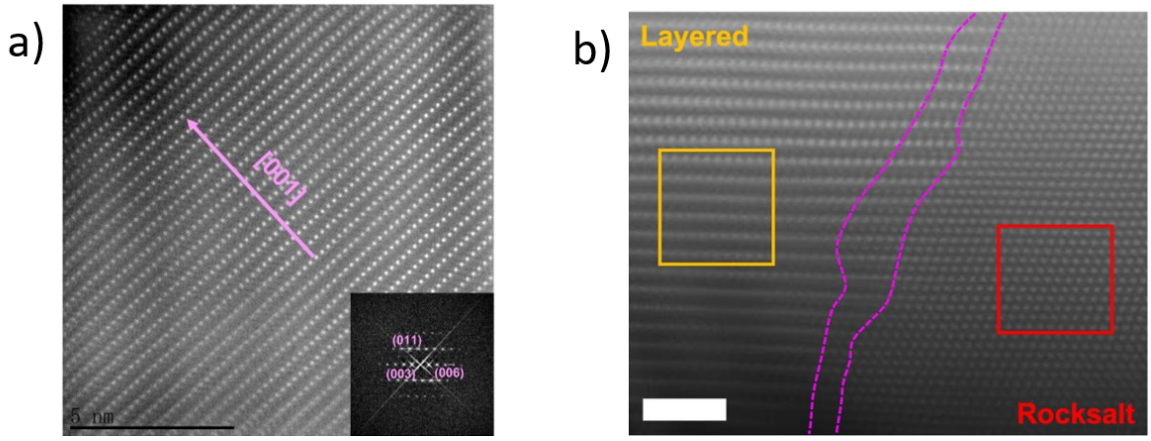

Figure 1.24: HAADF images of a) rhombohedral $LiCoO_2$ along the [100] ZA and b) $Li_{1.2}Ni_{0.4}Ru_{0.4}O_2$ containing a GB between the layered and rock salt phases of the LMO electrode material. Figures reprinted from references [43] and [42].

EDS and EELS provide the ability to achieve and understanding of detailed sample chemistry within a TEM in STEM mode. The scanning of the probe provides either x-ray or inelastic energy loss signal for the illuminated region. The resolution of EDS is determined by the interaction volume of the probe from which x-rays are generated, this limits the achievable resolution compared to EELS where AR chemical analysis is possible [175]. Investigations have used EDS to probe the bulk chemistry of battery materials, alongside chemical mixing at electrode electrolyte interfaces over tens of nanometres [4]. EELS at lower magnification provides similar analysis capabilities, although has the potential to probe the bonding states of elements within the bulk and interfacial regions [176, 177]. This has been useful in understanding the oxidation states and therefore stoichiometry of materials resulting from mixing of electrode electrolyte interfaces [88, 162].

It has been shown to be possible to grow LLZO with a dominant orientation on GGG(111) and (100), matching that of the substrate [131]. However, lithium deficiency often occurs after annealing thin films and is a clear limitation [154]. This provides the incentive to find deposition and annealing conditions were crystallinity and lithium retention are sufficient to develop LCO/LLZO heterostructures where a crystalline-to-crystalline interface can be analysed.

Successful high-resolution imaging has occurred within particles of Ta- and Ga-doped LLZO, whereby observations along the [111] and [133] ZA were concluded to have been achieved. The similarity in diffraction spot distances of LZO and LLZO make the use of FFTs or diffractograms unreliable unless calibration of the microscope is certain. Alongside observations where atomic plane spacing is inconsistent (Figure 1.25), these characteristics raise questions as to whether LZO or LLZO is being observed [178, 179]. The examples shown in Figure 1.25 focus on the diffusion of gallium into the layers of LLZO as an in-situ study. Images d to f provided images of Ta-doped LLZO through a lower temperature molten salt synthesis. The image along the [111] ZA confirms that LLZO can be imaged at high resolutions.

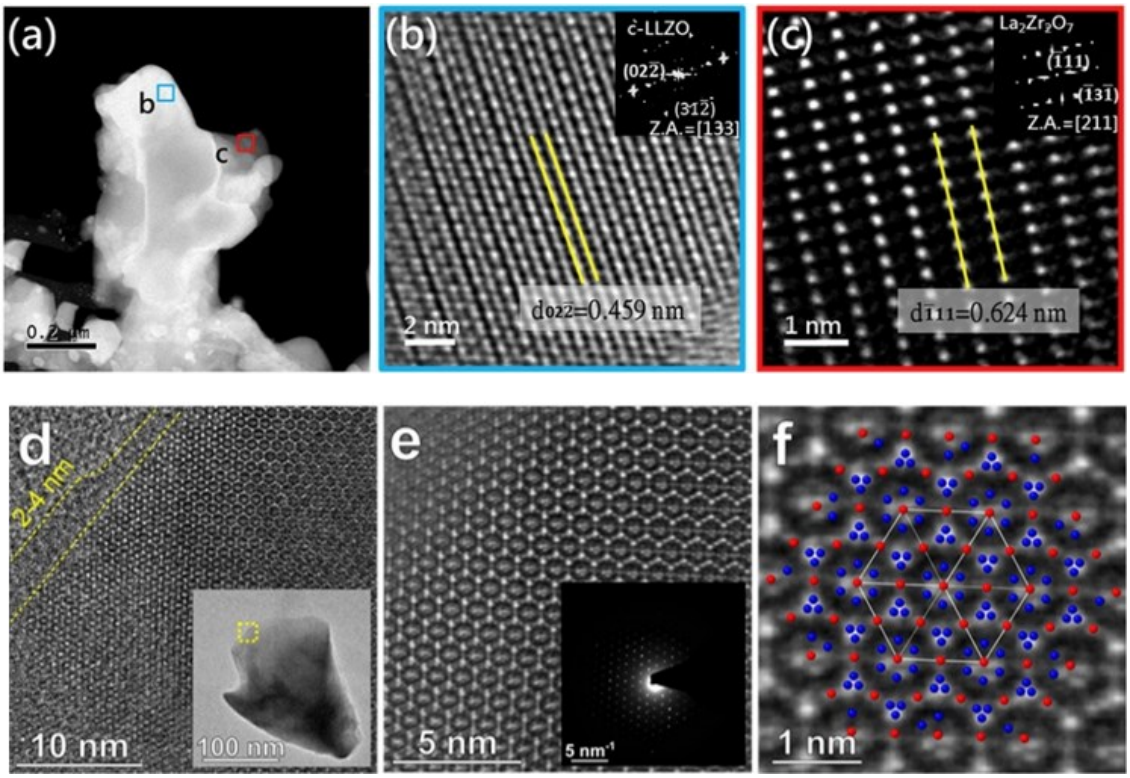

Figure 1.25: TEM and HAADF images of a) Ga-doped LLZO particle, b) LLZO phase during Li intercalation, c) LZO from (reference [178]). d,e,f) HAADF images along the [111] ZA of Ta-doped LLZO phases at increasing magnification within electron transparent region of LLZO particle on carbon grid (reference [179]).

1.8.2 Dynamic In-Situ Transmission Electron Microscopy

TEM is important for a variety of applications across nanoscale chemistry. Key uses have included investigations into catalysis, material structure and biological systems including protein imaging [180-184]. Focusing an electron beam through a thin (< 100 nm) sample, enables HR structural images and diffraction patterns to be produced. The images or patterns relate to the magnitude of electron scattering at the region being probed by the beam. The relative scattering angles relate to atomic number, elemental size and periodic structure of the sample. While a vast amount of information is obtainable from imaging initial and final structures (ex-situ), this limits observations to already complete processes, giving little insight to important transitions. The ability to record short movie-like sequences of dynamic nanoscale processes, is a more recent refinement of the TEM equipment. The development in technology, has allowed in-situ imaging to become a powerful technique across multiple scientific fields [180, 181, 185, 186]. With the power to view structural developments at atomistic scales, it is vital for researching battery electrodes under applied bias.

Modifications may be required from standard TEM techniques, in order to capture multiple images of processes occurring on second, down to nanosecond timescales [67, 187-189]. The technology behind rapid in-situ imaging, requires short bursts of high-density electron beams, to achieve adequate image brightness and contrast [187]. This high electron density results in space charge effects including electron-electron repulsion, which hinder operation and resolution. Accounting for this requires appropriate lenses and suitably wide apertures to accommodate dense electron beams [187, 188].

Viewing the dynamic processes within battery materials instead requires an understanding of the long-term effects the electron beam has on the material during image acquisition. Regarding intercalation and dynamic structural response in battery materials under bias, these are expected to occur on the second to minute timescales, depending on the desired charging or discharge rate. Electron-beam scan rate and dose are adjustable for tracking dynamic processes on these timescales, in tandem with beam sensitivity of LIB materials. This makes in-situ observations of battery materials where duration of data acquisition must account for the dose thresholds as the limiting factor to representative data collection of electrode and electrolyte. Use of rapid pulses of beams with high electron densities should not be required; rather ptychography and other dose limiting techniques are more appropriate for LIB materials [190, 191].

Beam damage can range from charging of the material's surface, to rapid structural or chemical degradation [192, 193]. It is therefore important to understand the dose limits of a given material and differentiate any beam specific effects from relevant experimental results. Battery specific artefacts may include structure degradation, leading to increased lattice disorder. This is commonly observed through weakening of diffraction patterns [194]. Chemical changes may also occur in many systems, including bond breaking and subsequent reactions. This is a side effect of beam energies (10 to 300 keV), being greater than those of covalent bonds. Most LMOs are noted to withstand up to 6×10^6 electrons $Å^{-2}$, without significant effect on structure [194]. Such doses can be calculated using Equation 6; where a is the irradiated area of the specimen, N number of electrons, D_c the critical dose, F the fraction of electrons reaching the detector and e the charge of an electron [195]. An example of quantifying beam damage is detailed by Brazier et al., who imaged two separate solid-state batteries on the same sample stage. One was subjected to charge/discharge cycles and the other purely to observe artefacts resulting from electron beam.[1] This helped differentiate bias related effects, from beam damage induced artefacts.

$$N = F[\frac{D_C}{e}]a^2 \qquad \text{Equation 6}$$

To apply bias to micro battery systems on the scale required for TEM, micro electrochemical systems (MEMS) are required. These take the form of TEM compatible sample holders, with the sample requiring in-situ biasing placed across two electrical terminals (Figure 1.26). A bias can then be applied to the sample during standard TEM analysis, such that the effects of charge cycles can be observed in-situ [196].

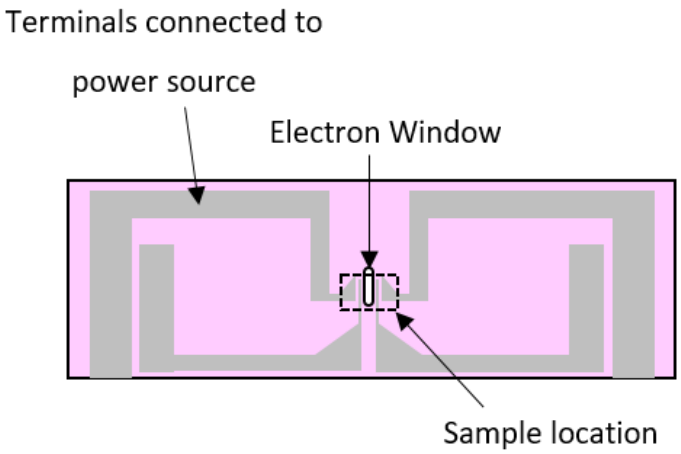

Figure 1.26: Scheme of MEMS chip for applying bias to fabricated nano-battery lamella. The sample is positioned in centre of chip, above the electron transparent window. Contacts allow the application of selected potential differences between the each side (e.g. anode and cathode) of the sample [196].

The benefits of in-situ TEM to batteries studies include; observation and modelling of the electrolyte and electrode changes, over multiple charge cycles. Conducting these dynamic studies on an atomic scale, would help progress understanding further. Structural disordering and pathways of ion intercalation would be important aspects to evaluate under bias. However, in-situ TEM alone cannot reveal to what extent any observed changes are affecting the batteries performance. Simultaneous acquisition of relevant electrochemical data would be ideal. A real time reference between structure, ion intercalation and electrochemistry, would link the physical and chemical changes.

1.9 State-of-the-Art and Project Aims

The electrochemical changes and cross-sectional imaging of devices on the micron and nanometre scales has provided insight into the performance changes during intercalation cycles and packing of particles with SEM [2, 32, 33, 40]. Investigations at the electron transparent edges of particles and cross-sections have evaluated phases of LMO with different lithium contents, allowing identification of lithium deficient grains with HR TEM. The importance of layered to rock salt GB is presented by different studies and highlight the importance of evaluating other boundaries at AR [42, 43, 48]. Phase transitions are shown to be of importance computationally and experimentally, where GB and electrode fracturing also occur [22, 197]. The process of calendering and heating solid electrodes for commercial devices makes understanding the influence of temperature on solid-state devices important. Subsequently determination of whether annealing is advantageous enough to be applicable to preparation of commercial devices or detrimental to the EEI. This creates incentive to track the changes between LCO and LLZO on the nanoscale by sintering samples combining both materials. The work on powders (Chapter 3) in this project aims to answer questions relating to the influence of sintering on grain size, phase of both materials, development of GB and extent of decomposition between electrode and electrolyte particles. Observations will consider the impact on Li capacity, mobility and trapping mechanisms relating to different crystallographic features on the nanoscale in SEM and TEM.

Growth of thin films of LCO has been achieved on three different substrates in literature, using the following substrates and respective orientations: ALO(0001),as well as (111) and (100) for STO and GGG. This has provided a basis for achieving orientated growth, where recent studies report depositions or annealing at temperatures up to 600 °C [48, 124, 150]. Depending on match between the substrate parameters, associated interfacial strain and deposition temperature, two Li-rich phases, c-LCO and r-LCO are expected favour LT and HT conditions respectively. Pursuing PLD of LCO at LT and LLZO at a range of temperatures, on ALO, STO and GGG, has three aims with this project. Firstly, to explore the growth orientations of the four potential phases within LCO depositions without substrate heating during PLD. Secondly, an approximation of Li content, within the LCO grown at LT and as grown or annealed LLZO, on each substrate is important to determine. Finally, conduct analysis of GB at AR using STEM, with the aim of furthering understanding of alignments between specific lattice directions relating to homogenous and heterogeneous phase GB. Compiling this analysis should determine the extent to which Li-rich and deficient grains comprise the thin films, as well as any dominant growth axis they adopt relative to the substrate. An assessment of the best choice of conductive STO substrate, between (111) and (100), can then be made for optimised heterostructure growth, whereby the ultimate goal is to create samples that

can be prepared for in-operando biasing (S)TEM experiments. Depositions of LCO on GGG investigate the quality and characteristics of LCO growth on a substrate yet to be reported in literature. If Li retention issues occur during similar deposition of LLZO films, this may allow the similar lattice constant and structure of GGG to provide insight into the orientations LCO may adopt if grown on an epitaxial LLZO(111) layer. The aims for LLZO deposition replicate those described for LCO, with optimisation of substrate temperature during PLD or post-deposition annealing requiring optimisation for the system at York to achieve crystalline growth on STO and replicate epitaxial growth on GGG [131].

Developing upon literature, can LLZO films on STO and GGG be analysed with HR (S)TEM to determine GB orientations between grains on the nanoscale, as achieved with LCO on ALO? Upon successful crystallisation of LLZO, does one phase dominate, and what insight do the orientations and boundaries Li transfer dynamics within electrolyte? Stability of such films under STEM probe irradiation is important to evaluate further given the importance of successful imaging of battery samples without significant beam damage influences. The use of PLD deposited LLZO on both GGG and STO with (111) and (100) surface orientations at vary growth and air-based annealing temperature will determine the single or polycrystallinity. XRD can assess phase and growth planes, with HRSTEM used to understand the single or polycrystalline characteristics achieved by growth and annealing temperatures. HR HAADF and BF images will support understanding of GB and inform potential modelling of these systems with respect to Li transfer across the normal to the adjoining planes of two neighbouring grains. In addition, could EELS analyse amorphous and crystalline films to confirm Li presence by resolving a peak at 55 eV, aided by the absence of Co in contrast to the electrode? This is attempted using STEM EELS on amorphous and crystallised LLZO films, aiming o resolve the Li signal from the background and nearby Co $M_{2,3}$-edge at 60 eV.

Current work on heterostructures has achieved chemical and interfacial decomposition analysis tracked at low resolutions, using STEM, EDS and EELS. Alongside electrochemical impedance studies, XRD and XPS, this has provided insight into the influence of thermal and electrical changes at interfaces inclusive of LCO and LLZO. Studies indicate the presence of LZO, $LaCoO_3$ and Li_2CO_3 within the SEI of these heterostructures. To advance upon these observations the important focuses of HR (S)TEM studies in Chapter 5 include the following. Firstly, can heterostructures of LCO and LLZO be deposited or prepared in such a way that both the electrode and electrolyte are crystalline at the interface? If LLZO remains amorphous after LT PLD, can annealing help form crystalline interfaces between LCO and LLZO? Establishing uniform LCO/LLZO interfaces aimed to provide a basis for AR imaging relating to the formation and crystallinity of lanthanum-cobalt-oxide layers forming during annealing or biasing of LCO/LLZO particle heterostructures. The use of GGG substrate aims to avoid thermal decompositions resulting from

LLZO crystallisation via annealing, the goal being to assess the interfacial characteristics relating to deposition of crystalline LLZO, then a crystalline LCO layer, both at LT. This has the potential to create a more effective heterostructure interface for in-situ biasing experiments where conductive GGG (e.g. $Ca^{(II)}$ or $Mg^{(II)}$ doped) would be used? Subsequently, does the LCO layer adopt a specific crystalline orientation on the surface of LLZO and how may this influence the Li-ion transfer dynamics of the resulting GB between LLZO and LCO?

Analysing the extent to which annealing time affects diffusion distances of elements within the two materials, will make effective use of EDS and EELS at high magnification and may be monitored in steady-state or dynamically if mounting onto a heating chip in-situ is successful. Similarly, ex-situ or in-situ biasing of these thin film heterostructures would expand upon electrode-electrolyte systems studied in literature. In-situ biasing is the ultimate aspiration if heterostructure preparation is effective. Work within this thesis lays the groundwork for in-situ experiments in future projects by attempting to effectively prepare a sample suitable for in-situ heating and biasing analysis. Further comparisons between structural changes and decompositions micron-scale (particles) and nanoscale (PLD heterostructures) can then be made.

Chapter 2

Experimental and Methodology

The methods and techniques fundamental to the completion of the project are presented in the following chapter. Techniques provide the methodology of creating and analysing particle-based and PLD samples of LCO and LLZO. The information provides covers the key sample preparation steps and annealing of each PLD specimen, alongside the milling conditions for lamella extraction, as well as parameters for imaging acquisition and spectroscopy within electron microscopy. Conditions utilised for TEM and STEM imaging, inclusive of beam energies and apertures, present the most common and effective parameters for various resolutions of image and spectroscopy acquisitions.

2.1 Powder Synthesis and Heterostructure Pellets

$LiCoO_2$ (LCO) with a purity of 99.5% was purchased from Alfar Aesar and used as received.

$Li_7La_3Zr_2O_{12}$ powders were synthesised to achieve an electrolyte with the desired stoichiometry and cubic phase. Mixing of Li_2CO_3 (STREM, 99%), La_2O_3 (Merck, 99.99%), ZrO_2 (Merck, 99%) was achieved with small additions of propanol to the mixture, grinding together with a mortar and pestle. A 10% excess weight of Li_2CO_3 was used to account for thermal evaporation of Li during the annealing process. The resulting powder was pressed into pellets (mass: 0.6 ± 0.1 g, diameter: 13 mm) at 10 tonnes, before being annealed at 850 °C (12 hours, ramp rate 10 °C min^{-1}), to induce a thermal decomposition into LLZO. Further grinding and re-pressing of pellets for sintering at 1150 °C (4 hours, ramp rate 20 °C min^{-1}) attempted to improve the percentage contribution of the cubic phase [98, 101, 198]. Cooling rates for sintered pellets were done at the maximum achievable with the furnace, beginning at approximately 20 $^oC\ min^{-1}$ before slowing to around 5 $^oC\ min^{-1}$. Removal of pellets occurred once the temperature was below 50 ^oC.

All sintering occurred with several LLZO pellets stacked (minimum stack height: four pellets) within an enclosed ZrO_2 crucible, attempting to limit Li evaporation from the exposed surface area. In addition, this provides an extent of protection from contaminants in the furnace. The use of a ZrO_2 crucible aimed to avoid Al doping of the structure if in the presence of an alumina crucible.

Heterostructure powder samples used the as purchased LCO, and as prepared LLZO powder after the thermal decomposition step (850 °C, 12 hours). LLZO, annealed to 850 °C, was mixed with LCO to limit the Li deficiency observed in the electrolyte seen after heating to 1150 °C (6 hours). Powders were ground together in a 1:1 mass ratio, with a combined mass of 0.35g ± 0.05 g providing suitable pellet thickness (≈ 2 mm) and structural stability. The pellets were a uniform grey-blue mixture with no significant LCO and LLZO segregation visible. The mixed powders were pressed into pellets (13mm diameter), at 10 tonnes and left in either a pristine state, annealed at 600 °C for 30 minutes (ramp rate 10 °C min^{-1}) or annealed at 900 °C for 4 hours (ramp rate 10 °C min^{-1}). Again, pellets were stacked during annealing to reduce Li evaporation from the surface. Pellets at the top and bottom of the stack were sacrificial.

XRD analysis was conducted using a Malvern Panalytical Aeries, with a CuKα X-ray source between angles of 5° and 70^o, with a step size of 0.022^o.

Samples were mounted onto pin stubs using conductive silver paint or conductive carbon tabs for SEM analysis and ion beam milling to create TEM compatible lamella.

2.2 Pulsed Laser Deposition of Thin Films

The research questions in this project depend on successful PLD of thin films, using an instrument with multiple target stages, which facilitates single layer and heterostructure deposition without venting the chamber. Substrate heating can induce crystallisation and potentially achieve the formation of desirable Li-conductive phases (e.g. r-LCO) during film formation. Dr Stuart Cavill in the University of York's Physics Department carried out deposition of the thin films. Decisions regarding deposition temperatures and film thicknesses considered both literature and the results of preceding thin film samples. PLD provides the necessary conditions and control for producing layers of electrode-electrolyte films of LCO and LLZO with amorphous and/or crystalline characteristics. A high-vacuum chamber (10^{-5} Pa) provides an inert atmosphere for material transfer and deposition, while partial oxygen or nitrogen pressure can be used to retain oxygen content, dope the material with nitrogen or aid the quality of material deposition. The LCO and Nb-doped LLZO target in the project did not contain an excess wt% of Li, with LT (no substrate heating) depositions aiming to determine the contribution of phases, grains, and boundaries without the influence of annealing the films.

Substrates selected aimed to induce controlled crystallisation within thin films of LCO and LLZO, based on the orientations shown to be achievable within literature for different substrate temperatures. The use of ALO(0001) would provide a lattice match and hexagonal symmetry well-suited to growth of r-LCO, while cubic STO substrates with (111) and (100) surface orientations would have greater strain between their surface and r-LCO. However, Nb-doped STO is suitable for creating thin film devices that can be developed into lamella for in-operando HR STEM experiments. Therefore, achieving a crystalline growth of LCO on STO, despite limitation relating to greater strain from lattice mismatch is advantageous compared to ALO.

To account for LLZO deposited not being crystalline on the LCO layer, PLD of the electrolyte onto a suitable substrate was attempted prior to making thin film heterostructures. To test the characteristics of LLZO PLD at LT, the use of STO allowed growth to be trailed on STO(100) and (111), to assess the orientations of crystalline growth and whether these provide an epitaxial or polycrystalline basis for deposition of an effective STO/LLZO/LCO heterostructure. Based on literature studies of LLZO growth on GGG [131], this provided an alternative substrate, with a small lattice mismatch (4.8%) between the repeating symmetry of the oxygen framework along the same ZA of LLZO.

2.2.1 Substrate Preparation

All compositions of substrate were cut into 5 × 5 mm^2 and cleaned by sonication in acetone, isopropanol, and deionised water (each for 15 minutes). STO substrates were annealed at 900 °C (ramp rate: 20 °C min^{-1}) for 10 minutes to remove any surface contamination. ALO and GGG substrate were cleaned with three sonication as above but not annealed.

2.2.2 $LiCoO_2$ Deposited on Al_2O_3, $SrTiO_3$ and $Gd_5Ga_3O_{12}$

LCO deposition was achieved by PLD with material ablated from a solid-state target of $LiCoO_2$ (supplier Testbourne Ltd.), forming a series of crystalline thin film on ALO, STO and GGG substrates. The laser was a Nd:YAG (wavelength 248 nm) laser; with the substrate remaining unheated during deposition. Laser repetition frequency was 10 Hz, with deposition time varied to achieve film thicknesses in the range of 40nm in single layers and 80 nm in heterostructures. Greater thickness in heterostructures was use to distinguish the bulk characteristics of LCO from the interface region.

Orientations in Table 2.1 and Table 2.2 are determined by either SAD or FFT of HR (S)TEM images acquired from within the substrate region of lamellae. The SAD or FFT are used to assign/reference the crystallographic direction of the substrate, along which the lamellae containing LCO, LLZO or the heterostructure thin film has been cut. Directions were commonly known prior to cutting the lamellae, based on the crystal symmetry and substrate orientation markings (e.g. cut corners), however the TEM and STEM data is used as an addition check to visually confirm the axis along which the substrate has been cut.

Table 2.1: Substrates and respective orientations upon which single layers of $LiCoO_2$ was deposited, with subsequent annealing conditions prior to lamella preparation and the ZA along which the lamella were cut.

Substrate	Surface orientation	Temperature during PLD / °C	Annealing prior to preparing lamella	ZA of substrate in lamella
Al_2O_3	0001	No heating	Remained pristine	$[12\bar{3}0]$
$SrTiO_3$	111	No heating	Remained pristine	$[1\bar{2}1]$
$SrTiO_3$	100	No heating	Remained pristine	Lamella 1: $[010]$ Lamella 2: $[110]$
GGG(111)	111	No heating	Remained pristine	Lamella 1: $[1\bar{2}1]$ Lamella 2: $[10\bar{1}]$

2.2.3 $Li_7La_3Zr_3O_{12}$ Deposited on $SrTiO_3$ and $Gd_5Ga_3O_{12}$

An Nb-doped LLZO ($Li_7La_3Zr_{2-x}Nb_xO_{12}$) target (MSE Supplies) was deposited onto single crystal STO substrates (5 × 5 mm^2), with surface orientations [100] and [111]. The dimensions of the LLZO target were a diameter of 25 mm and thickness of 2.5 mm. The PLD involved a Nd:YAG laser (266 nm), 10 Hz repetition rate with deposition temperatures ranging from 250 °C to 600 °C. Amorphous films were annealed between 350 °C and 1050 °C, for 4 hours (20 °C min^{-1} ramp rate) to induce crystallisation. Cooling rates for thin films were equivalent to the ramp rate (20 °C min^{-1}), although the rate of cooling decreased as the maximum rate of heat dissipation (below 300 °C) reduced rate of cooling to below the programmed value of 20 °C min^{-1}. No further annealing of LLZO films, deposited on STO(100), STO(111) and GGG(111) at 600 °C was conducted, as these crystallised during deposition. Depositions achieved LLZO film thicknesses of 60 nm to 80 nm, except for the heterostructure on STO(111) where 150 nm was observed.

Table 2.2: Substrates and respective orientations upon which single layers of Nb-doped $Li_7La_3Zr_2O_{12}$ was deposited, with subsequent annealing conditions prior to lamella preparation and the ZA along which the lamellae were cut.

Substrate	Surface orientation	Temperature during PLD / °C	Annealing prior to preparing lamella	ZA of substrate in lamella
$SrTiO_3$	100	250	Lamella 1: pristine Lamella 2: 450 °C (4 h)	[010]
$SrTiO_3$	100	350	550 °C (4 hours)	No lamella
$SrTiO_3$	100	350	1050 °C (4 hours)	[010]
$SrTiO_3$	100	600	Remained pristine	[010]
$SrTiO_3$	111	250	Lamella 1: pristine Lamella 2: 650 °C (4 h)	$[10\bar{1}]$ $[1\bar{2}1]$
$SrTiO_3$	111	350	950 °C (4 hours)	$[10\bar{1}]$
$SrTiO_3$	111	350	650 °C (30 minutes)	$[1\bar{2}1]$
$SrTiO_3$	100	600	Remained pristine	$[10\bar{1}]$
GGG(111)	111	600	Remained pristine	Lamella 1: $[1\bar{2}1]$ Lamella 2: $[10\bar{1}]$

2.2.4 Deposition of Heterostructures Containing LCO and LLZO

Using the same conditions for single layer describe above, heterostructure devices were deposited without heating onto STO(111) and (100) substrates, then annealed as a whole device in a furnace after PLD. Alternatively, LLZO was deposited at 600 °C on GGG(111) prior to LT LCO deposition and no post-PLD annealing was carried out. Samples are summarised in Table 2.3, covering substrate, layer ordering and specific annealing conditions. Samples were analysed by XRD in pristine condition and in (S)TEM after applying heat treatment for crystallisation (STO heterostructures only), and post-biasing at different voltage ranges (both STO and GGG heterostructures). This allowed for comparisons to be made between STO substrate orientations changing the growth direction of LCO, the order of deposition, and post-deposition annealing. At least two lamellae were prepared from each heterostructure to compare data along two ZA. Lamella for heterostructures on STO(111) were prepared along the $[10\bar{1}]$ and $[1\bar{2}1]$, similarly STO(100) samples were cut along both the $[110]$ and $[010]$ and GGG(111) the $[10\bar{1}]$ and $[1\bar{2}1]$ ZA.

Table 2.3: Heterostructure depositions of electrode and electrolyte onto single crystal substrates, each layer's composition, and respective thermal preparation conditions.

Substrate	Layer 1	Layer 2	PLD /Annealed	Temp. / °C	Duration / hours
STO(111) #1	LCO	LLZO	Annealed	600	4
STO(111) #2	LCO	LLZO	Annealed	600	0.5
STO(100)	LCO	LLZO	Annealed	600	0.5
GGG(111)	LLZO	LCO	Substrate heated during PLD	LLZO: 600 LCO: no heating	(During PLD)

2.2.5 X-ray diffraction

X-ray diffraction patterns were collected in two different instruments. With a Malvern Panalytical Aeries, with a Cu-Kα X-ray source, recording between angles (2θ) of 5° to 70° a step size of 0.022°. Alternatively, a Rigaku SmartLab rotating anode θ/2θ or 2θ-w diffractometer, using Cu-Kα radiation (λ = 1.54 Å), collecting data across various angle ranges between 0° and 90°, with a step size of 0.01°.

2.3 Ex-situ Application of Voltage Cycles to Sintered Particle and PLD LCO/LLZO Heterostructures

Biasing of samples was achieved using different voltage ranges between -12V and 12V with various numbers of charge cycles (Table 2.4 and Table 2.5) to replicate the conditions under which the LCO/LLZO interfaces are worked, and acquire voltage-current plots. Pristine and pellets sintered at 600 °C samples were used as these did not suffer from significant Li evaporation during annealing and thus tracking extent of any charge-related decomposition was potentially possible. A potentiostat was used to apply bias and acquire voltage-current plots for each cycle between two preselected voltage limits. Two probes brought into contact either side of the pellet (Figure 2.1, a), with bias cycle between the voltage limits carried out over a time period of 30 minutes. For example, 15 minutes from 12 V to -12 V and 15 minutes to return to 12V. Heterostructures were returned to a positive voltage to try to acquire a charge state with the Li occupying the LCO electrode.

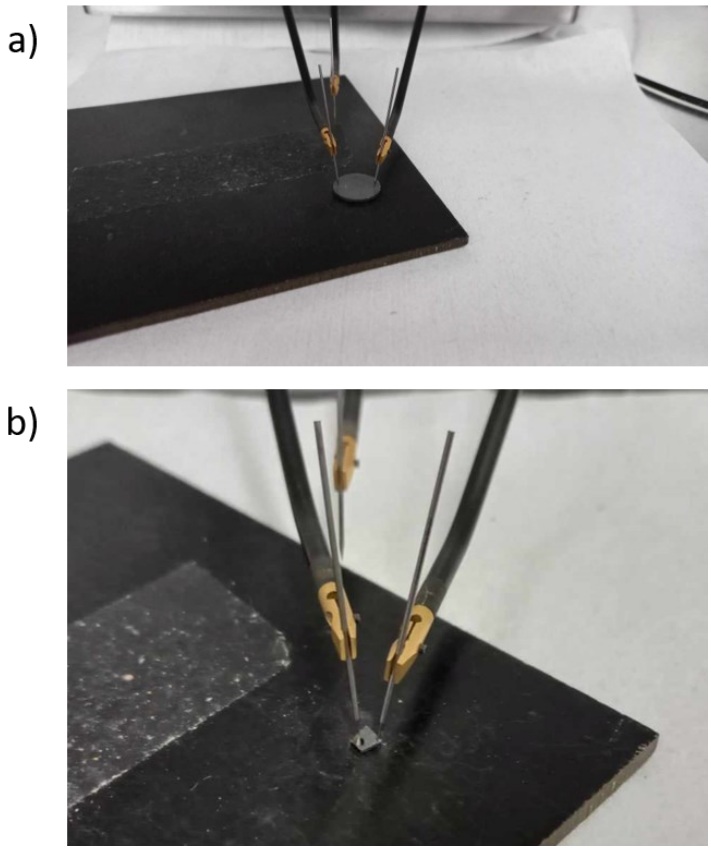

Figure 2.1: Probe setup for ex-situ voltage-current biasing experiments. a) Powder-based particle samples of LCO and LLZO. b) Thin film samples with on probe touching pristine substrate and the other the surface of the STO/LCO/LLZO or GGG/LLZO/LCO heterostructure.

Gold is deposited onto the surface of the single-layer LCO and LLZO sample set to improve conductivity with the potentiostat probes. Heterostructure samples, as well as pristine and sintered powder sample are not coated in gold as it was determined to be an unnecessary additional layer for crude biasing experiments.

IV sweeps were run using an Keysight B1500A semiconductor parameter analyser, running software by Agilent Technologies Inc. A pair of source measure units, in the form of sharpened graphite rods, are lowered onto the sample surface using the screw adjustments. These enabled precise alignment and gentle contact to be made with the surface of the thin film, substrate or sintered pellet samples. The two-probe set-up is inclusive of a common mode acting as a constant, while the second probe is a variable. The probes constitute a pair of source measure units, allowing application of potential different and subsequent simultaneous measurement of voltage and current response from the sample [199].

The voltage cycle runs were set up to sweep between two voltage limits, over 801 voltage steps, with the step size varied depending on the difference between the two voltage limits. This allowed charge cycles to occur over approximately 30 mins for each complete cycle (e.g. 4V to -4V and back to 4V).

The two-probe setup excludes a reference electrode such as Li/Li^+, limiting the accuracy of measurements given the absence of a stable reference with defined potential (Li/Li^+ $E^{\ominus}$ = -3.04 V). In addition, the probe nature of the electrochemical setup at York means that the distribution of electric field across the sample is unlikely to be uniform, potentially making the changes to the sample variable across samples surface. Ideally, a setup with a reference electrode and uniform contact across the surface of the sample would have been preferable but was not possible with the equipment available. This would be something to consider in the future, although likely more applicable to coin cells, whereas thin film samples are more compatible with the dimensions and techniques of in-situ biasing of solid-state battery lamellae.

Table 2.4: Biasing conditions applied to each type of annealed heterostructure sample. All cycles were carried out over a period of 30 minutes per cycle between the Voltage values.

Biasing range	Pristine pellet	600 ℃ pellet
2V to 4V	-	10 cycles
-6V to 6V	-	10 cycles
-12V to 12V	100 cycles	10 cycles

For PLD heterostructure samples, biasing experiments were run according to Table 2.5, to assess the effects of voltage window and number of charge cycles on the bulk crystal structure and EEI within STO/LCO/LLZO and GGG/LLZO/LCO. Varieties of voltage-current cycles were applied to samples of LCO and LLZO on STO and GGG substrates. The set-up aimed to run the current between the surface of the LCO or LLZO layer at the surface of heterostructures and pristine corner of the STO or GGG substrate (Figure 2.1, b). A constant separation distance (3 mm) between probe contacts was maintained across every sample and voltage-current cycle. To avoid shorting between the contacts if a Pt/Pd or Au coating had been applied this layer was scrapped off the corner of the sample not coated in LCO and LLZO.

Table 2.5: Voltages and number of cycles applied to heterostructures at room temperature. All samples were subjected to ten charge cycles at each voltage, with each cycle between the two-voltage values over 30 minutes.

Heterostructure	**Voltage range**
STO(100)/LCO/LLZO	2V to 4V
	6V to 0V
	6V to -6V
GGG(111)/LLZO/LCO	2V to 4V
	8V to -8V
	12V to 0V

2.4 Ion Beam Sample Preparation

Producing lamella suitable for HR TEM analysis, required cross-sections to be prepared with electron beam transparent thickness at a desired acceleration voltage. TEM compatible samples were milled from pellets and thin films with dimensions of millimetres, into micron sized rectangular wedges. Thicknesses below 150 nm were acceptable for HR (S)TEM at 200 keV, although reducing this to 100 nm facilitated atomistic imaging of phases and boundaries. The FIB utilises a dual beam setup containing a FEG-SEM and gallium ion source (GIS) to achieve respective imaging for alignment and milling of a sample from bulk to a state of electron transparency.[200-203] Secondary electron (SE) imaging, accompanied by limited exposure to the gallium beam, enabled sample alignment and tacking during milling without excessive damage [166, 204]. The angle between both sources in the FEI Nova 200 is 52°, the layout shown in Figure 2.2 [205, 206].

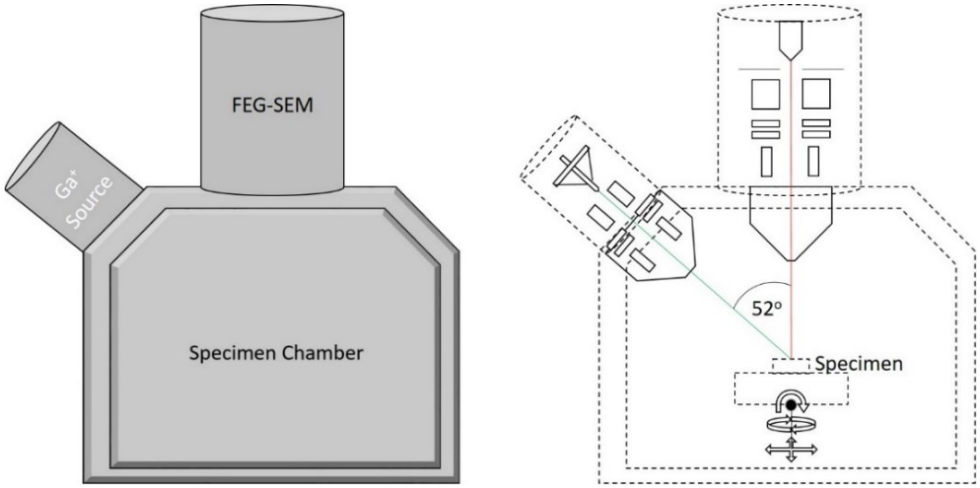

Figure 2.2: Diagram of FEI NOVA 200 FIB used throughout the project, with top mounted FEG-SEM and gallium source at 52° to the electron beam axis. Stage is mounted to the chamber door with computational and manual control of x, y, z, and rotational axis.

The steps of FIB-SEM preparation used in this project are displayed in Figure 2.3. Dwell times per pixel for electron and ion beam scanning was set to 0.3 µs, while for Pt deposition this was 1.0 µs. Standard Ga^+ beam milling operated with 200 ns per pixel during trenching and thinning of the lamella. The first step was protection of the region of interest (ROI) with platinum, using an ion beam current of 0.3 nA. Platinum is injected into the region above the sample through a needle attached to a reservoir of $(CH_3)_3Pt(CpCH_3)$. The ion beam scanned over the ROI, where transfer of

kinetic energy and heating of the local area deposited a rectangle of Pt, while the volatile organics evaporate through the beam induced heating. The following procedure was developed based on existing working practices within the facility, alongside the guidance of the FEI user manual and consideration of ion currents required to limit the damage to specimens containing Li [208, 209].

Pt coated ROI dimensions were length: 17 µm, width: 2 µm, depth: 6 µm to achieve a lamella that was durable enough for extraction and manipulation within the vacuum chamber, alongside being long enough to facilitate formation of a TEM transparent region of at least 2 µm. The rough cutting step required the use of high beam currents of 7.0 nA or 20 nA depending on the lamella size and substrate material (ALO, STO or GGG) [207]. A high current, high sputtering rate allowed for the rapid milling around the ROI. However, the greater interaction volume at large beam currents require consideration of excess milling and damage around the selected region [208, 209]. To compensate for error in the precision of milling and potential sample drift, approximately 1 to 2 µm of error was accounted for either side of the lamella to limit damage to the ROI. Significant redeposition of sputtered material also reoccurred onto the surrounding area of the sample, removed by lower ion beam currents during a later step. A milling depth of 6 microns was consistently sufficient with a 24 x 10 μm^2 region each side of the Pt region, allowing ion beam access at 0^o tilt for undercutting lamella.

After the rough milling around the ROI to achieve a lamella of suitable depth, the edges and end to be connected to the extraction needle were milled up to the Pt using a 1.0 nA ion beam. The left-most edge of the lamella remained attached to the bulk of the sample as an anchor point until lift-out was required. Using 1.0 nA allowed for formation of clean sides and ends to lamella in comparison to high beam currents. Tilting back to 0^o allowed the lamella to be undercut (1.0 nA), in preparation for extraction once the needle was attached. With the sample remaining at 0^o tilt (perpendicular to e-beam, 52^o to ion beam), the exposed edge was attached to the tungsten needle with a small region of platinum deposition (0.1 nA). Milling of the edge connected to the bulk of the sample freed the lamella, allowing for transferal to a copper grid. Platinum deposition welds the lamella to the grid, with the proceeding step being to cut the needle free. A copper grid was suitable given the absence of copper from electrode, electrolyte, and substrates.

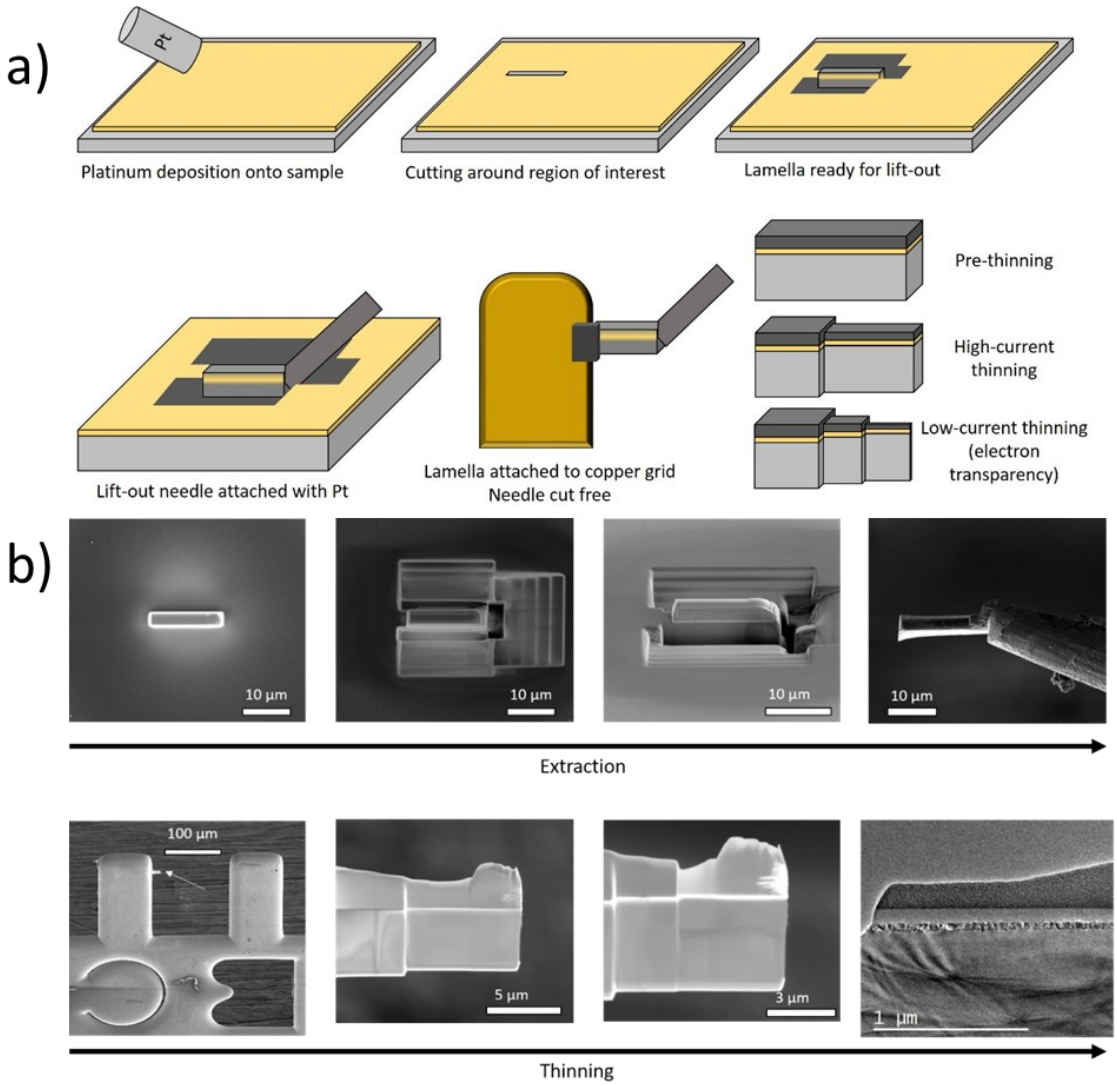

Figure 2.3: a) Schematic of process of lamella extraction from protection of ROI, through to mounting and thinning of sample to electron transparency. b) SEM images acquired during the extraction process of a lamella during the project, with the bottom right image showing the electron transparent region in a TEM after argon milling.

Low current milling is used to thin the sample to electron transparency (<150 nm thick). A slice-by-slice process is used along the front and back face of the lamella to incrementally reduce thickness. Starting at an ion beam current of 1 nA, the thickness was gradually reduced, following the steps in Table 2.6, until the contrast within the SE image acquired at 5 keV showed increased brightness in the thin region. This contrast change was indicative of sufficient electron transparency for TEM.

Table 2.6: Standard preparation steps with respective, sample tilts, alongside ion beam voltages and currents used to extract lamella, and then thin to electron transparency.

Preparation Step	Beam voltage / keV	Beam current / nA	Tilt / °	Thickness / nm
Rough milling	30	7.0	52	4000
Fine milling	30	3.0	52	2000
Undercutting	30	3.0	0	2000
Lit out	30	1.0	0	2000
Rough thinning (Front)	30	0.5	56	1200
Rough thinning (back)	30	0.5	48	800
Thinning	30	0.1	54	600
Thinning	30	0.1	50	400
Thinning	30	0.05	53	300
Thinning	30	0.05	51	200
Fine thinning	30	0.03	52.5	150
Fine thinning	30	0.03	51.5	120
Cleaning	5	0.03	45	100
Cleaning (180°)	5	0.03	45	100

2.1.1 Ion Polishing and Thinning

Further thinning and removal of gallium-damaged layers uses an argon ion-beam precision ion polishing system (PIPS) [167, 210, 211]. The PIPS setup is shown in Figure 2.4, with two ion guns, 85° apart at the front of the system, with the sample situated on a rotating stage at the centre of the vacuum chamber. A low acceleration voltage of 0.2 keV or lower allowed for reduction of sample thickness by around 40 nm to 50 nm per 10 minutes of milling. The PIPS guns were tilted to milling angles of ±6°, while the fixed sample rotates through 360°. In addition, to improve electron transparency the PIPS aided to reduce the influence of gallium implantation on AR imaging [212, 213].

Thickness of the lamella was gradually reduced at 0.2 keV until either the Pt layer was almost removed, or hole appeared in the sample. The latter is shown in Figure 2.5, where a hole formed in the LCO film after 15 minutes of milling. Either side of the hole is sufficiently thin for AR STEM. A summary of standard parameters for milling of lamella were 0.2 keV, gun currents ≈18 µA, gun tilt ±6°, modulated milling sector angles of 25°, milling duration per cycle of 5 minutes.

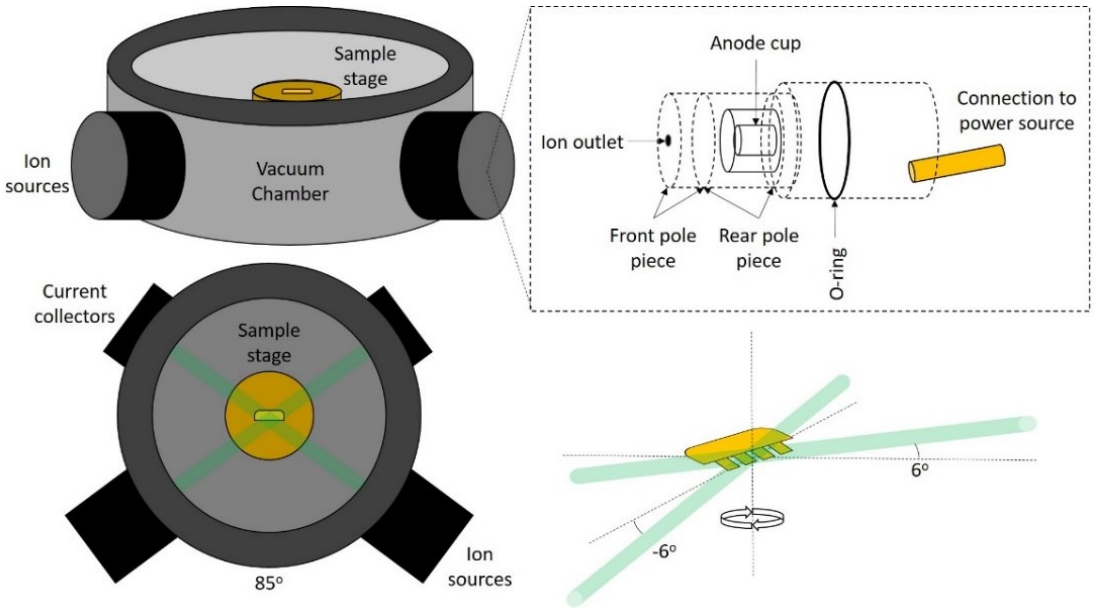

Figure 2.4: Diagram or PIPS layout with two ion guns with variable tilt angles and acceleration voltage suitable for gradual, low voltage cleaning and thinning of lamella. The sample is mounted in a central stage with 360° rotation, whereby customised milling segments allow the guns to selectively mill the lamella and avoid excessive Cu sputtering from the grid.

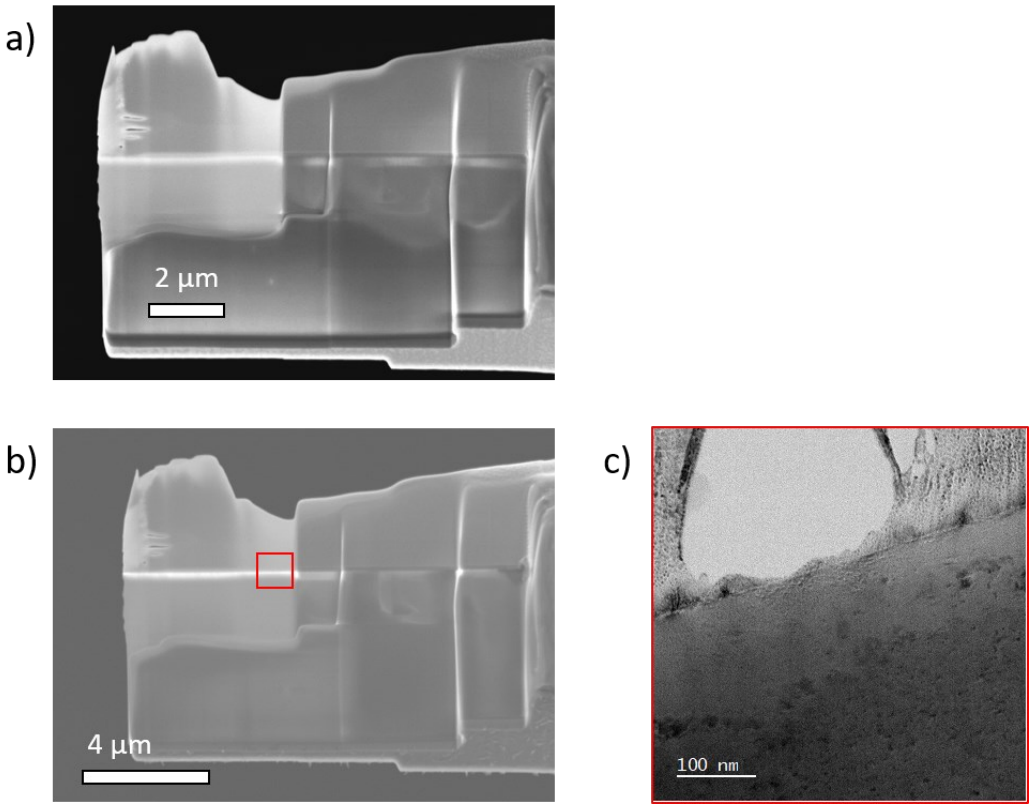

Figure 2.5: Sample before a) and after b) argon beam milling in the PIPS. The hole seen in c) formed at the thinnest region of the sample (red square) and a reference for effective sample preparation.

2.5 Scanning and Transmission Electron Microscopy for Imaging and Spectroscopic Studies of LCO and LLZO

2.5.1 Illumination Sources

To form an image in any microscope, a source of illumination in the form of particles or phonons interacting with the sample is required [214-217]. For electron microscopes, electrons ejected from the tip of a filament act as the source of illumination. In this project, applying a bias of between 5 keV and 300 keV accelerates electrons from the source's tip towards the sample.[218, 219] The SEM and TEM at York, SuperSTEM and ePSIC utilise either tungsten, LaB_6, Schottky-FEG or cold-FEG filaments (Figure 2.6). Each source has their own operation parameters, characteristics and design, with maximum brightness and obtainable resolution [220]. Common operational parameters for electron sources are shown in Table 2.7 [221].

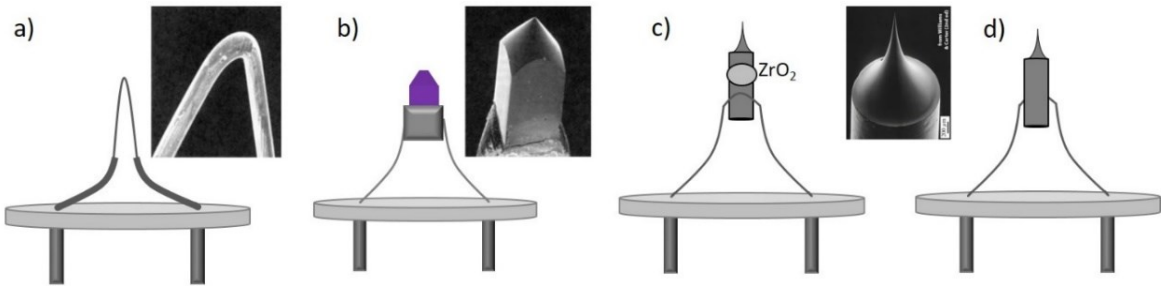

Figure 2.6: Thermionic and field emission source images and diagrams showing differences between a) tungsten, b) LaB_6, c) Schottky-FEG, with ZrO_2 reservoir, and d) cold-FEG sources. SEM images of source tips acquired from figures in references [222] and [216].

Ensuring the tip of a field emission source remains pristine required periodic removal of contaminations that reduce probe currents and increase the energy spread (ΔE) of the electron source. This is a significant disadvantage with respect to chromatic aberration and spectroscopic analysis (EELS), as well as lowering brightness, signal-to-noise ratios and therefore attainable resolution. The established method for contamination removal requires the gun to be heated to high temperatures [223]. This method was used prior to beam emission on the JEOL ARM200CF, ARM300CF and NeoARM instruments at ePSIC and York respectively.

Table 2.7: Important operational parameters of thermionic and FEG electron sources used in electron microscopes. Informed by reference [224]

	Tungsten	**LaB_6**	**Schottky-FEG**	**Cold-FEG**
Work function / eV	4.5	2.4	2.8	4.5
AC / $Am^{-2}K^2$	6×10^5	4×10^5	-	-
T / K	2700	1700	1800	300
Cross-over size / µm	50	10	<1	<0.01
Brightness / $Am^{-2}sr^{-1}$	$\times 10^9$	$\times 10^{10}$	$\times 10^{11}$	$\times 10^{12}$
Energy spread (ΔE) / eV	3	1.5	≈ 0.8	≈ 0.3
Required vacuum / Pa	10^{-2}	10^{-4}	10^{-8}	10^{-8}
Lifetime of source / hr	100	500	>1000	>1000

For the same emission current from different electron sources, the ability to focus the available current onto the first cross-over point determines the obtainable resolution of the microscope. A smaller diameter of the first-crossover point is achievable for FEG sources, compared to thermionic sources (Table 2.7), enabling higher resolutions to be achieved. The smaller the cross-over point, the higher the required source brightness, in order to ensure the beam has sufficient current density to generate a signal on the subsequent detectors. A smaller probe also requires less work by the electromagnetic lenses to demagnify the beam into a usable probe. These parameters of cross-over and high source brightness enable microscopes fitted with field-emission source to achieve the highest resolutions.To achieve transmission images of samples and acquire images at the ARs shown throughout this project the electrons are accelerated to velocities where relativistic effects become influential. Equation 7 describes the relativistic wavelength (λ) of an electron accelerated within a TEM. The mass and charge of an electron are m_e and e respectively, whilst h is the Plank constant and c is the speed of light in a vacuum. Relativistic effects are fundamental to electrons accelerated to the velocities of voltages on the order of keV. The theoretical maximum obtainable resolution is related to this wavelength alongside the aberrations induced by the magnetic lenses [225].

$$\lambda = \frac{\mathrm{h}}{\sqrt{2m_e eV\left(1+\frac{eV}{2m_e c^2}\right)}} \qquad \text{Equation 7}$$

The JEOL 7800F Prime SEM utilised a Schottky FEG, while the JEOL 2100+ TEM operates with a LaB_6 and JEOL ARM200CF and NeoARM STEM instruments operated with a cold-FEG.

2.5.2 Scanning Electron Microscopy

The JEOL 7800F Prime SEM provides topographic imaging with spectroscopy evaluating composition near the sample's surface. Layout of lenses and detectors is shown by the diagram in Figure 2.7. Applications within this work focus on bulk samples prior to creating a TEM transparent cross-section or viewing the TEM cross-section prior to loading into the transmission microscope. SEM of particle and thin film surfaces and lamella included; chemical mapping and phase analysis using EDS and EBSD, aiding selection of regions of interest to focus on in the TEM.[226-229] The JEOL 7800F Prime utilises a Schottky-FEG source with applied potentials between 1 keV and 30 keV, depending on the desired approach to imaging and spectroscopic data collection for each sample. Probe currents could range from 0.01 nA to 40 nA depending on the combination of probe current, acceleration voltage and aperture size (30 µm to 110 µm).

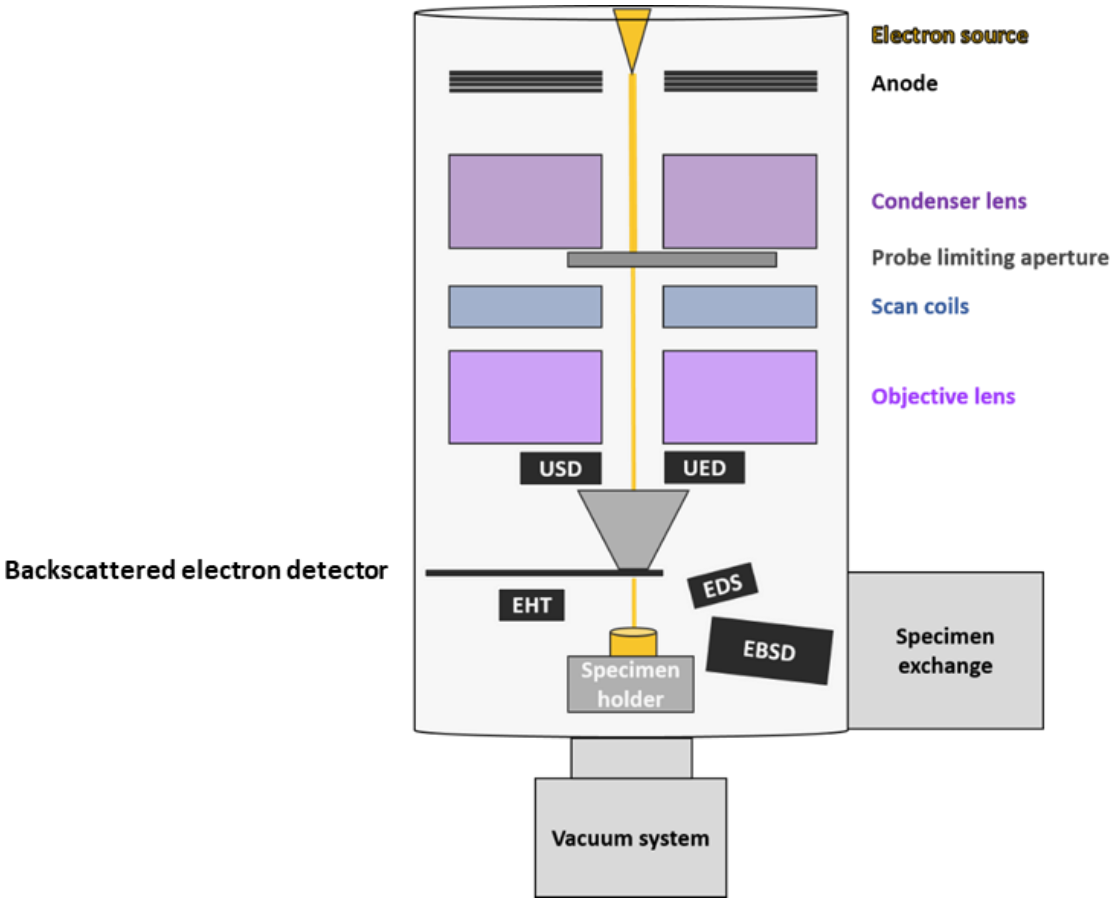

Figure 2.7: Diagram of SEM showing a standard aperture and lens arrangement in the JEOL 7800F Prime, with positions of detectors required for various imaging and spectroscopy modes including Everhart-Thornley Detetcor (EHT), SE, BSE, EDS and EBSD.

Elastic scattering of incident electrons follows the principles of Rutherford scattering, with a dependence on the average atomic number (Z) of the ROI [230-232]. Interaction volume with the sample reduces at lower beam energies or higher atomic mass, allowing analytical backscattered electron (BSE) imaging [233, 234]. At incident electron beam operating voltages over a few keV, the energy difference between BSE and SE is significant (Figure 2.8). BSE detectors positioned above the sample maximise collection efficiency, allowing less obstructed SE collection from an offset Everhart-Thornley detector.

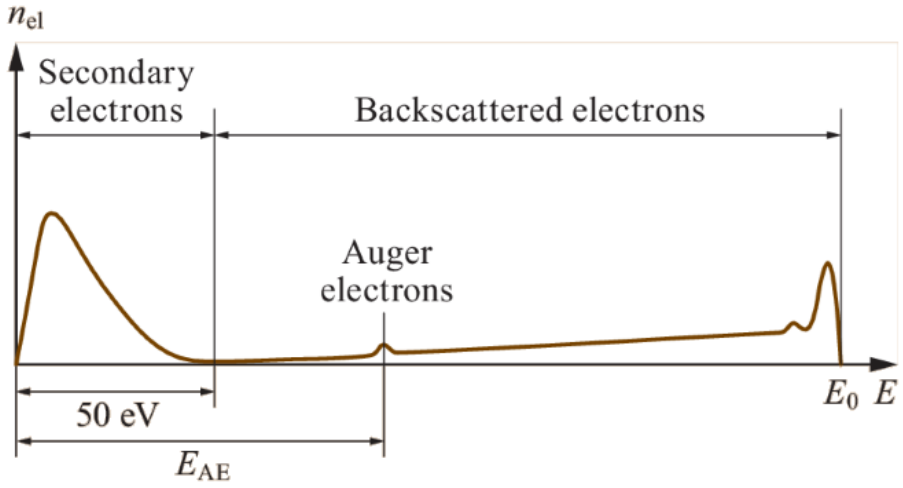

Figure 2.8: Plot of signals with repect to the beam energy E_0. Positions are indicative of their approximate energy dispersions that enable SE, Auger electron and BSE signals to be distinguised. BSE electrons possess energies similar to the incident beam E_0 (keV), while SE electrons have energy distributions on the scale of eV. Figure reprinted from reference [235].

The detectors within the JEOL 7800F Prime include an EHT, EDS and EBSD within the specimen chamber. Enhancing collection of SE is achieved via the use of detectors with an applied bias, the EHT in the JEOL 7800Prime detector is equipped with a faraday cage for this purpose. Given SE electrons have low energies relative to elastically scattered BSE, they are easily deflected by an applied positive electric field [236]. Applying a positive bias to the EHT cage attracts the low energy electrons meaning images are dominated by the SE signal. For BSE detectors, with geometry and working distance influence collection efficiency, with in-lens detectors requiring working distance of 2 to 4 mm used for sufficient signal-to-noise [237, 238]. Additional in-lens SE and BSE detectors are present above the pole piece and were utilised for short working distance. These enabled image acquisition across rough surfaces of PLD thin films, with crystallite features on the scale of tens of nanometres, requiring higher resolutions of imaging than the EHT provides.

For particle samples, SE and BSE imaging were used to assess porosity and compositional variation across the LCO/LLZO particle heterostructures. The Z dependant BSE signal contrast on allows analysis of areas within LCO/LLZO particle mixtures where EEIs were present for subsequent extraction of LCO/LLZO interfaces using the FIB. Imaging conditions with sufficient signal-to-noise and resolution acquired between 15 keV and 30 keV, with apertures of 30 µm and 50 µm providing control of current density. LCO and LLZO were stable at these voltages and tens of nanoamps of beam current for exposures lasting of several seconds (LLZO), to minutes (LCO).

2.5.3 Energy Dispersive Spectrometry

EDS is the use of the characteristic x-rays produced during inelastic electron interactions with elements comprising a given specimen in the SEM or TEM. Detection is achieved using a silicon drift detector (SDD) whereby incident x-rays are converted into electrical signal in a similar manner to backscattered electron detectors [239]. X-ray collection efficiency is dependent on the solid angle of emission from the sample. Two EDS detectors (Oxford Instruments, Ultim® Max, supported by Aztec software) were used in combination around the sample to increase collection angle for standard EDS acquisition [240]. One EDS detector was used above the EBSD detector when collecting EBSD and EDS data simultaneously. The processing time was adjusted depending on the number of x-rays emitted from the sample in the direction of the detector(s), with lower processing times used for powders and high values for lamella or combined EBSD-EDS experiments. This provided the ability to enhance the count rate alongside the use of apertures detailed below.

The radiative transitions between energy levels are characteristic of each element in the periodic table. Electron energies can be characterised as shells, labelled K to O in (Figure 2.9) relating to the specific electron orbitals to the 1^{st} (1s) 2^{nd} (2s, 2p) etc., with relaxations to the K shell (n=2 ➔ 1, n=3 ➔ 1 etc.) designated as K transitions. Suitable acceleration voltages were between 20 keV and 30 keV to facilitate detection of the Zr K-edge at 15.7 keV. A 30 µm aperture was frequently used, with the 50 µm diameter required when low count rates became a limitation, for example with lamellae thicknesses below 150 nm, where electron transmission through the sample increases. Electron beam and detector collection conditions ensured input counts rate exceeded 2×10^5 counts per second and detector dead times were above 20% but did not exceed 90%. Pixel resolution were either 1024×1024 or 512x512, depending on sample dimensions and desired scan rate.

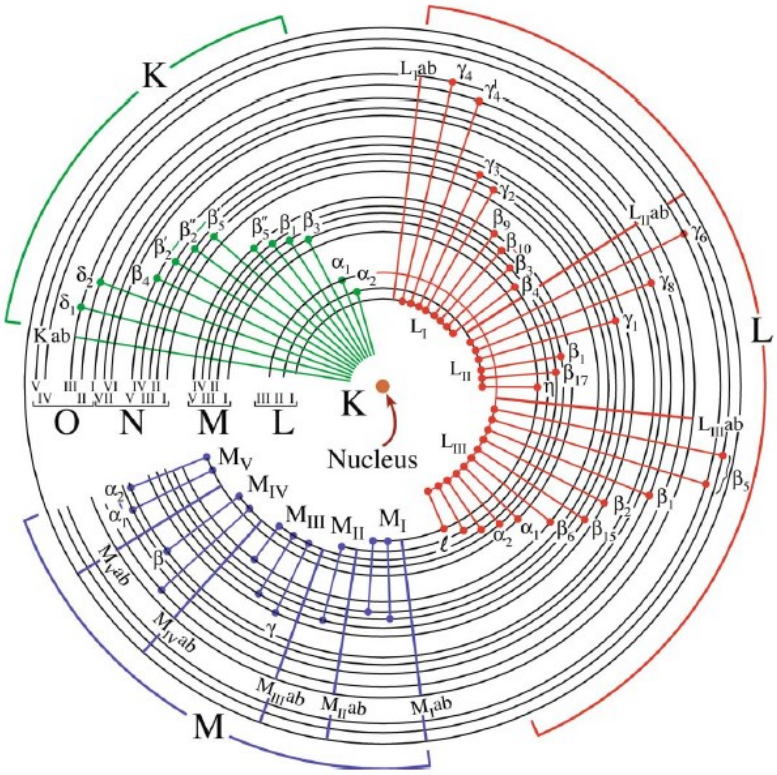

Figure 2.9: Characteristic EDS signals, relating to transitions between electron orbital energy levels within atoms. Illustration repsrinted from reference [225].

2.5.4 EBSD to Map Crystal Phase, Orientation and GB

Mapping crystal phase and orientation within complex samples can be a labour-intensive process, using diffraction patterns and local chemical data. EBSD utilises the patterns created bybackscattered electrons from crystal planes satisfying diffraction conditions, to determine phase, orientation, and boundaries between grains across the surface of a sample. This enabled analysis of phase variations and grains across suitable samples, whereby phase distributions, composition and structural characteristic can be determined [241]. The EBSD system comprises a phosphor screen detector (Figure 2.10); the sample was tilted to 70^{o} to align the diffracted electron with the detector and maximise signal. Working distance within the SEM was set to 14 mm to align the diffraction pattern with the phosphor screen.

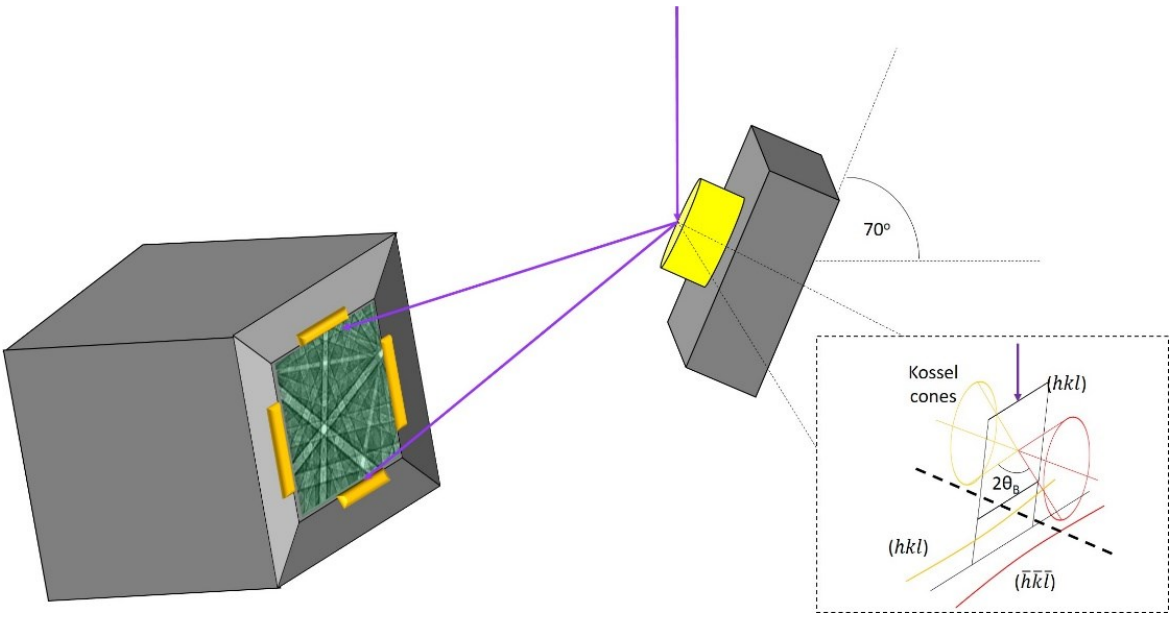

Figure 2.10: Diagram of EBSD dector positioned at 70° to the sample surface with inset diagram of Kikuchi line formation from crystal planes within the sample, leading to the projection of diffraction pairs (hkl) and ($\overline{\text{hkl}}$) onto the detector.

Applications for particle cross-section lamella of LCO and LLZO included; band contrast mapping to reveal GB within materials, phase detection if a sample contains two or more crystal phases, and orientation mapping to determine the orientation of each unique phase.[242] Data was collected using electron beam voltages of 25 keV and 30 keV, with an aperture size of 50 µm. The software requires informing of anticipated phases through atomic coordinate files (e.g. .cif) relating to LCO and LLZO, acquired from the Materials Project or literature published on the ICSD database [44, 51]. Detector exposure, adjusted within the software, optimised Kikuchi pattern signal-to-noise without overexposure, thus optimising detection of phase and orientation. Exposure times are varied within the magnitude of 10^2 ms. Image resolution was 622 x 512 pixels or 1244 x 1024 for sensitivity and resolution options respectively. The scale of PLD thin films were not compatible with the resolution achievable in the JEOL 7800F Prime.

For both the EDS and EBSD data, Aztec software from Oxford Instruments was used to interface with the detectors and construct associated elemental maps (EDS), as well as grain, phase and orientation maps (EBSD). EDS was acquired simultaneously with the EBSD to support identification of the phases within the grains or particle-based lamellae.

2.5.5 Transmission Electron Microscopy

Transmission electron microscopy can facilitate the observation of specimen structure from micron down to atomic spatial resolutions of 0.2 Å [243]. This allows for viewing and analysis of crystal structures, defects and chemical compositions where specific characteristics can reside over only a few nanometres. To improve the achievable resolution and simultaneously collect spectroscopic data, aberration correction and accompanying spectrometers for x-ray and inelastic collision analysis have been developed. The JEOL 2200FS, ARM200CF, ARM300CF, and NeoARM all make use of aberration correction and a combination of EDS, EELS or both. The parallel beam of conventional TEM (Figure 2.11, a) provides the capability for BF and DF imaging, alongside diffraction from selected areas. STEM (Figure 2.11, b) supported the acquisition of AR images through access to aberration-corrected microscopes, alongside EDS and EELS data relating to each probe position within the sample [225]. 4D-STEM in the form of pencil beam diffraction provides potential insight into nanograin phase and orientation within thin films samples.

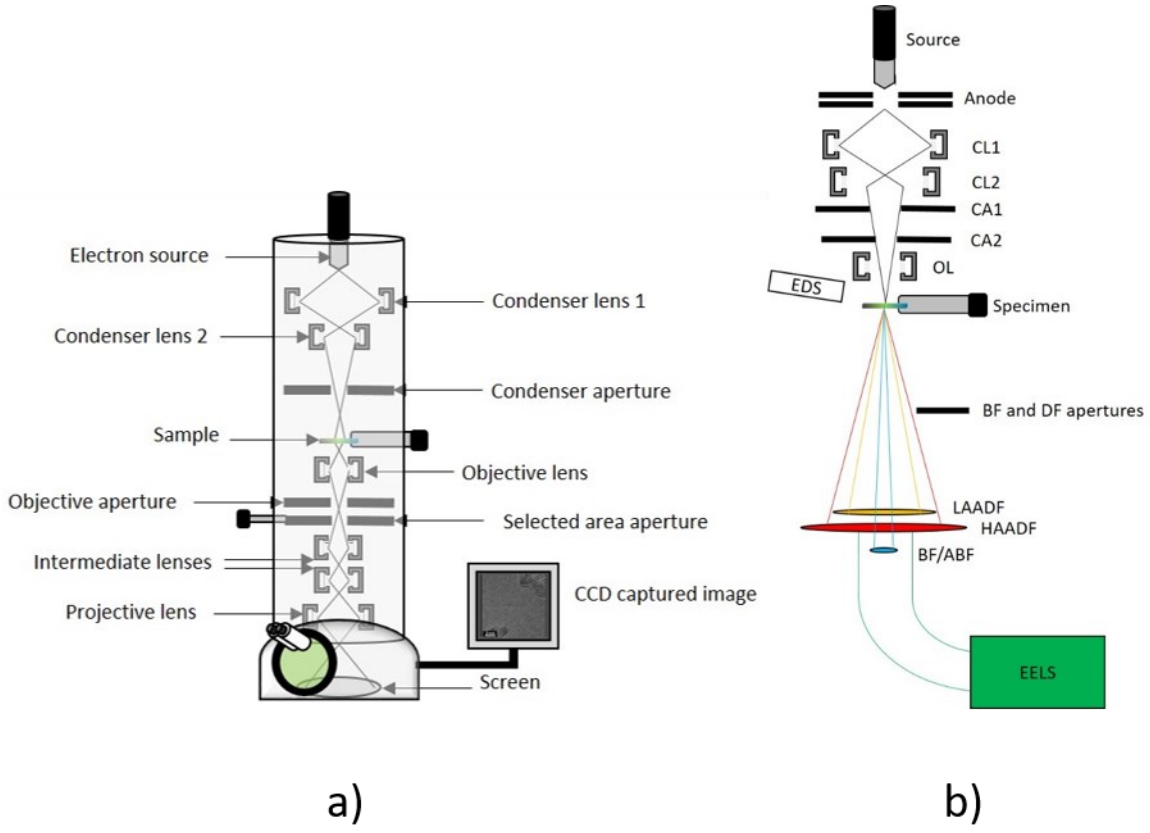

Figure 2.11: Schematic of a) conventional TEM and b) STEM setup illustrating electron path, condenser lenses (e.g. CL), apertures (e.g. CA) sample location and common detector positions.

To acquire projected images at various magnifications, electrons with sufficient energy to penetrate through the atomic lattice of a material, without excessive backscattering from within the lamella's thickness, are required. While in TEM and STEM modes, electrons between 30 and 300 keV passed through sample sufficiently thinned by the FIB [244]. Samples were thinned to at least 150 nm for 200 and 300 keV studies, with sub 100 nm thicknesses required for analysis with beam energies as low as 30 keV. Maximum theoretical resolution of the image is dependent on electron source as well as the specimen, design of lenses and aberration corrections in advanced microscopes [225, 245]. The focusing of electrons is achieved using a sequence of cylindrical lenses comprised of a coiled copper wire, wound around a soft iron core of each pole piece. The field strength for a given lens current is uniform within core of the lens, with the field strength tailing off at the edges of the entry and exit of the lens. Equation 8 describes the force on the electron within a magnetic lens at a given distance from the optical axis.

$$F = evBsin(\theta) = evB = \frac{mv^2}{r} \qquad \text{Equation 8}$$

F = force on electron, e = electron charge, E = electric field strength, v = electron velocity, B = magnetic field strength, m = mass (electron), r = radial distance of electron from optic axis, Θ = angle between electron velocity and magnetic field.

Resolutions achievable in STEM mode are dependent on the probe size and have the potential to exceed standard TEM imaging [225, 243]. However, the ability to run electron beams at energies in the MeV range, providing electrons with sub-angstrom wavelengths, alongside aberration correction in both STEM and TEM, means modern instruments have comparable resolution values. TEM has the advantage of spreading electron dose over a wide area for beam sensitive materials (e.g. Li electrolytes), although dose can also be controlled within modern STEM instruments through use of rapid exposure techniques. STEM has the advantage of providing local chemical and bonding data through precise positioning of the electron beam in probe form [216].

Within this project systems of two condenser lenses is used in JEOL 2100+, NeoArm and ARM200CF microscopes, while the ARM300CF uses three condenser lenses. These define the beam spread and illumination intensity; this is in combination with the condenser apertures (CA). The first condenser lens (CL1) operates on the electron beam after emission from the source and determines the spread of the beam passing through the second CL. A more excited first condenser lens (CL) allows a few electrons to pass through CL number two (CL2). Therefore, the condenser aperture determines the maximum spot size obtainable after CL1 has focused the beam. CL2 then focuses the electrons, converging the beam around the area of interest on the specimen. In the JEOL 2100+

this convergence formed a parallel beam condition for TEM imaging, while in the other microscopes the beam is converged into a probe for STEM imaging. Varying the post-sample intermediate lens conditions allows extraction of either an image, or the diffraction pattern from within the image forming plane (Figure 2.12).

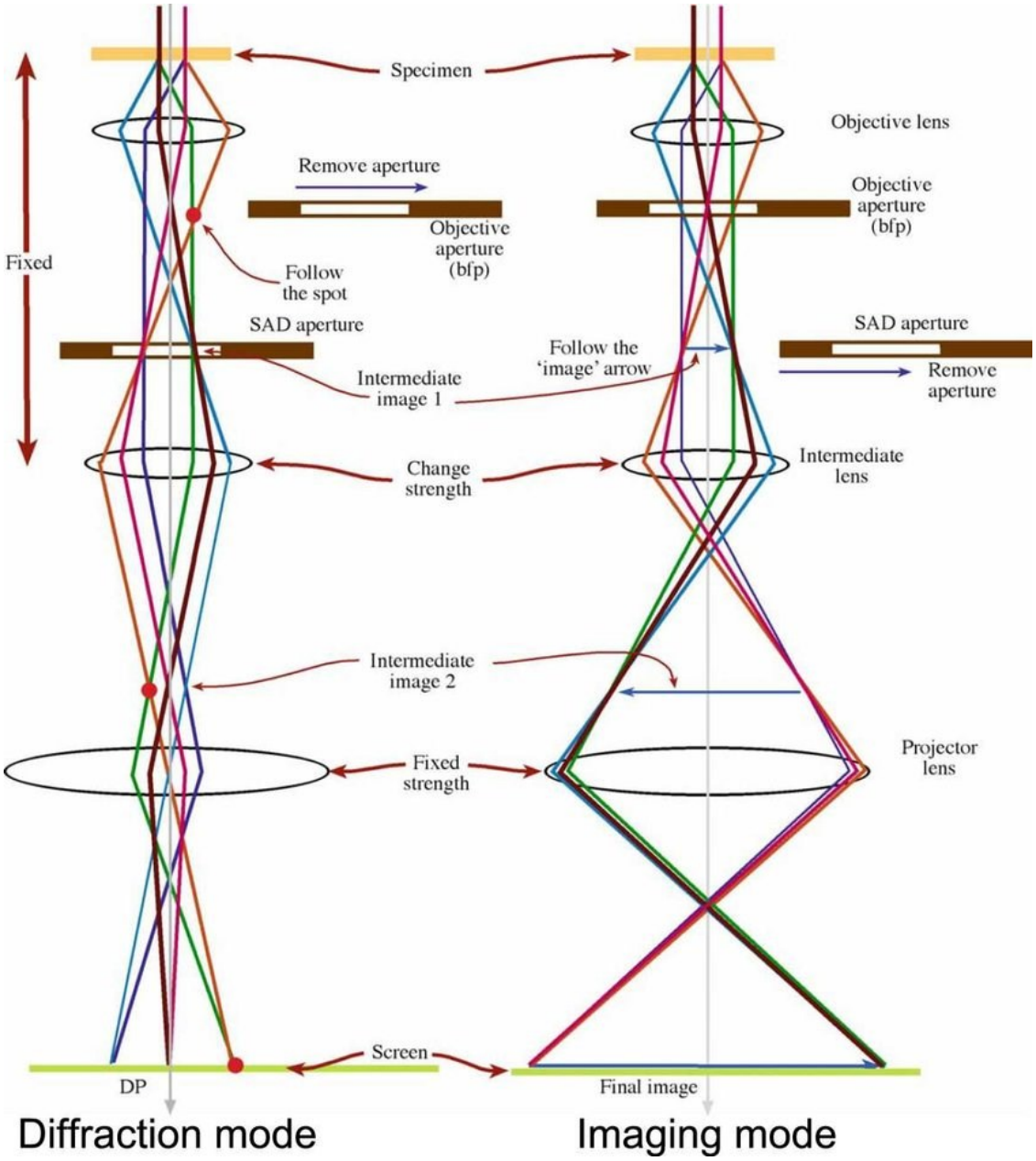

Figure 2.12: Diagrams showing difference between image forming (right) and diffraction mode (left) in TEM. Variation in the intermediate lens condition determines the resultant observation on the screen or camera. Introduction of the OA enhances contrast between diffracting planes by blocking higher-order diffractions at greater distances from the optical axis figure reprinted from reference [225, 247].

2.5.6 Apertures

The condenser aperture (CA) controlled the probe current/electron dose reaching the sample, as well as influencing the angular spread of electrons passing through the microscope. This also serves the role of controlling the maximum semi-angle of the electron beam, also limiting the extent to which the image suffers from spherical aberrations. The most common aperture diameters used in the JEOL 2100+ were 100 µm and 250 µm. For nanobeam diffraction the smallest (10 µm) CA was introduced for analysis with spot sizes of 5 nm to 15 nm. In the ARM200CF and NeoARM CL2 diameters were selected as 30 µm or 40 µm depending on the size of the aberration free region of the Ronchigram. Specific beam currents for camera lengths and apertures can be found on the ePSIC/Diamond Light Source Website.[248]

Objective apertures (OA) allowed for selection of specific proportions of the waveform emitted from the sample. Inserting a centrally aligned OA will select the central spot containing the bright-field information, while the size determines whether spots or rings diffracted away from the central axis are included. The narrower range of signals collected by the projector lens systems allows for greater contrast between diffracting and non-diffracting regions of the sample.[225, 249] They are used within literature and this project to create annular BF or DF images in a STEM system by blocking the angular distribution relating to the direct beam.[250]

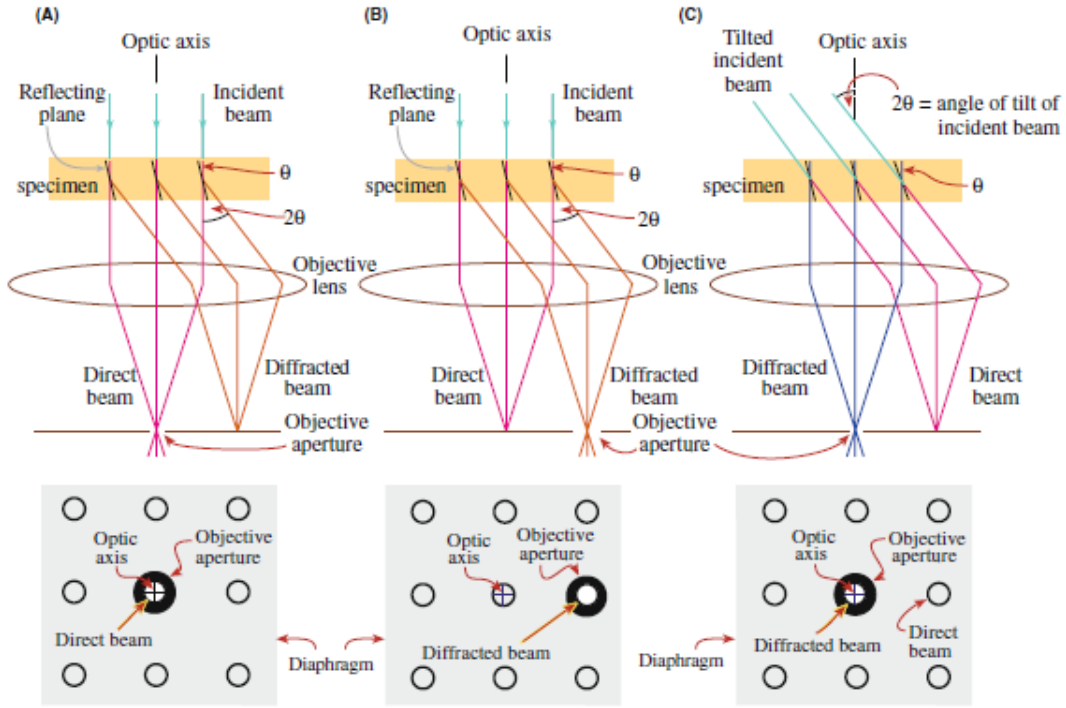

Figure 2.13: a) BF imaging condition with no offset OA or beam tilt. b) Shift of OA to align with a desired diffraction condition. c) Beam tilt with central OA alignment whereby the beam tilt matches the Bragg diffraction condition of the crystal plane of interest. Figure acquired from reference [225].

Using an OA heightens the contrast between the strongly diffracting crystallite and surrounding film. Using quadrupoles to tilt a diffraction spot in the DF onto the central axis of the image formation plane allows a small OA to select the signal provides within this part of the wave function. Using a sufficiently small OA to select either the BF or any DF spot allows for formation of a BF or DF image through re-selecting the image forming mode [225], These images can provide information on the regions of crystalline materials contributing to specific diffraction spots, for example phase and grain distributions and defect orientations [251-253]. For DF imaging of boundaries and defects in LCO the second smallest OA was used (20 μm). Owing to the spacing of intensities in the LLZO and LZO DPs, DF imaging was best approached with the smallest 5 μm OA in the JEOL 2100+.

2.5.7 Aberration Corrected Imaging

Modern microscopes can achieve ARs (0.2 Å) not only through improvements in gun brightness, stability, and energy monochromator but also the introduction of effective correction of aberrations of higher orders. Spherical aberration can simply be offset using a lens acting in convex fashion to correct for the difference in electron focal points as a function of orbit radius. To achieve correction of the spherical beam's aberrations the spherical symmetry must be broken and then refocused to achieve a common focus point for a greater angular radius of the electron beam. Higher-orders of aberration correction are achieved through the reduction of contributions from two- to five-fold astigmatisms, comma, and aberrations. Depending on the symmetry of the aberration, either a hexapole or octupoles/quadrupole arrangement is required for odd- or even-fold aberrations respectively [225]. A hexapole creates triangular distortion to the incident electron beam, allowing adjustment to odd orders of aberration, while quadrupoles and octupoles create square distortions to the spherical symmetry of the electron beam, correcting aberrations, and stigmatisms with even-fold symmetries. The corrections are achieved by computationally determining the beam tilts, shifts and defocus required to offset the aberrations in the uncorrected beam of spherical symmetry. The software (JEOL COSMO) controlling the lenses and high-order aberration correction, determines the amplitude of the aberration based off a under focussed Ronchigrams of an amorphous region of sample (e.g. carbon or platinum). Iterative steps are applied to correct aberrations to values suitable for atomistic BF and high-angle annular dark field (HAADF) imaging [254].

2.5.8 Detectors

In a TEM the position of detectors, relating to image formation, is below the specimen and proceeded by a set of projector lenses. The JEOL 2100+ TEM utilised a CCD for signal collection relating to the chosen BF or DF imaging condition. Exposure times of between 1 second for DP acquisitions, to protect the detector from overexposure, between 1 and 4 seconds for BF and up to 40 seconds for weak beam DF images were used. Some variations outside of these ranges were required for thin or thick regions of certain samples. The exposure for each sample and image accounted for the intensity of the beam for a given CA or spot size, alongside the brightness for a near-parallel beam condition at specific magnifications within the range of x8000 to x800k.

STEM detectors take the form of radial discs with holes in the centre. Similar to BSE detectors in the SEM section, these convert the energy supplied by the scattered or direct electron beam into charge through a p-n junction or photomultiplier tubes (PMTs). The semi-angles of collection are important with respect to the probe's convergence angle [225, 255]. The diagrams in Figure 2.14 show detectors up to the convergence angle (α) of the STEM probe can be used for BF and annular bright field (ABF) imaging, where the sites of atomic columns are dark. Wider-angle detectors with central radii above the probe's convergence angle translate the detected electron signal to an ADF or HAADF image. Based on the instrument parameters relating to the ARM200CF, ARM300CF and NeoARM, camera lengths between 8cm and 20 cm are used in conjunction with a specific radius of CA, such that the convergence angle is suitable for ADF or HAADF imaging. This information is provided within the instrument calibrations ePSIC provide online, as well as in the instruction manuals [248].

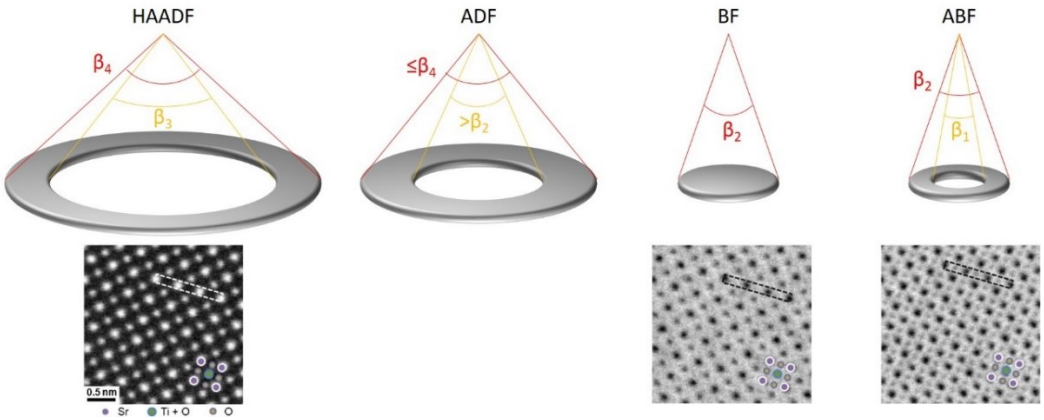

Figure 2.14: Annular detectors, where inner and outer collection angles of the detector are fundamental to the image contrast observed. The collection angle is dependant on apertures and camera lengths selected by user, with values commonly differing between specific makes and models of microscope. Example images acquired from reference [256].

To effectively deal with the lower signal incident at high-angles onto the HAADF detectors, low-noise electronics, and scintillator/photomultiplier tubes are commonly utilised to ensure suitable signal-to-noise ratios. These can detect electron signals at low fluxes, amplifying low signal count rates, optimising the contrast in images formed from the information detected by angular detectors [257].

The direct beam contains wave front information where atoms have deflected intensity away from the optical axis. While a mass relationship influences the intensities in the image to the intensity/contrast of the image, the direct beam is coherent and thus contrast depends on additional components, hence intensity doesn't directly relate to the mass of the atomic columns [258]. The use of ABF detectors excludes the direct beam, utilising the electrons scattered at small angles. ABF utilises either a annular detector or aperture blocking at least half of the internal semi-angle of the BF detector. This can enhance the contrast of the signal detected, enabling easier observation of light elements (e.g. Li) and low-mass atomic columns, simultaneously with heavier atoms, within an ABF image [259]. The feasibility of light element detection is proven with the resolving of single Li atoms in battery materials [256, 260]. As the intensity scales with the atomic mass of the elements illuminated by the probe, HAADF is effective in regions containing elements that have sufficient scattering coefficients to provide adequate intensity at high collection angles [261]. It makes compositional information can be assessed with HAADF as the intensities relate to the Z-number of the elements in the atomic column illuminated by the probe. The limitation with HAADF imaging providing atomic mass information for both heavy and light elements, for example within battery materials containing Li and La. This is related to the contrast difference between the two extremes being dependant on the square relationship between HAADF contrast and atomic number of the element. For example, in LLZO the atomic mass of La (Z=57) and Zr (Z=40) is far greater than Li (Z=3) and O (Z=8), making the latter elements challenging to observe in the image contrast relating to the scattering coefficients, hence La, Zr, O and Li intensities collected by a HAADF detector. ADF imaging collects electrons at lower scattering angles as potentially has applications for strain mapping in SSB materials [262]. All imaging conditions were applicable to samples containing LCO and LLZO with collection of BF, ABF and HAADF images consistently made on the JEOL ARM200CF and NeoARM STEM microscopes.

Typical STEM imaging conditions for the ARM200CF and ARM300CF were 12cm camera length, with a condenser aperture of 30 µm (semi angle: 23.0 mrad). EDS and EELS data was collected with the same convergence aperture but with a 3 cm camera length. Images on the ARM300CF were collected with either a 40 µm (semi angle: 33.6 mrad) or 50 µm (semi angle: 44.0 mrad) condenser aperture, in tandem with a 12 cm camera length. The condenser aperture diameters were selected based on the quality of the Ronchigram with respect to the semi-angle of

the aberration free region. Further details of beam currents, calibrations and semi-angles for various condenser lenses and camera lengths are available on the ePSIC (Diamond Light Source) confluence pages via references [248, 263]. On the ARM200CFthe JEOL BF, ADF and HAADF were used for image acquisition, while BF and HAADF detectors on the ARM300CF where used for image acquisition. On the ARM300CF an aperture was used to mask the centre of the BF detector for ABF imaging with a detector inner angle of 10.0 ± 1.3 mrad and outer angle of 20.8 ± 0.2 when using a 12 cm camera length.

2.5.9 Reducing contamination

The use of a cold trap within the instrument acts as a collection point for material or contamination emitted from the surface of the sample holder during (S)TEM experiments. The temperature gradient draws molecules onto the surface, cooled by liquid nitrogen. Consequently, improvements in vacuum quality around the sample are achieved, alongside avoidance of contaminants collecting on the pole-piece of the microscope. All TEM and STEM imaging was conducted with the use of the cold-trap installed on all instruments.

Contamination of the sample can also be a common problem, significantly limiting the achievable resolution across a given region. Carbon-based contaminants can be ablated and redeposited by the electron beam onto the surface of the sample, creating regions of contamination. This layer of carbon both increases sample thickness and obscures the atomic columns within the sample. To limit this type of contamination a ‘beam shower’ was used, exposing samples to a broad electron beam for several minutes to clean the surface of volatile hydrocarbons contributing to the contamination. Alternatives for beam sensitive materials included contamination reduction procedures prior to loading into the microscope, such as pre-pumping the specimen in the sample holder, low voltage argon or xenon ion milling of surface layers, or plasma cleaning. All methods were attempted during the project to varying success.

2.5.10 Spectroscopy in TEM and STEM

Chemical data can be acquired in both TEM and STEM microscopes, with the latter being able to resolve the composition of neighbouring atomic columns. The deflection of the beam in STEM mode is such that probe movement occurs without tilt effects with scan directions and patterns allowing control over aspects including specific illumination area and exposure time [264, 265]. The dwell time of the probe provides the signal at each position analysed, requiring consideration of maximum dose limits for each material, alongside obtaining sufficient signal counts for EELS and EDS acquisitions [266-268]. Potential exposure times vary greatly, between

nanoseconds for rapid in-situ or beam sensitive sample measurements, up to seconds for higher resolution EELS and EDS data acquisitions [269, 270]. Conditions used for imaging and spectroscopy of particle and thin film sample are covered below.

Acquiring chemical information from samples subjected to incident electrons is also achievable in TEM. However, for electrons with sufficient energy to penetrate a thin specimen it is possible to acquire chemical energy signatures in the form of X-ray or inelastic electron energy losses between source/pre-specimen and post specimen. EDS operates by the same principals as discussed in the SEM section, with the detector positioned just above the sample. In contrast, for electron energy loss spectroscopy (EELS) the energy loss detector on the ARM200CF and NeoARM was positioned at the end of the microscope column [225, 271]. The advantage for TEM-based EDS acquisition is the better vacuum conditions that enable the use of windowless detectors with improved efficiencies and potential for detection of light elements [260]. The lowest energy X-rays emitted from a given sample's surface are not blocked by the detector's window, potentially allowing signals relating to Bi, B and Li to be observed in EDS spectra. Li detection is likely to still require materials suitable to producing detectable quantities of Li signals, alongside specialised equipment and conditions including stable microscope environments and low-noise electronics [272].

Li has an EELS K-edge around 55 eV and requires a detector and signal that can resolve this peak from the zero peak and background signal. Detection of Li has been possible within EELS studies into Li_2CO_3 and Li_2O. These published articles highlight the need for the system to be sufficiently Li rich to produce an adequate signal strength for the K-edge. In addition, the 2S orbital needs to be occupied to facilitate the production of the K-edge signal [272]. The Li K edge is absorbed by the window (Be, silicon nitride or thinner polymers) of a standard EDS detector, requiring a windowless detector to collect the Li signal [26]. Energy resolution of the EDS and EELS detectors lay was expected to be below 2 eV, theoretically allowing characteristic signals from all elements to be resolved. However, the low intensity, broadness and background signals in EDS and EELS spectra limited the detectability of Li signals.

The EELS signal is a result of inelastic collisions that transfer of momentum from the electron in the incident beam to an electron in the orbital space of a constituent atom. If the energy transferred matches that required for a core electron to be ionised up to a higher, unoccupied orbital within the atom, this equates to a defined energy transition in the core-loss region of the EELS spectrum (usually above 100 eV). Ionisation of electrons in valence or weakly bound orbitals lead to a lower energy loss during the inelastic collision, therefore these energy losses are in the low-loss region, where the broad plasmon peak also resides [270]. This is in contrast to EDS where transitions are the result of radiative relaxation of electrons into orbitals from which electrons have

been ionised or excited from, leading to emissions of photons with wavelengths in the X-ray range. K-edge transitions describe the inelastic energy transfer with the innermost orbital (1s), L-edges relate to the 2p orbitals, M to the 3p and d orbitals and so on. The subsets (e.g. L_1, $L_{2,3}$) relate to the specific fine structure separation of characteristic peaks determined by the different spin states of electrons in occupied orbitals. The $2s_{1/2}$ (L_1) will have distinctly different energy signature compared to 2p ($L_{2,3}$). However, the two possible spin states in the p orbital ($^1/_2$ and $^3/_2$) equate to a small shift in energy loss of between below one and a few electron volts. The low-loss and core-loss energies for elements within LCO and LLZO detailed in Table 2.8, required consideration of energy dispersion and dwell time settings to detect specific characteristics edges effectively. The low- and core-loss energies for Zr and Nb are considerably greater than Co, La and O, hence STEM-EDS was used to detect and map these elements rather than select high dispersion setting for EELS acquisition. The intensity of the signals for Zr and Nb above 200 eV were also too weak to resolve at the chosen 'per-pixel' exposure times.

Table 2.8: Table of major EELS edges for constituent elements in LCO and LLZO. Values acquired from EELS Atlas [246].

Element	Edge 1 /eV	Edge 2/ eV	Edge 3 / eV	Edge 4 / eV	Edge 5 / eV
Li	55				
Co	60	779	794	7709	
O	532				
La	14	99	832	849	
Zr	29	180	182	1112	2307
Nb	34	205	207	2371	2465

This momentum transfer alters the energy of the incident electron and electron within the element. Excitations of the electrons are allowed between distinct values of energy levels within each element and thus changes in the incident beam electron energy can be related to these elemental fingerprints [273, 274]. As the detector is positioned on the BF/direct beam axis, very low angle elastically scattered and unscattered electrons are also recorded. These form the zero-loss peak, which can be used to determine the energy spread from the electron source as well as the sample thickness. Energy spread is commonly on the order of 0.2 to 2 eV and can be reduced through the use of a FEG source and a monochromator system.[270] A value for sample thickness can be computed from the integral of the zero loss intensity and intensity (I_o) of low-loss region of the spectra (I_t). Equation 8 provides a value of thickness in terms of mean free path, relating to the

expected number of scattering events for an electron of given energy passing through the sample. Table 2.9 provides ranges of thickness values from which different types of analysis can be considered acceptable. As the atomic weight of the sample also has an influence on mean free path between scattering events, this is a rough guidance and appropriate thickness for accurate quantification will be composition dependant.[275] For samples within the project, samples were measured to have values between 0.8 and 2 mean free paths.

$$\frac{t}{\lambda} = -\ln\left[\frac{I_o}{I_t}\right] \qquad \text{Equation 8}$$

Table 2.9:Sample thickness requirements with respect to mean free path for various analytical applications of collected EELS datasets [275].

Application	Sample thickness / mfp
Qualitative mapping (edges <800 eV)	0.1 – 1.2
Qualitative mapping (edges >800 eV)	0.3 – 2.5
Quantification	0.1 – 1.0
Quantification (edges >1.5 keV)	<1.5 – 2.0
Energy loss near edge structure (ELNES) mapping	~0.0 – 1.5
Thickness maps	<6.0
Plasmon energy analysis	0.1 – 6.0
Low-loss EELS analysis	0.1 – 3.0
Low-loss EELS analysis with deconvolution	0.5 – 6.0

The K-edge of oxygen has a characteristic core-energy loss signal between 520 eV and 550 eV, with the profile and peak positions providing insight into the bonding environments relating to specific s-, p-, d- and f- orbital interactions. The influence of crystal field effect, alongside covalence and oxidation states provide insight into specific characteristics within a material. Figure 2.15 shows the influence of changing geometry and covalence on the O K-edge for a series of $Li_xMn_yO_z$ stoichiometry [176]. This can provide insight into the composition within the bulk of both LCO and LLZO, as well as across the interfacial regions of heterostructures, depending on the Li deficiency of the material or the formation of secondary phases through thermal or electrochemical mechanisms. Dynamic studies using K-edge variations to track Li intercalation through an anode or cathode could provide information about composition and phases change on the nanoscale during charge cycles, alongside acquisition of TEM or STEM images.

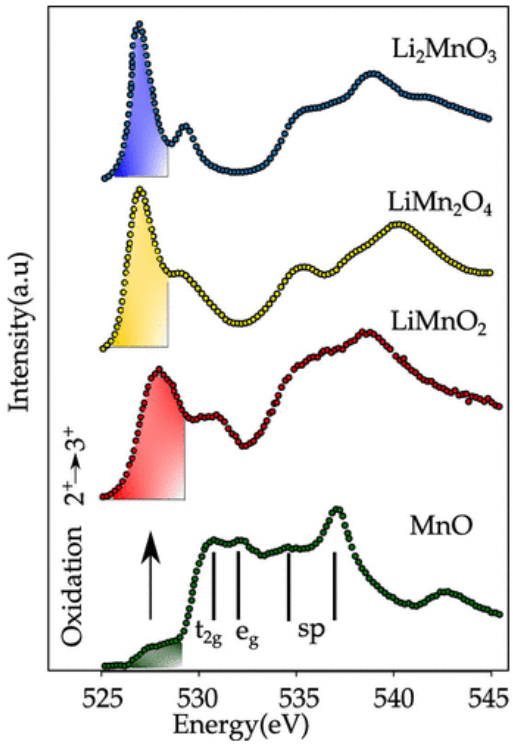

Figure 2.15: Impact of varying 3d electron occupancies and geometries of Li manganese oxides on the profile of O K-edges. Shifts and profiles of the O K-edge may be used as insight into Li deficiency, structure and composition variations. Figure acquired from reference [176].

The acquisition of EELS on modern microscopes relies on a three-dimensional data set with dual-EELS acquisition of low and core-loss spectra [276]. An EELS dataset for each pixel in the acquired image is comprised of x and y dimensions alongside a plot of the energy loss acquired by the respective energy channel. The low-loss region of the spectrum is high intensity, due to the energy loss of electrons in the region being minimal compared to the incident beam (0 to 200 eV). In contrast, the intensity of the background signal alongside any characteristics elemental energy losses diminishes exponentially towards high energy losses (> 200 eV). To ensure sufficient signal to noise ratios for core/high energy loss values the exposure time must before greater than for the low-loss spectrum. Dual acquisition from both low-loss and core-loss channels allows for efficient acquisition of data at each sample point, minimising the effects of charging and drift on the element signatures acquired.

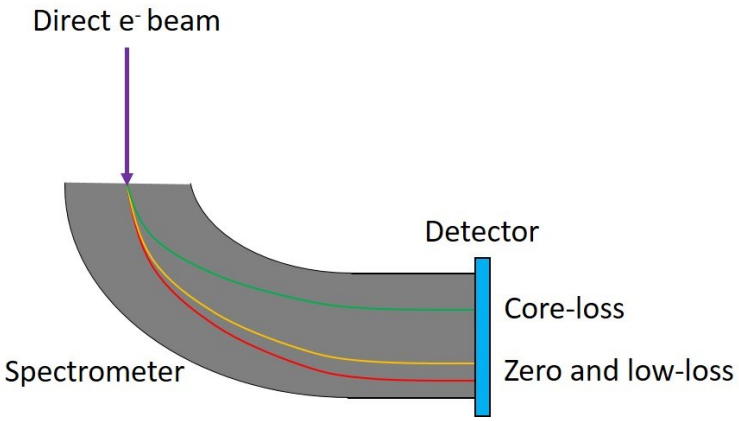

Figure 2.16: Dual-EELS detector achieving separation of low-loss and core-loss electrons through the applied field within a spectrometer. Separation prior to a detector with control over exposure time of each segment allows for combined acquisition of low- (red/yellow) and core-loss (green) data from each pixel.

For the system to achieve dual acquisition for each pixel in the EELS dataset the incident electrons are offset between two regions/channels of the detector, set up to acquire data at different exposure times. One segment is optimised for the acquisition of low-loss data, without overexposing the detector, while the other receives lower energy electrons, having experienced greater energy loss during passage through the sample. Switching between detector elements required the dynamic switching between electrostatic optical element settings to deflect electron intensity onto the low-loss and core-loss segments of the detector.

Elemental quantification requires the detection of quantifiable signals and their profiles with respect to the baseline intensity. If acquisition time and quantity of element within the probe area are sufficient compared to the simultaneously acquired background and noise, then it is possible to extract compositional information. This involved confirming the elements present in the sample in Digital Micrograph software (GATAN), before applying Hartree-Slater models to determine composition within each acquired pixel [277, 278].

All TEM and STEM images were acquired at 200 kV, in either a JEOL 2100+, aberration-corrected JEOL ARM200CF or NeoARM microscopes. Dual-EELS and EDS acquisition utilised a range of dispersion and exposure times. Energy dispersions on the order of 0.25 eV to 0.5 eV were used depending on the range of low and core loss energies inclusive of Co, La and Zr signals at 850 eV, 950 eV and 2200 eV respectively. Dual-EELS exposures were ≤ 2×10^{-4} seconds for the low-loss detection, while core-loss exposures were set to ≤ 0.2 seconds. This ensured suitable scan rates and resolution while avoiding excessive sample drift and sample contamination relating to longer exposure times.

2.5.11 Pencil beam diffraction

Four-dimensional STEM techniques, providing image and diffraction data for each probe position covered within the scan area. Subsequent combination of the signal and diffraction data sets allows for an intensity profile with respect to orientation to be complied across the area of interest.[279, 280] Site by site analysis can detect slight changes in phase, orientation and stress across a crystalline material, with the ability to provide detailed insight to the variations within multi-grain specimens where crystal orientation and phase are important characteristics.[280] Data was collected using the 300 keV JEOL ARM300CF, allowing polycrystalline films to be analysed with respect to the orientation and phase shifts over nanoscale distances unsuitable for SAD. Specific alignment conditions are set at ePSIC (Diamond Light Source) in order to calibrate and align the pencil beam. Steps involved calibration of the diffraction spacing and roundness of the polycrystalline diffraction pattern for gold nanoparticles on a carbon grid.[248, 263]

2.6 Modelling and STEM Simulation of Substrate, Electrode and Electrolyte Phases as well as Interfaces and GB

2.6.1 Crystal Models and Diffraction Simulation

For crystal models and diffraction simulations a combination of Vesta (JP-Minerals) and CrystalMaker (CrystalMaker Software Ltd.) were used [281]. These enabled the observations of multiple unit cell in three-dimensions and application of visual plane slices for aiding understanding of observations in TEM and STEM images data. CrystalMaker and JEMS (JEMS-SWISS, Dr. P. Stadelmann) both provide an interface from which the diffraction pattern deduced from the atom coordinate file of each phase observed and aligned along various ZA to assess the fit. They proved useful for understanding the plane alignments at GB and differences between similar phases including c-LCO, rs-CO and s-CO for the electrode, as well as LLZO and LZO for electrolyte analysis. Examples of the interfaces shown in Figure 2.17, cover the modelling, XRD simulation and TEM diffraction pattern simulation where appropriate.

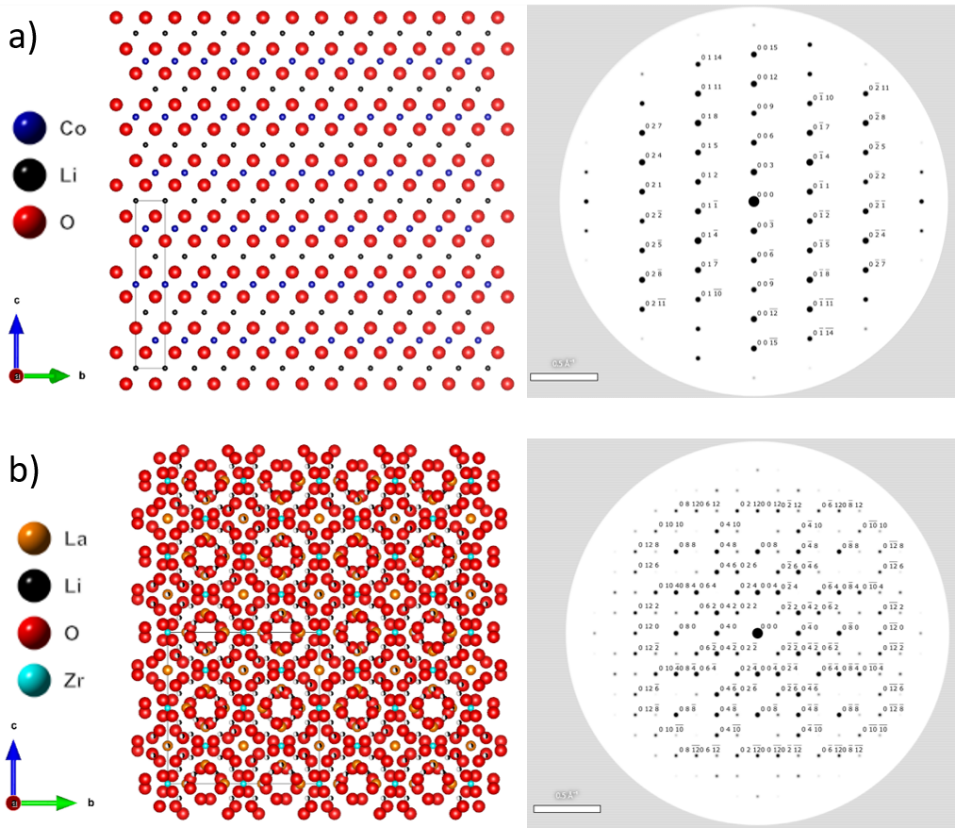

Figure 2.17: a) Model and simulated diffraction pattern of r-LCO, along the [100] ZA. b) Model and simulated diffraction pattern of c-LLZO, also along the [100] ZA. Structural models and simulations use atomic coordinate files for literature (ICSD) and The Materials Project databases [44, 51].

2.6.2 Use of QSTEM for BF and HAADF STEM image simulations

The implementation of simulations to support real electron microscopy image data is important to support conclusions drawn from atomic arrangements in samples. Two approaches to electron image simulation are commonly used, these being Bloch wave or multi-slice simulations [282]. In support of data collected by electron microscopy BF and HAADF simulation focused on the confirmation of phase and orientations. Diffraction and image simulations also could differentiate between cubic LCO structures closer to $LiCoO_2$ or CoO, achieved through use of structure models and Vesta, CrystalMaker, QSTEM and JEMS software. GBs were simulated to support the observations made with atomic-resolution analysis of crystalline LCO and LLZO thin films.

Two simulation programs are used to produce images from structural models of orientations specific to a single phase of LCO or LLZO, as well as specific interfaces between substrates and GB orientations. Models of the specific phases are acquired from the materials project or inorganic crystal database [44, 51]. Inserting these atomic coordinate files into the QSTEM model builder (Figure 2.18), allowed for the formation of interfaces between substrate and LCO or LLZO, as well as GB within the bulk of these materials. Selection of ZA and alignment between the lattice orientations has full freedom of rotation and movement for aligning models with the information provided in STEM images. Applying separate atom coordinate files to each region provides the ability to rotate and align two regions along theoretical boundaries, such as the interface between substrate and thin film or two grains within a single material.

Simulation of images utilised QSTEM for both STEM and TEM images. Atom coordinate files relating to single crystals of electrode and electrolyte phases, or interface models built in QSTEM model builder were imported. Expansion of the models in all three dimensions was used to produce images with sufficient fields of view to compare to HAADF and BF data. The thickness of the sample was increased to include simulation thicknesses of up to 40 nm of multi-slice simulations. Electron microscope parameters including accelerating voltage and focus were adjusted to relate to the conditions at which the crystal phase or GB data was collected. An example of a HAADF and BF simulation for the r-LCO and cubic LLZO phase are shown in Figure 2.18. Thicknesses for image simulations were determined by creating model parameters in QSTEM, of sufficient thickness to form contrast and intensities representative of real images, while also being achievable within reasonable simulation times (2 hours). This was such that multiple simulated STEM images of grain boundaries could be produced, compared to real data (BF and HAADF images), with suitable improvements made to the model to describe the contrast and structure observed at grain boundaries. This meant limiting simulations to thicknesses of 20 nm to 40 nm for most phase and GB simulations, where the update time to render adjustments to models of greater depth, along the simulated observation axis, also became a limitation.

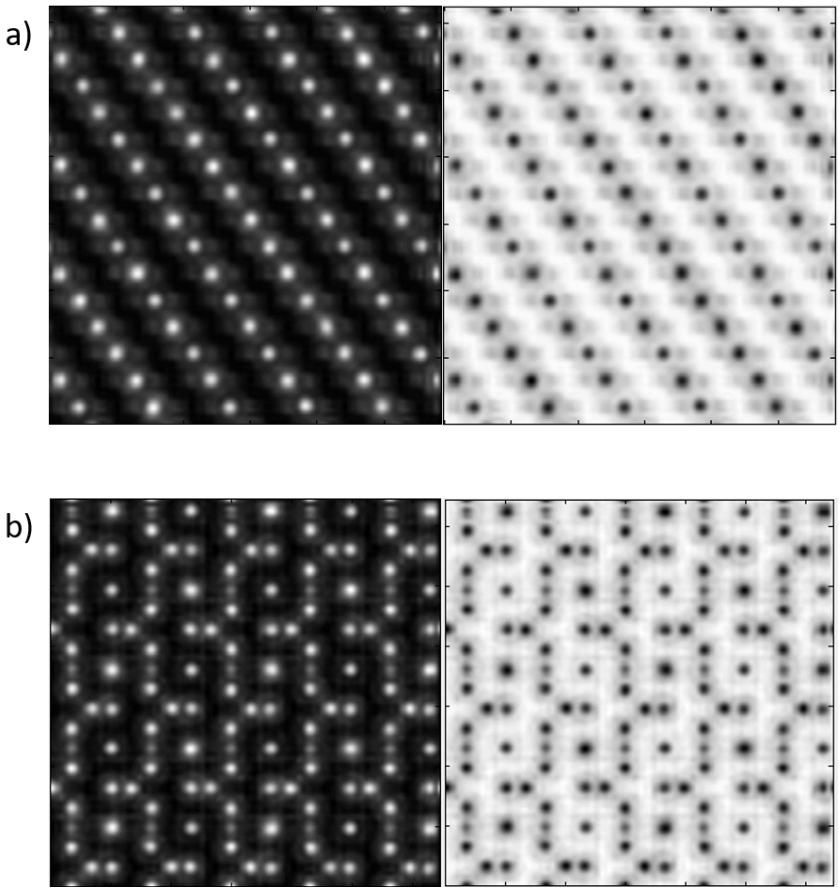

Figure 2.18: a) HAADF and BF simulations of r-LCO phase along the [100] ZA, showing Co and O atom positions. b) HAADF and BF simulations of c-LLZO along the [100] ZA, where La and Zr atoms dominate the contrast. Both examples are produced using QSTEM simulation software.

Chapter 3

Structure and Defects of Sintered $LiCoO_2/Li_7La_3Zr_2O_{12}$ Heterostructures on the Micron Scale

Commercial devices utilise electrodes and electrolytes on the micron to millimetres scales in batteries compatible with applications on small to large scales (e.g. phones and cars). This requires combining active Li conductive materials, with layer thicknesses of tens of microns [283-285]. As introduced in Chapter 1, heat treating (calendering) the system during the rolling process, aims to improve the grain size, phases and optimise active material density within the device [29-31]. The consequences of this thermal treatment results in desirable phase changes with altering the interfacial chemistry between two solid-state materials, where altering particle size, phase and composition can change Li mobility through EEIs [161, 162, 286]. Investigating the bulk properties of materials on the micron scale, more applicable to commercial devices, allows comparison with nanostructures observed in thin films (Chapter 5). The range of magnifications and resolutions achievable by electron microscopy are utilised in this Chapter to further the understanding characteristics from the micron, nano and atomistic scales within LCO and LLZO grains.

Work conducted on sintered samples comprised of LCO and LLZO, is focusing on the differences between pristine and annealed (600 °C and 900 °C) heterostructures. A comparison of grain size, phases and interfacial compositions was done by a combination of electron microscopy techniques, including SEM and TEM imaging, alongside EDS and EBSD. Low-magnification TEM can observe the distributions of GB and defects within microns of material, applied effectively within this project to LCO and LLZO. Comparisons of results relating to each sintering method, consider the influences on characteristics affecting transition of Li through a micron scale device [119, 287, 288].

Binders are important components of commercial batteries, providing adhesion between the particles comprising the particles within the electrode layers. They form a component of the electrode slurries used for pasting the positive and negative electrode material onto the current collectors.

While work presented in this thesis focuses on binder-free particles and thin film heterostructure depositions, it is important to consider the role binders may have and their composition, given they play a fundamental role in to design and performance of commercial batteries. The design of an effective binder achieves good slurry and electrode film formation during deposition and drying. Also remaining stable while subjected to the harsh temperature and electrochemical conditions experienced during battery operation. Binders including, resins, rubbers and polymers are therefore designed to be pliable and suitable for maintaining electrode integrity over thousands of charge cycles [26]. Electron transfer from within the active electrode material, to the current collectors requires an electrically conductive binder or additives to facilitate efficient movement of charge during the intercalation and deintercalation of Li between cathode (e.g. LCO) and anode (e.g. graphite). Typical binder materials include polyvinylidene fluoride and styrene butadiene copolymer [289].

The exclusion of binders within the work presented is based on the potential volatility of the polymers and rubbers at high annealing temperatures, alongside the susceptibility to damage, sputtering and contamination of LCO and LLZO during FIB-SEM processing to form lamellae of suitable quality for HRSTEM. The presence of high-carbon materials in HRSTEM would have also been a potential limitation with respect to beam damage and subsequent carbon contamination of the electrode and electrolyte surfaces. Excluding the binder provided what was considered the best environment for effectively analysing the particle and grain interfaces in pristine and annealed states.

Regarding the analysis of alignments between grains in a solid-state battery system, the absence of these binders does not negatively impact understanding of GB between crystal planes in LCO, LLZO and the heterostructures. The main limitation may have been understanding the impact of a binder on particle aggregation during annealing, given they would have occupied the space between electrode and electrolyte particles. Also, any potential diffusion of carbon into the LCO and LLZO during annealing is not accounted for in the binder-free samples presented in this thesis.

The work has focused on defining the consequences of a set of sintering conditions on the phase, Li content, interfacial chemistry and GB of LCO and LLZO heterostructures, that develops insight into the potential benefits of heat treatment of electrode and electrolyte particle systems, alongside the limitations. The contribution of results towards how phase, GB, defect and interfacial decomposition develop with temperature can inform studies and refinements of these materials within the preparation parameters defined in this chapter.

3.1 Structure and Morphology of $LiCoO_2$ and $Li_7La_3Zr_2O_{12}$ Powders

As purchased LCO and as synthesised LLZO powders were analysed by SEM, to observe morphology and surface features resolvable using a variety of beam energies, current, and magnifications. The combination of XRD signals at 19° (r-LCO(001)), 45° (r-LCO(104) alongside the two peaks at 66° and 67° (LCO(108) and (110)) relate to the r-LCO phase (Figure 3.1 a). In the SEM images (Figure 3.1, b and c) the presence of layers possibly relates to where Li and CoO_2 layers are periodically slipping along glide planes, forming the layering effect. The detection of the r-LCO phase suggests good Li content within the powder, as this is expected to be present under Li-rich conditions. Thus any subsequent phase changes to into c-LCO, rs-CO or s-CO phases could be attributed to Li losses during sample annealing. These Li-deficient phases, relating to Li evaporation are presented in literature [49, 290], occurring at substrate temperatures of 550 °C during PLD, as well as at 500 °C during attempts to reprocess used LCO cathodes . No visible damage to the particles occurs during exposure to the scanning electron beam, using nanoamp currents at voltages between 5 keV and 30 keV. This resistance to electron beams between 5 keV and 300 keV and nanoamps of current density (A cm^{-2}), allows effective use of SEM and atomic-resolution TEM throughout the project. Most LCO particles from the as-purchased powder have distinct layers along a consistent direction within the particles (Figure 3.1, c). The presence of these layers, consistently 100 to 200 nm thick, likely relates to glide planes within the crystal structure.

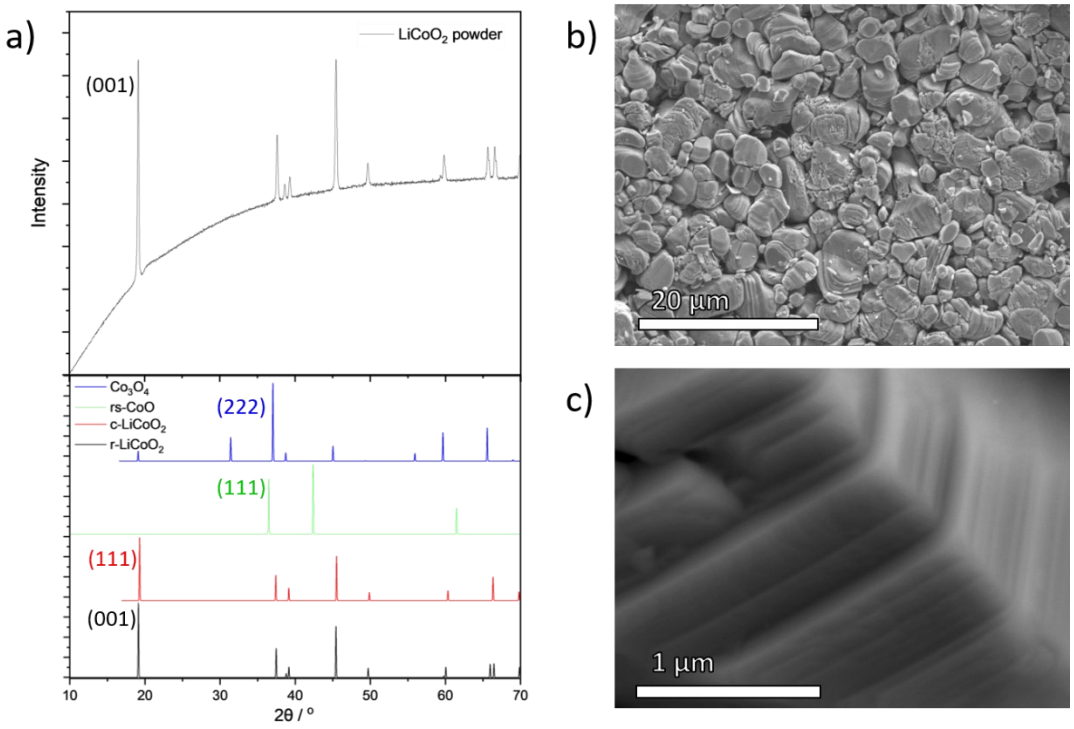

Figure 3.1: a) XRD of pure LCO powder (top), as sourced from Alfar Aesar at 99.5% purity, with simulated XRD patterns for rhombohedral, cubic and spinel phases included as reference (bottom). b) Low magnification SE SEM image of surface of pellet pressed at 10 tonnes for 20 mins. c) Higher magnification (x43k) SE image region of pellet showing variation in LCO particle size and shape. XRD collected in Panalytical Aries, SEM acquired using JEOL 7800F Prime.

The LLZO prepared by thermal decomposition (850 °C), shows an inhomogeneous particle morphology, with a near complete conversion of precursors (Li_2CO_3, La_2O_3 and ZrO_2) into the electrolyte. In addition to particle shape and composition, susceptibility to beam damage at low voltages was assessed at varying magnifications whereby the sample was charged with electrons. Figure 3.2 shows smooth particles of varying size, ranging from below 5 µm to 20 µm. The packing of inhomogeneous particle sizes creates porosity across the surface and bulk of the electrolyte, reducing the Li capacity of LLZO for a given volume of electrolyte. Despite this, well defined interfaces between particles, show a clear contact area for possible Li mobility through the porous sample. The incorporation of binders into this material, to form a flexible electrolyte can make use of the porosity, such that controlling LLZO particle size may allow tuning a balance of capacity and flexibility characteristics of devices [291-293]. SEM data for the LLZO pellet was mostly acquired under a beam energy of 20 keV to 30 keV, for EDS purposes (Zr K-edge 15.7 keV) and beam currents between 7 nA and 20 nA to provide sufficient count rates. At low magnifications under these conditions the material appears stable over time periods of minutes.

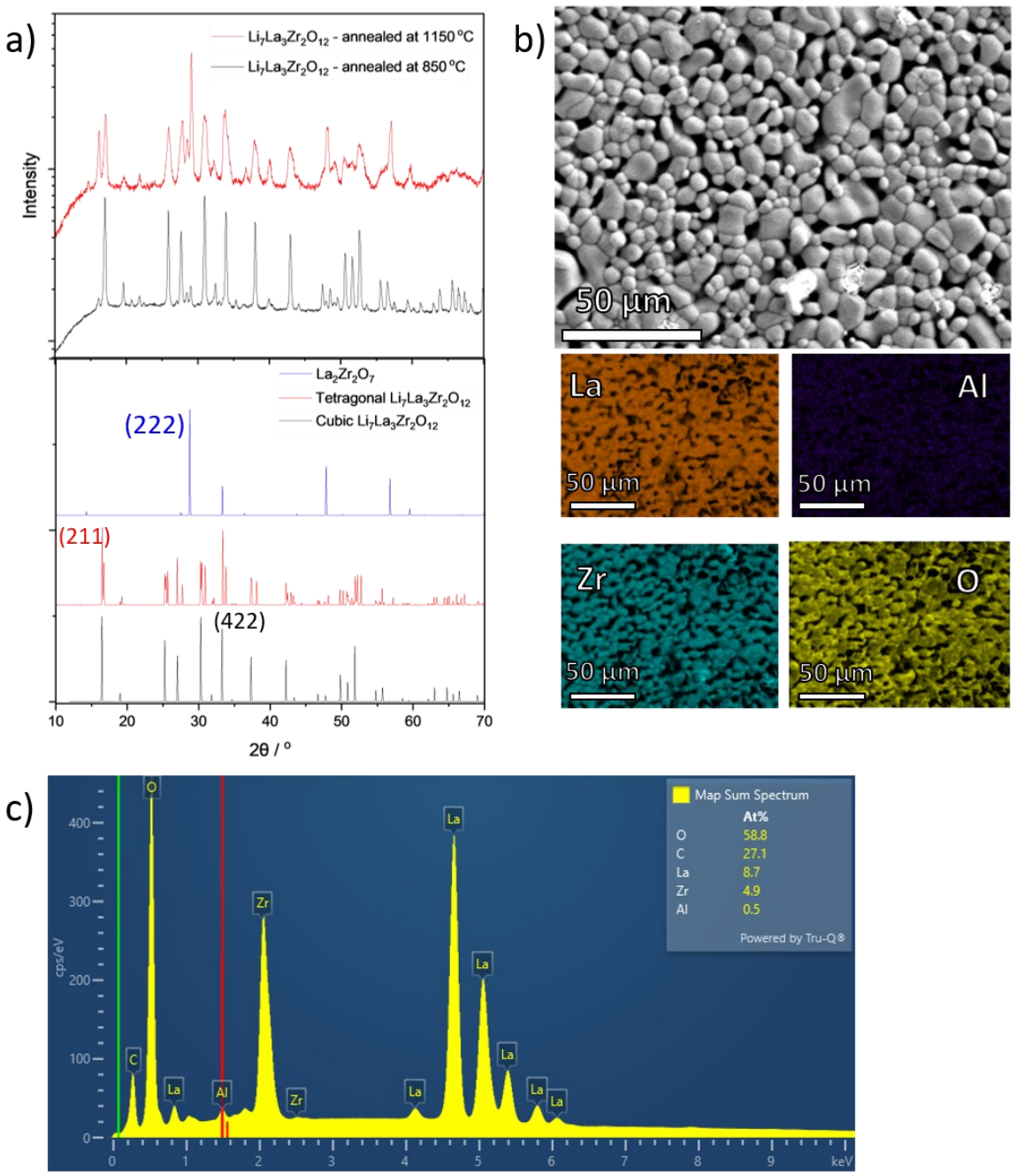

Figure 3.2: a) XRD of as-synthesised LLZO powder, sintered at 850 °C (12 hours) and 1150 °C (4 hours), the latter showing Li deficient characteristics (LZO(222) at 28°). Simulations of c-LLZO, t-LLZO and LZO are included below as reference. b) Image of LLZO particles on the surface of the sintered pellet with accompanying EDS spectra. The spectra contained La, Zr and O signals, with a weak Al signal, suggesting contamination during thermal decomposition. c) EDS spectrum of LLZO powder with atomic percentage compositions suggesting a 3 : 1.7 ratio between La and Zr (expected to be 3 : 2). Data acquired in JEOL 7800F Prime.

Charging of the specimen under the electron beam was minimal, showing LCO and LLZO had sufficient electron conductivity to facilitate SEM analysis at low (micron scales) and high (tens of nanometres) magnifications. Areas detected by EDS as unreacted ZrO_2 precursor did show signs of charge accumulation during irradiation (Figure 3.2, b). Grains of La_2O_3 are also present in some lamellae of particle cross-sections, support the observation that complete thermal decomposition was not achieved, though its presence has a minor contribution of the synthesised LLZO. Remaining La_2O_3 and ZrO_2 grains in an active device will be a disadvantage regarding Li conduction through the electrolyte. This potential limitation also highlights the need to check for segregation of LLZO into ZrO_2 and La_2O_3 grains during PLD (Chapter 4 and 5).

The LLZO surface had varying coverage of small particles (Figure 3.3) likely to be the result of reaction between Li and CO_2, forming a Li_2CO_3 layer across the surface [294, 295]. The EDS data acquired across regions of both LCO and LLZO particles shows differing carbon content on the surface of each material. Examples of larger carbon content on LLZO are shown in Figure 3.4, relating to a sample of LCO/LLZO sintered at 600 °C. The relative atomic percentages in EDS maps provide ratios of La to Zr of 3 : 1.7 (pure pellet, Figure 3.2), with a similar ratio in a sample sintered at 600 °C (Figure 3.4). This is not far from the target 3 : 2 stoichiometry of $Li_7La_3Zr_2O_{12}$ and correlates with the XRD throughout this chapter containing peak positions indicative of c-LLZO rather than Li deficient LZO for samples in pristine and post sintering at 600 °C.

LLZO imaging at higher SEM magnification conditions (15 keV, 2.0 nA, 3 mm working distance), was used to investigate regions of contact between particles. During exposure at these conditions, the dynamic formation of structures growing from the surface, occurring over tens of seconds, was imaged (Figure 3.3). These are likely to be rapidly forming Li_2CO_3 dendrites, induced by the beam current charging the electrolyte [296]. Tang et al., provide similar observations with Li dendrite growth along GB within their samples during irradiation by electrons. Similar formations develop close to the edges of lamella during FIB preparation, showing Li loss could occur at multiple stages of preparation and analysis of Li containing materials. Throughout the project, potential mechanisms of Li loss can therefore be attributed to kinetic energy transfer (sputtering in SEM, TEM and FIB), electrical charge accumulation (SEM, TEM and FIB) or thermal evaporations (annealing, PLD, FIB) [297].

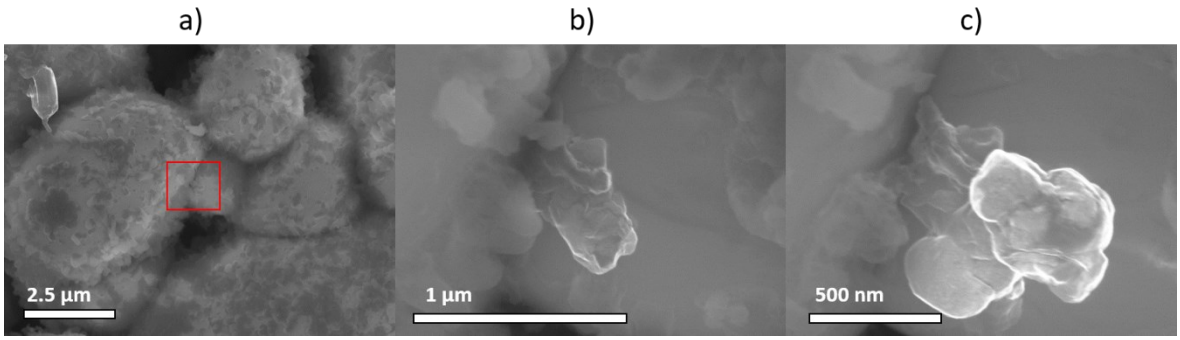

Figure 3.3: Observation of electron beam induced formation of possible contamination structure or Li_2CO_3 dendrites. The red box in a) indicates the area magnified in images b) and c). b) and c) were taken one minute apart and show the growth of a structure occurring from the surface of the LLZO particle-particle boundary. Collected on JEOL 7800F Prime at a working distance of 3 mm, 15 keV aperture: 50 µm.

3.2 SEM Imaging and EDS of Sintered Heterostructure Samples in the Form of Pellets and Cross-Section Lamella

Upon mixing LCO and LLZO powders and pressing into pellets, they were sintered at 600 °C and 900 °C, with aim to facilitate transformation into r-LCO and c-LLZO for maximum Li conductivity. This also heightens the chance for thermal decomposition between the two materials through element diffusion, rather than electrochemically induced SEI formation. Therefore, a range of annealing conditions were explored to determine the best approach to heating the two materials that optimises phase and grain structure, without inducing excessive interfacial degradation. A set of samples were kept in pristine conditions in order to provide a baseline in terms of crystal phase, grain size and boundaries within LCO and LLZO particles.

Assessing the samples in the form of pellets within the SEM using BSE detector (Figure 3.4), demonstrate that there are clear differences in contrast between LCO and LLZO. The contrast differences in combination with EDS maps allowed assessment of the regions where electrode and electrolyte particles were well-mixed, allowing ROI to be selected. Both materials were well mixed with numerous regions where LCO and LLZO particles are in contact and thus suitable for lamella containing heterostructure interfaces. Surface assessment only provides a rough guideline to optimal regions from which to mill lamella. Multiple lamella from pristine (mechanically pressed) and sintered samples contain varying amounts of porosity and composition were prepared, and used for analysis of LCO, LLZO or their interfaces.

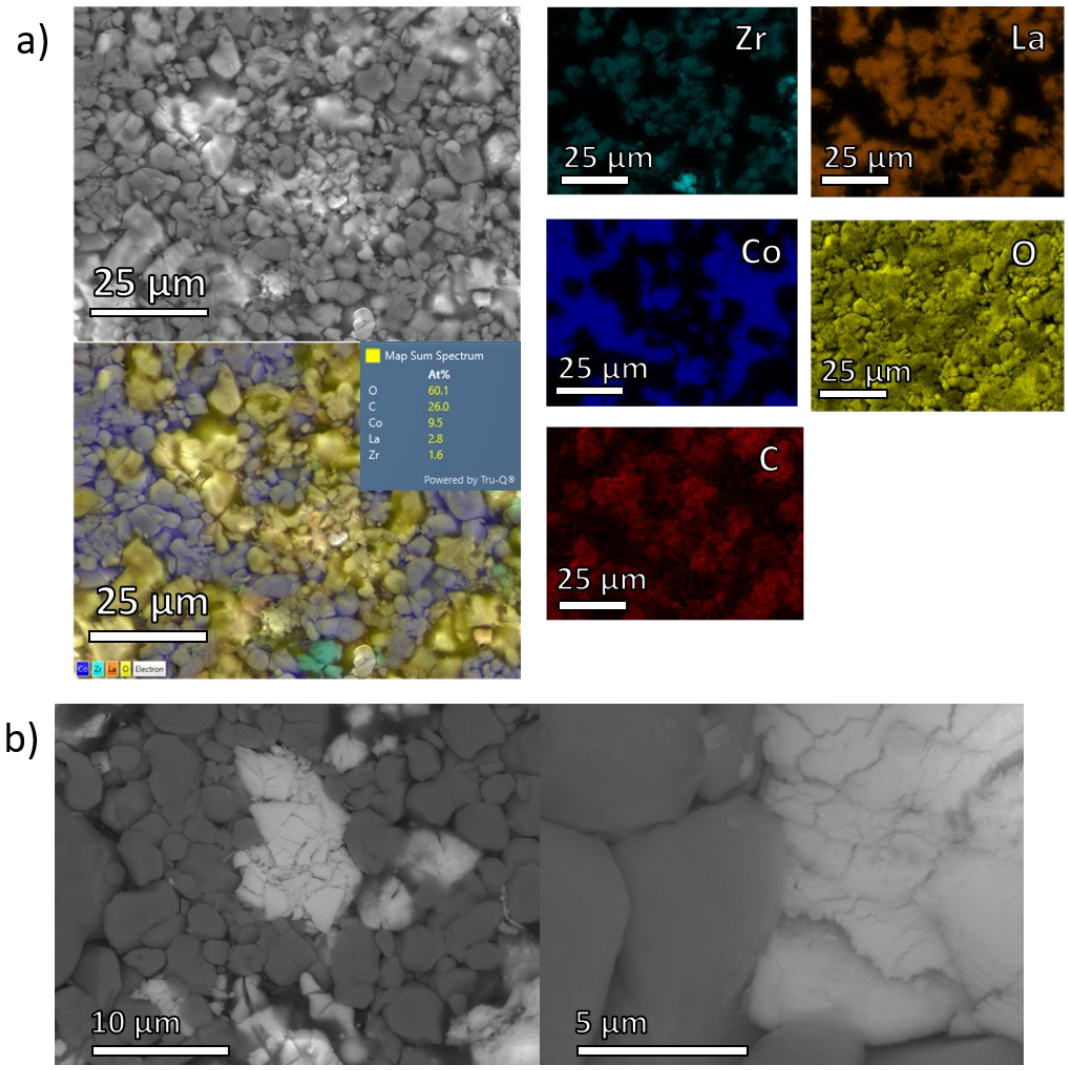

Figure 3.4: a) SEM-EDS element signal overlay in pristine LCO/LLZO pellet, with respective elemental maps and electron image (30 keV and 10 nA). b) BSE image of LCO (dark-grey) and LLZO (light-grey) particles with a higher magnification of the LCO/LLZO interface (right). Data acquired on JEOL 7800F Prime at 25 keV (aperture, 30 µm)

XRD results are shown in Figure 3.5 and Figure 3.6. The bulk crystal phases are also shown for comparison, also to easier follow a possible decomposition of sintered electrode-electrolyte particles subjected to the different temperatures and subsequently voltage cycled pellets. Figure 3.5 compares the samples with different annealing temperatures of the pellets, with both the pristine and 600 °C (1 hour) samples providing very similar diffraction results with the rhombohedral phase of the LCO powder dominating the intensity alongside a clear set of c-LLZO peaks. The effect of annealing at 600 °C is difficult to assess since the peak intensities relating to LLZO broaden, hinting a LLZO phase distribution with smaller grains is occurring after an hour of sintering. Sintering at 900 °C (4 hours) leads to a significant proportion of the Li deficient LZO phase dominating the diffraction intensity. This is shown by the presence of the strong peak at 29°, not

seen in pristine and 600 °C sintered samples. The XRD is dominated by the rhombohedral r-LCO(001) peaks at 19°, while no signs of rs-CoO (rs-CO) or s-Co_3O_4 (s-CO) presence after sintering, suggests greater susceptibility to Li evaporation from the LLZO compared to LCO.

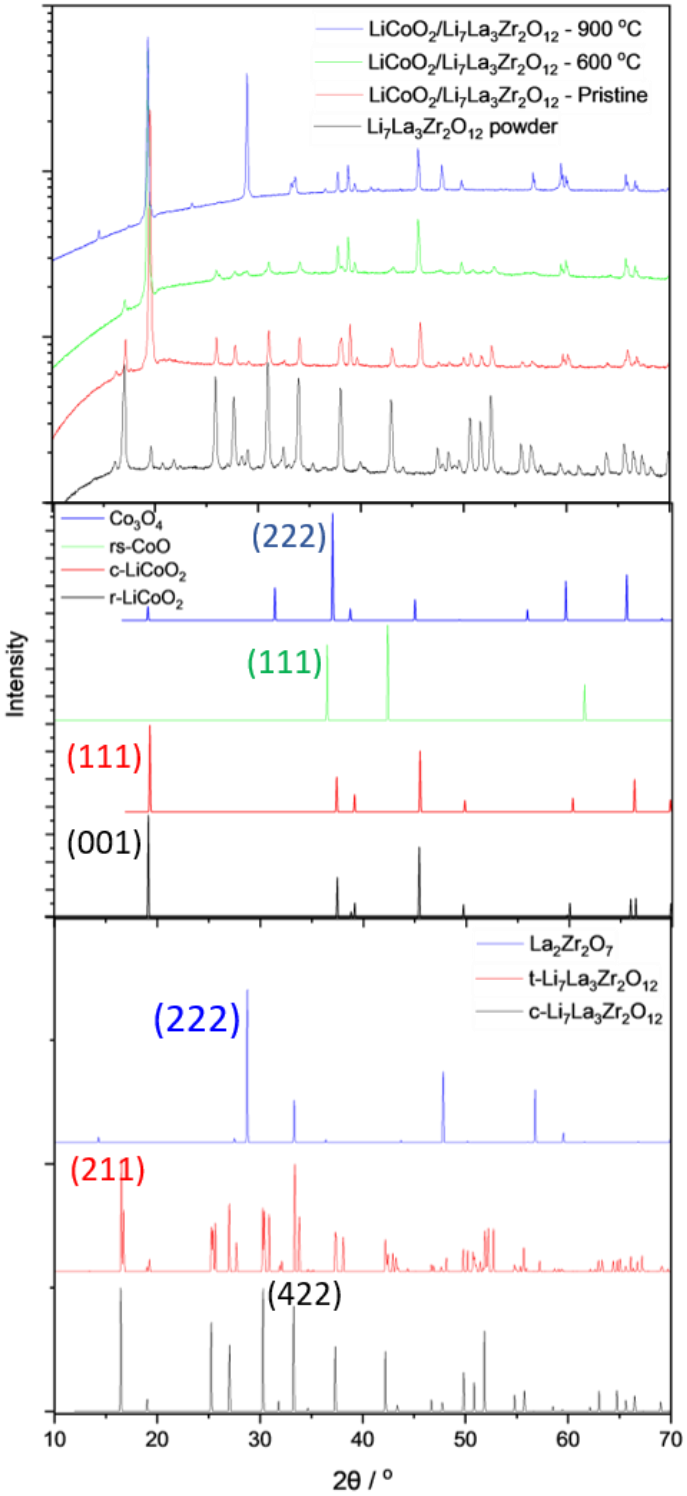

Figure 3.5: Top) XRD data acquired for pure LLZO powder and mixtures of LCO and LLZO in pristine condition, annealed at 600 °C for 1 hour or 900 °C for 4 hours. Spectra below this include simulations of LCO and LLZO phases, alongside Li vacant LZO and $LaCoO_3$ secondary phase. Structural files for simulation acquired from ICSD and Materials Project databases [51, 290, 298-302].

The biasing of sample at a variety of voltages was performed to determine if any decomposition occurs. The XRD data and of these heterostructure pellets is shown in Figure 3.6. Voltage cycles were conducted at 4V, 6V and 12V to assess the extent of interfacial decomposition induced by increasingly harsh electrochemical conditions. The XRD results show that after the voltage application there are no new phases or phase changes within the samples tested. The r-LCO(001) peak at approximately 19° remains dominant, the pristine samples also retain the LLZO distribution of XRD signals, while the appearance of a signal at 28° for LZO(222) is again present for samples annealed at 600 °C. The higher voltage experiments contained some hysteresis within voltage-current curves, suggesting potential electrochemical change (Appendix II). However, no clear development of LZO or lanthanum-cobalt-oxide phase occurs when investigated by XRD. A doublet of peaks near 33° would be expected for $LaCoO_3$, relating to the $LaCoO_3$(110) and (104) planes. While potentially weakly present in pristine and 600 °C samples biased between 6 V and -6 V, as well as 12 V and -12 V, the similarity in position to LLZO(442) means assigning them as $LaCoO_3$ cannot be done confidently without supporting SEM-EDS, TEM, STEM-EELS or other chemical data such as XPS. The extent of interface decomposition into $LaCoO_3$ in pellets sintered at 900 °C is also undetected with XRD, though later shown that this phase is present on micron-scale (e.g. Figure 3.9). Seen within literature and this project, the scale of electrochemical degradation appears to be on the nanoscale, making higher resolutions of microscopy and spectroscopy fundamental for detecting SEI [303, 304].

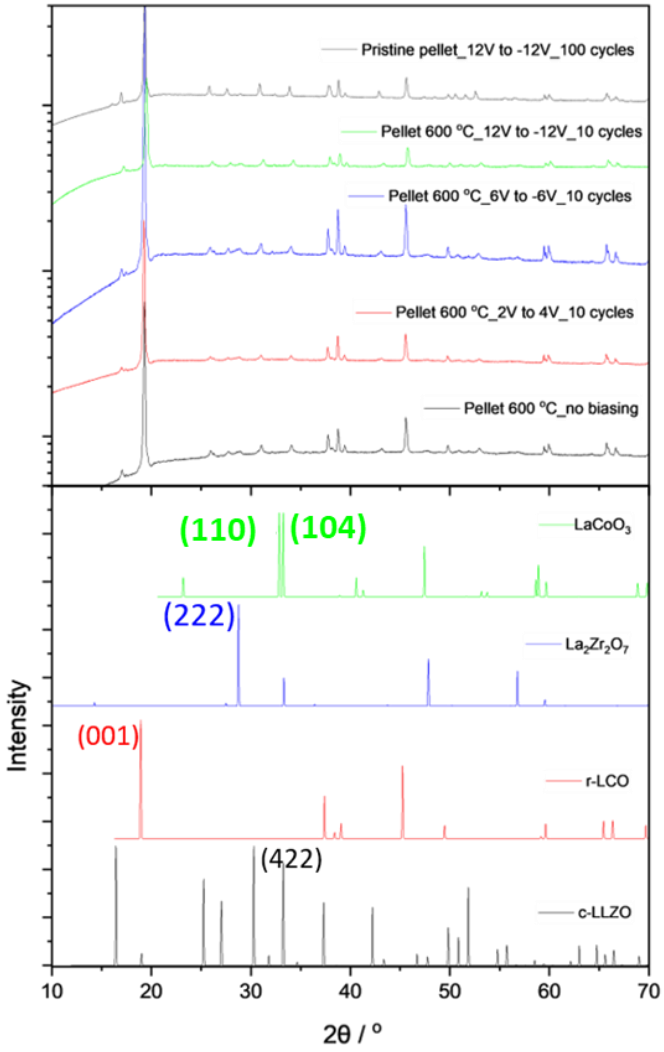

Figure 3.6: Upper) XRD data for pristine and voltage cycled LCO/LLZO mixed pellets for the voltage values detailed in Table 2.4. Lower) Theoretical XRD peaks for phases expected to be present in the simples. Simulated from .cif files from ICSD and the Materials Project [51, 290, 298-302].

3.3 Electron Microscope-Based Analysis of Pristine and Sintered Heterostructures Containing LCO and LLZO

Lamella from pristine cross-sections contains no visible intermixing, when observed by the SEM (JEOL 7800F Prime). There are many instances, as in Figure 3.7, where small particles of LCO occupied regions between larger particles. These small particles with limited inter-particle surface contact will limit a devices performance, owing to the voids between them, through which Li cannot transfer. Annealing can develop smaller grains into larger regions of the same phase and orientation, hence sintering attempts to achieve similar conversions of small LCO and LLZO particles into larger volumes. This may reduce the volume of isolated material within the electrode, maximising the volume within which Li can transfer without encountering a boundary with vacuum or air. While formation of larger particles is beneficial, the effect of variable grain orientations and phases within sintered particle cross-section is an area of importance. Small grains of LCO consistently dominate the pristine particles, while the electrolyte LLZO grains are consistently larger.

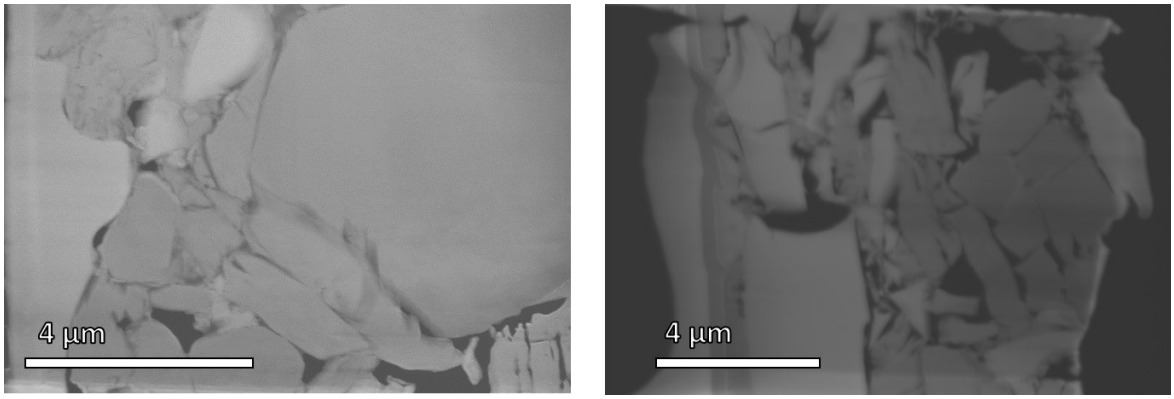

Figure 3.7: SE SEM images of pristine sample showing individual small particles of LCO with variable dimensions and gaps rather than continuous and close contact. The brighter particles are identified as LLZO or LZO using EDS. Data acquired on JEOL 7800F Prime.

Heating the pellets to 600 °C for 1 hour allowed analysis of the grains, boundaries and phases within particles subjected to the annealing conditions that avoid large Li evaporation. This sintering temperature and duration provides some differences when compared to pristine and long-sintered samples. Cross-sectional areas revealed larger grains of LCO with similarities to high temperature sintering (900 °C). SEM-EDS of the pellet annealed at 600 °C for 1 hour assesses the

chemistry between different LCO and LLZO regions, with interfaces observed in multiple cross-section specimens. The first indications of decomposition relating to sintering of the heterostructure occur within these samples, with carbon rich regions (Figure 3.8) occupying space between LCO and LLZO, most likely to be Li_2CO_3. The EDS in Figure 3.8 highlights a region of this material and as with later LLZO thin film specimens the potential presence of Li_2CO_3 appears to correlate with a greater lithium content in LLZO particle or thin films. Further TEM work provides insight into the characteristics of sintered LCO, LLZO regions, as well as a high rate of Li_2CO_3 damage, in the form of these regions disappearing within seconds of irradiation.

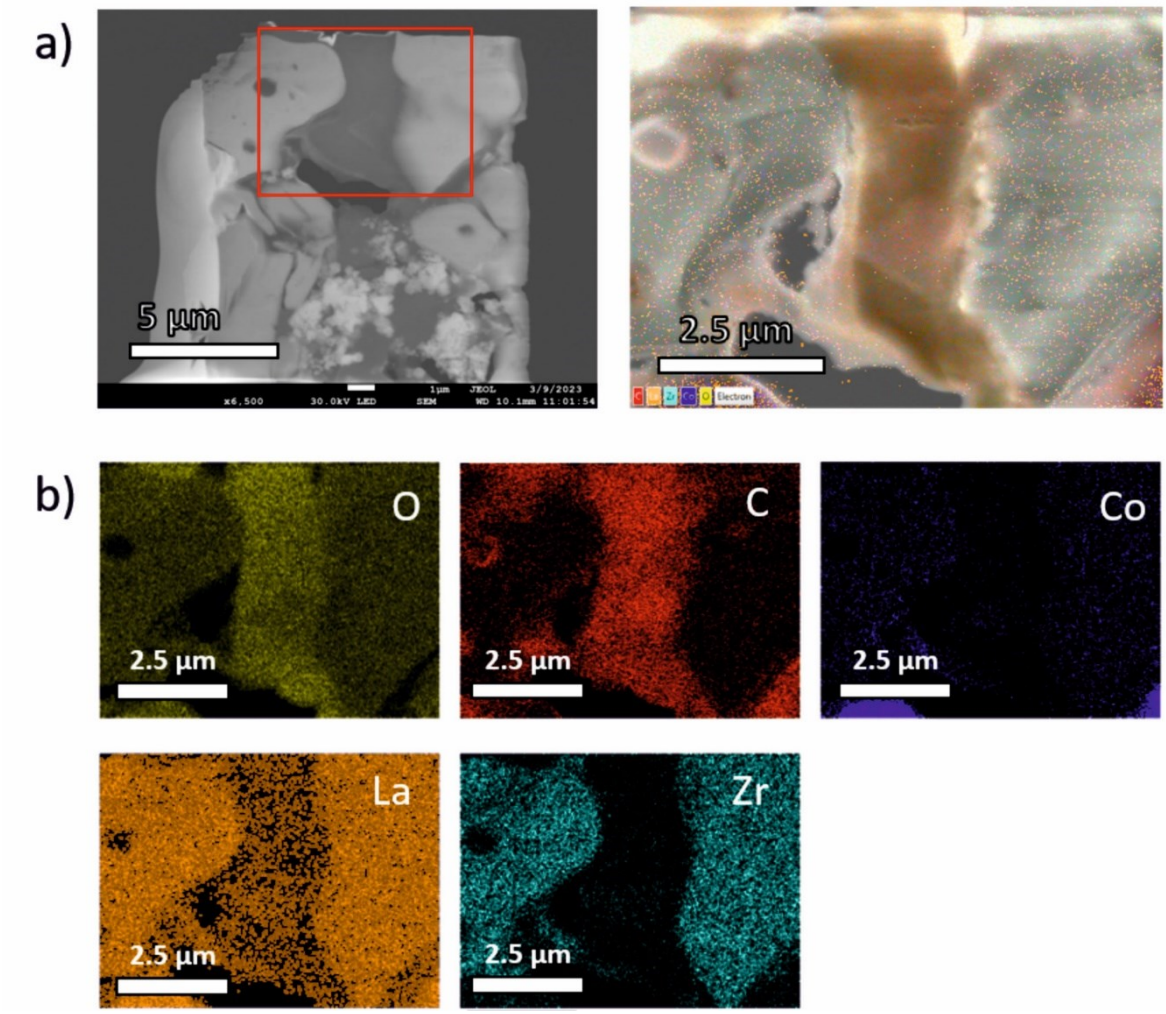

Figure 3.8: a) SEM and EDS overlay image of region between two LLZO particles. b) Respective EDS of this region indicating presence of C and O but no Co, La or Zr. This suggests the formation of Li_2CO_3 regions occurs between particles during annealing or possibly FIB preparation.

In Figure 3.9 the comparison between all three annealing approaches contains cross-sections with interfaces between LCO and LLZO. EDS mapping differentiated between regions of LCO and other particles comprised of La, Zr and O. Some areas providing a La signal were devoid of any Zr, instead containing a Co Kα signal and formed between regions mapped as LCO and LLZO. $LaCoO_3$ would be expected either as a thermally or electronically induced product of decomposition between electrode and electrolyte in this system.[305] This has been detected using Raman spectroscopy and XPS within mixtures of LLZO and transitional metal (Co, Mn, Ni) electrode materials annealed at 900 °C [306]. The energetic stability of this stoichiometry is favourable compared to $LaCoO_3$ [51]. The extent to which annealing or biasing the system leads to the growth of this lanthanum cobalt oxide phase was a question approached by ex- or in-situ sintering experiments.

With respect to the presence of Li_2CO_3 and $LaCoO_3$ after sintering at 600 °C and 900 °C respectively, the carbonate is assignable to the surfaces of LLZO rather than a product of LCO-LLZO decomposition. The lack of $LaCoO_3$ grains resolved by SEM after annealing at 600 °C suggests the intermixing is on either a nanoscale requiring TEM-EDS analysis or initiates at a temperature threshold between 600 °C and 900°C. In contrast, the intermixing at 900 °C is an attribute of decomposition resulting from the contact between LCO and LLZO, while this temperature likely has exceeded the temperature limit of Li_2CO_3 decomposition, removing it from these cross-sections.

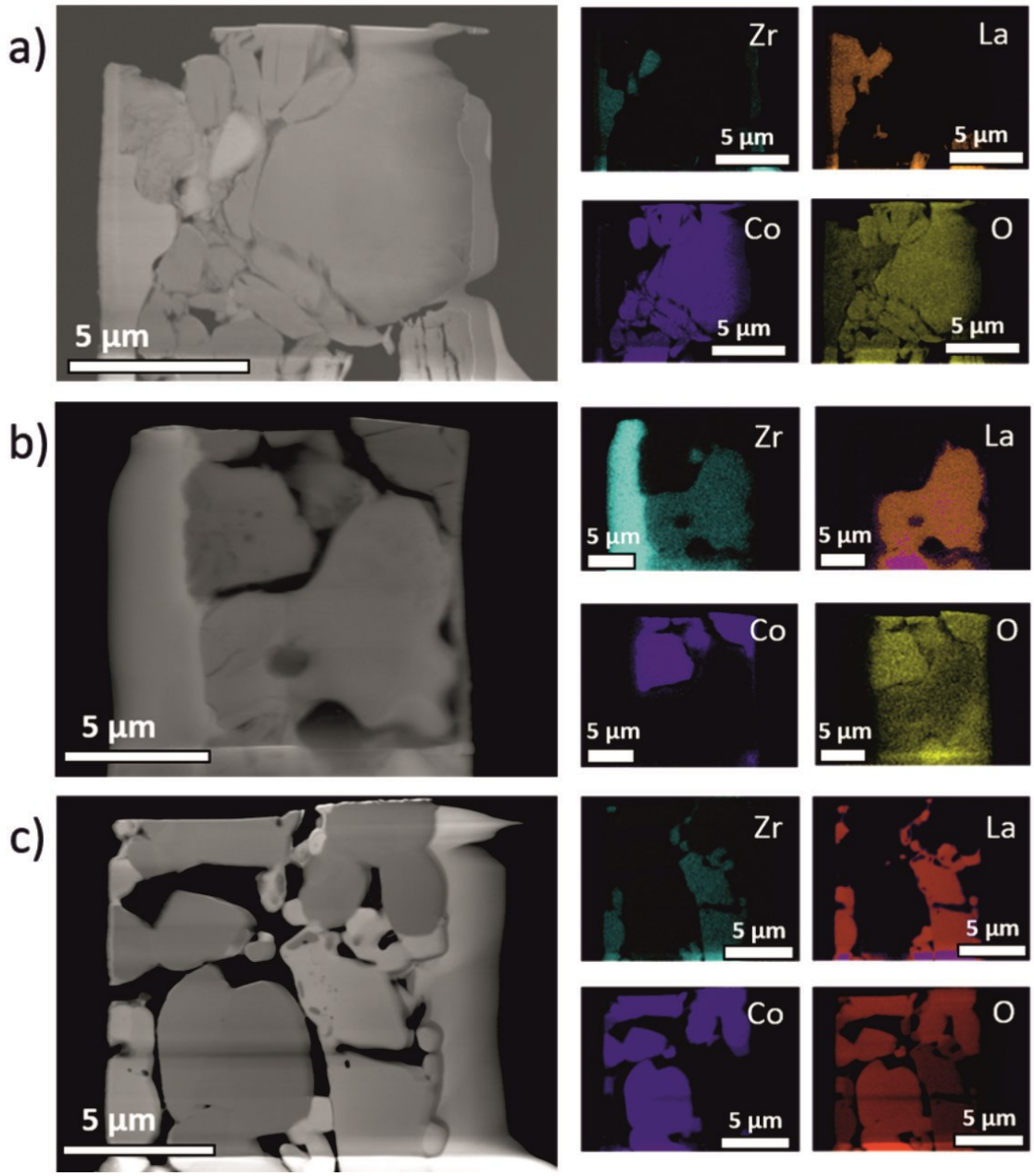

Figure 3.9: SE SEM images of; a) A pristine cross-section with LCO and LLZO interfaces showing no obvious secondary phase. b) Cross-section of sample heated to 600 °C (1 hour) with no clear formation of a SEI phase between electrode and electrolyte. Instead, some gaps between LCO and LLZO are occupied by high carbon contents (likely Li_2CO_3). c) Cross-section of lamella annealed at 900 °C (4 hours) containing particles of LCO and LLZO and highlighted regions of $LaCoO_3$ forming between particles of LCO and LLZO. Data acquired on JEOL SEM 7800F Prime at 30 keV.

3.4 Using EBSD to Map the Positions of GB in Cross-sections

Here we present the EBSD of the sintered specimen, on LCO/LLZO lamella, where several micron scale features important for Li dynamics were present. EBSD mapping acquired data provides structural indexing of individual particles and their grains. The simultaneously acquired EDS maps has provided chemical characterisation of the grains, which turn out to be very useful since solely analysis based on indexing was not sufficient to differentiate between the LCO, rs-CO, s-CO and LLZO or LZO phases. While the phase data sets for cross-sections of electrode and electrolyte particle were ambiguous, they indicated most of the regions in 900 °C sintered samples kept the crystalline structure sufficiently long to acquire Kikuchi patterns. In contrast, the particles with a La, Zr and O signal in pristine and 600 °C sintered samples return successful indexing within LCO regions; however, LLZO particles do not provide Kikuchi pattern intensity, indicating beam damage. The Li deficient LZO phase dominates the XRD spectra of 900 °C sintered samples, while the XRD of pristine and 600 °C sintered samples show the presence of LLZO. This data therefore suggests Li content appears to limit the material stability under a focused probe even at 30 keV in SEM. Consequently, the LLZO is has likely been damaged/transformed into amorphous or polycrystalline state (evidence in later TEM work). The susceptibility to beam damage could be an indication of Li presence in the lanthanum-zirconium-oxide structure.

The band contrast did map GB locations within the cross-sections of LCO and LZO particles in pristine and sintered samples. In Figure 3.10 the grains within particle with no contrast variations in SEM images are distinguished by dark lines in the band contrast maps. These indicated that large LCO particles contain multiple grains. Use of TEM contrast and SAD confirms the presence of the GB shown by EBSD, as well as orientation variations between the grains. The large particles in sintered samples contain multiple grains, supporting the assumption that smaller LCO particles coalesce during the annealing process. Large GB within particles have the potential to act as region for Li accumulation, allowing ions to move between grains. The GB can be beneficial by enabling channelling of Li between LCO and LLZO, or a detrimental role if the GB terminates within the electrode or electrolyte particle [119, 288].

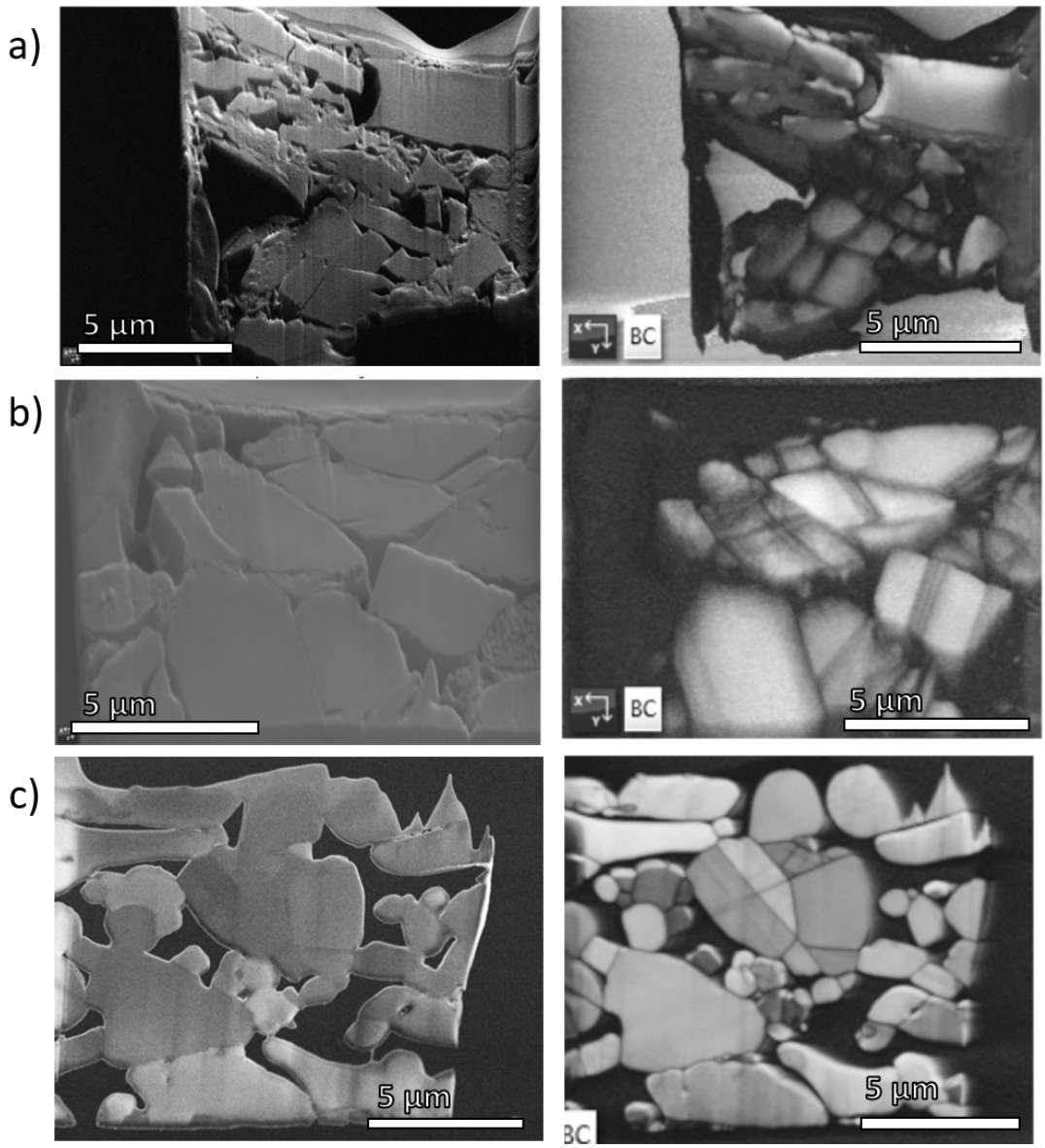

Figure 3.10: Tilt corrected SEM images (left) and band contrast maps (right) of lamella derived from a) pristine, b) 600 °C and c) 900 °C sintered LCO/LLZO powder samples. Band contrast maps reveal GB (dark lines) within smooth looking particles. Some particle cross-sections did not produce Kikuchi patterns of suitable quality for indexing by the software. c) was not tilt corrected by the software at the point of data acquisition. Data acquired at 30 keV on the JEOL 27800F Prime with probe currents between 4 nA and 20 nA using the 30 µm CA.

GB within LCO were more frequent than within LLZO particles of the sample. No grains of electrode or electrolyte appeared to be amorphous when combining EBSD and TEM diffraction information throughout the project, with LLZO being more susceptible to rapid damage at imaging conditions where LCO and LZO were stable. The influence of GB on Li intercalation is expected to increase as they integrate within particles that have been annealed. Their impact on Li mobility is likely to be beneficial as GB networks within LCO interconnected and terminate at the particle

surfaces. If particle surfaces have a boundary with another LCO or LLZO particle, these annealed GB networks could benefit the Li transfer compared to the smaller particle in pristine specimens. The SEM images for heterostructure particle samples, tilted to 70° for EBSD, had significant roughness to their surface, either due to non-uniform milling or via decomposition occurring on the surface during lamella storage. The pristine surface required for EBSD mean these regions provide low-quality Kikuchi patterns and thus limiting the successful indexing of grain boundary contrast and phase indexing. TEM imaging and diffraction acquisition suffers less from the surface's roughness and reaction of the surface with air. Hence, diffraction patterns to assess orientation and phase are more reliable using TEM. Improving the preparation of the sample's surface, would improve the quality of the EBSD data, as this remains a more efficient method of mapping phase and orientations across large areas.

3.5 Transmission Electron Microscopy to Study Crystallinity, Grains and Defects within Sintered Heterostructures

TEM analysis of the polycrystalline films/heterostructures involved sample tilting to align individual particles on their ZAs and thus reliably determine phase of LCO and LLZO. Acquisition of diffraction, phase information and HR imaging within micron-scale grains of both materials observes details of nanoscale to atomistic structure, including defects of varying scale. EBSD data in previous section has highlighted that GB exist within the particles, resolvable by SEM. The inaccuracy of EBSD phase assignment has been improved by SAD phase identification, within particles. Crystalline phases were identified utilising the characteristic diffraction patterns for each phase in different zone axes [44, 51].

Below we present the TEM results from the pristine and sintered samples, focusing on crystallography and visualisations of defects such as GB, dislocations, etc. Potential conductivity influencing structural characteristics are highlighted with respect to the impacts these can have on efficiency of Li mobility and device degradation over a battery's lifespan. The main LCO phase in pristine samples appeared to be r-LCO, with common diffraction patterns relating to $[100]$, $[1\bar{1}0]$ and $[001]$ ZAs. Figure 3.11 shows examples of diffraction patterns from pristine and sintered samples, the latter containing rs-CO. The diffraction patterns in pristine specimens (Figure 3.11 a) show that the majority phase is r-LCO in the electrode grains. For the 600 °C sintered sample both r-LCO and rs-CO were found in the electrode, with the latter reflecting Li deficiency (as discussed in Chapter 1), distinction between rs- CO and c-LCO was made by measuring the spacing of the diffraction spots. Some Li may still be present within these rs-CO grains, but would require

spectroscopic signature of Li, by EELS to confirm this assumption. The lamellae from samples sintered at 900 °C were comprised of the rs-CO phase, with r-LCO phases becoming a minority. This contradicts the XRD, where the electrode signal retains a dominant r-LCO signal even after sintering at 900 °C. This is indicative of Li deficiency near the surface, from which the lamella were extracted, whereas within the bulk of the sintered samples the XRD shows Li-rich grains of r-LCO likely remain as the majority. The diffraction along the [100] axis of rs-CO and s-CO are similar with only a 6% difference in reciprocal spacing for the observed spots. The visual symmetry of atomic columns in HR imaging, analysed later in this chapter, confirms the presence of the rs-CO phase, rather than the s-CO.

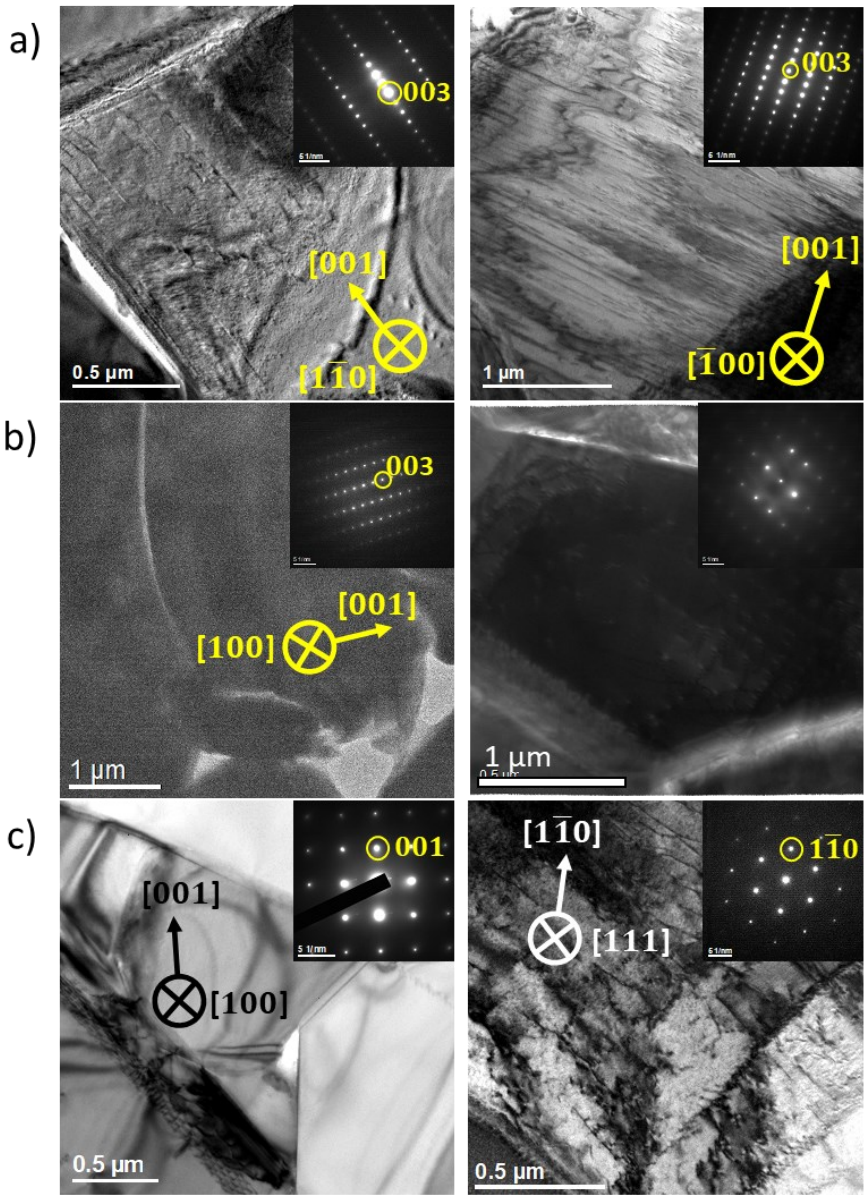

Figure 3.11: Particles within cross-sections of a) Pristine, b) 600 °C and c) 900 °C samples. The inset DPs show a variation between r-LCO (a and b) and rs-CO (c) phases of LCO. The grain to the right of b) remains unidentified and could be r-LCO or rs-CO. All TEM images are BF, acquired in JEOL 2100+ with varying SAD aperture sizes, (camera length: 25 cm).

The presence of large regions of r-LCO suggests reasonable Li retention for pristine and 600 °C sample, advantageous for capacity and conductivity of the electrode, while the deficiencies above 900 °C create rock salt phases, lessening Li conductivity [49]. The balance for annealing appears to be between inducing the merging of small particles, without over exposing the LCO to HT such that Li evaporates. This association between reduced Li content and the formation of the rs-CO or s-CO phases, shown by XRD and TEM of LCO prepared in literature with Li contents ranging from 0% (CoO and Co_3O_4) to 100% ($LiCoO_2$) [162, 304, 308].

Electrolyte grains within pristine and sintered samples (Figure 3.12) where located in the TEM using SEM-EDS data. The SAD from grains in pristine samples (Figure 3.12, a) shows they are LZO, with no LLZO grains present in the sample set of pristine lamellae. This is despite the strong presence of LLZO in the XRD for pristine samples. In contrast, samples sintered at 600 °C, also retaining an XRD signal indicative of LLZO, contained grains where beam exposure resulted in rapid loss of diffraction information and formation of damage spots (Figure 3.12, b and Figure 3.15, b). While condensing the probe for accurate alignment of ZA is possible on grains of LCO and LZO, the beam dose this provides forms circles of damage on grains containing La, Zr and O thought to be Li-rich. This is based on the absence of damage in Li poor $La_2Zr_2O_7$[309]. The lamella from samples sintered at 600 °C are likely to contain Li-rich electrolyte grains and while difficult to identify the specific ZA of observation, provide insights into the phase changes resulting from specimen charging during FIB preparation and high electron doses. Examples of damaged LLZO in Figure 3.12, b provide polycrystalline SAD patterns containing nanograins (Appendix I). Given the stability of the DP obtained from these regions, the locations have likely having decomposed into LZO.

ZA where LZO is identified within pristine and 900 °C sintered samples [110] and $[1\bar{2}1]$ axis are shown in Figure 3.12. The 600 °C annealed sample did have a grain where a diffraction pattern with LLZO characteristics were visible. However, this was challenging to align, prior to disappearance of diffraction information, owing to rapid damage under the 200 keV electron beam. Susceptibility of LLZO to Li evaporation during sintering (XRD), and damage during electron and ion beam exposure (FIB and TEM) can explain the consistent dominance of LZO in particle and highlights the limitations of HR (S)TEM for analysis of SSE. DP from within samples sintered at 900 °C are related to LZO, based on the intensities, absences and spacing between identifiable planes, e.g. (000) and (111) spots (LZO: 1.6 nm^{-1}, LLZO: 1.8 nm^{-1}). Despite limitations with Li retention, analysing GB and defects within the identified LLZO and LZO grains remains important for furthering the understanding of this SSE. While literature has acquired STEM images at ARs, within particles of LLZO, the distribution of boundaries on the nano-to-micron scales remains an important area to investigate [178, 179].

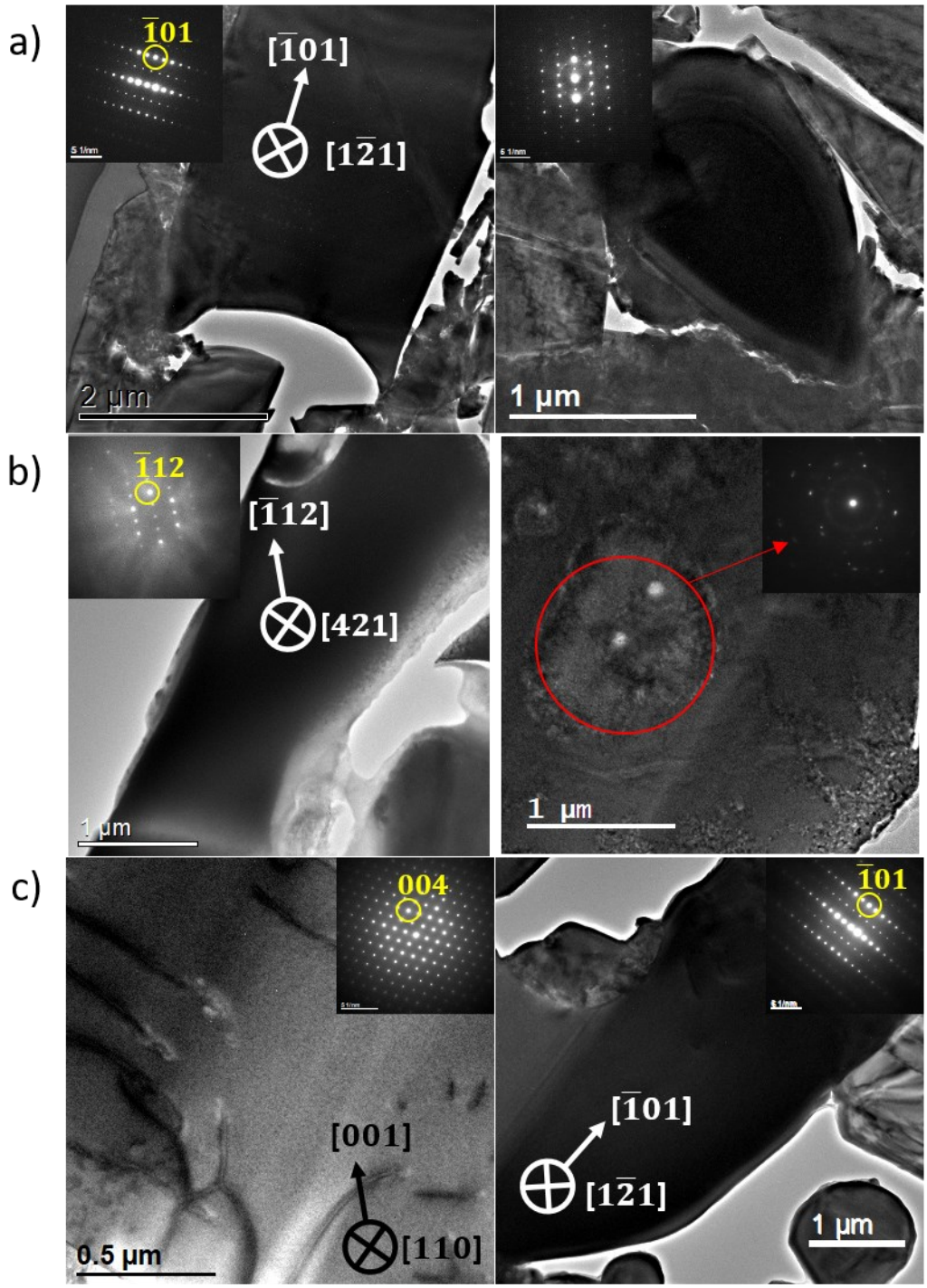

Figure 3.12: Particles within cross-sections of a) Pristine, b) 600 °C and c) 900 °C samples. The inset FFTs show a variation between Li deficient LZO phases are weak LLZO phases that were quick to disappear alongside the emergence of beam damage. All data are BF images taken in JEOL 2100+ with varying SAD aperture sizes, (camera length: 25 cm).

Low magnification TEM images of electrode and electrolyte particles (Figure 3.14 and Figure 3.15) reveal numerous defects in isolation or combining to form networks within individual grains. These range from lone dislocations to complex clusters in an extensive network spanning micrometre of both materials. Figure 3.14 focuses on particles within pristine (a) and sintered (b and c) LCO, where defects exist within the bulk, and near the GBs or interfaces between neighbouring particles. Defect networks mostly span pristine particles of cluster close to GB, while individual defects are randomly scattered throughout the bulk of r-LCO and rs-CO grains. The lengths vary greatly, from nanometres parallel to the surface or microns when combined into defect networks. Defects running at an angle to the aligned ZA are distinguishable by their zigzag or spotty appearance, owing to the effects of extinction distances within the electrode and electrolyte. Lengths of defects not parallel to the optical axis are undetermined. The 3D structure of defects within LCO creates complex pathways for Li movement within the grains. Conductivities limiting the efficiency of Li intercalation along specific lattice planes within r-LCO and rs-CO may be improved by defects directing Li along a more efficient lattice plane, or towards GB.

Dislocations are excited when the tilt angle meets the Bragg condition of the defect's direction through the crystalline material. Tilting the sample onto a two-beam condition allows for the excitation of a single g-vector ($\vec{g}$) and the direct/zero beam (g_0). Defects satisfying the condition for diffracting beam intensity onto the spot relating to a given $\vec{g}$ vector of the crystal's lattice. These defects have a Burgers vector relating to the respective crystal plane represented by the excited diffraction spot (e.g. $\vec{g}_{100}$). Defects with a dot product ($\vec{g}.\vec{b}$=0) will not appear illuminated in a DF image, whereas dislocations satisfying $\vec{g}.\vec{b}$=n (n being an integer) are observed as bright features in the DF image. This brightness is representative of the excited g-vector in the diffraction pattern, from which the DF image is projected by via selection of the spot with an objective aperture. The orientations of dislocations can be determine using the cross-product of two g vectors, $\vec{g}_1$ and $\vec{g}_2$, where $\vec{b}$ = $\vec{g}_1$x$\vec{g}_2$ [216, 310].

The formation of defect networks is driven by the combinations of deformation within the crystal structure, commonly occur near to grain boundaries or structural interfaces (e.g. substrate and film), where the effects of stress and strain lead to the formation of defects along different directions. The orientation and plane along which the defects climb can vary within the material, with the distributions dependant on the phase, formation process and boundary orientations. Where two or more defects growing along the same or differing burgers vectors meet they have the ability to attractively combine or annihilate, creating various interfaces within the defect network pattern [26, 307]. Defects have the ability to combine or annihilate each other dependant on their orientation, creating a continuous network or termination points within a complex combination of defects. Depending on the planes upon which the defects climb within a network

and the symmetry of the defect system, defect networks can combine to form irregular (Figure 3.13 a) or patterned networks (Figure 3.13, b) [307]

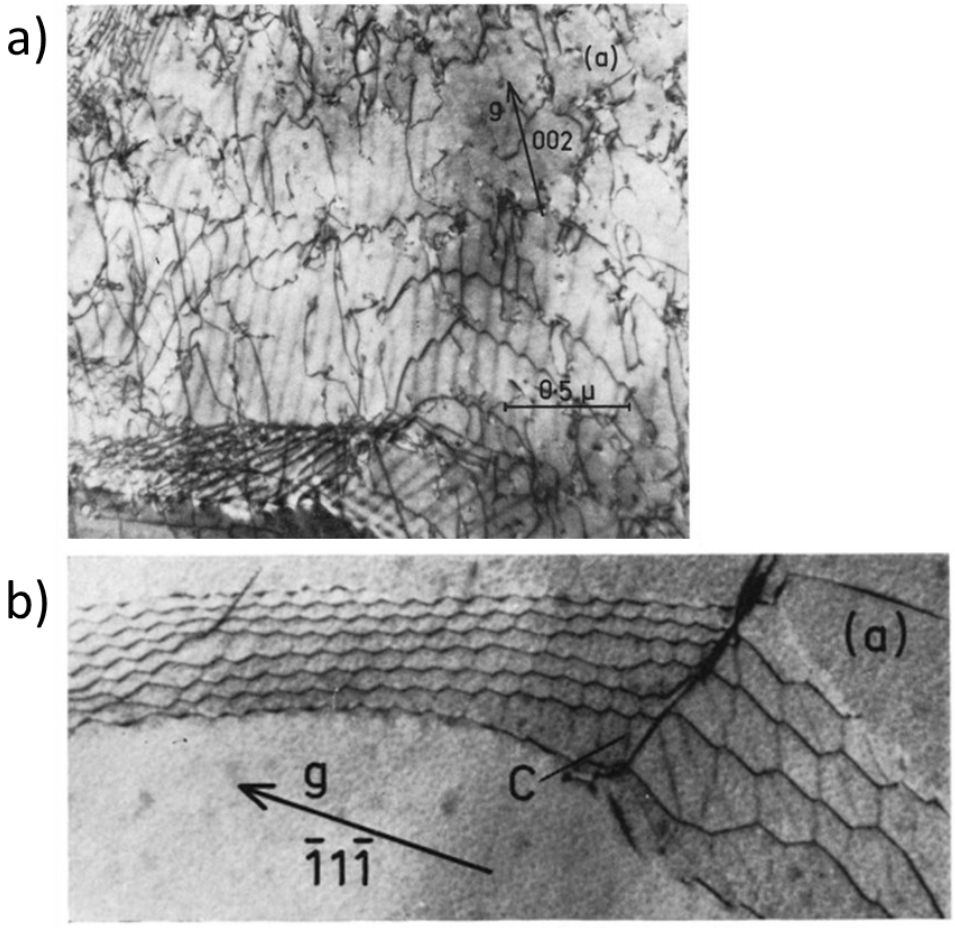

Figure 3.13: a) Tangled dislocation network in Al-2%Mg alloy creating an irregular pattern of combining defects, b) Network formed from three-fold nodes in Al-6%Mg alloy, displaying a network with a repeating pattern. Images reprinted from reference [307].

There are differences between the defects in relation to variation of annealing temperature. Pristine LCO had fewer defects, seemingly adopting longer structures with a specific direction through a particle (Figure 3.14, a), compared to sintered samples (Figure 3.14, b and c). Annealing appeared to create networks combining shorter defects forming along various orientations in 3D throughout r-LCO and rs-CO. The density of defects within the bulk of the grains after sintering at 600 °C and 900 °C also increases. Within large, single crystal grains of r-LCO, fewer defects would be advantageous for allowing uninterrupted ion migration through the LCO phase of highest conductivity. In an electrode comprised of polycrystalline nanograins, the presence of defects may provide routes of lower resistance for Li mobility through rs-CO and s-CO grains. Unlike GB networks spanning the micron-scale cross-sections of particles, isolated defects may trap Li in

the bulk to the electrode. However, the networks of defects that appear in both LCO and LLZO may be effective at channelling Li towards the GB, benefiting mobility. Further study of the defect networks is required to determine whether these defects have a net positive or negative effect. In-situ TEM studies to observe the changes in defects during annealing are possible and an important future experiment to carry out.

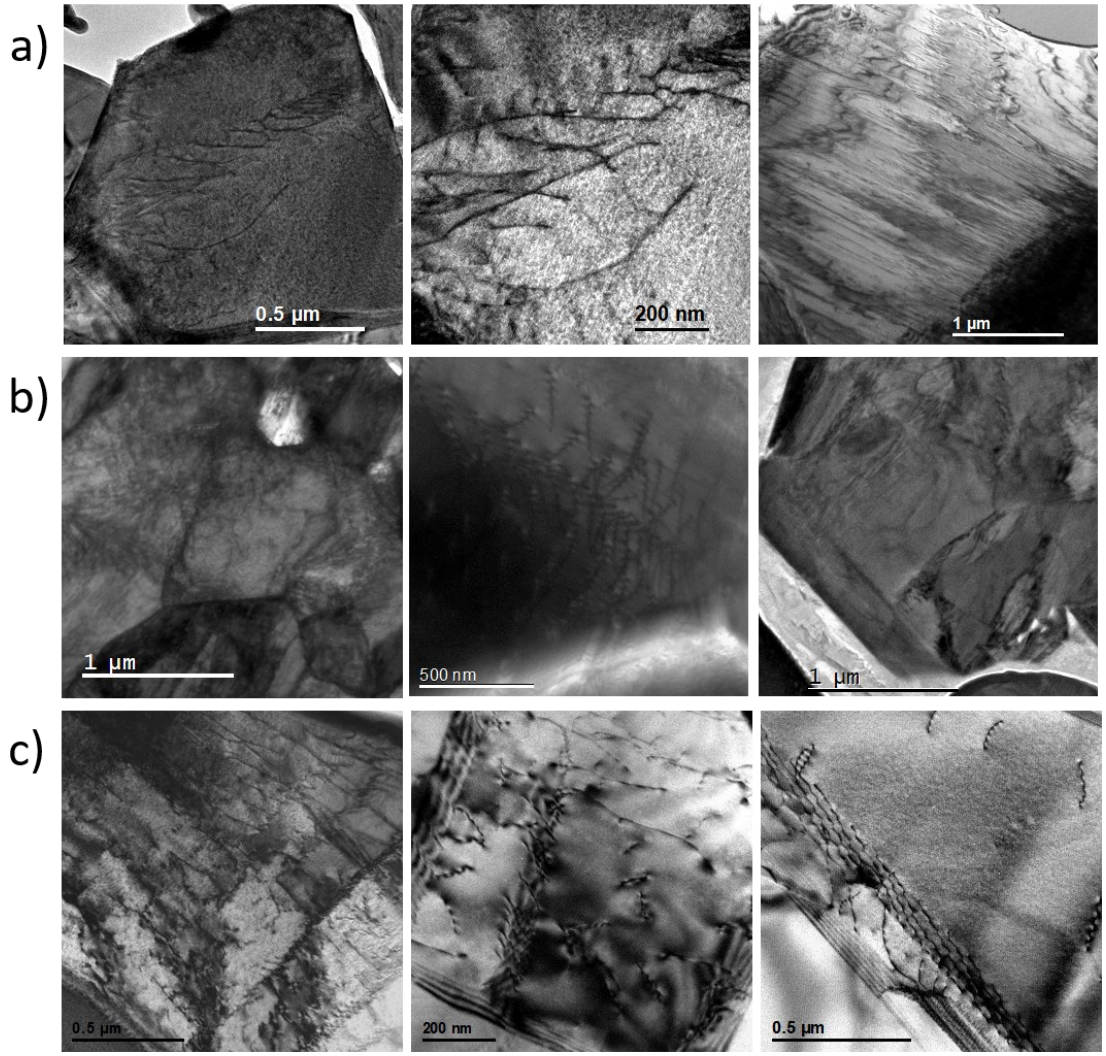

Figure 3.14: Defects and grains observed in samples of pristine LCO particles. a) Pristine sample. b) LCO/LLZO powder sintered at 600 °C. c) LCO/LLZO powder sintered at 900 °C. BF images acquired at 200 keV in JEOL 2100+

In the electrolyte, defects were also found in LLZO and LZO particles (Figure 3.15). The difference between pristine (Figure 3.15, a), 600 °C and 900 °C (Figure 3.15, b and c) annealing is more challenging to assess, owing to the sample size of electrolyte grains and beam damage (Figure 3.15, b), where differentiating defects from the changes as LLZO is damaged is not possible. While extended networks of defects were present in LCO, fewer of them were observed within the grains of electrolyte. Increased number of defects appeared to be present after sintering at 900 °C (Figure 3.15, c), appearing to aggregate in clusters rather than of long networks. The reason for greater defect formation after sintering at 900 °C could be due to the decomposition of LLZO into LZO.

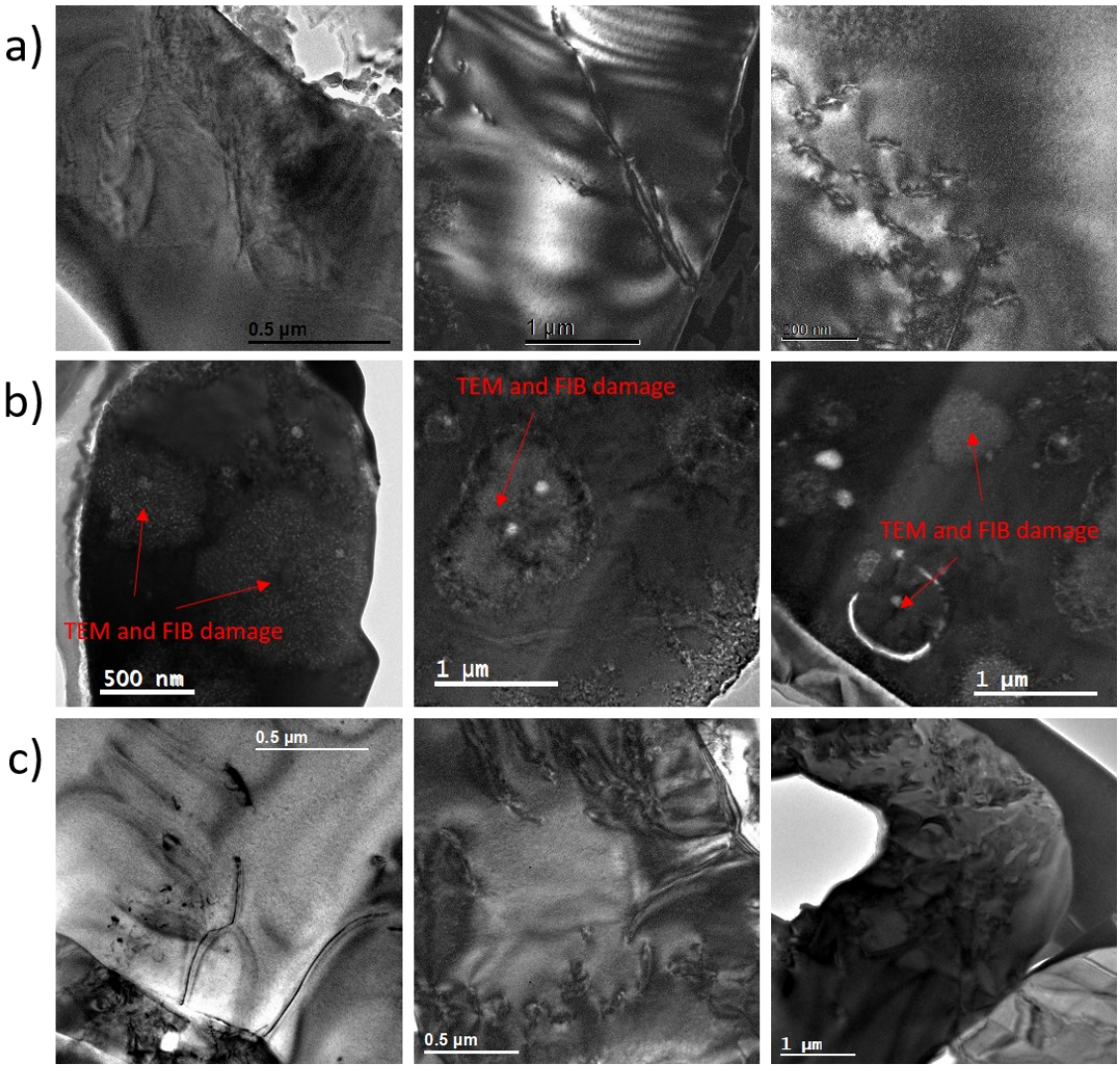

Figure 3.15: Defects and grains observed in samples of pristine LLZO particles. A) Pristine, b) sintered at 600 °C. c) sintered at 900 °C. Defects in the LZO grains of a) and c) are similar, although more appear to be present post-sintering. The electron ion beam damage makes resolving defects in LLZO grains in the images shown in b) challenging. Data acquired in JEOL 2100+ at 200keV.

BF and DF imaging at a variety of tilts observes the defects and attempts to assess their respective orientations within the different networks present in LCO or LLZO. Figure 3.16 to Figure 3.18 provide examples of this work into both materials where specific network of defects was imaged at higher magnifications. A distinct set of network defects running parallel to a GB and $[1\bar{1}0]$ diffraction vector for the rs-CO ZA [100] is shown in Figure 3.16. The extended network of defects evolves along the direction parallel to the GB. We have also acquired DF images of this region by tilting towards two-beam and subsequent weak beam (g – 3g) diffraction conditions for BF and DF analysis from the [001] ZA. Diffraction patterns for tilts relating to DF images are labelled with respective g vectors. Within pairs of BF and DF images, there were tilt conditions where intensity of specific defects reduces significantly. Given clusters of defects do not meet the same $\vec{g} \,.\, \vec{b} = 0$ condition; this suggests multiple $\vec{b}$ (Burgers) vectors of complex dislocation system. These defects are likely to have significant influence on the Li mobility across different crystallographic directions.

The network of defects in Figure 3.16 was representative of a few regions in LCO where tightly packed clusters of dislocations existed. Through two-beam (Figure 3.16) and weak-beam (Figure 3.17) imaging of this defect network, some dependence on the (010) or $(\bar{1}10)$ plane became apparent. With both planes containing defects illuminated in their respective DF images the network allows interconnection of defects that may be active to Li intercalation through different LCO planes.

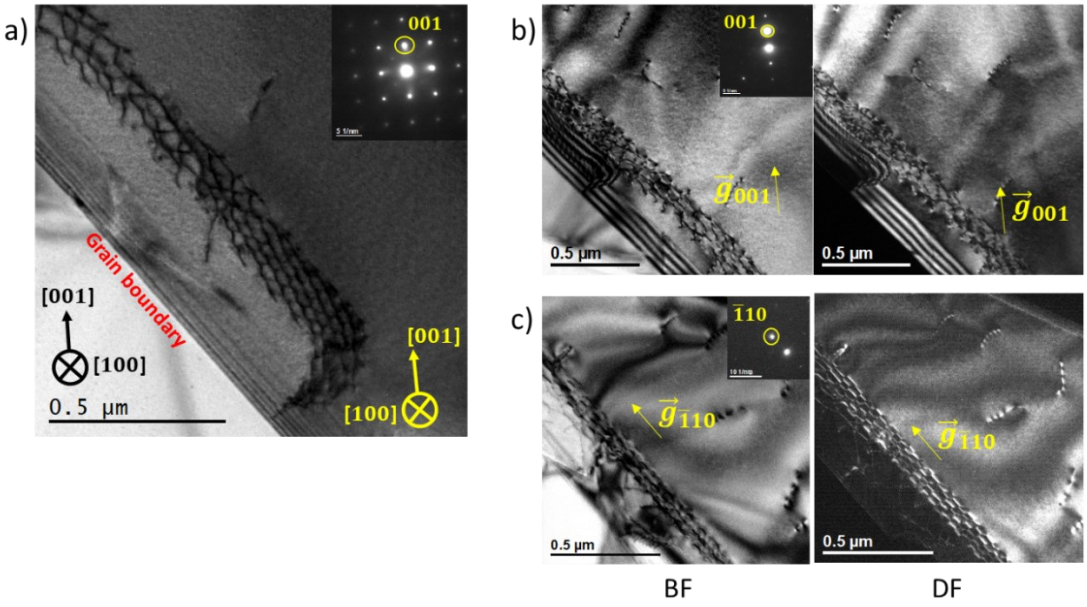

Figure 3.16: BF image of defect network parallel to GB in a particle of LCO. a) rs-CO grain on [100] zone axis. b) Two-beam BF (left) and DF (right) images with sample tilted onto the two-beam condition, exciting the 001 spot. c) BF (left) and DF (right) when the grain is tilted to create a two-beam condition with the $\bar{1}10$ diffraction condition. Data acquired on the JEOL 2100+ at 200 keV. DF images utilised the 20 µm OA.

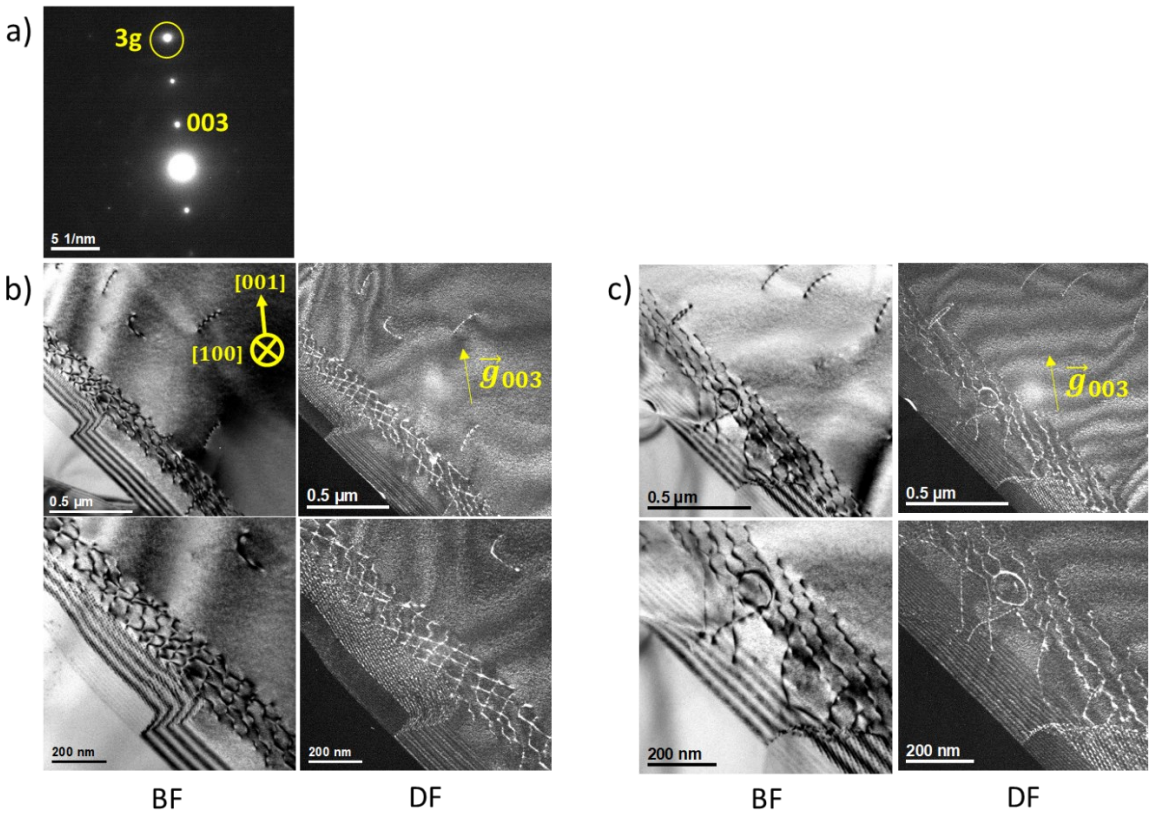

Figure 3.17: a) Weak beam condition for defect imaging along the 001 direction in rs-CO grain shown. b) Low (upper images) and higher magnification BF and DF image relating to an area with a more closely packed defect network where most defects excite. c) Low (upper images) and high magnification BF and DF images of region further down the sample with different defect structure. The defect are also excited at this weak beam within this region of the defect network. Data acquired on the JEOL 2100+ at 200 keV. Weak beam DF images utilised the 20 µm OA to maximise signal.

BF and DF sets of images around $[001]$ r-LCO ZA are shown in Figure 3.18, with different defects becoming visible in the DF at more than one $\vec{g}$ vector condition. Within the cluster of dislocations in a grain of r-LCO, viewed along the [001] zone axis, g vector orientations used for imaging appeared to satisfy $\vec{g}.\vec{b}$ = n along planes such as the $[\bar{1}20]$ and $[2\bar{1}0]$. In contrast, diffraction spots relating to the $[110]$ and $[\bar{1}\bar{1}0]$ directions did not display defect contrast, as observed in the respective DF images (Figure 3.18), thus satisfy a $\vec{g}.\vec{b}$ = 0 condition. The defects shown in this grain are not as interconnected as in Figure 3.17, alongside having an apparent orientation dependence. The density of defects suggests that within a device they can have a considerable influence with respect to the volume they occupy, their overall impedance to Li transfer would be important to determine. This will likely depend on the phase of the grain they occupy, their orientation, length and proximity to GBs.

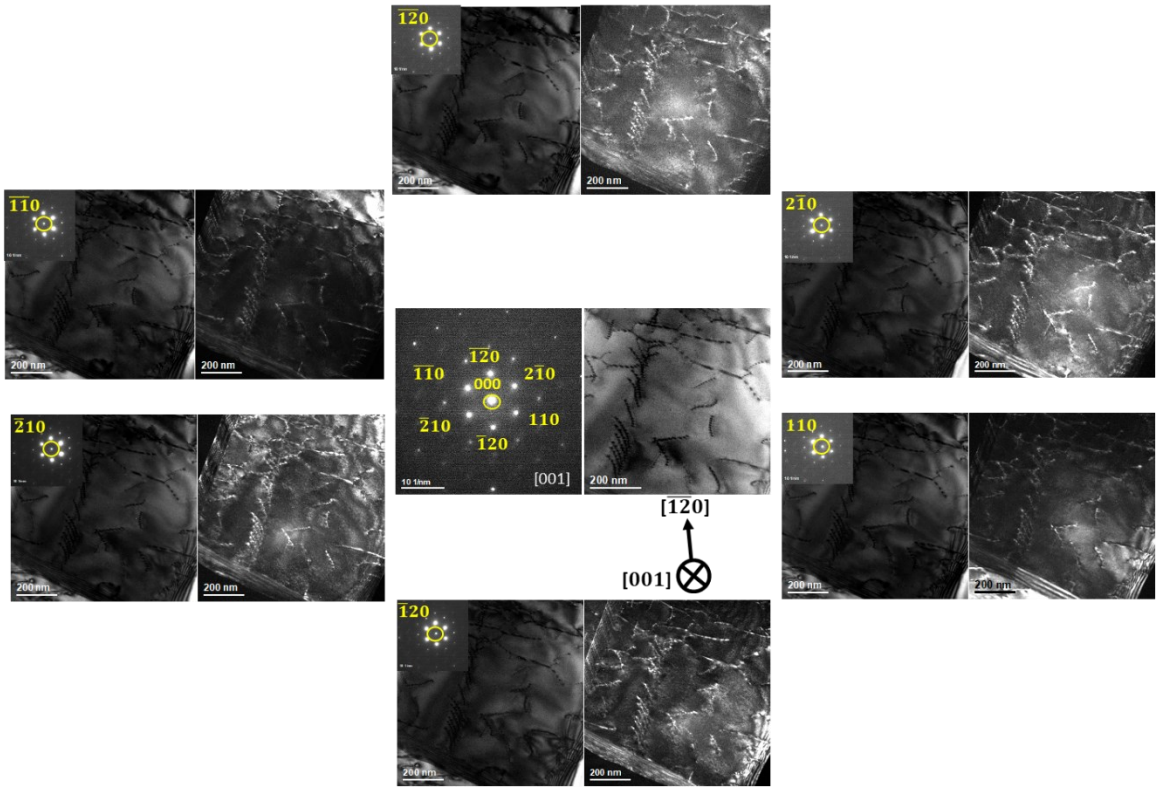

Figure 3.18: BF and DF imaging of the spots around the [001] zone axis of an r-LCO particle cross-section. Most defects appeared to be illuminated with the aperture selecting the series of $[2\bar{1}0]$ diffraction spots. Selection of the [110] and $[\overline{11}0]$ spots illuminated significantly fewer defects. BF images are shown to the left of each image pair and DF displayed on the right. Data acquired on the JEOL 2100+ at 200 keV. DF images utilised the 20 µm OA to maximise signal.

Similar BF and DF images collected within the LLZO (Figure 3.19) provides less insight into orientation, with fewer visible defects and the spacing of the LLZO or LZO DP too small for one spot to reside within the 5 to 20 µm apertures for DF imaging. Dislocation defects, seen in Figure 3.19 c), were now visible, unlike within the LCO grains. The dislocations in Figure 3.19 appeared to be mostly parallel to the [110] axis based on the lack of contrast variation along their length. Although while providing strong contrast in the BF images for two-beam tilt conditions there, we did not find appropriate $\vec{g}$ vector conditions that would clearly show dislocation defect contrast changes to assign directions.

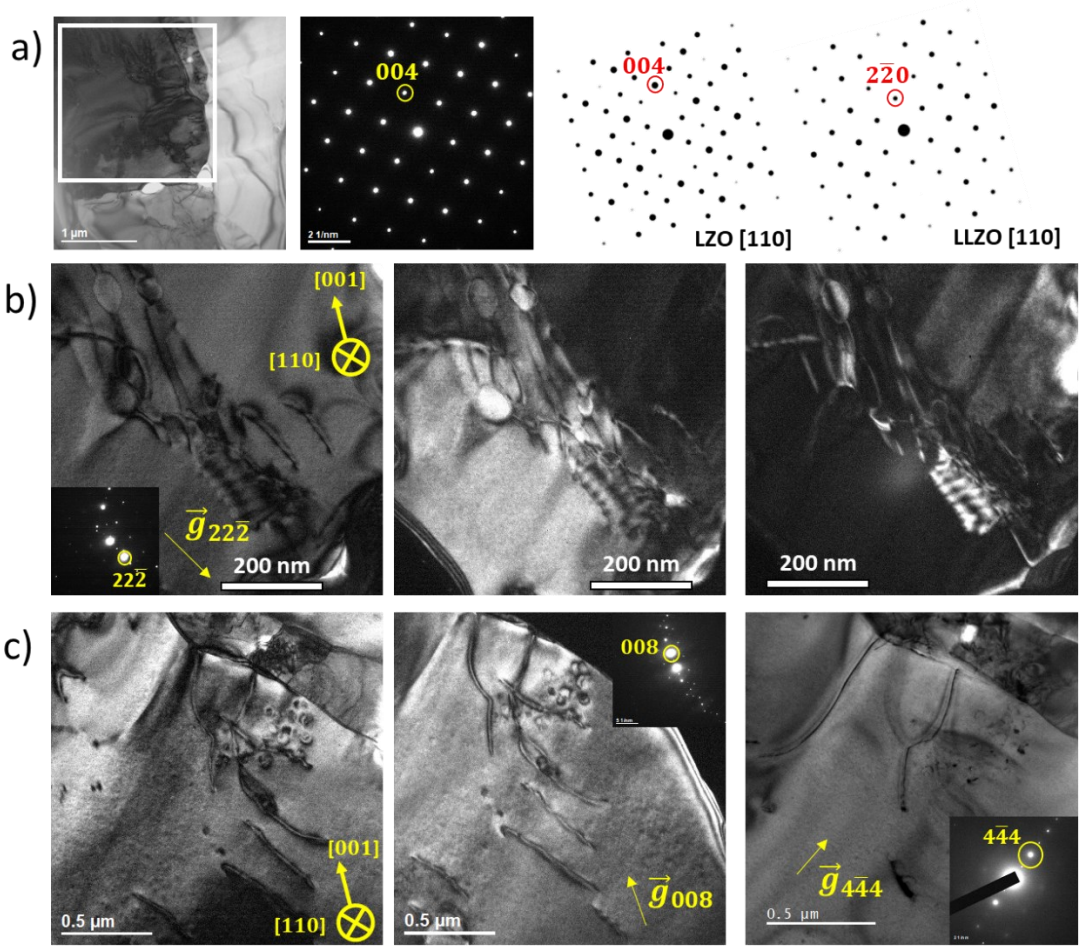

Figure 3.19: a) ROI with SAD pattern from grain orientated onto the $[110]$ ZA of LZO or LLZO. The lattice parameters determined from the distance to the direct beam (000) are closer to the LZO phase than LLZO. b) Left to right: TEM, BF and DF images with the $22\bar{2}$ diffraction spot near a two-beam condition. c) Left to right: BF, DF image through selection of the 008 spot (centre image) and DF relating to the $4\bar{4}4$ diffraction (right image) plane of LZO. Data acquired in JEOL 2100+ at 200 keV, using the 5 µm OA for DP of LZO or LLZO.

As an overall influence on electrode and electrolyte performance, the presence of defects has the potential to provide regions of disorder within the grains of electrode and electrolyte, whereby Li may accumulate or be channelled, with lower resistance, through the device, with literature suggesting they are closely related to diffusion characteristics [24]. A high concentration or network of defects near to a GB or LCO-LLZO interface is likely to support Li movement into boundaries and through a grain. In contrast, isolated defects within the bulk of a particle's grain are more likely to act as Li traps if they do not provide a more efficient route into an adjacent grain [24, 119, 288]. Computational analysis of screw and edge defects coupled with experimental studies is required to understand their effect on the Li mobility, i.e. whether inducing formation of defect networks with controlled annealing, helps or hinders device performance.

3.6 HR (S)TEM of LCO, LLZO and $LaCoO_3$ Phases in Sintered Particles, Resolving Atomic Structure at GB and Interfaces

In this part, we provide HR STEM imaging of LCO, LLZO and $LaCoO_3$ (secondary phases) that result from thermal decomposition of LLZO, in attempt to determine the nanoscale details of phases and orientations at GB and EEIs. In Figure 3.20, the LCO structure (a) and a grain showing rs-CO (b) are resolved. The layer spacing in the r-LCO grain is 0.48 nm, close to the 0.46 nm expected for r-LCO, which is within the error of spacing determination from FFT. Resolving of atomic columns within these planes is likely limited by the thickness of the sample or slight misorientation from the ZA. Imaging across the GB and defect network in Figure 3.20, b shows the rs-CO phase within this grain as well as overlapping grains and orientations at the GB.

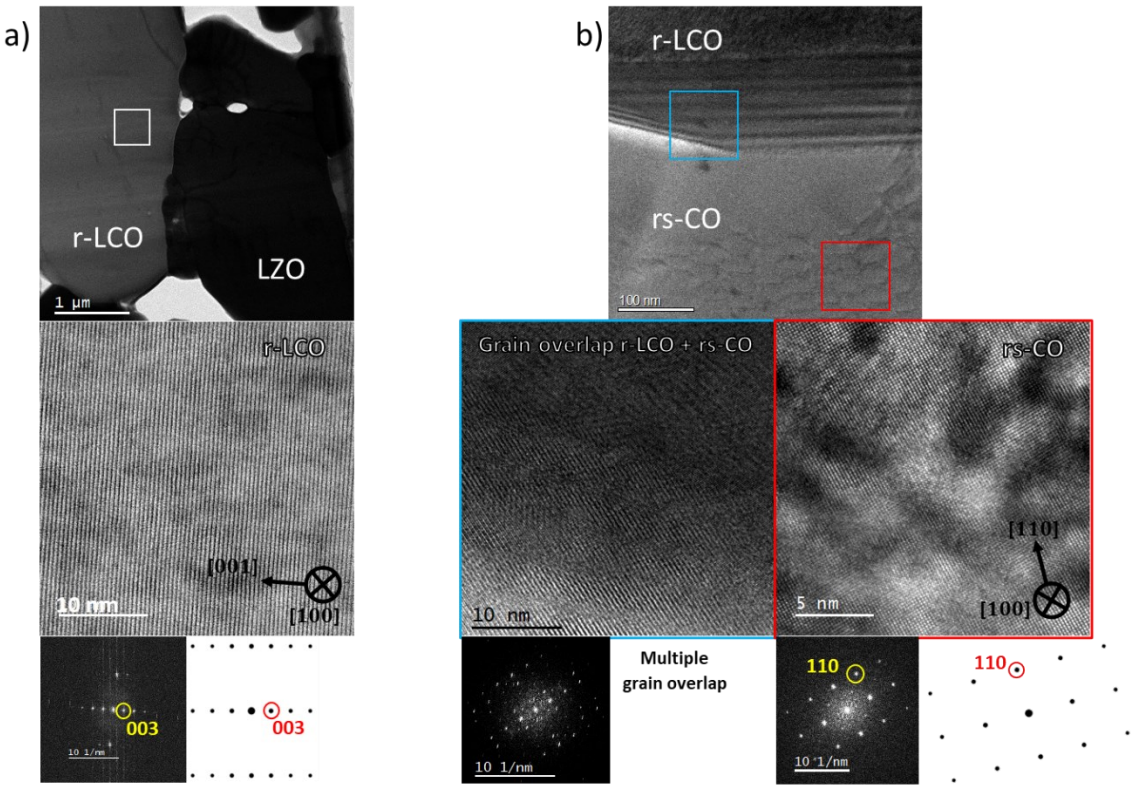

Figure 3.20: a) Region of r-LCO with structure resolved along the $[1\bar{1}0]$ ZA in the HAADF image. The CoO_2 layers relating to the [001] plane run horizontally across the image. b) Two HAADF images of LCO taken from region inclusive of a GB and defect network. A mix of orientations appearing to be the r-LCO phase along the $[1\bar{1}0]$ ZA. In contrast, the red square returned HR image data of the rs-CO phase with defects visible. Acquired on JEOL 2200FS, at 200 KeV.

The bulk of particles remained too thick for effective analysis of defects and lattice alignments at GB on atomic scale. While the edges of LCO and LLZO particles were thinner, Ga^+ and Ar^+ damaged during milling lead to amorphisation of these thin regions. The porosity of the particle samples is the limiting factor when attempting to thin the LCO and LLZO to the extent that characteristics of GB and defects on the atomic scale can be analysed. The use of PLD thin films in Chapters 4 and 5 resolves this problem.

Figure 3.21 shows regions of electrolyte where atomic columns are resolved. The FFT diffractograms and SAD diffraction are used to find the spacing which is consistent with LZO, as covered in Appendix I.

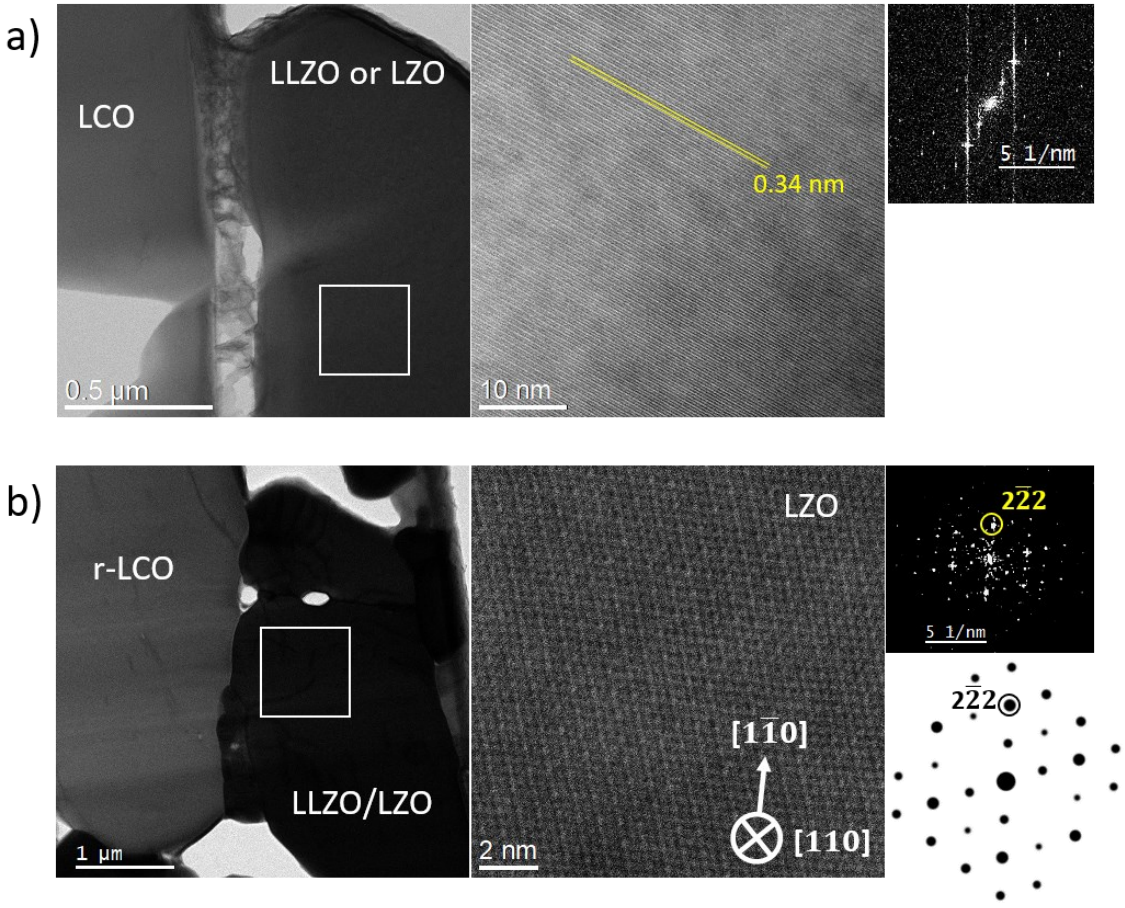

Figure 3.21: a) HAADF images of LZO or LLZO grain with spacing of spots and lattice planes (0.34 nm) lying between the values expected for both phases and thus undeterminable within calibration errors and diffractogram measurement accuracy. b) HAADF images of LLZO grain observed along the [110] axis with the atomic structure resolved. The separate atomic columns along this zone axis have been resolved. JEOL 2200FS, 200 KeV

Atomic columns were observable near EEI, providing insight into the bulk structure of grains as well as LCO/LZO interfaces. At the interface with LCO, the misorientation between the grains of adjacent particles is such that simultaneous atomically resolved imaging was not possible (Figure 3.22). The example in Figure 3.22 shows the [110] axis of LZO or LLZO in contact with LCO, near to the $[1\bar{1}0]$ zone axis and touching along the (001) plane. The lattice planes of likely CoO layers are visible but alignment with the nearby $[1\bar{1}0]$ r-LCO axis was not simultaneously possible. A layer of 4 nm between the two materials is present, with crystallinity resolvable with additional defocus Figure 3.21, c. This region could have either been an overlap between the two materials or an SEI formed by La and Co intermixing during annealing. The lack of a large $LaCoO_3$ grain between the LCO and LLZO particle in Figure 3.22 suggests that interfaces away from the particle-air interface are less susceptible to significant La-Co intermixing. This was also the case in thin film heterostructures (Chapter 5), where the interfaces do not have contact with air during annealing. An interface on the scale of a few nanometres (Figure 3.21 b and c) will be significantly less detrimental to Li conduction in comparison to micron scale secondary phases of $LaCoO_3$ as shown in Figure 3.22. Maximising the contact between particles of LCO and LLZO at their interface could limit the formation of $LaCoO_3$ on the micron scale and create EEIs dominated by the thin SEI seen in Figure 3.22.

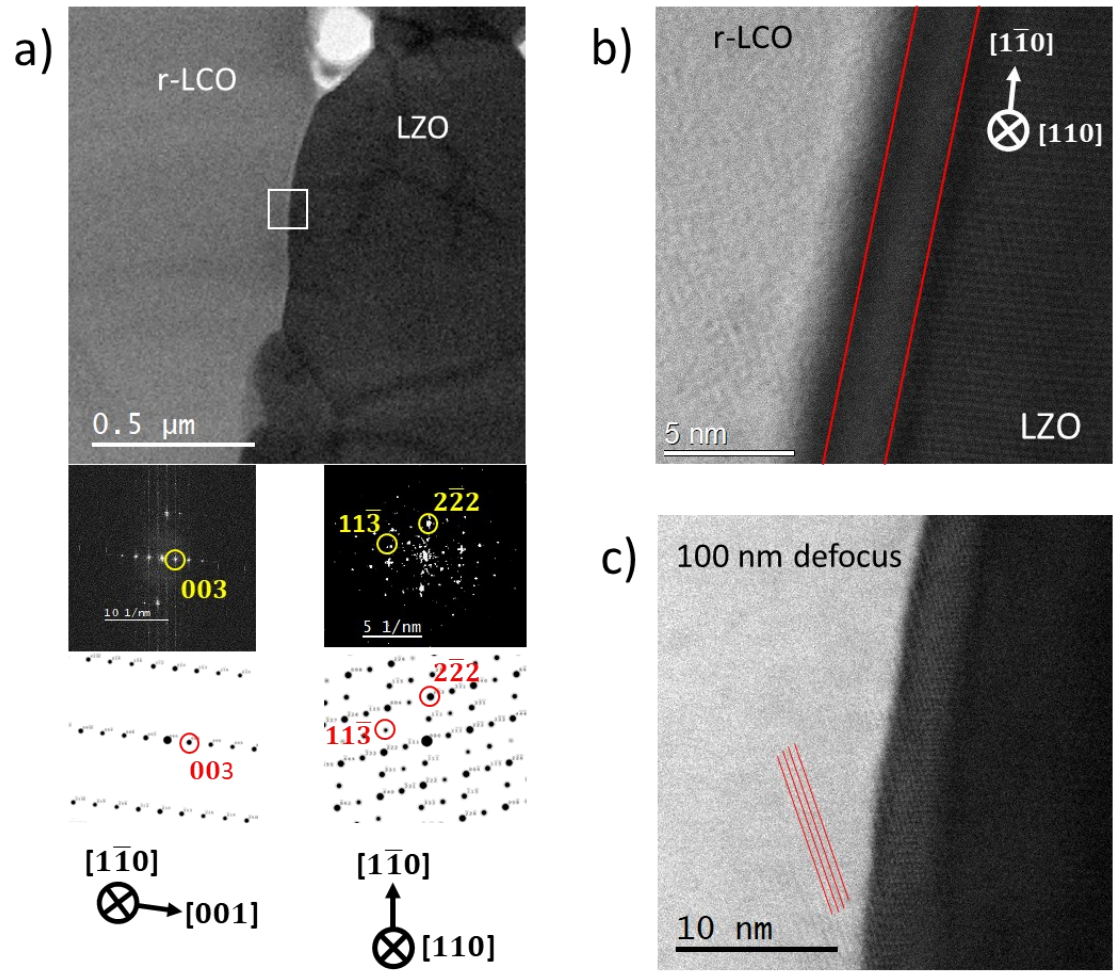

Figure 3.22: a) Region of interface between electrode and electrolyte imaged, with the closest zone axis of each displayed. These relate to an interface between the [001] of r-LCO and [1$\bar{1}$3] of LZO. b) Interface region with LLZO/LZO on the [110] zone axis, while the r-LCO lattice planes are not aligned and poorly resolved. An interface region with intermediate contrast is also present and focus adjusted (100 nm defocus) to resolve the interface structure in image in image c). Data acquired on JEOL 2200FS at 200 keV

Figure 3.22 is from a region where LCO and $LaCoO_3$ grains are shown to have been formed during the sintering at 900 °C. The cut lamella provides opportunity for HR imaging within these grains and their interfaces with either electrode or electrolyte. An example of one LCO/$LaCoO_3$ interface is displayed in Figure 3.23, alongside an EELS element map showing the shape transition between LCO and the decomposition phase. The $LaCoO_3$ was shown to match the diffraction spacing along the [010] axis of spinel structure [306, 311]. The spinel structure of $LaCoO_3$ provides potential for Li migration; however, it does not provide a highly conductive route for Li as an interface layer between LCO and LLZO, due to rather low conductivity of $\times 10^{-8}$ S cm^{-1} [312, 313].

The less energetically favourable $Li_xLa_2Co_{1-x}O_4$ composition is possible but not seen within $LaCoO_3$ and therefore formation of these near micron-scale decomposition layers between LCO and LLZO would be significantly limiting within devices.

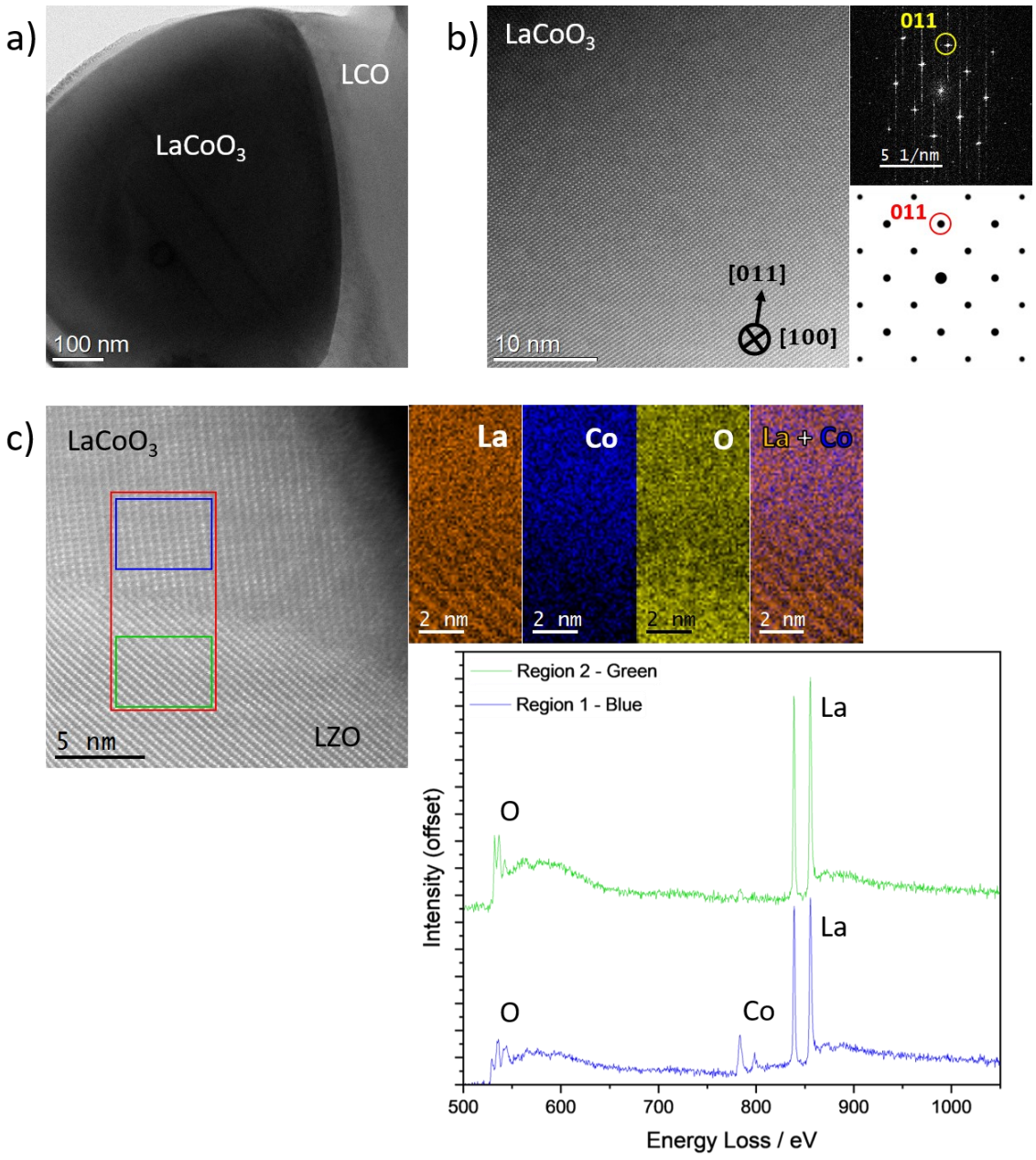

Figure 3.23: a) Particle of $LaCoO_3$ with respective high magnification image b) showing the cubic spinel structure along the [010] ZA. c) Interface from another region between $LaCoO_3$ and LZO with a sharp interface. EELS maps are included for the scanned region (red), with the core-loss spectra relating to the two phases also displayed (blue and green), highlighting the presence of Co in the upper grain and absence in the low grain. Data acquired at York on JEOL 200FS at 200 keV (a, b) and SuperSTEM at 60 keV (c).

The other clear challenge created by LCO and LLZO with respect to imaging across the interfaces within heterostructures was the difference in atomic weight. This has the consequence of creating large contrast gradients across the sharp interfaces of materials. This presented difficulties in particle samples, washing out the contrast in atomic planes within grains either side of the LCO/LLZO interfaces. Atomic structure could still be resolved, although methods of deposition LCO and LLZO in a controlled manner have the potential to create EEI where both materials were had a ZA aligned with the electron beam axis allowing imaged containing lattice information LCO and LLZO simultaneously. This approach was utilised and data presents in Chapter 4 and 5.

3.7 Conclusions from Investigation into the Micron and Nanoscale Crystallographic features in Sintered LCO/LLZO Heterostructures

Using a range of sintering conditions on samples containing LCO and LLZO particles, assesses the composition, grain, and defect structures, as well as interfacial decomposition between the electrode and electrolyte on the micron to atomic scale. Each sintering method causes changes to compositional and structural features, including coalescing smaller LCO grains seen in pristine samples, into larger particles containing multiple grains and boundaries after heat treatment. Distributions of defects also change alongside the formation of large regions of $LaCoO_3$, between LCO and LLZO particles, when the EEIs are exposed to 900 °C. These changes can have important influences on a devices performance relating to the Li-ion conduction through electrode and electrolyte. The XRD of pristine and 600 °C samples show these contain Li rich r-LCO and c-LLZO, while heat treatment at 900 °C provides strong evidence of Li deficiency within the LLZO. Retention of the r-LCO phase after sintering at 900 °C suggests the electrode is less thermally sensitive to Li evaporation than the electrolyte. Susceptibility to beam damage and annealing thin film samples in literature and later chapters reported from my work, further support the susceptibility of LLZO to Li evaporation [143, 314].

The apparent coalescence of smaller LCO particles into larger, multi-grain particles during sintering can be advantageous for maximising the density of material in electrodes, potentially improving the capacity and efficiency of the device. The formation of GB systems through the merging of smaller LCO grains, create new routes for Li intercalation through LCO electrodes. Increasing the size of LLZO particles due to sintering was not seen, potentially a result of particle growth/decomposition during sintering process and fewer adjacent LLZO grains to coalesce with during sintering. Evaporation of Li will offset improvements due to grain size enlargement by

reducing capacity during annealing over 600 °C for timespans of hours. Li conductivity through LCO and LLZO also will reduce as the contribution of rs-CO and LZO phases increases, as identified in this Chapter. A greater weight excess of Li in starting LCO and LLZO would be advantageous when subjecting the samples in this chapter to sintering/annealing. This would lessen the influence of lithium deficiency when applying temperatures of 900 °C, while retaining the apparent growth of LCO grain sizes.

GB and interfaces appear to have a role in inducing dislocation/dislocation networks within the electrode and electrolyte grains, most visible through the presence of defects forming close to boundaries or staking faults. The latter is dependent on whether the contrast variations at the GB are related to overlapping grains or crystallographic defects forming stacking faults. The extended network of defect loops (Figure 3.16) is one example of the range and potential significance of increased defects regions within crystalline grains of LCO. Two-beam and weak-beam experiments have tried to find $\vec{g} \,.\, \vec{b} = 0$ conditions for defects, with future work, focusing on additional and refined two-beam datasets, to accurately determine orientations of Burger's vectors. Given their significant volume defects, appear likely to occupy a significant volume of LCO electrodes. Experimentally determining defect types and their orientations can enable important computational work focused on the Li dynamics within these complex features. With literature focusing on analysing, crystallographic and compositional details electrodes and electrolytes at nano-to-ARs [124, 163, 315], determining the impact of defects on performance, relating to type (edge, screw etc.), orientation and scale, is an important area of research to pursue further. Controlling defect length, network formation and developing insight into their influence on mobility, through computational work, are all interesting avenues to research.

SEI formation between LCO and LLZO, through La and Co intermixing occurs during annealing at 900 °C, creating grains of $LaCoO_3$ with low Li conductivity, detrimental to performance. The potential for excessive decomposition between solid-state electrode and electrolyte is significant and thus thermal treatment of the two in direct contact is undesirable. Annealing separately with an excess of Li before forming the EEI, would optimise the system of LCO grain interconnection, and phase of both materials without La and Co intermixing.

Chapter 4

Orientation and Grain Boundary Analysis of $LiCoO_2$ and $Li_7La_3Zr_2O_{12}$ Grown by Pulsed Laser Deposition

This chapter aims to build upon the thin films of LCO and LLZO presented in literature [131, 147, 148] by focusing on the distribution of phases and coherence between grains of equivalent and different phases. Understanding and refining single layer depositions, for formation of thin film electrode-electrolyte heterostructures, required the investigation of crystalline properties at various PLD growth conditions and annealing temperatures. We show in this chapter multi-phase growth of LCO occurred, originating from Li deficiency throughout the thin films. The growth orientation of r-LCO, c-CO and s-CO films is variable but controlled across the used substrates, ALO(0001), GGG, STO(111) and STO(100), although with varying dominant growth directions. While LCO provides crystalline films on all substrates at low deposition temperatures, LLZO is crystallised using temperatures of 600 °C, up to 1050 °C for annealing and 600 °C during PLD. HR STEM was used to investigate the orientations and GB in crystalline electrode and electrolyte samples.

For LCO a focus on LT PLD aims to develop methodology where Li retention between target and substrate is high. This is potentially at the expense of epitaxial growth, therefore provides the opportunity for gaining insight into phase distributions and consequent modelling of lithium dynamics in polycrystalline LCO thin films. LLZO preparation continues with the LT PLD approach for improving Li retention during deposition, but in response to the results obtained then attempts to define suitable parameters for annealing thin films. Locating the minimum onset temperature for crystallisation of amorphous thin films and applying this to PLD such that crystalline growth can be achieved in the system at York and potentially elsewhere. Analysis of grains and their boundaries within crystalline LLZO films then match the objectives set for LCO studies, providing HRSTEM data as the basis for observing coherence at GB in LLZO and thus acting as a basis for modelling potentially complex grain systems in LLZO and other garnet electrolytes.

Figure 4.1 displays the anticipated orientations for LCO on ALO(0001), STO(111) and STO(100), based on the lattice parameters in Table 4.1 and films acquired at higher temperatures in literature [51, 316, 317]. The a/b lattice parameters and periodic oxygen atom spacing of Al_2O_3, on the (0001) plane are 4.76 Å, with a γ angle of 120 °C for the rhombohedral crystal structure ($R\bar{3}c$). For epitaxial orientated r-LCO, the lattice dimensions along the a/b vectors are 2.82 Å. This creates a 0.88 Å (30%) mismatch between O atom spacing on the 001 plane of LCO, deposited upon

the Al_2O_3(0001) plane. Significant strain should occur due to this scale of mismatch between substrate and LCO at their interface. Despite the mismatch the periodicity of major defects along the interface is later shown to be infrequent. Either through lack of interfacial strain or aided by the hexagonal symmetry of ALO sharing similarities with r-LCO, the interface did not appear excessively strained or defect dense.

Table 4.1: Table of lattice parameters for substrates, LCO and potential phases resulting from Li deficiency.

Composition	Phase	Space group	Lattice Parameters / Å			Angles / °		
			a	b	C	α	β	γ
Substrates								
Al_2O3	Hexagonal	$R\bar{3}c$	4.76		13.00	90		120
$SrTiO_3$	Cubic	$Pm\bar{3}m$	3.90			90		
$Gd_3Ga_5O_{12}$	Cubic	$Ia\bar{3}d$	12.55			90		
Electrode phases								
$LiCoO_2$	Rhombohedral	$R\bar{3}m$	2.82		14.05	90		120
$LiCoO_2$	Cubic	$Fd\bar{3}m$	8.22			90		
rs-CoO	Cubic	$Fd\bar{3}m$	4.26			90		
Co_3O_4	Cubic	$Fd\bar{3}m$	8.05			90		
Electrolyte								
$Li_7La_3Zr_2O_{12}$	Tetragonal	I_{41}/acd	13.20		12.87	90		
$Li_7La_3Zr_2O_{12}$	Cubic (>900 °C)	$Ia\bar{3}d$	13.18			90		
$La_2Zr_2O_7$	Cubic	$Fd\bar{3}m$	10.75			90		

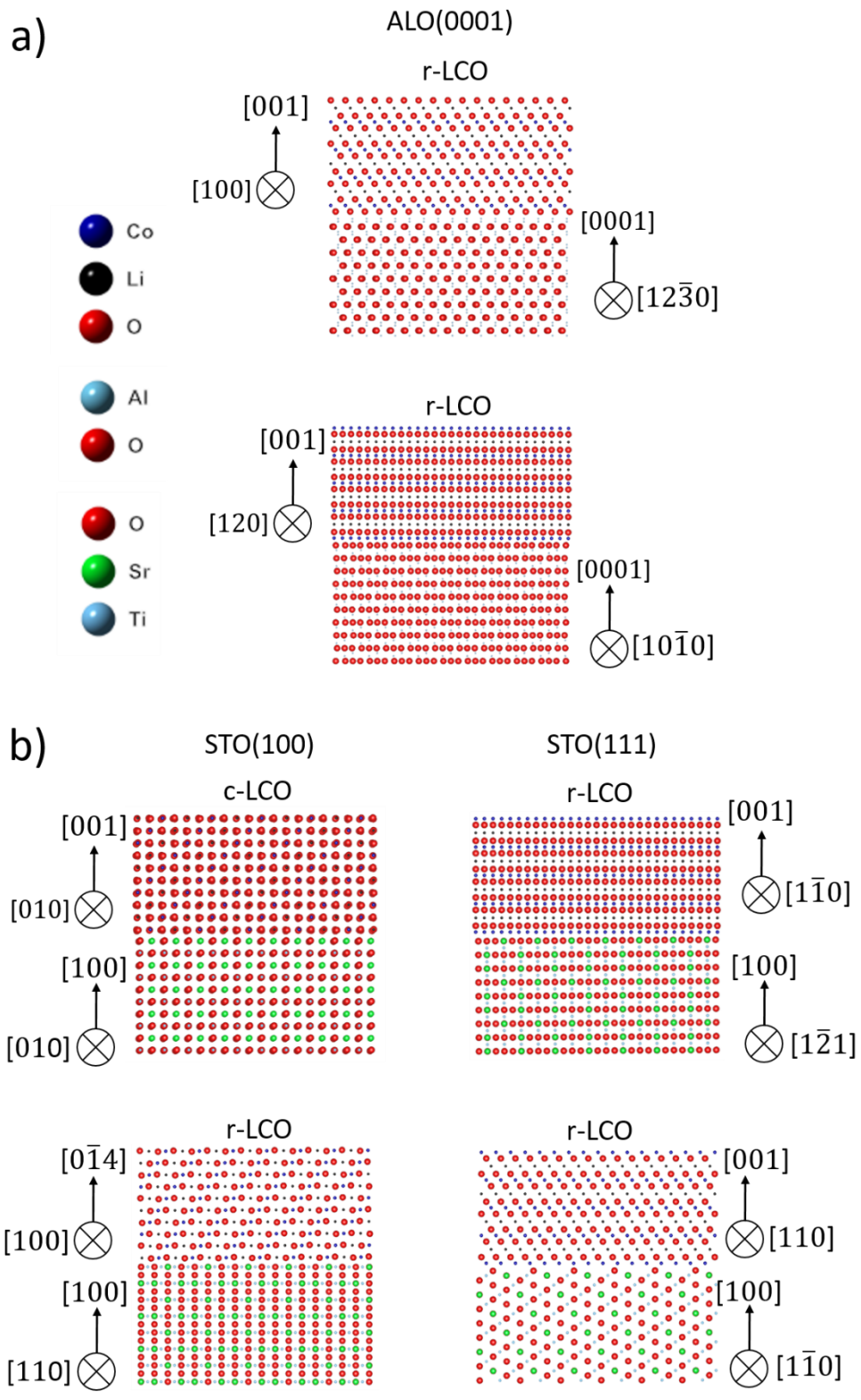

Figure 4.1: Models of possible orientations of LCO growth on a) Al_2O_3(0001) viewed along the [$2\bar{1}\bar{1}0$] (upper), [$01\bar{1}0$] (lower) ZA. b) STO(111) viewed along [$1\bar{1}0$] (upper), [$11\bar{2}$] (lower) ZA, c) STO(100) viewed along the [010] direction, with c-LCO (upper) and r-LCO (lower) phases, where LCO would be expected to grow along ($0\bar{1}4$) plane, as shown. These were informed by studies into LCO growth above 500 °C [316]. Structure files acquired from literature and computational databases [52, 124, 150].

4.1 LT Deposition of LCO onto ALO, STO and GGG substrates

Deposition onto ALO(0001) provides the opportunity to observe the influence of LT deposition of LCO and correlate possible Li losses during PLD could contribution to variable Li content within the thin film, inclusive of phase and GB contributions. The orientations of Li rich and deficient phases are important with respect to Li mobility across GB and within the electrode [124, 130].

Surface analysis of LCO thin films was using a combination of SEM and TEM, monitors surface roughness, crystallite morphology (Figure 4.2) and profile of crystal facets along the cross-section (Figure 4.5). Film thickness is used as a reference for deposition time when aiming to produce films between 80 nm to 100 nm thick in heterostructure devices. In the depositions on ALO(0001) and STO(100) or (111) substrates, film thickness was in the range of 35 nm to 50 nm. The variations result from an uneven, faceted nature of the film's surface when grown on ALO(0001) (Figure 4.5). Depositions on STO(100) were more uniform at the surface (Figure 4.17), deposited with a consistent thickness of 50 nm (± 2 nm).

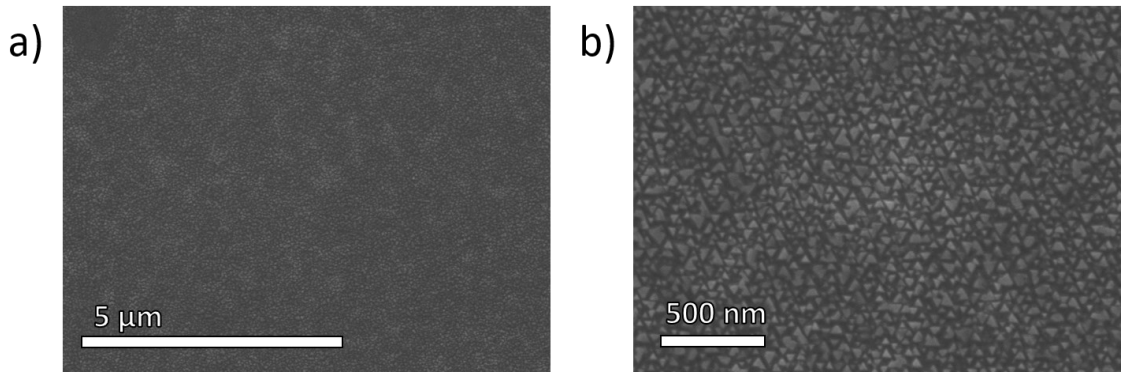

Figure 4.2: a) LCO on ALO(0001) showing triangular crystallite morphology anticipated for r-LCO[001] growth [124]. Both images acquired at 15 keV, in JEOL 7800F SEM.

However, the match and symmetry between hexagonal ALO(0001) and r-LCO(001), provides a basis for inducing consistently orientated LCO growth. The surface morphology observed in SEM differed between LCO on all substrates, ALO(0001), STO(100), STO(111) and GGG(111). As based on literature reports for LCO grown on ALO(0001), a film should be dominated by growth along the [001] axis of LCO with triangular facets on the surface. The triangular crystallites are indicative of LCO growing along the (001) plane, with edges to the triangles representing exposure of (014) and (012) lattice planes of r-LCO.[130]

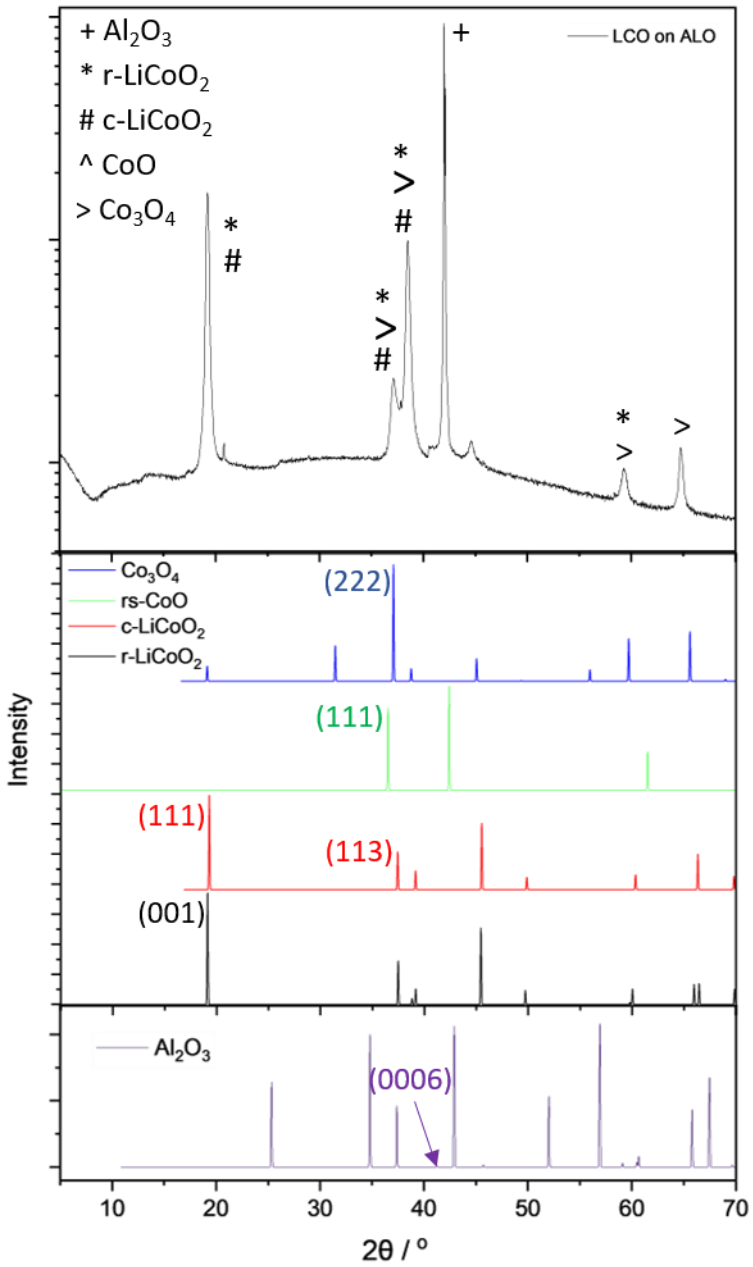

Figure 4.3: XRD for single layer depositions of LCO onto ALO(0001), showing intensities relating to multiple potential LCO phases (top), simulations of the possible LCO and CO phases (middle), with the simulation for ALO (bottom) labelled where the weakly diffracting (0006) exists. XRD data acquired on Panalytical Aries, using a Cu-Kα source.

The three main phases observed with HR STEM imaging were the rhombohedral, cubic and spinel phases (Figure 4.4). The cubic phase was shown to relate closely to the Li deficient atomic column intensity and diffraction pattern of rock salt CoO rather than Li rich LCO. The direct detection of Li content is a challenge to quantify, due to very low sensitivity of atoms with low Z values and overlap with the Co $M_{2,3}$-edge in the low-loss EELS spectra. It is assumed that a small amount of Li remains in the rs-CO phase if the s-CO phase has not formed. These rs-CO are Li

deficient with respect to the $LiCoO_2$ PLD target. This correlates well with the XRD in Figure 4.3 where the r-LCO, rs-CO and s-CO phases all have the potential to be present, with the Li deficiency of the cubic phase suggesting the rs-CO phase XRD signal may be visible on LCO grown on STO substrates instead on c-LCO. The presence of the Li deficient rock-salt structure appears to be consistent in this project and when reference in similar cathode materials such as $Li_{1.2}Ni_{0.4}Ru_{0.4}O_2$ in literature [42]. The main distinguishing feature between the c-LCO and rs-CO phase is the intensities in HAADF images, where rather than alternating bright, dark atomic columns (shown in the c-LCO simulation (Figure 4.4, b)) the near uniform intensity distribution exists in all HAADF images containing a cubic electrode phase. This suggests stoichiometry closer to CoO, where Li content in Li_xCoO_2 can be assumed to be between $0<x<0.4$, while a negligible Li content ($x \approx 0$) is more likely to form to s-CO phase. Assessment of the precise Li content is near impossible, hence while approximations can be made based on the observed spacing in DP and diffractograms, shown to be close to $LiCoO_2$ for the r-LCO phase and potentially nearly completely Li deficiency in rs-CO and s-CO grains. Deviation from the lattice parameters of DP simulations relating to r-$LiCoO_2$, rs-CoO and s-Co_3O_4 is small, as well as lying within the error ranges of diffractograms and microscope calibrations shown in Appendix I.

The contribution and orientation of r-LCO and s-CO phases in the LCO on ALO correlates with the XRD intensities of the r-LCO(001) and s-CO(111) signals in Figure 4.3. Shown later, the AR STEM imaging of grains also support the approximations made from XRD results regarding contribution and orientation within the electrode grown on ALO at LT. The presence of rs-CO and s-CO phase are both restrictive to Li mobility within and around these grains, as well as the potential for Li trapping upon intercalation into the regions. Device performance will be dependent on the ability for these grains to facilitate Li intercalation as well as retrieval when transferring Li capacity to the anode during device discharging.

Where crystalline material forms a boundary between either substrate and thin film or grains within LCO and LLZO, the boundary is referred to by the normal to the plane at which the two crystal orientations meet. For example, a boundary between the r-LCO(001) and r-LCO(012) plane of two LCO grains is labelled in reference to the direction these two grains are touching, rather than parallel to the boundary. In Figures this is noted by g vectors, hence for this system to $\vec{g}_{001}$ and $\vec{g}_{120}$ would be pointing towards to GB.

The r-LCO phase, observed in two ZA with respect to ALO, has an orientation where the [100] and [120] ZA align with the alternate [120] and [100] axis of Al_2O_3. Crystallinity along the ALO-LCO interfaces was dominated by the r-LCO phase, orientated along the [001] direction. The observed crystallographic alignments between substrate and the film create anisotropic lattice mismatch which are: ALO$[12\bar{3}0]$||LCO$[100]$, with a mismatch of 1.3% between repeating columns. Rotating through 90° the ALO$[10\bar{1}0]$||LCO$[120]$ have a 9.4% mismatch when assessing the distances of repeating symmetry along the planes of contact between film and substrate. A minority of growth at the interfaces occurs with the r-LCO phase adopting a $(0\bar{1}2)$ growth plane, driven by the minimisation of the strain energy at the ALO-LCO interface, additionally the strain can be relieved by formation of twin boundaries, where were observed in the grown films.

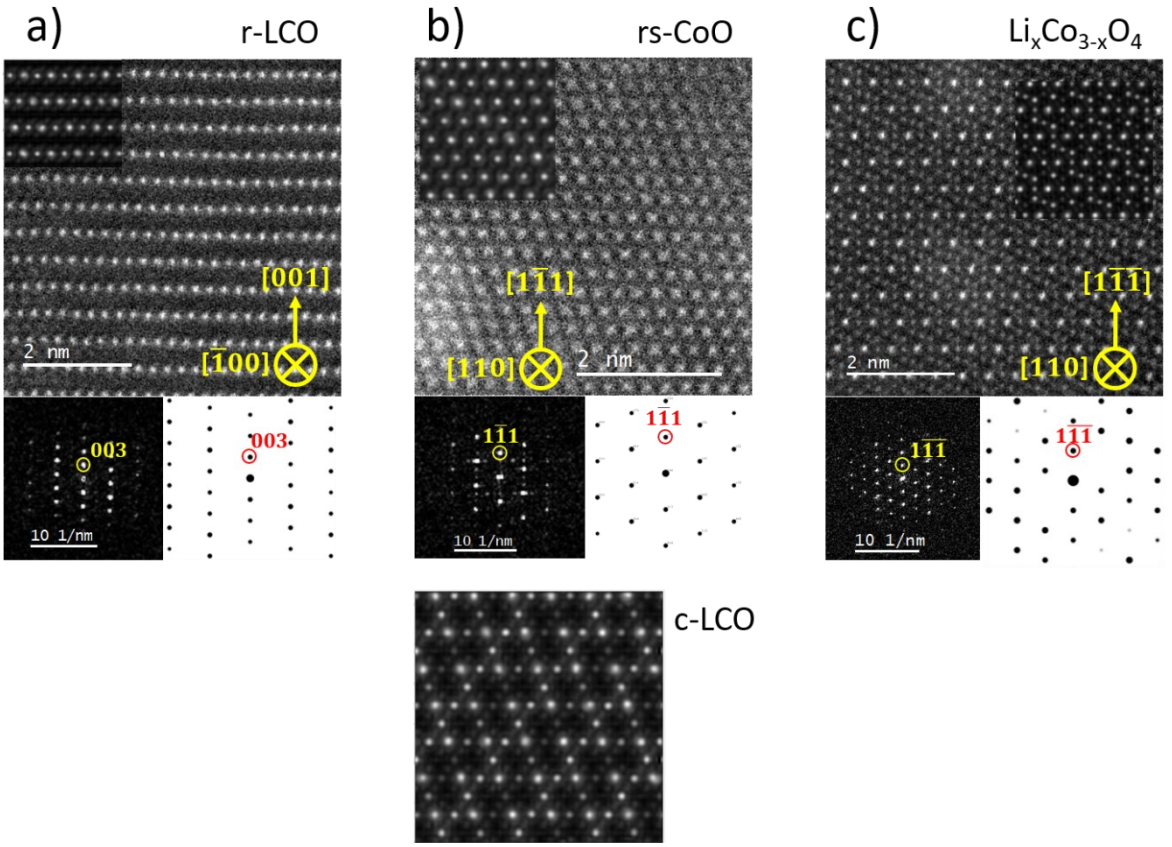

Figure 4.4: Three phases imaged in thin films of LCO on Al_2O_3(0001) substrate. a) r-LCO ($LiCoO_2$), b) rs-CO (CoO) with simulated HAADF of c-LCO included for reference to differences in intensity between the Li depleted and Li rich cubic phases. c) s-CO ($Li_xCo_{3-x}O_4$), where x is likely to be near to zero. All images collected using JEOL ARM300F (ePSIC) at 300 keV.

Deposition of LCO onto ALO created the faceted surface structure seen in the SEM image (Figure 4.2) with a more in-depth analysis achieved through TEM imaging of the cross-section (Figure 4.5). The faceted surface islands contain all three main phases identified by XRD, nanobeam diffraction and HRSTEM images (r-LCO, rs-CO and s-CO). These island surfaces have variation with respect to the (001) surface of r-LCO. The angles related to r-LCO facets exposing the $(0\bar{1}2)$ and $(0\bar{1}4)$ lattice planes, (001) and $(1\bar{1}\bar{1})$ for rs-CO, as well as (001) for s-CO contribute to the uneven electrode surface. Most of the islands contain the rock salt or spinel CO, as shown by HR imaging revealing the susceptibility to Li deficiency within the surface regions. This may have occurred through evaporation during PLD, or through surface decomposition extracting the Li to form Li_2CO_3. FIB preparation could also be contributing to Li loss and could not be dismissed as one of the causes of Li deficiency, although less likely for the LCO films [318].

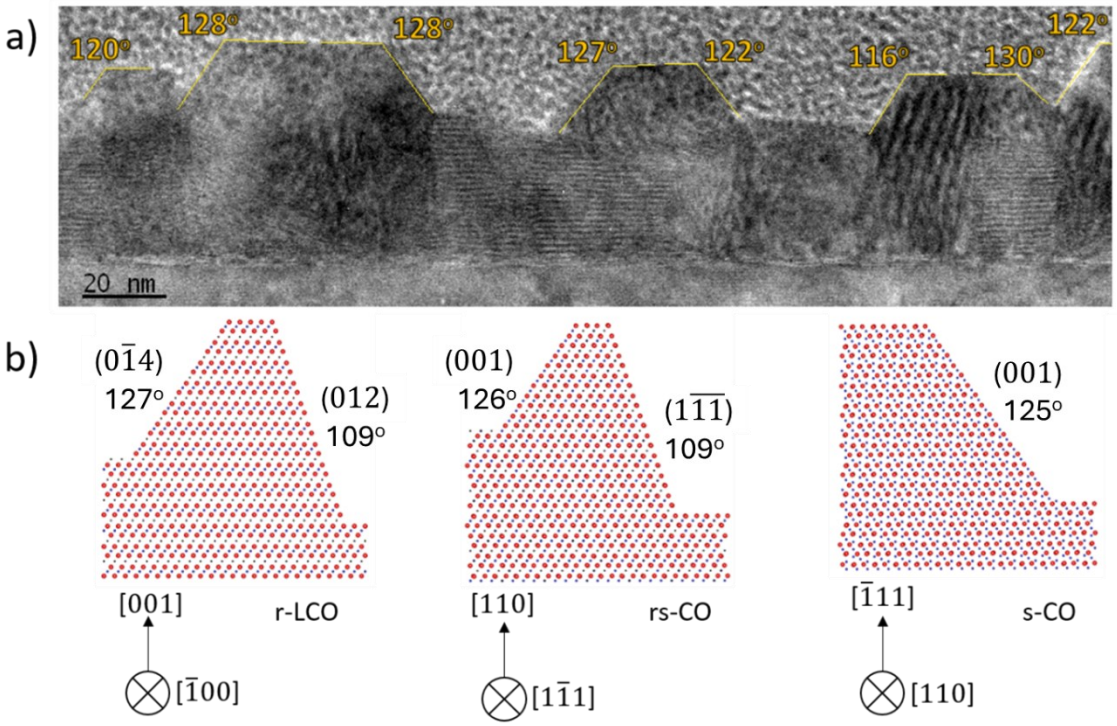

Figure 4.5: a) Low magnification BF TEM image of LCO film cross-section with surface facets relating to the edges of triangular crystallites observed in SEM surface images. b) Structure models of r-LCO, c-LCO and Co_3O_4 with planes relating closely to the angles observed within the faceted surface structure. Data acquired on JEOL 2200CF at 200 keV.

Absence of flat LCO films should not be detrimental in forming well-defined crystallographic heterostructured interfaces between LCO and LLZO. Such structures will have multiple routes of Li transfer across the electrode and electrolyte. Efficient Li transfer has the potential to be occur from the LCO crystal planes exposed by the faceted surface, or through the GBs running between the different phases with exit routes at the film's surface. The surface contains many regions of Li deficient cubic and spinel phase, which will restrict the efficient movement of Li from bulk to surface of the electrode. However, r-LCO facets exposing $(0\bar{1}4)$ and $(0\bar{1}2)$ planes would promote greater Li mobility through an EEI given the exposure of Li planes directly with an electrolyte. If Li deficiency at the surface is avoided the faceted structure of the r-LCO phase is consequently beneficial to r-LCO grown along the (001) plane, given intercalation along the [001] ZA is restricted by the cobalt oxide (CoO_2) layers. In addition, the greater surface area between LCO and LLZO created by interlinking with LCO facets should facilitate a improved rate of Li transfer between the two materials with reduced risk of bottleneck and Li plating [319]. This assumes the interface is not adversely affected by limitations of SEI formation specific to a faceted structure and subsequent enhanced impedance [162, 163, 165, 170, 311]. Passivation layers on the faceted LMO would preserve the greater surface area of electrode-electrolyte with minimised influence of thermal or electrochemical interfacial degradation [162].

4.2.2 Grain Boundary symmetries and Defects

The presence of three phases in the LT deposited LCO films creates conditions where a variety of GB form between different combinations of phases creating variety of homogeneous or heterogeneous interfaces between lattice vectors suitable for HR STEM. The HR data in Figure 4.6 to Figure 4.10 provides additional insights to the GB introduced within literature. Current research focuses on twin and anti-phase boundaries between r-LCO grains, grown at higher temperature within a Li-rich electrode [43, 48, 124]. A variety of grains with heterogeneous GB between different phases are presented here, this has provided a diverse sample set for investigation of how Li-rich and poor grains may combine in a device. This analysis provides a basis for considering potential Li routes between each phase relating to the lattice directions forming the GB shown below. During charge cycling grain phases and dimensions dynamically vary as Li is removed and inserted from LCO. The strains from lattice mismatches along each identified GB may therefore have a potential impact on electrode structural stability, especially in a working device. The resolution achieved by HR STEM, at 300 keV, provides a dataset for building accurate models to potentially to serve as a basis for realistic computational modelling of ion mobility across the GB. The goal would be to address Li mobility across these specific types of multi-phase boundaries to understand their impact within a charged (Li-poor LCO) and discharged (Li-rich LCO) device [119].

Within BF and HAADF STEM images it is apparent that some of these grains are twins (Figure 4.6), viewed along the [100] and $[\bar{1}00]$ ZA of the r-LCO phase, with the (010) and $(0\bar{1}4)$ lattice planes in contact. The twinning was determined using the symmetry of the lattice within the phase alongside support from nanobeam diffraction and FFT information. Misorientation between these r-LCO nanograins occurs, creating the twin boundaries between the $(0\bar{1}4)$ planes of the two mirrored r-LCO grains (Figure 4.6, a) seen in literature [124]. These relate to an interface between a $(0\bar{1}4)$ plane of the r-LCO grain, growing with the r-LCO(001)||ALO(0001), in contact with the $(0\bar{1}4)$ of another r-LCO grain growing along the (012) plane. The exposed lattice plane along the misorientated r-LCO grains is the $(0\bar{1}4)$, an energetically preferential direction for Li intercalation between electrode and electrolyte [124, 320]. The interface between (001) and $(0\bar{1}2)$ orientated grains has the potential to provide escape routes for Li ions in [001] surface via transfer into Li channels between CoO_2 layers with a component of the lithium layers directed towards the film's surface [321]. This would create a more efficient route for Li between in electrode and electrolyte in heterostructures.

In Figure 4.6, b), the HAADF and respective diffractogram information relates to the [100] and $[\bar{1}00]$ ZA of r-LCO grains, forming an anti-phase twin (APT) GB. Across the APT boundary the Co atomic planes are misaligned, this will be restrictive of Li mobility across the boundary, given the blocking effect from the misaligned CoO_2 layers [320]. The intensity at the incoherent interface is indicative of either intermixing of Co in the Li layer or overlapping grains along the viewing axis, with a misorientation into the plane of the image, which is not resolvable by viewing the cross-section. The decreasing intensity of these anti-phase cobalt layers further into the neighbouring grain suggests intermixing is the cause rather than overlap of the grains along the viewing axis. This does however highlight the importance of considering lattice alignment in three-dimensions. It is possible an offset between Co layers exists along the observation axis, improving the alignment of Li layers between two grains, that otherwise appear to be blocking in the two-dimensional cross-section.

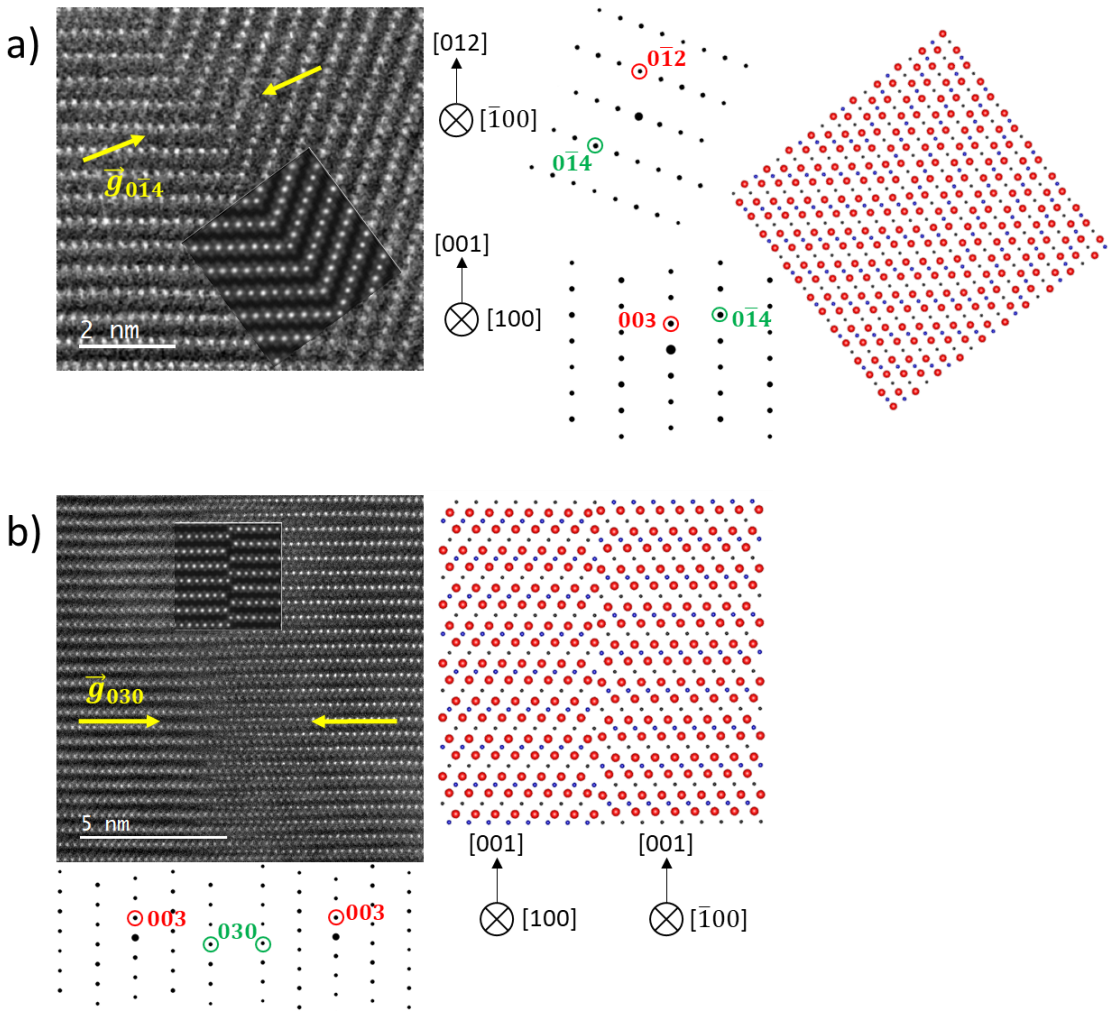

Figure 4.6: a) HAADF image of twinned boundary between two r-LCO phases, joining along their $(0\bar{1}4)$ lattice planes with atom model and HAADF simulation. b) HAADF of anti-phase twin (APT) boundary between two r-LCO phases joined along their $(0\bar{1}0)$ plane. Red indices indicate the growth directions and green the lattice axis at which the GB form. Images acquired at 300 keV on JEOL ARM300CF.

Variation in the Co layer spacing is a common characteristic of GBs within the grown layers, and could be attributed to the offset the strain caused by slight incoherence between in lattice parameters and symmetry between GBs where equivalent or different phases combine (e.g. r-LCO-to-r-LCO and r-LCO-to-rs-CO) [42]. Depending on the mismatch of lattice parameters between specific lattice vectors of r-LCO, rs-CO and s-CO phases, these phases create a compression or widening of layer spacing, most noticeable in r-LCO grains. This likely will have a measurable effect on the ion mobility through the electrode depending on the extent to which Li channels are closed or widened. The exact influence of these strains would require computational analysis of Li diffusion in accurate atomic models based on this work.

Grains of the rs-CO and s-CO present throughout LCO film on ALO(0001) create GB between different combinations of the three phases, as well as some minor occurrences of twinned rs-CO grains, the latter being shown in Figure 4.10. The presence of GB forming between different phases, along a variety of lattice directions and crystal orientations, creates distinctly different routes where Li transfer could occur at varying rates and dynamically changing strain compromising the electrodes structural integrity [22, 46, 125].

The r-LCO, rs-CO, s-CO create boundaries which are slightly strained due to difference in lattice constants with some being coherent interfaces, and in some areas they appeared disordered, for example atomic columns at the very boundary are not resolved. (Figure 4.7 to Figure 4.10). A minority of rs-CO and r-LCO combinations result in poor alignment due to mismatch in atomic symmetry (Figure 4.10, orange boundary), forming GB with (amorphous like region) between the grains. Phase analysis could be further supported with nano and pencil beam diffraction in future work, the latter potentially being able to illustrate the distribution of phases when effectively processed in the future. . Digital diffractograms are used in this chapter and assignments in Appendix I.

Continuing with boundaries containing the r-LCO, the Figure 4.7 illustrates examples of interfaces between r-LCO and rs-CO, while r-LCO and s-CO are presented in Figure 4.8. These phases consistently appeared to form coherent GB with well-defined boundaries between rs-CO and r-LCO inclusive of contact between the (110) and $(\bar{1}00)$ planes of the cubic and rhombohedral phases. Other boundaries formed between the rs-CO $(\bar{1}1\bar{1})$ and r-LCO (001) plane (Figure 4.7, a), rs-CO $(11\bar{2})$ and r-LCO (010) (Figure 4.7 b), as well as rs-CO $(\bar{1}11)$ and r-LCO (001) (Figure 4.7, c) lattice planes. The Li-deficient rs-CO grains are Li-ion mobility limiting, although shares similarities in terms of cubic symmetry with Li-rich c-LCO. It may accept lithium during intercalation into LCO and therefore undergo phase transition in an active device, changing the lattice match and strain at the GB with r-LCO [42, 322]. The rs-CO$(\bar{1}1\bar{1})$ interfacing with the r-LCO(001) creates a combination between a phase of lower Li conductivity and planes of r-LCO (i.e. (001) planes) where Li mobility is limited by passing through CoO_2 layers.

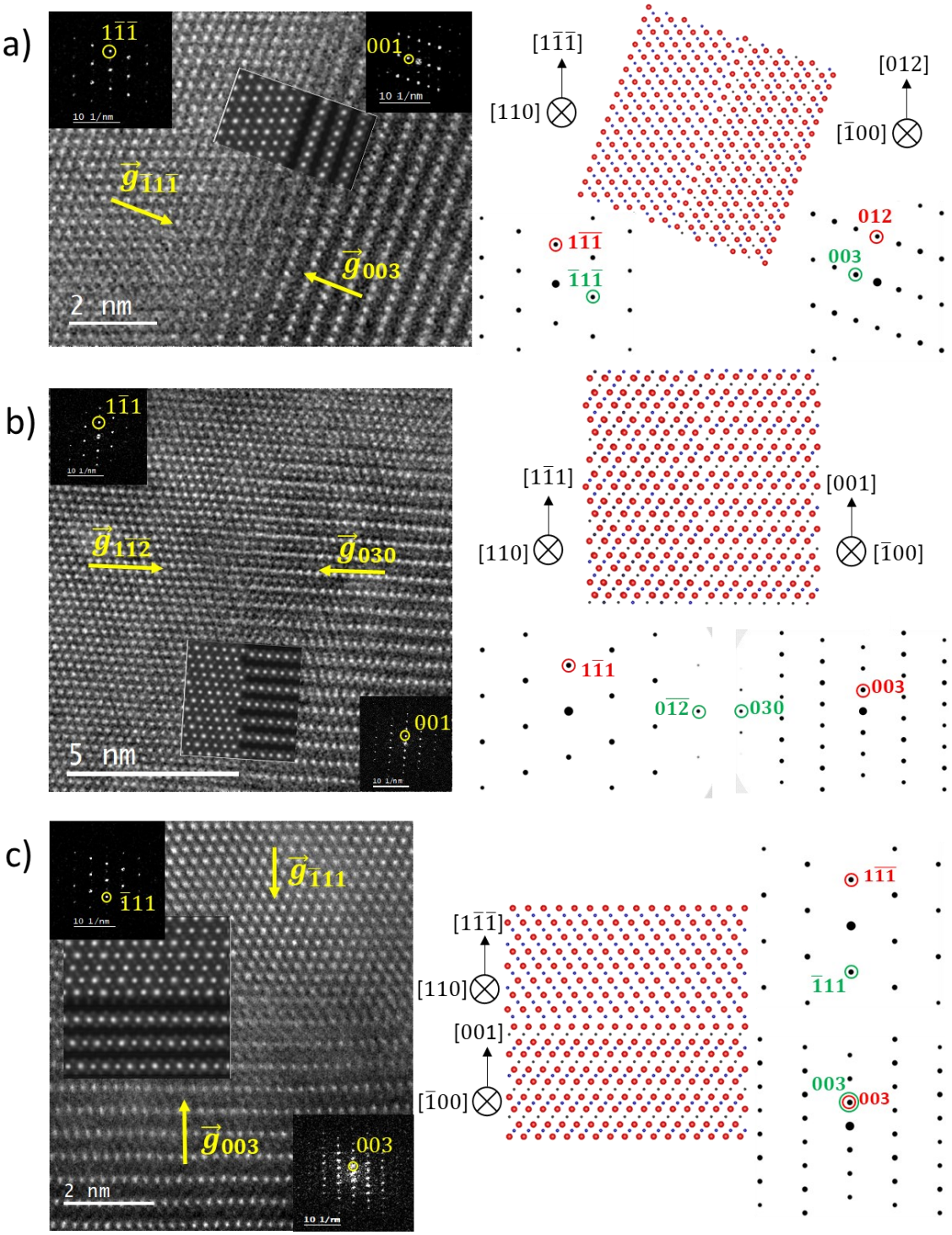

Figure 4.7: HAADF images of GB in LCO thin film on ALO(0001). Phases include the HT r-LCO growing along the [100] and $[\bar{1}00]$ directions, cubic phase along the $[\bar{1}10]$ and [110] axis, as well as the spinel phase along the [110] axis. Inset are simulated HAADF images along the respective ZA of each grain. Red indices indicate the growth directions and green the lattice axis at which the GB form. Images acquired at 300 keV using the JEOL ARM300F microscope at ePSIC. Inset HAADF simulations were produced in QSTEM from interfaces between theoretical r-LCO and rs-CO phase models.

Other types of two-phase GB combine the r-LCO with s-CO, Figure 4.8 contains two HAADF images of well-resolved boundaries. The first example (Figure 4.8, a) is an interface forming along the [001] direction of the r-LCO phase. This combines the (001) plane of r-LCO with the $(1\bar{1}\bar{1})$ plane of the spinel phase. Figure 4.8, b) illustrates the interface between the $(\bar{1}1\bar{2})$ axis s-CO and (010) of the r-LCO phases, with a 1 nm region of transitional contrast in the HAADF between the layered and spinel structure. Interfaces between Li rich r-LCO and s-CO (Li free), are likely to create a region at which Li is blocked or one where s-CO absorbs the Li ions, balancing the Li content between the two phases [323]. Subsequent phase transitions during electrode charge cycling may include the formation of a larger grains of Li deficient s-CO or rs-CO phase, a hypothesis which could be supported through in-situ biasing experiments focusing on a s-CO-to-r-LCO GB.

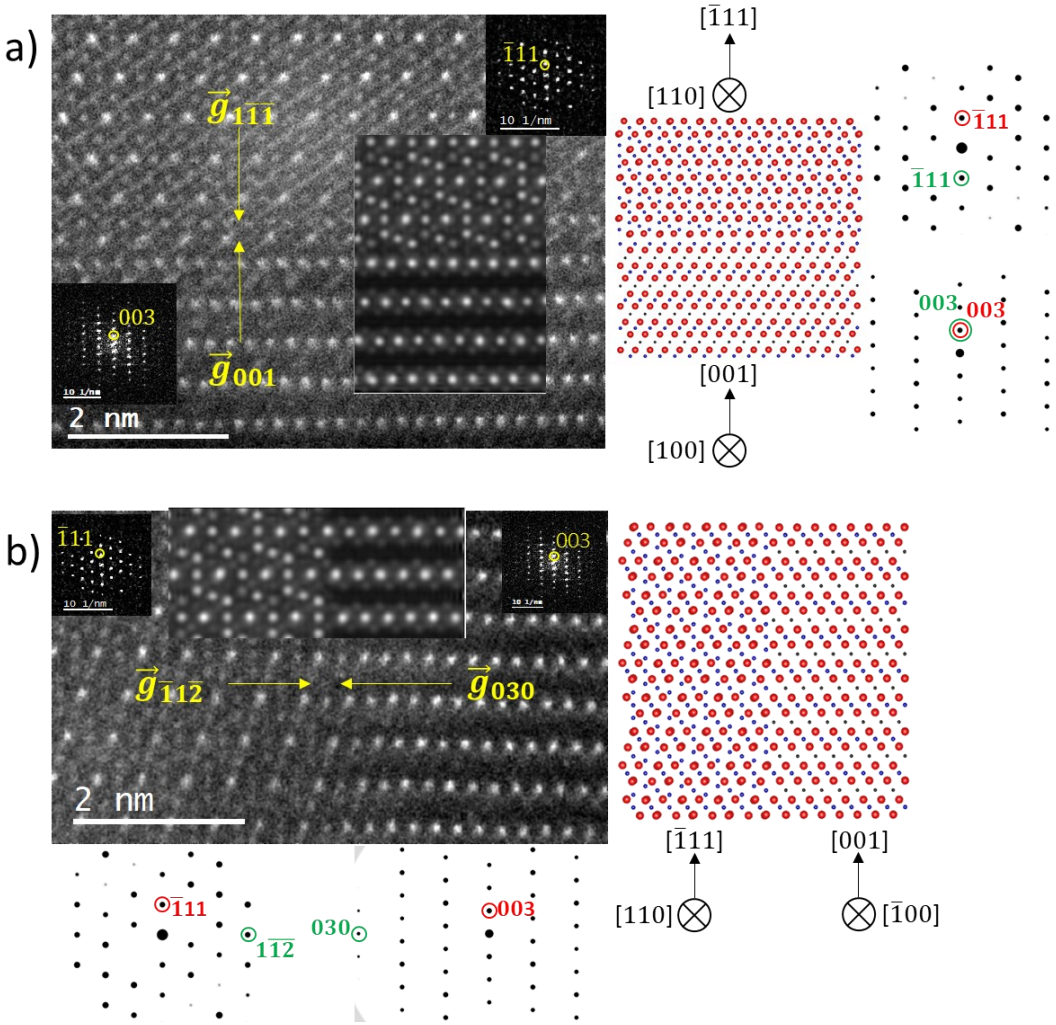

Figure 4.8: HAADF images of r-LCO to s-CO GB. a) r-LCO to s-CO boundary with r-LCO growth plane (001) in contact with the $(1\bar{1}\bar{1})$ of the spinel phase. b) An r-LCO to s-CO interface with the respective (010) and $(\bar{1}1\bar{2})$ planes forming the boundary. Red indices indicate the growth directions and green the lattice axis at which the GB form. Acquired in a JEOL ARM300F aberration corrected STEM at 300 keV. Inset HAADF simulations were produced in QSTEM from interfaces between theoretical r-LCO and s-CO phase models.

The final phase combination within the cross-section is rs-CO to s-CO GBs (Figure 4.9), whereby Li transfer between two significantly, Li deficient phases is of less significance compared to boundaries with r-LCO. Alignment between the s-CO ($\bar{1}11$) and rs-CO ($\bar{1}1\bar{1}$) creates a twin-like boundary with atomic columns mirroring at the interface. The boundaries shown in Figure 4.9 contain coherent interfaces with moderate lattice mismatch between the rs-CO and s-CO, leading to visible dislocations along the stepped interface (Figure 4.9, a (red arrow)). Incoherent interfaces between the two Li-deficient phases, that would be spatially advantageous for Li migration between rs-CO and s-CO were not observed, therefore routes for Li around these grains require a local r-LCO grain. Therefore, the cubic to spinel boundaries are both unlikely to experience significant volumes of Li migration or provide a route between these phases, limiting the efficiency of Li intercalation into and out of the electrode.

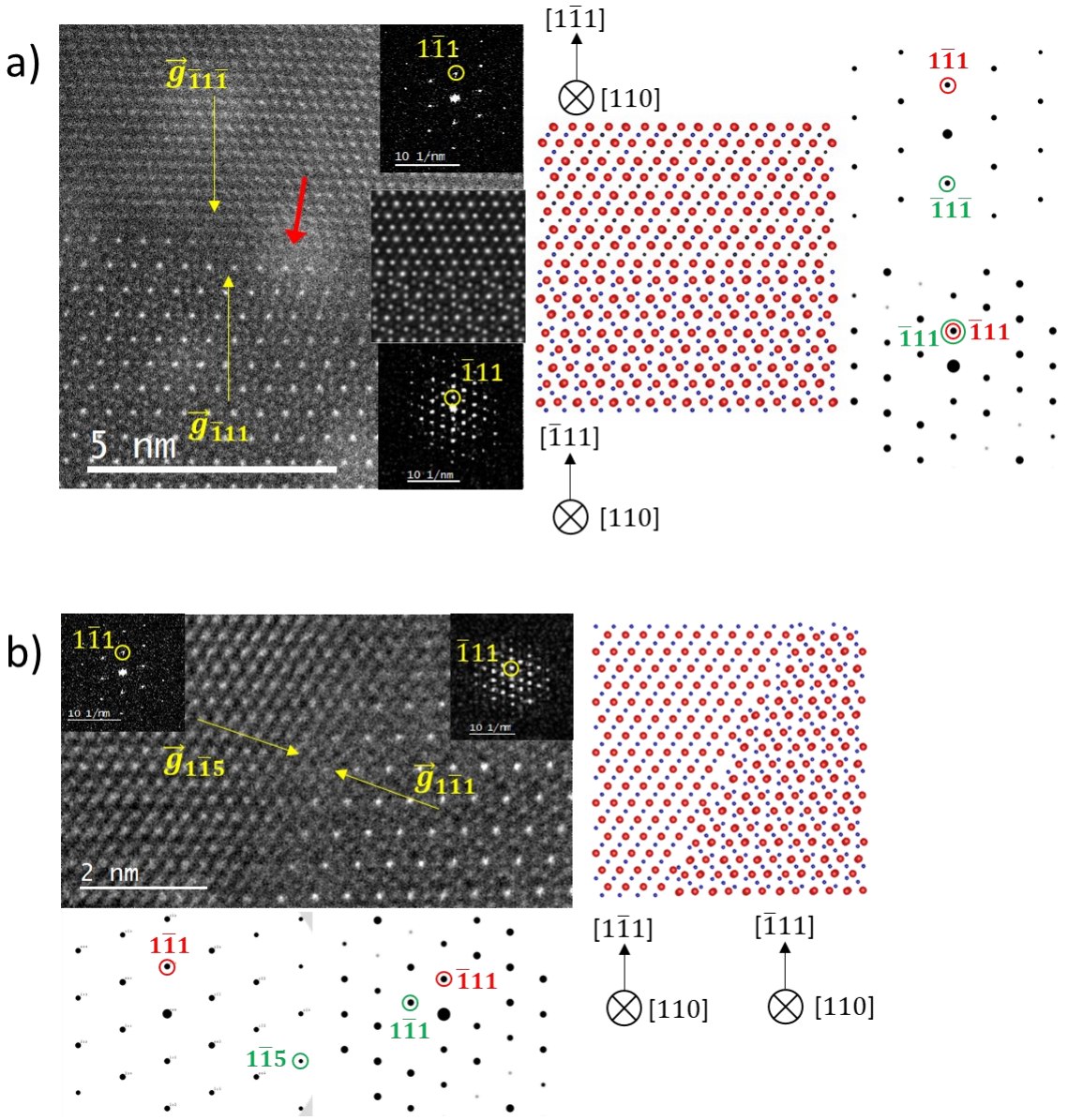

Figure 4.9: HAADF images of rs-CO to s-CO boundaries forming within the LCO film a) Contact between $(\bar{1}11)$ plane of s-CO and $(\bar{1}1\bar{1})$ of rs-CO with periodic steps at the interface. b) $(1\bar{1}5)$ plane of rs-CO in contact with $(1\bar{1}1)$ of s-CO. Red indices indicate the growth directions and green the lattice axis at which the GB form. Acquired in a JEOL ARM300F aberration corrected STEM at 300 keV. Inset HAADF simulations were produced in QSTEM from interfaces between theoretical rs-CO and s-CO phase models.

The presence of the spinel phase indicates potential significant Li deficiency and limited Li-ion mobility through these films deposited at LT. Future work determining the Li content in $Li_xCo_{3-x}O_4$ and rs-CO may help understand the abundance of these phases based on thresholds of Li content [323]. Spinel phases are not consistently near the substrate or surface (greater rs-CO content) of the films where deficiency is be anticipated (Figure 4.5). Their presence within the bulk of the thin films creates strain during the dynamic processes of charge cycles. Electrode fracturing in addition to blocking Li migration through these deficient grains are two areas of limitation to lifespan and performance.

Phase changes or growth of specific grains during charge and discharge cycles will lead to the constantly varying combinations of the GB presented, each with varying effects on Li mobility. Figure 4.10 is an example where the r-LCO and rs-CO phases form GB, where several different lattice vectors form homogeneous and heterogeneous GB within a film depth of about 40 nm. The changes in lattice alignments at the GB every 5 nm to 20 nm (Figure 4.10, b) can be attributed to the system reaching limits of strain and thus realigning onto an energetically preferable set of GB planes. Such shifts in GB orientations on the nanoscale will result in varying conductivities along an interface between two grains. The samples in Chapter 3 suggest grains are consistently larger in particles, with a few long GB traversing the micron scale of particles. Nano size grains may only be more relevant to electrodes and electrolytes in the form of thin films, but particle samples were not compatible with thinning to thicknesses where HR STEM analysis within the bulk of the grains could confirm this.

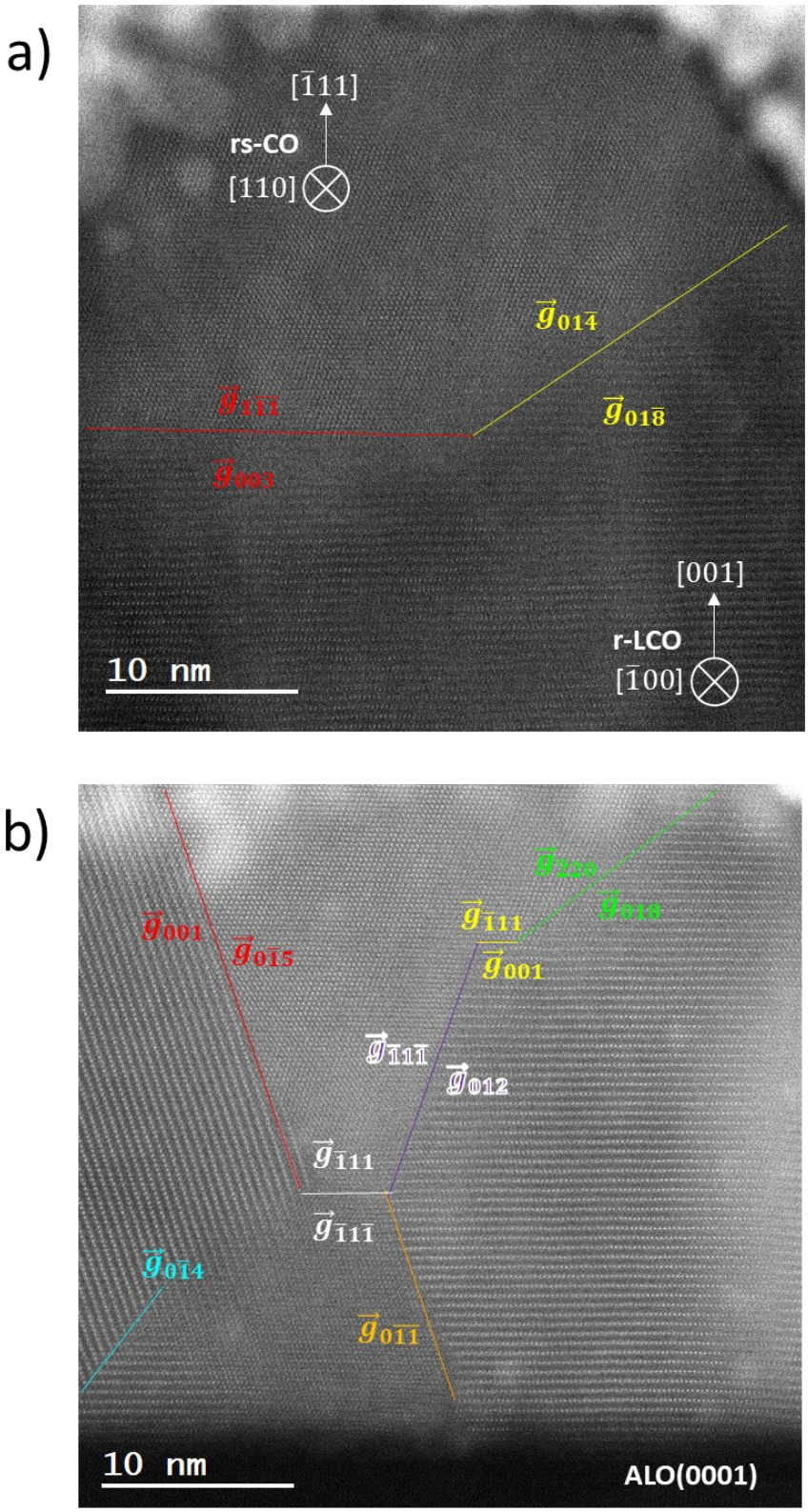

Figure 4.10: HAADF images containing examples of regions with multiple GB, providing insight into the complexity of Li dynamics throughout the approximate 45 nm depth of the grown film. a) r-LCO to rs-CO grain from the bulk to surface region of LCO. b) Four r-LCO to rs-CO grains in the bulk of the LCO thin film where GB vary continuously. GB within the multi-grain SYSTEM form coherent (light blue, white), semi-coherent (purple, red, yellow) or incoherent (orange) boundaries. Data acquired in JEOL ARM 300CF at 300 keV.

4.2.3 Low Temperature Growth of $LiCoO_2$ on $SrTiO_3$(111) Substrate

The use of STO substrates aims to develop similarly controlled LCO growth at low substrate temperatures during PLD, whereby the orientations of all three phases and dominant axis of crystal grown relating to STO(111) and (100) can be assessed at AR. Attributes of LCO on STO are compared to ALO, alongside evaluating combinations of phases forming GB not yet shown. Importantly for development of good heterostructures samples, potentially compatible with in-situ experiments, the suitability of STO(111) and/or STO(100) regarding growth of LCO layers with preferable characteristics (lattice orientations and surface structure) is discussed. Beginning with growth of LCO on STO(111), literature expects similarities to the orientation control achieved on ALO, where the [001] axis of LCO can be analysed at the interface with LLZO [124].

In the SE SEM image in Figure 4.11 the same triangular crystallite morphology, seen on ALO, is not for LCO deposited onto STO(111). Instead, in smaller crystallites of inconsistent shape are present, with larger spherical particles protruding from the surface. While potentially the consequence of decomposition into Li_2CO_3 in air, these are not observed in other samples, e.g. the EDS maps do not show presence of high carbon content within.

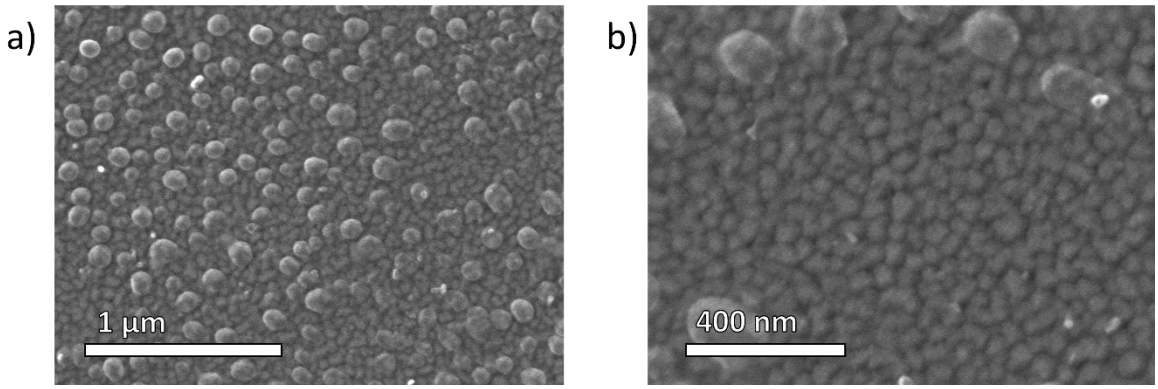

Figure 4.11: SE SEM of LCO deposited onto STO(111), showing fine crystallites structure with spherical growths upon the surface. Data acquired on JEOL 7800F Prime at 15 keV.

Acquisition of XRD from the STO(111) sample (Figure 4.12) provides similar insights to Figure 4.3 where both r- and c- LCO phases are likely present, identifiable by signals relating to their respective (001) and (111) growth planes at 19°. The broad peak around 38° and weak feature at 35° could be assigned to the s-CO, rs-CO phases, again requiring the use of TEM cross-section to determine the contribution of either the spinel or RS structure and their position within the bulk or surface of the thin film. The intensity and ratio between the signals at 19° and 38° suggest similar contributions from LCO and CO phases within the thin film.

Sharp onsets in the XRD spectra, for example, around 45° for STO(100) in Figure 4.16 are a result of emission impurity from the X-ray source. They are not a property of the LCO or LLZO thin films, rather an artefact resulting from the operation of the machine. They may be obscuring crystal phases present within the LCO and LLZO thin films, while quantification of any peaks relating to LCO and LLZO that are resolved within these steps is avoided.

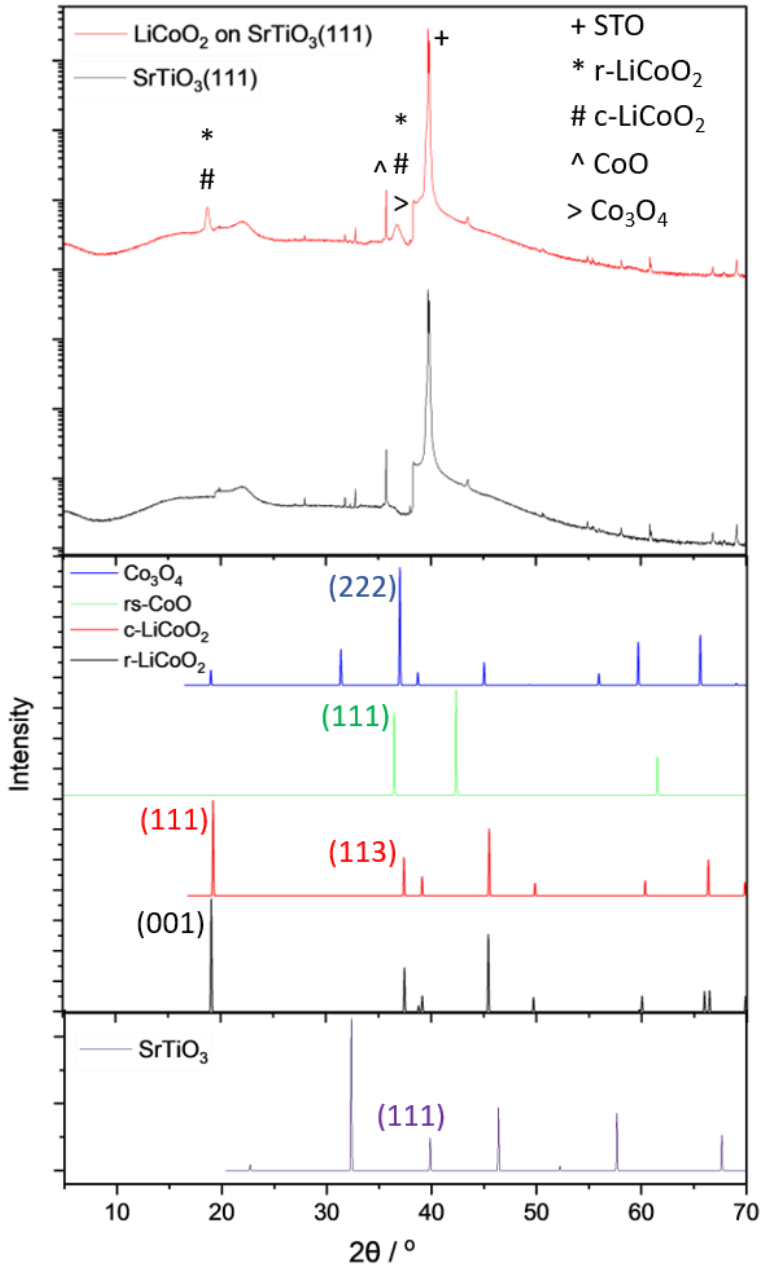

Figure 4.12: XRD figures for single layer depositions of LCO onto STO(111), showing intensities relating to multiple potential LCO phases (top), simulations of the possible LCO and cobalt oxides phases (middle), and substrate simulation where the signal relating to the (111) plane of STO is labelled. Data acquired on Panalytical Aries, using a Cu-Kα source.

Across the film depth (37 nm to 47 nm) (Figure 4.13), many different nanograins and phases appear to be present, based on the contrast effects of overlapping crystal lattices. The cubic lattice dimensions of STO are 3.9 Å and therefore a greater degree of mismatch exists in terms of lattice dimension and symmetry differences between STO and LCO, compared to the hexagonal surface of ALO(0001). The surface of LCO on STO(111) still contains the rough, faceted structure, although with less defined set of surface structures. Therefore, more strain is anticipated at the interface between STO and LCO, potentially leading to inducing greater disorder in the electrode material, with Figure 4.13 supporting this thesis.

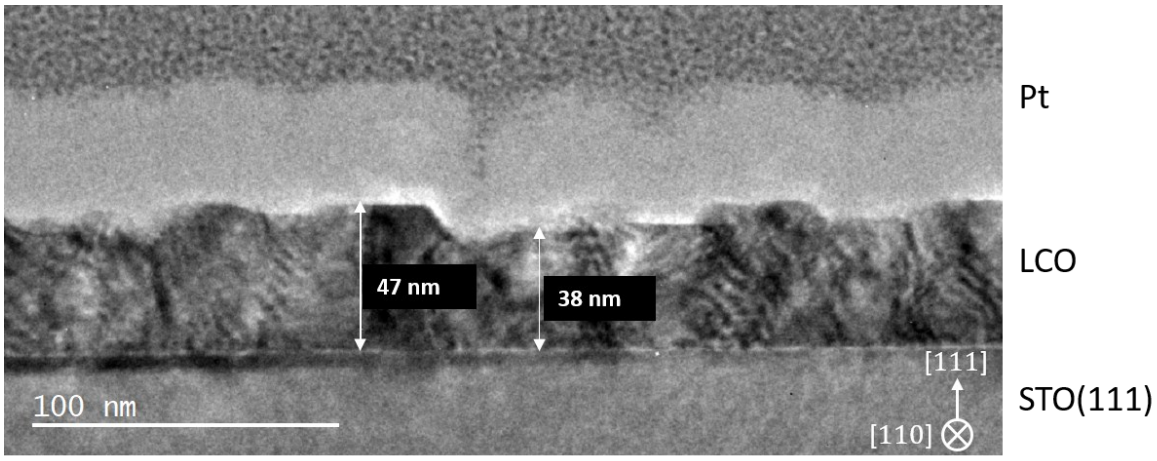

Figure 4.13: BF TEM cross-section of LCO on STO(111), showing STO/LCO/Pt layers, with LCO film thickness ranging from 37 to 46 nm in depth, owing to the irregular, faceted nature of the film's surface. Data acquired on JEOL 2100+ at 200 keV.

Similarly, to ALO, deposition onto STO(111) resulted in another polycrystalline single layer of LCO, with a mixture of all three phases. Despite some directional growth of the r-LCO phase along the $[001]$ axis, misorientations, defects and phase variations were observed across the thin film. Unlike ALO(0001), the defects and strain along the interface between the STO and deposited LCO was clearly visible (Figure 4.14Figure 4.13, a). An r-LCO-to-r-LCO GB between the (001) and (012) lattice planes is visible in Figure 4.14, a) as well as rs-CO grains (Figure 4.14, b). Moiré fringes indicated consistently varying overlapping of different orientations and phases, visually suggesting the increase variation in growth compared to LCO on ALO. There appeared to be a greater content of r-LCO growing along the $(0\bar{1}2)$, likely due to greater strain effects at the STO-LCO interfaces. Conductivity along the [100] or [010] ZA (4.0×10^{-6} S cm^{-1}) of LCO is two orders of magnitude greater than the along the [001] axis (2.4×10^{-8} S cm^{-1}) [324]. A greater volume of r-LCO with crystal growth orientated along the $(0\bar{1}2)$ plane would improve the overall Li-ion mobility from within the electrode towards an EEI due to the vertical component of the [010] axis.

For LCO on STO(111) the GB between to r-LCO grains, in contact along the respective (001) and (012) lattice planes stood out in the sample's cross-section. Li migration across the boundary is made difficult by the low conductivity of the [001] ZA. This GB may not be as detrimental to uninterrupted Li flow through the electrode as the APT (Figure 4.6, b) but will hinder Li mobility more than the twin where both grains join along their $(0\bar{1}4)$ plane, with CoO_2 layers remaining in phase.

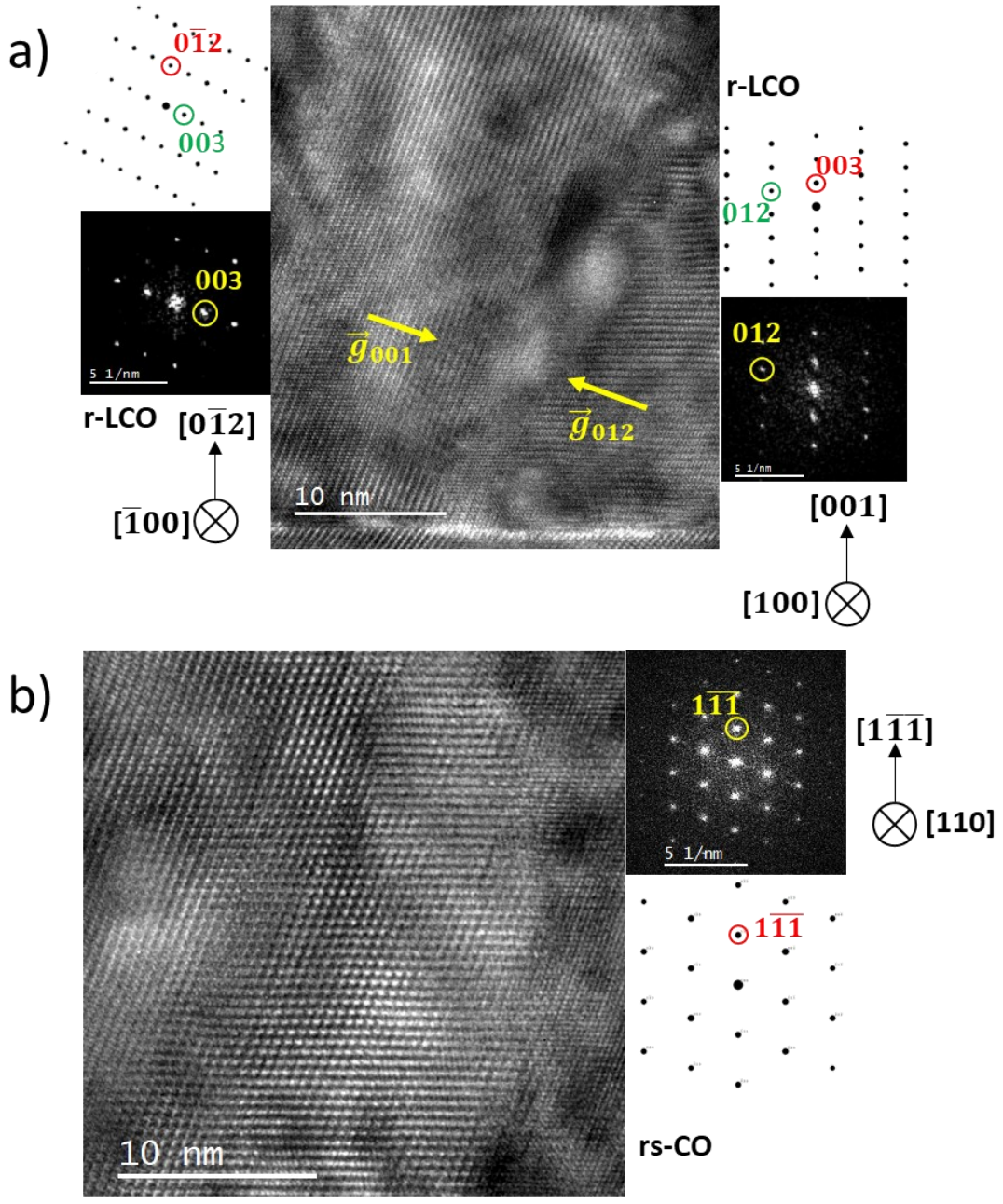

Figure 4.14: HR TEM (BF) of LCO grown on STO(111). a) Boudnary between the normal of the (001) and (012) lattice planes of the r-LCO phase. Red indices indicate the growth directions and green the lattice axis at which the GB form b) BF image of a rs-CO grain gowing along the $(1\bar{1}\bar{1})$ plane. Acquried on JEOL 2100+ at 200 keV.

4.3.4 Low Temperature Growth of $LiCoO_2$ on $SrTiO_3$(100) Substrate

On STO(100) the aim was to achieve growth dominated by an r-LCO phase growing along the $(0\bar{1}4)$ plane. This is beneficial regarding the intercalation pathways for Li towards the surface of the electrode material using LT PLD, based on literature observations and ion diffusion calculations [124]. The match between LCO and STO(100) surface should have been suitable for such growth, developing upon literature with AR observation of phases. Different growth orientations on the (100) substrate surface has the potential to create a new dataset of GB between the three main phases observed on ALO and STO(111). The SEM image in Figure 4.15 contains crystallites smaller than observed for LCO on ALO(0001) and with a square morphology compared to the triangular shapes of LCO with the r-LCO(001) growth and associated rhombohedral, RS and spinel planes exposed on these surface islands. The structure seen in Figure 4.15 is likely to be more representative of the cubic phase or r-LCO growing along the more conductive $(0\bar{1}4)$ plane [124].

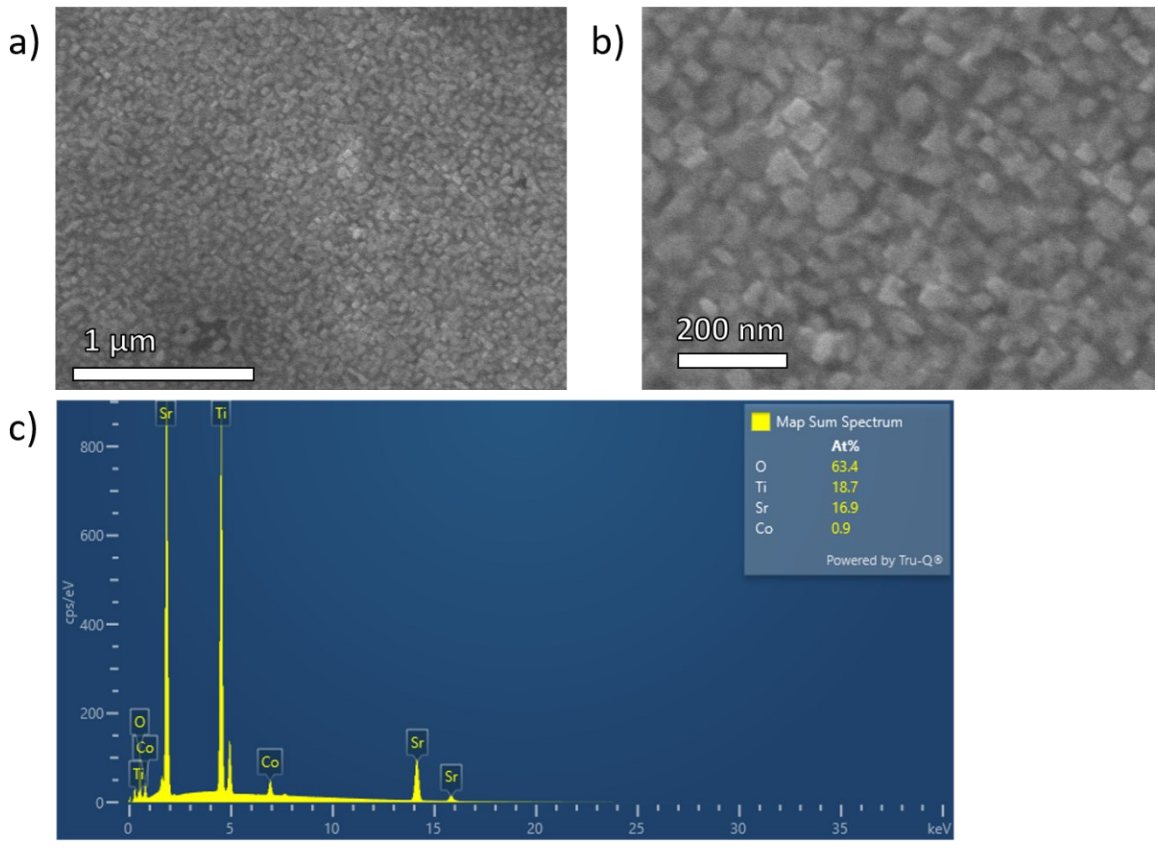

Figure 4.15: a, b) SE SEM images of LCO surface deposited onto STO(100). c) Accompanying EDS spectra acquired from the sample. Data acquired on the JEOL 7800F at 15 keV for imaging and 25 keV for EDS.

The XRD was supportive of crystalline growth on STO(100) with a differing orientation to growth on ALO(0001) and STO(111). The absence of a signal at 19° suggests neither the r-LCO(001) or c-LCO(111) were present in significant proportions within the thin film. In contrast, the emergence of the signals at 42° and 45° are representative of LCO phases along the r-LCO($0\bar{1}4$) and rs-CO(001) growth planes. This correlates with the surface orientation of STO(100) inducing growth of LCO and CO phases along planes differing from ALO and STO(111) examples. The presence of the r-LCO($0\bar{1}4$) growth needed confirmation with TEM imaging with respect to either the STO[010] and [110] ZA to assess r-LCO and rs-CO or s-CO contributions. This was achieved and displayed later in this section. The r-LCO phase is identified growing along the ($0\bar{1}4$) plane. In addition, data relating to heterostructures grown on STO(100) (Chapter 5) show the ($0\bar{1}4$) plane of growth more clearly after annealing the respective samples.

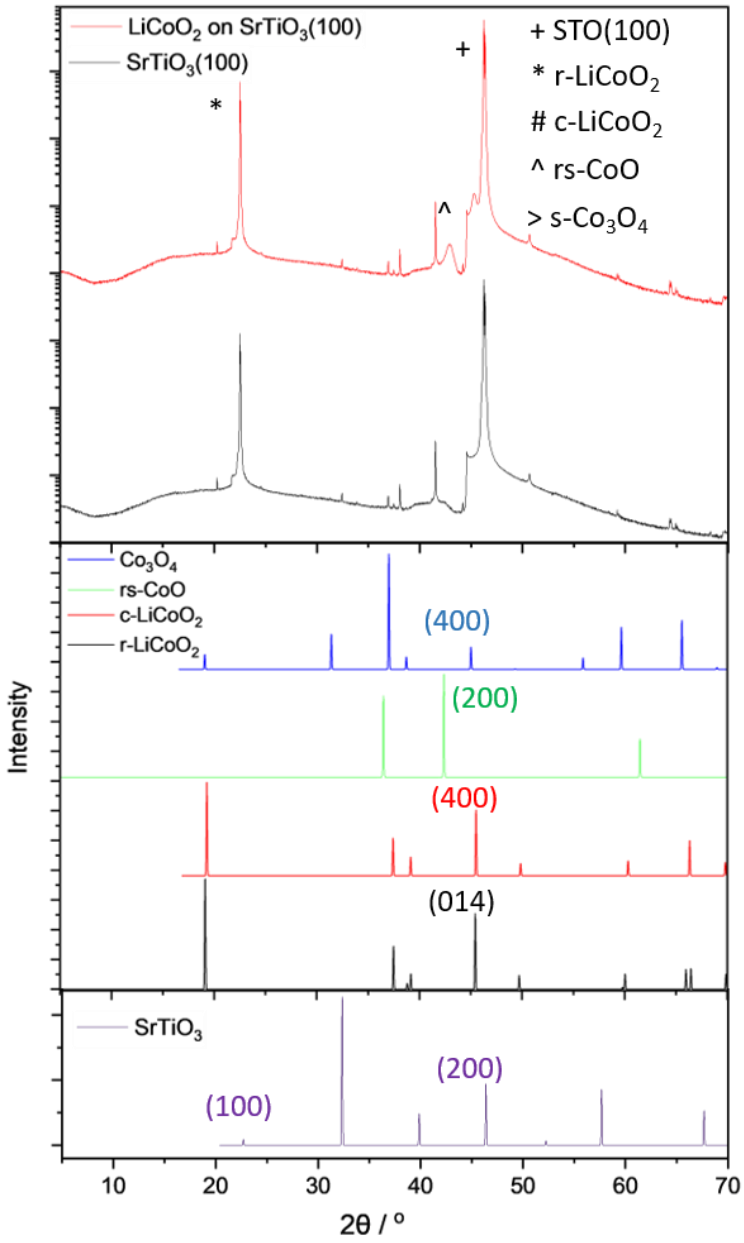

Figure 4.16: XRD figures for single layer depositions of LCO onto STO(111), showing intensities relating to multiple potential LCO phases (top), simulations of the possible LCO and cobalt oxides phases (middle), and substrate simulation (bottom) where the (100) and (200) relating to the surface are labelled. Data acquired on Panalytical Aeries (Cu Kα X-ray source)

The low-magnification cross-section images in the TEM shows a flatter surface compared to the LCO film than the facets on ALO(0001) and STO(111). This would contribute to a consistent Li transfer from the surface of the electrode into the electrolyte, assuming a single crystal growth of the Li-rich r-LCO c-LCO or rs-CO phase. The LCO film thickness is consistent, while the Moiré fringes indicted grain overlap along the observation axis. Understanding the combination of grain orientations creating the complex image contrast in Figure 4.17 required HR STEM imaging.

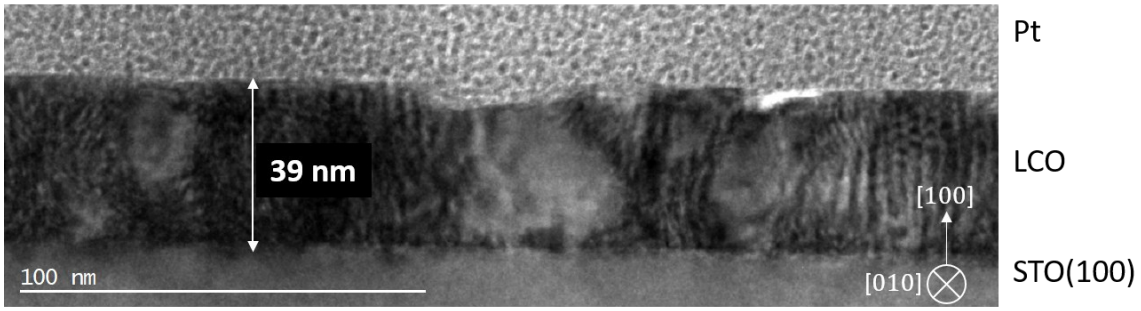

Figure 4.17: BF TEM image of LCO grown on STO(100). The low-magnification of the STO/LCO/Pt cross-section showing an almost uniform LCO layer, with a thickness of around 39 nm. Data acquired at 200 keV on JEOL 2100+

In Figure 4.18 and Figure 4.19, two differing axis of observation are shown with respect to the STO(100) substrate. Observing the LCO growth along the [010] and [110] ZA reveals the presence of r-LCO, rs-CO and s-CO phases, although clarity is restricted by the similarity of the phase dimensions along their [010] ZA. In Figure 4.18 the rs-CO and s-CO are identified by the slight differences in the two patterns spacings within the diffractograms. The use of the [110] ZA for samples grown on STO(100) (Figure 4.19) provides a ZA where the three phases of LCO were more easily distinguished along the respective r-LCO[100], rs-CO[110] and s-CO[110] ZA respectively. The lattice growth occurred along r-LCO($0\bar{1}4$) (Figure 4.19, a) and rs-CO/s-CO(100) (Figure 4.18 and Figure 4.19, b), with growth of these grains creating a multi-phase system similar to growth on ALO and STO(111). The contribution from the rs-CO phase appears to be greater compared to LCO on ALO and STO(111), possibly aided by the cubic symmetry of the STO(100) surface. The growth of the r-LCO phase along the ($0\bar{1}4$) lattice plane is beneficial for extraction of Li between the CoO layers into electrode-electrolyte boundaries, making STO(100) a best substrate in heterostructures if PLD conditions allow r-LCO to become the dominant phase. HR STEM data in Chapter 5 provides a greater resolution for clearer assignment of all three of these phases.

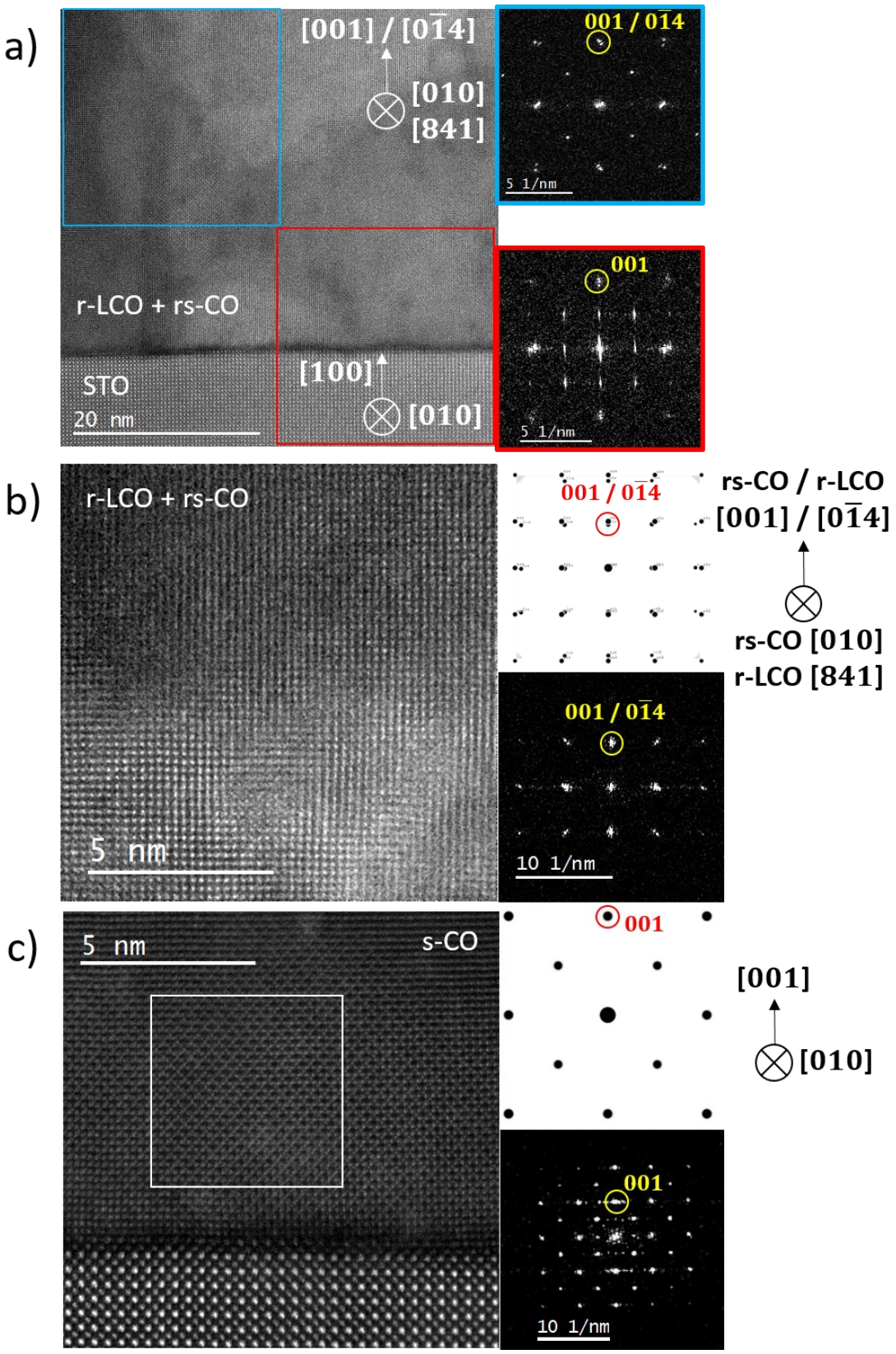

Figure 4.18: a, b) HAADF images from the cross-section along the [010] axis of STO substrate, showing rs-CO and r-LCO within the same diffractogram. Growth of r-LCO along the [0$\bar{1}$4] axis is observed along the [841] ZA, with a slightly larger spacing of spots (≈ 4%) within the diffractogram compared to the [100] ZA on rs-CO. c) s-CO grain, distinguishable by diffractogram and different structural symmetry. Data acquired on the JEOL ARM200CF at 200 keV.

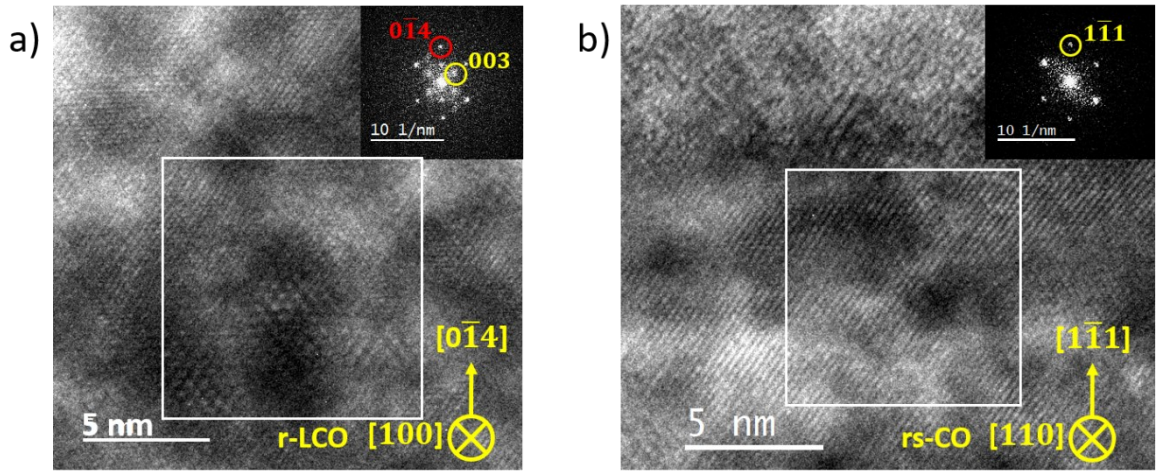

Figure 4.19: BF TEM images of lamella cut along the [110] ZA of the STO(100) substrate showing r-LCO and rs-CO phases. a) Overlapping r-LCO grains in the bulk of the LCO layer, viewed along their [100] and [$\bar{1}$00] ZA, with associated diffractogram. Both grains grown along the (0$\bar{1}$4) plane. b) rs-CO grain and diffractogram near surface of thin film, growing along the (1$\bar{1}$1) plane. Images taken on JEOL 2100+ at 200 keV.

4.3.5 Low Temperature Growth of $LiCoO_2$ on $Gd_5Ga_3O_{12}$(111) Substrate

The deposition of LCO onto gadolinium gallium garnet is not covered by literature. Rather the large lattice constant is better suited to the epitaxial growth of LLZO [131], however four consistent orientations were observed to grown upon the GGG(111) substrate (Figure 4.23). The lattice match between the lattice parameter of GGG (111) plane (7.1 Å) and a/b vectors of LCO (2.8 Å) is a 1:2 ratio with 21.1% mismatch, while with the c axis of LCO (12.99 Å) this is only 8.5% in a 2:1 between GGG(111) and LCO[001] [51]. This suggests it would be well suited to achieving some extent of orientated growth during PLD of a LCO film, similar to the multi-phase systems using STO as the substrate.

Looking at the surface crystallite morphology in the SEM it is apparent crystallisation has likely occurred during LT deposition of the LCO film (Figure 4.20). An assortment of crystallite shapes are present, indicating that growth along one dominant ZA has not occurred on GGG(111), rather a mixture of orientations, dissimilar from controlled axis of LCO growth on ALO and STO. Again, the surface roughness is significant, creating different planes of exposure to Li layers/channels along the edges of these islands, resulting in a surface of inhomogeneous ion transfer efficiency with the electrolyte. The surface roughness may also be interesting to analyse in a GGG/LCO/LLZO heterostructure but is not a sample construction attempted within this project.

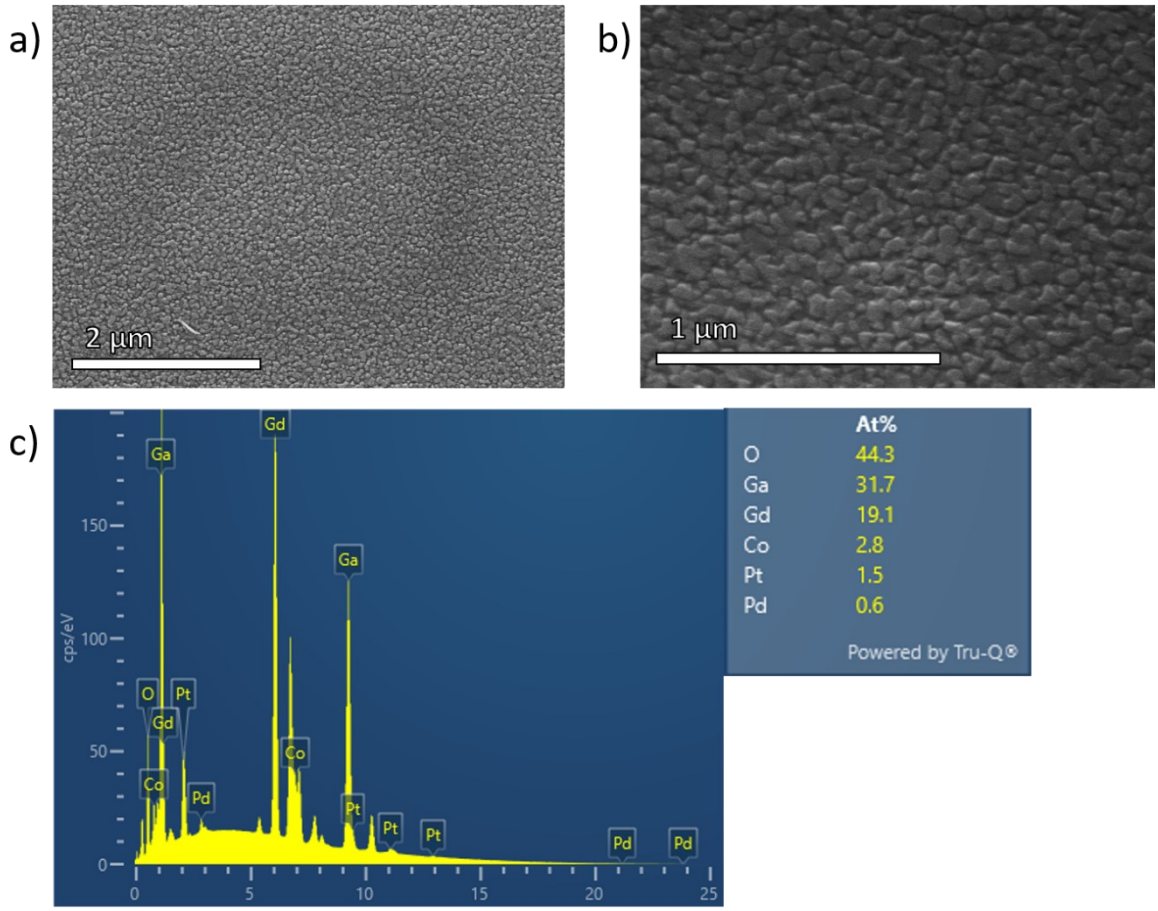

Figure 4.20: a, b) Surface images of LCO deposited onto GGG(111), showing a variety of crystallite sizes and shapes across the surface of the thin film. c) Accompanying EDS spectrum detecting Ga, Gd, O and Co, with Pt and Pd signals from the conductive coating. Data acquired in JEOL 7800F Prime

Signals detected in Figure 4.21's XRD related to the presence of the same phases seen on STO and ALO substrates. The XRD for data acquired on the Rigaku SmartLab has a greater noise compared to data acquired on the Malvern Panalytical Aeries due to the grazing angle sampling a smaller volume of material, alongside a lower step size resolution. This is also observed for later data related to LCO, LLZO and heterostructures samples, also acquired on the Rigaku Smartlab. The signals for r-LCO, c-LCO, rs-CO and s-CO were shown to potentially be present prior to further investigation with HR STEM imaging. The intensities of signals at both 19° and 45° show the (001) and $(0\bar{1}4)$ growth planes of r-LCO were present with the absence of c-LCO in the data above suggesting this phase remains absent. Overall, the XRD indicate a multi-phase thin film with greater variance in film orientation than LCO on ALO and STO substrates owing to the additional rs-CO and s-CO intensities at 37° (rs-CO or s-CO(111)) and 42° (rs-CO(100)).

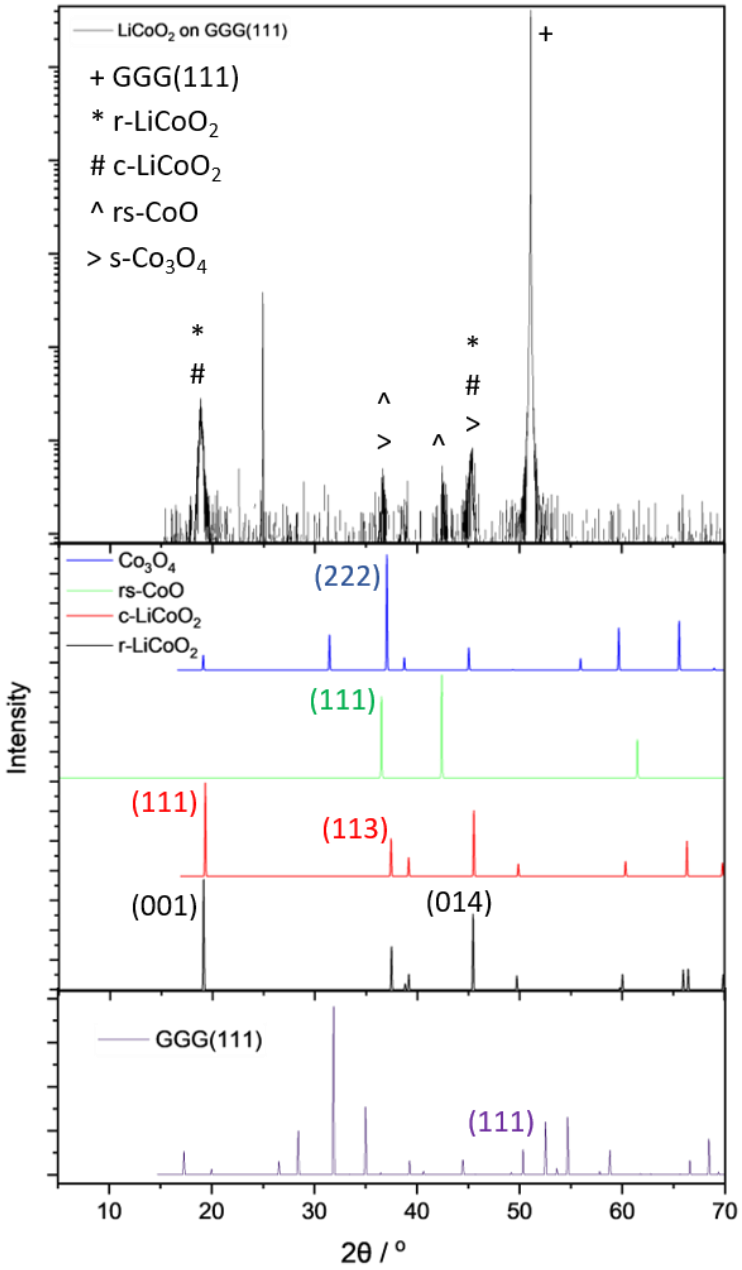

Figure 4.21: XRD figures for single layer depositions of LCO onto GGG(111), showing intensities relating to multiple potential LCO phases (top), simulations of the possible LCO and cobalt oxides phases (middle), and substrate simulation where the (111) orientation of STO is labelled. Data acquired on Rigaku SmartLab.

In Figure 4.22, LCO on GGG(111) is deposited at a layer thickness of approximately 50 nm (± 5 nm), with the height of irregularly shaped islands varying along a seven-micron cross-sectional area of TEM transparency. The surface roughness is consistent with SEM observations with various angles to facets. While similar to those seen on ALO and STO, the surface on LCO on GGG(111) is less regularly shaped with respect to the angles at the edges of these islands, suggesting variation in growth directions.

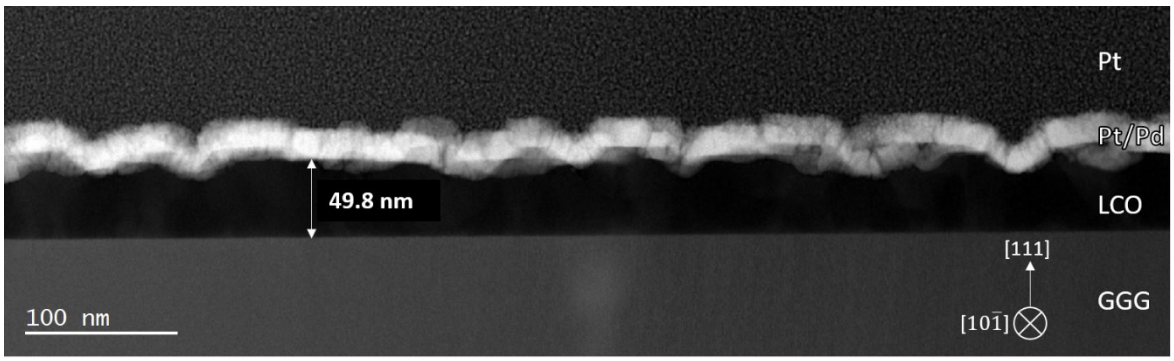

Figure 4.22: Low-magnification cross-section of LCO thin film deposited onto GGG(111). The surface was coated in a layer of Pt/Pd to reduce charging and drift in the FIB-SEM. LCO film depth varied reaching close to 50 nm at the tips of facets. HAADF acquired at 200 keV in JEOL ARM200CF

Multiple regions at the substrate-LCO interface were imaged to understand any relationships between the (111) surface of GGG and growth directions of LCO, expected to be present in grains of r-LCO, rs-CO and s-CO. We see a few different orientations of LCO phases relating to the atomic structure of the GGG substrate (Figure 4.23). The layered structure of the r-LCO phase appeared to dominate the electrode layer, with a varying growth direction. The dominant phase on all the substrates after PLD at LT does not seem to be dependent on heating above the c-LCO to r-LCO transition temperature [325].

The HAADF images in Figure 4.23 show crystalline grains present from several nanometres from the films surface, up to the full height of the film. Direction of the grains was assessed at higher resolutions, also shown in Figure 4.23, where three dominant orientations appeared to exist. Firstly, the phase in Figure 4.23, a), has an offset of the layers at 18° from the substrate surface. Alternatively, a grain with r-LCO grown along the (001) plane, is only 7.5° from being parallel to the GGG(111) surface (Figure 4.23, b and d). This is either a result of competing preferential alignments with the atomic column symmetry of the GGG substrate or a consequence of difference between the symmetries of the r-LCO twin orientations ([100] and [$\bar{1}$00]). Other regions were occupied by layers running vertically from the substrate surface (Figure 4.23, c), likely along the r-LCO(001) plane, based on spacing of the layers. The closer layer spacing was thought to potentially relate to observing the r-LCO phase along the [122] ZA, where growing occurs along the (0$\bar{1}$1) plane. Excluding these layers observed to form parallel to the substrate surface, there was no identifiable low-index plane of intersection at the GGG(111)-LCO interface. It was difficult to assess the extent to which LCO on GGG(111) was comprised of multiple phases given the ZA of the electrode material did not align nicely with the [1$\bar{2}$1] of GGG.

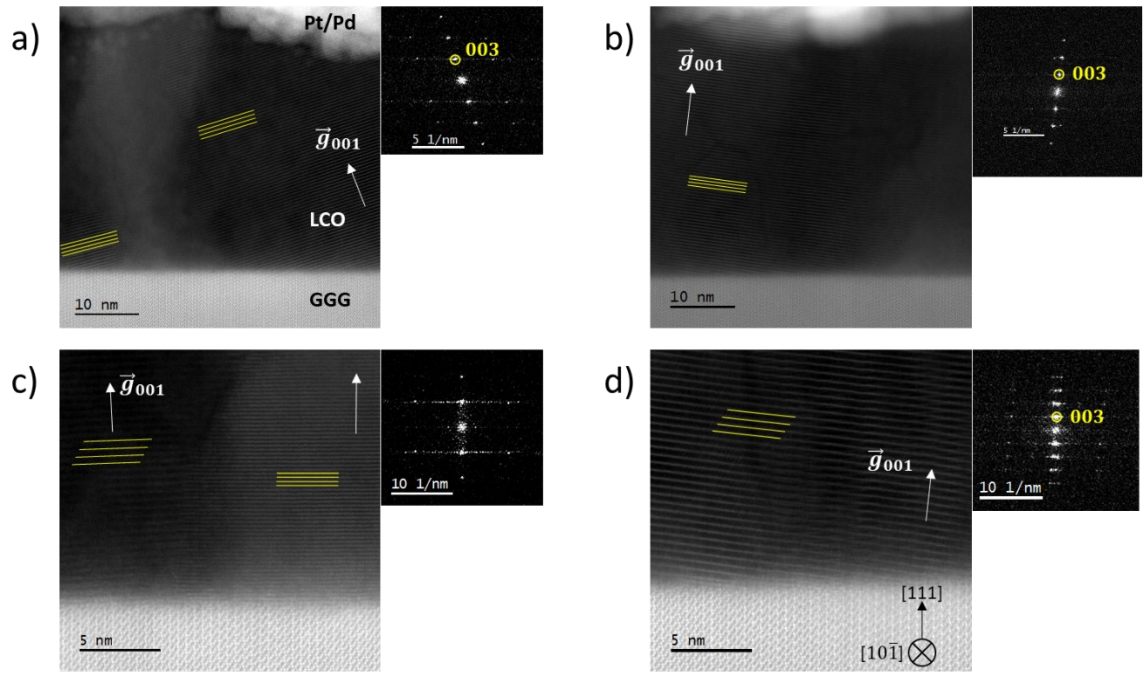

Figure 4.23: HAADF images Resolving lattice planes within LCO film deposited onto GGG(111) substrate, cut along the [101] ZA. Lattice planes within the LCO layer are marked by yellow lines. a) r-LCO growth with [001] growth axis offset 18° from the (111) plane of GGG. b) r-LCO growth with the (001) plane, offset 7.5° from surface of GGG. c) Two different orientations and therefore an interface between r-LCO grains or GB between r-LCO and rs-CO. d) Higher magnification of two grains overlapping with orientations relating to b) and c). Images acquired at 200 keV on JEOL ARM200CF

With respect to advantage of LCO growth with the characteristics seen on GGG(111), the orientation of Li routes towards the surface will improve efficiency of Li transfer towards an electrolyte. In addition, the similarities between GGG and LLZO with respect to lattice parameter and crystal structure make these orientations suitable for insight and comparison into growth of LCO and Li mobility at the interfacial boundary. The results here suggest the variable angle of CoO layer resolved in HAADF image would allow more efficient Li intercalation into LLZO than if the LCO on GGG was dominated by the r-LCO[001] oriented growth seen on ALO.

4.3 Growth and Structural Characteristics of Single Layer LLZO Thin Films at Different PLD Deposition Temperatures

The growth of LLZO is firstly approached with PLD around 200 °C, aiming to minimise Li evaporation, before progressing to higher temperature deposition, and annealing to induce crystallisation. STO and GGG were used as substrates for the controlled growth of LLZO, where lattice parameters are compared in Table 4.2. The closest lattice parameter ratio between STO and LLZO is a 3:1 mismatch of 1.48 Å (11%) relative to the lattice parameters of c-LLZO or 0.95 Å (8%) relative to c-LZO. In contrast, GGG is a 1:1 ratio with a mismatch of 0.63 Å (4.7%) relative to cubic LLZO and 1.8 Å (14%) of LZO. With similar structure and symmetry between GGG and LLZO the potential for well-orientated electrolyte growth for potential applications to LCO/LLZO heterostructures. As covered in Chapter 1, GGG has been shown by XRD studies to achieve orientated growth in an LLZO film along the same atomic plane as the GGG's surface [131]. This would be advantageous with respect to providing a consistent electrolyte and based on which to grow LCO in GGG/LLZO/LCO heterostructures, if well-orientated growth is not achievable on STO.

Table 4.2: Lattice parameters for STO and GGG substrates used in this section of the Chapter, with t-LLCO, c-LLCO and c-LZO phases as reference to the crystal growth in data presented

Composition	Phase	Space group	Lattice Parameters / A			Angles / °		
			a	b	c	A	β	γ
Substrates								
$SrTiO_3$	Cubic	$Pm\bar{3}m$	3.90			90		
$Gd_3Ga_5O_{12}$	Cubic	$Ia\bar{3}d$	12.55			90		
Electrolyte								
$Li_7La_3Zr_2O_{12}$	Tetragonal	I_{41}/acd	13.20		12.87	90		
$Li_7La_3Zr_2O_{12}$	Cubic (>900 °C)	$Ia\bar{3}d$	13.18			90		
Li deficient phase								
$La_2Zr_2O_7$	Cubic	$Fd\bar{3}m$	10.75			90		

4.3.2 Deposition of Amorphous $Li_7La_3Zr_2O_{12}$ Layers and Consequences of Annealing on Crystallinity

SEM images of LLZO depositions at LT on STO formed rough, fractured surfaces with variable particle dimensions (Figure 4.24). It was not clear if the roughness was related to crystallinity given a lack of regular shape to any particles. Another possibility is that the roughness is reflective of Li_2CO_3, given the electrolyte's susceptibility to reaction with CO_2 in air [318]. A 10 nm to 20 nm Pt/Pd layer is deposited on samples containing LLZO films in Chapter 4 and 5, to provide sufficient sample conductivity for SEM imaging. A side effect is it is also likely contributed towards roughness observed at the film's surface. However, without the conductive coating the sample drift did not allow for acceptable SEM resolutions or effective FIB preparation at beam voltages between 5 keV and 30 keV.

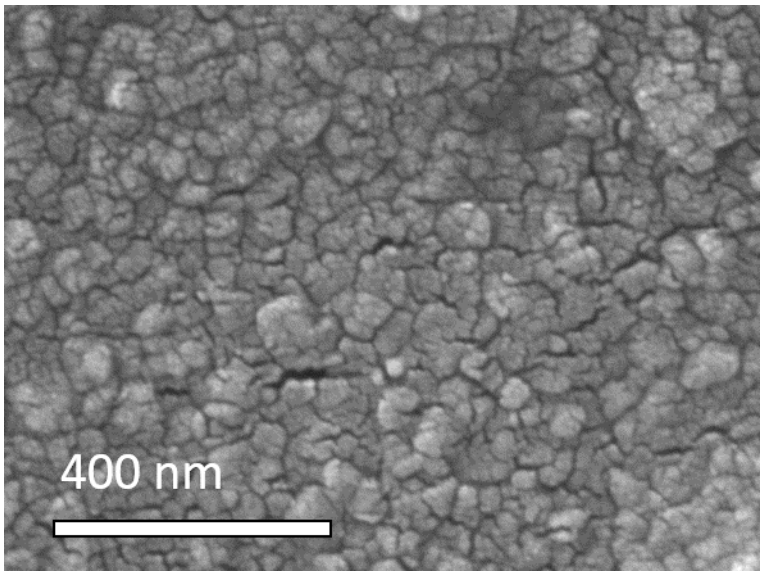

Figure 4.24: SE SEM image of LLZO film, deposited onto STO(100) at 250 °C. A rough, fractured surface is present across the electrolyte with no regular structures. Acquired in JEOL 7800F Prime at 15 keV.

The XRD of LLZO deposited at 250 °C, shown in Figure 4.25, has no visible intensities relating to crystallisation in the form of LLZO or LZO phases. TEM is later used to confirm the lack of crystallinity and crystallographic order near to the interface between LLZO and STO substrates. The low conductivity of amorphous LLZO again makes LT PLD undesirable for bulk electrolyte conductivity and transfer of lithium between lattice planes at the EEI.

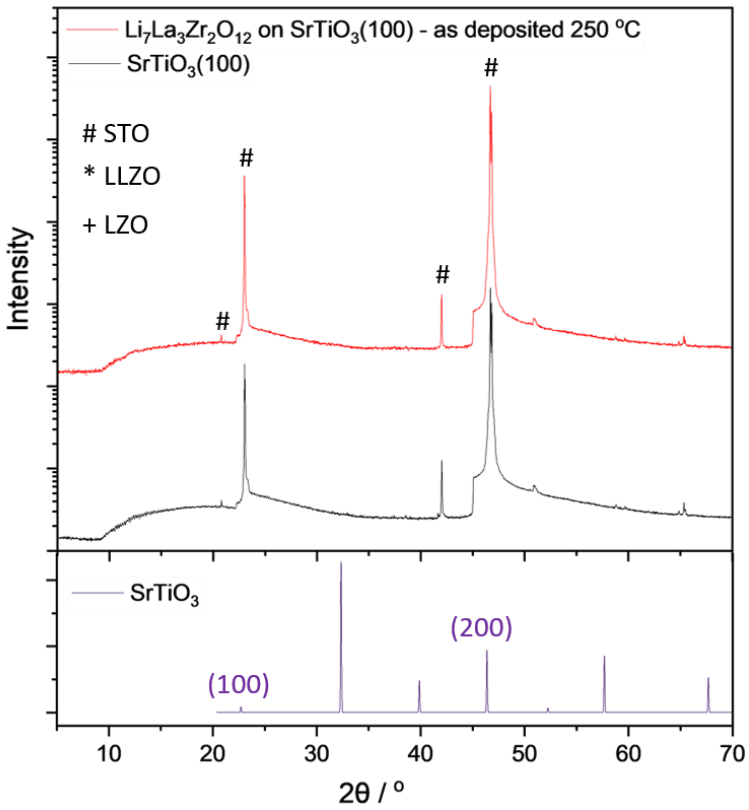

Figure 4.25: XRD of LLZO deposited at a substrate temperature of 250 °C during PLD with pristine STO reference and simulation of STO diffraction pattern. No signals relating to LLZO are visible above the baseline.

A lamella prepared from a sample of LLZO on STO(100), formed with a substrate temperature of 250 °C during PLD, can be seen in Figure 4.26. Figure 4.26, a) shows a uniform contrast to the LLZO layer, with a flat surface, with b) and c) using higher resolutions showing no ordering of atoms near substrate/electrolyte interface, neither within bulk of the electrolyte. Given the conductivity value of $\times 10^{-7}$ S cm^{-1} for amorphous LLZO, it was deemed important to achieve crystallisation, via either annealing or raising substrate temperature during PLD of LLZO [326].

The TEM observations, of the films deposited at 250 °C, show no signs of crystallinity across microns of the lamella. Higher resolutions and SAD patterns support the majority of these films being amorphous. Short range order may be indicated by spots in the amorphous SAD, in Figure 4.26, c), but this is likely a consequence of diffraction from crystalline grains in the Pt layer at the edge of the areas selected by the smallest SAD aperture. A Li_2CO_3 decomposition layer around 20 nm thick was visible at the surface, resulting from reaction of the electrolyte's Li content with the air. This decomposition layer is clearly visible in Figure 4.26, a) between the amorphous LLZO and Pt/Pd coating (dark contrast). This would not be a problem in commercial devices, where fabrication would be optimised/isolated to decomposition reactions with air.

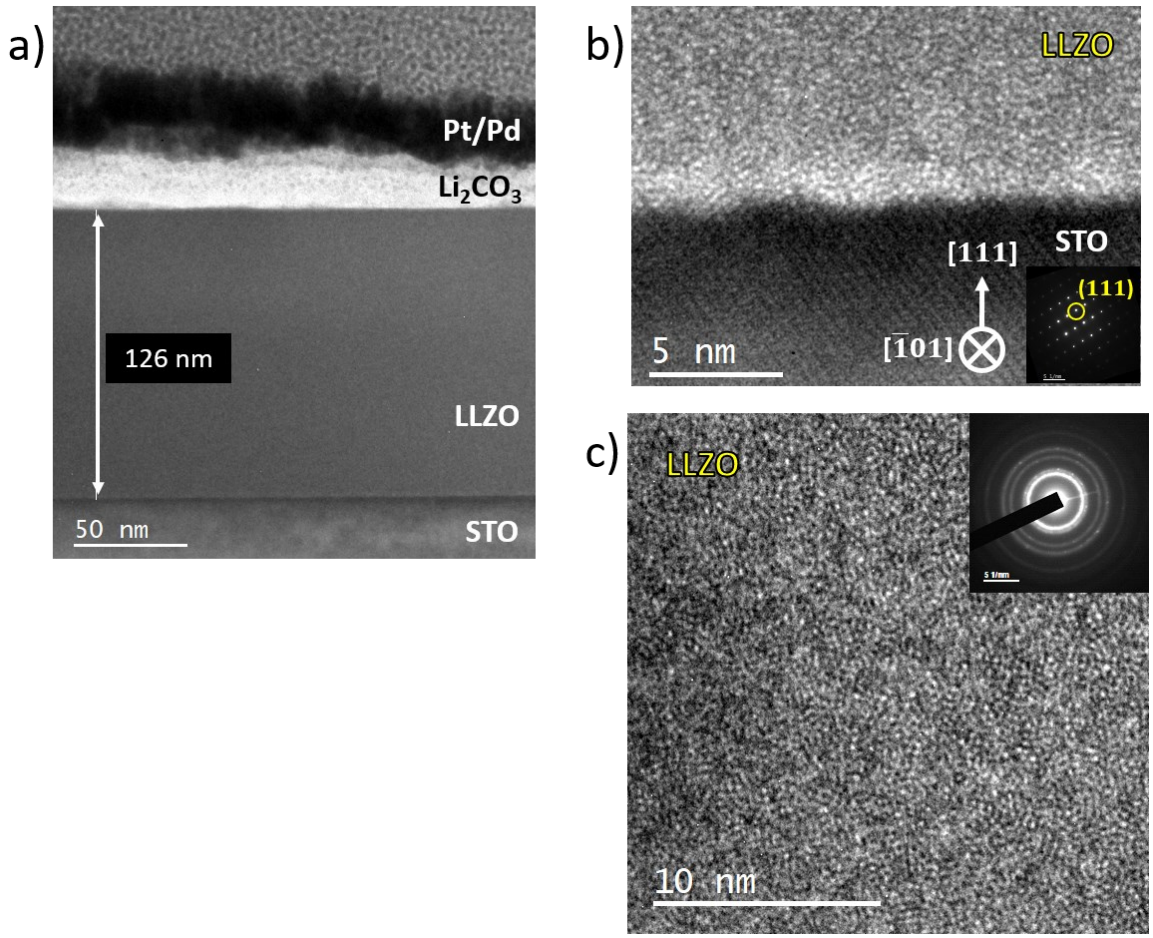

Figure 4.26: a) Low magnification BF TEM image of LLZO layer grown at 250 °C on STO(111). b) HR TEM image of interface, with inset FFT of [110] ZA for STO, with no crystallinity evident at the substrate-film interface. c) HR TEM image of amorphous LLZO within the bulk of the film, with an inset SAD showing amorphous rings from the LLZO layer, alongside faint diffraction spots where the SAD aperture overlapped slightly with the Pt layer deposited during FIB-SEM preparation. Data acquired on JEOL 2100+ at 200 keV, SAD with aperture diameter of 10 µm.

The lack of long-range crystallinity coincides with XRD observations, where Figure 4.27, a) show no significant LLZO or LZO signals after annealing amorphous samples between 350 °C and 550 °C, with crystallinity only apparent at 650 °C and above Figure 4.27, b). Relevant to samples containing amorphous LLZO is the attempt at shortening the annealing duration of films in section 4.4, from 4 hours to 30 minutes (ramp rate; 50 °C min^{-1}). A film LLZO film (PLD, 250°C) was annealed at 650 °C using this shorter duration of annealing. This contained some nanograins but the amorphous phase still dominated, indicating longer annealing was required. Considerations need to be made with respect to crystallisation versus Li loss as can result in significant Li evaporation, which becomes apparent in the data presented below [110, 143].

4.4 Annealing of Amorphous LLZO Films to Determine Crystallisation Temperature and Consequent Crystal Structure of the Electrolyte

Annealing of amorphous LLZO films, formed during PLD at substrate temperatures up to 450 °C, aimed to determine the threshold temperature for crystallisation. The use of this threshold annealing temperature as a substrate temperature during PLD then assessed the extent to which crystallinity is induced during deposition (section 4.5) and if a specific growth direction is achieved. This threshold temperature would be applied to growth on GGG substrates, shown by XRD in literature to induce growth of thin films matching the substrate's crystal orientation [131]. For post-PLD annealed samples, focus at HR is placed into determining structural differences indicative of LLZO or LZO grains and correlating orientation and Li content with furnace or PLD substrate temperatures.

The XRD analysis of annealed films shows the temperature threshold for significant crystallisation of LLZO grown on STO. Definitive peak intensities for LLZO or LZO did not appear for depositions or annealing below 650 °C. This is apparent in the series of XRD relating the increased annealing temperatures in Figure 4.27. A weak signal may be present at 32^{o} for samples annealed at 450 °C and 550 °C on STO(100), which matches with the (332) plane of LLZO (Figure 4.27, a), but this is not intense enough to be certain. An LZO signal for the (111) plane appeared at 28^{o} for samples exposed to temperatures of 650 °C, 950 °C and 1050 °C (Figure 4.27, b). The signal at 34^{o} could be assigned to the (001) or (211) plane of LZO and LLZO respectively. Prior to TEM confirming the presence of crystallinity the XRD suggests the threshold for crystallisation was somewhere between 550 °C and 650 °C, with 600 °C being used as a substrate temperature during PLD for data presented in section 4.5.

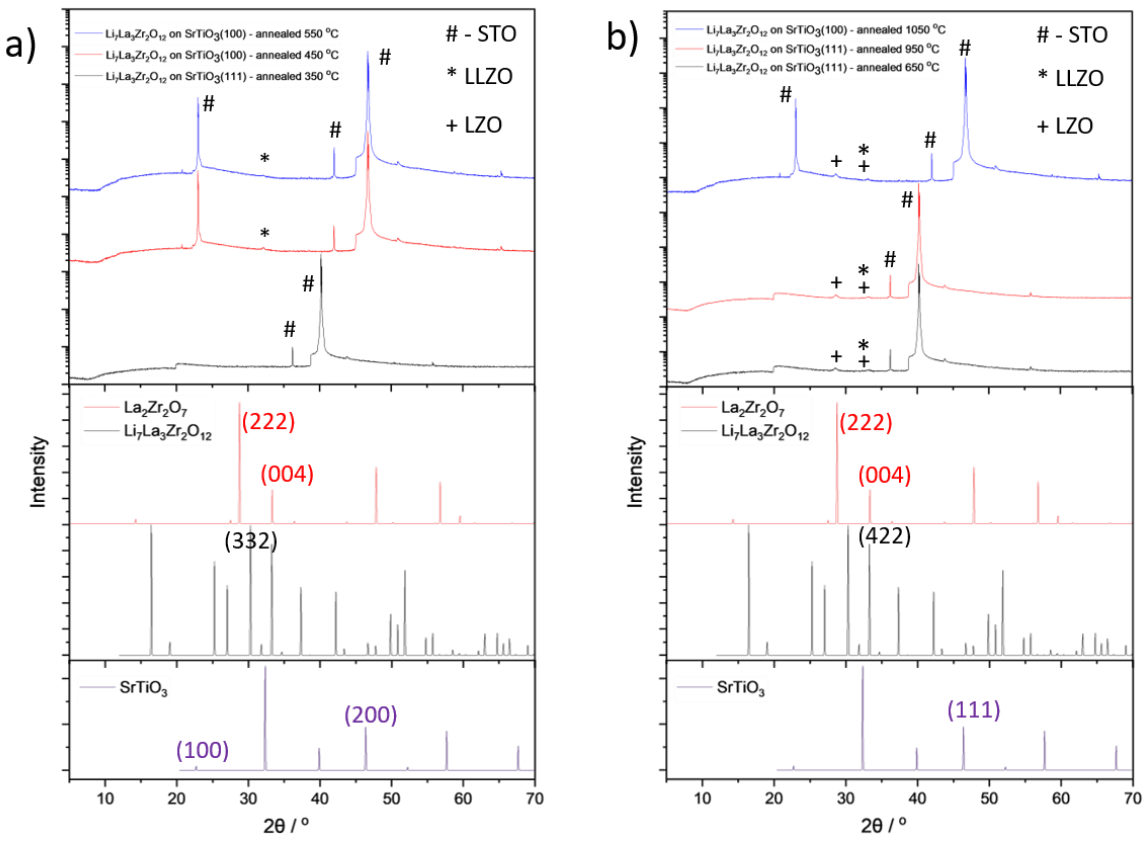

Figure 4.27: XRD of furnace annealed samples (4 hours, ramp-rate 20 °C min^{-1}) showing no clear crystallisation in a) after attempts at 350 °C, 450 °C and 550 °C. b) Emergence of signals relating to the LZO phase at 650 °C, 950 °C and 1050 °C and potentially some c-LLZO. Data acquired on Panalytical Aeris powder XRD (source: Cu-Kα)

A plot of the ratio between LZO(222) at 28° and LLZO(422) or LZO(004) at 33° and substrate peaks 40° (STO(111)) and 46° (STO(200)) after annealing is shown in Figure 4.28. There is a positive correlation between the annealing temperature (4 hours) and the intensity of both of the LLZO or LZO peaks relative to the substrate intensity. The outliers relating to the signal at 33° when annealing at 450 °C and 750 °C are indicative of either error in data analysis, due to noise in the spectrum, or optimisation of the temperature for crystallisation of a thin film with an orientation of LLZO(422) or LZO(004).

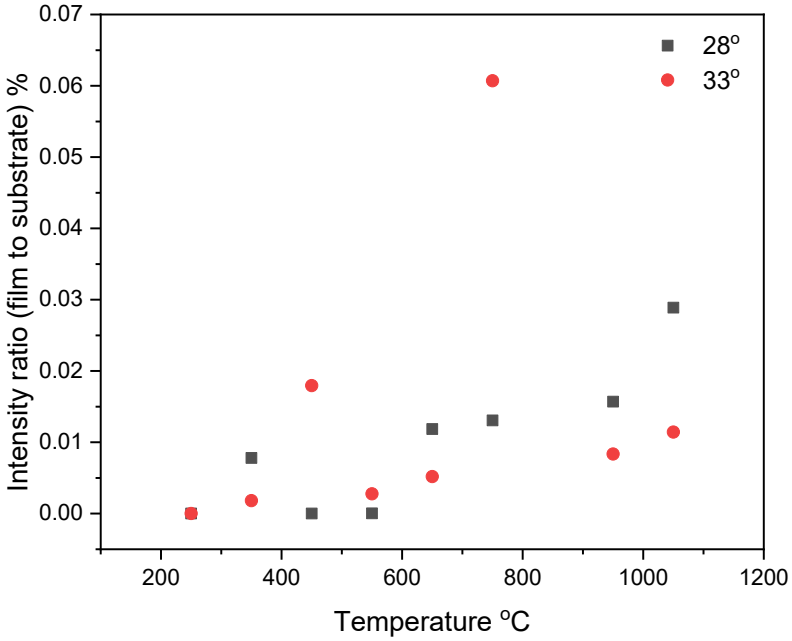

Figure 4.28: Intensity ratios between LZO(222) at 28° and LLZO(422) or LZO(004) at 33° and substrate peaks 40° (STO(111)) and 46° (STO(200)) after annealing. The data points show a tread of increasing intensity in both peaks as temperature increases, suggesting a greater degree of crystallisation. The intensity of the peak at 33° after annealing at 750 °C suggests either optimised growth for the LZO(004) or LLZO(422) growth or is an outlier.

The presence of LZO signals in the XRD is indicative of Li evaporation, detrimental to the electrolyte's capacity, and conductivity within the volume occupied by these Li-deficient grains. Electron microscopy studies aim to determine if the peaks labelled at LLZO and LZO in Figure 4.27 related to significant crystallisation within these samples or if a significant proportion of amorphous electrolyte remained. Li evaporation is undesirable and would require a method of offsetting to maintain LLZO conductivity and capacity within a device. SEM of films (Figure 4.29) annealed at 950 °C (a) and 1050 °C (b) show porous films on both STO(100) and (111). This creates a network of electrolyte with inactive volume and internal surface areas exposed to decomposition in contact with air. Porosity at 1050 °C appeared slightly greater, although both show evidence of reduction in the volume of contact between LLZO where Li transfer can occur. Crystallisation without inducing this level of porosity is preferable; however, TEM analysis was still undertaken to understand the characteristics of these films annealed at HT.

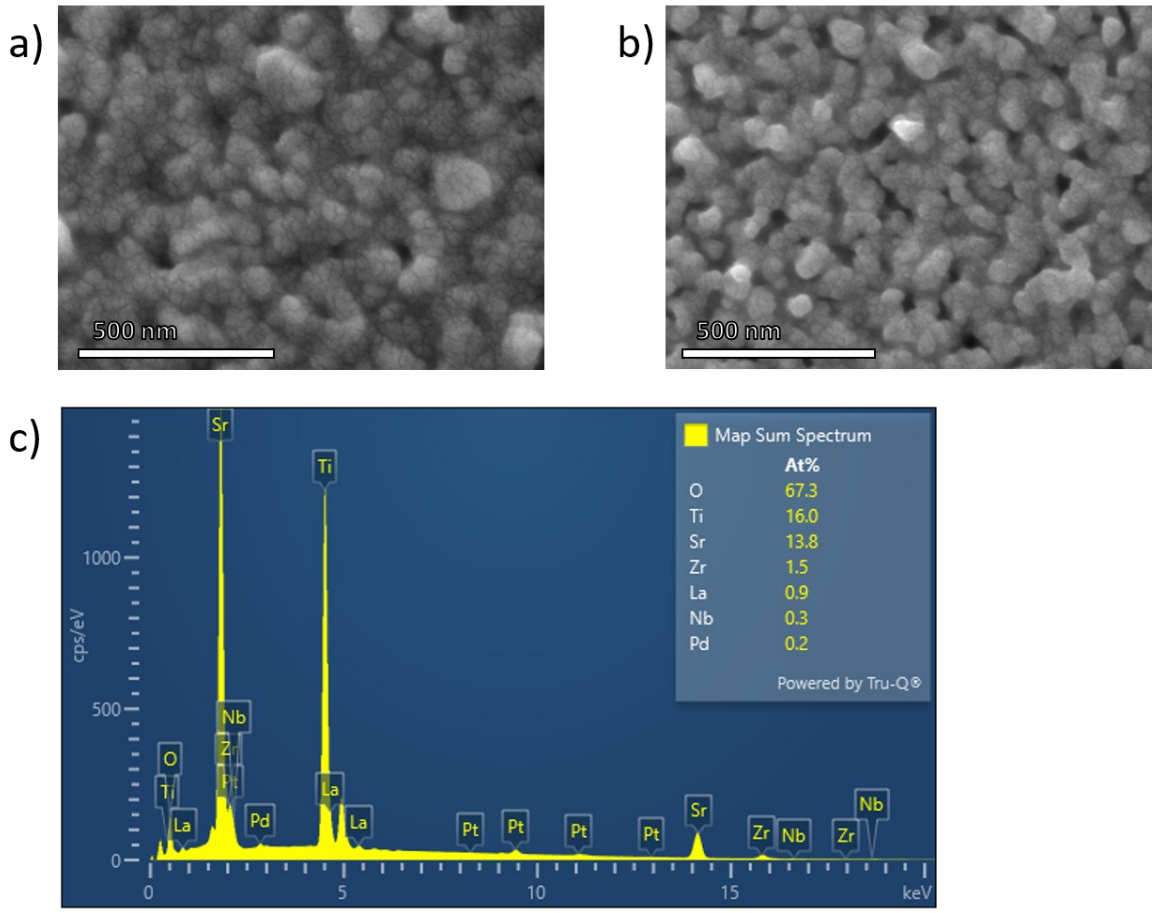

Figure 4.29: SE SEM images of furnace annealed LLZO film on a) STO(100) and b) STO(111) substrates. Both films are porous, which is indicative of a significant change in structure during annealing above the temperature threshold for crystallisation of amorphous LLZO. Images taken on JEOL 7800F Prime at 15 keV, EDS data acquired at 25 keV.

Variation in contrast across the cross-section (Figure 4.30, a) illustrated regions providing different diffraction conditions. This is an indicator of the widespread polycrystallinity running throughout the thin film after crystallisation at 950 °C and 1050 °C. The surface roughness and contrast are similar on both STO(100) and (111), suggesting the single crystal substrate has no significant influence over orientation of the crystallised material. Data from nanoscale to atomic resolutions is presented in (S)TEM Figures due to phase and orientation characteristics being indistinguishable between the two substrates and temperatures. SAD patterns from the film further supported the highly polycrystalline nature of the film, with many regions relating to the LZO phase.[51]

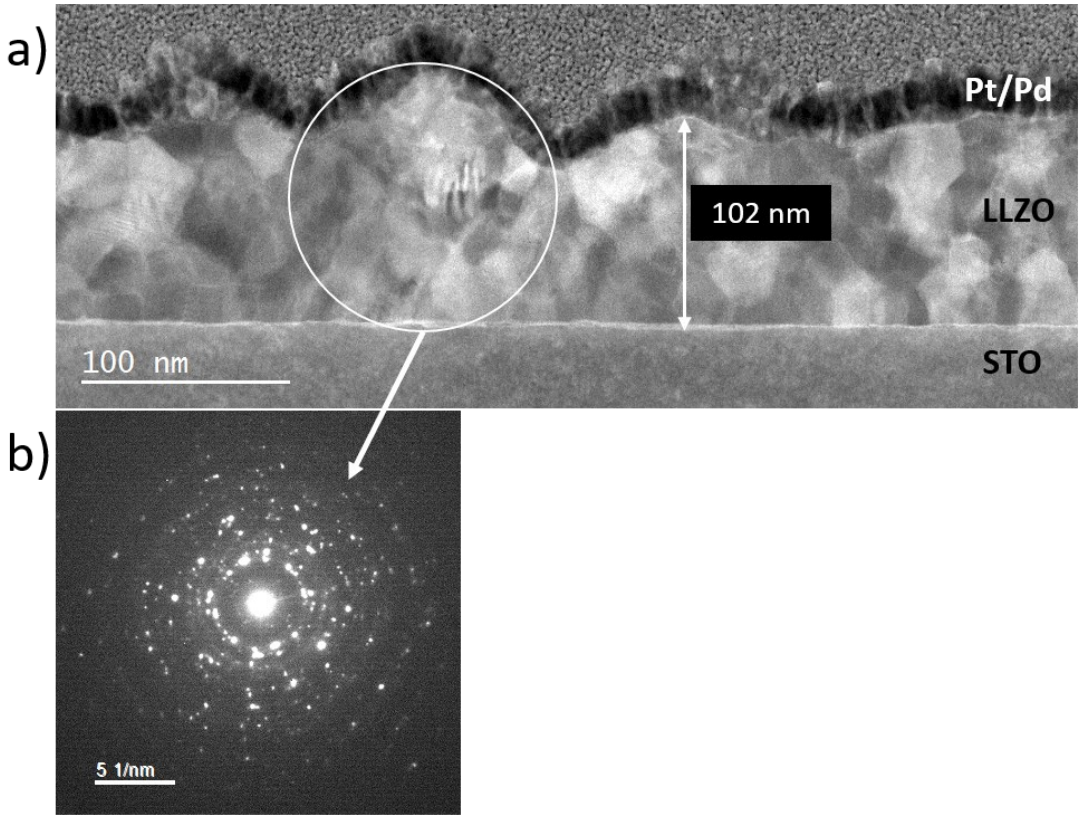

Figure 4.30: a) Low magnification TEM image of 2 micrometres of polycrystalline cross-section with several on-axis nanograins (dark contrast). SADP from circled region illustrates the polycrystallinity b) SAD pattern from circled region in TEM image, showing the polycrystallity of the LLZO film after annealing at 950 ^{o}C.. Data taken in JEOL 2100+ TEM at 200 keV, with DP acquisition using the 10 µm SAD aperture.

Compared to the amorphous LLZO (Figure 4.26), the TEM taken across lamella after annealing contains a distinct change in surface roughness, also shown by the low-magnification TEM images in Figure 4.30. The lack of a Li_2CO_3 layer between LLZO and Pt/Pd (Figure 4.30, a) suggests a deficiency in Li available for surface decomposition. The approximate method of tilting the sample to align to constituent nanograins onto a ZA was achieved,either by maximising the contrast of a specific grain or using Kikuchi lines where possible (e.g. larger grains), as this is a method of greater accuracy. Cross-sections of nanograins ranged from around 10 nm to 40 nm. Such diversity of grain structure creates wide ranging dependence for Li conductivity on the alignment of planes between each grain and space for Li to move within the GBs. The use of STEM resolving the nanograin structure attempted to accurately determine the phase and orientations within these polycrystalline films of LLZO or LZO.

HAADF images (Figure 4.31 and Figure 4.32) confirmed a dominance of crystalline nanograins throughout the film's cross-section. A minority of amorphous grains remain uncrystallised or are a result of the porous structure being filled with amorphous redeposited material during FIB-based preparation. Crystallisation from the initially amorphous LLZO would have either occurred from the surface or nucleated randomly throughout the thin film. LZO nanograins dominated the structure, with lattice plane spacings of 0.31 nm (Figure 4.31, b), or resolved structures and their diffractograms indicative of this Li-vacant phase (Figure 4.32). Some LLZO appears to exist, assigned by their greater lattice spacings (0.36 nm), although a significant minority. Variations caused by image drift and expected errors in microscope calibrations, alongside lattice strain, may lead to misidentification of LLZO and LZO phases, owing to similar spacings along similar ZA. This is possible within the data presented in this project as well as literature working on HR STEM of LLZO [178, 179]. Prolonged, annealing above 900 °C is clearly significantly detrimental to Li content and therefore capacity of LLZO electrolytes. Powders annealed at 850 °C during synthesis do not show significant Li deficiency in XRD, but do in lamella extracted near the surface, showing the volume of material in thin films is more susceptible to Li deficiency throughout the sample. The temperatures used for polycrystalline films were effective at creating a crystalline network of nanograins whereby a complex route for Li transfer is formed. This assumes LLZO had crystallised into similar nanograins prior to Li evaporation, with short annealing durations (e.g. 10 minutes) at 950 °C, or lower temperature is required to avoid development of LZO grains.

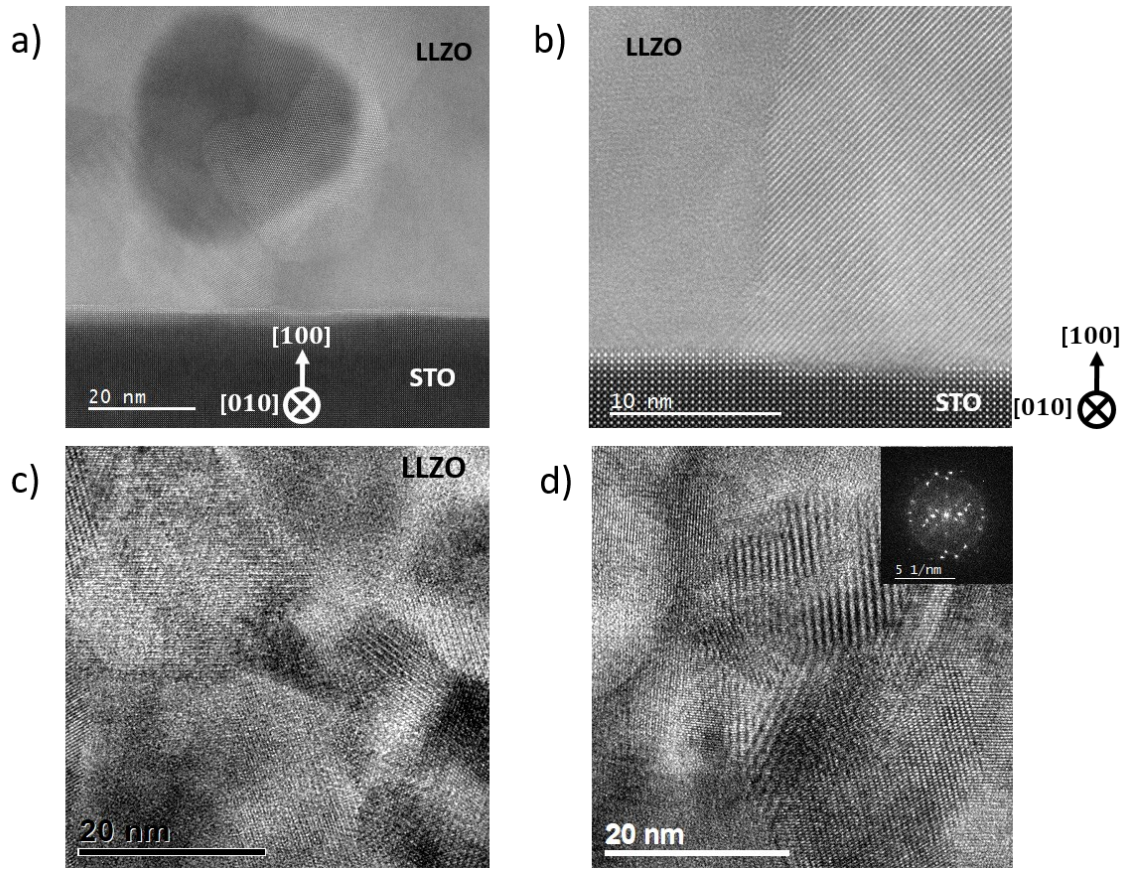

Figure 4.31: Images showing variation in LLZO film's orientation relative to the surface of an STO(100) (a and b) and STO(111) (c and d) substrates. The nanoscale grain dimensions and apparent independence of orientation relative to the STO(100)'s surface is indicated in a) and b). c and d) BF TEM images of GB and overlapping nanograins within the bulk of the LLZO layer. The polycrystalline nanograins were formed during annealing at 950 °C and 1050 °C for 4 hours. a, b) HAADF acquired on JEOL ARM200CF, c, d) BF TEM from JEOL 2100+, all datasets taken at 200 keV

Higher resolution examples, including HAADF images in Figure 4.32, identified some GB alignments between grains of LZO. The rock-salt structure provides easy identification of the lattice axis, phase and therefore the planes at which the grains meet. In Figure 4.32, a) grains between two LZO grains viewed along the $[1\bar{2}1]$ and [110] axis touch close to the $(31\bar{1})$ and $(1\bar{1}1)$ lattice planes, while in b) lattice planes of an undetermined orientation, create a boundary with the $(\bar{1}11)$ plane of a grain viewed along LZO$[110]$ ZA. Based on the HAADF contrast, atom symmetry and FFT between the two LZO planes in Figure 4.32, c), a symmetrically equivalent twin boundary appears to have formed. This interface between LZO twins, viewed along their [110] axis, create a boundary between the $(1\bar{1}1)$ and $(1\overline{11})$ lattice planes. The contrast in the upper-right grain indicative of grain overlap along the observation axis.

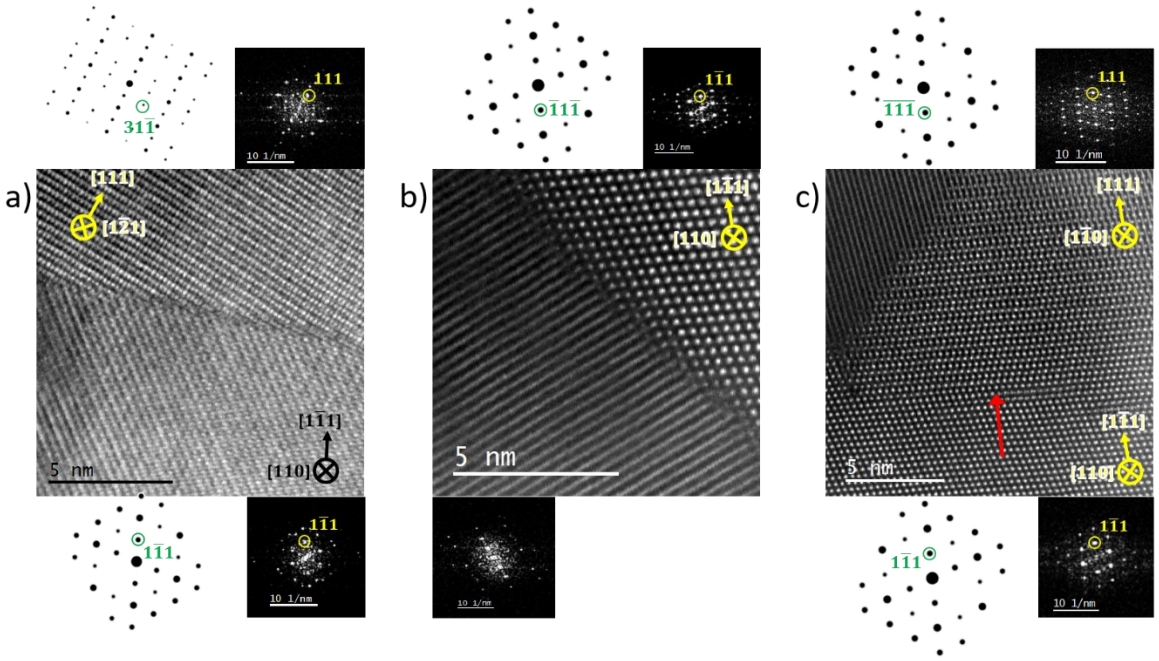

Figure 4.32: HAADF images of GB between the a) $(\bar{1}\bar{1}\bar{1})$ and $(1\bar{1}1)$ planes of LZO observed along the respective $[1\bar{2}1]$ and $[110]$ ZA, b) $[110]$ and undetermined LZO orientation, c) LZO boundaries between three grains with twin boundary (red arrow) joining along the (111) and $(1\bar{1}1)$ planes of LZO. a) and b) are symmetry inequivalent while the twin in c) forms with a symmetrically equivalent plane. The GB runs horizontally across the image, the midpoint marked by the red arrow. Data acquired on JEOL ARM200F at 200 keV.

As mentioned in section 4.3, heating to 650 °C for 30 minutes at a ramp rate of 50 °C min^{-1} achieves a small degree of crystallisation within the thin film, although the majority remains amorphous. A layer of Li_2CO_3/Li_2O was present at the surface, suggesting Li content remained within the LLZO film. This supports shorter durations of heating at higher temperatures potentially promoting crystallisation of the cubic phase, without excessive Li evaporation from the bulk of the electrolyte. Future work on the rapid crystallisation of amorphous LLZO films would develop understanding of whether crystallisation of this electrolyte is possible at temperatures near 1000 °C on sub-10 minutes timescale. This differs from the longer timescales and lower temperatures used in this work (minutes to hours) and current literature (hours) [97, 143].

4.5 Surface and Structural Analysis of Crystalline LLZO Deposited onto STO Substrates Heated to 600 °C during PLD

The heating of the STO substrates to 600 °C during PLD of LLZO also results in the formation of different surface roughness compared to amorphous and annealed thin films. The topography of the LLZO illustrates differences between the electrolyte grown on STO(111) (Figure 4.33, a) and (100) (Figure 4.33, b). The film on STO(111) has greater roughness, with varying crystallite size and shape, potentially suggesting inhomogeneous grain sizes and variable growth orientations across the sample. The LLZO on STO(100) has a more uniform surface, closer to the appearance of the amorphous films in Figure 4.24.

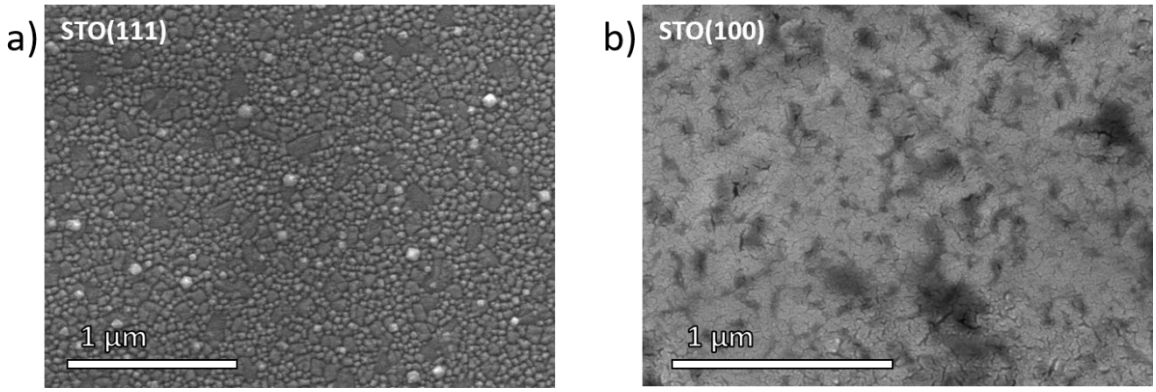

Figure 4.33: Secondary electron surface images of LLZO depositied onto a) STO(100), b) STO(111). The porosity seen in annealed LLZO samples was not evident in these films grown at 600 °C. LLZO grown on STO(111) exhibits small and large crystallites, while the film on STO(100) is more uniform/flat. Aquired on JEOL 7800F Prime at 15 keV.

XRD spectra in Figure 4.34, acquired from the thin films on both STO substrates, indicate a dominance of LZO. The signal at 33° for LZO on STO(100) is likely to relates to a dominant [001] growth orientation within the electrolyte layer. This is shown later to match well with the most common grain orientations observed in TEM cross-sections of both samples (Figure 4.38 to Figure 4.40). A couple of weaker signals at 17° and 34° may relate to the presence of LLZO regions, although a minority in comparison to the LZO phase. For LLZO on STO(111) the XRD are similarly Li-deficient, with strong peaks relating to the LZO phases at 28° and 33°, assignable as a potential dominance of LZO grains growing along the [111] and [001] axis. The broad feature between around 44° was potentially LLZO but analysis of crystal structure in (S)TEM was required to confirm or exclude the presence of any Li-rich grains.

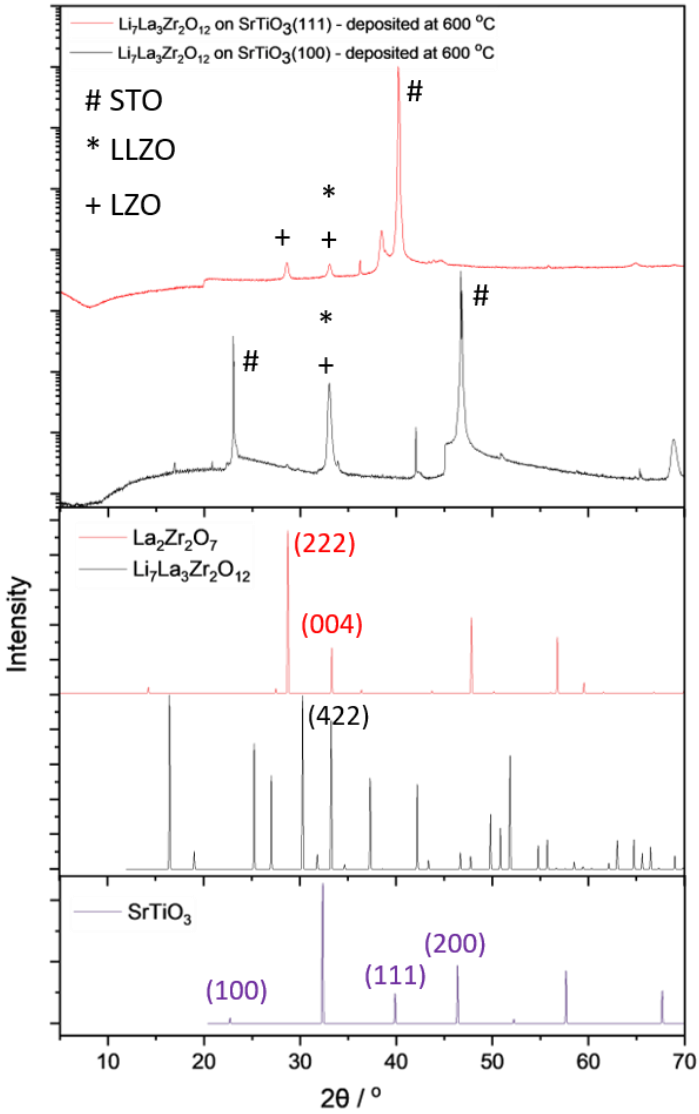

Figure 4.34: XRD of films deposited at 600 °C substrate temperature during PLD, showing crystallisation relating to the LZO phase a) LLZO on STO(100) with LZO signals at 28° and 33°, (001), alongside potential weak LLZO signals at 16.5°, (211) and 33.2°, (422). b) LLZO on STO(111) with similar prominence of LZO peaks, suggesting significant Li deficiency. Weak signals at high angles (42° to 44° and 64°) may be related to a minority LLZO phase. Data acquired on Panalytical Aeris powder XRD (source: Cu-Kα).

The plot of thin film intensity at 28° (LZO(222)), 33° (LLZO(422) or LZO(004)) and 38° (LLZO(521), in Figure 4.35 shows that, growth of LLZO onto STO(100) at substrate temperatures of 600 °C during PLD, the main crystallisation direction relates to the LZO(004) as the intensity of the signal at 33° is dominant. In contrast, all three orientations are present within the film grown at 600 °C on STO(111). Here the peak at 38°, possible related to LLZO(521) is the dominant peak intensity. In order to confirm and clarify these observations in XRD, work to observe the presence of these phases and their orientation is analysed by TEM and STEM was therefore required and is presented later in this chapter.

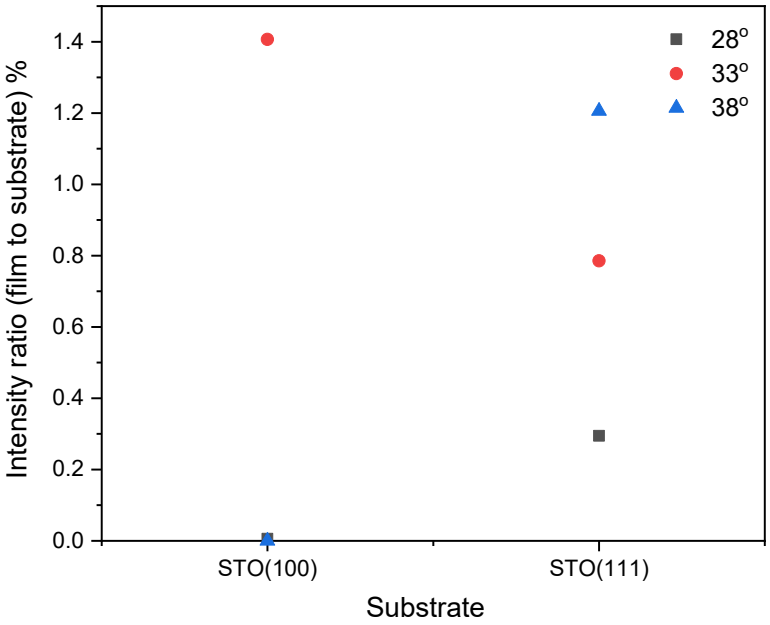

Figure 4.35: Intensity ratios between LLZO film and substrate peaks 40° (STO(111)) and 46° (STO(200)) when grown at substrate temperatures of 600 °C during PLD. The data points show relative percentage of LZO(222) at 28°, LZO(004) or LLZO(422) at 33° and potentially LLZO(521) at 38°. LLZO deposited onto STO(111) contained a great number of orientations of either LLZO or LZO.

Figure 4.36 provides low-magnification TEM images, the roughness apparent in Figure 4.33 is shown to relate to an uneven surface with no consistent angles, unlike LCO grown on ALO(0001) and STO(111). Nanobeam diffraction indicates the dominance of a grains observed along the [100] ZA (or equivalent), relating to growth of LZO along the [001] direction, relative to the $[1\bar{2}1]$ and $[1\bar{1}0]$ ZA of STO(111).

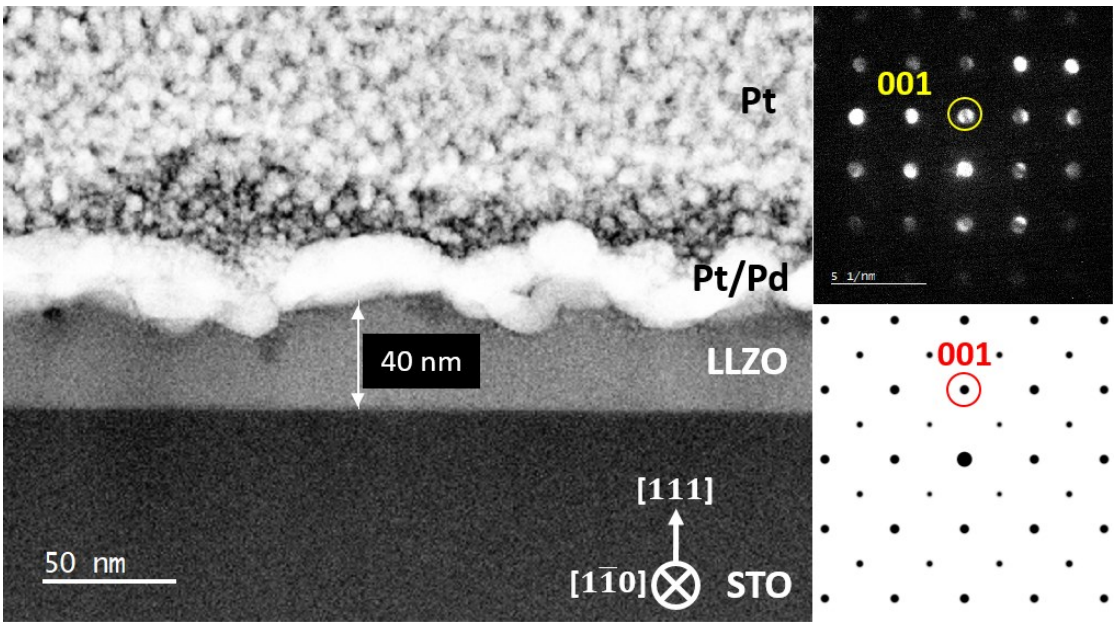

Figure 4.36: a) Low magnification HAADF image of electrolyte deposited on STO(111) at substrate temperatures of 600 °C, with a 40 nm film depth. Nanobeam diffraction was representative of the spacings relating to the most intense spots in the diffraction pattern simulated for the [100] ZA of LZO. HAADF acquired at 200 keV with JEOL ARM200CF.

Magnifications suitable for resolving atomic structure reveal a crystalline film, dominated by LZO, without any visible porosity. The lack of porosity benefits utilisation of the full volume of electrolyte material between cathode and anode for Li transfer. In Figure 4.37 (a), large grains cover the depth of the deposited electrolyte with some variation in the form slight variations in growth axis and GB with grain occupying a minority of the sample. Despite the consistent and significant proportion of LZO[100], the contribution of GB with and defects Is significant enough to have an impact on the electrolyte. In some regions the growth close to the [001] axis deviates from 4° relative to the STO surface, to 8°, creating the Moiré pattern seen in Figure 4.37, a) (highlighted by a red box). Regarding the misorientations relative to the substrate, the lattice mismatch between STO(111), LZO and LLZO is such that this tilted growth is thought to be energetically preferable to the [001] orientation growing directly parallel to the substrate's surface. The second grain orientation, occurring in the minority, are the lattice planes running approx. 16° from parallel to the STO(111) (Figure 4.37, b). These provide diffractogram spacings relating to the LLZO phase, viewed along the $[\bar{1}01]$ ZA. While the diffractogram suggests LLZO, the structure adopts layering of atomic planes similar to LZO viewed along the $[1\bar{2}1]$ ZA. The small grain observed in Figure 4.37, b), near the STO interface, were present at irregular intervals along the cross-section. The diffractogram suggests either overlapping grains or a phase that nano or pencil beam diffraction is needed to confirm as LLZO or LZO.

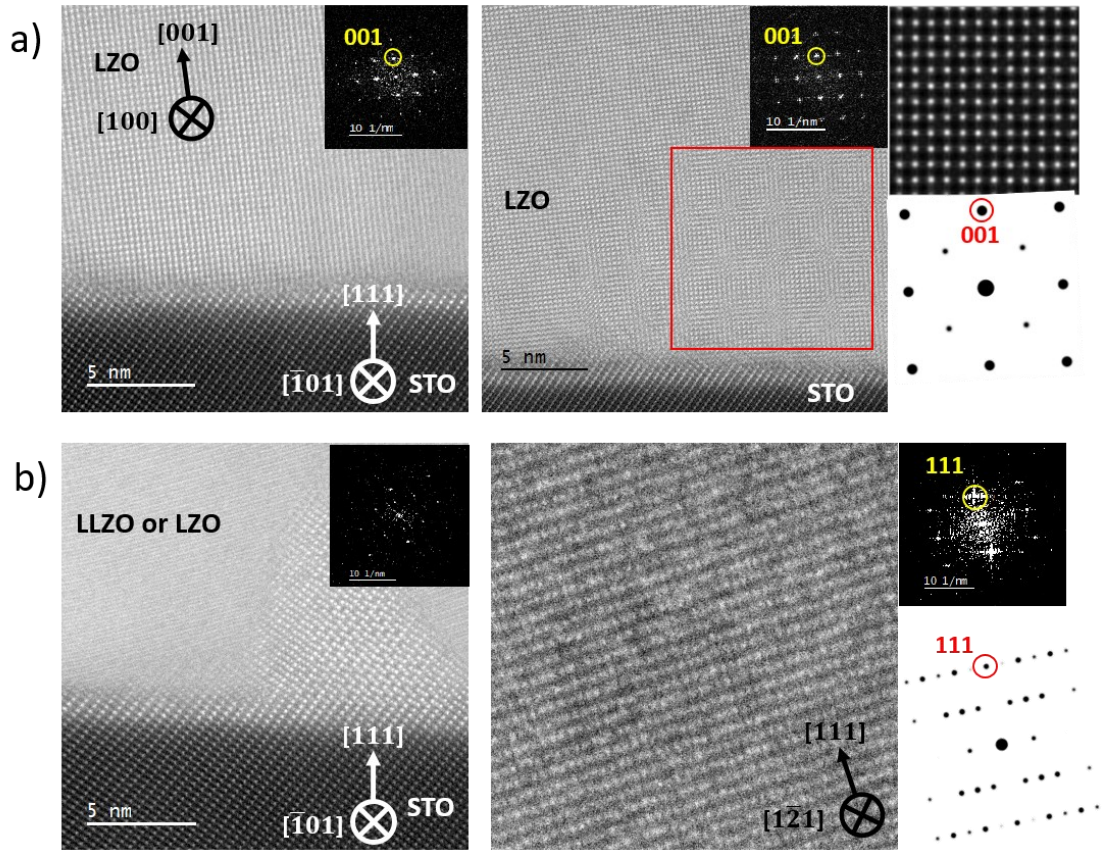

Figure 4.37: a) HAADF images of LZO grains grown at substrate temperatures of 600 °C during PLD, on STO(111) (lamella cut along [$\bar{1}$01] ZA). a) HAADF simulation along the [100] of LZO accompanies the STEM images. b) HAADF image of alternative grain orientations within the electrolyte film, with diffractogram symmetry and spacing suggesting a minor grain orientation of the LZO or LLZO (111) plane growing at 16° to the substrate's surface (simulated DP of LLZO included). Inset diffractograms show the slight misorientation from the (001) plane of the [100] ZA. Acquired on JEOL GrandARM300CF at 300 keV.

On STO(100) a well-crystallised film is also achieved with substrate temperatures of 600 °C during PLD (Figure 4.38), with contrast suggesting a columnar structure with grains (Figure 4.38, a). The observation axis, shown by the SAD from the electrolyte film shown in Figure 4.38, is representative of LZO or LLZO along the [110] ZA. Assuming both phases are present, their respective growth direction would be along the [001] for LZO and [1$\bar{1}$0] for LLZO, where either STO or energetic stability of this growth orientation leads to adopting these orientations. Spacing of the diffraction pattern is closer to LZO than LLZO, suggesting similar Li deficiency as films grown on STO(111). The cutting of the STO(100) substrate along the [110] ZA mean the LZO phase is observed along a different direction to the [100] of LZO in Figure 4.37 despite a near equivalent growth orientation. PLD at a substrate temperature of 600 °C, onto an amorphous layer would define whether the [001] growth is dependant or independent of STO as a substrate.

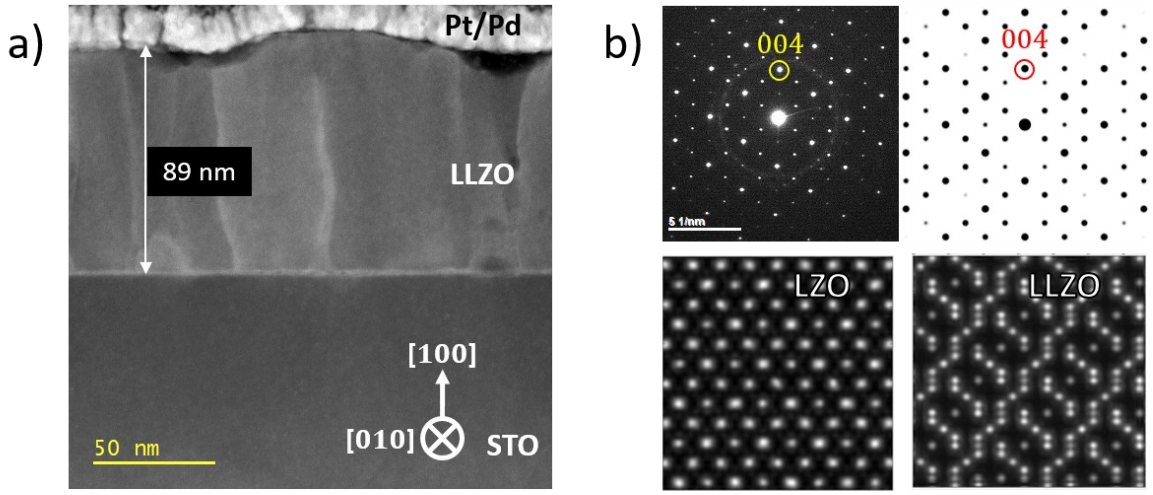

Figure 4.38: a) HAADF image of LLZO on STO(100), showing a 90 nm film depth and contrast variation. b) Diffraction pattern from SAD within the LLZO film, accompanying diffraction simulation of [110] ZA for LLZO phase. The orientation of the diffraction related to the [001] or $[1\bar{2}1]$ orientations of LZO or LLZO respectively, with diffraction spacings closer to the LZO phase. Data acquired on NeoARM200CF at 200 keV.

HR STEM provides more detailed analysis of the orientated growth of electrolyte on STO(100). The electrolyte growing is resolved along the [110] ZA in Figure 4.39 with consistent phase and orientation between the STO/LLZO interface up to the surface of the deposited material. While boundaries and defects do exist, their distribution and number are fewer compared to furnace annealing, reducing potential barriers to Li transfer relating to diffusion through GB interfaces and networks. Figure 4.40 illustrates lateral variation in crystallinity, observed as contrast variations in low magnification images (a) and shifting crystallinity in HR STEM (b and c). Columns where LZO growing along the [001] axis was not resolved, may either be amorphous or a different axis of growth, where the crystalline structure of the electrolyte does not align well with the [010] ZA of the STO substrate in the lamellae analysed.

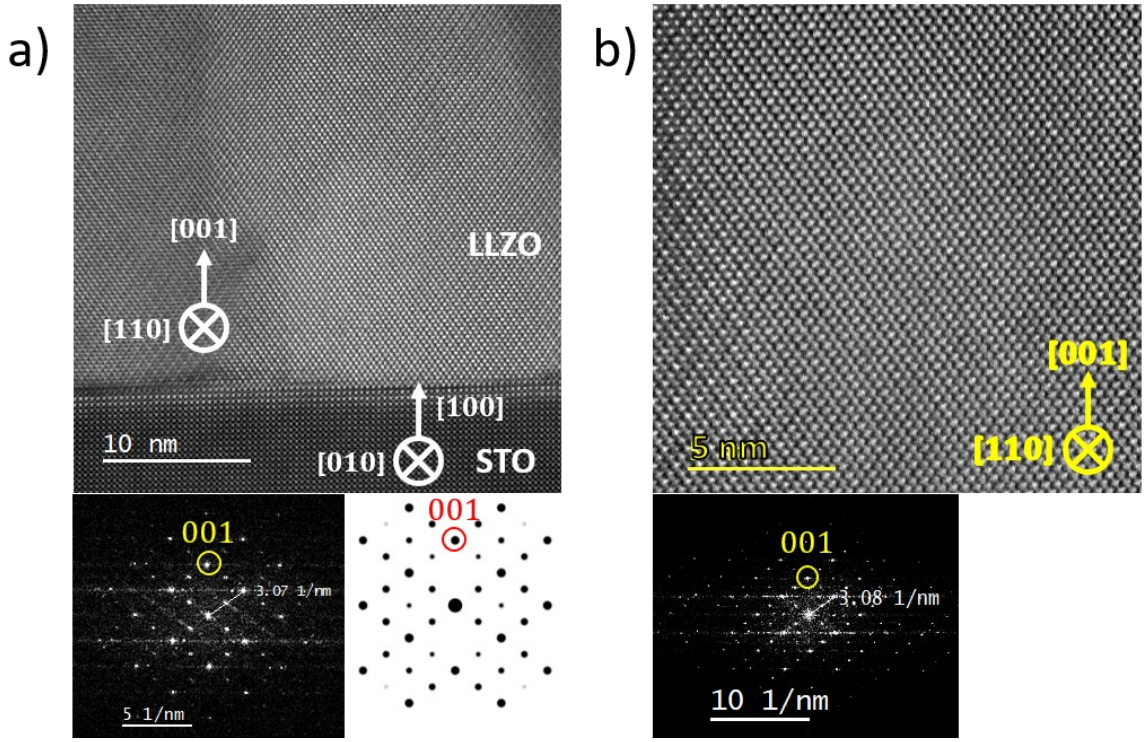

Figure 4.39: HAADF images of the LLZO film deposited onto STO(100) (lamella cut along the [010] ZA) with the diffractogram pattern and spacing (≈ 3.1 nm^{-1}) relating to the [110] ZA of LZO instead of LLZO. This shows the sample is likely to have substantial Li deficiency. Images acquired in JEOL ARM200CF at 200 keV.

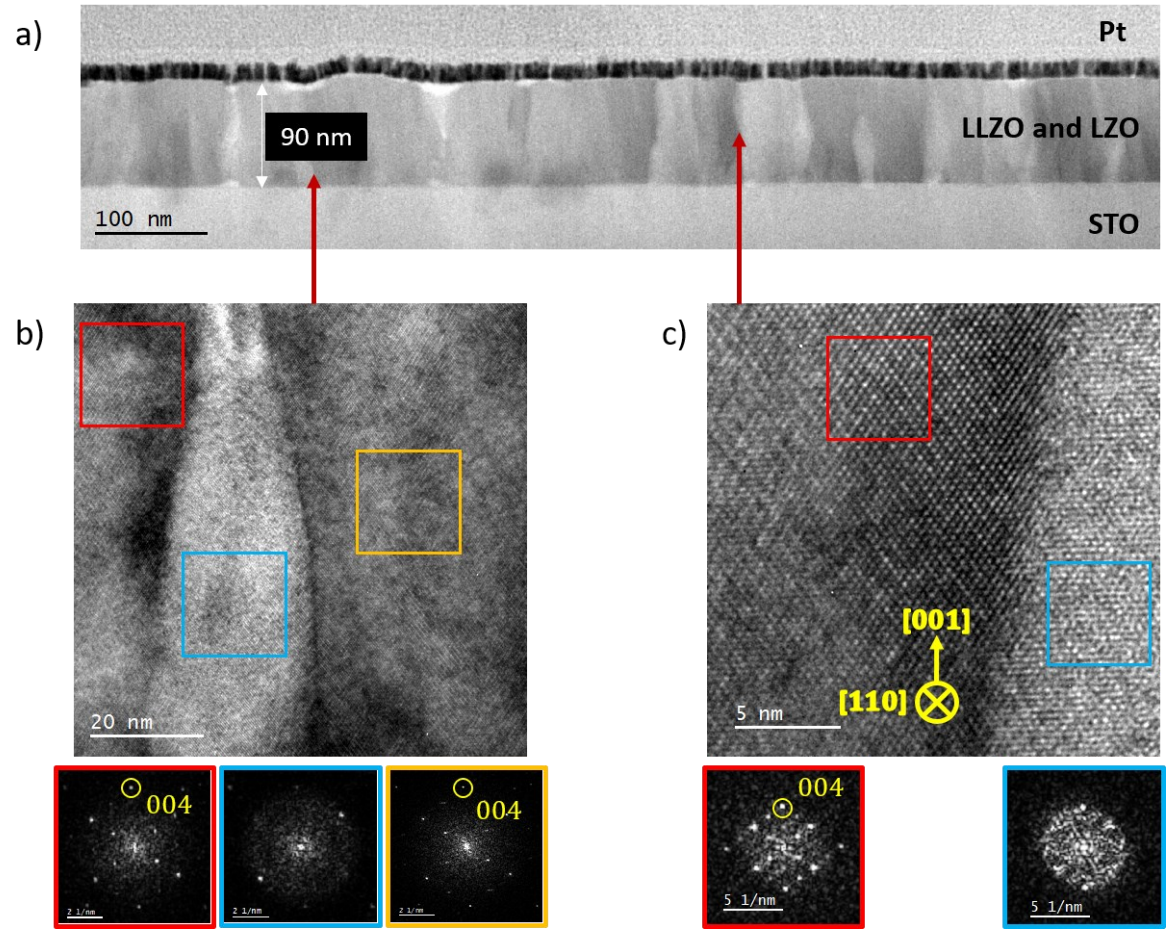

Figure 4.40: Boundaries showing misorientations and changes in crystallinity between adjacent grains. a) Low magnification BF image, displaying the contrast variations where boundaries are present (red arrows) along the cross-section of the LLZO film. b) Transition between boundaries close to the [110] axis of LZO with variation in both orientation and degree of crystallinity. c) Higher magnification of grain boundary between [110] axis and partially amorphous grain. JEOL ARM200CF at 200 keV.

EELS (Figure 4.41, a)) and EDS (Figure 4.41, b)) measurements detect the presence of La, Zr and O within the LLZO layer near the STO substrate. Dwell time versus specimen drift and contamination rate meant that an acquisition time of 0.2 seconds per pixel was suitable when acquiring data with resolutions of at least 20x10 pixels without excessive sample drift or degradation. This meant accurately quantifying at% of Zr was not possible. The dispersion required for detection of a weak core-loss Zr signal at 1112 eV and 2307 eV was not compatible with drift rate (approx. 0.4 nm in x axis, 20 seconds) versus dwell time. Drift correct was applied but this also required consideration of contamination rate given the requirements for a reference frame to be acquired for appropriate correction.

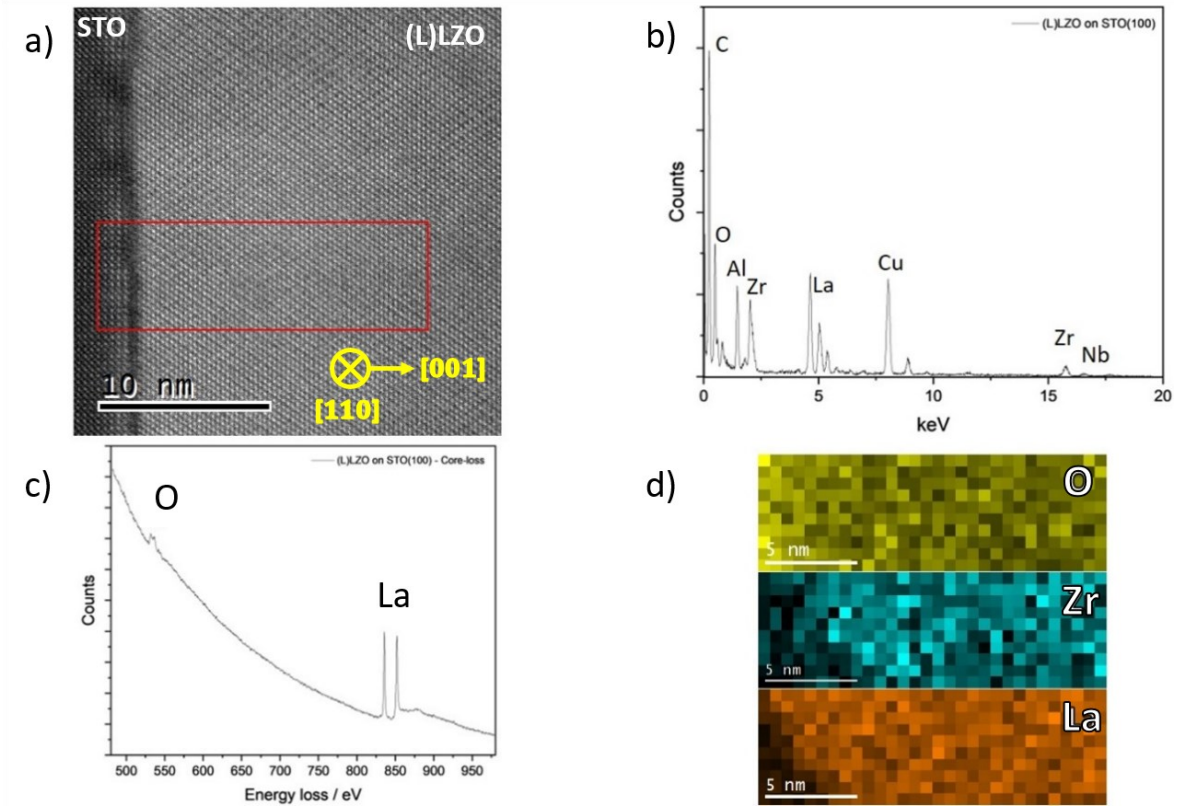

Figure 4.41: a) Image with ROI (red box) for EELS and EDS acquisition and core-loss EELS spectra. b) EDS spectra and associated maps of O, Zr and La distributions for each pixel/probe position. c) Core-loss EELS spectrum relating to the ROI, with O and La signals. d) Chemical map from EDS spectrum confirming presence of O, Zr and La in the electrolyte layer. Data acquired at 200 keV in JEOL ARM200CF at 200 keV.

Summarising annealing versus in-PLD crystallisation, inducing crystallisation of LLZO during PLD appears to lead to directional growth of both the LLZO and LZO phases present in these films, in contrast to the polycrystallinity of annealing amorphous films. Having oriented LLZO growth can promote a more consistent energy barrier to ion mobility through the crystal. The formation of crystalline layers with substrate temperatures of 600 °C during PLD matches the crystallinity in LLZO layers induced by annealing between at 650 °C (e.g. XRD in Figure 4.27). Similar to annealing, the limitation with elevated substrate temperature during PLD is the rate of Li loss, versus the time required to deposit a film to the desired thickness (50 nm to 100 nm). Subsequent work attempted growth on GGG(111) at 600 °C (presented in section 4.6), with ongoing studies into use of lower temperatures for LLZO on GGG(100) as well as annealing at 900 °C (less than 10 minutes) aimed at achieving a crystalline LLZO layer with consistent lattice orientation without significant Li deficiency.

4.6 High-Resolution Electron Microscopy of LLZO Grown on GGG(111) at 600 °C, Aiming to Achieve Epitaxial Growth of the Electrolyte

Deposition onto GGG substrates with a [111] single crystal surface orientation has been shown by XRD in literature, to acquire LLZO film growth by PLD along the respective (111) planes of c-LLZO.[131] Applying this with a focus of analysing the film growth at AR aimed to assess the epitaxy, grain structure and Li content of individual grains. In addition, the potential for orientated LLZO growth would provide a basis for easier analysis of the SSE-electrode interface by deposition of LCO onto the LLZO layer where GB between the two materials exist.

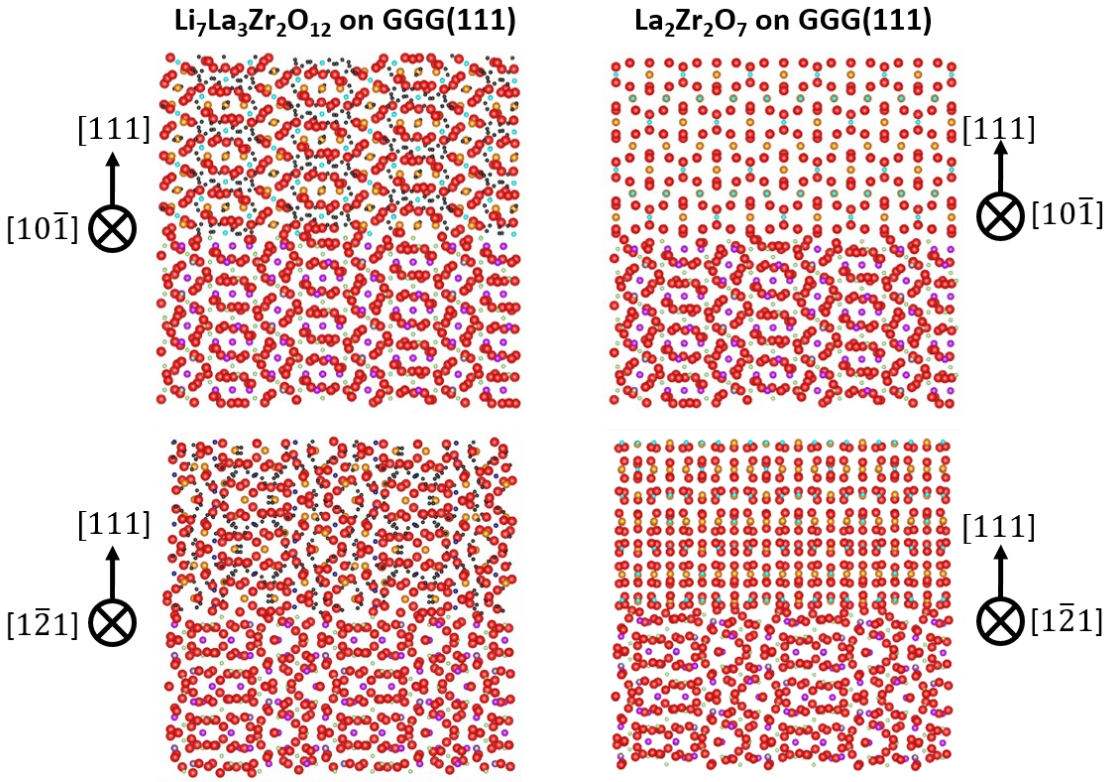

Figure 4.42: Models of LLZO growth anticipated on GGG(111) substrate, accounting for potential formation of LZO phase in regions of significant Li evaporation. Models show growth of LLZO and LZO viewed along matching [10$\bar{1}$] and [1$\bar{2}$1] axis cut along the edges of GGG(111) substrates. Interface models produced using QSTEM model builder and structure files from online databases [44, 51].

The SEM images in Figure 4.43 show a more textured surface compared to amorphous layers on STO, although are different from crystalline electrolyte films deposited onto STO(111) and (100) at 600 °C. While the SEM observations show crystallinity has likely occurred, based on comparisons to similar surface structures in LCO and LLZO on ALO and STO, the variation in shape and size indicates potential polycrystallinity owing to inconsistent distribution of larger crystallites. Understanding the atomistic features of LLZO growth on GGG(111) at 600 °C includes investigations of phase and grain orientation using XRD and (S)TEM presented in Figure 4.44 to Figure 4.47.

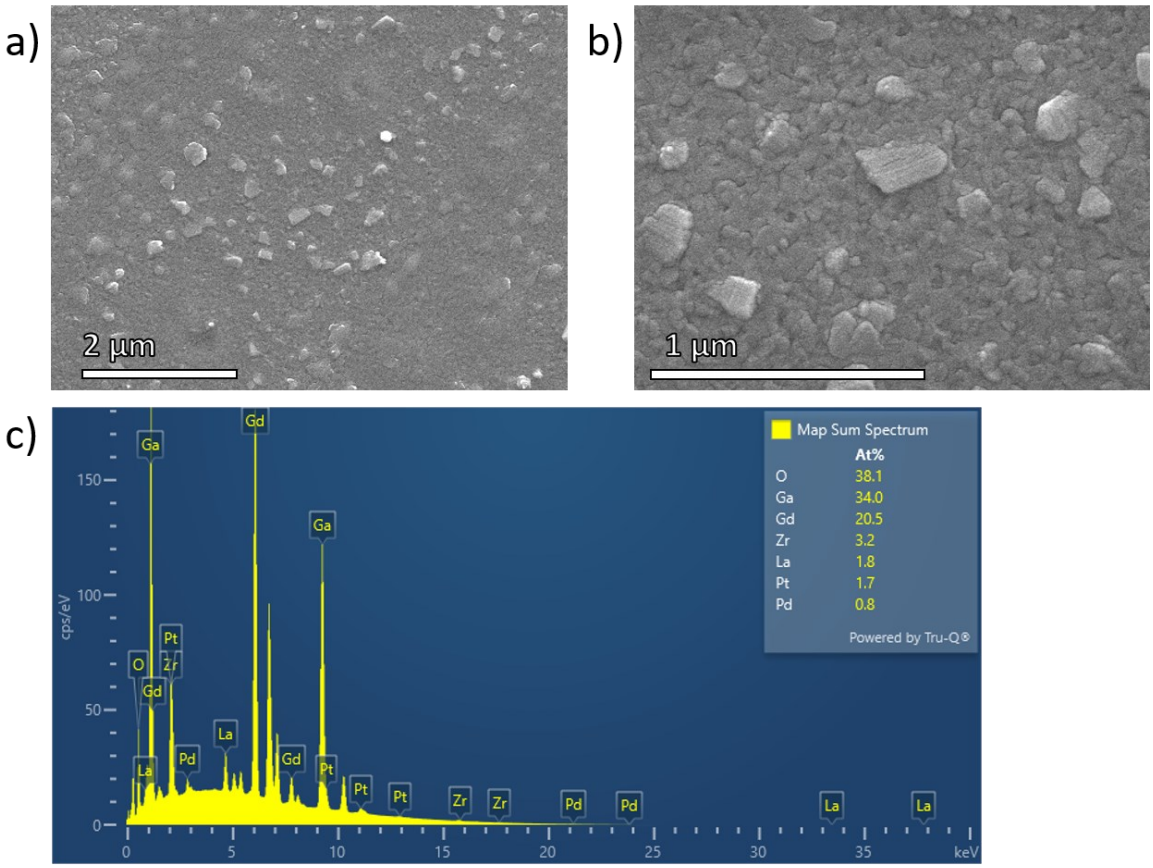

Figure 4.43: a, b) SEM images of LLZO films deposited onto GGG(111), containing a dense film with crystallite structures across the surface. c) EDS spectrum of sample containing all anticipated elements. High at% of Zr could again be attributed to the use of a Pt/Pd coating to reduce sample charging and drift to acceptable levels. Images and EDS data acquired on JEOL 7800F Prime.

Owing to the challenges producing crystalline LLZO through PLD onto STO substrates at temperatures below 600 °C, deposition at 600 °C aimed to produce epitaxial electrolyte crystalline films without the need to anneal LLZO on GGG. This substrate temperature was expected to create Li-deficient LZO grains within the layer of LLZO on GGG(111), however ideally retaining some Li-rich grains along the same crystal plane as the substrate. The XRD in Figure 4.44, taken from the LLZO film after deposition onto GGG(111) shows a dominant signal at 28°, relating to the (111) plane of LZO. The dominant intensity of this LZO signal is indicative of a well-orientated growth of the film, but with clear Li deficiency.

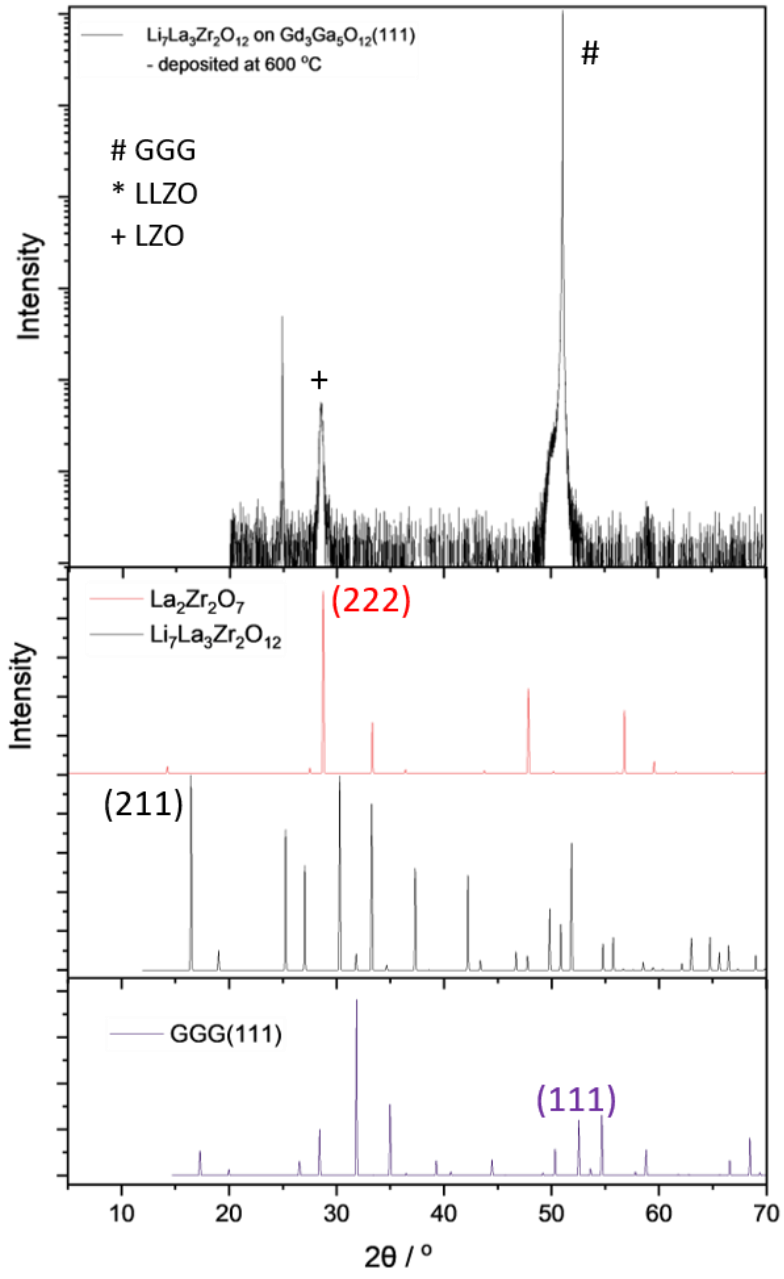

Figure 4.44: XRD of LLZO on GGG(111) showing clear presence of the c-LZO phase through the (111) peak close to 28°. This is also representative of the film's dominant growth orientation along the (111) plane. XRD acquired on Rigaku SmartLab, using Cu-Kα radiation (λ = 1.54 Å).

Initial low-magnification TEM imaging of the samples revealed an approximately 70 nm thick film is relatively flat on the surface, with no facet/island formation, relative to the $[1\bar{2}1]$ axis of the GGG substrate along which the lamella was cut. Slight contrast variations (red arrows) may be indicative of grains within the deposited film. HRSTEM presented in subsequent figures investigating the orientation and granular properties of LLZO on GGG(111).

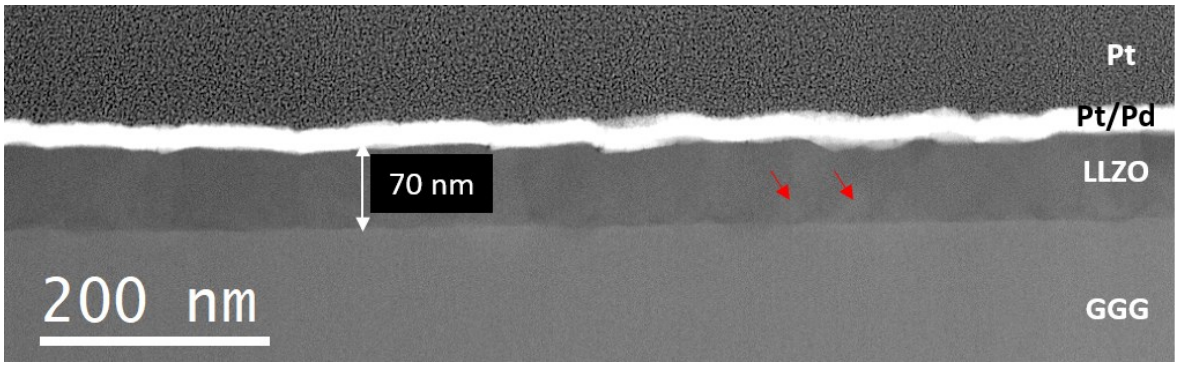

Figure 4.45: Low magnification HAADF image of LLZO on GGG(111), with a electrolyte film thickness of approximately 70 nm. The film's surface is slightly rough, slight contrast variations in the film potentially indicative on grains or orientation variation. Data acquired on JEOL ARM200CF at 200 keV.

The cross-sections of LLZO deposited onto GGG(111) shows epitaxial growth of films containing the LZO phase throughout most of the film's depth. This counteracts the data in literature where Li-rich LLZO films are obtained on GGG at substrate temperatures of 600 °C to 800 °C [131]. The deficiency is most likely occurring during PLD given the XRD is indicative of LZO prior to FIB preparation. A predominantly LZO film was imaged using HR STEM, where the LZO phase is visible along the $[1\bar{2}1]$ ZA, growing along the (111) plane (Figure 4.46). While, epitaxial growth of LZO dominates the thin film, small grains within the structure, indicative of LLZO were observed close to the interface, also growing along the (111) plane of the lattice. The HAADF, and EDS in Figure 4.47 show these grains contained La, Zr, Nb, O and Ga, whereby the additional Ga diffusion may have stabilised the LLZO phase closer to the interface [327].

If the Li loss at these deposition temperatures can be offset, a well-orientated LLZO film grown on conductive GGG substrates would provide a strong basis for creating heterostructures where analysis of the c-LLZO(111) plane is in contact with a crystalline LMO electrode.

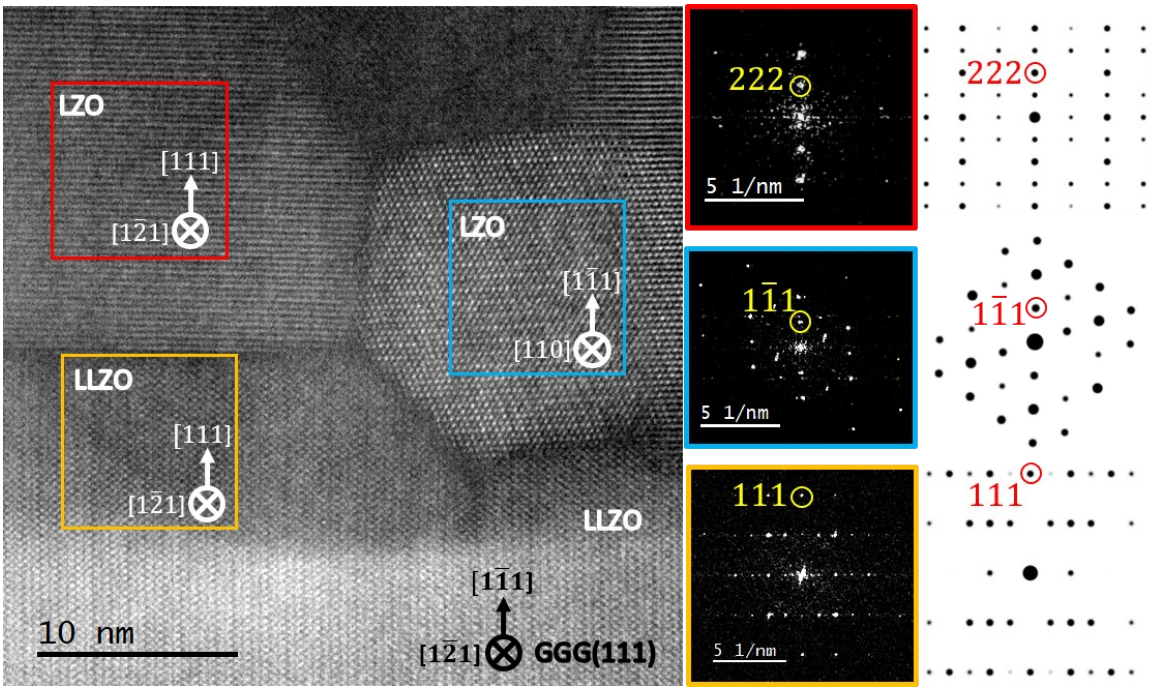

Figure 4.46: a) HAADF of grains with LLZO (yellow) and LZO (red) growing along the [111] axis, viewed along their [1$\bar{2}$1] ZA. A grain of LZO observed along the [110] ZA (blue region). The respective diffractograms from each grain and simulated DP for the respect ZA are included as reference to lattice parameters in literature databases.[44, 51] Images acquired at 200 keV with JEOL ARM200CF.

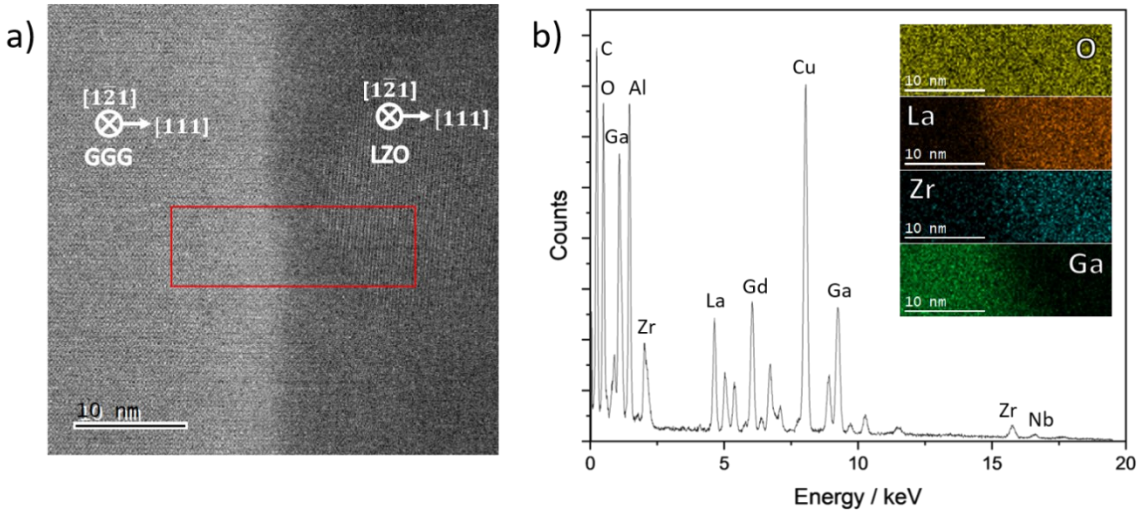

Figure 4.47: a) HAADF images of GGG/(L)LZO interface, with EDS acquired from ROI (red box) covering the transition from substrate to deposited electrolyte. b) EDS spectrum showing presence of elements anticipated in both layers of the sample. The inset chemical maps indicate a few nanometres of gallium diffusion into the LLZO or LZO. Acquired on JEOL ARM200CF at 200 keV.

Compared to literature, which shows the presence of Li in XRD [131] and some STEM images [179], the data presented in this project does not show the same trends for deposition at over 600 ^{o}C on either STO or GGG substrates. The LLZO powder synthesised in labs is Li-rich, based on XRD data, the limitation being beam sensitivity rather than preparation. Annealing of thin films is a clear limitation within this project, where the duration of annealing is likely to be a significantly damaging factor with respect to Li retention. However, this does not explain the Li-rich, epitaxially grown films achieved by Kim et al. achieving epitaxial growth on GGG at over 600 ^{o}C during PLD [131]. This is likely achieved using an excess of Li in their LLZO target used for deposition, although they do not state a value for Li excess in their experimental information. Literature providing HRSTEM images of what they claim to be LLZO, base their assignments on the spacing between planes in the images [178]. The complexity of the crystal structure and the small differences between plane spacings in LLZO and LZO leave analysis open to analytical errors regarding accurately measuring the spacing and coming to incorrect conclusions when assigning the LI-rich or deficient phase. When comparing the contrast in their STEM images to Li-deficient phases in annealed thin film samples (Figure 1.25) the similarities raise significant scepticism regarding correct assignment of LLZO in some literature. This is in addition to discrepancies between simulated HAADF images of the ZA literature claims to be viewing (e.g. along ZA [133], in ref. [178]). Ambiguity in assignment of phase made have been due to the number of ZA in LLZO and LZO, where atomic columns can be resolved as well as similar d-spacings that may be misassigned (DPs or FFT from HR images) within reasonable error due to calibration or microscope instability (e.g. noise).

4.7 Conclusions to Analysis of Crystal Structure and GB within Single Layer LCO and LLZO Films Grown on ALO, STO and GGG

This chapter has worked through the analysis of LCO and LLZO thin films deposited onto a range of substrate compositions. Temperature has been varied for LLZO films during and after deposition on the electrolyte materials allowing crystallisation temperature and orientation relationships to be explored.

Thin film deposition of LCO onto single crystal ALO and STO substrates at LT in relation to the cubic-to-rhombohedral transition results in the formation of multiple Li-rich and Li-deficient cobaltate phases. Rhombohedral LCO grows along the (001) and $(0\bar{1}2)$ planes, switching between the mirrored [100] and $[\bar{1}00]$ ZAs to create systems of twinned and misorientated GBs. The rs-CO phase also displays two possible mirror growth directions on ALO(0001), along the $(1\bar{1}\bar{1})$ and $(1\bar{1}1)$ planes, while s-CO only grew along the $[\bar{1}11]$ plane. Grains of r-LCO are dominant and contained a variety of twinned and APT GBs. The surface facets where occupied by Li-deficient rs-CO and s-CO phases, which is limiting to Li conductivity nearer to the electrode's surface. The complexity of multi-phase, nanograin LCO creates a variety of homogeneous (e.g. r-LCO to r-LCO) and inhomogeneous (e.g. r-LCO to rs-CO) GB. The dynamics of Li transition through the three-phase electrode material are therefore considerably more complex than large grains observed in particles. From the GB data collected there is considerable scope to computationally model and understand the lattice matching, strain, and Li intercalation dynamics across each combination of phase and orientation. These LCO films deposited at LT provide a good basis for creating and observing orientations at GB in a LCO/LLZO heterostructure.

LCO on STO(111) contained similar contributions of r-LCO, rs-CO and s-CO to ALO(0001), displaying the same growth orientations (r-LCO(001) and $(0\bar{1}2)$, rs-CO$(1\bar{1}1)$) for each phase, although grain size and orientation is ore variable. Regarding application to heterostructures, this remains a acceptable method of LCO deposition onto conductive STO substrate intending to create a LCO/LLZO device for in-situ STEM experiments. LCO grown on STO(100) contained a predominantly rs-CO phase, with a minor contribution from r-LCO and s-CO. The growth of rs-CO was along the (100) plane, matching the substrate orientation. The change of LCO growth axis makes these useful for alternative LCO/LLZO heterostructure, although improving the percentage contribution of the r-LCO phase is desirable. LCO on GGG(111) was also crystalline, growing close to a plane orientation of(001) in relation to the $[1\bar{2}1]$ ZA of GGG(111). Orientations of the r-LCO layers have some relationship to the lattice structure of GGG, although are significantly more variable than on ALO and STO.

Thin films deposited via PLD from a target of LLZO are amorphous on STO, below temperatures of 550 °C during deposition and after subjected to post deposition annealing. When annealed from 650 °C up to 1050 °C, porous, polycrystalline films for with significant Li deficiency, leading to a dominance of LZO. Assuming retention of Li and LLZO phase with similar polycrystalline characteristics after annealing, the numerous GB and porosity may limit lithium conductivity but provide an interesting basis for analysis of LCO-to-LLZO GBs, using HR STEM-EELS experiments. Films crystallising at substrate temperatures of 600 °C during PLD creates growth of large, crystalline grains, dominated by LZO(001) or LLZO($\bar{1}$10) orientated growth. Spacing of the diffraction spots and lattice planes is indicative of LZO rather than successful acquisition of LLZO, continuing the trend of Li deficient crystallisation at 600 °C. This contrasts, retention of LLZO at substrate temperatures over 600 °C in literature [131]. On STO(111) LZO grains adopted a slight misorientation (1.5° to 6.8°) from the [001] growth direction, with potential LLZO grains (lattice plane spacing: 0.36 nm) having a 20° misorientation with the substrate. On STO(100) the orientation of LZO and LLZO are also along the [001] axis, with a columnar structure to the grains where either amorphous or different orientation of electrolyte occupy the space between grains viewed along the [110] ZA, relative to the [110] of STO(100).

On GGG the LLZO film was similarly dominated by Li deficiency, although grains of LLZO near to the surface and the dominant LZO phase both grew along the [111] plane and were viewed along the same ZA as the GGG was cut. Small grains along the [110] ZA and some intermixing of gallium into the LLZO layer occurred near the interface, possibly driven by the 600 °C substrate temperature during deposition.

The limitation for HR (S)TEM of LLZO films within this project may therefore be the extent to which Li is lost during PLD, due to annealing, or damage during FIB preparation.[318] Conductivities for amorphous LLZO films PLD at LT will have low conductivity ($\times 10^{-7}$ S cm^{-1}) even if Li retention is good when annealing below 600 °C [156, 328-330]. The results on STO and GGG shows potential, but refinement is required to achieve single orientations of the LLZO phase rather than LZO.

Table 4.3: Summary of single layer growth of LCO and LLZO films on ALO, STO and GGG substrates. Data is inclusive of substrate temperatures during PLD, alongside annealing conditions, as well as phases and dominant growth orientations indexed by SAD and digital diffractograms from HR STEM image.

Substrate	PLD substrate temperature	Phases	Dominant Plane of Growth
		$LiCoO_2$	
ALO(0001)	No heating	r-LCO	(001) and some $(0\bar{1}2)$
		rs-CO	$(\bar{1}11)$
		s-CO	$(\bar{1}1\bar{1})$
STO(111)	No heating	r-LCO	(001) and $(0\bar{1}2)$
		rs-CO	$(\bar{1}11)$
STO(100)	No heating	r-LCO	$(0\bar{1}4)$
		rs-CO	(001)
		s-CO	(001)
GGG(111)	No heating	r-LCO	Variable growth directions
		rs-CO	Variable growth directions
		$Li_7La_3Zr_2O_{12}$	
STO(100)	250 °C	Amorphous	-
-	Furnace annealed 450 °C	Amorphous	-
-	Furnace annealed 550 °C	Partially crystalline (from XRD)	-
-	Furnace annealed 1050 °C	Polycrystalline	No dominant orientation
STO(111)	350 °C	amorphous	-
-	Furnace annealed 650 °C	Polycrystalline	No dominant orientation
-	Furnace annealed 950 °C	Polycrystalline	No dominant orientation
STO(100)	600 °C	LZO	(001)
STO(111)	600 °C	LZO	(001) (Minor contribution from other grains with undefined growth axis)
GGG(111)	600 °C	LZO and some LLZO	LZO: (111) LLZO: (111)

Chapter 5

Interfaces in Thin Film LCO/LLZO Heterostructures

Building upon the work on single layer LCO and LLZO, we deposited heterostructures with aim to study the interface between the two materials at nano and atomic scales. Using HR STEM, advancements on literature are made by focusing on the crystalline structure between LCO and LLZO with attention on the influence of Li conductivity and device degradation mechanisms. Controlled growth of LCO and LLZO on STO and GGG substrates, with interchanged order of deposition created samples were ex-situ characterised and investigated, with the evaluation of compatibility with in-situ experiments. The following chapter focuses on the growth of heterostructures, comparing pristine, annealed and voltage-cycled interfaces. Imaging and spectroscopy within TEM and STEM, resolve atomic structures in the bulk and at the EEI.

The intention is to progress the understanding of LCO/LLZO interfaces built by previous electrochemical, XPS, XRD and low magnification microscopy in literature [163, 165, 170]. Using HR STEM, EELS and EDS attempted to answer questions related to crystalline or amorphous interface layers impact on Li transfer. Assessments of the possible consequences on Li impedance and potential structural failure mechanisms are considered within the data discussed. Heterostructure sample preparation was informed by LCO and LLZO growth in Chapter 4, whereby LCO deposited at LT provides reasonable Li retention and controlled, directional growth of r-LCO, rs-CO and s-CO. LLZO as a primary layer on GGG or secondary layer on LCO required two post-deposition approaches to heterostructures. Crystalline electrolyte growth was possible on GGG, while the requirement to anneal LLZO deposited below 600 °C onto LCO are covered with respect to heterostructure samples on STO(111) and (100) (Table 2.3). Covering the STO samples with a pellet of LLZO during annealing also aimed to offset Li evaporation from the LLZO surface layer. The process of annealing heterostructures at 600 °C, enables the bulk of LCO to be analysed after this heat treatment, with comparisons made to the single layers containing three-phases in Chapter 4, alongside depositions at higher temperature in literature [124, 130]. With respect to the interfacial regions, STEM and EELS were used to analyse thermally and ex-situ biasing induced structure and compositional features at the interface, providing insight into how these may influence performance of a device.

5.1 Structure and Chemical Analysis of STO(111)/$LiCoO_2$/$Li_7La_3Zr_2O_{12}$ Heterostructure

Heterostructures grown on STO(111) include the growth of LCO as the first layer. This aims to replicate the multi-phase thin films in Chapter 4 with oriented growth along the r-LCO[001] and [111] of rs-CO and s-CO, creating a polycrystalline base for LLZO deposition. The combination of the three phases may allow analysis of alignments between crystalline electrolyte-electrolyte GB at ARs. To avoid Li evaporation from the LCO layer if depositing LLZO at substrate temperatures of 600 °C, the electrolyte is deposited as an amorphous layer without heating the STO(111)/LCO sample during PLD.

To observe the structural characteristics in the heterostructure prior to annealing, XRD aims to understand to what extent crystalline phases of LCO and LLZO were present. Figure 5.1 shows that there is crystalline LCO in the heterostructure, with the peak at 19° indicative of r-LCO(001), while the broad signal at 38° to 40° could contain contributions from r-LCO, rs-CO or s-CO. It is possible this broad signal also contains c-LLZO(211), however, the lack of other distinct electrolyte peaks and data in Chapter 4 for LT LLZO deposition, supports the presence of an amorphous electrolyte layer in the pristine heterostructure. The limited conductivity ($\times 10^{-7}$ S cm^{-1}) and absence of lattice planes for analysis of crystalline GB at the heterostructure interface is a clear drawback of amorphous LLZO. Hence, annealing at 600 °C (4 hours) attempts to induce crystallinity in the electrolyte layer and observe the impacts this has on the atomic scale using HR (S)TEM and EELS.

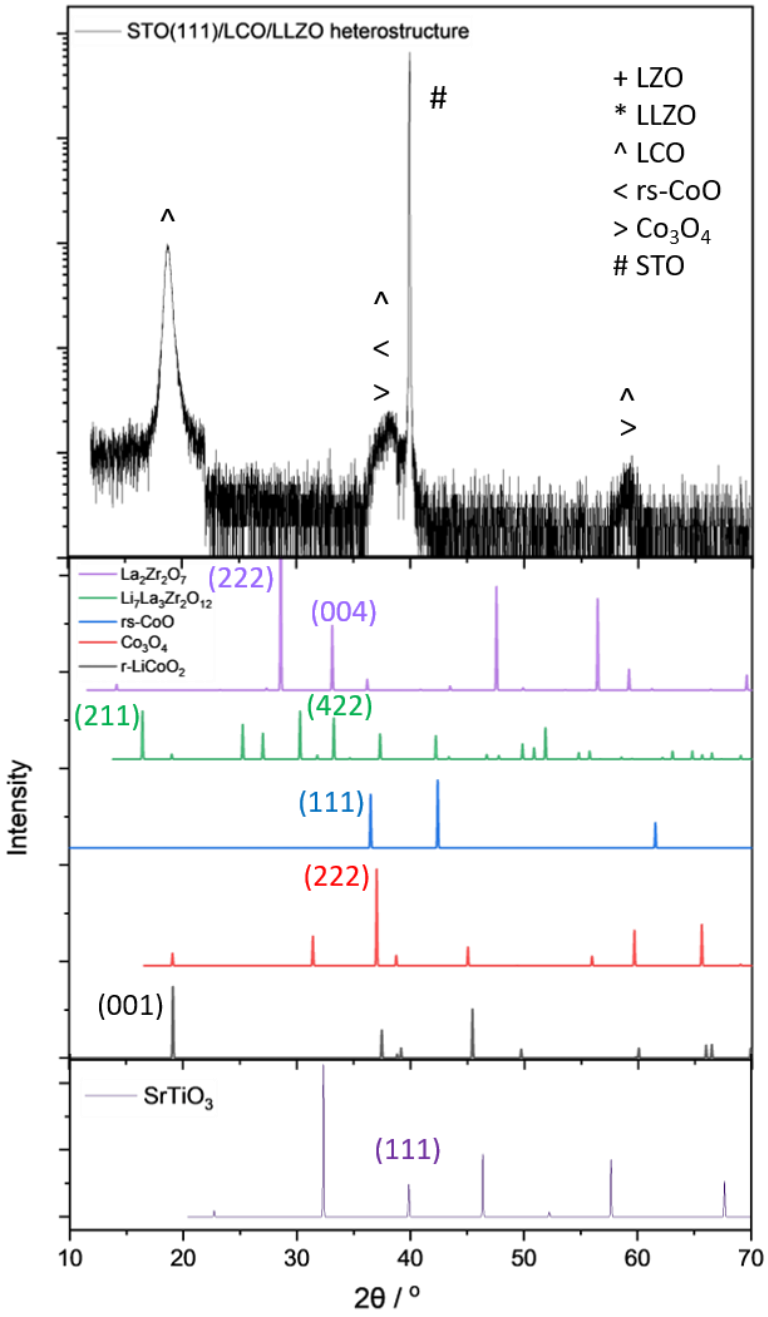

Figure 5.1: XRD of pristine STO(100)/LCO/LLZO heterostructure, with simulated XRD of Li rich and deficient phases of both materials between 10° and 70°. Signals relating to crystalline LCO are present, however unless contributing to the LCO signals, crystalline LLZO appears to be absent. Acquired on Rigaku SmartLab rotating anode θ/2θ or 2θ-w diffractometer, using Cu-Kα radiation.

Figure 5.2 shows the surface of the LLZO layer grown on LCO, after annealing at 600 °C for 4 hours. Based on LLZO films deposited onto STO and crystallised above 600 °C in the furnace, the annealing of the heterostructure aims to form polycrystalline nanograins of LLZO in contact with the LCO layer. The surface has adopted a porous structure of electrolyte particles with nanoscale

dimensions, similar to the polycrystalline films annealed at 950 °C and 1050 °C. Subsequent inspection of crystallinity within the bulk of the electrode and electrolyte, as well as across the LCO/LLZO interface is approached with HR (S)TEM analysis (Figure 5.3 to Figure 5.9). The orientations and chemistry influencing routes Li transfer between the two materials are investigated in atomic detail, to further the XRD and nanoscale studies within literature studies. Li evaporation is expected during annealing, although the Li content in the LCO layer could offset deficiencies near the interface, retaining a region where crystalline LCO and LLZO for interfaces.

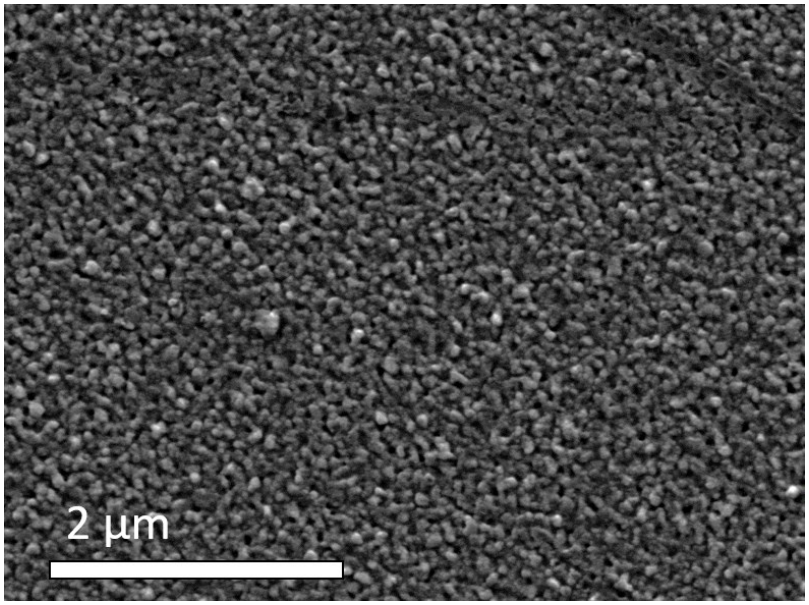

Figure 5.2: SEM SE image of STO(111)/LCO/LLZO heterostructure surface showing a porous structure of particles or crystallites with dimensions on the nanoscale. Image acquired in JEOL 7800F Prime at 5 keV (due to sample drift at high voltages).

The low magnification BSE images of heterostructure lamella show the depth of deposited films, alongside structural and chemical distributions mapped by EDS. Figure 5.3, a) shows an LCO thickness of 60 nm and LLZO thickness of 150 nm for the heterostructure on STO(111) with uniform electrolyte deposition. The HR BSE images and EDS (Figure 5.3, b) identifies the LLZO layer in the form of columns containing La and Zr, rather than the contrast distribution expected for polycrystalline nanograins forming during annealing (Figure 4.30). The formation of a porous electrolyte is likely to have exposed the voids to redeposition of sputtered material during ion milling. Rather than creating a polycrystalline film, during annealing at 600 °C a different process has occurred to form the column structure where nanograins are not observed to be present. The porosity likely limits the efficiency of Li transfer between electrodes, assuming the columns of La, Zr and O contain grains of crystalline LLZO.

A four-hour annealing at 600 °C may have been too gradual to crystallise amorphous LLZO effectively. The polycrystallinity seen in LLZO films crystallising at 950 °C in Chapter 4 may therefore have relied on more rapid crystallisation of the electrolyte, prior to Li evaporation. The different characteristics of the annealed electrolyte are thought to be the result of a different crystallisation rate, where rate of crystallisation alongside lithium evaporation forms a more porous structure. The columnar formations match with LLZO deposited on STO(100) at a substrate temperature of 600 °C during PLD as well as studies at 700 °C by Garbayo et al [143]. HR STEM attempts to understand the characteristics of the LCO and interface regions alongside any crystal structure within this porous LLZO.

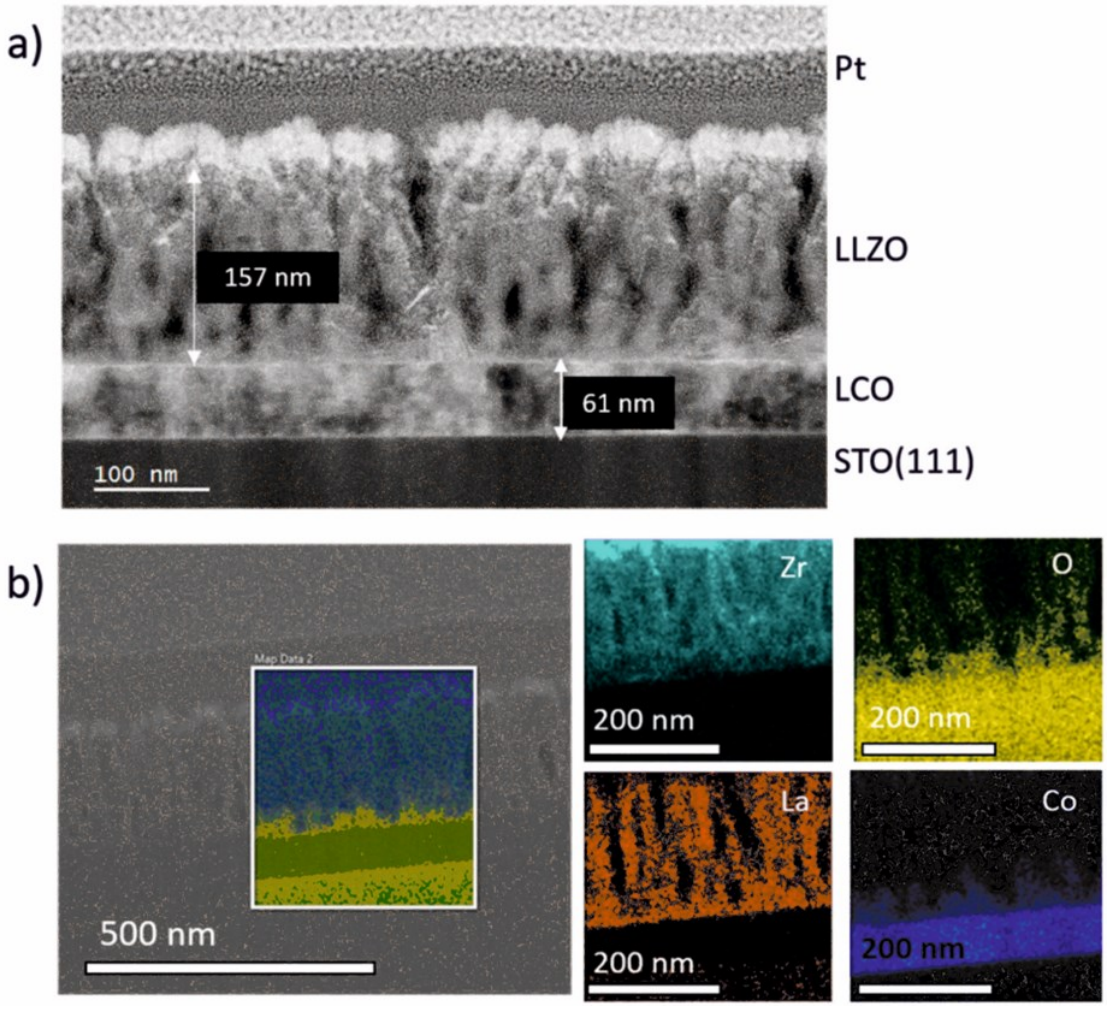

Figure 5.3: a) Low magnification images of the Nb-doped STO(111)/LCO/LLZO. The cross-section contains platinum from FIB processing throughout the electrolyte layer, creating the contrast variations. b) EDS maps from selected region of heterostructure, showing Zr, O, La and Co maps, where diffusion of Co into the LLZO layer is observable in the Co map. Images taken at 200 keV using JEOL ARM200F at ePSIC.

In the EDS data (Figure 5.3, b) the bulk of LLZO and LCO are distinguishable from the interface region where Co diffuses non-uniformly into the electrolyte, up to distances of approximately 100 nm. La diffusion into the LCO layer does not match the distance of Co diffusion into the electrolyte. The change to composition on this scale, through the formation of thick interface comprised of La, Co, O and Zr, creates a significant Li conductivity disadvantage through annealing LCO and LLZO when in contact. The intermixing is thought to be the precursor to the formation of $LaCoO_3$ grains in the samples sintered at 900 °C analysed in Chapter 3, although occurring on the nanoscale in these thin film heterostructures. As with the formation of $LaCoO_3$ in particle systems, the development of amorphous and/or crystalline SEI through thermal decomposition, is detrimental to device performance, due to the lower conductivity of these secondary phases [304]. With $LaCoO_3$, Li_2CO_3 and LZO detected by XRD and XPS in literature [170], the sample in Figure 5.3 is analysed using STEM-EELS to evaluate the composition and atomic structure within the SEI formed at 600 °C.

It is also important to determine why the electrolyte layer crystallises differently at 600 °C compared to 950 °C. In-situ heating experiments would be most informative for understanding the changes at 600 °C, as well as higher temperatures (e.g. 950 °C). Data collection would focus on nucleation points, crystallisation rates and transition between LLZO and LZO as Li evaporates. This would further the work present on ex-situ annealing studies into crystallisation of electrode or electrolyte and consequent decompositions presented within this project and relevant literature [110, 163, 294]. For electrolytes forming a porous network, mapping the LLZO film using slice-by-slice FIB, combined with EDS and EBSD, can construct a 3D model of the heterostructure. This could give insight into the density and composition of LLZO networks shown in Figure 5.3, and to what extent capacity and Li transfer rates are impacted on the wider scale.

HR STEM focused on the bulk of the LCO, acquiring images of atomic structure and the orientation of the electrode phases present, this is summarised by Figure 5.4. The bulk of the LCO layer is dominated by the r-LCO phase, orientated along the (001) plane, with no detection of rs-CO or s-CO in the LCO layer of heterostructures on STO(111) after annealing for 4 hours. These HAADF images (Figure 5.4 a, b and c) for the LCO layer after annealing at 600 °C all suggest phase transitions have occurred during heating, from the substrate to the LCO/LLZO interface. Li deficient grains in the single layer could be transforming into the r-LCO phase through Li diffusion from the LLZO layer, or the temperature of annealing is forcing r-LCO formation despite partial Li deficiency.

Compared to multi-phase single layer depositions at LT, the enhanced presence of the r-LCO phase is beneficial for conductivity between the CoO_2 layer compared to the structure of rs-CO and s-CO. Twinned phases between the $(0\bar{1}4)$ planes (Figure 4.6) are not observed, appear to be lost during annealing. APT GB were still present within the r-LCO(001) orientated electrode (Figure 5.4, b), creating barrier to Li at the resultant boundaries between the (010) planes where CoO_2 block efficient transfer of Li into the twinned grain. Starting with a single crystal r-LCO electrode for in-situ biasing experiments would allow analysis of strain development during the growth of rs-CO and s-CO grains during Li deintercalation. Literature has provided some insight into this with experiments observing transitions from r-LCO to c-LCO or rs-CO [22, 80]. However observing the changes with respect to characteristics such as nanograin formation in LCO/LLZO heterostructures would provide direct observation of grain growth, GB formation and structural failure mechanisms.

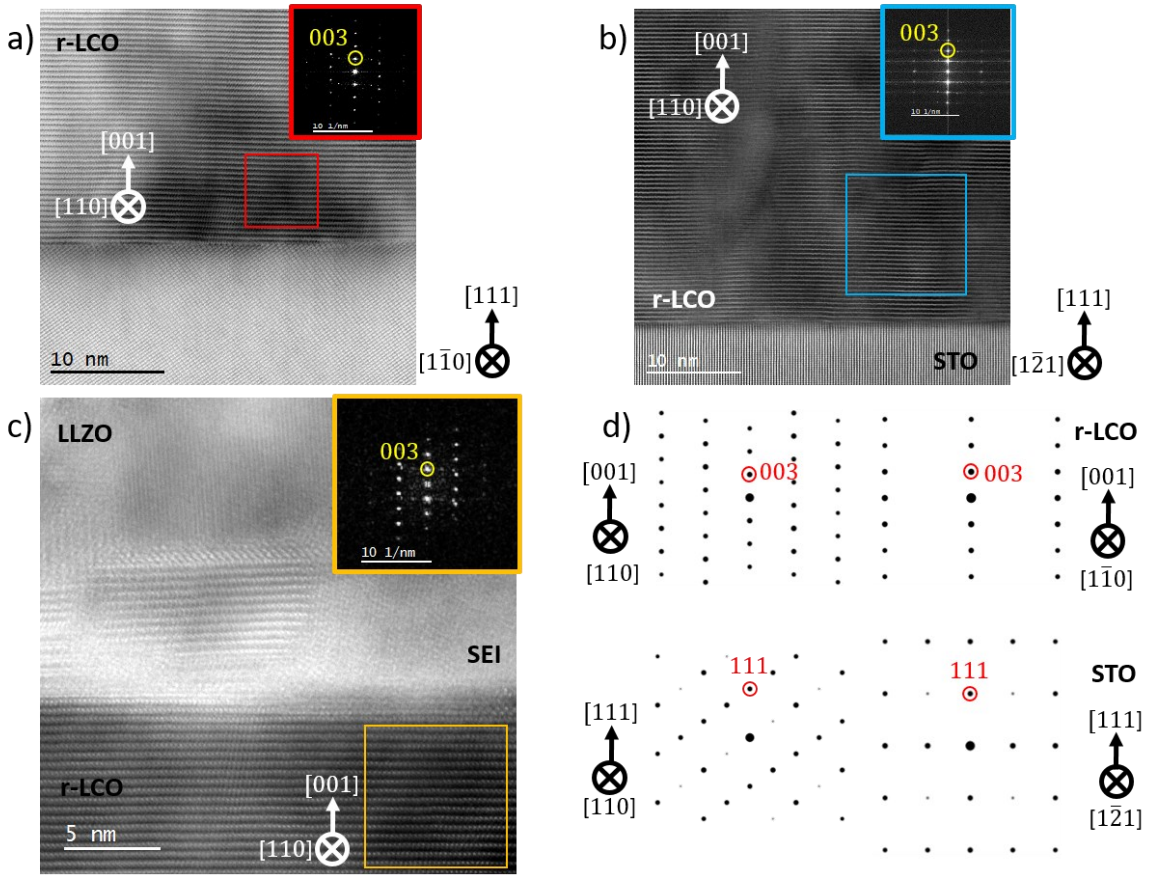

Figure 5.4: HAADF images of LCO structure from the surface of STO(111), to the LCO/LLZO interface. a) Epitaxial r-LCO(001) layer after heating to 600 °C for 4 hours. Lamella cut along the $[10\bar{1}]$ ZA of STO shows this ZA align with the $[100]$ ZA (or equivalent) of r-LCO b) Lamella cut along the STO $[1\bar{2}1]$ ZA showing same epitaxial r-LCO(001) lattice orientation by viewed along the $[1\bar{1}0]$ ZA of r-LCO. c) The r-LCO phase is present up to the surface of the electrode/electrode interface. Amorphous material, intermixed with crystalline structures, are observed within 20 nm the interface. d) Diffraction patter simulation relating to the observed ZA for LCO (top) and STO (bottom). Images taken at 200 keV on JEOL ARM200.

Also shown in Figure 5.4 is an interface region of r-LCO in contact with the brighter contrast of the LLZO layer in the HAADF image. The phase of the electrode is r-LCO up to the sharp change in contrast at the interface with the electrolyte (Figure 5.5), with a mixture of amorphous and crystalline regions seen within the intermixed (Co, La and O) region. This posed questions with respect to the exact composition of the intermixed region and if the atomic structure of any crystalline grains could be resolved, as achieved for $LaCoO_3$ in particle samples. STEM, EELS and diffractogram information, targeting the amorphous and crystalline regions at the interface, is used to determine the composition and phases of crystallites (Figure 5.4, c and Figure 5.5) and amorphous regions near the interface.

The dominant structure along the interface consists of amorphous material occupying the first 5 to 10 nm from the LCO surface into the LLZO. This is seen as a bright, uniform band in HAADF images and matches the thickness expected for SEI in literature [162, 303, 331]. After the first 5nm to 10 nm of amorphous SEI, a change in contrast or the presence of crystallinity extends. Although a minority of the cross-section, compared to amorphous intermixed regions, these crystalline regions near the interface, examples of which are shown in Figure 5.5, are consistency present. They can therefore be considered an important contributor to Li dynamics within the interfacial region. These crystallites contained consistent spacing between the lattice planes, alongside atomic columns near enough to the selected ZA of the STO to be individually resolved. This structure was identified as the r-LCO phase owing to both the atom symmetry and diffractograms taken from the crystallites (Appendix I). Their orientation is different to the r-LCO(001) electrode layer and dimensions of each crystallite vary in length and width along the r-LCO[010] and r-LCO[001] directions. The number of lattice planes along the r-LCO(001) axis creates crystallites consistently shorter in this direction compared to the length of crystallites along the r-LCO(010). Spectroscopic analysis of the crystallites determines their composition and further support the conclusions that the composition of crystallites in Figure 5.5 is LCO, likely forming at 600 °C as Co diffuses into the electrolyte layer. While the surrounding region contains La, Co and O, the presence of LCO crystals suggests 600 °C is sufficient for segregation of LCO from the large region of intermixed lanthanum, cobalt, and oxygen.

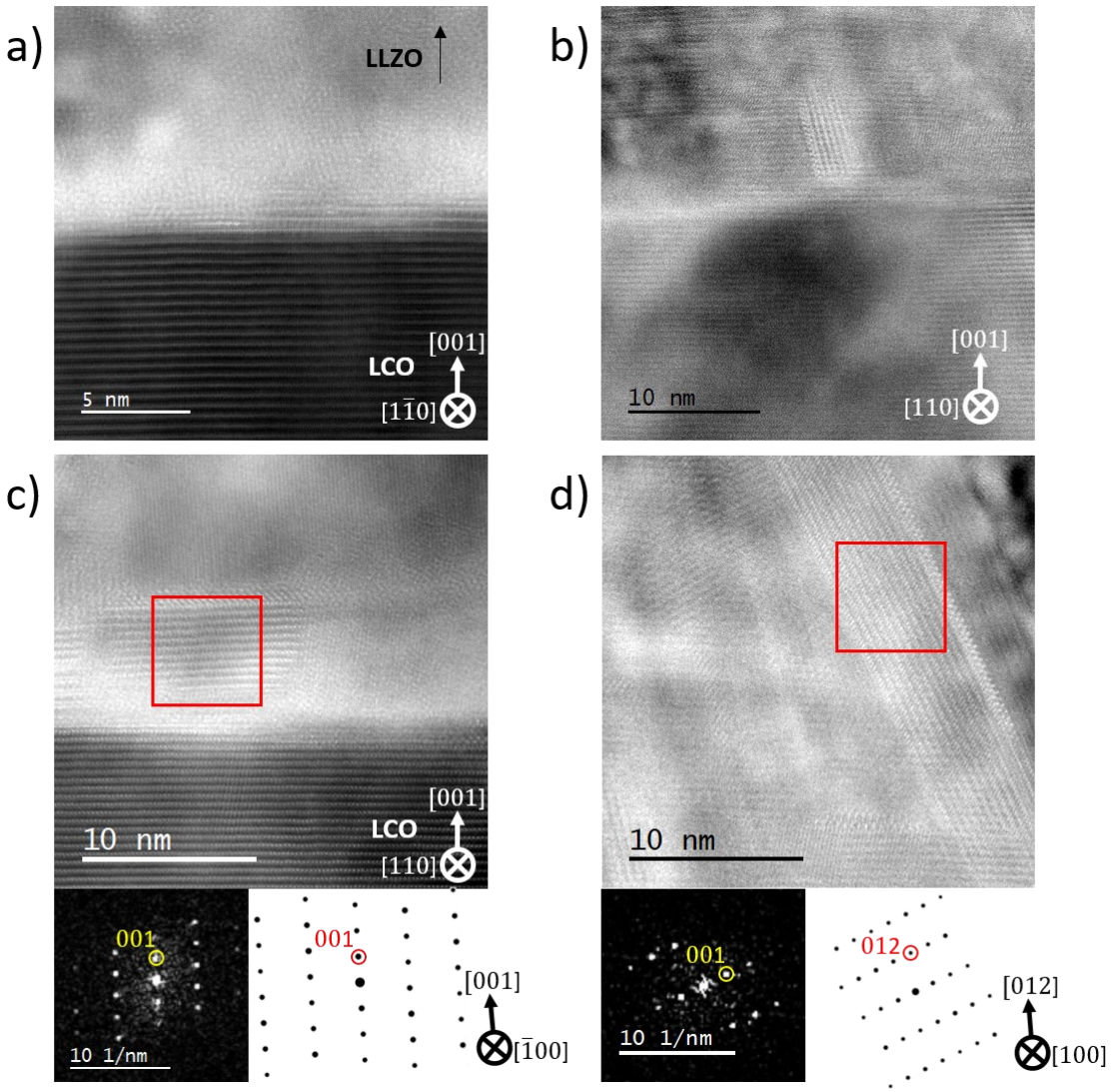

Figure 5.5: HAADF images of amorphous and crystalline regions along the LCO/LLZO interface. a) Amorphous interface layer at the surface of the r-LCO(001) layer. b) Varying orientations of crystalline regions near the surface of r-LCO. c) Higher magnification of crystallite, with the diffractogram acquired from highlighted region (red box), relating to the r-LCO phase viewed along the [$\bar{1}$00] ZA. The growth direction is close to the [001] axis of r-LCO. d) A crystallite where the structure of r-LCO is resolved along the [100] ZA, growing along the (012) lattice plane. Crystallites are anisotropic, with dimensions significantly shorter along the (001) growth plane (CoO_2 layers) of r-LCO. Images taken at 200 keV using JEOL ARM200F at ePSIC.

Figure 5.6 shows the STEM-EELS data acquired from different regions across the LCO/LLZO interface. The data highlights the Co content in a crystallite emerging from the amorphous SEI layer of greater La content than both the crystallite and LCO layer. Alongside the diffractograms (Figure 5.5), the strong Co signal within the crystallite, further supports this interface structure being LCO, although with seemingly no correlation to the bulk [001] orientation of the r-LCO electrode layer. The residual La signal in line scans is likely to be material above or below these crystallites along the observation axis. This has made analysis more complex, especially when understanding crystallite composition and the profile of O K-edges.

The brighter amorphous layer seen in Figure 5.6, at the surface of the LCO, was consistently present and uniform across most of the interface, always preceding further Co diffusion into the electrolyte. The at% across the interface indicate a ratio between La and Co of approximately 1:1, while at% of O is higher than anticipated for the stoichiometry of $LaCoO_3$. Without accurate quantification of Zr or Li content, the precise composition of this amorphous SEI was not certain. Detection of the core-loss Zr signal was not achieved with dwell time limitations relating to sample drift, damage, and contamination rates. Therefore, the zirconium content is unknown in this 5 nm layer and EDS analysis did not provide sufficient resolution to conclusively say Zr is absent. However, Figure 5.3 and Figure 5.12 do lower contrasts in element maps of Zr when transitioning from the bulk of the LLZO layer into the SEI. If annealing thin films replicates the characteristics of $LaCoO_3$ formation at LCO/LLZO interfaces in Chapter 3, it would be expected that upon the formation of a lanthanum-cobalt-oxide layer, Zr does not participate in the composition of these regions.

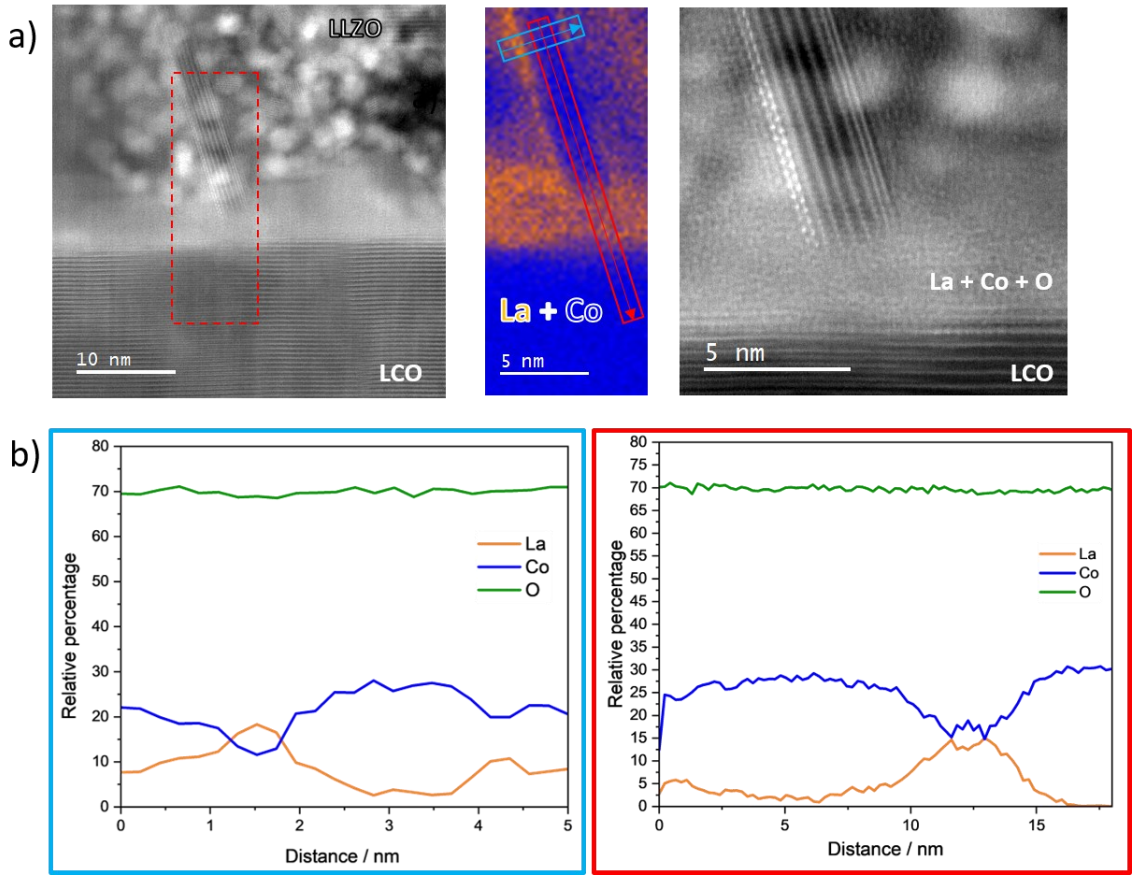

Figure 5.6: Element intensity maps formed from EELS spectra across a small region of the interface containing a crystallite. Co diffusion clearly occurs more than 10 nm into the electrolyte layer, whereas La diffusion into the electrode is approximately 2 nm. Acquired in JEOL ARM200CF at 200 keV.

The O K-edge is sensitive to changes in bonding environment within the sample, allowing assessment and identification of specific attributes (e.g. bonding) and compositions across the complex heterostructures [176, 177]. EELS were acquired at a several regions along the interface containing epitaxial LCO, interface crystallites of unknown composition and within the LLZO layer. EELS and EDS acquired within the bulk of the electrolyte layer contained the anticipated La, Zr, O peaks, with the addition of a platinum signal in EDS spectra. The acquisition of EELS data within the bulk of the LCO and LLZO or LZO layers provides measurable shifts between the main O K-edges expected throughout the transition between electrode and electrolyte are clear, Figure 5.7. The oxygen EELS system shows clear transitions between electrode and electrolyte layers are shown to be variable with a region of extensive lanthanum and Co intermixing. Figure 5.7 shows the O K-edges taken from the LCO and LLZO layers within the electrode-electrolyte systems as well as the interface region and crystalline $LaCoO_3$, as shown in Figure 3.23 in Chapter 3.

Supporting HAADF data and chemical maps, the O K-edges helped inform assignment of potential phases within the heterostructure device. The overlap between amorphous and crystalline materials with different compositions was a challenge where K-edge profiles relating to LCO and LLZO could help distinguish two phases overlapping along the viewing axis. There was a clear change through the interface region between the two materials, were the signal relating to LCO at 528 eV and 540 eV reduces in intensity during the appearance of the LLZO or LZO related signal at 532 eV. The interfacial region is distinct in the HAADF and BF images, with a O K-edge profile indicative of LCO and LLZO of varying intensities. The profile of $LaCoO_3$, acquired from interfacial decomposition in Chapter 3, were not clearly observed in core-loss spectra. While the amorphous interface layers (Figure 5.5) may have composition of $LaCoO_3$, this was not certain from EELS data. Improvements to assignment of these amorphous layers closest to the interface would require thinner samples and reducing energy dispersion in the STEM-EELS acquisition such that the important core-loss edges within LCO, LLZO or lanthanum cobalt oxide could be resolved [176, 177].

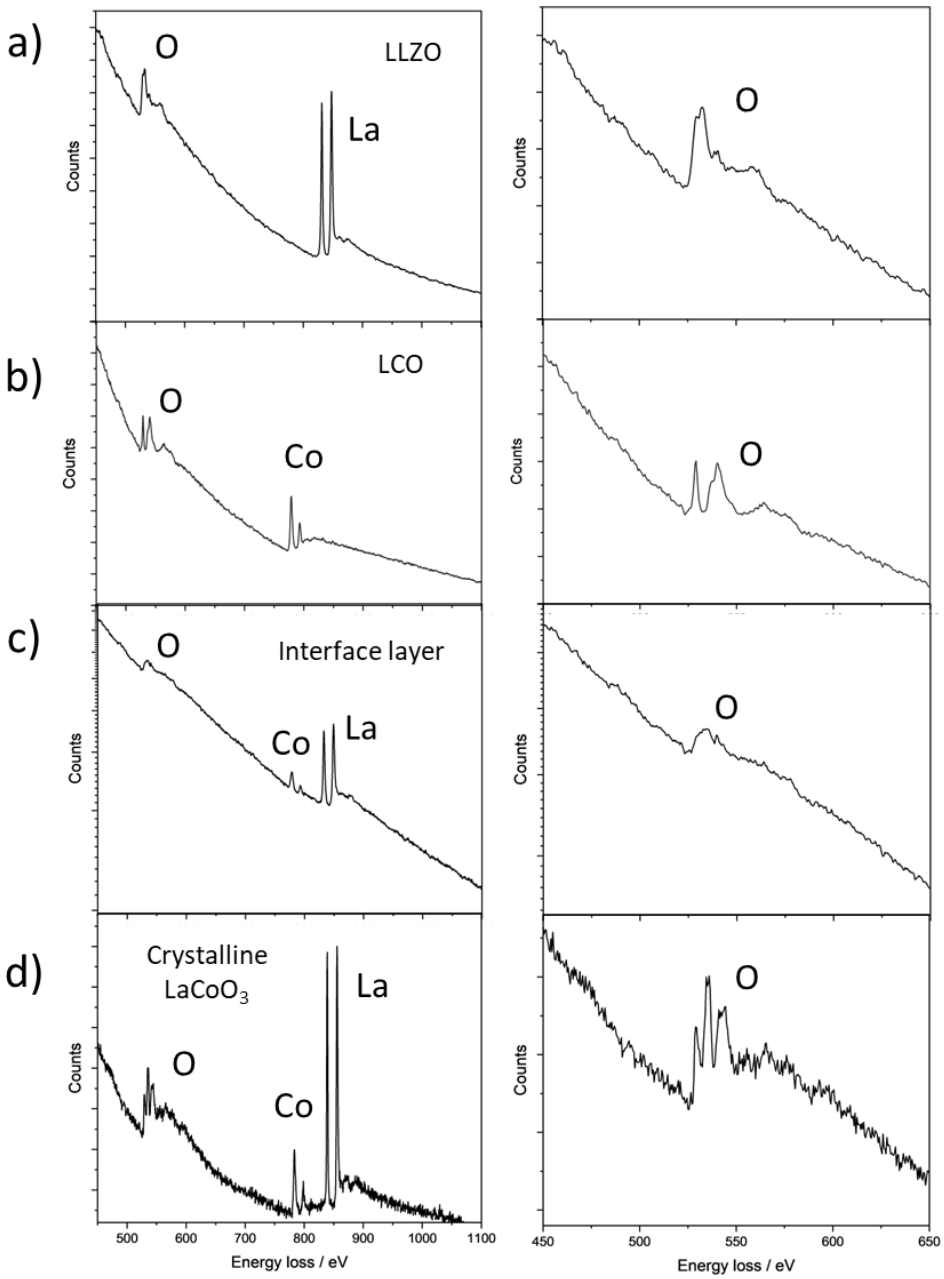

Figure 5.7: Left) core-loss spectra and right) O K-edges relating to a) LLZO, b) LCO, c) the interface layer from heterostructures (Chapter 5), and d) crystalline $LaCoO_3$ from sintered particle samples (Chapter 3). Data acquired in JEOL ARM200CF, at 200 keV.

Application of O K-edge structure to the bulk and interfacial regions helped with the determination of composition of the crystallites (Figure 5.8). The profile within the crystallite has strong peaks relating to the bulk of the LCO electrode and is clearly distinguishable from the LLZO and broad SEI layer (Figure 5.7). The Co:La signal ratio significantly differs between the interface and crystallite regions and while La remains in the EELS spectrum the combined information from HAADF, EELS chemical maps and diffractogram pattern spacing strongly supports the crystallites being LCO, adopting the rhombohedral phase.

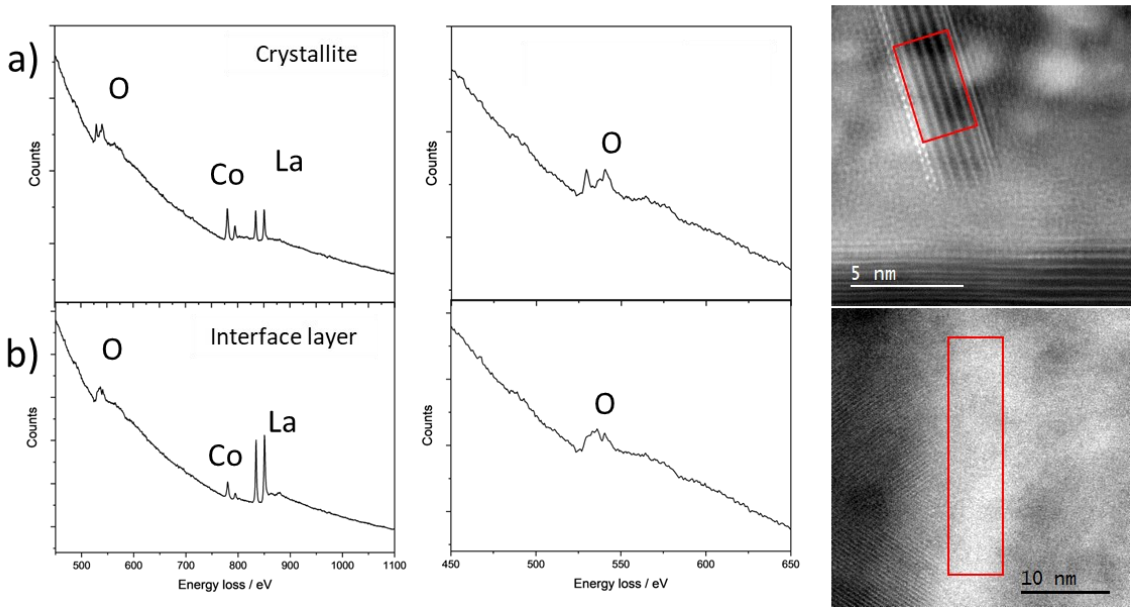

Figure 5.8: Core-loss (left) and O K-edge (right) profiles taken from within; a) an interfacial crystallite, b) the interface layer. The regions from which the EELS spectra were acquired are shown in the HAADF images by red boxes. Acquired in JEOL ARM200CF at 200 keV.

These crystallites have the potential to provide Li pathways through the nanometres of elementally complex SEI, the variance in dimension and orientation LCO dendrites, may create strain within a crystalline LLZO layer, potentially leading to structural failures during charge cycles. The influence of reducing annealing time on the intermixing and formation of such crystallites is important to understand the thresholds of intermixing distance and crystallite formation and possibly the influence they have on structural stability within the electrolyte. Annealing at 900 °C for 4 hours led to evaporation of Li down to the base LCO-substrate interface. In Figure 5.9 we can see the [110] ZA of the spinel phase in contact with the STO, with an epitaxial orientation growing along the $(1\bar{1}1)$ plane of Co_3O_4. The full phase transition from r-LCO to s-CO suggests that at least some Li content in cubic phases observed within LCO thin films in Chapter 4. Accounting for the limitations of applying temperature to Li-rich heterostructures, annealing conditions were subsequently kept at 600 °C for no more than 30 minutes of annealing to try and limit both Li evaporation and interfacial mixing for the heterostructure on STO(100).

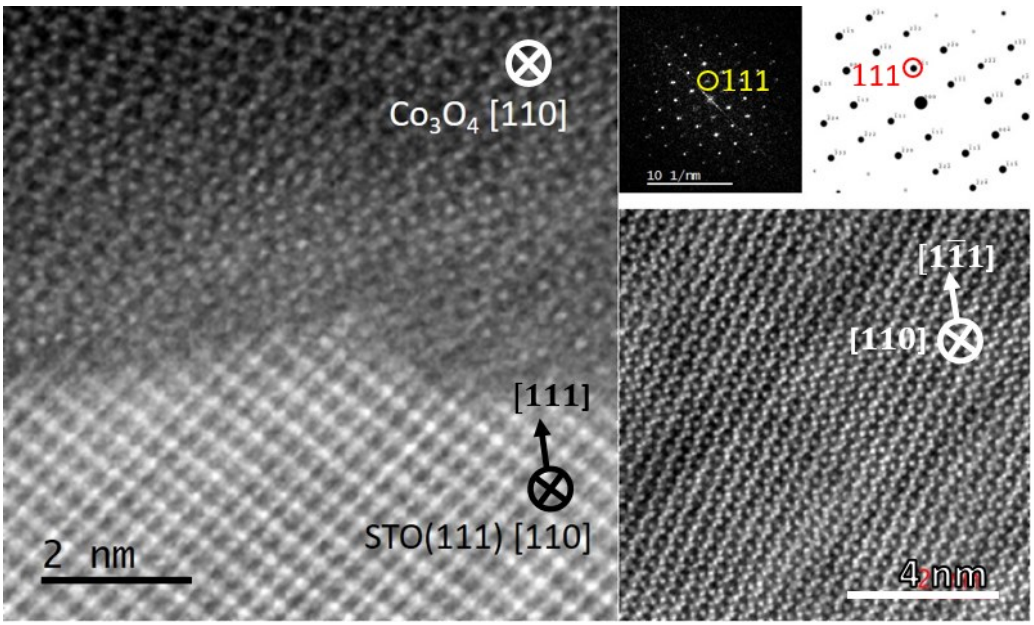

Figure 5.9: HAADF images of s-CO layer on STO(111) substrate after annealing the heterostructure to 900 °C for 4 hours. The s-CO Li phase dominates throughout the electrode layer, suggesting the presence of s-CO reflect near complete Li deficiency in these grains. s-CO is observed along the [110] ZA with a $(1\bar{1}1)$ growth , as illustrated by the diffractogram and supporting simulation. Data acquired at SuperSTEM by Khalil El Hajraoui.

5.2 Structure and Chemical Analysis of STO(100)/$LiCoO_2$/$Li_7La_3Zr_2O_{12}$ Heterostructure

The process of depositing STO(100)/LCO/LLZO heterostructures was pursued with achieving a similarly the well-orientated LCO layer to the observations on the STO(111) heterostructure. The aim was to achieve films with the anticipated $(0\bar{1}4)$ growth of the r-LCO phase when deposited onto STO(100), creating a preferable orientation of Li channels towards the LLZO.[174] The same LT PLD conditions were used for LCO on STO(100) and LLZO onto LCO, although given the porosity and damage to the LLZO layer in heterostructures on STO(111) the STO(100) heterostructure was only annealed for 30 mins at 600 °C. Differences in LLZO crystallinity, extent of Co diffusion and crystallite formation are compared as a function of annealing time.

The XRD in Figure 5.10 contains strong support for a film with r-LCO and s-CO phases growing along their respective $(0\bar{1}4)$ and (001) crystal planes (signal between 42° to 47°). No peak at 19° shows LCO growth along the (001) plane is less prevalent than in the STO(111) heterostructure sample. The absence of LLZO or LZO peaks indicates amorphous electrolyte growth at low substrate temperatures during PLD.

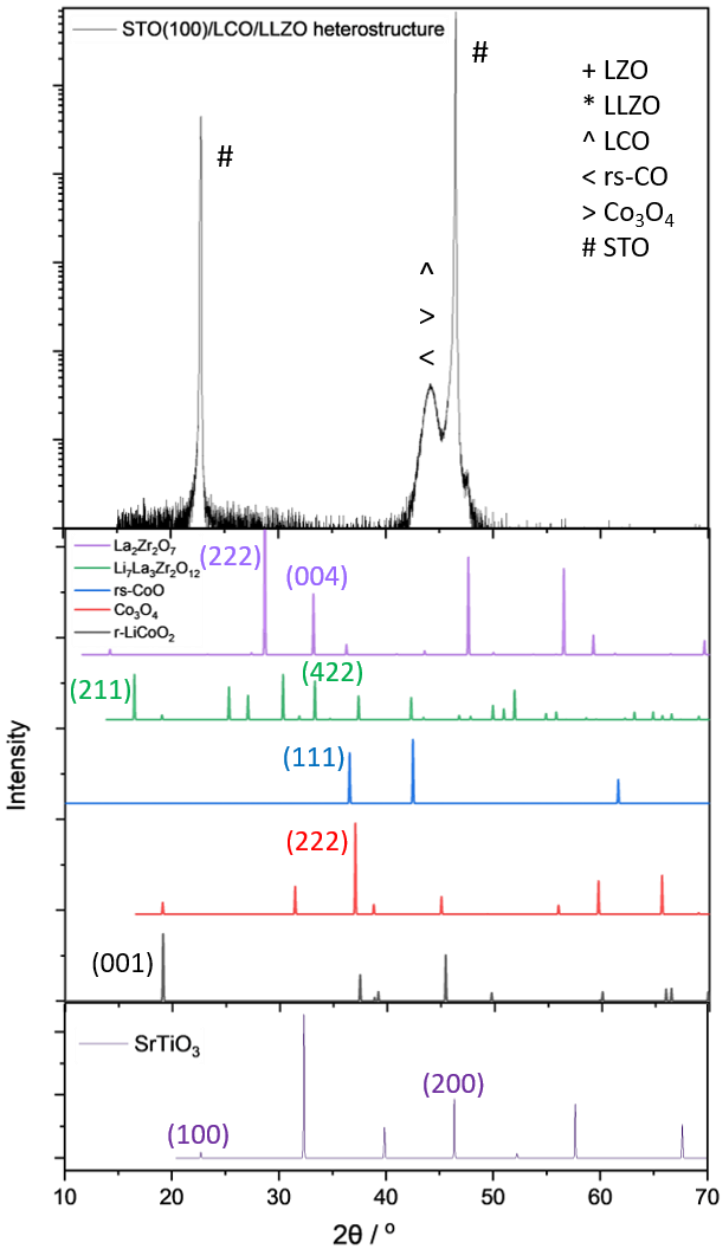

Figure 5.10: a) XRD of as deposited film showing LCO or CO signal at 42° to 47°, alongside STO(100) signals. Supporting XRD simulations are included below the data from the as-deposited STO(100)/LCO/LLZO heterostructure. Acquired on Rigaku SmartLab rotating anode θ/2θ or 2θ-w diffractometer, using Cu-Kα radiation.

SEM images of the heterostructure surface show the same rough, slightly fractured structure observed for amorphous depositions of LLZO on STO in Chapter 4. The EDS confirmed the presence of each element within the heterostructure, although at% of Zr is uncertain due to overlapping Lα x-ray (2.042 keV) and with the M-edge of Pt (2.048 keV) in the Pt/Pd conductive layer required to offset sample charging and drift for SEM and FIB. This correlates with the lack of LLZO or LZO signals in the XRD spectrum before and after annealing, therefore 30 minutes appeared unsuitable for extensive crystallisation of the electrolyte layer although the extent of Co diffusion and interface changes would be assessed by (S)TEM of cross-sections.

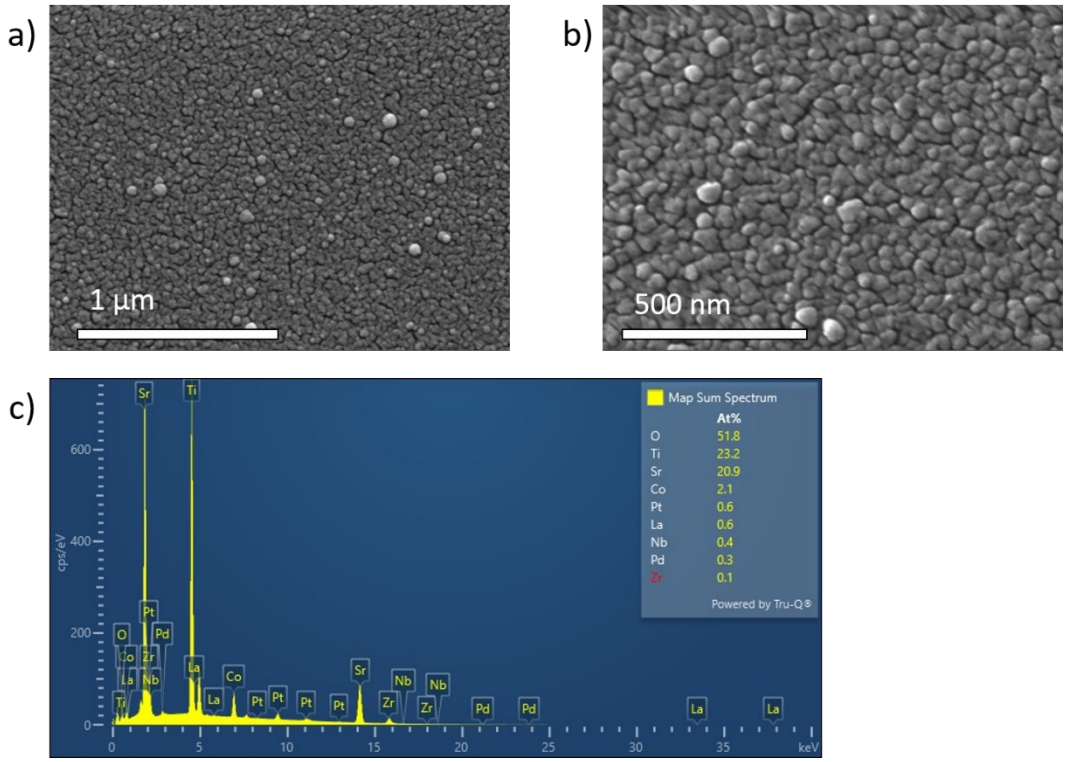

Figure 5.11: a, b) SE SEM images of LLZO surface in the STO(100)/LCO/LLZO heterostructure. B) EDS spectrum acquired from sample, showing element from film and substrate. Acquired in JEOL 7800F Prime using 15 keV for managing and 25 keV (10 µm aperture) for EDS.

Similarly to the STO(111) heterostructure, irregular diffusion of Co into LLZO was shown by the low-magnification EDS of the cross-section (Figure 5.12). Given single layer deposition of LCO onto STO(100) had a flat surface, diffusion rather than overlap of a faceted LCO structure was concluded as the route of intermixing during annealing. The smooth, amorphous layer of LLZO in the STO(100)/LCO/LLZO heterostructure clearly differs from the electrolyte layer after annealing at 600 °C (4 hours). The LLZO was only 60 nm in depth and returned EDS showing a dense electrolyte layer, rather than the porous columns of La and Zr seen in Figure 5.3.

EDS spectra closer to the interface, illustrated a transition from Co and O within the electrode, to a mix of La, Co and O in the crystallites near the interface. The line scans are indicative of around 30 nm of Co diffusion to form a slightly thinner intermixed layer than after 4 hours of annealing. Another distinct region of contrast 5 to 10 nm thick between the two layers, prior to further Co diffusion further into the LLZO. Higher magnification STEM and EELS was used to assess this thin SEI with brighter HAADF contrast. The La signal again decreases more sharply into the LCO layer, supporting Co dominating the diffusion of metal ions during annealing.

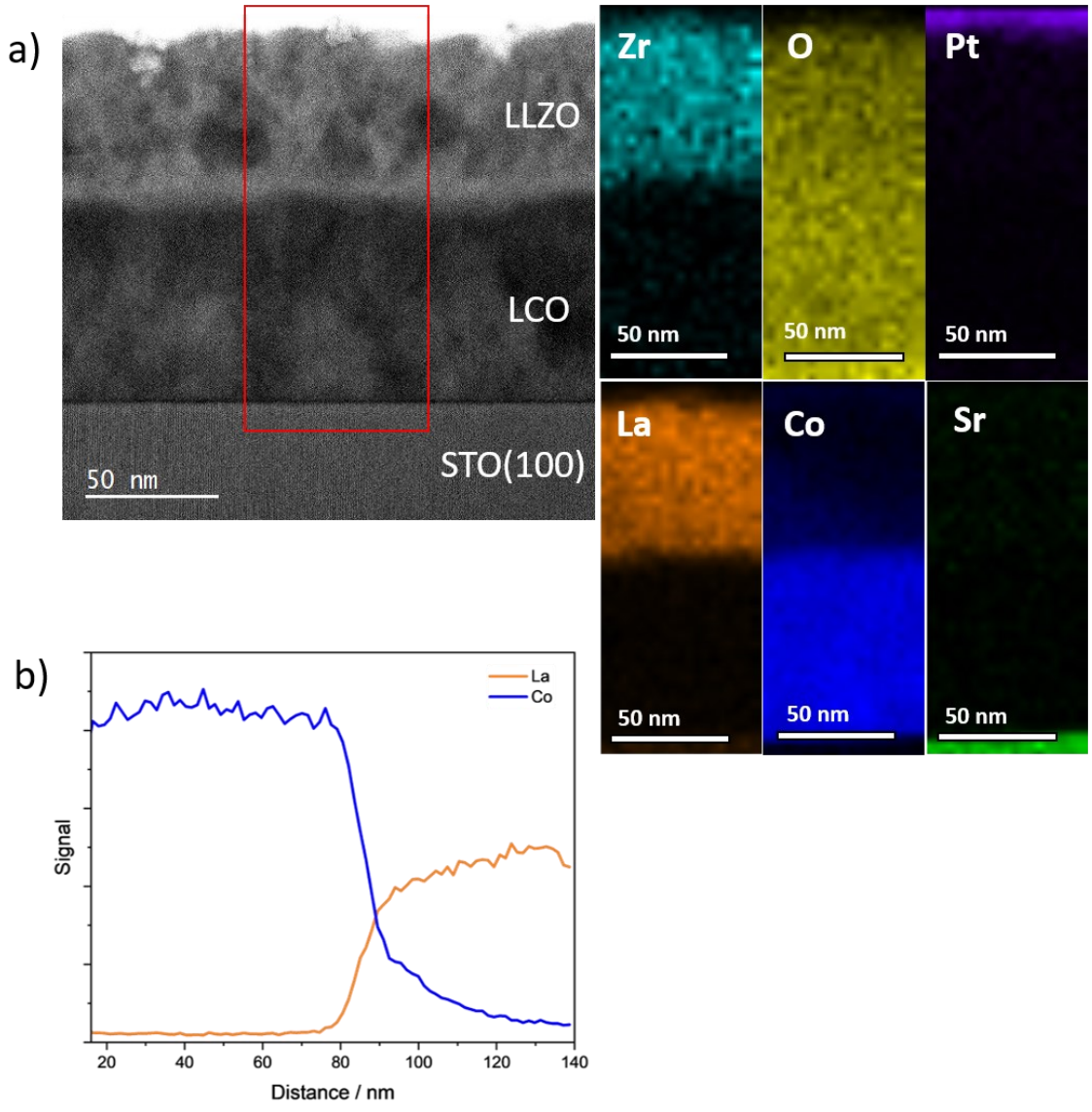

Figure 5.12: a) Cross-section of STO(100)/LCO/LLZO heterostructure with EDS maps showing distribution of elements across the interface. Region from which composition is analysed is shown by the red box. Co diffusion into the LLZO layer, seen in the elemental maps, is measured to be approximately 40 nm using a line scan b) where La is orange and Co blue. Data acquired on JEOL ARM 200CF at 200 keV.

For LCO within the heterostructure on STO(100) (Figure 5.13), shorter annealing duration at 600 °C, contains a mostly r-LCO film orientated along the ($[0\bar{1}4$) plane. A component of Li deficiency in the form of cubic and spinel phases was more prevalent in the annealed STO(100)/LCO structure cross-sections. The retention of multiple phases after 30 minutes of annealing show this duration was insufficient to create the apparent full phase conversion to r-LCO seen on STO(111) after 4 hours of sintering. Accounting for the selectivity of lamella compared to the 5 × 5 mm^2 scale of the bulk sample, the quantity r-LCO may be circumstantial with respect to the ROI. Additional lamella derived from heterostructures on STO(100), annealed at 600 °C for 30 minutes show similar contribution from r-LCO, with small grains cubic and spinel phase.

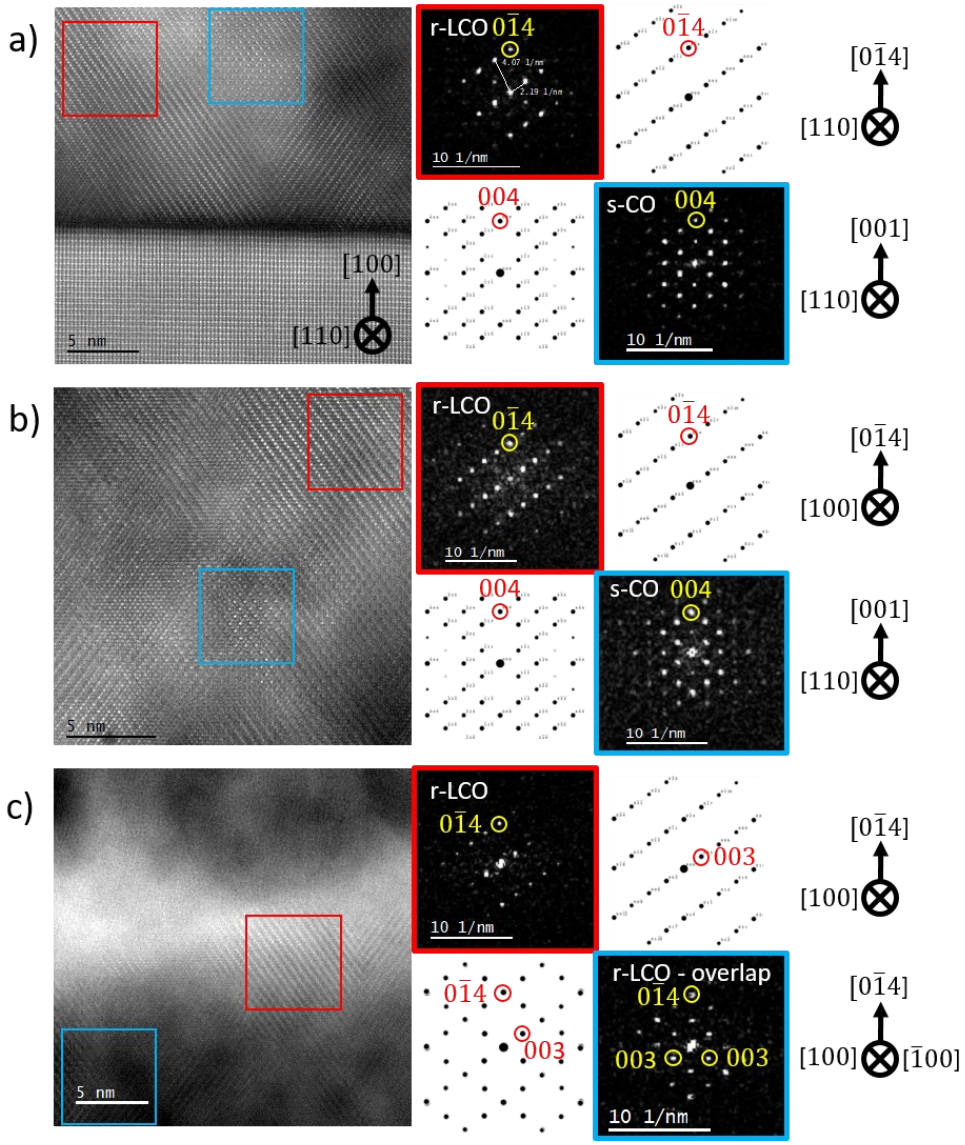

Figure 5.13: LCO layer on STO(100) after annealing of heterostructure sample at 600 °C for 30 minutes. a) STO/LCO interface, b) bulk of LCO layer, c) LCO near to interface with amorphous LLZO. All three LCO phases are present in the electrode layer after annealing, with dominant orientations relating to growth along the r-LCO($0\bar{1}4$), rs-CO(001) and s-CO(001) planes. HAADF images collected on JEOL 200ARMCF at 200 keV.

The surface structure of the LCO film remains predominantly rhombohedral phase with the layers of Co oxide terminating at an amorphous interface with the LLZO layer (Figure 5.14). Presence of Li in the electrolyte was again likely to be offsetting Li deficiency at the LCO surface, although rs-CO and s-CO remained present in the bulk. Retention of the layered structure of LCO along the $(0\bar{1}4)$ plane this is preferential for Li intercalation form the surface of the electrode layer into an electrolyte. Common GB within the electrode layer include transitions between rs-CO$(1\bar{1}0)$ plane in contact with s-CO$(\bar{1}10)$, alongside interfaces between the $(0\bar{1}4)$ planes of the r-LCO phase along the respective [100] and $[\bar{1}00]$ ZA. Figure 5.14 displays examples of these boundary types, with a variety of influences on Li intercalation. Boundaries with the cubic and spinel phases will have reduced Li transfer efficiency compared to overlapping r-LCO grains. The overlapping of r-LCO grains, with GB along the viewing axis contain channels of Li, for efficient transfer into overlapping grains. This twin boundary along the $(\bar{2}10)$ planes at the BG of the overlapping r-LCO phases therefore create potentially efficient route between the two grains. These Li columns are expected to be periodic regions of no intensity between CoO_2 layers in the HAADF images. While potentially occupying the regions of low intensity between these CoO_2 layers, future work implementing methods like ptychography and ABF would potentially allow observation of Li to visually confirm its presence.

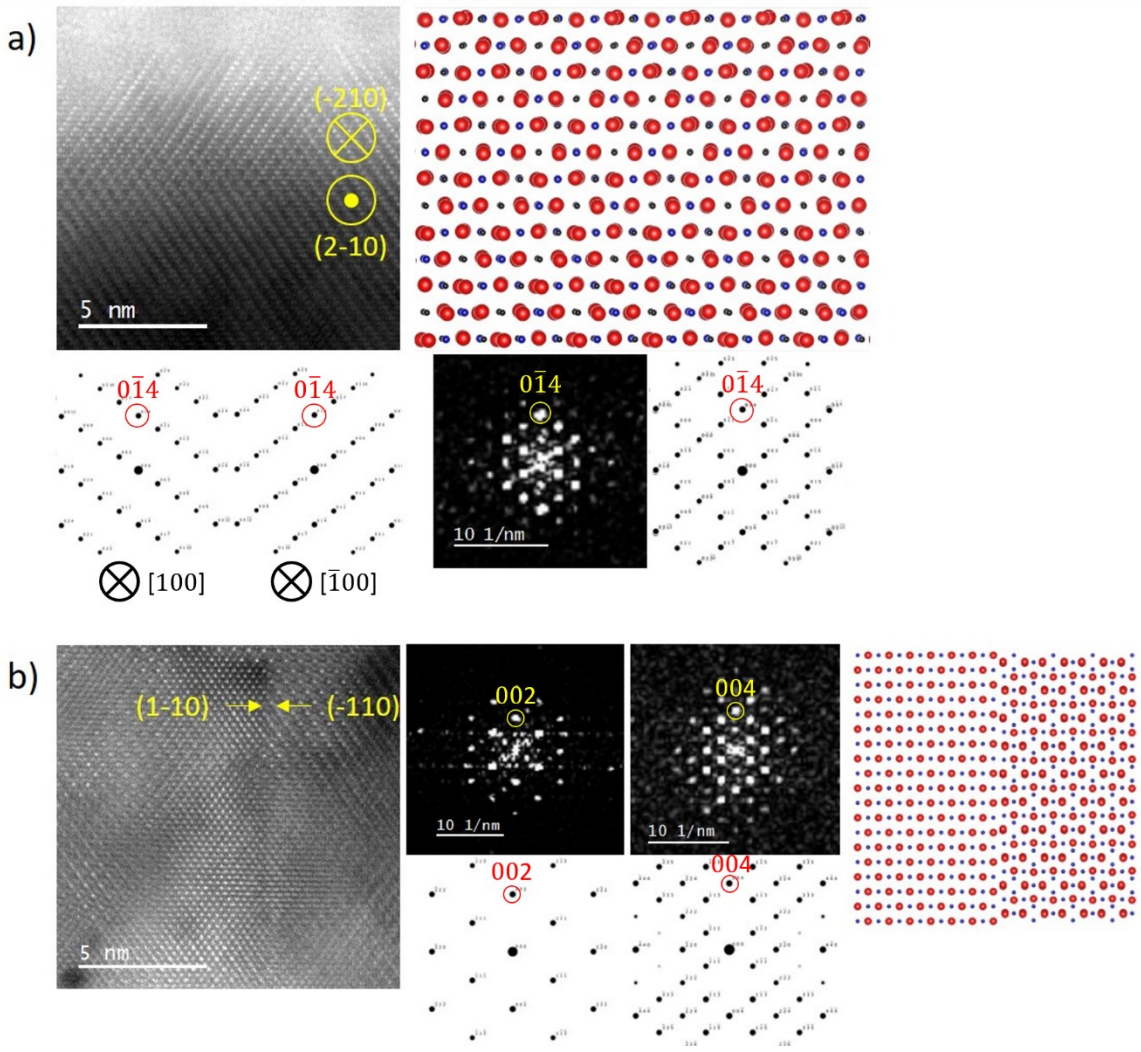

Figure 5.14: GB in LCO grown on STO(100) between r-LCO, rs-CO and s-CO phases. a) HAADF image of overlap between two twinned r-LCO grains growing along the (0$\bar{1}$4) plane, with Li expected to occupy the region within the diamond-shaped voids. Here GB exist between the ($\bar{2}$10) and (2$\bar{1}$0) plane of r-LCO. b) rs-CO and s-CO grains growing along their [001] planes with various GB alignments, with an interface between (1$\bar{1}$0) of rs-CO and ($\bar{1}$10) of s-CO labelled on the image. Acquired at 200 keV in JEOL ARM200CF

The BF and HAADF STEM images show no crystalline regions within the bulk of the amorphous LLZO layer. The HR images also contain the same 5 to 10 nm thick SEI layer, which remains amorphous throughout the thin film's cross-section, for example Figure 5.3, Figure 5.8, b) and Figure 5.13, c). Diffusion of Co extends tens of nanometres into the amorphous electrolyte, with sporadic clusters of anisotropic crystallites that match the layered structure of r-LCO with respect to the spacing of atomic layers and atom symmetry. The extent of Co diffusion into the electrolyte suggests even 30 minutes, thermal treatment would have a negative impact on the Li mobility. This is despite the formation of r-LCO crystallites seen to form after 4 hours of annealing,

also forming after 30 minutes. Given the challenge of achieving LLZO crystallisation at 600 °C from 30 minutes to 4 hours, utilising much higher temperatures (e.g. 950 °C) for annealing times of at most 10 minutes is the best future approach to attempt LLZO crystallisation. This facilitates the conditions of crystallisation temperature, alongside minimising time for Li evaporation and element diffusion. This method of rapid HT annealing the heterostructures could create conditions not reported in the literature for treatment of electrode and electrolytes, if proved effective.

Similarly, to the samples of STO(111)/LCO/LLZO, heated to 600 °C for 4 hours, regions of crystallites could be analysed in detail (Figure 5.15). For the STO(100) heterostructure the crystallites were sporadic in comparison to the amorphous region where CO had diffused into the LLZO. EELS data supports the presence of Co within the structures, with the crystallites consistently penetrating around 20 nm into the electrolyte, with HAADF contrast hinting at La or Zr presence along the edges of the crystallites. The chemical mapping again indicated the heavier elements along the edge of the crystallites was La. Co content of the crystallites was less distinct in the EELS data from the STO(100) heterostructure compared to within STO(111) is likely to be a result of amorphous LLZO and lanthanum-cobalt-oxide overlaying the crystallites, Figure 5.6. Diffractograms, atomic structures and lattice plane spacing within the crystallites matching r-LCO were therefore used for assigning the structures in conjunction to chemical mapping. While the amorphous lanthanum cobalt oxide SEI will increase impedance to Li transfer between the electrode and electrolyte, the presence of these crystallites penetrating the electrolyte may facilitate routes for Li intercalation between the two materials. Crystallite penetration of tens of nanometres into the electrolyte suggested consequences of even short durations of thermal treatment are extensive with respect channelling Li into the electrolyte through LCO channels.

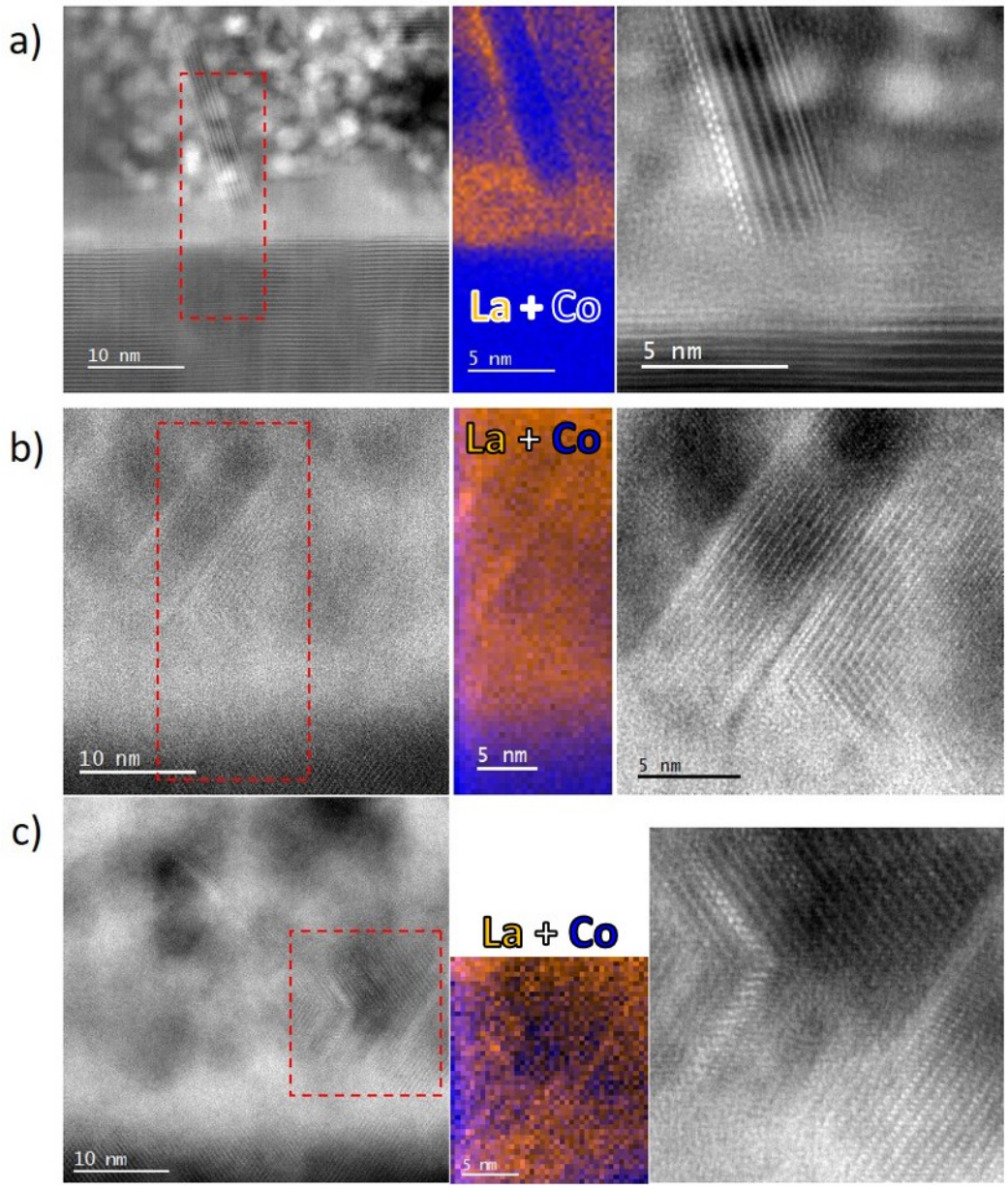

Figure 5.15: HAADF images and La-Co EELS maps within crystallite regions forming along the interface between LCO and LLZO during annealing. a) STO(111) lamella annealed at 600 °C for 4 hours for references. b, c) STO(100) lamella annealed at 600 °C for 30 minutes. Data acquired in JEOL ARM200CF at 200 keV.

The orientations of r-LCO crystallites remained close to the $(0\bar{1}4)$ plane with some minor angular deviations and GB. Lanthanum remains consistently implanted along the edges of the crystallites with a combination of HAADF contrast and La intensity in EELS maps used to conclude this. Some overlap along the viewing axis and $(0\bar{1}4)||(0\bar{1}4)$ twin GB between crystallites were also present. A future question to investigate would be the extent to which lanthanum along the edges of the crystallites limits Li diffusion out along the (001) plane of the r-LCO phase.

Despite the lack of LLZO crystallisation it would be possible to prepare such sample for in-situ experiments to observe changes occurring through heating or biasing experiments. This would further the depth of determining the processes in thermal and electrical degradations with a focus on LLZO crystallisation and formation crystallite during annealing, alongside changes when a bias is applied. The interfacial structure and chemistry for heterostructures on STO substrates annealed for 4 hours and 30 minutes has many similarities. A region of roughly 8 nm to 20 nm along the interface between the LCO and LLZO layer shows distinctly different contrast to the LCO and LLZO layers. This initial interface region was consistently amorphous, even when crystallites were growing into the LLZO layer. The EDS data across the interface supports the intermixing of Co and La in this region, while Zr appears to remain in the electrolyte layer. The uniformity of the SEI layer will provide a consistent impedance to Li mobility across the interface.

Imaging and EELS data (Figure 5.15) revealed the extent of intermixing of La and Co had occurred over 20 nm along the LCO/LLZO interface heated to 600 °C. This was to a lesser extent than for the samples heated for longer on STO(111) (Figure 5.3), but substantial with respect to expected electrochemical SEI mentioned in literature [331, 332], The SEI is clearly amorphous, alongside the majority of the LLZO electrolyte layer, indicating the annealing was sufficient to cause interfacial decomposition but without crystallisation of the electrolyte.

Crystallites forming at the interface (Figure 5.5) are one of the most interesting findings, even present after shortening the annealing time. The LCO crystallisation in the STO(100) interface region retains similar orientation to the bulk of the electrode layer. In contrast, the deviation in crystallite orientation from the (001) in the STO(111) heterostructure interface suggested a degree of independence as crystallites form. Intermixed amorphous regions were more dominant than the occurrence of crystallites, however the presence of crystallites occurrence at least every few microns in both heterostructure likely makes their contribution to performance significant on larger scales. While mostly obscured by the SEI layer, some crystallites could be resolved to be in contact with the LCO layer, indicating a direct contact route for Li could possibly circumnavigate a SEI layer with low Li conductivity. There is potential for in-situ STEM heating experiments of pristine STO/LCO/LLZO heterostructures focusing on observation of crystallite formation mechanisms and potential strain they induce upon successful crystallisation of the LLZO layer. Fracturing and grains in the surrounding electrolyte as the LLZO layer crystallises would be important when concluding the benefits, versus structural damaged LCO crystallites creates at the interface.

5.3 Structure and Chemical Analysis of $Gd_5Ga_3O_{12}(111)/Li_7La_3Zr_2O_{12}/LiCoO_2$ Heterostructure

Due to the low lattice mismatch the GGG substrates provides a strong basis for potentially producing heterostructures whereby a pristine, crystalline EEI could be created. LLZO and LZO were seen to form epitaxial layers along the same direction as the GGG substrate's surface plane owing to the close lattice match between the two. Therefore, depositing the electrolyte onto GGG, prior to LCO, provides the opportunity to acquire a crystalline electrolyte layer. The SEM in Figure 5.16 shows a LCO surface layer with irregular crystallites, similar to when deposited onto GGG(111), as shown in Chapter 4.

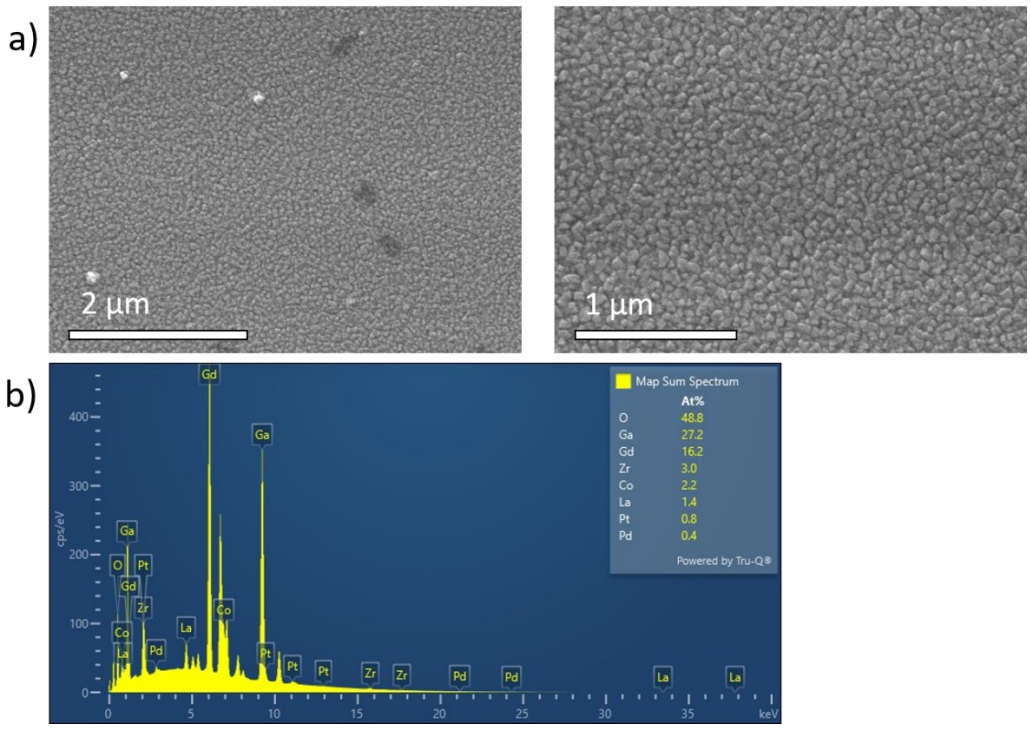

Figure 5.16: SE SEM images of LCO surface layer on GGG(111)/LLZO/LCO heterostructure, showing a rough surface of irregular structures. The EDS spectrum show the presence of both layers on the GGG substrate. Data collected in JEOL 7800F Prime

While the XRD peak at 30° in Figure 5.17 suggests some LLZO (211) planes presence in the initial deposition of GGG/LLZO/LCO films, the intensity of LZO phase signals at 28° LZO(111) and 58° LZO(444) dominates the bulk of this layer. The direction of LZO growth is along the (111) plane (as in Chapter 4), correlates with these XRD signals for the GGG/LLZO/LCO heterostructure. No significant LCO signals are present to help determine crystallinity or orientation, hence the importance for HR STEM analysis.

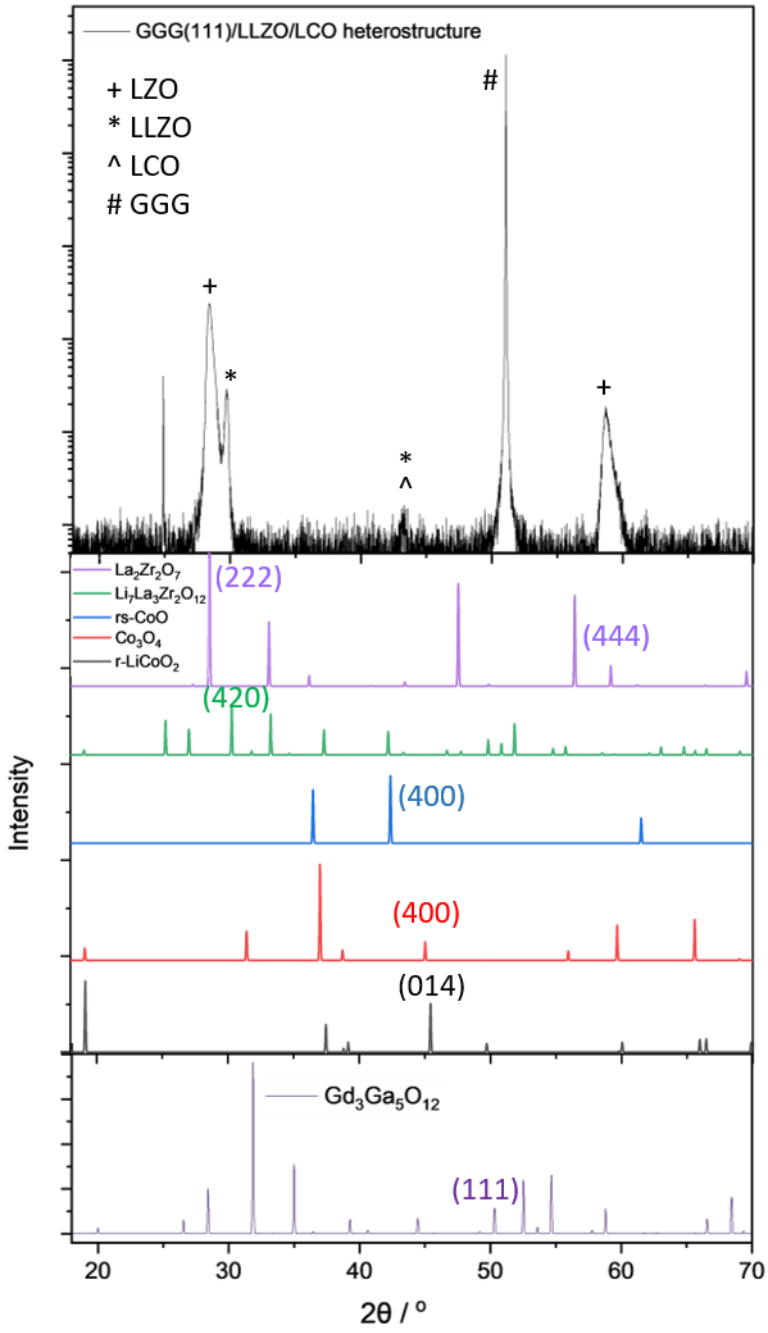

Figure 5.17: Thin film XRD spectra of GGG(111)/LCO/LLZO heterostructure sample, with respective simulations of phases anticipated within the electrode and electrolyte, as well as GGG substrate included below the experimental data. Peaks at 28° and 58 ° indicate presence of LZO, while the peak at 30° may represent the (420) plane of LLZO. XRD acquired on Rigaku SmartLab rotating anode θ/2θ or 2θ-w diffractometer, using Cu-Kα radiation

A low magnification image is shown in Figure 5.18 to assess the layering of the GGG/LLZO/LCO heterostructure with the electrolyte layer roughly 12 nm thicker than the LCO. The interface appears mostly flat and uniform with some irregular contrast (red arrow).

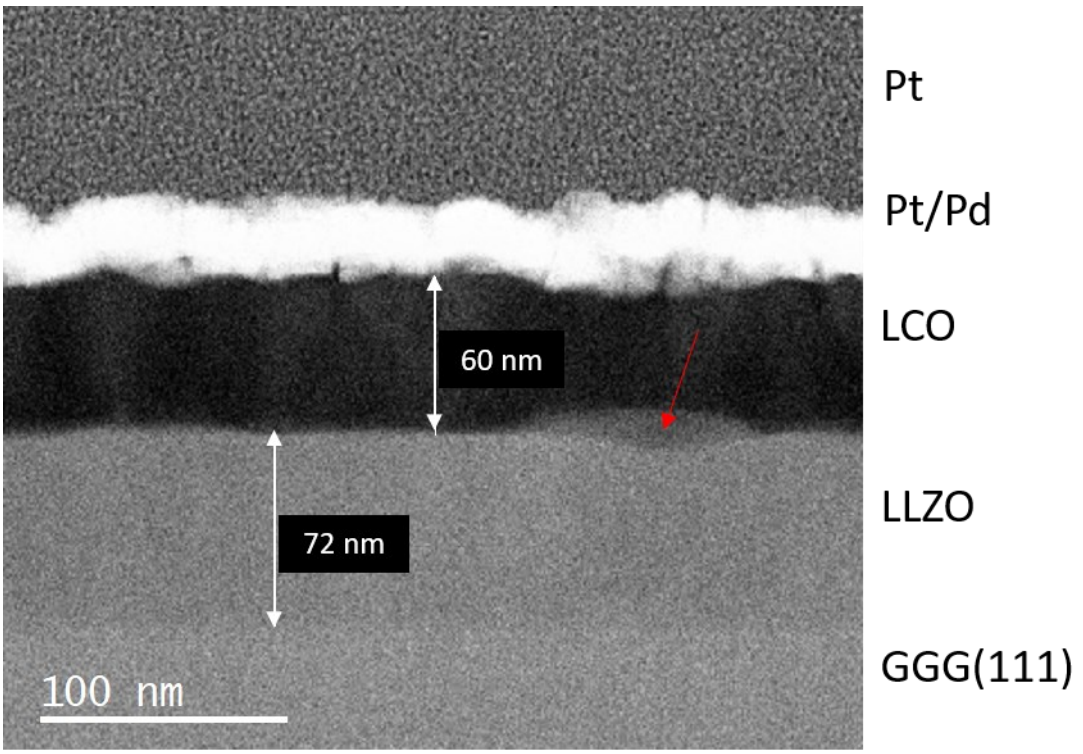

Figure 5.18: Low-magnification HAADF image with clear contrast different between the 72 nm (±5 nm) thick LLZO layer and 60 nm (±10 nm) thick LCO layer. Data taken on JEOL ARM300CF at 300 keV.

Lattice planes of LZO, viewed along the $[1\bar{2}1]$ axis are visible in Figure 5.19, with this structure running consistently throughout the electrolyte layer in the pristine GGG(111) heterostructure. Both sides of the interface were crystalline, with the LCO adopting a range of orientations whereby CoO layers, with spacing relating to the r-LCO phase, grew with the Li channels directed into the electrolyte layer. The layered LCO growth shared similarities with the variable orientation seen when grown on GGG substrates. While not epitaxial, the growth of crystalline LCO with these orientations at interface with a LLZO layer are promising for efficient Li transfer, if Li rich LLZO growth on GGG can be achieved.

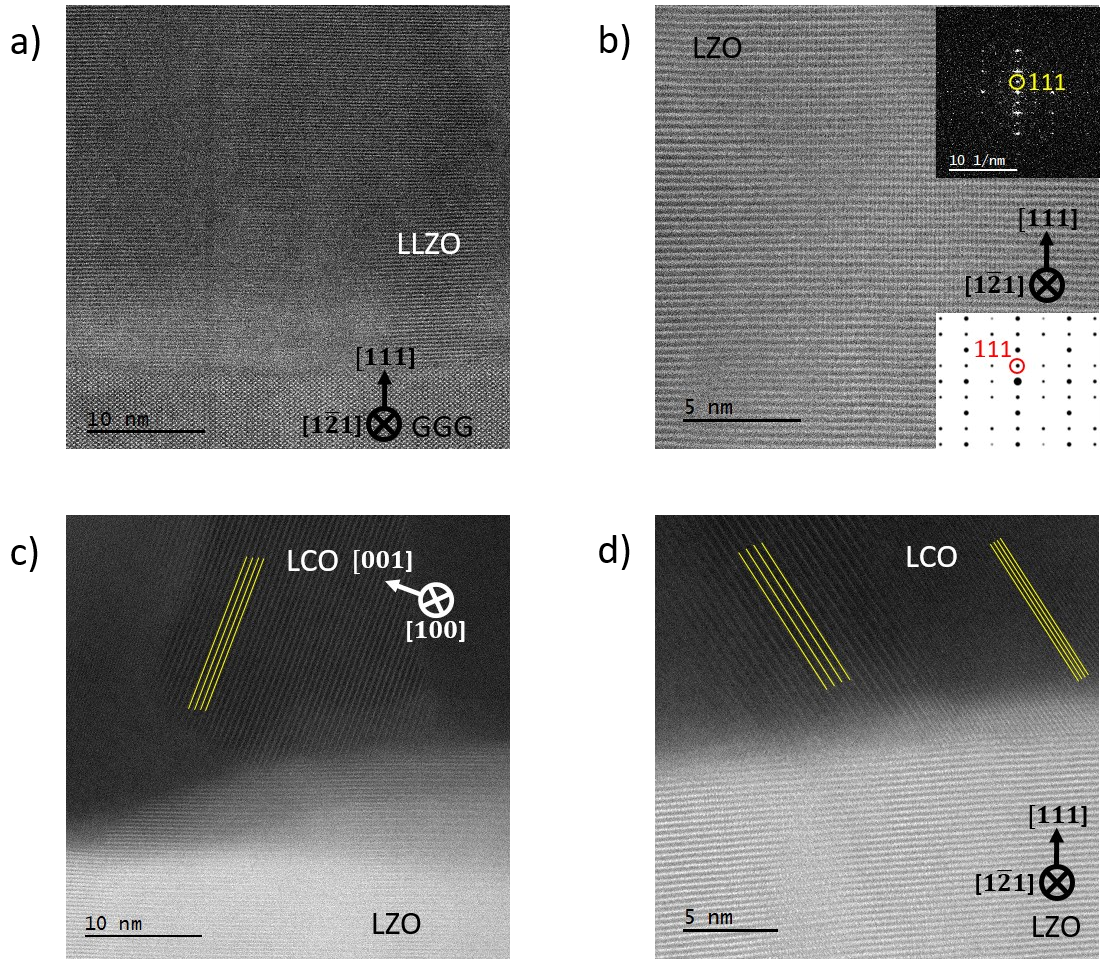

Figure 5.19: HAADF STEM images of a) GGG(111)/LLZO interface with Li deficient LLZO or LZO structure orientated along the (111) plane, shown clearly by the higher magnification image b). c), d) Interfaces between crystalline electrolyte layer and LCO, showing an interface of crystalline material with no amorphous SEI layer. Due to the sharp contrast between electrode and electrolyte, yellow lines mark LCO lattice planes. Images acquired at 200 keV on JEOL ARM200CF

Depositions at of LLZO as a single layer and heterostructure on GGG(111) both suffered from Li deficiency. The presence of the LCO layer, in contact with the electrolyte, did not appear to facilitate any LLZO grain retention or formation along the interface as a pristine sample. The intermixing and formation of an SEI were minimal compared to annealing the heterostructure, with most of the LZO/LCO interface having no significant amorphous layer between the two layers. This is shown in the HAADF images and EELS maps across the interface shown in Figure 5.19 and Figure 5.20, where either a negligible or at most 10 nm overlap/intermixing were seen to have occurred. Absence of LCO crystallites in the LLZO layer was also apparent, and therefore could be concluded to be a feature specific to Co diffusion and crystallisation during annealing. Avoiding annealing and achieving a crystalline interface as seen in Figure 5.19 would be ideal for future analysis and in-situ experiments if a Li rich electrolyte can be retained during PLD.

The EDS and EELS data collected for samples grown on GGG(111) highlights the effects of thermal treatment on an LCO/LLZO system from particles and heterostructures on STO. In Figure 5.20, containing the element maps of an as deposited interface, significant intermixing was not visible in STEM or EELS data along most of the interface. LT LCO deposition onto the LLZO layer is clearly insufficient to create the same extent of intermixing and amorphous SEI formation as observed in heterostructures furnace annealed to 600 °C. This would be advantageous with respect to order of devices fabrication, where the LLZO is heat treated to crystallisation prior to application of the electrode layer, without further annealing that would thermally degrade the interface. In both Figure 5.20 a) and b) there is a suggestion of oxygen deficiency in regions where Co appears to be more abundant close to the interface. This is supported by a slight dip in the relative percentage of oxygen in the associated interfacial line scans in Figure 5.20, prior to the greater O content of the LZO/LLZO layer. La diffusion appears to be minor (< 5 nm), hence this could either be a layer of CoO or metallic Co near to the interface, where the relative percentage of O is lower than in the bulk of the LCO film. Given the difficulty aligning grains of LCO in HRSTEM imaging it is difficult to be certain where O deficiency is real at the interface or an error of EELS element mapping and pixel value assignment when processing the data in DigitalMicrograph.

Later application of bias would therefore become the contributor to SEI formation. Regarding crystal structure, no obvious change was observed in the LLZO layer with the layering of Li deficiency LZO phase running epitaxially from the substrate through to the interface with LCO. The interface retained LCO and LZO separation, with at most 10 nm of intermixing or overlapping grains between slight roughness along the electrolyte's surface. A thin band of brighter contrast is potentially visible in Figure 5.20 a), suggesting some SEI formation, similar to the amorphous $LaCoO_3$ layer seen in STO heterostructures. This remains significantly less than thermal decomposition of the SEI in heterostructures on STO as well as data presented later in this chapter relating to GGG(111) heterostructures that were subjected to voltage-current cycles. The minor SEI formation and mixing in pristine GGG samples may be a result of intermixing during deposition of the first LCO atomic layers onto the electrolyte's surface. Alternatively, some electron transfer and charge balancing at the interface of the two materials when first coming into contact may have resulted in a small layer of electrochemical decomposition in pristine samples.

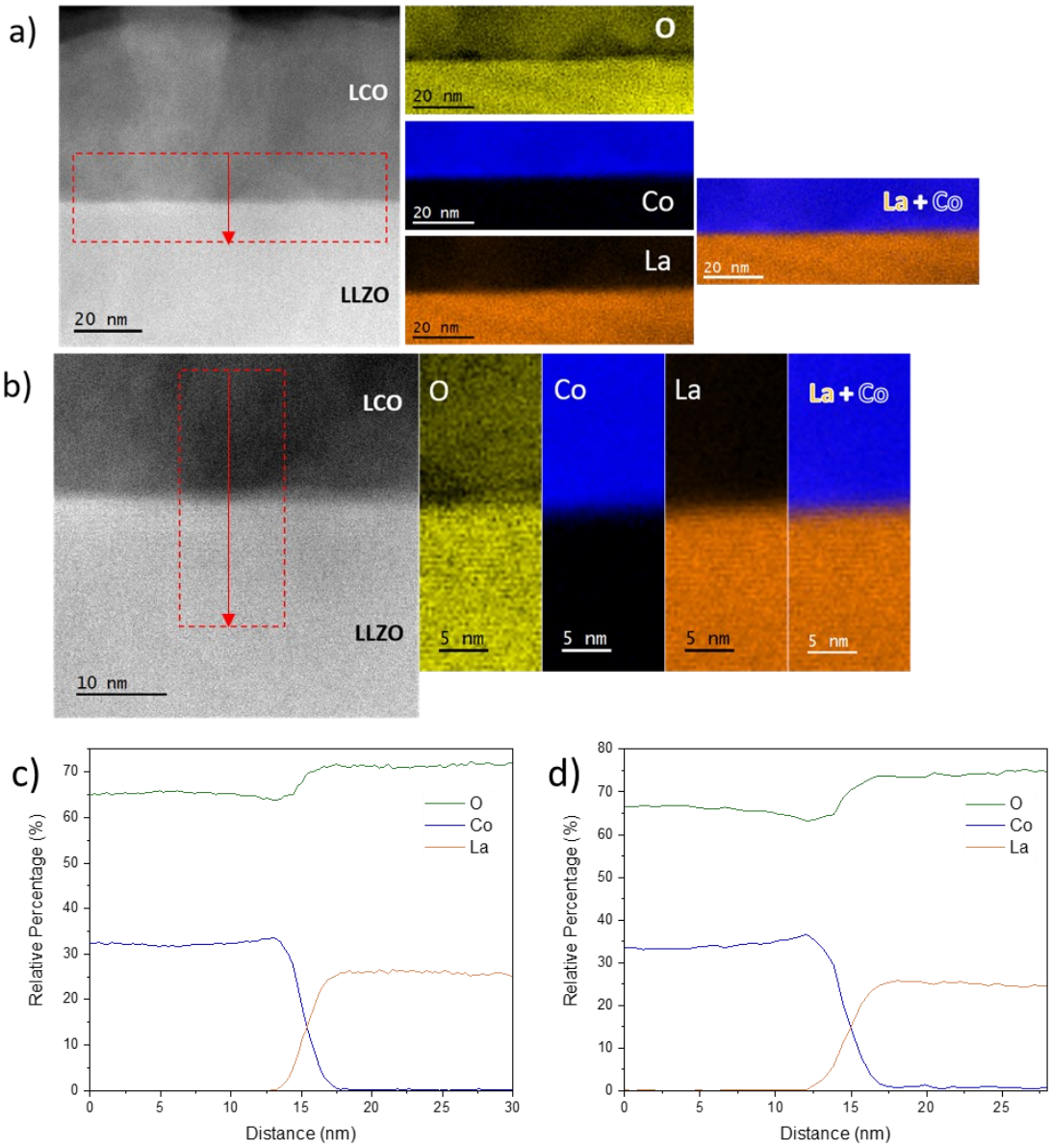

Figure 5.20: HAADF images EELS of an as-deposited GGG(111)/LLZO/LCO heterostructure, showing no significant intermixing of La and Co at the interface. a) ROI ≈ 100nm across the interface, b) higher magnification analysis of the interface at higher resolution. c) and d) Line scans integrated across the EELS acquisition regions in of a) and b) respectfully, where the red arrows on the ADF image show the direction of both line scans. Data acquired on JEOL ARM200CF at 200 keV.

Along the three heterostructures/interfaces created through LT PLD and annealing or crystalline deposition of LLZO, similarities and difference are apparent. In annealed interfaces, the electrolyte either remained amorphous or became porous with tens of nanometres of Co diffusion from the electrode into the LLZO. This is not observed in the GGG/LLZO/LCO samples where crystalline LCO and LZO are in contact at the boundary, without significant La or Co diffusion occurring. Growth of LCO crystallites is common within annealed heterostructures but absent in the GGG sample. All three types of sample show difficult in either retaining Li or alternatively limit by significant Co diffusion during annealing, reducing Li mobility over the interface.

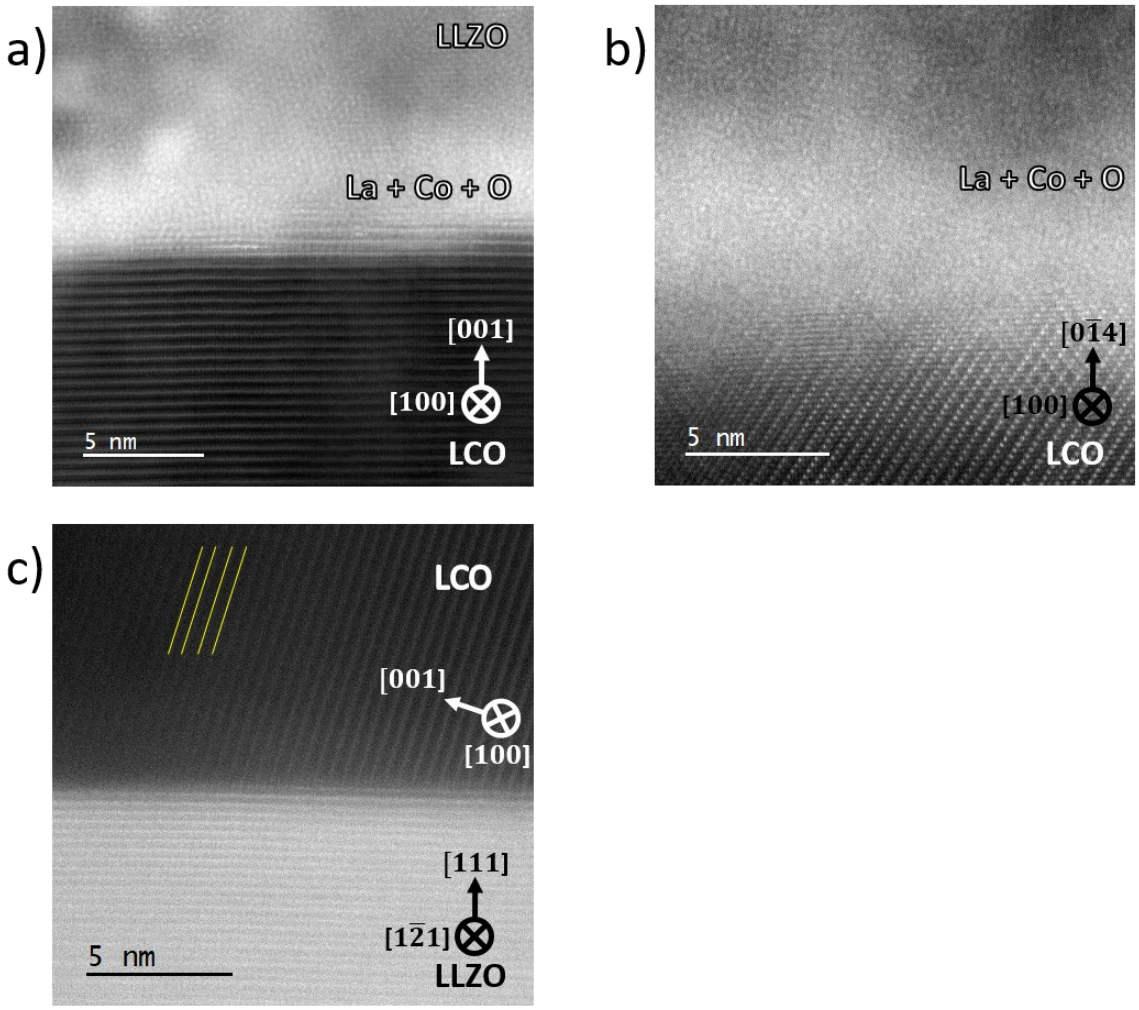

Figure 5.21: HAADF images as comparisions between; a) STO(111)/LCO/LLZO interface, b) STO(100)/LCO/LLZO interface, and c) GGG(111)/LLZO/LCO interface, showing the crystallin-to-amorphous transition in STO heterostructures and a crystalline-to-crystalline EEI in the GGG heterostructure. Data acquired on ARM200CF at 200 keV.

5.4 Interfaces within Biased STO(100)/LCO/LLZO Heterostructure

With respect to biasing a variety of voltage-current cycles were applied to samples of LCO and LLZO on GGG. The set-up aimed to run the current between the surface of the top layer and substrate upon which the heterostructure was deposited. Common set-up for the probe positions on the heterostructure films aimed to apply one contact to the film's surface and other to the corner of the substrate with not material coverage during PLD. Ten, thirty-minute biasing cycles between the voltage values in Table 2.5 attempted to assess the effects of voltage windows on the crystal structure and interfaces within the STO(100)/LCO/LLZO and GGG(111)/LLZO/LCO systems. These two systems were selected as they represented a system that had been annealed and therefore already thermally degraded at the interfaces (STO heterostructure), compared to the GGG heterostructures with no significant thermally induced element diffusion. The influence of charge on the system could then be analysed on both the degraded and pristine heterostructures, with the consequence of ex-situ biasing on element diffusion and SEI formation compared between the two types of sample.

The application of bias to the samples appeared to have no influence on the phase of the LCO layer within the STO(100)/LCO/LLZO samples (Figure 5.22). With the same orientation and phases present in the cross-sections after milling. The voltage-current profile had a varying hysteresis throughout the 10 charge cycles, suggesting changes were occurring, however image data does not indicate significant change in the contribution of r-LCO, rs-CO and s-CO. All were still present in lamella cut along the [110] and [100] ZA of STO, as shown in Figure 5.22.

The extent of interface decomposition caused by thermal treatment at 600 °C appeared to be significantly greater than any changes occurring during the cycling of the heterostructures between the various voltage limits. The interfacial composition and extent of Co diffusion may have altered during ex-situ biasing but without in-situ EDS or EELS experiments observing a change within the intermixed region of STO heterostructures confirmation was difficult. The bulk of the LLZO layer was still amorphous with crystallites running through the region of Co diffusion and SEI of greater contrast and La content near the LCO surface. Even voltage cycles between 8V and -8V provides no distinguishable difference in interface chemistry.

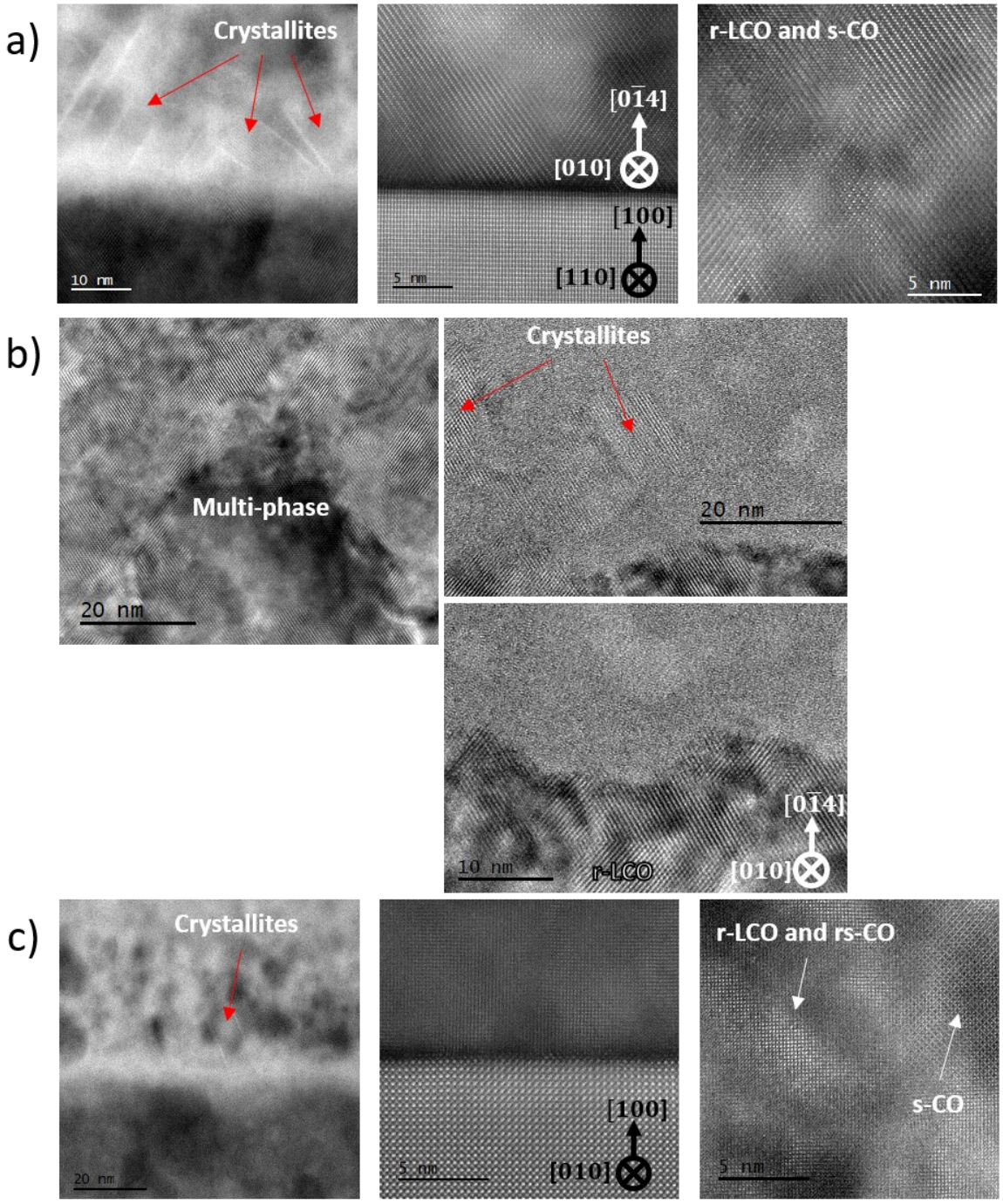

Figure 5.22: a) Bulk LCO and LCO/LLZO interface after 600 °C annealing for 30 minutes. b, c) After application of 10 ex-situ biasing cycles between 6V and -6V, with b) cut along the [110] ZA of STO and c) the [010]. Both show a multi-phase electrode of r-LCO, rs-CO and s-CO is still present and no obvious changes in contrast from the annealed sample have occurred. HAADF images acquired at 200 keV in JEOL ARM200CF

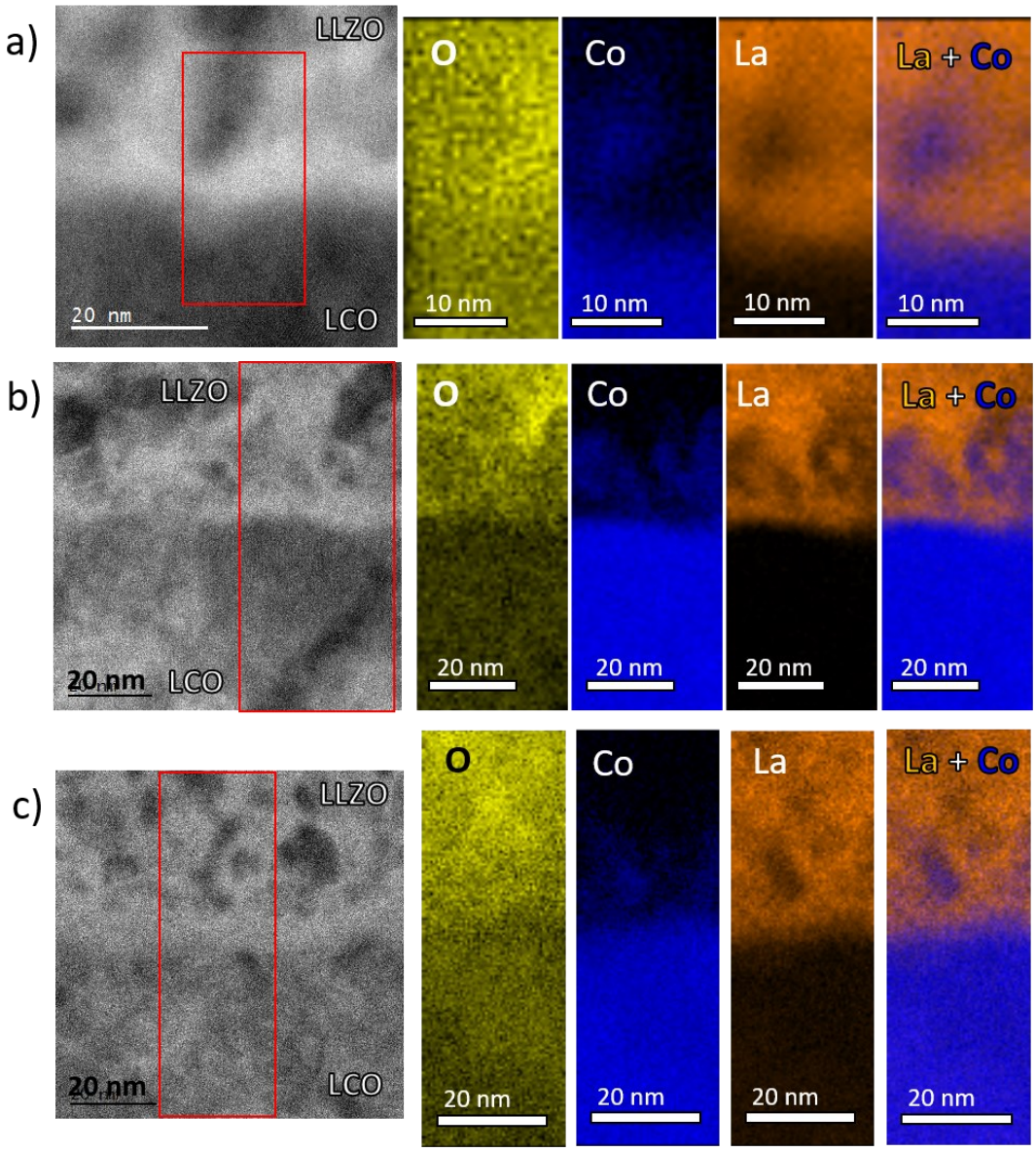

Figure 5.23: ADF images and associated EELS maps from the ROI (red boxes), showing Co and La distribution across the interface of STO/LCO/LLZO heterostructure. a) annealed (600 °C, 30 mins), b) biased 2V to 4V for ten cycles, c) biased 6V to -6V for ten cycles. Each charge cycle was approximately 30 minutes in length, EELS collected at 200 keV DualEELS setup with collection time per pixel of at most 0.02 seconds (JEOL ARM200CF).

The application of bias cycles (Table 2.5) to heterostructures on GGG(111) provides a basis to assess any clear changes to the electrode, electrolyte and their interfaces up to applied voltages of 8V. The charge curves acquired during the biasing show the passing of current, although in the nano Amp range rather than micro-Amps of STO samples. This may be related to the resistivity of the GGG substrate or Li poor LZO layer observed in the pristine sample. The retention of an amorphous structure after current cycles and heating provides no crystalline channels or GBs for Li to migrate through.

A slight hysteresis, showing deviation from resistor-like (linear voltage-current plots) behaviour of single layers and heterostructures on GGG(111), was present in heterostructures on STO(100), as shown in Appendix II. This suggests some charge and ion flow in the STO(100) heterostructure. The predominantly resistor behaviour of samples and absence of oxidation and reduction peaks within the voltage-current cycles suggests absence or insufficient charge and ion flow for battery-like behaviour to be seen in the data collected. Either the setup and voltage ranges chosen for the voltage-current cycles are insufficient to cause any Li flow from electrode to electrolyte or the process was not detectable by the sensitivity of the equipment. Refinement to the electrochemical measurement setup and technique for thin film analysis is required to effective ex-situ experiments where confident correlations between voltage-current experiments and (S)TEM observation may be made. Alternatively, coin cell scale tests could have the potential to be more compatible with setups that can effectively and accurately measure electrochemical changes during charge cycles and understand how LCO and LLZO interact when prepared under the conditions of crystallisation chosen for thin film samples. This would be an avenue for future work.

STEM-EELS shown in Figure 5.24 suggested that some SEI formation through redox activity or La diffusion had occurred (blue arrows). The bright layer with La and Co intermixing of around 3 nm suggests some change because of charging the heterostructure when compared to the pristine sample. This change needs to be observed in-situ to confirm the change occurs during biasing. Use of conductive GGG substrates make such experiments possible, ideally with improved Li retention to analyse crystalline-to-crystalline LLZO-LCO interfaces.

The oxygen map for the sample biased up to between 0 V and 12 V shows a region of oxygen deficiency along the interface where a contrast change between the bulk of the LCO and LLZO layers occurs. This appears to coincide with a greater Co content within the element maps, in the region of the deficiency in the O maps. It is difficult to know for certain from the data acquired but this could be related to CoO formation, segregation of metallic Co at the interface during preparation or biasing, as well as potentially misassignment during data processing in DigitalMicrography. The presence of Co does however suggest this is not a gap between LCO and LLZO at the interface, rather a change in chemical composition.

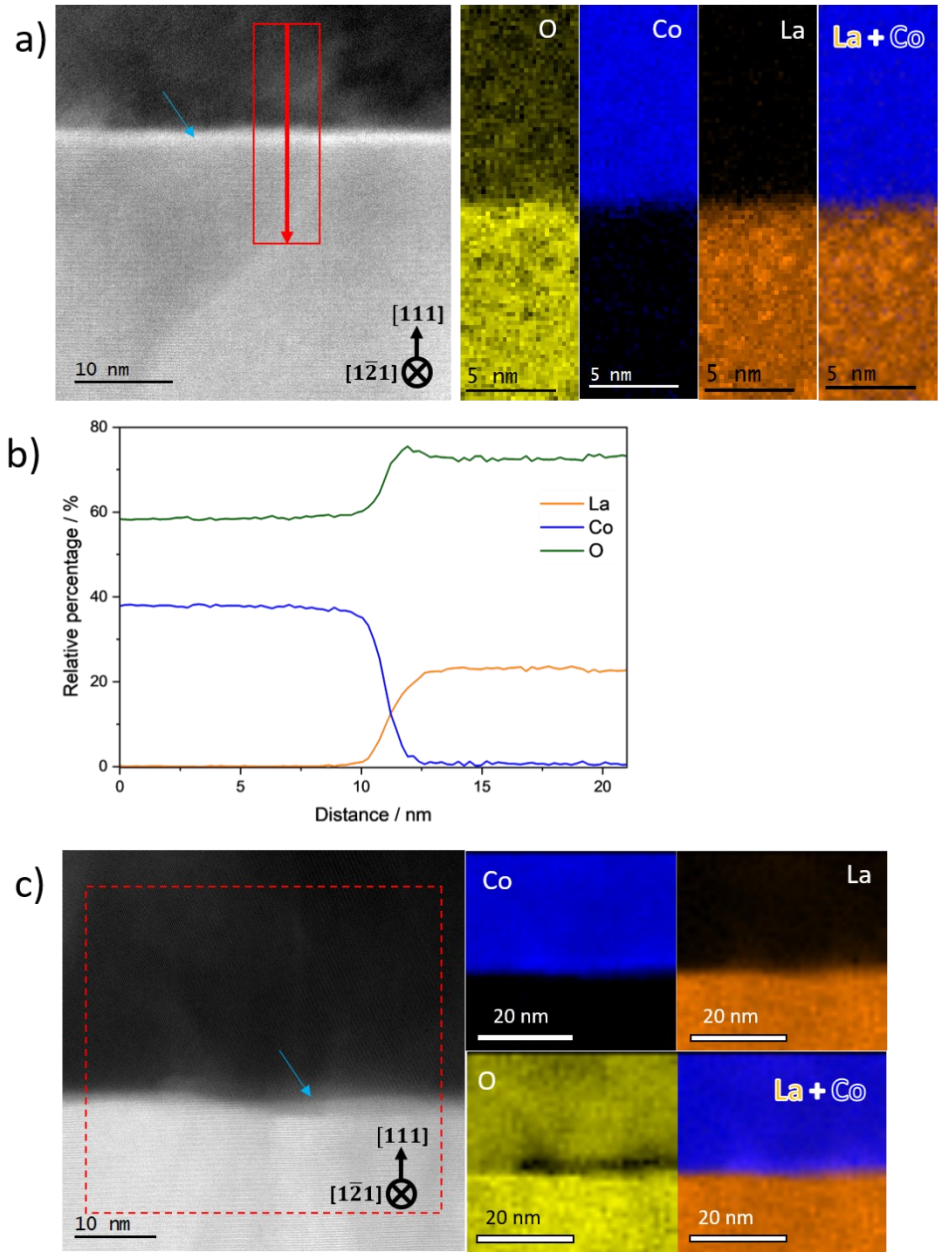

Figure 5.24: a) HAADF image and EELS maps of interface where biasing had occurred for 10 charge cycles between 2V and 4V. Contrast at the interface and intermixing in the EELS maps suggested presence of a 3 nm thick SEI layer, as shown by the line scan in (b), along the direction of the red arrow. c) Sample biased between 0V and 12V (10 cycles) where some La and Co diffusion has based on the combined information regarding HAADF contrast and EELS. Images and EELS data acquired on JEOL ARM200CF at 200 keV.

s

5.5 Conclusions from Investigation into PLD LCO/LLZO Heterostructures Subjected to Annealing and Biasing on STO and GGG substrates

Heterostructures containing interfaces between LCO and LLZO are deposited using PLD, with investigation and comparison of the bulk and interfacial characteristics between as-deposited, annealed, and ex-situ biased LCO-to-LLZO boundaries. The results provide insight into crystallinity as well as extents of thermal and potential electrochemical decompositions, with varying degrees of success and clarity.

The process of electrolyte deposition at temperatures below crystallisation, aimed at retaining Li, requires the input of thermal energy to achieve crystallisation of the electrolyte layer. This appears to lead to rapid La, Co, O intermixing within 30 minutes at temperatures of 600 °C, without significant crystallisation of the LLZO layer. Changes within amorphous LLZO films after annealing at 600 °C for 4 hours create a porous electrolyte with visible regions of crystallinity. At 600 °C the LCO layer on STO(111) and STO(100) was dominated by the r-LCO phase, oriented along the (001) and $(0\bar{1}4)$ planes respectively. Annealing in presence of the Li-rich LLZO layer and above the rs-CO-to-r-LCO transition temperature potentially promotes the improved proportion of r-LCO compared to three-phase, single layers in Chapter 4, with Li deficiency. After 4 hours a completely r-LCO layer was observed on STO(111), while some s-CO and rs-CO grains remained after 30 minutes at 600 °C on STO(100).

Intermixing of Co into the LLZO layer after 30 minutes and 4 hours of annealing was similar, with Co signal consistently observed up to 50 nm into the electrolyte layer. This is greater than the height of the facets in the single-layer LCO films and does not resemble the regular angular structure. While diffusion of Co is potentially occurring from overlap between the LLZO and small surface islands of LCO, the presence of similar mixing between LCO on STO(100), expected to form a flat electrode surface, supports the argument for diffusion over overlapping material. The presence of LCO crystallites, not seen in literature, growing within the electrolyte layer in both lamellae are of significant interest. The atomic symmetry and spacing of spots in the diffractogram support identification as LCO in regions where overlapping LLZO or LZO complicate the EELS spectra. Their ability to grow through the amorphous SEI, potentially allows them to channel Li between electrode and electrolyte, through the low-conductivity interfacial region. In-situ heating and biasing can attempt to determine their formation mechanisms and contribution to Li mobility across the SEI, alongside phase changes during charge cycles.

The deposition of LLZO onto GGG substrates at 600 °C provides an epitaxial LLZO or LZO film, with clear Li deficiency. While Li deficient the lack of porosity is encouraging regarding the potential deposition of epitaxial LLZO layers in a heterostructure system. The dominance of the Li deficient phase suggests a significant percentage excess in the LLZO target is required to offset losses during HT deposition The interface did not show the same extent of intermixing from deposition of LCO at LT during PLD, relative to the annealed samples. This suggests that thermal degradation of the interface could be avoided by acquisition of crystalline LLZO prior to coating of the electrolyte in electrode materials. Despite the lack of well-orientated growth, the crystallinity of the LCO electrolyte on the Li-deficient electrolyte layer is promising given this order of deposition would not require annealing if the first layer deposition of LLZO achieved crystallinity.

Biasing appears to have some effect on the GGG/LLZO/LCO interface where a SEI appears to have formed in HAADF data, however in-situ experiments are required to confirm development this layer under ex-situ charging or if crystallite and diffusion characteristics dynamically change in annealed heterostructures. No clear change between annealed and biased heterostructures on STO substrates (STO/LCO/LLZO) is observed due to the extent of non-uniform decomposition and diffusion of Co across annealed interfaces. Again in-situ analysis would be fundamental for observing real-time changes at interfaces already heavily degraded by annealing.

The certainty in conclusions relating to the effect of biasing is limited based on the equipment and potential effect of FIB-SEM charge accumulation on the samples. The potential for non-uniform electric fields across the sample during I/V sweep experiments, using the source measure unit probes, and degradation from current accumulation during lamella preparation mean the changes between ‘pristine’ and ‘biased’ sample may be the effect of the biasing experiment or artefacts of preparation technique. In-situ experiments based on the preparation of optimised heterostructure samples, with pristine interfaces (GGG/LLZO/LCO).

Chapter 6

Conclusions and Future Work

6.1 Project Conclusions

Studying particles and thin films, with a focus on atomic structure and composition has furthered the understanding of how LCO and LLZO evolve function within their bulk structure and structural changes owing to chemical interactions at an EEI. The aims set out in Chapter 1 described development of heterostructures of LCO and LLZO with characteristics defined by annealing and PLD conditions suitable for future dynamic studies of SSB interfaces of lamella devices. HR (S)TEM for develops understanding of the coherence in LCO GBs in sintered particles and thin films, alongside defect distributions and networks, as well as interface characteristics from the micron to atomistic scales using imaging and spectroscopy. The acquisition and analysis of the structures and compositions in this thesis across EEI at these resolutions, as well as STEM-based EDS and EELS adds to the available knowledge in the literature [16, 22, 88, 161, 162, 304]. From this project, the use of GB resolved at atomic resolutions, which provide a basis for accurate modelling of coherent and semi-coherent GB with varying influence on Li conductivity related to alignment between lattice planes, defects and strain. The chemical and structural insights into LCO/LLZO interfaces show crystal alignments between electrode and electrolyte can be resolved to understand boundaries between the materials in a steady state and are therefore applicable to in-situ studies. The data here provides the opportunity to index the coherent and incoherent relationships between different phases and planes at which GB form. Processes through which strain is managed between two phases at their boundary (e.g. dislocations) can aid modelling of Li dynamics at the GB.

Sintering LCO and LLZO particles influences particle morphology, and characteristics of disorder on the micron scale. Merging of smaller LCO particles during sintering, forms GB networks spanning cross-sections of larger post-sintering particles, potentially improving Li conductivity. Annealing also appeared to increase the density of defects in isolation and as networks. These are thought to include dislocations, point and line defects, with type and orientation varying along their length and direction within the lattice. Individually these are nanoscale scale features, combining into networks on the micro scale. Two possible impacts relating to defects are Li accumulation [319] or creating spatially advantageous routes [197, 333] for improved Li mobility within grains of LCO. The benefits of defects will rely on their size and termination points, where Li may transfer from within the bulk of LCO or LLZO to a GB or adjacent particle, rather than becoming accumulation

sites. After sintering, the number of LZO and rs-CO grains observed increased because of Li evaporation. This is detrimental to capacity and conductivity, despite improvements in particle size and GB networks. The XRD of annealed particle samples show Li evaporation from LCO is limited to the surface, from which the lamellae were acquired, whereas the decomposition of LLZO to LZO occurred throughout the millimetre thick pellets of LCO and LLZO.

Thermally induced SEI formation also followed a temperature-dependant trend, with significant formation of $LaCoO_3$ on the micron scale at 900 °C. Pristine and 30 minutes of heating at 600 °C did not contain noticeable intermixing of La and Co on the same scale. However, Li_2CO_3 was prevalent in the space between both LLZO and LCO particles after exposure to 600 °C, a route of Li loss through thermal decomposition. This is likely to be a reaction with CO_2 in air, rather than any decomposition specific to contact between LCO and LLZO. Exclusion of air or thermally resistant binder filling of porosity could avoid this Li_2CO_3 formation, although electrode-electrolyte intermixing would persist. Overall, a combined insight into the micron and nanoscale is achieved, linking decomposition between LCO and LLZO within thin films also analysed with XRD, XPS and impedance measurements in literature [6, 163, 165]. Particles of electrode and electrolyte provide insights on to scales that more representative of commercial devices, while thin films are better suited for AR imaging in electron microscopy.

PLD of LCO at LT maintains sufficient Li content that a high proportion of the r-LCO phase remains present within the thin films on ALO, STO and GGG. This was apparent in XRD (r-LCO peak at 19^o), in addition to most LCO films containing large grains of r-LCO across micrometres of TEM transparent lamella. Precise contributions of each phase are difficult to determine based on broadness of XRD signals potentially containing signals from r-LCO, rs-CO and s-CO lattice planes. Lamellae provide a method of directly observing the contribution of each phase, while specific to the micro-scale region selected, enable a better assessment of the amount of each phase and dominant growth orientations.

The presence of rs-CO and s-CO grains, due to Li deficiency, allow atomic-resolution analysis of the phase disorder expected in commercial LMO electrodes. The combination of multiple nanograins with varying orientations and phases provides additional insight into the ranges of routes Li can take within the electrode. GB between rs-CO, s-CO and r-LCO grains had various lattice mismatch depending on the axis of contact between planes (e.g. r-LCO(001)||rs-CO($\bar{1}1\bar{1}$) and r-LCO(010)||s-CO($1\bar{1}2$)) likely resulting in widely varying Li mobility across the GB observed, with rs-CO shown in literature as providing lower Li conductivity but able to accept Li during charging [197, 333]. The LCO depositions on all substrates were suitable for heterostructures for HR STEM analysis between r-LCO, rs-CO and s-CO and a crystalline LLZO, providing a basis for modelling and computational studies of Li conductivity along real lattice directions of LCO and LLZO at a GB. The

variety of GB and the networks within thin films on ALO, and STO substrates have provided addition insight beyond the homogeneous and heterogeneous combinations on phases creating GB observed in literature [22, 43, 48]. For example, in this work the numerous lattice alignments between the three main phases, creating GB throughout LCO films, are expected to create dynamic changes in Li mobility on the nanoscale, alongside fatigue from strain as the device ages during charge cycles [22]. The data presented provides references for GB systems that could develop as Li moves in and out of LCO, which can inform realistic models of how the electrode may evolve during charge cycles and associated Li-ion conductivities.

Deposition of LLZO onto two substrates, allowed investigation of thin film crystallisation and Li retention. Study of temperature conditions for crystallisation either in-situ during PLD or by sintering ex-situ, identified conditions potentially suitable for heterostructure samples within which crystalline interfaces between LCO and LLZO would form. The crystalline phases of LCO and LLZO are orders of magnitude more conductive than their amorphous counterparts and therefore a system where both are crystalline is important to develop when considering a commercial-scale device [107].

Temperatures below 600 °C during PLD or annealing did not result in a significant crystallisation of LLZO, nor did shorter annealing times to 30 minutes at higher temperature (650 °C). However, while successful at acquiring crystalline electrolyte films, annealing at 950 °C and PLD with substrates heated at 600 °C were detrimental to Li content. A relationship between the STO orientation and polycrystalline films was unclear, suggesting random nucleation within the amorphous layer. This granular structure forms many GB with may lead to variations in conductivity owing to the diversity in nanograin alignments [197]. This would require ensuring sufficient Li retention to observe LLZO-to-LLZO GB, informing accurate modelling and computational studies of Li conductivity across the boundaries, as is possible from the HRSTEM data for LCO. The network of GB running between these grains would have the potential to direct Li throughout the electrolyte from bulk to interface with cathode or anode. PLD of LLZO at 600 °C on STO and GGG all created crystalline films of Li-deficient LZO with dominant orientations and some residual grains of LLZO near the substrate-electrolyte interface.

In Chapter 5 the process of preparing and investigating heterostructures of LCO and LLZO subjected to various annealing conditions has expanded insight into interfacial intermixing and crystallisation phenomena. HR STEM, EDS and EELS data, of LCO/LLZO heterostructure were obtained in the interfacial region, resolving crystallites after annealing on STO substrate. These were structures that, as to my knowledge, are not currently presented in literature, where previous studies have focused on the chemical composition and Li diffusion across the interface rather than the crystalline features and GB at the electrode-electrolyte interface [163, 165, 168, 170]. These

small interfacial crystalline of LCO may be important structural feature with respect to the interfacial impedance and resultant electrochemical performance of SSB. The HR STEM BF and HAADF data, supported by EELS, across the LCO/LLZO interface has achieved additional insight into the electrode-electrolyte system than data provided by previous literature.

Annealing produced dominant diffusion of Co into the LLZO layer with minor La transfer into the electrode. While the intermixed region remains predominantly amorphous, periodic regions of crystallites could be observed determined to be channels of r-LCO, in contact with the electrode surface, indicating they might act as a route of greater Li-ion mobility through the SEI [163]. LLZO/LCO heterostructures on GGG enabled the growth of an interface without annealing promoting intermixing of La and Co between electrode and electrolyte. Crystalline-to-crystalline contact between LCO and LLZO shows orientated growth of LCO could be achieved on LLZO and LZO phases, with similarities to the variable growth directions of LCO on GGG(111). Refinement of the electrolyte deposition on GGG is still required to improve Li retention, thus determine the dependence of r-LCO orientation during PLD onto epitaxial LLZO. The lack of intermixing and amorphous SEI further illustrates the rapid detrimental impact annealing has on the interface between these two SSB materials. Ex-situ biasing appeared to form thin amorphous layers in the GGG heterostructure with intermixing of La and Co, like that for STO heterostructures. Co and La diffusion further than 10 nm is not substantial in the EELS data, showing more localised decomposition at the interface during charge cycles compared to annealing. While still detrimental to Li conduction at the interface, the volume of lanthanum-cobalt-oxide ions is less than in annealed samples. Crystallinity and orientation of the electrode and electrolyte appeared to remain stable after applying charge cycles up to 12V.

Crystalline-to-crystalline contact between LCO and LLZO was possible on the sample utilising GGG as a substrate, without the need to anneal the heterostructure to induce LLZO crystallisation. The preparation method for GGG/LLZO/LCO is therefore better suited to achieving in-situ studies of a pristine-to-charge cycled SSB device, using conductive GGG substrates. While an anode cannot be included in a sample prepared by depositing LLZO as the first layer, it would provide insight into a device where annealing electrode and electrolyte is achieved separately. Insight may be obtainable into how a pristine interface between LCO and LLZO electrochemically degrades independent of annealing. Including the work presented, the limitations of annealing LCO and LLZO when in contact are consistent on the nanoscale in this project (Chapter 5) and literature, alongside more significant decomposition microscale (Chapter 3) [170]. On a commercial scale, the extent diffusion related decomposition between LCO and LLZO, means combined annealing should be avoided. Therefore, further research into pristine interfaces under thermal and electrochemical stresses related to final applications is required [163, 334].

6.2 Future Work

Future focus within the field of LMOs and LLZO may include refinements to the preparation conditions of particle or thin film samples. Focus should be applied to optimising annealing temperatures and duration to maximise the potential benefits of annealing these materials (e.g., phase, grain size and density of particles) and limit undesired elemental diffusion of La and Co that form SEI that reduce Li-ion mobility between electrode and electrolyte. Using the best preparation processes for heterostructure growth, developed in Chapters 4 and 5, HR STEM could achieve insights into LCO/LLZO into the dynamic (in-operando heating and biasing (S)TEM experiments) structural changes within GB and interfaces susceptible to electrochemical degradation. The best sample for this is deposition of LLZO onto GGG and finally LCO as the top layer, where the interface remained crystalline and pristine for HR STEM data uninfluenced by annealing. This would progress upon literature in the form of resolving crystal structure at the interface, alongside facilitating samples suitable for dynamic in-operando annealing and biasing experiments.

Studies on practical micron-scale powder systems, relevant to devices should focus on the refinement of particle-based heterostructures aiming to GB and defects within an LCO/LLZO heterostructure device. To achieve this, an effective method of combining EDS and EBSD would enable improved indexing through determination of phases and crystallographic orientations, based on information provided by simultaneous EDS. Developing these into 3D datasets for particle samples using FIB-EBSD is achievable, allowing the influence of particle size, grain orientation, GB networks and decomposition to be mapped throughout a device replicating commercial scales.

In-situ annealing to track the development of $LaCoO_3$ decomposition phases can be achieved through heating experiments within (S)TEM. Forming an amorphous or crystalline SEI with nanometre to micron dimensions, this would be relevant to commercial-scale devices where heat is applied to the electrode and electrolyte whilst in contact during deice fabrication.[30] If aiming to optimise SSBs analysis of annealing LCO and LLZO whilst in contact is of less interest as interfacial decomposition on scales of 100 nm would be too detrimental to Li-ion conduction throughout a commercial device. However, the extent to which a passivation layer supresses diffusion during annealing may be an area of research to pursue regarding testing if the benefits of sintering are maintained without the La and Co intermixing forming the secondary phase.

Operating temperatures of Li-ion devices are such that thermal decomposition between LCO and LLZO in a commercial device during use is unlikely but may still occur on a nanoscale. Long-term effects of 60 ^{o}C on the solid-state interface would be one area of investigation relating to non-electrochemical changes [334].

It is also relevant as a thin SEI resulting from device charge and discharge, with ex-situ biasing on particles and thin films giving a rough insight into the development of a thin lanthanum-cobalt-oxide interface layer. In-situ work on the micron-scale particle can provide valuable insight into the decompositions, as well as dynamic changes to GB and defect networks. These crystallographic characteristics will be important to the efficiency of Li conduction throughout the materials and their interfaces, as well as lifespan of solid-state batteries. HR electron microscopy experiments must consider of LLZO's beam sensitivity with low-dose or ptychography experiments utilised to ensure effective analysis of the Li-rich structure. Li deficiencies may be addressed by the following considerations:

1. Limiting target temperatures caused by laser irradiation during ablation, where Li evaporation could occur prior to deposition
2. Reduction of annealing temperatures and durations, that lead to Li evaporation during crystallisation occurs.
3. Loss of Li through sample damage and charging when preparing lamella in the FIB or PIPS.

Advancing the understanding of SSE with electron microscopy requires careful preparation (e.g. cryogenic FIB conditions) with limitation of charge, electron beam or heat induced damage mechanisms. Crystallisation temperature with respect to single layer and heterostructure samples should be adjusted. Flash annealing at temperatures in significant excess to those required for crystallisation (e.g. >900 °C), over 10 minutes or less may be a a potential route to achieving LLZO crystallisation from amorphous films, while avoiding excess Li deficiency and thermal interface degradation. The progress made with heterostructure illustrates the applications of HR electron microscopy to interfaces between solid-state electrode and electrolyte to successfully resolve the SEI and resolve crystal structure either side of the interface. Continued development of LCO/LLZO heterostructure samples would also focus on testing the application of rapid annealing above 900 °C to try to achieve LLZO crystallisation without excessive Li loss. In terms of in-situ experiments, focus should be applied to how atomic structures within the bulk of electrode and electrolyte develop over the first charge cycles of experiments. Using both the thermally decomposed interfaces and pristine LLZO to r-LCO heterostructure could enable dynamic observation of changes to interfaces, Co, and La diffusion, as well as influence of crystallites during the application of bias. These are all structural features of interest arising from data within this project, which are of interest to dynamic microscopy studies aimed at understanding the influence of specific lattice orientations at EEI and the consequences of crystallites when the LLZO layer crystallises.

Outside of microscopy, the new HR STEM GB and interface data can then be applied to computational studies, whereby the impact of orientations and LCO-to-LLZO crystallographic alignments on Li conductivity can be modelled. This would give further insight into the importance of specific GB and optimising the lattice alignments of electrode and electrolyte in fabrication methods where controlled deposition of heterostructures is possible.

Appendix I

Identification of Phases within Particle and Thin Film Samples Using Selected Area Diffraction and Diffractograms

The determination of phase and orientations discussed in the results Chapters requires the identification of phases within particles and thin films in through the application of simulation with respect to databases of crystal models. SAD and nanodiffraction in TEM (JEOL 2100+ and diffractograms from HR STEM (JEOL ARM200CF) allow for calibration of d-spacing from atomic-resolution images of the ALO, STO and GGG substrate, that are applied to the HAADF and BF images of LCO and LLZO films to determine phase and orientation throughout single layer and heterostructure samples.

Below are examples relating to each important samples, where the key phases have been identified from the symmetry of the diffraction patterns and the spacing between spots in the SAD or diffractogram patterns. Theoretical spacings for spots in the LCO and LLZO phases are displayed in individual in , while Figure AI.1 to Figure AI.19 work through samples of important to show how the phases in each sintered pellet or PLD sample are identified.

Figures provide identification of important diffraction spots within simulated DPs, where the distances from the (000) (direct beam) to lattice plane of importance are labelled. These are shown in red and used to compare the theoretical or experimentally derived lattice parameters for LCO, LLZO, LZO and $LaCoO_3$ in literature, to those acquired during (S)TEM experiments in this project. Where possible the diffraction patterns or diffractograms relating to substrates (ALO, STO and GGG) are presented as a reference to a lattice of known and consistent dimensions, independent of Li content. The spacings from the substrates are used for each dataset as a calibration to account for error in the scaling provided by the any of the (S)TEM instruments used at York, ePSIC or SuperSTEM.

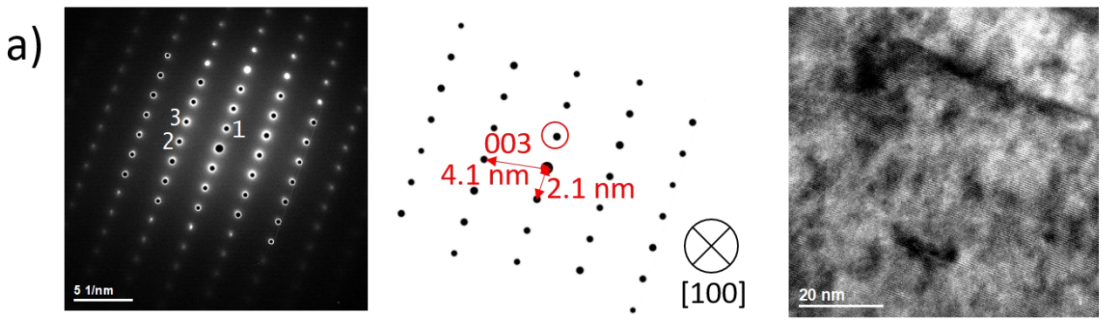

Spot#	d-Spacing (nm)	Rec. Pos.(1/nm)	Degrees to Spot 1	Degrees to x-axis
1	0.5496	1.820	0.00	70.33
2	0.2892	3.457	101.68	172.01
3	0.2827	3.537	71.85	142.18

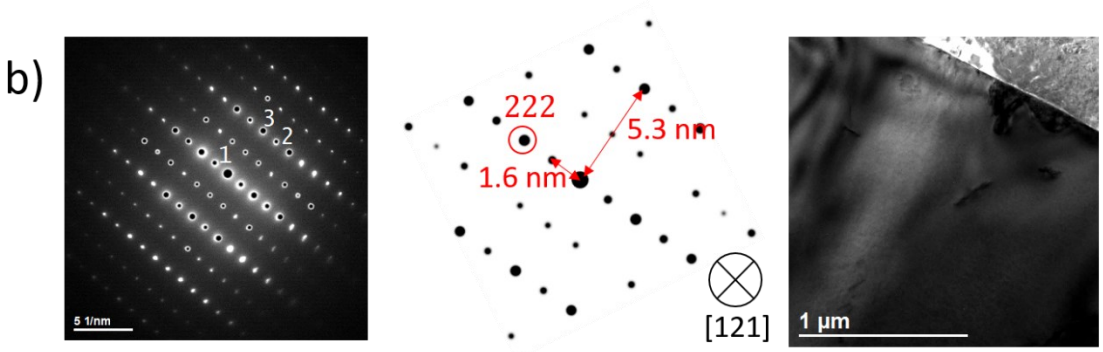

Spot#	d-Spacing (nm)	Rec. Pos.(1/nm)	Degrees to Spot 1	Degrees to x-axis
1	0.6989	1.431	0.00	137.86
2	0.2077	4.814	87.10	50.76
3	0.2000	5.001	71.22	66.64

Figure AI.1: Examples of electrode and electrolyte grains in pristine powder heterostructures. a) r-LCO grain observed along the [100] ZA with a 13% difference between simulated and experimental lattice spacing. b) LZO along the $[1\bar{2}1]$ ZA with an 11% error in experimental and simulated lattice spacing. Data acquired on JEOL 2100+ at 200 keV, camera length 25 cm.

a)

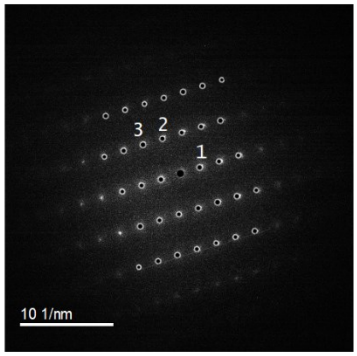

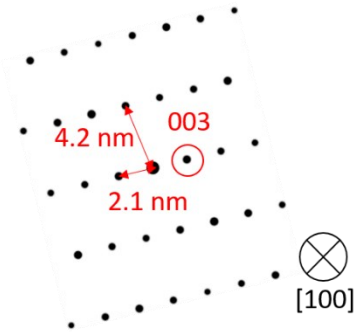

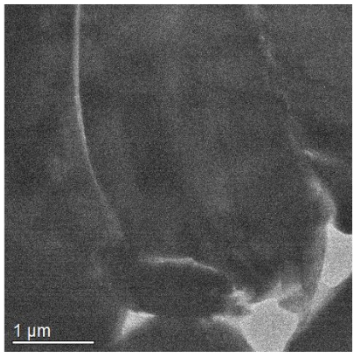

Spot#	d-Spacing (nm)	Rec. Pos.(1/nm)	Degrees to Spot 1	Degrees to x-axis
1	0.4401	2.272	0.00	18.44
2	0.2315	4.319	97.22	115.65
3	0.1971	5.073	123.15	141.58

b)

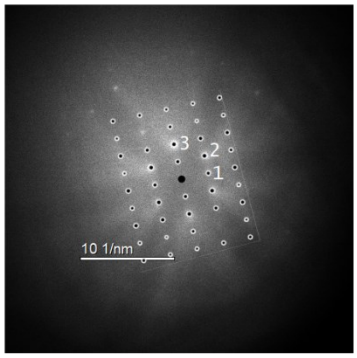

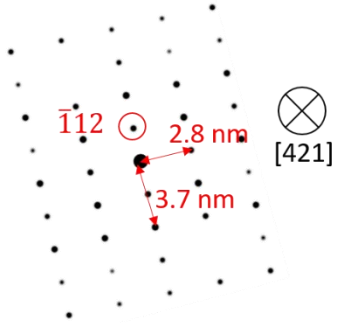

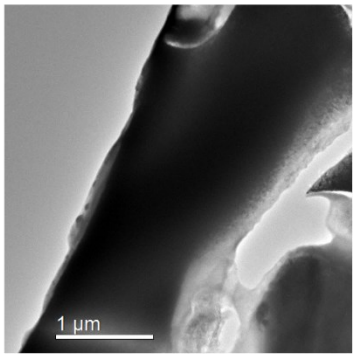

Spot#	d-Spacing (nm)	Rec. Pos.(1/nm)	Degrees to Spot 1	Degrees to x-axis
1	0.3433	2.913	0.00	10.42
2	0.2866	3.490	32.49	42.91
3	0.2750	3.636	91.68	102.11

Figure AI.2: Examples of electrode and electrolyte grains in 600 °C sintered powder heterostructures. a) r-LCO grain observed along the [100] ZA with a 3% difference between simulated and experimental lattice spacing. b) LLZO along the [421] ZA with a 4% error in experimental and simulated lattice spacing. Data acquired on JEOL 2100+ at 200 keV, camera length 25 cm

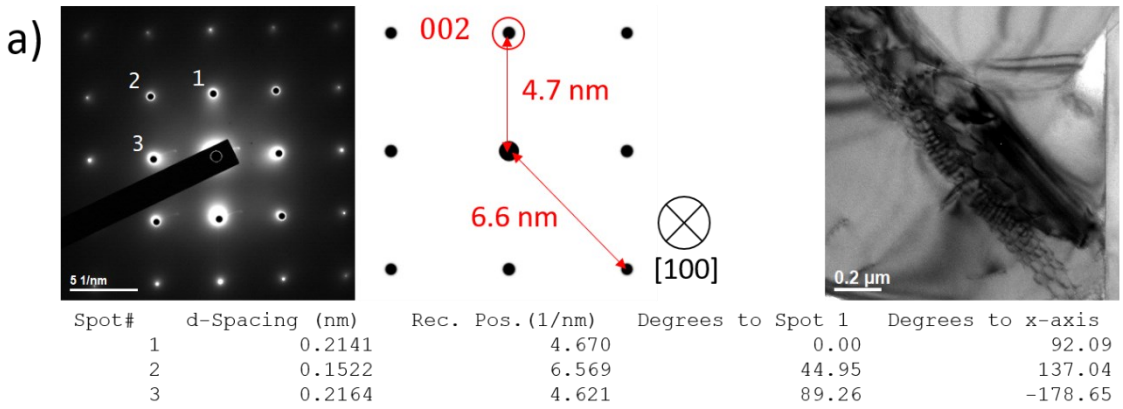

Spot#	d-Spacing (nm)	Rec. Pos.(1/nm)	Degrees to Spot 1	Degrees to x-axis
1	0.2141	4.670	0.00	92.09
2	0.1522	6.569	44.95	137.04
3	0.2164	4.621	89.26	-178.65

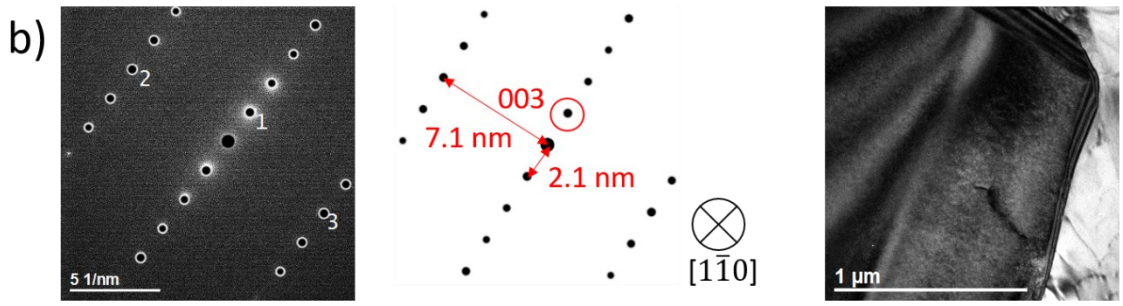

Spot#	d-Spacing (nm)	Rec. Pos.(1/nm)	Degrees to Spot 1	Degrees to x-axis
1	0.5063	1.975	0.00	52.45
2	0.1535	6.516	90.25	142.70
3	0.1539	6.496	89.93	-37.48

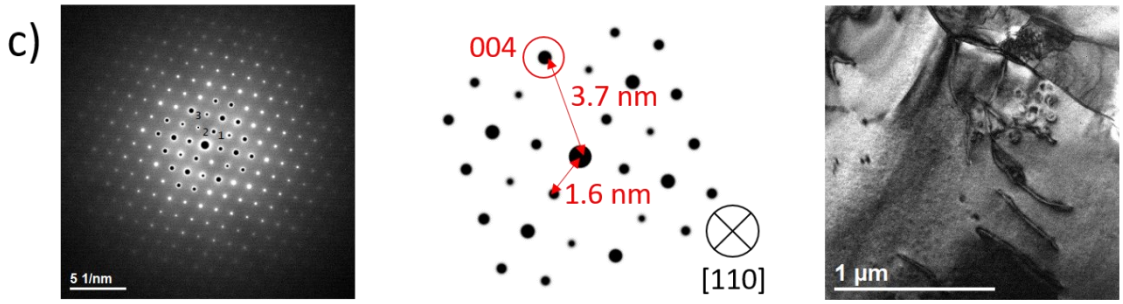

Spot#	d-Spacing (nm)	Rec. Pos.(1/nm)	Degrees to Spot 1	Degrees to x-axis
1	0.7008	1.427	0.00	57.11
2	0.6179	1.618	54.20	111.30
3	0.3087	3.239	54.35	111.46

Figure AI.3: Examples of electrode and electrolyte grains in 900 °C powder heterostructures. a) rs-CO grain along the [100] ZA with a 1% error in simulated and experimental diffraction spacings. b) r-LCO grain observed along the [1$\bar{1}$0] ZA with an 8% difference between simulated and experimental lattice spacing. c) LZO along the [110] ZA with a 12% error in experimental and simulated lattice spacing. Data acquired on JEOL 2100+ at 200 keV, camera length 25 cm

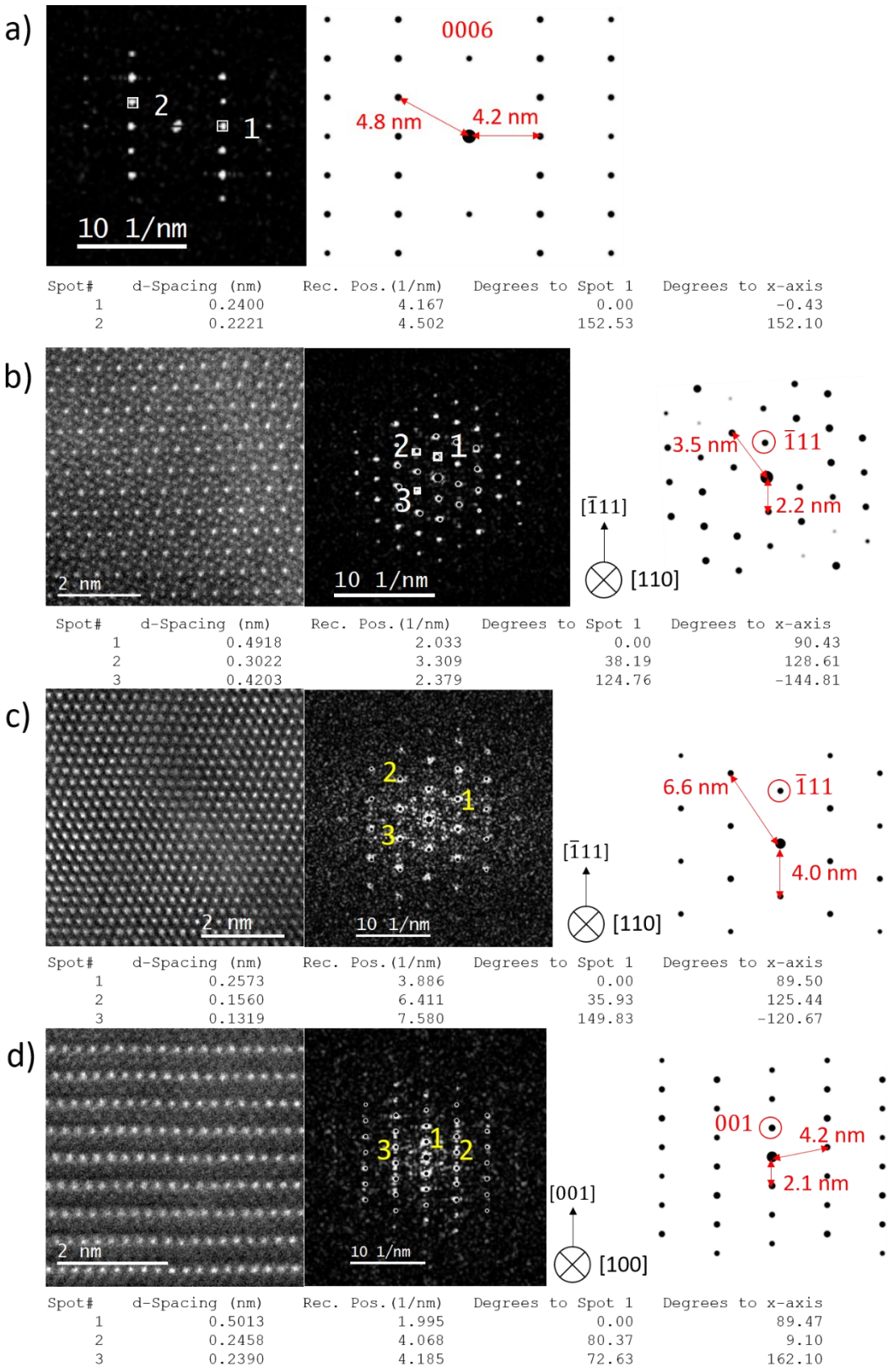

Spot#	d-Spacing (nm)	Rec. Pos.(1/nm)	Degrees to Spot 1	Degrees to x-axis
1	0.2400	4.167	0.00	-0.43
2	0.2221	4.502	152.53	152.10

Spot#	d-Spacing (nm)	Rec. Pos.(1/nm)	Degrees to Spot 1	Degrees to x-axis
1	0.4918	2.033	0.00	90.43
2	0.3022	3.309	38.19	128.61
3	0.4203	2.379	124.76	-144.81

Spot#	d-Spacing (nm)	Rec. Pos.(1/nm)	Degrees to Spot 1	Degrees to x-axis
1	0.2573	3.886	0.00	89.50
2	0.1560	6.411	35.93	125.44
3	0.1319	7.580	149.83	-120.67

Spot#	d-Spacing (nm)	Rec. Pos.(1/nm)	Degrees to Spot 1	Degrees to x-axis
1	0.5013	1.995	0.00	89.47
2	0.2458	4.068	80.37	9.10
3	0.2390	4.185	72.63	162.10

Figure AI.4: a) Diffractogram from ALO substrate along the [120] with a 0.7% error on the y-axis and 6% error along x axis. b) s-CO phase along the [110] ZA with a 6% error between acquired and simulated DP. c) rs-CO phase along [110] ZA with a 3% error in the selected spots in experimental and simulated DPs. d) r-LCO grain along [100] ZA, with a 5% error between experiment and simulation. Data acquired on JEOL ARM300CF at 300 keV

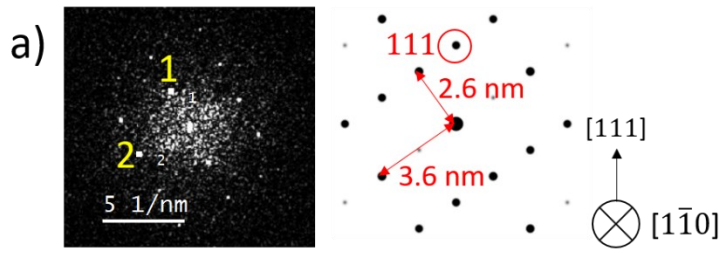

Spot#	d-Spacing (nm)	Rec. Pos.(1/nm)	Degrees to Spot 1	Degrees to x-axis
1	0.4223	2.368	0.00	118.58
2	0.2978	3.358	90.87	-150.55

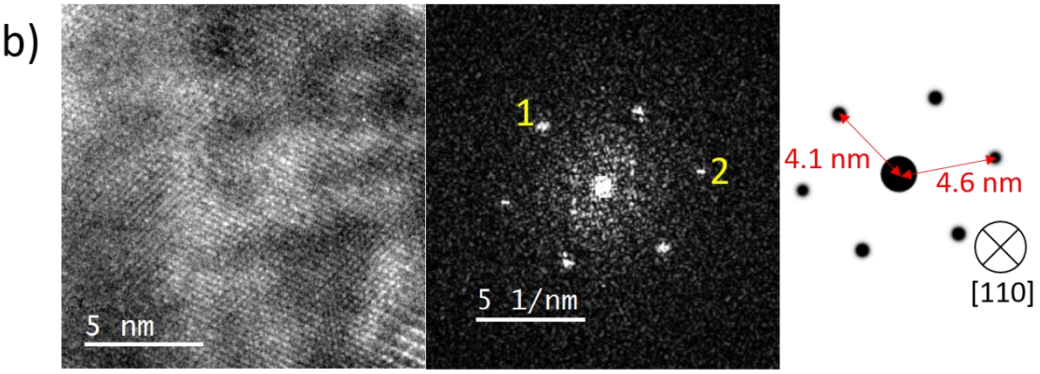

Spot#	d-Spacing (nm)	Rec. Pos.(1/nm)	Degrees to Spot 1	Degrees to x-axis
1	0.2600	3.846	0.00	135.77
2	0.2280	4.385	126.66	9.11

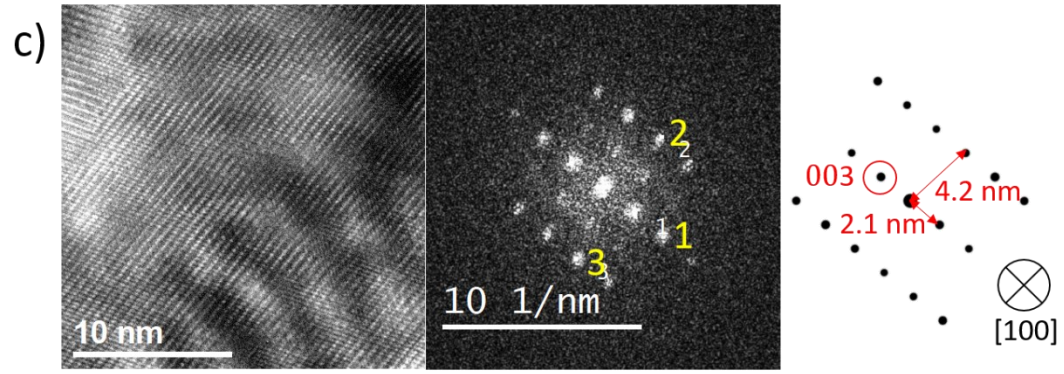

Spot#	d-Spacing (nm)	Rec. Pos.(1/nm)	Degrees to Spot 1	Degrees to x-axis
1	0.5013	1.995	0.00	-39.26
2	0.2618	3.819	80.90	41.64
3	0.2617	3.821	70.73	-109.99

Figure AI.5: a) Diffractogram from STO(111) substrate along the [1$\bar{1}$0] ZA with a 8% error between simulated and experimental lattice parameters. b) rs-CO grain on STO(111), along [110] ZA with a 6% error between experimental and simulated diffraction spots. c) r-LCO phase along [100] ZA with a 9% error between experiment and simulation. Data acquired on JEOL 2100+ at 200 keV

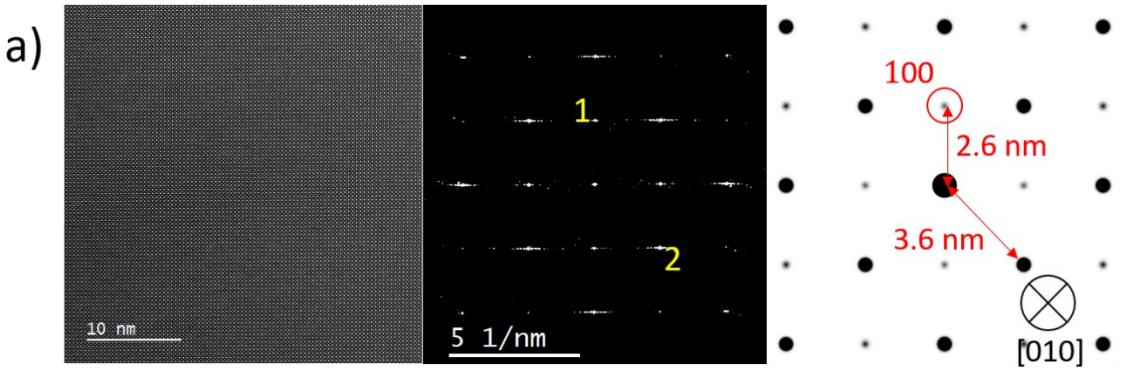

Spot#	d-Spacing (nm)	Rec. Pos.(1/nm)	Degrees to Spot 1	Degrees to x-axis
1	0.4116	2.430	0.00	89.71
2	0.2874	3.480	133.73	-44.01

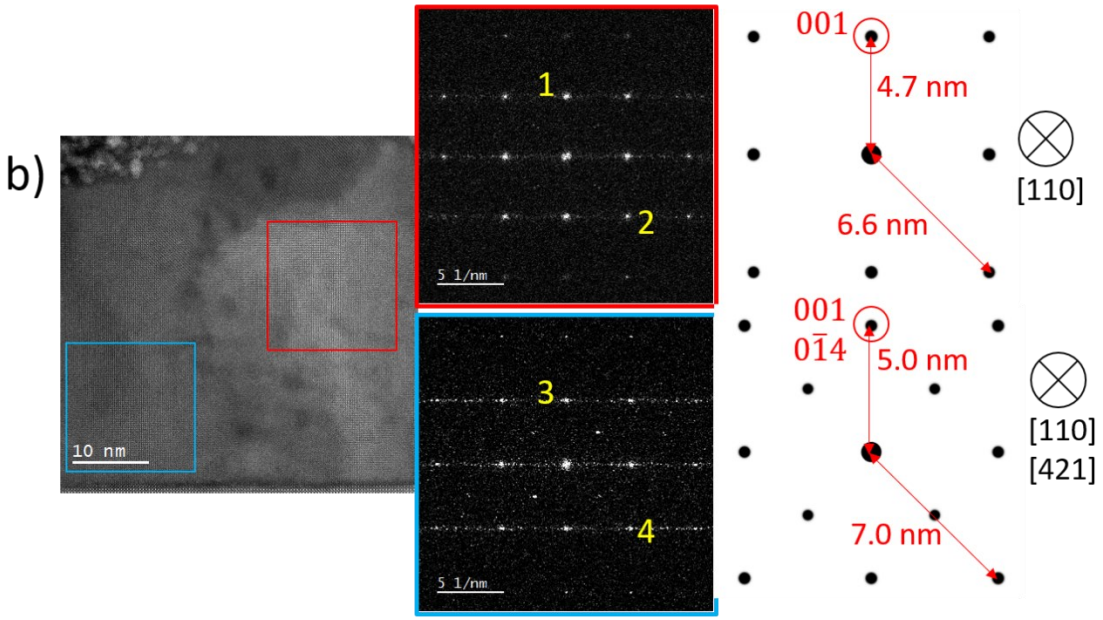

Spot#	d-Spacing (nm)	Rec. Pos.(1/nm)	Degrees to Spot 1	Degrees to x-axis
1	0.2232	4.480	0.00	89.49
2	0.1566	6.384	134.06	-44.57

Spot#	d-Spacing (nm)	Rec. Pos.(1/nm)	Degrees to Spot 1	Degrees to x-axis
3	0.2102	4.758	0.00	89.91
4	0.1473	6.789	134.56	-44.65

Figure AI.6: a) STO substrate along [010] ZA with a 6% error relative to simulation. b) rs-CO (red) with a 5% error and r-LCO or s-CO along the respective [110] or [421] ZA with a 5% error between experimental DP and simulated spacings for the associated ZA. Data acquired at 200 keV on JEOL ARM200CF

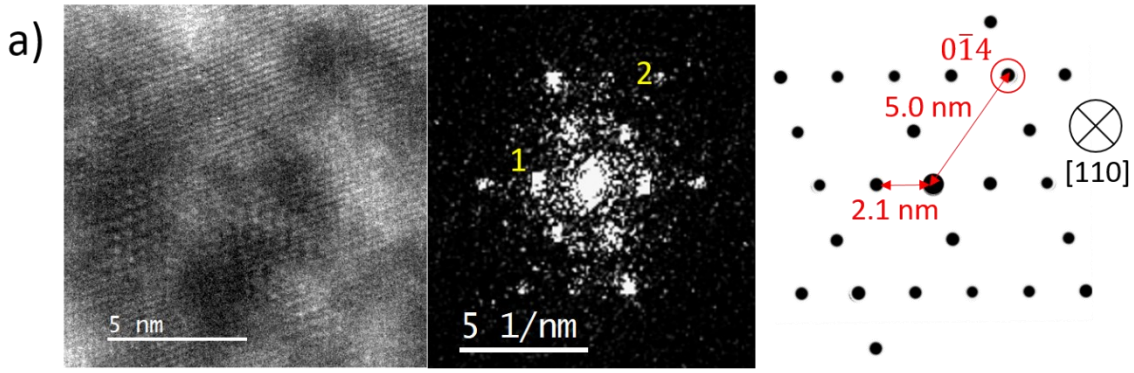

Spot#	d-Spacing (nm)	Rec. Pos.(1/nm)	Degrees to Spot 1	Degrees to x-axis
1	0.4982	2.007	0.00	-174.65
2	0.2028	4.931	128.71	56.65

Figure AI.7: Overlapping r-LCO grains along the [100] and [$\bar{1}$00] on STO(100) substrate, with a 5% error between DP spacing and simulated values. Data acquired on JEOL 2100+ at 200 keV.

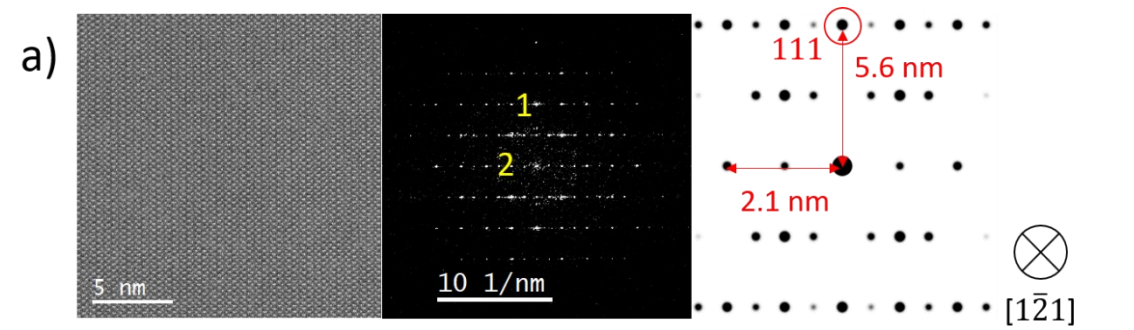

Spot#	d-Spacing (nm)	Rec. Pos.(1/nm)	Degrees to Spot 1	Degrees to x-axis
1	0.1880	5.319	0.00	90.03
2	0.4631	2.160	90.25	-179.72

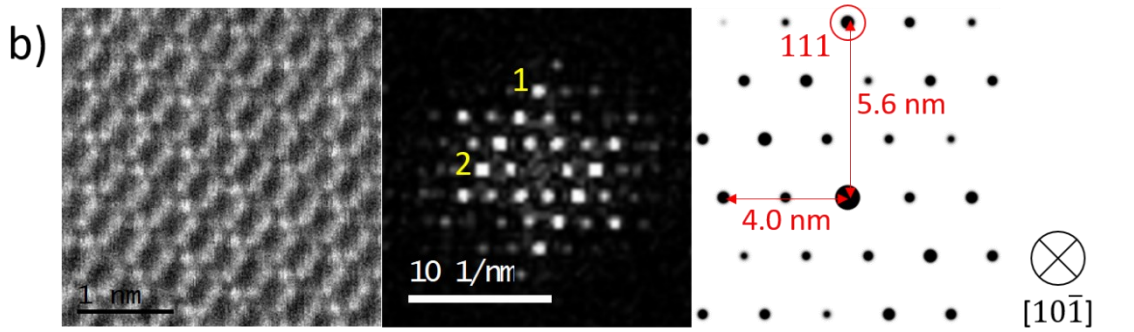

Spot#	d-Spacing (nm)	Rec. Pos.(1/nm)	Degrees to Spot 1	Degrees to x-axis
1	0.1851	5.404	0.00	89.18
2	0.2588	3.864	91.10	-179.72

Figure AI.8: GGG(111) substrate along a) [121] ZA with a 5% and b) [101] ZA with a 3% error between simulated and experimental diffraction patterns. Data acquired on JEOL ARM200CF at 200 keV

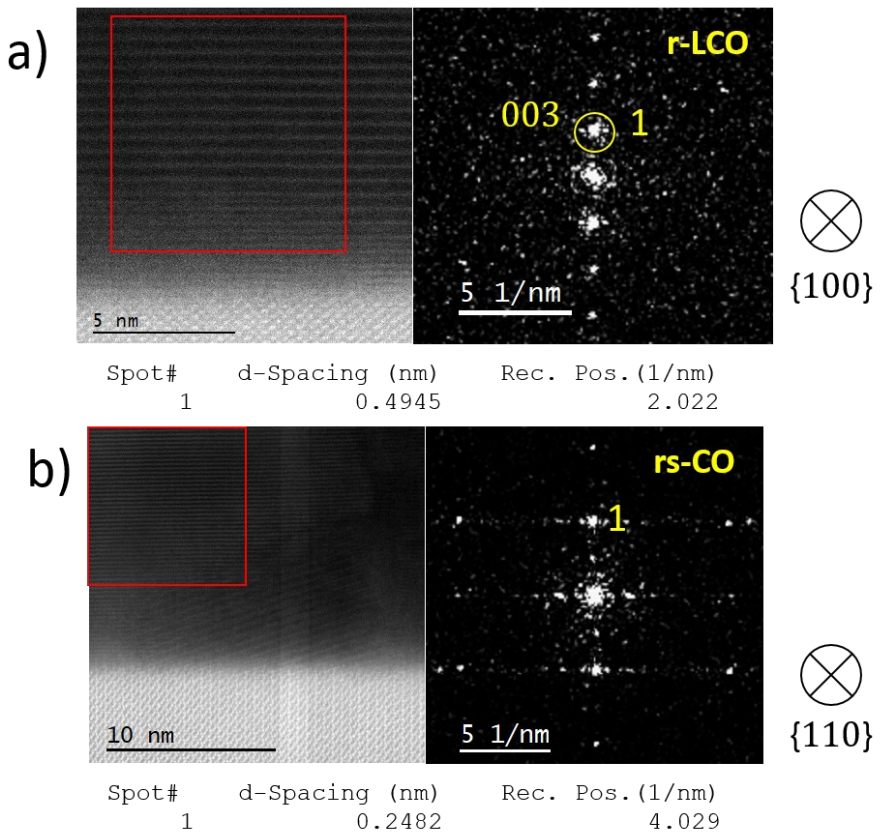

Figure AI.9: LCO films grown on the GGG(111) (same sample at Figure A.8). a) Spacing for the 001 diffraction spot is 4% shorter than simulated. b) Spacing relating to the 111 direction (4.0 nm^{-1}) of rs-CO is the closest simulated spacing accounting for the error in GGG spacing within the same sample, 2% short of the simulated value. JEOL ARM200CF, at 200 keV

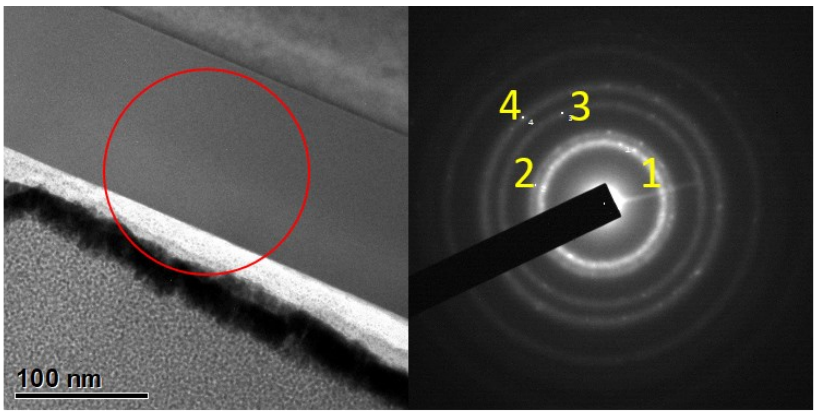

Spot#	d-Spacing (nm)	Rec. Pos.(1/nm)	Degrees to Spot 1
1	0.2600	3.846	0.00
2	0.2187	4.572	90.30
3	0.1577	6.343	40.76
4	0.1324	7.555	58.99

Figure AI.10: Amorphous LLZO on STO substrate with possibly some short-range order from within electrolyte or Pt/Pd layer. Image and DP taken on JEOL 2100+ at 200 keV, camera length: 25 cm

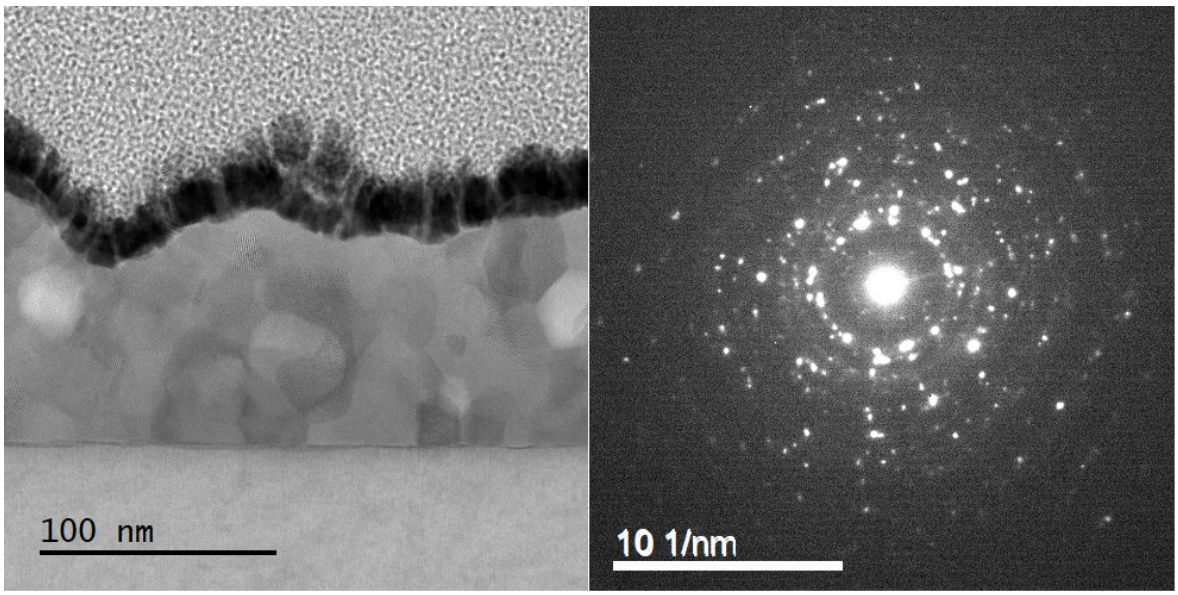

Figure AI.11: Polycrystalline LLZO and LZO on STO substrate with rings of diffraction spots potentially relating to both phases. ADF Image taken on JEOL ARM 200CF for best representation of grain contrast. DP acquired on JEOL 2100+ at 200 keV, camera length: 25 cm

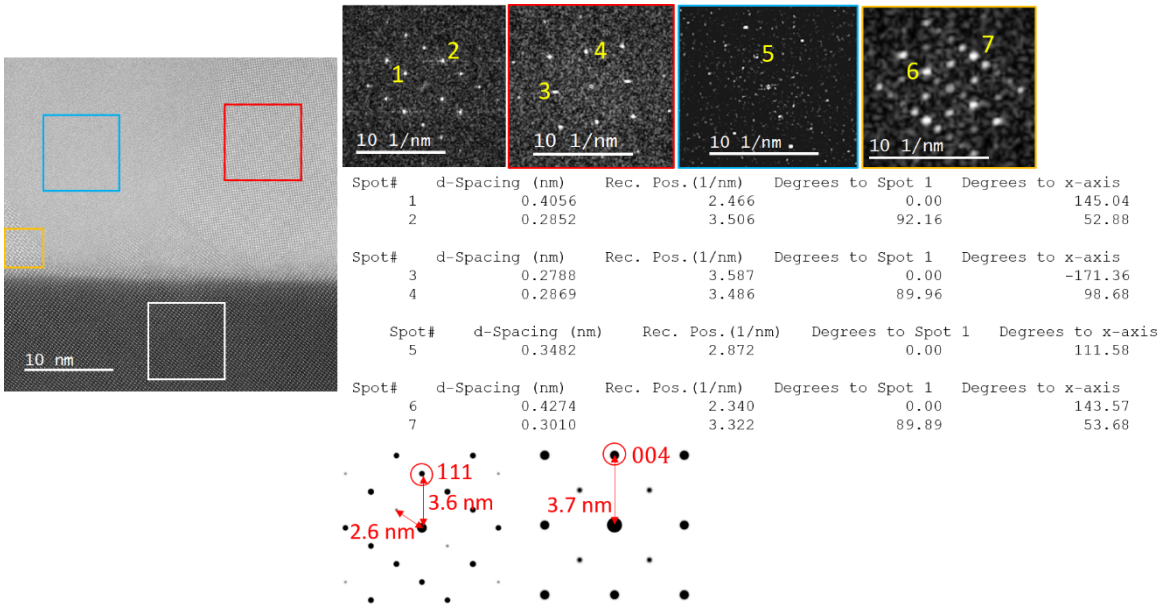

Spot#	d-Spacing (nm)	Rec. Pos.(1/nm)	Degrees to Spot 1	Degrees to x-axis
1	0.4056	2.466	0.00	145.04
2	0.2852	3.506	92.16	52.88

Spot#	d-Spacing (nm)	Rec. Pos.(1/nm)	Degrees to Spot 1	Degrees to x-axis
3	0.2788	3.587	0.00	-171.36
4	0.2869	3.486	89.96	98.68

Spot#	d-Spacing (nm)	Rec. Pos.(1/nm)	Degrees to Spot 1	Degrees to x-axis
5	0.3482	2.872	0.00	111.58

Spot#	d-Spacing (nm)	Rec. Pos.(1/nm)	Degrees to Spot 1	Degrees to x-axis
6	0.4274	2.340	0.00	143.57
7	0.3010	3.322	89.89	53.68

Figure AI.12: White box) STO(111) along $[10\bar{1}]$ ZA with a 10% error between experimental and simulated DPs. Red box) c-LZO, along [100] ZA, with a 6% difference between simulated and experimental spacings. Red and yellow box) Unidentified ZA either relating to the $[1\bar{2}1]$ of LLZO or LZO (blue), yellow remains unknown and could be a combination of grains overlapping. Data acquired on JEOL ARM 300CF at ePSIC (300 keV)

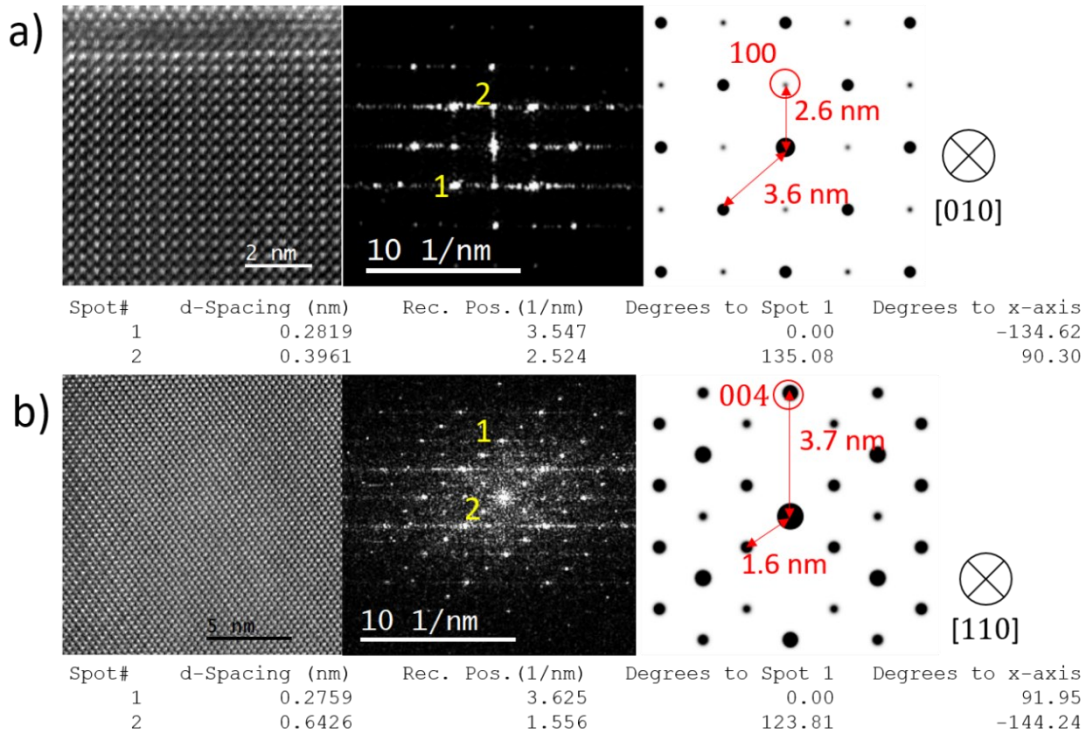

Figure A.13I: a) [010] ZA on STO(100) substrate with a 3% error in experimental DP spacing to the 100 spot. b) [110] ZA of LLZO or LZO, with a 3% error short of the spacing expected for LZO (simulation shown) and 14% short of the simulated spacing for LLZO. Relative to the 3% error of the STO diffractogram the film is identified as LZO. Data acquired on JEOL ARM200CF at 200 keV.

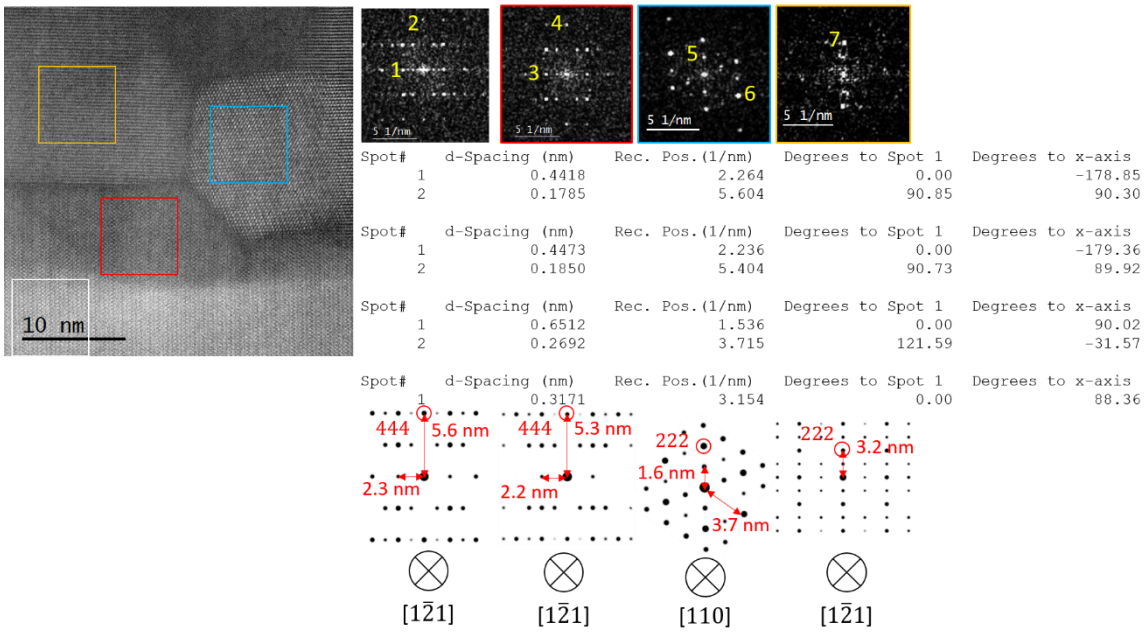

Figure AI.14: White box) GGG(111) substrate along [121] ZA with a 2% error in experimental and theoretical DP spacing. Red box) [121] ZA of LLZO with 2% error, blue box) [110] ZA of LZO with a 4% error, and yellow box) [121] ZA of LZO with a 1% error between experimental and simulated DP. Data taken on JEOL ARM200CF at 200 keV

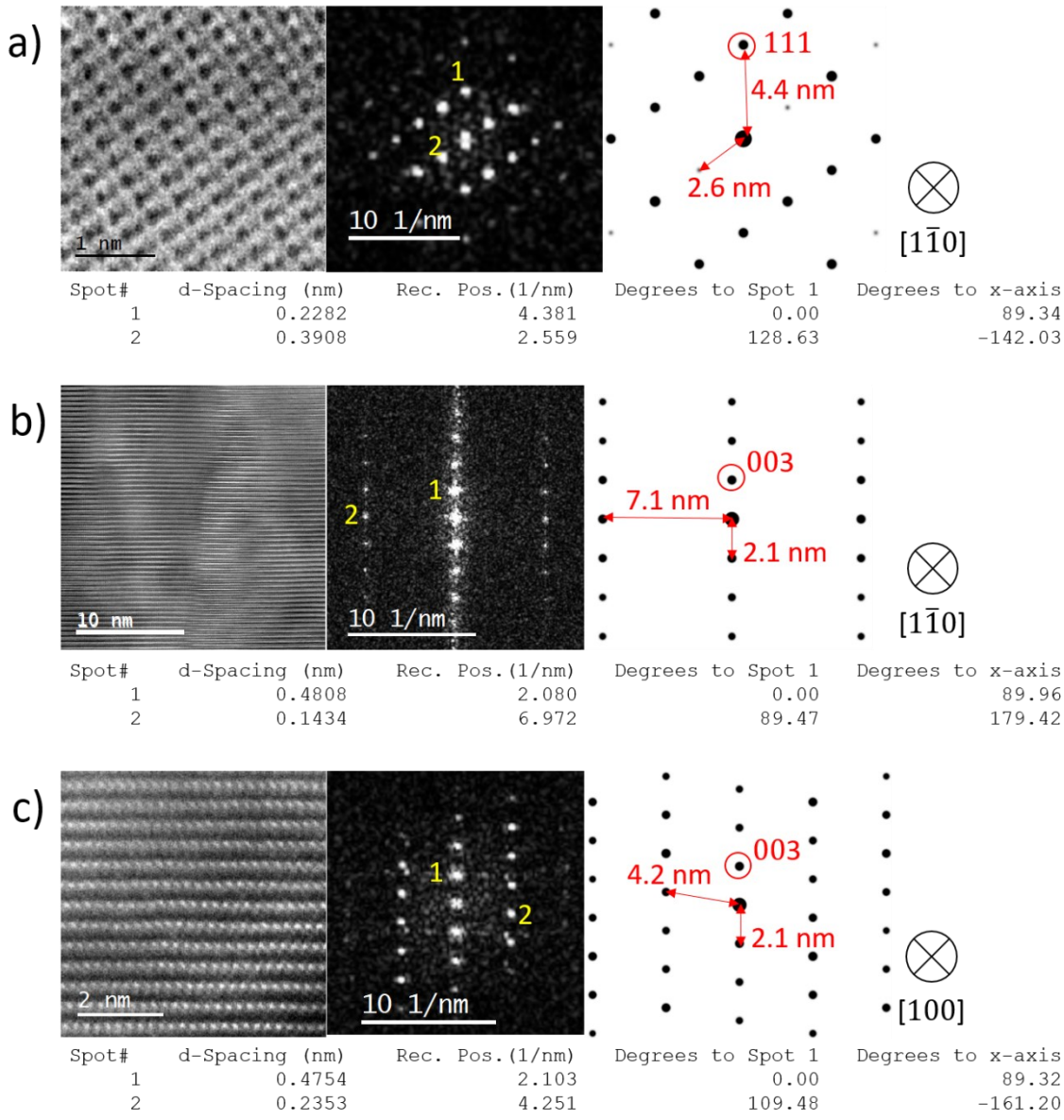

Figure AI.15: a) STO(111) substrate along [110] ZA in STO/LCO/LLZO heterostructure samples, with a 1% error in experimental and simulated DP distances. B) r-LCO along the [110] ZA, with a 1% error and c) r-LCO along [100] ZA with a 1% error between experimental on simulated DP values. Data acquired on JEOL ARM200CF at 200 keV

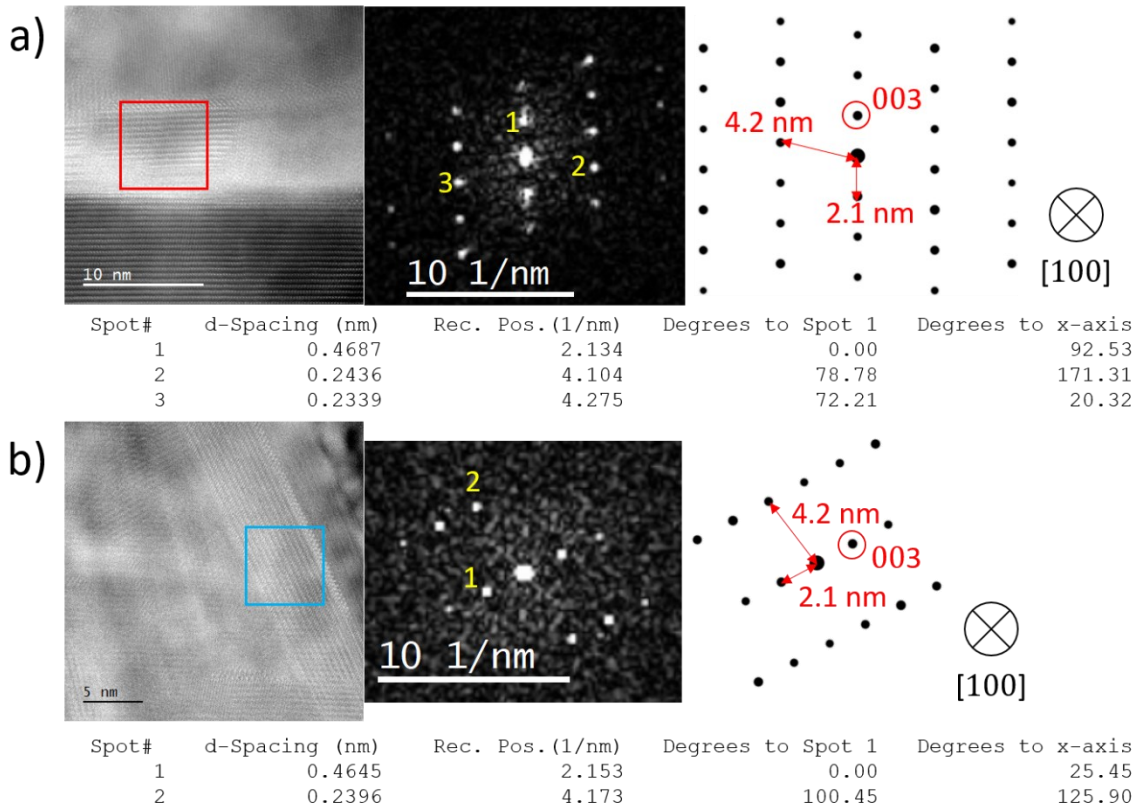

Spot#	d-Spacing (nm)	Rec. Pos.(1/nm)	Degrees to Spot 1	Degrees to x-axis
1	0.4687	2.134	0.00	92.53
2	0.2436	4.104	78.78	171.31
3	0.2339	4.275	72.21	20.32

Spot#	d-Spacing (nm)	Rec. Pos.(1/nm)	Degrees to Spot 1	Degrees to x-axis
1	0.4645	2.153	0.00	25.45
2	0.2396	4.173	100.45	125.90

Figure AI.16: Crystallites at LCO/LLZO interface on STO(111) substrate (calibrated in Figure AI.15). a) 2% error in simulated r-LCO phase, although with matching symmetry between the experimental DP and simulated DP for the [100] ZA. b) Second example of r-LCO simulation matching the spacing of the diffractogram within a 2% error, alongside equivalent angles between the constituent spot in the patterns. Data acquired on JEOL ARM200CF at 200 keV.

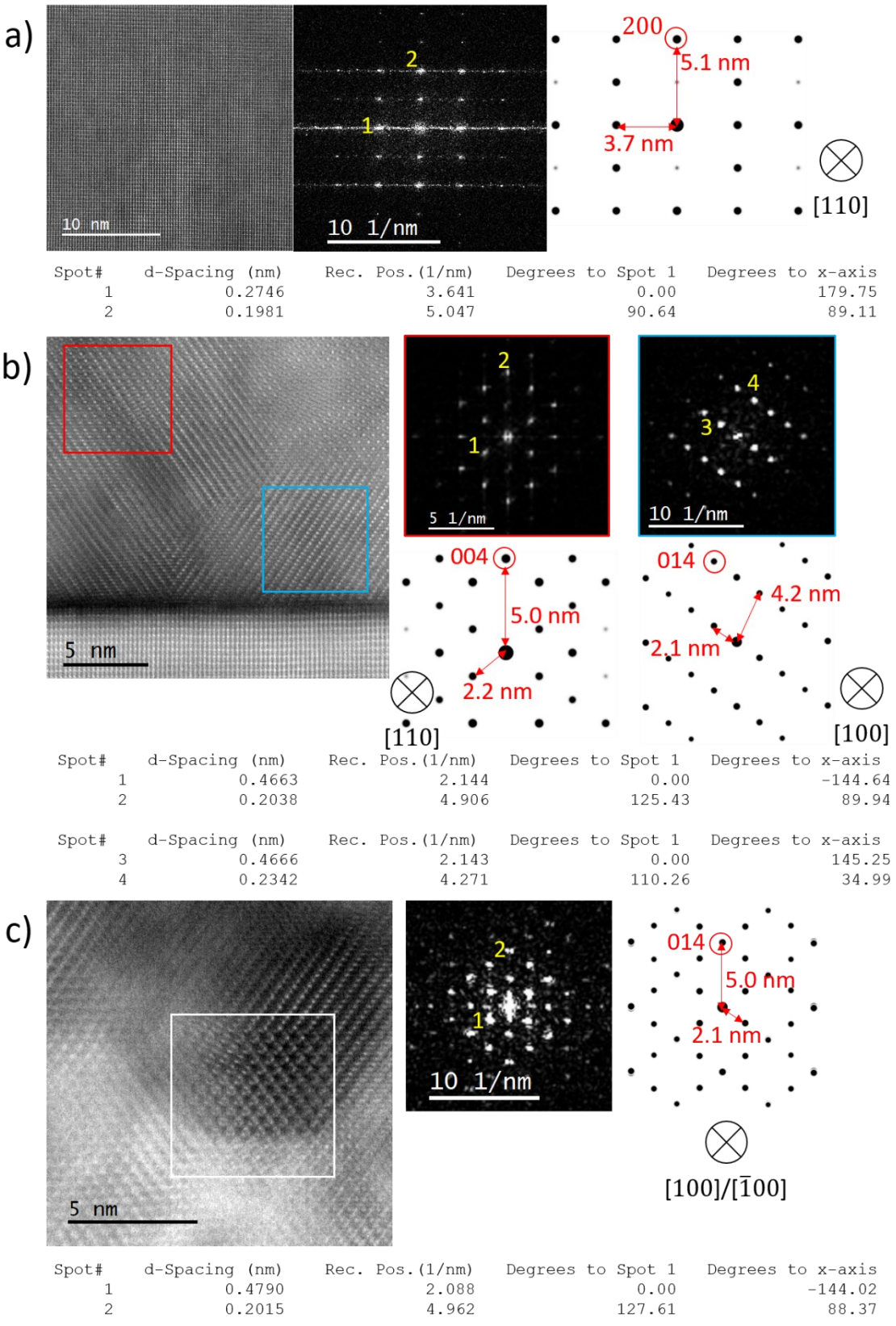

Spot#	d-Spacing (nm)	Rec. Pos.(1/nm)	Degrees to Spot 1	Degrees to x-axis
1	0.2746	3.641	0.00	179.75
2	0.1981	5.047	90.64	89.11

Spot#	d-Spacing (nm)	Rec. Pos.(1/nm)	Degrees to Spot 1	Degrees to x-axis
1	0.4663	2.144	0.00	-144.64
2	0.2038	4.906	125.43	89.94

Spot#	d-Spacing (nm)	Rec. Pos.(1/nm)	Degrees to Spot 1	Degrees to x-axis
3	0.4666	2.143	0.00	145.25
4	0.2342	4.271	110.26	34.99

Spot#	d-Spacing (nm)	Rec. Pos.(1/nm)	Degrees to Spot 1	Degrees to x-axis
1	0.4790	2.088	0.00	-144.02
2	0.2015	4.962	127.61	88.37

Figure AI.17: a) STO(100) substrate in STO/LCO/LLZO heterostructure, viewed along [110] ZA with 1% in experimental and simulated values. b) s-CO (red box) along [110] ZA with 2% error and r-LCO (blue box) with a 2% error along the [100] ZA. c) Overlapping r-LCO grains, along the [100] and [100] ZA as HAADF contrast does not match that of s-CO, with a 1% error between experimental and simulated lattice parameters. Data acquired on JEOL ARM200CF at 200 keV.

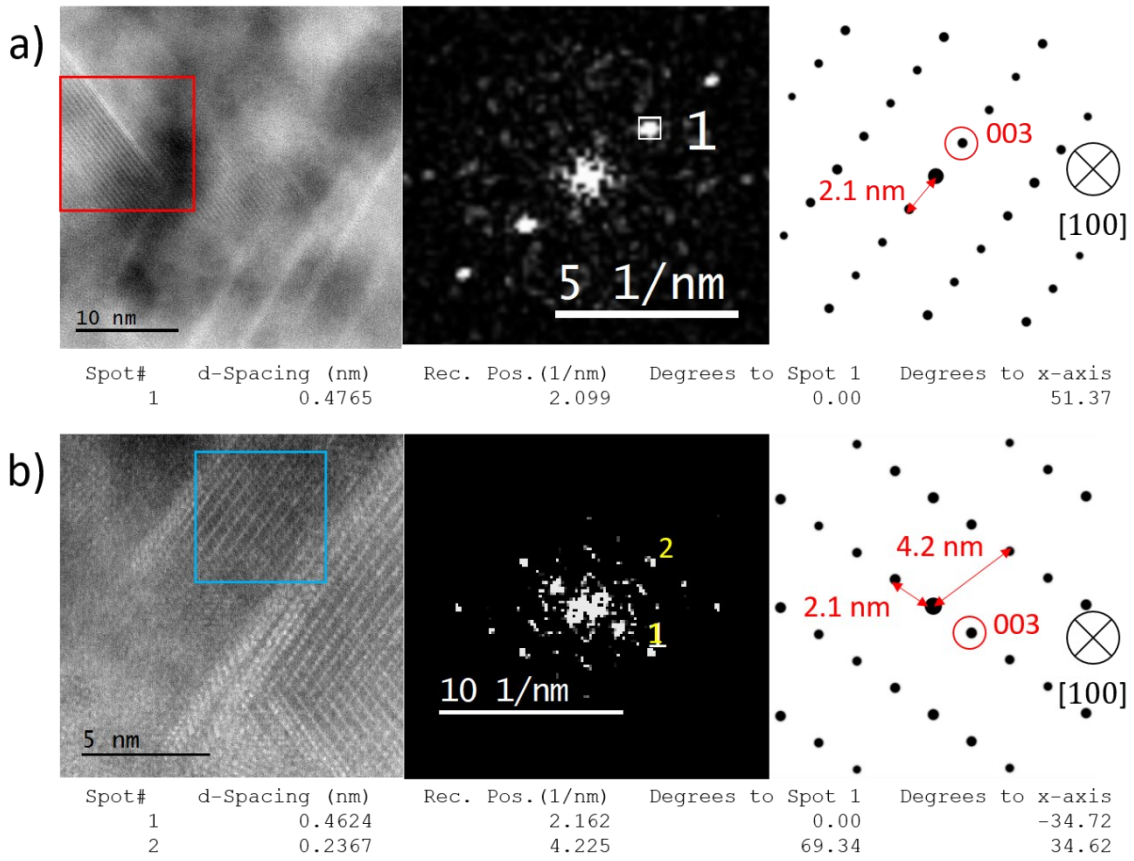

Figure AI.18: LCO crystallites on sample presented in Figure AI.17. a) r-LCO with spacing of lattice planes within 1% of simulated values. b) Crystallites close to a ZA, matching the [100] of r-LCO within a 1% to 3% error relative to the simulated r-LCO[100] DP. Error here is likely to originate from the size of the spots and pixel contribution in the diffractogram. Data acquired on JEOL ARM200CF at 200 keV

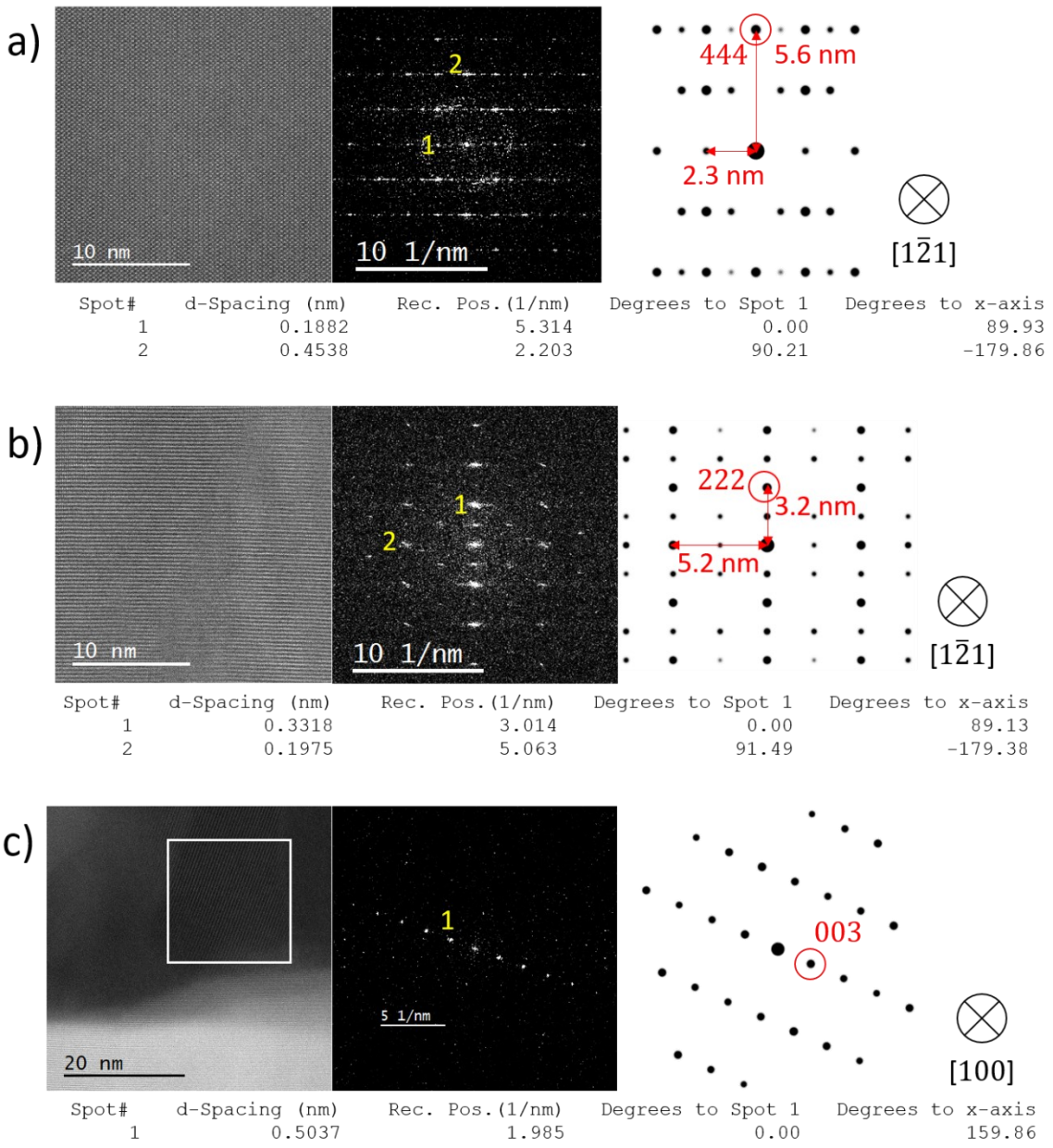

Figure AI.19: a) GGG(111) substrate viewed along the [121] ZA, with a 5% error in observed and simulated DP. b) LZO along the [121] ZA with a 3% error between experimental and expected values. c) Lattice planes of crystalline LCO in contact with electrolyte surface, diffraction pattern spacing of the spot relating to the 003 DP spot in the simulation has a 5% error from the experimentally observed distance. The LCO grains is likely r-LCO, viewed near to the [100] or equivalent ZA. Data acquired on JEOL ARM 300CF at 300 keV

Appendix II

Voltage-Current Plots Relating to Charge Cycled Particle and Heterostructure Samples

Below are Tables and Figures relating to the process of charge cycling through all three heterostructure samples. Table x contains the detailed information of biasing applied to sections cut from each lamella, including the particle samples. Subsequent voltage current curves are displayed in Figure x to Figure x whereby current was passed through the samples ten times, with the exception of one pristine pellet sample subjected to a hundred cycles. Each cycle between the two voltage limits lasted 30 minutes (± 2 minutes). For clarity of plotting the voltage cycles, every second voltage cycle over ten cycles, or every tenth cycle for a hundred cycles are plotted on the graphs.

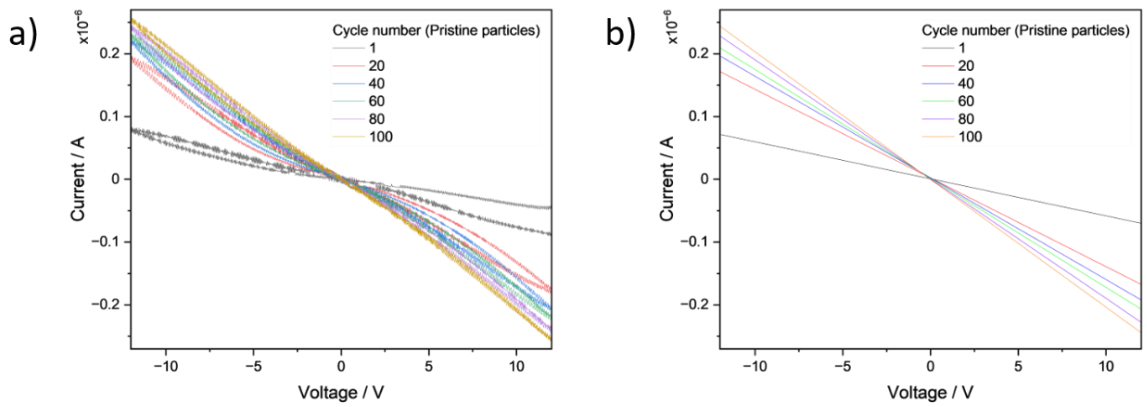

Figure AII.1: Selected voltage cycles between 12V and -12V, applied to a pristine pellet of LCO/LLZO powders. A large increase in resistance (gradient) is seen between charge cycle one and charge cycle 20, with a more gradual increase up to chare cycle 100. a) Raw data, b) linear fits to curves in a) as a visual guide to approximate changes in gradients.

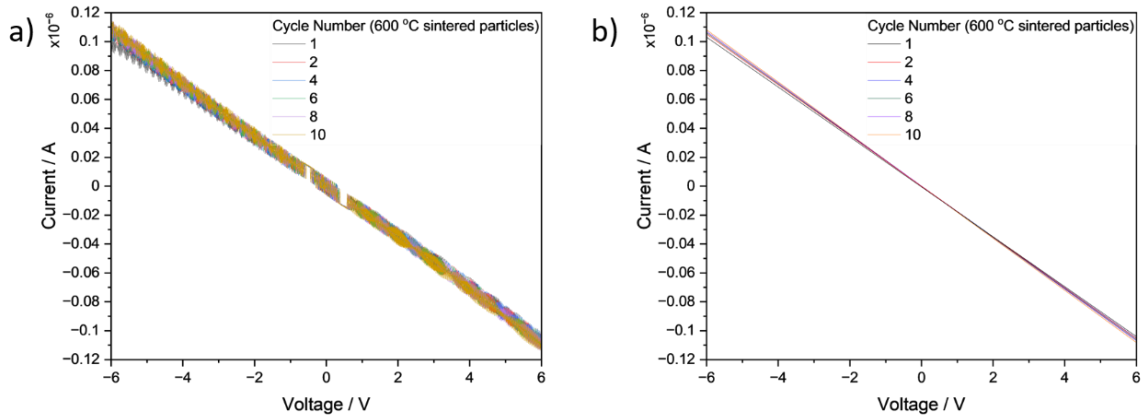

Figure AII.2: Selected voltage cycles between 6V and -6V, applied to a samples of LCO/LLZO powders sintered at 600 °C. No considerable increase in resistance is observed after 10 cycles, suggesting electrochemical changes in the pristine samples do not occur in on a scale clearly distinguishable from thermal decomposition cause by sintering at 600 °C for 1 hour. a) Raw data, b) linear fits to curves in a) as a visual guide to approximate changes in gradients.

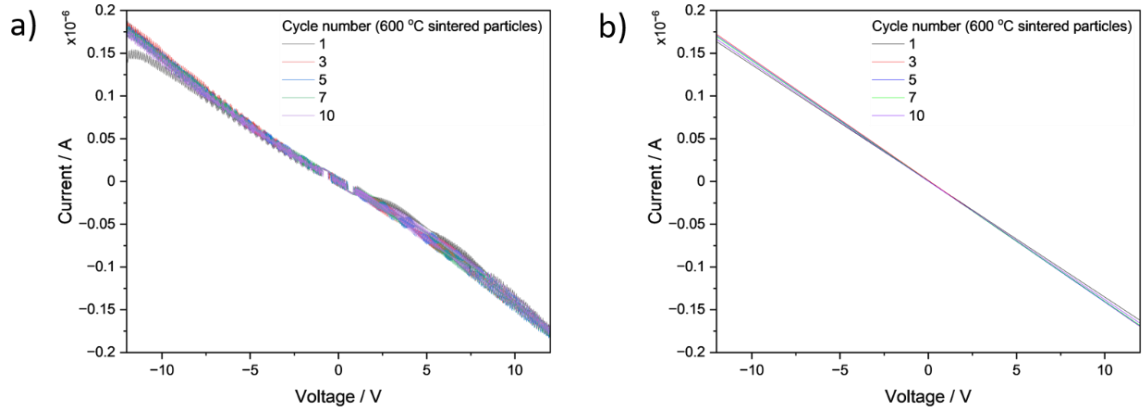

Figure AII.3: Selected voltage cycles between 12V and -12V, applied to samples of LCO/LLZO powders sintered at 600 °C. No considerable increase in resistance is observed after 10 cycles, although some hysteresis is present suggesting minor electrochemical changes at these extreme voltage limits. This further supports that major contribution to reduction in Li conductivity in particle and heterostructure samples being thermal decomposition cause by sintering. a) Raw data, b) linear fits to curves in a) as a visual guide to approximate changes in gradients.

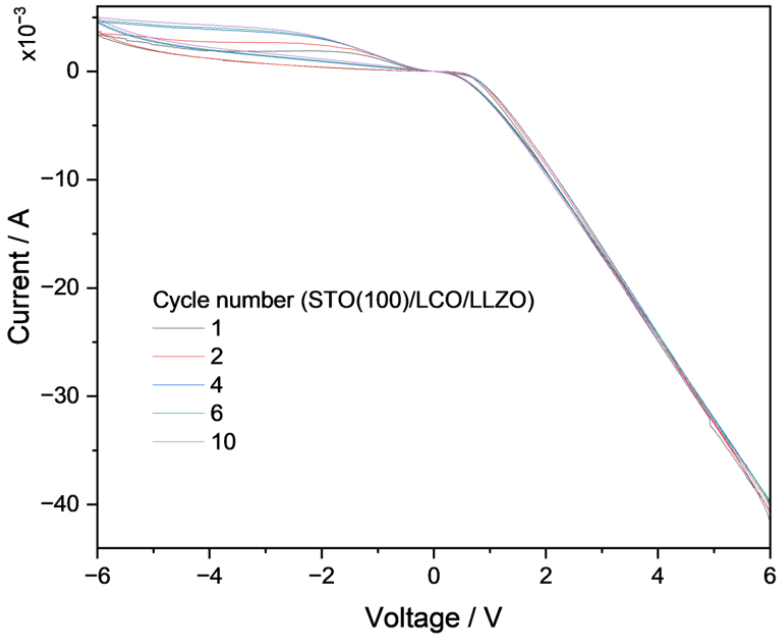

Figure AII.4: Selected voltage cycles between 6V and -6V, applied to a STO(100)/LCO/LLZO heterostructure annealed at 600 °C for 30 minutes. A linear increase in negative current is observed at positive potentials, with small positive currents under negative applied bias.

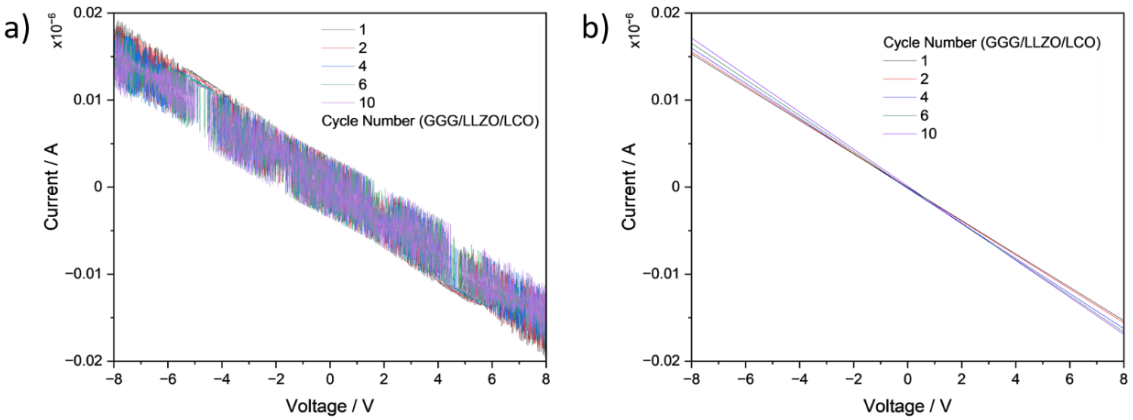

Figure AII.5: Selected voltage cycles between 8V and -8V, applied to a GGG/LLZO/LCO heterostructure annealed in pristine condition. The current changes linearly at all applied voltages and did not significantly change across 10 charge cycles.

Abbreviations

Aluminium oxide	ALO
Annular bright field	ABF
Anti-phase twin	APT
Atomic resolution	AR
Backscattered electron	BSE
Bright field	BF
Cobalt	Co
Cobalt Oxide	CO
Condenser aperture	CA
Condenser lens	CL
Dark field	DF
Diffraction pattern	DP
Dimethyl carbonate	DMC
Electrode-electrolyte interface	EEI
Electron backscatter diffraction	EBSD
Electron energy loss spectroscopy	EELS
Energy dispersive spectroscopy	EDS
Ethylene carbonate	EC
Everhart-Thornley	EHT
Focused ion beam	FIB
Gadolinium gallium garnet	GGG
Grain boundary	GB
High angle annular dark field	HAADF
High resolution	HR

Highest occupied molecular orbital	HOMO
Lanthanum	La
Liquid electrolyte	LE
Lithium	Li
Lithium cobalt oxide	LCO
Lithium lanthanum zirconium oxide	LLZO
Lithium metal oxide	LMO
Lithium phosphoxinitride	LiPON
Low angle annular dark field	LAADF
Low temperature	LT
Lowest unoccupied molecular orbital	LUMO
Manganese	Mn
Nickle	Ni
Objective aperture	OA
Photomultiplier tube	PMT
Precision ion polishing system	PIPS
Pulsed laser deposition	PLD
Rock salt	RS
Secondary electron	SE
Selected area diffraction	SAD
Sodium	Na
Solid electrolyte interface	SEI
Solid-state battery	SSB
SSE	SSE
Strontium titanate	STO
Transmission electron microscopy	TEM

Upper electron detector	UED
Upper secondary electron detector	USD
Window of stability	WOS
X-ray diffraction	XRD
X-ray Photoelectron spectroscopy	XPS
Zirconium	Zr

Bibliography

1. Brazier A. First Cross-Section Observation of an All Solid-State Lithium-Ion “Nanobattery” by Transmission Electron Microscopy. Chem Mater. 2008;20(6):2352 – 9.
2. Ostfeld AE, Gaikwad AM, Khan Y, Arias AC. High-performance flexible energy storage and harvesting system for wearable electronics. Scientific Reports. 2016;6(1):26122.
3. Browning JF. In Situ Determination of the Liquid/Solid Interface Thickness and Composition for the Li Ion Cathode $LiMn_{1.5}Ni_{0.5}O_4$. ACS Appl Mater Interfaces. 2014;6:18569 − 76.
4. Gauthier M. Electrode−Electrolyte Interface in Li-Ion Batteries: Current Understanding and New Insights. J Phys Chem Lett. 2015;6:4653−72.
5. Richards WD. Interface Stability in Solid-State Batteries. Chem Mater. 2016;28:266 - 73.
6. Tatara R. The Effect of Electrode-Electrolyte Interface on the Electrochemical Impedance Spectra for Positive Electrode in Li-Ion Battery. Journal of The Electrochem Soc. 2019;166(3):A5090 - A8.
7. Hwang S, Kim D-H, Shin JH, Jang JE, Ahn KH, Lee C, Lee H. Ionic Conduction and Solution Structure in $LiPF_6$ and $LiBF_4$ Propylene Carbonate Electrolytes. The Journal of Physical Chemistry C. 2018;122(34):19438-46.
8. Hayashi A. High lithium ion conduction of sulfide glass-based solid electrolytes and their application to all-solid-state batteries. Journal of Non-Crystalline Solids. 2009;355:1919 – 23.
9. Popovici D. Preparation of Lithium Aluminum Titanium Phosphate Electrolytes Thick Films by Aerosol Deposition Method. J Am Ceram Soc. 2011;94(11):3847 – 50.
10. Hayashi A. superionic glass-ceramic electrolytes for room-temperature rechargeable sodium batteries. Nat Comm. 2012:1 - 5.
11. Kim S. Epitaxial growth and lithium ion conductivity of lithium-oxide garnet for an all solid-state battery electrolyte. Dalton Trans. 2013;42:13112 – 7.
12. Gai J. Improving the Li-ion conductivity and air stability of cubic $Li_7La_3Zr_2O_{12}$ by the co-doping of Nb, Y on the Zr site. Journal of the European Ceramic Society. 2018;38:1673 – 8.
13. Shin DO. Synergistic multi-doping effects on the $Li_7La_3Zr_2O_{12}$ solid electrolyte for fast lithium ion conduction. Scientific RepoRts. 2015;Dong Ok Shin.
14. Hanc E, Zając W, Molenda J. Synthesis procedure and effect of Nd, Ca and Nb doping on structure and electrical conductivity of $Li_7La_3Zr_2O_{12}$ garnets. Solid State Ionics. 2014;262:617-21.
15. Zhang M, Pan P, Cheng Z, Mao J, Jiang L, Ni C, et al. Flexible, Mechanically Robust, Solid-State Electrolyte Membrane with Conducting Oxide-Enhanced 3D Nanofiber Networks for Lithium Batteries. Nano Letters. 2021;21(16):7070-8.
16. Dawson JA. Atomic-Scale Influence of Grain Boundaries on Li-Ion Conduction in Solid Electrolytes for All-Solid-State Batteries. J Am Chem Soc. 2018;140:362 − 8.
17. Birkl CR. Degradation diagnostics for lithium ion cells. Journal of Power Sources. 2017;341:373 - 86.
18. Dahéron L. Electron Transfer Mechanisms upon Lithium Deintercalation from $LiCoO_2$ to CoO_2 Investigated by XPS. Chem Mater. 2008;20:583 – 90.
19. Porthault H. Raman study of the spinel-to-layered phase transformation in sol–gel $LiCoO_2$ cathode powders as a function of the post-annealing temperature. Vibrational Spectroscopy. 2012;62:152 - 8.
20. Jorn R. Atomistic Modeling of the Electrode−Electrolyte Interface in Li-Ion Energy Storage Systems: Electrolyte Structuring. J Phys Chem C`. 2013;117:3747 − 61.
21. Kitaura H. Fabrication of electrode–electrolyte interfaces in all-solid-state rechargeable lithium batteries by using a supercooled liquid state of the glassy electrolytes. J Mater Chem. 2011;21:118 – 24.
22. Kim NY. Microstructural study on degradation mechanism of layered $LiNi_{0.6}Co_{0.2}Mn_{0.2}O_2$ cathode materials by analytical transmission electron microscopy. Journal of Power Sources. 2016;307.

23. Yan Z. Effect of niobium doping on the structure and electrochemical performance of $LiNi_{0.5}Co_{0.2}Mn_{0.3}O_2$ cathode materials for lithium ion batteries. Ceramics International. 2017;43:3866 – 72.
24. Fu Z-H, Chen X, Zhang Q. Review on the lithium transport mechanism in solid-state battery materials. WIREs Computational Molecular Science. 2023;13(1):e1621.
25. Kim T, Song W, Son D-Y, Ono LK, Qi Y. Lithium-ion batteries: outlook on present, future, and hybridized technologies. Journal of Materials Chemistry A. 2019;7(7):2942-64.
26. Asenbauer J, Eisenmann T, Kuenzel M, Kazzazi A, Chen Z, Bresser D. The success story of graphite as a lithium-ion anode material – fundamentals, remaining challenges, and recent developments including silicon (oxide) composites. Sustainable Energy & Fuels. 2020;4(11):5387-416.
27. Luiso S, Fedkiw P. Lithium-ion battery separators: Recent developments and state of art. Current Opinion in Electrochemistry. 2020;20:99-107.
28. He K. Battery Manufacturing Basics from CATL's Cell Production Line 2021 [Available from: https://medium.com/batterybits/battery-manufacturing-basics-from-catls-cell-production-line-part-1-d6bb6aa0b499.
29. Qian G, Monaco F, Meng D, Lee S-J, Zan G, Li J, et al. The role of structural defects in commercial lithium-ion batteries. Cell Reports Physical Science. 2021;2:100554.
30. Meyer C, Bockholt H, Haselrieder W, Kwade A. Characterization of the calendering process for compaction of electrodes for lithium-ion batteries. Journal of Materials Processing Technology. 2017;249:172-8.
31. ScienceDirect Cotcpfcoefl-ib-. Anode Binders For Lithium Batteries 2023 [Available from: https://www.targray.com/li-ion-battery/anode-materials/binders.
32. Aryal S. Structural Studies of Capacity Activation and Reduced Voltage Fading in Li-Rich, Mn-Ni-Fe Composite Oxide Cathode. Journal of The Electrochem Soc. 2018;165(2):71 - 8.
33. Ovejas VJ, Cuadras A. Effects of cycling on lithium-ion battery hysteresis and overvoltage. Scientific Reports. 2019;9(1):14875.
34. Kong F. Ab initio study of doping effects on $LiMnO_2$ and Li_2MnO_3 cathode materials for Li-ion batteries. J Mater Chem A. 2015;3:8489 – 500.
35. Montoro LA. Changes in the Electronic Structure of Chemically Deintercalated $LiCoO_2$. Electrochemical and Solid-State Letters. 2000;3(9):410 - 2.
36. Dahbi M. Comparative study of EC/DMC LiTFSI and $LiPF_6$ electrolytes for electrochemical storage. Journal of Power Sources. 2011;196:9743 – 50.
37. Nowak S. Ultra-thin LiPON films - Fundamental properties and application in solid state thin film model batteries. Journal of Power Sources. 2015;275:144 - 50.
38. Larcher D. Towards greener and more sustainable batteries for electrical energy storage. Nature Chemistry. 2015;7:19 - 29.
39. Famprikis T. Fundamentals of inorganic solid-state electrolytes for batteries. Nat Mat. 2019;18:1278 – 91.
40. Kang K. Electrodes with High Power and High Capacity for Rechargeable Lithium Batteries. Science. 2006;311:977 - 80.
41. Dahéron L. Electron Transfer Mechanisms upon Lithium Deintercalation from LiCoO2 to CoO2 Investigated by XPS. Chem Mater 2008;20:583 - 90.
42. Li N, Sun M, Kan WH, Zhuo Z, Hwang S, Renfrew SE, et al. Layered-rocksalt intergrown cathode for high-capacity zero-strain battery operation. Nature Communications. 2021;12(1):2348.
43. Li S, Sun Y, Gao A, Zhang Q, Lu X, Lu X. Sustainable $LiCoO_2$ by collective glide of CoO_6 slabs upon charge/discharge. Proceedings of the National Academy of Sciences. 2022;119(20):e2120060119.
44. Hellenbrandt M. The Inorganic Crystal Structure Database (ICSD)—Present and Future. Crystallography Reviews. 2004;10(1):17-22.
45. Mishra A. Electrode materials for lithium-ion batteries. Materials Science for Energy Technologies. 2018;1:182 – 7.
46. Spinner N. Investigation of metal oxide anode degradation in lithium-ion batteries via identical-location TEM. J Mater Chem A. 2014;2(6):1627 – 30.

47. Song M. Recent Advances in Zn-Ion Batteries. Adv Funct Mater. 2018;28.
48. Sun G, Yu F-D, Lu M, Zhu Q, Jiang Y, Mao Y, et al. Surface chemical heterogeneous distribution in over-lithiated $Li_{1+x}CoO_2$ electrodes. Nature Communications. 2022;13(1):6464.
49. Antaya M, Cearns K, Preston JS, Reimers JN, Dahn JR. In situ growth of layered, spinel, and rock-salt $LiCoO_2$ by laser ablation deposition. Journal of Applied Physics. 1994;76(5):2799-806.
50. Porthault H, Baddour-Hadjean R, Le Cras F, Bourbon C, Franger S. Raman study of the spinel-to-layered phase transformation in sol–gel $LiCoO_2$ cathode powders as a function of the post-annealing temperature. Vibrational Spectroscopy. 2012;62:152-8.
51. Jain A, Ong SP, Hautier G, Chen W, Richards WD, Dacek S, et al. Commentary: The Materials Project: A materials genome approach to accelerating materials innovation. APL Materials. 2013;1(1).
52. Momma K, Izumi F. VESTA: A Three-Dimensional Visualization System for Electronic and Structural Analysis. Journal of Applied Crystallography - J APPL CRYST. 2008;41:653-8.
53. Anderson DL. Theory of the Earth. USA: Blackwell Scientific Publications; 1989.
54. McManus MC. Environmental consequences of the use of batteries in low carbon systems: The impact of battery production. Applied Energy. 2012;93:288 – 95.
55. Thackeray MM. Advances in manganese-oxide 'composite' electrodes for lithium-ion batteries. J Mater Chem A. 2005;15:2257 – 67.
56. Slater MD. Sodium-Ion Batteries. Adv Funct Mater. 2013;23:947 – 58.
57. Doeff MM. Titanate Anodes for Sodium Ion Batteries. J Inorg Organomet Polym. 2014;24:5 - 14.
58. Aryal S. Structural Studies of Capacity Activation and Reduced Voltage Fading in Li-Rich, Mn-Ni-Fe Composite Oxide Cathode. Journal ofThe Electrochemical Society. 2018;165(2):71 - 8.
59. Li F. Sodium-based batteries: from critical materials to battery systems. J Mater Chem A. 2019;7:9406 – 31.
60. Yan Z. A tightly integrated sodium titanate-carbon composite as an anode material for rechargeable sodium ion batteries. Journal of Power Sources. 2015;274:8 - 14.
61. Farahani S. Chapter 6 - Battery Life Analysis. In: Farahani S, editor. ZigBee Wireless Networks and Transceivers. Burlington: Newnes; 2008. p. 207-24.
62. Liao Y, Yuan L, Xiang J, Zhang W, Cheng Z, He B, et al. Realizing both high gravimetric and volumetric capacities in Li/3D carbon composite anode. Nano Energy. 2020;69:104471.
63. Liu C, Neale ZG, Cao G. Understanding electrochemical potentials of cathode materials in rechargeable batteries. Materials Today. 2016;19(2):109-23.
64. Orendorff CJ. The Role of Separators in Lithium-Ion Cell Safety. The Electrochemical Society Interface. 2012;21(2):61.
65. Bachman JC. Inorganic Solid-State Electrolytes for Lithium Batteries: Mechanisms and Properties Governing Ion Conduction. Chem Rev. 2016;116:140 − 62.
66. Balasubramanian M. In situ X-ray diffraction and X-ray absorption studies of high-rate lithium-ion batteries. Journal of Power Sources 2001;92:1 - 8.
67. Ramachandramoorthy R. Pushing the Envelope of In Situ Transmission Electron Microscopy. ACS Nano. 2015;9(5):4675 – 85.
68. Takada K. Progress and prospective of solid-state lithium batteries. Acta Materialia. 2013;61:759 – 70.
69. Nowak S. Ultra-thin LiPON films e Fundamental properties and application in solid state thin film model batteries. Journal of Power Sources. 2015;275:144 - 50.
70. Bachman JC, Muy S, Grimaud A, Chang H-H, Pour N, Lux SF, et al. Inorganic Solid-State Electrolytes for Lithium Batteries: Mechanisms and Properties Governing Ion Conduction. Chemical Reviews. 2016;116(1):140-62.
71. Sakuda A. Sulfide Solid Electrolyte with Favorable Mechanical Property for All-Solid-State Lithium Battery. Sci Rep. 2013;3.
72. Chen L-J. Oxygen vacancy in $LiTiPO_5$ and $LiTi_2(PO_4)_3$: A first-principles study. Phys Lett A. 2011;375:934–8.
73. Lim M-S. First-principles study of lithium-ion diffusion in β-Li_3PS_4 for solid-state electrolytes. Curr Appl Phys. 2018;18:541 – 5.

74. Senevirathne K. A new crystalline LiPON electrolyte: Synthesis, properties, and electronic structure. Solid State Ionics. 2013;233:95 - 101.
75. Sommer C. Quasiparticle band structure of alkali-metal fluorides, oxides, and nitrides. Phys Rev B. 2012;85.
76. Zajac W. Towards control over redox behaviour and ionic conductivity in $LiTi_2(PO_4)_3$ fast lithium-ion conductor. Acta Materialia. 2017;140:417 - 23.
77. Liu D. Positive film-forming effect offluoroethylene carbonate (FEC) on highvoltage cycling with three-electrode $LiCoO_2$/Graphite pouch cell. Electrochemical Acta. 2018;269:378 - 87.
78. Yu X. Electrode−Electrolyte Interfaces in Lithium−Sulfur Batteries with Liquid or Inorganic Solid Electrolytes. Acc Chem Res. 2017;50:2653 - 60.
79. Shen C. In Situ AFM Imaging of Solid Electrolyte Interfaces on HOPG with Ethylene Carbonate and Fluoroethylene Carbonate-Based Electrolytes. ACS Appl Mater Interfaces 2015;7:25441 − 7.
80. Cherkashinin G. Electron Spectroscopy Study of $Li[Ni,Co,Mn]O_2$/Electrolyte Interface: Electronic Structure, Interface Composition, and Device Implications Chem Mater. 2015;27:2875 − 87.
81. Wu H. Stable cycling of double-walled silicon nanotube battery anodes through solid–electrolyte interphase control. Nat Nanotech. 2012;7:310 - 5.
82. Zeng Z, Liang W-I, Liao H-G, Xin HL, Chu Y-H, Zheng H. Visualization of Electrode–Electrolyte Interfaces in $LiPF_6$/EC/DEC Electrolyte for Lithium Ion Batteries via in Situ TEM. Nano Letters. 2014;14(4):1745-50.
83. Paraschiv GL. Structural stability of NaPON glass upon heating in air and nitrogen. Journal of Non-Crystalline Solids. 2018;482:137 – 46.
84. Wei K. Lithium phosphorous oxynitride (LiPON) coated $NiFe_2O_4$ anode material with enhanced electrochemical performance for lithium ion batteries. Journal of Alloys and Compounds. 2018;769:110 - 9.
85. Zhao S. A solid-state electrolyte lithium phosphorus oxynitride film prepared by pulsed laser deposition. Thin Solid Films. 2002;415:108 - 13.
86. Ponrouch A. Non-Aqueous Electrolytes for Sodium-Ion Batteries. Journal of Materials Chemistry A. 2012:1-21.
87. Kamaya N, Homma K, Yamakawa Y, Hirayama M, Kanno R, Yonemura M, et al. A lithium superionic conductor. Nature Materials. 2011;10(9):682-6.
88. Wang Z. In Situ STEM-EELS Observation of Nanoscale Interfacial Phenomena in All-Solid-State Batteries. Nano Lett. 2016;16:3760 − 7.
89. Paraschiv GL. Impact of nitridation of metaphosphate glasses on liquid fragility. Journal of Non-Crystalline Solids. 2016;441:22 - 8.
90. Kamaya N. A lithium superionic conductor. Nat Mat. 2011;10:682 - 6.
91. He X. Origin of fast ion diffusion in super-ionic conductors. Nat comm. 2017;8.
92. Jalem R. Concerted Migration Mechanism in the Li Ion Dynamics of GarnetType $Li_7La_3Zr_2O_{12}$. Chem Mater. 2013;25:425 − 30.
93. Koerver R. Chemo-mechanical expansion of lithium electrode materials – on the route to mechanically optimized all-solid-state batteries. Energy & Env Sci. 2018;11:2142 - 58.
94. Ross FM. Opportunities and challenges in liquid cell electron microscopy. Science. 2015;350(6267).
95. Shibata N. Atomic resolution electron microscopy in a magnetic field free environment. Nat comm. 2019;10.
96. Jinschek JR. Achieve atomic resolution in in situ S/TEM experiments to examine complex interface structures in nanomaterials. Curr Opn in Solid State and Mat Sci. 2017;21:77 – 91.
97. Liu G. Synthesis of $Li_7La_3Zr_2O_{12}$ Solid Electrolyte by Solid Phase Sintering Method. Mater Sci Eng. 2019.
98. Liu G, Li T, Xing Y, Pan W. Synthesis of $Li_7La_3Zr_2O_{12}$ Solid Electrolyte by Solid Phase Sintering Method. IOP Conference Series: Materials Science and Engineering. 2019;678(1):012150.
99. Ma C. Interfacial Stability of Li Metal−Solid Electrolyte Elucidated via in Situ Electron Microscopy. Nano Lett. 2016;16:7030−6.

100. Yang T. Nanostructured Garnet-Type Solid Electrolytes for Lithium Batteries: Electrospinning Synthesis of $Li_7La_3Zr_2O_{12}$ Nanowires and Particle Size-Dependent Phase Transformation. J Phys Chem C. 2015;119:14947−53.
101. Awaka J, Kijima N, Hayakawa H, Akimoto J. Synthesis and structure analysis of tetragonal $Li_7La_3Zr_2O_{12}$ with the garnet-related type structure. Journal of Solid State Chemistry. 2009;182(8):2046-52.
102. Jalem R, Yamamoto Y, Shiiba H, Nakayama M, Munakata H, Kasuga T, Kanamura K. Concerted Migration Mechanism in the Li Ion Dynamics of Garnet-Type $Li_7La_3Zr_2O_{12}$. Chem Mater. 2013;25(3):425-30.
103. Murugan R. Fast Lithium Ion Conduction in Garnet-Type $Li_7La_3Zr_2O_{12}$. Angew Chem Int Ed. 2007;46:7778 – 81.
104. He X, Zhu Y, Mo Y. Origin of fast ion diffusion in super-ionic conductors. Nature Communications. 2017;8(1):15893.
105. Villa A. Ionic conductivity optimization of composite polymer electrolytes through filler particle chemical modification. Ionics. 2021;27:2483 – 93.
106. Li C. Solid-state reactive sintering of dense and highly conductive Ta-doped $Li_7La_3Zr_2O_{12}$ using CuO as a sintering aid. J Mater Sci. 2020;55:16470 – 81.
107. Huang X. Synthesis of Ga-doped $Li_7La_3Zr_2O_{12}$ solid electrolyte with high Li+ ion conductivity. Ceramics International. 2021;47:2123 – 30.
108. Hanc E. Synthesis procedure and effect of Nd, Ca and Nb doping on structure and electrical conductivity of $Li_7La_3Zr_2O_{12}$ garnets. Solid State Ionics. 2014;262:617 – 21.
109. Shin DO. Synergistic multi-doping effects on the Li7La3Zr2O12 solid electrolyte for fast lithium ion conduction. Nat Sci Rep. 2015;5.
110. Thompson T. Tetragonal vs. cubic phase stability in Al – free Ta doped $Li_7La_3Zr_2O_{12}$ (LLZO). J Mater Chem A. 2014;2.
111. Gastol D, Capener M, Reynolds C, Constable C, Kendrick E. Microstructural design of printed graphite electrodes for lithium-ion batteries. Materials & Design. 2021;205:109720.
112. Fuchsbichler B. High capacity graphite–silicon composite anode material for lithium-ion batteries. Journal of Power Sources. 2011;196:2889 – 92.
113. Shannon RD. Revised Effective Ionic Radii and Systematic Studies of Interatomie Distances in Halides and Chaleogenides. Acta Cryst. 1976;32:751 - 67.
114. Marsh H. Activated Carbon. UK: Elsevier; 2006.
115. Dou X. Hard carbons for sodium-ion batteries: Structure, analysis, sustainability, and electrochemistry. Materials Today. 2019;23:87 - 104.
116. Dahbi M. Synthesis of hard carbon from argan shells for Naion batteries. J Mater Chem A. 2017;5:9917 – 28.
117. Zuo X. Silicon based lithium-ion battery anodes: A chronicle perspective review. Nano Energy. 2017;31:113 – 43.
118. Aoki Y, Oda M, Kojima S, Ishihama T, Nagashima T, Doi T, Inaba M. Predictive Characterization of SEI Formed on Graphite Negative Electrodes for Efficiently Designing Effective Electrolyte Solutions. ACS Applied Energy Materials. 2022;5(1):1085-94.
119. Dawson JA, Canepa P, Famprikis T, Masquelier C, Islam MS. Atomic-Scale Influence of Grain Boundaries on Li-Ion Conduction in Solid Electrolytes for All-Solid-State Batteries. Journal of the American Chemical Society. 2018;140(1):362-8.
120. He X, Sun H, Ding X, Zhao K. Grain Boundaries and Their Impact on Li Kinetics in Layered-Oxide Cathodes for Li-Ion Batteries. The Journal of Physical Chemistry C. 2021;125(19):10284-94.
121. Yu S, Siegel DJ. Grain Boundary Softening: A Potential Mechanism for Lithium Metal Penetration through Stiff Solid Electrolytes. ACS Applied Materials & Interfaces. 2018;10(44):38151-8.
122. Winiarski B, Gholinia A, Mingard K, Gee M, Thompson G, Withers PJ. Correction of artefacts associated with large area EBSD. Ultramicroscopy. 2021;226:113315.
123. Neumann A, Hamann TR, Danner T, Hein S, Becker-Steinberger K, Wachsman E, Latz A. Effect of the 3D Structure and Grain Boundaries on Lithium Transport in Garnet Solid Electrolytes. ACS Applied Energy Materials. 2021;4(5):4786-804.

124. Li Z, Yasui S, Takeuchi S, Creuziger A, Maruyama S, Herzing AA, et al. Structural study of epitaxial $LiCoO_2$ films grown by pulsed laser deposition on single crystal $SrTiO_3$ substrates. Thin Solid Films. 2016;612.
125. Birkl CR, Roberts MR, McTurk E, Bruce PG, Howey DA. Degradation diagnostics for lithium ion cells. Journal of Power Sources. 2017;341:373-86.
126. Jain A. The Materials Project: A materials genome approach to accelerating materials innovation. APL Mat. 2013;1.
127. Nomura Y, Yamamoto K, Hirayama T, Igaki E, Saitoh K. Visualization of Lithium Transfer Resistance in Secondary Particle Cathodes of Bulk-Type Solid-State Batteries. ACS Energy Letters. 2020;5(6):2098-105.
128. Zhu C, Fuchs T, Weber SAL, Richter FH, Glasser G, Weber F, et al. Understanding the evolution of lithium dendrites at $Li_{6.25}Al_{0.25}La_3Zr_2O_{12}$ grain boundaries via operando microscopy techniques. Nature Communications. 2023;14(1):1300.
129. Fu S, Arinicheva Y, Hüter C, Finsterbusch M, Spatschek R. Grain Boundary Characterization and Potential Percolation of the Solid Electrolyte LLZO. Batteries. 2023;9(4):222.
130. Katsui H, Yuji Y, Goto T. Orientation and Morphology of $LiCoO_2$ Prepared by Chemical Vapor Deposition on Al_2O_3 Single Crystal. Key Engineering Materials. 2012;508:300-3.
131. Kim S, Hirayama M, Taminato S, Kanno R. Epitaxial growth and lithium ion conductivity of lithium-oxide garnet for an all solid-state battery electrolyte. Dalton Transactions. 2013;42(36):13112-7.
132. Rasic D. Epitaxial Growth of Thin Films2019.
133. Mihailescu IN, György E. Pulsed Laser Deposition: An Overview. In: Asakura T, editor. International Trends in Optics and Photonics: ICO IV. Berlin, Heidelberg: Springer Berlin Heidelberg; 1999. p. 201-14.
134. McGinnis WC, Hening A. Relative effects of pulsed laser deposition parameters on the stoichiometry of thin films. Thin Solid Films. 2023;764:139603.
135. Lu F-F, Tian H-K. Dopant-induced modulation of lithium-ion conductivity in cubic garnet solid electrolytes: a first-principles study. Physical Chemistry Chemical Physics. 2023;25(28):18973-82.
136. Thompson T, Yu S, Williams L, Schmidt RD, Garcia-Mendez R, Wolfenstine J, et al. Electrochemical Window of the Li-Ion Solid Electrolyte Li7La3Zr2O12. ACS Energy Letters. 2017;2(2):462-8.
137. Mustaffa DT, Kamarulzaman N, Taib MFM, Rusdi R, Ibrahim AB. Theoretical investigations of Li+ and Co3+ positions for layered LiCoO2 Lithium ion battery cathode material using first principle method. AIP Conference Proceedings. 2017;1877(1):080005.
138. Menazea AA, Mostafa AM, Al-Ashkar EA. Impact of CuO doping on the properties of CdO thin films on the catalytic degradation by using pulsed-Laser deposition technique. Optical Materials. 2020;100:109663.
139. Jeong SH, Vu TKO, Kim EK. Post-annealing effects on Si-doped Ga_2O_3 photodetectors grown by pulsed laser deposition. Journal of Alloys and Compounds. 2021;877:160291.
140. Indrizzi L, Ohannessian N, Pergolesi D, Lippert T, Gilardi E. Pulsed Laser Deposition as a Tool for the Development of All Solid-State Microbatteries. Helvetica Chimica Acta. 2021;104(2):e2000203.
141. Dai W, Qiao Y, Ma Z, Wang T, Fu Z. All-solid-state thin-film batteries based on lithium phosphorus oxynitrides. Materials Futures. 2022;1(3):032101.
142. Li J, Lai W. Structure and ionic conduction study on Li_3PO_4 and LiPON (Lithium phosphorous oxynitride) with the Density-Functional Tight-Binding (DFTB) method. Solid State Ionics. 2020;351:115329.
143. Garbayo I, Struzik M, Bowman WJ, Pfenninger R, Stilp E, Rupp JLM. Glass-Type Polyamorphism in Li-Garnet Thin Film Solid State Battery Conductors. Advanced Energy Materials. 2018;8(12):1702265.
144. Wang Z, Luo C, Anwand W, Wagner A, Butterling M, Rahman MA, et al. Vacancy cluster in ZnO films grown by pulsed laser deposition. Scientific Reports. 2019;9(1):3534.

145. Su D, Yamada T, Gysel R, Tagantsev AK, Muralt P, Setter N, Jiang N. Growth-mode induced defects in epitaxial $SrTiO_3$ thin films grown on single crystal $LaAlO_3$ by a two-step PLD process. Journal of Materials Research. 2011;26(6):770-4.
146. Korte C, Peters A, Janek J, Hesse D, Zakharov N. Ionic conductivity and activation energy for oxygen ion transport in superlattices—the semicoherent multilayer system YSZ (ZrO_2 + 9.5 mol% Y_2O_3)/Y_2O_3. Physical Chemistry Chemical Physics. 2008;10(31):4623-35.
147. Nishio K. Crystal orientation of epitaxial LiCoO2 films grown on SrTiO3 substrates. Journal of Power Sources 2014;247:687 - 91.
148. Tsuruhama T. Preparation of Layered-Rhombohedral $LiCoO_2$ Epitaxial Thin Films Using Pulsed Laser Deposition. Appl Phys Express. 2009;2.
149. Sastre J. Lithium Garnet Li7La3Zr2O12 Electrolyte for All-Solid-State Batteries: Closing the Gap between Bulk and Thin Film Li-Ion Conductivities. Adv Mater Interfaces. 2020;7.
150. Julien C, Camacho-Lopez MA, Escobar-Alarcon L, Haro-Poniatowski E. Fabrication of $LiCoO_2$ thin-film cathodes for rechargeable lithium microbatteries. Materials Chemistry and Physics. 2001;68(1):210-6.
151. Huang R, Hitosugi T, Fisher CAJ, Ikuhara YH, Moriwake H, Oki H, Ikuhara Y. Phase transitions in $LiCoO_2$ thin films prepared by pulsed laser deposition. Materials Chemistry and Physics. 2012;133(2):1101-7.
152. Xia H, Lu L, Ceder G. Li diffusion in $LiCoO_2$ thin films prepared by pulsed laser deposition. Journal of Power Sources. 2006;159(2):1422-7.
153. Maiyalagan T, Jarvis KA, Therese S, Ferreira PJ, Manthiram A. Spinel-type lithium cobalt oxide as a bifunctional electrocatalyst for the oxygen evolution and oxygen reduction reactions. Nature Communications. 2014;5(1):3949.
154. Sastre J, Priebe A, Döbeli M, Michler J, Tiwari AN, Romanyuk YE. Lithium Garnet Li7La3Zr2O12 Electrolyte for All-Solid-State Batteries: Closing the Gap between Bulk and Thin Film Li-Ion Conductivities. Advanced Materials Interfaces. 2020;7(17):2000425.
155. Budida J, Srinivasan K. Review of thin film deposition and techniques. Materials Today: Proceedings. 2023;92:1030-3.
156. Lobe S, Dellen C, Finsterbusch M, Gehrke HG, Sebold D, Tsai CL, et al. Radio frequency magnetron sputtering of Li7La3Zr2O12 thin films for solid-state batteries. Journal of Power Sources. 2016;307:684-9.
157. Ohnishi T, Takada K. Sputter-Deposited Amorphous Li(3)PO(4) Solid Electrolyte Films. ACS Omega. 2022;7(24):21199-206.
158. Liang Q, Yan C-s, Meng Y, Lai J, Krasnicki S, Mao H-k, Hemley RJ. Recent advances in high-growth rate single-crystal CVD diamond. Diamond and Related Materials. 2009;18(5):698-703.
159. Benedek P, Wenzler N, Yarema M, Wood VC. Low temperature hydrothermal synthesis of battery grade lithium iron phosphate. RSC Advances. 2017;7(29):17763-7.
160. Lobe S, Bauer A, Uhlenbruck S, Fattakhova-Rohlfing D. Physical Vapor Deposition in Solid-State Battery Development: From Materials to Devices. Advanced Science. 2021;8(11):2002044.
161. Fingerle M, Buchheit R, Sicolo S, Albe K, Hausbrand R. Reaction and Space Charge Layer Formation at the $LiCoO_2$–LiPON Interface: Insights on Defect Formation and Ion Energy Level Alignment by a Combined Surface Science–Simulation Approach. Chemistry of Materials. 2017;29(18):7675-85.
162. Vardar G, Bowman WJ, Lu Q, Wang J, Chater RJ, Aguadero A, et al. Structure, Chemistry, and Charge Transfer Resistance of the Interface between $Li_7La_3Zr_2O_{12}$ Electrolyte and $LiCoO_2$ Cathode. Chemistry of Materials. 2018;30(18):6259-76.
163. Müller A, Okur F, Aribia A, Osenciat N, Vaz CAF, Siller V, et al. Benchmarking the performance of lithiated metal oxide interlayers at the $LiCoO_2$|LLZO interface. Materials Advances. 2023;4(9):2138-46.
164. Umeshbabu E, Zheng B, Yang Y. Recent Progress in All-Solid-State Lithium−Sulfur Batteries Using High Li-Ion Conductive Solid Electrolytes. Electrochemical Energy Reviews. 2019;2(2):199-230.

165. Sastre J, Chen X, Aribia A, Tiwari AN, Romanyuk YE. Fast Charge Transfer across the $Li_7La_3Zr_2O_{12}$ Solid Electrolyte/$LiCoO_2$ Cathode Interface Enabled by an Interphase-Engineered All-Thin-Film Architecture. ACS Applied Materials & Interfaces. 2020;12(32):36196-207.
166. Nowakowski P, Bonifacio CS, Campin MJ, Ray ML, Fischione PE. Accurate Removal of Implanted Gallium and Amorphous Damage from TEM Specimens after Focused Ion Beam (FIB) Preparation. Microscopy and Microanalysis. 2017;23(S1):300-1.
167. Sato T, Aizawa Y, Matsumoto H, Kiyohara M, Kamiya C, Von Cube F. Low damage lamella preparation of metallic materials by FIB processing with low acceleration voltage and a low incident angle Ar ion milling finish. Journal of Microscopy. 2020;279(3):234-41.
168. Wang Z, Santhanagopalan D, Zhang W, Wang F, Xin HL, He K, et al. In Situ STEM-EELS Observation of Nanoscale Interfacial Phenomena in All-Solid-State Batteries. Nano Letters. 2016;16(6):3760-7.
169. Zhou W, Pennycook SJ, Idrobo J-C. Localization of inelastic electron scattering in the low-loss energy regime. Ultramicroscopy. 2012;119:51-6.
170. Kim Y, Waluyo I, Hunt A, Yildiz B. Avoiding CO_2 Improves Thermal Stability at the Interface of $Li_7La_3Zr_2O_{12}$ Electrolyte with Layered Oxide Cathodes. Advanced Energy Materials. 2022;12(13):2102741.
171. Park N-Y, Ryu H-H, Park G-T, Noh T-C, Sun Y-K. Optimized Ni-Rich NCMA Cathode for Electric Vehicle Batteries. Advanced Energy Materials. 2021;11(9):2003767.
172. Sakuda A, Hayashi A, Tatsumisago M. Sulfide Solid Electrolyte with Favorable Mechanical Property for All-Solid-State Lithium Battery. Scientific Reports. 2013;3(1):2261.
173. Lozano JG, Martinez GT, Jin L, Nellist PD, Bruce PG. Low-Dose Aberration-Free Imaging of Li-Rich Cathode Materials at Various States of Charge Using Electron Ptychography. Nano Letters. 2018;18(11):6850-5.
174. Takeuchi S, Tan H, Bharathi KK, Stafford GR, Shin J, Yasui S, et al. Epitaxial $LiCoO_2$ Films as a Model System for Fundamental Electrochemical Studies of Positive Electrodes. ACS Applied Materials & Interfaces. 2015;7(15):7901-11.
175. Klie RF, Arslan I, Browning ND. Atomic resolution electron energy-loss spectroscopy. Journal of Electron Spectroscopy and Related Phenomena. 2005;143(2):105-15.
176. Frati F, Hunault MOJY, de Groot FMF. Oxygen K-edge X-ray Absorption Spectra. Chemical Reviews. 2020;120(9):4056-110.
177. Yoon W-S, Kim K-B, Kim M-G, Lee M-K, Shin H-J, Lee J-M, et al. Oxygen Contribution on Li-Ion Intercalation−Deintercalation in $LiCoO_2$ Investigated by O K-Edge and Co L-Edge X-ray Absorption Spectroscopy. The Journal of Physical Chemistry B. 2002;106(10):2526-32.
178. Huang C-Y, Tseng Y-T, Lo H-Y, Chang J-K, Wu W-W. In situ atomic scale investigation of $Li_7La_3Zr_2O_{12}$-based Li^+-conducting solid electrolyte during calcination growth. Nano Energy. 2020;71:104625.
179. Weller JM, Chan CK. Reduction in Formation Temperature of Ta-Doped Lithium Lanthanum Zirconate by Application of Lux–Flood Basic Molten Salt Synthesis. ACS Applied Energy Materials. 2020;3(7):6466-75.
180. Avanesian T. Quantitative and Atomic-Scale View of CO-Induced Pt Nanoparticle Surface Reconstruction at Saturation Coverage via DFT Calculations Coupled with in Situ TEM and IR. Journal of The American Chemical Society. 2017;139:4551 − 8.
181. Evans JE. Visualizing macromolecular complexes with in situ liquid scanning transmission electron microscopy. Micron. 2012;43:1085 – 90.
182. Figg CA. Polymerization-induced thermal self-assembly (PITSA). Chem Sci. 2015;6:1230–6.
183. Mirsaidov UM. Imaging Protein Structure in Water at 2.7 nm Resolution by Transmission Electron Microscopy. Biophysical Journal. 2012;102:15 - 7.
184. Vara M. Understanding the Thermal Stability of Palladium−Platinum Core−Shell Nanocrystals by In Situ Transmission Electron Microscopy and Density Functional Theory. ACS Nano. 2017;11:4571 − 81.
185. Gregorczyk KE. In Situ Transmission Electron Microscopy Study of Electrochemical Lithiation and Delithiation Cycling of the Conversion Anode RuO_2. ACS Nano. 2013;7(7).

186. Hansen PL. Atom-Resolved Imaging of Dynamic Shape Changes in Supported Copper Nanocrystals Science. 2002;295:2053 - 5.
187. Browning ND. Recent developments in dynamic transmission electron microscopy. Current Opinion in Solid State and Materials Science. 2012;16:23 - 30.
188. LaGrange T. Nanosecond time-resolved investigations using the in situ of dynamic transmission electron microscope (DTEM). Ultramicroscopy. 2008;108:1441 – 9.
189. Taheri ML. In Situ Laser Synthesis of Si Nanowires in the Dynamic TEM. Nono Micro Small. 2008;4(12):2187 - 90.
190. Buban JP, Ramasse Q, Gipson B, Browning ND, Stahlberg H. High-resolution low-dose scanning transmission electron microscopy. J Electron Microsc (Tokyo). 2010;59(2):103-12.
191. Lv J, Zhang H, Zhang D, Liu L, Han Y. Low-Dose Electron Microscopy Imaging of Electron Beam-Sensitive Crystalline Materials. Accounts of Materials Research. 2022;3(5):552-64.
192. Egerton RF. Radiation damage in the TEM and SEM. Micron. 2004;35:399 - 409.
193. Egerton RF. Control of radiation damage in the TEM. Ultramicroscopy. 2013;127:100 - 8.
194. Lin F. Chemical and Structural Stability of Lithium-Ion Battery Electrode Materials under Electron Beam. Scientific Reports. 2014;4.
195. EGERTON RF. Mechanisms of Radiation Damage in Beam-Sensitive Specimens, for TEM Accelerating Voltages Between 10 and 300 kV. Microscopy Research and technique. 2012;75:1550 - 6.
196. DENSsolutions. In Situ TEM Biasing & Heating https://denssolutions.com/products/lightning/2019 [
197. Sarkar S, Hoffmann JA, Park J. Micro-macroscopic modeling of a lithium-ion battery by considering grain boundaries of active materials. Electrochimica Acta. 2021;393:139052.
198. Yoon SA, Oh NR, Yoo AR, Lee HG, Lee HC. Preparation and Characterization of Ta-substituted $Li_7La_3Zr_{2-x}O_{12}$ Garnet Solid Electrolyte by Sol-Gel Processing. J Korean Ceram Soc. 2017;54(4):278-84.
199. Mercer D. What Is a Source Measurement Unit or SMU? : Analog Devices; 2017 [Available from: https://www.analog.com/en/resources/analog-dialogue/studentzone/studentzone-december-2017.html.
200. Steve R, Robert P. A review of focused ion beam applications in microsystem technology. Journal of Micromechanics and Microengineering. 2001;11(4):287.
201. Giannuzzi LA, Stevie FA. A review of focused ion beam milling techniques for TEM specimen preparation. Micron. 1999;30(3):197-204.
202. Lee JZ, Wynn TA, Schroeder MA, Alvarado J, Wang X, Xu K, Meng YS. Cryogenic Focused Ion Beam Characterization of Lithium Metal Anodes. ACS Energy Letters. 2019;4(2):489-93.
203. Langford RM. Focused ion beams techniques for nanomaterials characterization. Microscopy Research and Technique. 2006;69(7):538-49.
204. Russo MF, Maazouz M, Giannuzzi LA, Chandler C, Utlaut M, Garrison BJ. Trench formation and lateral damage induced by gallium milling of silicon. Applied Surface Science. 2008;255(4):828-30.
205. Li J, Malis T, Dionne S. Recent advances in FIB–TEM specimen preparation techniques. Materials Characterization. 2006;57(1):64-70.
206. Schaffer M, Schaffer B, Ramasse Q. Sample preparation for atomic-resolution STEM at low voltages by FIB. Ultramicroscopy. 2012;114:62-71.
207. Ampere AT, Ivan AI, Jong-Seung P, Chii DC. Milling yield estimation in focused ion beam milling of two-layer substrates. Journal of Micromechanics and Microengineering. 2005;15(1):20.
208. Burnett TL, Kelley R, Winiarski B, Contreras L, Daly M, Gholinia A, et al. Large volume serial section tomography by Xe Plasma FIB dual beam microscopy. Ultramicroscopy. 2016;161:119-29.
209. Hong-Wei L, Dae-Joon K, Blamire MG, Wilhelm TSH. Focused ion beam fabrication of silicon print masters. Nanotechnology. 2003;14(2):220.
210. Erdman N, Campbell R, Asahina S. Precise SEM Cross Section Polishing via Argon Beam Milling. Microscopy Today. 2006;14(3):22-5.
211. Stegmann H, Ritz Y, Utess D, Hübner R, Zschech E. Enhanced TEM Sample Preparation Using In-situ Low Energy Argon Ion Milling. AIP Conference Proceedings. 2009;1173(1):275-9.

212. Lotnyk A, Poppitz D, Ross U, Gerlach JW, Frost F, Bernütz S, et al. Focused high- and low-energy ion milling for TEM specimen preparation. Microelectronics Reliability. 2015;55(9):2119-25.
213. Legras L, Lescoat ML, Jublot-Leclerc S, Gentils A. Optimisation of TEM preparation in metallic materials using low voltage ions. European Microscopy Congress 2016: Proceedings. p. 443-4.
214. Heintzmann R, Ficz G. Breaking the resolution limit in light microscopy. Briefings in Functional Genomics. 2006;5(4):289-301.
215. Spencer M, Spencer M, Michael Spencer F. Fundamentals of light microscopy: CUP Archive; 1982.
216. Carter CB, Williams DB. Transmission electron microscopy: Diffraction, imaging, and spectrometry: Springer; 2016.
217. Egerton RF. Physical principles of electron microscopy: Springer; 2005.
218. Iqbal M, Elahi F, Rehman A, Wasy Zia A, Islam Gu, Zusheng Z. Design and beam dynamics of a Transmission Electron Microscope electron gun assembly. Vacuum. 2019;165:283-9.
219. OZAKI K, UCHIKAWA Y, MARUSE S. Dependence of Brightness Characteristics upon Point Cathode Electron Gun Geometries. Journal of Electron Microscopy. 1982;31(2):137-43.
220. Joy DC. The theory and practice of high-resolution scanning electron microscopy. Ultramicroscopy. 1991;37(1):216-33.
221. Latreche A. Combined thermionic emission and tunneling mechanisms for the analysis of the leakage current for Ga_2O_3 Schottky barrier diodes. SN Applied Sciences. 2019;1(2):188.
222. Henning S, Adhikari R. Chapter 1 - Scanning Electron Microscopy, ESEM, and X-ray Microanalysis. In: Thomas S, Thomas R, Zachariah AK, Mishra RK, editors. Microscopy Methods in Nanomaterials Characterization: Elsevier; 2017. p. 1-30.
223. Ross IM, Walther T. Configuring a 300kV cold field-emission gun for optimum analytical performance. Journal of Physics: Conference Series. 2012;371(1):012012.
224. Schwind GA, Magera G, Swanson LW. Comparison of parameters for Schottky and cold field emission sources. Journal of Vacuum Science & Technology B: Microelectronics and Nanometer Structures. 2006;24(6):2897.
225. Williams DB, Carter CB. Transmission Electron Microscopy: A Textbook for Materials Science: Springer; 2009.
226. Edwards TEJ, Di Gioacchino F, Clegg WJ. High resolution digital image correlation mapping of strain localization upon room and high temperature, high cycle fatigue of a TiAl intermetallic alloy. International Journal of Fatigue. 2021;142:105905.
227. Wang M, Li Z, Raabe D. In-situ SEM observation of phase transformation and twinning mechanisms in an interstitial high-entropy alloy. Acta Materialia. 2018;147:236-46.
228. Honold T, Volk K, Retsch M, Karg M. Binary plasmonic honeycomb structures: High-resolution EDX mapping and optical properties. Colloids and Surfaces A: Physicochemical and Engineering Aspects. 2016;510:198-204.
229. Chen D, Kuo J-C, Wu W-T. Effect of microscopic parameters on EBSD spatial resolution. Ultramicroscopy. 2011;111(9):1488-94.
230. Marassi R, Nobili F. Measurement Methods | Structural and Chemical Properties: Scanning Electron Microscopy. In: Garche J, editor. Encyclopedia of Electrochemical Power Sources. Amsterdam: Elsevier; 2009. p. 758-68.
231. Lloyd GE. Atomic number and crystallographic contrast images with the SEM: a review of backscattered electron techniques. Mineralogical Magazine. 1987;51(359):3-19.
232. Assa'd A, El Gomati M. Backscattering coefficients for low energy electrons. Scanning Microscopy. 1998;12(1):185-92.
233. Tian J, Wu J, Chiu Y-L. Monte Carlo simulation and theoretical calculation of SEM image intensity and its application in thickness measurement. Ultramicroscopy. 2018;187:13-9.
234. Joy DC. Beam interactions, contrast and resolution in the SEM. Journal of Microscopy. 1984;136(2):241-58.
235. Erdman N, Bell DC, Reichelt R. Scanning Electron Microscopy. In: Hawkes PW, Spence JCH, editors. Springer Handbook of Microscopy. Cham: Springer International Publishing; 2019. p. 229-318.

236. Griffin BJ. A comparison of conventional Everhart-Thornley style and in-lens secondary electron detectors—a further variable in scanning electron microscopy. Scanning. 2011;33(3):162-73.
237. Eggert F, Rafaelsen J, Reinauer F, Camus P, Gernert U. The Detector Efficiency Question with EDS. Microscopy and Microanalysis. 2021;27(S1):1674-6.
238. Agemura T, Sekiguchi T. Collection efficiency and acceptance maps of electron detectors for understanding signal detection on modern scanning electron microscopy. Microscopy. 2018;67(1):18-29.
239. Lechner P, Fiorini C, Hartmann R, Kemmer J, Krause N, Leutenegger P, et al. Silicon drift detectors for high count rate X-ray spectroscopy at room temperature. Nuclear Instruments and Methods in Physics Research Section A: Accelerators, Spectrometers, Detectors and Associated Equipment. 2001;458(1):281-7.
240. Xu W, Dycus JH, Sang X, LeBeau JM. A numerical model for multiple detector energy dispersive X-ray spectroscopy in the transmission electron microscope. Ultramicroscopy. 2016;164:51-61.
241. Zaefferer S. On the formation mechanisms, spatial resolution and intensity of backscatter Kikuchi patterns. Ultramicroscopy. 2007;107(2-3):254-66.
242. Winkelmann A, Cios G, Tokarski T, Nolze G, Hielscher R, Kozieł T. EBSD orientation analysis based on experimental Kikuchi reference patterns. Acta Materialia. 2020;188:376-85.
243. Erni R, Rossell MD, Kisielowski C, Dahmen U. Atomic-Resolution Imaging with a Sub-50-pm Electron Probe. Physical Review Letters. 2009;102(9):096101.
244. Li S, Chang Y, Wang Y, Xu Q, Ge B. A review of sample thickness effects on high-resolution transmission electron microscopy imaging. Micron. 2020;130:102813.
245. Rose HH. Optics of high-performance electron microscopes. Sci Technol Adv Mater. 2008;9(1):014107.
246. Ahn CC, Krivanek OL, Gatan I, Arizona State University High Resolution Electron Microscopy F. EELS atlas : a reference collection of electron energy loss spectra covering all stable elements. Warrendale, Pa.: Gatan, Inc. Warrendale, Pa.; 1983.
247. Haberfehlner G. 3D nanoimaging of semiconductor devices and materials by electron tomography. 2013.
248. Taylor M. ePSIC Instruments https://diamondlightsource.atlassian.net/wiki/spaces/EPSICWEB/pages/1511758/ePSIC+Instruments: Diamond Light Source; 2020 [
249. Schumacher P, McKay BJ. TEM investigation of heterogeneous nucleation mechanisms in Al–Si alloys. Journal of Non-Crystalline Solids. 2003;317(1):123-8.
250. Bals S, Kabius B, Haider M, Radmilovic V, Kisielowski C. Annular dark field imaging in a TEM. Solid State Communications. 2004;130(10):675-80.
251. Wu G, Zaefferer S. Advances in TEM orientation microscopy by combination of dark-field conical scanning and improved image matching. Ultramicroscopy. 2009;109(11):1317-25.
252. Wang ZL. Dislocation contrast in high-angle hollow-cone dark-field TEM. Ultramicroscopy. 1994;53(1):73-90.
253. An J, Voelkl E, Suk JW, Li X, Magnuson CW, Fu L, et al. Domain (Grain) Boundaries and Evidence of “Twinlike” Structures in Chemically Vapor Deposited Grown Graphene. ACS Nano. 2011;5(4):2433-9.
254. Sannomiya T, Sawada H, Nakamichi T, Hosokawa F, Nakamura Y, Tanishiro Y, Takayanagi K. Determination of aberration center of Ronchigram for automated aberration correctors in scanning transmission electron microscopy. Ultramicroscopy. 2013;135:71-9.
255. Ooe K, Seki T, Ikuhara Y, Shibata N. High contrast STEM imaging for light elements by an annular segmented detector. Ultramicroscopy. 2019;202:148-55.
256. Okunishi E, Sawada H, Kondo Y. Experimental study of annular bright field (ABF) imaging using aberration-corrected scanning transmission electron microscopy (STEM). Micron. 2012;43(4):538-44.
257. Jones L. Quantitative ADF STEM: acquisition, analysis and interpretation. IOP Conference Series: Materials Science and Engineering. 2016;109(1):012008.

258. Findlay SD, Shibata N, Sawada H, Okunishi E, Kondo Y, Ikuhara Y. Dynamics of annular bright field imaging in scanning transmission electron microscopy. Ultramicroscopy. 2010;110(7):903-23.
259. Bin F, Gao P, Ikuhara Y, Ishikawa R, Shibata N. Better Contrast for Imaging Defects by ABF. Microscopy and Microanalysis. 2017;23(S1):480-1.
260. Oshima Y, Sawada H, Hosokawa F, Okunishi E, Kaneyama T, Kondo Y, et al. Direct imaging of lithium atoms in LiV_2O_4 by spherical aberration-corrected electron microscopy. Journal of Electron Microscopy. 2010;59(6):457-61.
261. Yamashita S, Kikkawa J, Yanagisawa K, Nagai T, Ishizuka K, Kimoto K. Atomic number dependence of Z contrast in scanning transmission electron microscopy. Scientific Reports. 2018;8(1):12325.
262. Jones L, Wenner S, Nord M, Ninive PH, Løvvik OM, Holmestad R, Nellist PD. Optimising multi-frame ADF-STEM for high-precision atomic-resolution strain mapping. Ultramicroscopy. 2017;179:57-62.
263. Source DL. ePSIC Documentation https://diamondlightsource.atlassian.net/wiki/spaces/EPSICWEB/overview: Diamond Light Source; 2023 [
264. Su Z, Ding J, Song M, Jiang L, Shi T, Li Z, et al. Enhancing the radiation tolerance of high-entropy alloys via solute-promoted chemical heterogeneities. Acta Materialia. 2023;245:118662.
265. Titus MS, Mottura A, Babu Viswanathan G, Suzuki A, Mills MJ, Pollock TM. High resolution energy dispersive spectroscopy mapping of planar defects in $L1_2$-containing Co-base superalloys. Acta Materialia. 2015;89:423-37.
266. Zhang D, Zhu Y, Liu L, Ying X, Hsiung C-E, Sougrat R, et al. Atomic-resolution transmission electron microscopy of electron beam-sensitive crystalline materials. Science. 2018;359(6376):675-9.
267. Maaz K. The Transmission Electron Microscope: IntechOpen; 2012.
268. Lee Z, Rose H, Lehtinen O, Biskupek J, Kaiser U. Electron dose dependence of signal-to-noise ratio, atom contrast and resolution in transmission electron microscope images. Ultramicroscopy. 2014;145:3-12.
269. Longo P. Fast STEM spectrum imaging using simultaneous EELS and EDS in Gatan Microscopy Suite software https://www.gatan.com/fast-stem-spectrum-imaging-using-simultaneous-eels-and-eds-gatan-microscopy-suite-software#:~:text=The%20EELS%20spectrum%20image%20(SI,ms%20and%2030%20ms%2C%20respectively: GATAN; 2023 [
270. Bosman M, Keast VJ. Optimizing EELS acquisition. Ultramicroscopy. 2008;108(9):837-46.
271. Longo P, Twesten RD. Fast STEM Spectrum Imaging Using Simultaneous EELS and EDS. Microscopy Today. 2013;21(1):28-33.
272. Hovington P, Timoshevskii V, Burgess S, Demers H, Statham P, Gauvin R, Zaghib K. Can we detect Li K X-ray in lithium compounds using energy dispersive spectroscopy? Scanning. 2016;38(6):571-8.
273. Egerton RF. Electron energy-loss spectroscopy in the TEM. Reports on Progress in Physics. 2009;72(1):016502.
274. Hofer F, Schmidt FP, Grogger W, Kothleitner G. Fundamentals of electron energy-loss spectroscopy. IOP Conference Series: Materials Science and Engineering. 2016;109(1):012007.
275. Malis T, Cheng SC, Egerton RF. EELS log-ratio technique for specimen-thickness measurement in the TEM. Journal of Electron Microscopy Technique. 1988;8(2):193-200.
276. Scott J, Thomas PJ, MacKenzie M, McFadzean S, Wilbrink J, Craven AJ, Nicholson WAP. Near-simultaneous dual energy range EELS spectrum imaging. Ultramicroscopy. 2008;108(12):1586-94.
277. Leapman RD, Rez P, Mayers DF. K, L, and M shell generalized oscillator strengths and ionization cross sections for fast electron collisions. The Journal of Chemical Physics. 2008;72(2):1232-43.
278. Verbeeck J, Van Aert S. Model based quantification of EELS spectra. Ultramicroscopy. 2004;101(2):207-24.

279. Wu M, Harreiß C, Ophus C, Johnson M, Fink RH, Spiecker E. Seeing the Structure and Structural Evolution of Nano-crystallites in Soft Materials Using 4D Scanning Confocal Electron Diffraction. Microscopy and Microanalysis. 2022;28(S1):464-6.
280. McAuliffe T, Ackerman A, Savitzky B, Kwok T, Danaie M, Ophus C, Dye D. 4D-STEM elastic stress state characterisation of a TWIP steel nanotwin. arXiv preprint arXiv:200403982. 2020.
281. Momma K. VESTA 3 for three-dimensional visualization of crystal, volumetric and morphology data. J Appl Crystallogr. 2011;44:1272-6.
282. Ishizuka K. A practical approach for STEM image simulation based on the FFT multislice method. Ultramicroscopy. 2002;90(2):71-83.
283. Kovachev G, Ellersdorfer C, Gstrein G, Hanzu I, Wilkening M, Werling T, et al. Safety assessment of electrically cycled cells at high temperatures under mechanical crush loads. eTransportation. 2020;Volume 6.
284. Kovachev G, Schröttner, Gstrein G, Aiello L, Hanzu, Wilkening M, et al. Analytical Dissection of an Automotive Li-Ion Pouch Cell. Batteries. 2019;5:67.
285. USA J. Achieving Pristine Cross Sections Of Battery Samples For Scanning Electron Microscopy: JEOL USA, Inc.; 2022 [Available from: https://www.jeolusa.com/NEWS-EVENTS/Blog/pristine-cross-sections-of-batteries.
286. Tatara R, Karayaylali P, Yu Y, Zhang Y, Giordano L, Maglia F, et al. The Effect of Electrode-Electrolyte Interface on the Electrochemical Impedance Spectra for Positive Electrode in Li-Ion Battery. Journal of The Electrochemical Society. 2019;166(3):A5090.
287. Miyakawa S, Matsuda S, Tanibata N, Takeda H, Nakayama M, Saito T, Fukuchi S. Computational studies on defect chemistry and Li-ion conductivity of spinel-type $LiAl_5O_8$ as coating material for Li-metal electrode. Scientific Reports. 2022;12(1):16672.
288. Gregori G, Merkle R, Maier J. Ion conduction and redistribution at grain boundaries in oxide systems. Progress in Materials Science. 2017;89:252-305.
289. Zou F, Manthiram A. A Review of the Design of Advanced Binders for High-Performance Batteries. Advanced Energy Materials. 2020;10(45):2002508.
290. Liang Q, Yue H, Zhou W, Wei Q, Ru Q, Huang Y, et al. Structure Recovery and Recycling of Used $LiCoO_2$ Cathode Material. Chemistry – A European Journal. 2021;27(57):14225-33.
291. Cheng EJ, Kimura T, Shoji M, Ueda H, Munakata H, Kanamura K. Ceramic-Based Flexible Sheet Electrolyte for Li Batteries. ACS Applied Materials & Interfaces. 2020;12(9):10382-8.
292. Li L, Deng Y, Chen G. Status and prospect of garnet/polymer solid composite electrolytes for all-solid-state lithium batteries. Journal of Energy Chemistry. 2020;50:154-77.
293. Lu W, Xue M, Zhang C. Modified $Li_7La_3Zr_2O_{12}$ (LLZO) and LLZO-polymer composites for solid-state lithium batteries. Energy Storage Materials. 2021;39:108-29.
294. Delluva AA, Kulberg-Savercool J, Holewinski A. Decomposition of Trace Li_2CO_3 During Charging Leads to Cathode Interface Degradation with the Solid Electrolyte LLZO. Advanced Functional Materials. 2021;31(34):2103716.
295. Cheng L, Liu M, Mehta A, Xin H, Lin F, Persson K, et al. Garnet Electrolyte Surface Degradation and Recovery. ACS Applied Energy Materials. 2018;1(12):7244-52.
296. Leenheer AJ, Jungjohann KL, Zavadil KR, Sullivan JP, Harris CT. Lithium Electrodeposition Dynamics in Aprotic Electrolyte Observed in Situ via Transmission Electron Microscopy. ACS Nano. 2015;9(4):4379-89.
297. Tang S, Chen G, Ren F, Wang H, Yang W, Zheng C, et al. Modifying an ultrathin insulating layer to suppress lithium dendrite formation within garnet solid electrolytes. Journal of Materials Chemistry A. 2021;9(6):3576-83.
298. Øygarden V, Lein HL, Grande T. Structure, thermal expansion and electrical conductivity of Nb-substituted $LaCoO_3$. Journal of Solid State Chemistry. 2012;192:246-54.
299. Dong B, Yeandel SR, Goddard P, Slater PR. Combined Experimental and Computational Study of Ce-Doped $La_3Zr_2Li_7O_{12}$ Garnet Solid-State Electrolyte. Chemistry of Materials. 2020;32(1):215-23.
300. Garcia B, Barboux P, Ribot F, Kahn-Harari A, Mazerolles L, Baffier N. The structure of low temperature crystallized $LiCoO_2$. Solid State Ionics. 1995;80(1):111-8.

301. Bhowmik RN, Kumar A, Sinha AK, Yusuf SM. Probing low temperature non-equilibrium magnetic state in $Co_{2.75}Fe_{0.25}O_{4+\delta}$ spinel oxide using dc magnetization, ac susceptibility and neutron diffraction experiments. Journal of Alloys and Compounds. 2020;849:156614.
302. Paul B, Singh K, Jaroń T, Roy A, Chowdhury A. Structural properties and the fluorite–pyrochlore phase transition in $La_2Zr_2O_7$: The role of oxygen to induce local disordered states. Journal of Alloys and Compounds. 2016;686:130-6.
303. Wang A, Kadam S, Li H, Shi S, Qi Y. Review on modeling of the anode solid electrolyte interphase (SEI) for lithium-ion batteries. npj Computational Materials. 2018;4(1):15.
304. Adenusi H, Chass GA, Passerini S, Tian KV, Chen G. Lithium Batteries and the Solid Electrolyte Interphase (SEI)—Progress and Outlook. Advanced Energy Materials. 2023;13(10):2203307.
305. Sastre J. Fast Charge Transfer across the $Li_7La_3Zr_2O_{12}$ Solid Electrolyte/$LiCoO_2$ Cathode Interface Enabled by an Interphase-Engineered All-Thin-Film Architecture. ACS Appl Mater Interfaces. 2020;12:36196 − 207.
306. Ren Y, Liu T, Shen Y, Lin Y, Nan C-W. Chemical compatibility between garnet-like solid state electrolyte $Li_{6.75}La_3Zr_{1.75}Ta_{0.25}O_{12}$ and major commercial lithium battery cathode materials. Journal of Materiomics. 2016;2(3):256-64.
307. Miekk-Oja HM, Lindroos VK. The formation of dislocation networks. Surface Science. 1972;31:422-55.
308. Spotte-Smith EWC, Kam RL, Barter D, Xie X, Hou T, Dwaraknath S, et al. Toward a Mechanistic Model of Solid–Electrolyte Interphase Formation and Evolution in Lithium-Ion Batteries. ACS Energy Letters. 2022;7(4):1446-53.
309. Tong Y, Zhu J, Lu L, Wang X, Yang X. Preparation and characterization of Ln2Zr2O7 (Ln=La and Nd) nanocrystals and their photocatalytic properties. Journal of Alloys and Compounds. 2008;465(1):280-4.
310. Hirsch PB, Howie A, Nicholson R, Pashley DW, Whelan MJ, Marton LL. Electron Microscopy of Thin Crystals. Nature. 1977;197:438-.
311. Zhang H, Zhang J, Yang H, Lan Q, Hong D, Wang S, et al. Structural and Magnetic Properties of $LaCoO_3$/$SrTiO_3$ Multilayers. ACS Applied Materials & Interfaces. 2016;8(28):18328-33.
312. Chen J, Wang P-F, Kang Y, Zhang Y-H, Yang D-X, Shi F-N. Co_3O_4/$LaCoO_3$ nanocomposites derived from MOFs as anodes for high-performance lithium-ion batteries. Inorganic Chemistry Communications. 2022;140:109447.
313. Mu J, Zhang L, He R, Li X, Bai X, Tian L, et al. Enhancing the electrochemical performance of $LiNi_{0.5}Mn_{1.5}O_4$ cathode material by a conductive $LaCoO_3$ coating. Journal of Alloys and Compounds. 2021;865:158629.
314. Shim J-H, Kang H, Kim Y-M, Lee S. In Situ Observation of the Effect of Accelerating Voltage on Electron Beam Damage of Layered Cathode Materials for Lithium-Ion Batteries. ACS Applied Materials & Interfaces. 2019;11(47):44293-9.
315. du Baret de Limé A, Lein T, Maletti S, Schmal K, Reuber S, Heubner C, Michaelis A. Impact of Electrode Defects on Battery Cell Performance: A Review. Batteries & Supercaps. 2022;5(10):e202200239.
316. Maruyama S. Combinatorial Synthesis of Epitaxial $LiCoO_2$ Thin Films on $SrTiO_3$(001) via On-Substrate Sintering of Li_2CO_3 and CoO by Pulsed Laser Deposition. ACS Comb Sci. 2016;18:343−8.
317. Nishio K. Crystal orientation of epitaxial LiCoO2 films grown on SrTiO3 substrates. Journal of Power Sources. 2014;247:687-91.
318. Ding Z, Tang Y, Chakravadhanula VSK, Ma Q, Tietz F, Dai Y, et al. Exploring the influence of focused ion beam processing and scanning electron microscopy imaging on solid-state electrolytes. Microscopy. 2022.
319. Cannarella J, Arnold CB. The Effects of Defects on Localized Plating in Lithium-Ion Batteries. Journal of The Electrochemical Society. 2015;162(7):A1365.
320. Moriwake H, Kuwabara A, Fisher CAJ, Huang R, Hitosugi T, Ikuhara YH, et al. First-Principles Calculations of Lithium-Ion Migration at a Coherent Grain Boundary in a Cathode Material, $LiCoO_2$. Advanced Materials. 2013;25(4):618-22.

321. Bouwman PJ, Boukamp BA, Bouwmeester HJM, Notten PHL. Structure-related intercalation behaviour of $LiCoO_2$ films. Solid State Ionics. 2002;152-153:181-8.
322. Reimers JN, Dahn JR. Electrochemical and In Situ X-Ray Diffraction Studies of Lithium Intercalation in Lix CoO_2. Journal of The Electrochemical Society. 1992;139(8):2091.
323. Liu W-W, Lau W-M, Zhang Y. The electrochemical properties of Co_3O_4 as a lithium-ion battery electrode: a first-principles study. Physical Chemistry Chemical Physics. 2018;20(38):25016-22.
324. Khandaker MR, Maruyama Y, Nagao M, Watauchi S, Munakata H, Kanamura K, Tanaka I. TSFZ Growth and Anisotropic Ionic Conductivity of Zr-Doped $LiCoO_2$ Single Crystals. Crystal Growth & Design. 2022;22(9):5624-8.
325. Porthault H. Raman study of the spinel-to-layered phase transformation in sol–gel LiCoO2 cathode powders as a function of the post-annealing temperature. Vibrational Spectroscopy. 2012;62:152– 8.
326. Awaka J. Synthesis and structure analysis of tetragonal $Li_7La_3Zr_2O_{12}$ with the garnet-related type structure. Journal of Solid State Chemistry. 2009;182:2046–52.
327. Jalem R, Rushton MJD, Manalastas W, Jr., Nakayama M, Kasuga T, Kilner JA, Grimes RW. Effects of Gallium Doping in Garnet-Type $Li_7La_3Zr_2O_{12}$ Solid Electrolytes. Chemistry of Materials. 2015;27(8):2821-31.
328. Loho C, Djenadic R, Bruns M, Clemens O, Hahn H. Garnet-Type $Li_7La_3Zr_2O_{12}$ Solid Electrolyte Thin Films Grown by CO_2-Laser Assisted CVD for All-Solid-State Batteries. Journal of The Electrochemical Society. 2017;164(1):A6131.
329. Saccoccio M, Yu J, Lu Z, Kwok SCT, Wang J, Yeung KK, et al. Low temperature pulsed laser deposition of garnet $Li_{6.4}La_3Zr_{1.4}Ta_{0.6}O_{12}$ films as all solid-state lithium battery electrolytes. Journal of Power Sources. 2017;365:43-52.
330. Kalita DJ, Lee SH, Lee KS, Ko DH, Yoon YS. Ionic conductivity properties of amorphous Li–La–Zr–O solid electrolyte for thin film batteries. Solid State Ionics. 2012;229:14-9.
331. Meda US, Lal L, M S, Garg P. Solid Electrolyte Interphase (SEI), a boon or a bane for lithium batteries: A review on the recent advances. Journal of Energy Storage. 2022;47:103564.
332. Li Y, Leung K, Qi Y. Computational Exploration of the Li-Electrode/Electrolyte Interface in the Presence of a Nanometer Thick Solid-Electrolyte Interphase Layer. Accounts of Chemical Research. 2016;49(10):2363-70.
333. Abakumov AM, Li C, Boev A, Aksyonov DA, Savina AA, Abakumova TA, et al. Grain Boundaries as a Diffusion-Limiting Factor in Lithium-Rich NMC Cathodes for High-Energy Lithium-Ion Batteries. ACS Applied Energy Materials. 2021;4(7):6777-86.
334. Ma S, Jiang M, Tao P, Song C, Wu J, Wang J, et al. Temperature effect and thermal impact in lithium-ion batteries: A review. Progress in Natural Science: Materials International. 2018;28(6):653-66.